National Technical University of Athens

School of Mechanical Engineering

Thermal Engineering Section

Laboratory of Steam Boilers and Thermal Plants

PhD Thesis

EXPERIMENTAL AND MODELING INVESTIGATION OF CLEANING TECHNOLOGIES FOR CARBON DIOXIDE, TAR AND SULFUR COMPOUNDS CONTAINED IN GASIFICATION PRODUCT GASES

Dimitrios T. Grimekis

Dipl. Mechanical Engineer NTUA

Supervisor: Prof. Sotirios Karellas

Athens, 2019

Επιβλέπων Καθηγητής

Δρ. Σ. Καρέλλας
Καθηγητής ΕΜΠ

Τριμελής Συμβουλευτική Επιτροπή

Δρ. Κ. Πανόπουλος
Ερευνητής Β', ΕΚΕΤΑ

Δρ. Ε. Κακαράς
Καθηγητής ΕΜΠ

Δρ. Σ. Καρέλλας
Καθηγητής ΕΜΠ

Επταμελής Εξεταστική Επιτροπή

Δρ. Σωτήριος Καρέλλας	Καθηγητής ΕΜΠ
Δρ. Εμμανουήλ Κακαράς	Καθηγητής ΕΜΠ
Δρ. Αθανάσιος Κωνσταντόπουλος	Καθηγητής ΑΠΘ
Δρ. Χρήστος Αργυρούσης	Καθηγητής ΕΜΠ
Δρ. Jürgen Karl	Καθηγητής FAU
Δρ. Αθανάσιος Στούμπος	Ερευνητής Α', ΕΚΕΦΕ «ΔΗΜΟΚΡΙΤΟΣ»
Δρ. Κυριάκος Πανόπουλος	Ερευνητής Β', ΕΚΕΤΑ

Στην οικογένειά μου

Acknowledgements

I would like to thank Professor Sotirios Karellas for offering me the opportunity to pursue a PhD thesis in the Laboratory of Steam Boilers and Thermal Plants of the National Technical University of Athens, for his invaluable support and for the great collaboration we had these years.

I would also like to express my gratitude to Dr. Kyriakos Panopoulos from CERTH for supporting this research and for providing technical expertise on aspects related to gasification and syngas cleaning.

A significant part of the work presented in this dissertation has been funded through the EU research projects CO2freeSNG2.0 (EC Grant Agreement No. RFCR-CT-2013-00008) and BRISK (EC-FP7, Grant agreement No. 284498). I would like to thank Professor Jürgen Karl, Michael Neubert and Peter Treiber from FAU (Germany) for all technical discussions and fruitful collaboration during the CO2freeSNG2.0 project. In addition, I would like to thank all institute staff members that provided facilities, expertise and personal effort during the gasification and sorbent tests in the framework of the BRISK project. From CIUDEN (Spain), I would like to thank Miguel Angel Delgado Calvo for coordinating the gasification tests. From PSI (Switzerland), I would like to thank Dr. Serge M.A. Biollaz for hosting the lab-scale sorbent tests. In addition, I would like to thank Dr. Philip Edinger for the excellent collaboration during the AC tests and all technical discussions that followed them. Also, I am thankful to Dr. Olov Öhrman, Dr. Magnus Marklund and Henry Hedman from ETC for their support and guidance during the campaigns in Sweden.

From the LSBTP, I would like to thank the technical personnel Euthymios Dimitriadis and Labros Adamos for assisting with the construction of the test rigs at NTUA, as well as Platon Pallis and Dr. Aggelos Doukelis for providing technical feedback. Special thanks to colleagues Dr. Konstantinos Braimakis, Petros Vlavakis, Tryfon Roumpedakis, Stratis Varvagiannis, Aris-Dimitrios Leontaritis, Antonis Charalampidis and Despina Magiri-Skouloudi for their recommendations and our great collaboration. It is essential for me to express my gratitude to Christos Pavlis, Sotiris Giannoulidis, Konstantina Manou, George Desypris, Nikos Zygourakis and all students that we worked together. We exchanged knowledge and experience during these years conducting experiments and simulations. I am also thankful to Maria Prokopou and Vasianna Barmparitsa, who handled many administration issues on my behalf.

Finally, I would like to thank with all my heart my family and friends, who have been there for me over the years. You really supported me during this trip and this thesis is dedicated to you.

Dimitrios Grimekis
Athens, 2019

Η έγκριση της Διδακτορικής Διατριβής από τη Σχολή Μηχανολόγων Μηχανικών του Εθνικού Μετσόβιου Πολυτεχνείου δεν υποδηλώνει αποδοχή των γνωμών του συγγραφέα (Ν. 5343/ 1932, Άρθρο 202).

Summary

The scope of the present thesis covers the investigation of solvents, sorbents and processes for CO_2, tar and sulfur removal from syngas prior to its utilization for synthesis and/or power generation. Carbon capture through "warm gas cleaning" (processes at temperatures up to 200 °C) is an important aspect for both applications. During substitute natural gas (SNG) production, methanation with carbon monoxide in a CO_2-free syngas decreases the demand for hydrogen and the size and cost of process equipment. In addition, high-temperature acid gas removal (AGR) permits hydrocarbons to pass through the cleaning unit. Benefits can also be noted for methanol (MeOH) synthesis plants. In addition, pre-combustion CO_2 capture at elevated temperatures in integrated gasification combined cycle (IGCC) plants comprises an important solution for reducing the environmental impact of power generation from solid fuels through Carbon Capture, Utilization and Storage (CCUS), while increasing the cycle efficiency compared to cold gas cleaning processes (e.g. Rectisol™). In this framework, this PhD thesis investigated the characteristics, benefits and limitations of applying hot potassium carbonate solutions for AGR. This thesis aims to provide a holistic approach through experimental work, thermodynamic modeling, as well as modeling of the AGR process and its integration in an IGCC plant for power and MeOH cogeneration. Since the process cannot achieve deep desulfurization especially regarding organic-sulfur species, gas cleaning (particularly organic/inorganic sulfur and tar) by activated carbon was experimentally investigated at "warm gas cleaning" conditions. A coupling of hot potassium carbonate process with sorbent beds would be essential for synthesis processes, in which sulfur poisoning of catalysts (e.g. nickel, copper) is often an issue even at concentrations in the range of 1 ppmv. Next, a brief summary of the thesis chapters is provided.

In *Chapter 1*, an overview of the global status and projections regarding the utilization of solid fuels for energy, fuels and chemicals is presented. The overview covers coal and biomass, with a special emphasis on the latter due to its sustainability. The major biochemical and thermochemical conversion pathways are reviewed emphasizing on gasification, which is of interest in the present dissertation. The main syngas contaminants from coal and biomass gasification are analyzed and an extensive literature review is provided regarding their content and speciation in the raw product gas. Moreover, gas cleaning requirements depending on downstream processes for power generation or catalytic synthesis are presented. Finally, an overview of syngas cleaning technologies is provided as a link to the processes studied in the context of the PhD thesis.

In *Chapter 2*, an experimental study was carried out on biomass gasification in order to investigate the syngas composition from a 3 MW_{th} air blown bubbling fluidized bed gasification plant operating with woody biomass. The experimental results were used to develop a steady-state, equilibrium Aspen Plus™ model for the gasifier. In this model, the formation of methane and ethylene were taken into account, as well as the char content in fly ash. The model was based on the minimization of Gibbs free energy for the estimation of the main product gas components, as well as on the effect of the water-gas shift (WGS) reaction equilibrium at the reactor outlet. The implementation of a WGS model reactor contributed to the approximation of experimental data since the reaction can be still active after the gasifier outlet. When only methane formation was considered, the simulation data greatly deviated from the experimental results. For this reason, the formation of ethylene was incorporated in the model in a stoichiometric reactor. The improved model managed to adequately predict the main syngas components. Deviations when operating conditions, such as fuel and oxidant feed rates changed, were also discussed. Correlations for char production, organic sulfur and tar distribution can further improve the model performance.

In *Chapter 3*, physical adsorption of organic and inorganic sulfur onto activated carbon was investigated experimentally. Organic sulfur adsorption was carried out in a lab-scale fixed bed reactor at elevated temperature (100-200 °C). Thiophene (C_4H_4S) was considered as the model species in the gas phase based on its concentration in syngas. The study covered a wide range of operating parameters, such as the gas flow rate (or gas hourly space velocity, GHSV), temperature, C_4H_4S concentration and moisture content. Temperature was found to influence significantly the capacity, while on the other hand, *GHSV* did not have a notable impact other than a reduction in breakthrough time. A comparison of experimental data with two isotherm models implementing one (Henry model) and two parameters (Langmuir model) followed and a good agreement was found for the latter model. As a next step, a study on the combined removal of sulfur and tar species by activated carbon was conducted. Real syngas produced by a 1 MW_{th} entrained-flow gasifier was used during the experiments. The investigation concluded that selectivity issues arise since the AC material could adsorb H_2S

less efficiently in the presence of C_6H_6. Moreover, difficulties encountered during AC evaluation under real gasification conditions are discussed (mainly due to the variability of syngas quality).

In *Chapter 4*, an experimental investigation of CO_2 solubility and absorption rate into pure and promoted K_2CO_3 solutions is presented. The study was carried out in a stirred reactor by applying a batch-type pressure decay experimental method. For the pure K_2CO_3 aqueous solutions, tests were carried out at temperatures between 80 and 120 ^oC with two different K_2CO_3 concentrations. The experimental measurements were found to be in agreement with estimations of electrolyte-NRTL thermodynamic model. In a next step, Glycine, MDEA, MEA and PZ were tested as additives in the K_2CO_3 aqueous solution. As far as K_2CO_3 solvents are concerned, solubility increases with a decrease in temperature or with a denser solvent. Concerning the addition of promoters, the use of PZ greatly improves CO_2 solubility and absorption rate at the same time. The use of MEA is also beneficial for both solubility and absorption rate, but to a lesser extent compared to PZ. On the other hand, MDEA can potentially improve solvent capacity when added in lower quantities, however, when used at higher concentrations, it lowers CO_2 solubility. Finally, Glycine addition at a low molarity deteriorated CO_2 solubility. Based on solvent screening results, MEA and PZ were selected as promoters for further investigation.

In *Chapter 5*, an experimental study on the removal of CO_2/light tar mixtures by pure and MEA-promoted K_2CO_3 aqueous solutions is presented. Two model compounds which have the potential to be valorized in downstream synthesis applications were selected (benzene and toluene) e.g. reforming of benzene during methanation is possible. This study can be considered as an extension of the work performed in *Chapter 4*. The experimental apparatus used in the batch-type experiments was modified to allow continuous gas phase analysis through FTIR spectroscopy. The effect of absorption temperature, MEA concentration, and tar partial pressure on the co-absorption of CO_2/C_6H_6 and CO_2/C_7H_8 is reported. The low affinity of K_2CO_3 solutions towards light tar species is confirmed, since very low tar capacities were measured.

In *Chapter 6*, an Aspen Plus™ model for the hot potassium carbonate process aiming at the simultaneous capture of CO_2 and H_2S from coal syngas is presented. The study was carried out in the framework of process integration in a Coal-to-SNG plant based on allothermal gasification. Both pure K_2CO_3 and PZ-promoted K_2CO_3 solvents with varying PZ fractions were evaluated. Adjustment of electrolyte-NRTL parameters was performed through experimental data regression, since default Aspen Plus™ parameters did not accurately model the thermodynamics of the liquid solution. Detailed rate-based models were used to describe the absorber and desorber columns. The effect of process parameters on H_2S capture efficiency, liquid circulation rate and specific reboiler duty was investigated for all solvents. It was found that when the process operates with PZ-promoted solutions, similar reboiler duties to the pure K_2CO_3 solvents can be achieved at lower absorber pressure. A higher lean solvent loading is required for the former due to their high heat of desorption, while PZ volatility issues must also be considered. In addition, operation of the desorber column at elevated pressure was found to benefit solvents with a higher PZ fraction. Finally, H_2S removal efficiency was consistently above the CO_2 capture level (set to 95% in all cases). Strategies for further reducing the H_2S content in clean syngas are also discussed.

In *Chapter 7*, Aspen Plus™ process models encompassing the integration of the hot potassium carbonate process in a biomass IGCC (BIGCC) plant are presented. Three configurations were considered, particularly a) an electricity-only BIGCC plant without CCS, b) an electricity-only BIGCC plant with pre-combustion CCS by means of aqueous K_2CO_3 solutions for CO_2 and H_2S capture and c) an electricity and MeOH cogeneration BIGCC plant with pre-combustion CCS by means of aqueous K_2CO_3 solutions for CO_2 and H_2S capture. In all configurations, autothermal pressurized gasification with steam/O_2 mixtures and hot syngas cleaning were considered for coupling with the hot potassium carbonate process. The effect of steam-to-biomass ratio, carbon capture rate and MeOH cogeneration share on the plant energy efficiency, exergy efficiency and exergy destruction ratio per process was investigated. The air separation unit, N_2 compressors for syngas dilution and compressors for CO_2 storage/sequestration account for the major electric power consumptions of the plant. Energy efficiency for the BIGCC w/o CCS was found to exceed 46%, while the integration of hot potassium carbonate technology caused an efficiency penalty in the range of 6.5-11.5 percentage points. A high share of exergy destruction was found to occur in the gas turbine, autothermal gasifier and CCS unit.

Finally, the main conclusions of the thesis, its contribution to knowledge and suggestions for future work, are presented in *Chapter 8*.

Περίληψη

Αντικείμενο της παρούσας εργασίας είναι η διερεύνηση διαλυτών, στερεών προσροφητών και διεργασιών για τη δέσμευση CO_2, πισσών και θειούχων ενώσεων από αέρια σύνθεσης πριν από τη χρήση τους για καταλυτική σύνθεση ή/και παραγωγή ηλεκτρικής ενέργειας. Η δέσμευση CO_2 μέσω "θερμού καθαρισμού αερίων" (“warm gas cleaning”, διεργασίες σε θερμοκρασίες έως 200 ° C) αποτελεί σημαντική πτυχή και για τις δύο εφαρμογές. Κατά την παραγωγή υποκατάστατου φυσικού αερίου (SNG), η μεθανοποίηση με μονοξείδιο του άνθρακα (χωρίς CO_2 στο αέριο) μειώνει την κατανάλωση υδρογόνου, το μέγεθος και το κόστος του εξοπλισμού. Επιπλέον, η δέσμευση όξινων αερίων (AGR) σε υψηλές θερμοκρασίες επιτρέπει στους υδρογονάνθρακες να διαφύγουν από τη μονάδα καθαρισμού. Οφέλη μπορούν επίσης να σημειωθούν για τις μονάδες σύνθεσης μεθανόλης (MeOH). Ακόμη, η δέσμευση CO_2 πριν την καύση υπό συνθήκες θερμού καθαρισμού σε μονάδες συνδυασμένου κύκλου με αεριοποίηση (IGCC) αποτελεί σημαντική εναλλακτική για τη μείωση των περιβαλλοντικών επιπτώσεων της παραγωγής ηλεκτρικής ενέργειας από στερεά καύσιμα μέσω της δέσμευσης, αξιοποίησης και αποθήκευσης άνθρακα (CCUS). Επιπρόσθετα, συνεισφέρει στην αύξηση της απόδοσης του κύκλου σε σύγκριση με τις ψυχρές διεργασίες AGR (π.χ. Rectisol®). Στο πλαίσιο αυτό, η παρούσα διδακτορική διατριβή διερεύνησε τα χαρακτηριστικά, τα οφέλη και τους περιορισμούς της εφαρμογής θερμών διαλυμάτων ανθρακικού καλίου σε διατάξεις AGR. Η εργασία αποσκοπεί στην επίτευξη μιας ολιστικής προσέγγισης μέσω πειραματικής μελέτης, θερμοδυναμικής μοντελοποίησης, μοντελοποίησης της διεργασίας AGR, καθώς και μοντελοποίηση της ενσωμάτωσής της σε μονάδα IGCC για συμπαραγωγή ενέργειας και MeOH. Δεδομένου ότι η διεργασία δεν μπορεί να επιτύχει πλήρη αποθείωση, ειδικά όσον αφορά θειούχες οργανικές ενώσεις, πραγματοποιήθηκε επιπλέον πειραματική διερεύνηση της απομάκρυνσης προσμίξεων (οργανικού/ανόργανου θείου και πισσών) από ενεργό άνθρακα, επίσης υπό συνθήκες "θερμού καθαρισμού". Η σύζευξη της διεργασίας θερμού ανθρακικού καλίου με τέτοιες προσροφητικές κλίνες θα ήταν απαραίτητη για διεργασίες σύνθεσης, στις οποίες η δηλητηρίαση των καταλυτών (π.χ. νικέλιο, χαλκός) με θείο αποτελεί συχνό πρόβλημα, ακόμη και σε συγκεντρώσεις που κυμαίνονται κοντά στο 1 ppmv. Στη συνέχεια, παρουσιάζεται μια σύντομη περίληψη των κεφαλαίων της διατριβής.

Στο *Κεφάλαιο 1* παρουσιάζεται μια επισκόπηση της τρέχουσας κατάστασης και των προβλέψεων σχετικά με τη χρήση στερεών καυσίμων για ενέργεια, καύσιμα και χημικά σε παγκόσμιο επίπεδο. Η επισκόπηση καλύπτει τον ορυκτό άνθρακα και τη βιομάζα, με ιδιαίτερη έμφαση στη δεύτερη λόγω της βιωσιμότητάς της. Οι κυριότερες βιοχημικές και θερμοχημικές διεργασίες μετατροπής αναλύονται, δίνοντας έμφαση στην αεριοποίηση, η οποία παρουσιάζει ενδιαφέρον για την παρούσα διατριβή. Ακόμη, περιγράφονται οι σημαντικότερες προσμίξεις που προκύπτουν κατά την αεριοποίηση στερεών καυσίμων και παρουσιάζεται εκτεταμένη βιβλιογραφική ανασκόπηση σχετικά με τη σύστασή τους στο ακατέργαστο αέριο. Στη συνέχεια, παρουσιάζονται οι απαιτήσεις καθαρισμού των προσμίξεων αυτών βάσει των κατάντη διεργασιών παραγωγής ενέργειας ή καταλυτικής σύνθεσης. Τέλος, γίνεται μια επισκόπηση των τεχνολογιών καθαρισμού αερίου σύνθεσης, ως σύνδεσμος με τις διεργασίες που μελετήθηκαν στο πλαίσιο της διδακτορικής διατριβής.

Στο *Κεφάλαιο 2* πραγματοποιήθηκε πειραματική μελέτη της αεριοποίησης, προκειμένου να διερευνηθεί η σύσταση του αερίου σύνθεσης. Οι μετρήσεις πραγματοποιήθηκαν σε μονάδα αεριοποίησης ξυλώδους βιομάζας ισχύος 3 MW_{th} τεχνολογίας ρευστοποιημένης κλίνης. Τα πειραματικά αποτελέσματα χρησιμοποιήθηκαν για την ανάπτυξη ενός μοντέλου ισορροπίας σταθερής κατάστασης στο λογισμικό Aspen Plus™. Σε αυτό το μοντέλο ελήφθησαν υπόψη ο σχηματισμός του μεθανίου και του αιθυλενίου, καθώς και η περιεκτικότητα εξανθρακώματος της ιπτάμενης τέφρας. Το μοντέλο βασίστηκε στην ελαχιστοποίηση της ελεύθερης ενέργειας Gibbs για την εκτίμηση των κύριων συστατικών του αερίου προϊόντος, καθώς και στην επίδραση της ισορροπίας της αντίδρασης μετατόπισης (water-gas shift, WGS). Η διόρθωση της αντίδρασης WGS συνέβαλε στην προσέγγιση των πειραματικών δεδομένων, δικαιολογώντας την υπόθεση πως η αντίδραση μπορεί να παραμείνει ενεργή μετά την έξοδο του αεριοποιητή. Όταν εξετάστηκε αποκλειστικά ο σχηματισμός μεθανίου, τα αποτελέσματα της προσομοίωσης βρέθηκαν να αποκλίνουν σημαντικά από τα πειραματικά αποτελέσματα. Για το λόγο αυτό, ο σχηματισμός αιθυλενίου ενσωματώθηκε στο μοντέλο. Το βελτιωμένο μοντέλο κατόρθωσε να προβλέψει επαρκώς τα κύρια συστατικά του αερίου σύνθεσης. Παρατηρήθηκαν επίσης αποκλίσεις κατά τη μεταβολή των συνθηκών λειτουργίας, όπως ο ρυθμός τροφοδοσίας καυσίμου και οξειδωτικού μέσου (αέρας). Συσχετίσεις για την παραγωγή εξανθρακώματος, την κατανομή θειούχων ενώσεων και πισσών μπορούν να βελτιώσουν περαιτέρω τις προβλέψεις του θερμοδυναμικού μοντέλου.

Στο *Κεφάλαιο 3* πραγματοποιήθηκε πειραματική μελέτη της φυσικής προσρόφησης οργανικού και ανόργανου θείου σε ενεργό άνθρακα. Οι μετρήσεις προσρόφησης οργανικού θείου πραγματοποιήθηκαν σε υψηλές θερμοκρασίες (100-200 °C) σε μια εργαστηριακή διάταξη σταθερής κλίνης. Ως αντιπροσωπευτική θειούχος οργανική ένωση στην αέρια φάση θεωρήθηκε το θειοφαίνιο (C_4H_4S) βάσει και της σύστασής του στο αέριο σύνθεσης. Η μελέτη κάλυψε ένα σημαντικό εύρος παραμέτρων λειτουργίας, όπως η παροχή αερίου (*GHSV*), η θερμοκρασία, η συγκέντρωση του C_4H_4S και η ύπαρξη υγρασίας στο αέριο. Βρέθηκε πως η θερμοκρασία επηρεάζει σημαντικά τη χωρητικότητα του προσροφητή, ενώ από την άλλη πλευρά, η επίδραση της παροχής του αερίου βρέθηκε να μην είναι αξιοσημείωτη πέραν της μείωσης του χρόνου διέλευσης (breakthrough time). Ακολούθησε αντιπαραβολή των πειραματικών αποτελεσμάτων με δύο μοντέλα ισόθερμων προσρόφησης με μία (Henry) και δύο μεταβλητές (Langmuir) και βρέθηκε πως μια συσχέτιση τύπου Langmuir μπορεί να επιτύχει μια ικανοποιητική προσέγγιση. Σε επόμενο βήμα, πραγματοποιήθηκε πειραματική διερεύνηση του συνδυασμένου καθαρισμού θειούχων ενώσεων και πισσών από ενεργό άνθρακα σε υψηλές θερμοκρασίες. Κατά τη διάρκεια των μετρήσεων χρησιμοποιήθηκε πραγματικό αέριο σύνθεσης από μονάδα αεριοποίησης βιομάζας ισχύος 1 MW_{th} τεχνολογίας κονιοποιημένου καυσίμου. Τα αποτελέσματα υπέδειξαν πως η προσρόφηση του H_2S πραγματοποιήθηκε λιγότερα αποδοτικά με την παρουσία πισσών στο αέριο σύνθεσης (κυρίως C_6H_6). Επιπλέον, αναλύονται δυσκολίες που αντιμετωπίστηκαν κατά τη διάρκεια της πειραματικής μελέτης υπό συνθήκες πραγματικής αεριοποίησης και οφείλονται κυρίως στη μεταβλητή ποιότητα του αερίου σύνθεσης.

Στο *Κεφάλαιο 4* παρουσιάζεται η πειραματική διερεύνηση της διαλυτότητας και του ρυθμού απορρόφησης του CO_2 σε υδατικά διαλύματα K_2CO_3 χωρίς και με χρήση προσθέτων. Η μελέτη διεξήχθη σε αναδευόμενο αντιδραστήρα με εφαρμογή ασυνεχούς (batch) πειραματικής μεθόδου. Για τα υδατικά διαλύματα K_2CO_3 χωρίς πρόσθετα, διεξήχθησαν δοκιμές σε θερμοκρασίες στο εύρος 80-120 °C με δύο διαφορετικές συγκεντρώσεις K_2CO_3. Οι πειραματικές μετρήσεις βρέθηκαν να συμφωνούν με τις εκτιμήσεις του θερμοδυναμικού μοντέλου electrolyte-NRTL. Σε επόμενο βήμα, δοκιμάστηκαν ως πρόσθετα στο υδατικό διάλυμα K_2CO_3 οι ενώσεις γλυκίνη, μεθυλο-διεθανολαμίνη (MDEA), αιθανολαμίνη (MEA) και πιπεραζίνη (PZ). Όσον αφορά τα υδατικά διαλύματα καθαρού K_2CO_3, η διαλυτότητα του CO_2 αυξάνεται με μείωση της θερμοκρασίας ή με πυκνότερο διαλύτη. Αναφορικά με τη χρήση προσθέτων, η προσθήκη PZ βελτιώνει σημαντικά τη διαλυτότητα και το ρυθμό απορρόφησης του CO_2. Η χρήση MEA είναι επίσης ευεργετική τόσο για τη διαλυτότητα όσο και για το ρυθμό απορρόφησης, ωστόσο σε μικρότερο βαθμό σε σύγκριση με την PZ. Από την άλλη πλευρά, η MDEA μπορεί να βελτιώσει την απορροφητική ικανότητα όταν προστίθεται σε μικρότερες ποσότητες, ωστόσο, όταν χρησιμοποιείται σε υψηλότερες συγκεντρώσεις, μειώνει τη διαλυτότητα του CO_2. Τέλος, η προσθήκη γλυκίνης σε χαμηλή συγκέντρωση στο διάλυμα έχει αρνητική επίδραση στη διαλυτότητα του CO_2. Με βάση τα πειραματικά αποτελέσματα, οι MEA και PZ επιλέχθηκαν ως πρόσθετες ενώσεις για περαιτέρω μελέτη.

Στο *Κεφάλαιο 5* παρουσιάζεται μια πειραματική μελέτη για τη συνδυασμένη δέσμευση CO_2/ελαφρών πισσών από υδατικά διαλύματα καθαρού K_2CO_3, αλλά και με MEA ως πρόσθετο. Επιλέχθηκαν δύο πρότυπες ενώσεις οι οποίες μπορούν να αξιοποιηθούν κατάντη του αεριοποιητή (βενζόλιο και τολουόλιο) π.χ. μέσω αναμόρφωσης του βενζολίου κατά τη μεθανοποίηση. Η συγκεκριμένη πειραματική διερεύνηση μπορεί να θεωρηθεί ως επέκταση της μελέτης που παρουσιάζεται στο Κεφάλαιο 4. Η πειραματική διάταξη που χρησιμοποιήθηκε στο Κεφάλαιο 4 τροποποιήθηκε για να επιτρέψει τη συνεχή ανάλυση της αέριας φάσης μέσω φασματοσκοπίας FTIR. Στο κεφάλαιο αυτό μελετάται η επίδραση της θερμοκρασίας απορρόφησης, της συγκέντρωσης MEA και της μερικής πίεσης των πισσών στη συνδυασμένη απορρόφηση των CO_2/C_6H_6 και CO_2/C_7H_8. Η καταλληλότητα των θερμών διαλυμάτων K_2CO_3 να επιτρέπουν τη διέλευση πισσών επιβεβαιώθηκε, καθώς μετρήθηκαν πολύ χαμηλές τιμές διαλυτότητας.

Στο *Κεφάλαιο 6* παρουσιάζεται η μοντελοποίηση της διεργασίας απορρόφησης/εκρόφησης CO_2 και H_2S από αέριο σύνθεσης μέσω θερμών υδατικών διαλυμάτων K_2CO_3 στο λογισμικό Aspen Plus™. Η μελέτη πραγματοποιήθηκε στο πλαίσιο της ενσωμάτωσης της διεργασίας σε μονάδα σύνθεσης SNG από λιγνίτη μέσω αλλοθερμικής αεριοποίησης (χωρίς να συμπεριληφθούν ωστόσο στη μοντελοποίηση οι ανάντη και κατάντη διεργασίες αεριοποίησης και καταλυτικής σύνθεσης, αντίστοιχα). Αξιολογήθηκαν τόσο υδατικά διαλύματα καθαρού K_2CO_3, όσο και μίγματα H_2O-K_2CO_3-PZ με μεταβαλλόμενη σύσταση PZ. Αρχικά, πραγματοποιήθηκε ρύθμιση των παραμέτρων αλληλεπίδρασης του μοντέλου electrolyte-NRTL μέσω ανάλυσης παλινδρόμησης με πειραματικά δεδομένα, καθώς οι προεπιλεγμένες τιμές των παραμέτρων στο Aspen Plus™ παρουσιάζουν περιορισμένη ικανότητα πρόβλεψης των θερμοδυναμικών ιδιοτήτων των διαλυμάτων. Μοντέλα ρυθμού (rate-based) χρησιμοποιήθηκαν για τη μοντελοποίηση των στηλών απορρόφησης και εκρόφησης. Στη συνέχεια, μελετήθηκε η επίδραση διαφόρων παραμέτρων λειτουργίας της διεργασίας στην απόδοση δέσμευσης του H_2S,

στην απαιτούμενη παροχή μάζας υγρού διαλύτη και στην ειδική κατανάλωση θερμικής ενέργειας στον αναβραστήρα για όλες τις περιπτώσεις διαλυτών. Βρέθηκε πως στις περιπτώσεις που χρησιμοποιούνται διαλύτες με πρόσθετη PZ είναι εφικτή η επίτευξη αντίστοιχης θερμικής κατανάλωσης με τα διαλύματα καθαρού K_2CO_3 σε σημαντικά χαμηλότερη πίεση της στήλης απορρόφησης. Επιπλέον, για τα διαλύματα που περιέχουν PZ απαιτείται μεγαλύτερος λόγος ανθράκωσης του πτωχού διαλύτη εξαιτίας της μεγαλύτερης ειδικής θερμότητας αναγέννησης, ενώ επίσης πρέπει να εξεταστούν ζητήματα σχετικά με την πτητικότητα της PZ. Επιπρόσθετα, η λειτουργία της στήλης εκρόφησης σε υψηλή πίεση βρέθηκε να ευνοεί διαλύτες με υψηλότερη περιεκτικότητα σε PZ. Η απόδοση δέσμευσης H_2S ήταν σταθερά μεγαλύτερη από το ποσοστό δέσμευσης CO_2 (σταθερό και ίσο με 95% σε όλες τις περιπτώσεις). Τέλος, περιγράφονται στρατηγικές για την περαιτέρω μείωση της συγκέντρωσης του H_2S στο καθαρό αέριο σύνθεσης.

Στο *Κεφάλαιο 7* αναλύεται η μοντελοποίηση σταθμών συνδυασμένου κύκλου με αεριοποίηση βιομάζας (BIGCC) στο Aspen Plus™, όπου ενσωματώνεται ως τεχνολογία AGR η διεργασία χημικής απορρόφησης με θερμό υδατικό διάλυμα K_2CO_3. Μελετήθηκαν τρεις διαφορετικές διατάξεις και συγκεκριμένα α) ένας σταθμός BIGCC για ηλεκτροπαραγωγή χωρίς CCS, β) ένας σταθμός BIGCC για ηλεκτροπαραγωγή με CCS και διεργασία χημικής απορρόφησης των CO_2 και H_2S μέσω διαλυμάτων K_2CO_3 και γ) ένας σταθμός BIGCC για συμπαραγωγή ηλεκτρικής ενέργειας και MeOH με CCS και διεργασία χημικής απορρόφησης των CO_2 και H_2S μέσω διαλυμάτων K_2CO_3 (μονάδα AGR πριν την καύση). Σε όλες τις περιπτώσεις θεωρήθηκε πως πραγματοποιείται αυτοθερμική αεριοποίηση σε υψηλή πίεση με μίγματα H_2O/O_2 και καθαρισμός αερίου σε υψηλή θερμοκρασία για τη σύζευξη με την προτεινόμενη τεχνολογία AGR. Με βάση τα μοντέλα των διατάξεων αναλύθηκε η επίδραση του λόγου ατμού/βιομάζας (στάδιο αεριοποίησης), του ποσοστού δέσμευσης CO_2 και του ποσοστού συμπαραγωγής MeOH στον ενεργειακό βαθμό απόδοσης, στον εξεργειακό βαθμό απόδοσης και στο ποσοστό καταστροφής εξέργειας ανά διεργασία. Η μονάδα διαχωρισμού αέρα, οι συμπιεστές N_2 για την αραίωση του αερίου σύνθεσης και οι συμπιεστές για την αποθήκευση CO_2 συντελούν στο σημαντικότερο ποσοστό των ιδιοκαταναλώσεων ηλεκτρικής ενέργειας. Ο βαθμός ενεργειακής απόδοσης για το σταθμό BIGCC χωρίς εφαρμογή CCS υπερέβη το 46%, ενώ η ενσωμάτωση της διεργασίας απορρόφησης/εκρόφησης με υδατικά διαλύματα K_2CO_3 προκάλεσε τη μείωσή του κατά 6.5-11.5 ποσοστιαίες μονάδες. Επιπλέον, ένα σημαντικό ποσοστό της συνολικής καταστροφής εξέργειας στο σταθμό συντελείται στον αεριοστρόβιλο, στον αυτοθερμικό αεριοποιητή και στη μονάδα CCS.

Τέλος, στο *Κεφάλαιο 8* παρουσιάζονται τα κύρια συμπεράσματα της διδακτορικής διατριβής και τα στοιχεία καινοτομίας της, καθώς και προτάσεις για μελλοντική εργασία.

Contents

Nomenclature

Acronyms

AARD	Average absolute relative deviation
ABE	Acetone-butanol-ethanol
AC	Activated Carbon
AD	Anaerobic Digestion
AGR	Acid Gas Removal
ASU	Air Separation Unit
BA	Boric acid
BET	Brunauer-Emmett-Teller
BEV	Battery Electric Vehicle
BFBG	Bubbling fluidized-bed gasifier
BGGE	Biomass gasification with Gas Engine
BGSOFC	Biomass gasification with solid oxide fuel cell
BIGCC	Biomass-fueled Integrated Gasification Combined Cycle
BPR	Backpressure regulator
BT	Benzothiophene
BtL	Biomass to Liquid
BTX	Benzene-toluene-xylenes
CCE	Carbon Conversion Efficiency
CCS	Carbon Capture and Storage
CCUS	Carbon Capture, Utilization and Storage
CFBG	Circulating fluidized-bed gasifier
CFD	Computational Fluid Dynamics
CGE	Cold Gas Efficiency
CHP	Combined Heat and Power
CV	Coefficient of Variation
DBT	Dibenzothiophene
DFBG	Dual fluidized bed gasifier
DMDS	Dimethyl disulfide
DME	Dimethyl ether
DMS	Dimethyl sulfide
DOE	Department Of Energy
DRS	Data Regression System
ECN	Energy research Centre of the Netherlands
EDS	Ethyl disulfide
EFG	Entrained-flow gasifier
EM	Ethyl mercaptan
EOR	Enhanced Oil Recovery
EOS	Equation of state
EQM	Equilibrium model
ER	Equivalence ratio
ETC	Energy Technology Center
EU	European Union
FB	Fixed bed
FBG	Fluidized-bed gasifier
FFT	Fast Fourier Transform (algorithm)
FICFB	Fast internally circulating fluidized bed
FID	Flame Ionization Detector
FT	Fischer-Tropsch
FTIR	Fourier Transform Infrared
FXBG	Fixed-bed gasifier
GC	Gas chromatography/gas chromatograph

GDP	Gross Domestic Product
GHSV	Gas Hourly Space Velocity
GT	Gas turbine
HETP	Height equivalent to a theoretical plate
HPT	High-pressure turbine
HRSG	Heat recovery steam generator
HTC	Hydrothermal carbonization
HTG	Hydrothermal gasification
HTL	Hydrothermal liquefaction
ICE	Internal combustion engine
ID	Internal diameter
IEA	International Energy Agency
IGCC	Integrated Gasification Combined Cycle
IGT	Institute of Gas Technology
IHS	Iron oxide hydroxide sorbent
IMTP	Intalox Metal Tower Packing
IR	Infrared
IUPAC	International Union of Pure and Applied Chemistry
KLG	Karhunen–Loève Galerkin
LCA	Life Cycle Assessment
LCOE	Levelised cost of electricity
LFG	Landfill gas
LHHW	Langmuir-Hinshelwood-Hougen-Watson
LLE	Liquid-liquid equilibrium
LOD	Limit of Detection
LOQ	Limit of Quantification
LPG	Liquefied Petroleum Gas
LPT	Low-pressure turbine
MAE	Methyl aminoethanol
MBM	Meat and bone meal
MCFC	Molten carbonate fuel cell
MDEA	Methyl diethanolamine
MEA	Monoethanolamine
MFC	Mass flow controller
MM	Methyl mercaptan
MOO	Multi-objective optimization
MPT	Medium-pressure turbine
MPZ	Methylpiperazine
MS	Mass spectrometer, magnetic stirrer
MT	Mixing tee
NG	Natural gas
NGCC	Natural Gas Combined Cycle
NMR	Nuclear Magnetic Resonance
NREL	National Renewable Energy Laboratory
NRTL	Non-random Two Liquid (theory, model)
OECD	Organization for Economic Co-operation and Development
OPD	Optical path difference
ORC	Organic Rankine Cycle
OSC	Organic Sulfur Compound
PAH	Polyaromatic hydrocarbon
PFPD	Pulsed Flame Photometric Detector
PID	Proportional-Integral-Derivative
PMF	Particulate matter filter
PPP	Purchasing Power Parity
PR-BM	Peng-Robinson with Boston–Mathias alpha function

PSA	Pressure Swing Adsorption
PSD	Particle size distribution
PSI	Paul Scherrer Institute
PTFE	Polytetrafluoroethylene
PV	Photovoltaics
PVC	Polyvinyl chloride
PZ	Piperazine
PZEA	2-(1-piperazinyl)-ethylamine
RBM	Rate-based model
RES	Renewable Energy Sources
RH	Relative humidity
RM	Rotameter
RMSE	Root-mean-square error
RP	Reflux pump
SC	Steam cycle
SCD	Sulfur chemiluminescence detector
SCGP	Shell Coal Gasification Process
SNG	Substitute natural gas
SOFC	Solid oxide fuel cell
SP	Sampling port, syringe pump
SPA	Solid-phase adsorption
SRK	Soave-Redlich-Kwong
SS	Stainless steel
SSA	Specific surface area
STBR	Steam-To-Biomass Ratio
SU	Sampling unit
SV	Switch valve
TCD	Thermal Conductivity Detector
TDL	Tunable diode laser
TEPA	Tetraethylenepentamine
THT	Tetrahydrothiophene
TIT	Turbine Inlet Temperature
TRL	Technology Readiness Level
UNFCCC	United Nations Framework Convention on Climate Change
UNIQUAC	Universal Quasi-chemical (theory, model)
VLE	Vapor-liquid equilibrium
VP	Vacuum pump
WBA	World Bioenergy Association
WGS	Water-gas shift
WGSHT	Water-Gas Shift reactor at High Temperature
WGSLT	Water-Gas Shift reactor at Low Temperature
WI	Weight indicators
WWSQ	Weighted Sum of SQuares

Parameters and variables

a	specific interfacial area (m^{-1})
A_{φ}	Debye-Hückel parameter
CCE	carbon conversion efficiency (–)
CGE	cold gas efficiency (–)
C_{CO_2}	CO_2 solubility (mol L^{-1})
C_e	adsorbate concentration (mol m^{-3})
D_L	liquid diffusivity (m^2 s^{-1})
d_b	bubble size in reactor (m)
d_p	particle diameter (μm)

e	specific exergy (J mol^{-1})
E_i	exergy (W)
$e_{0,k}$	specific reference chemical exergy of species *k* (J mol^{-1})
f	fugacity coefficient
g	gravitational constant (m s^{-2})
G	Gibbs free energy of system (J)
$GHSV$	gas hourly space velocity (h^{-1})
h_w	enthalpy of water evaporation (MJ kg^{-1})
h	specific enthalpy (J mol^{-1})
H	enthalpy (J)
HHV	higher heating value (MJ kg^{-1})
I	irreversibility (W)
I_x	ionic strength (segment mole fraction scale)
K	equilibrium constant
K_H	Henry equilibrium constant (m^3 kg^{-1})
K_L	Langmuir equilibrium constant (m^3 mol^{-1})
$k_L a$	volumetric mass transfer coefficient (s^{-1})
k_i	kinetic constant
k_{ind}	consistency index in power-law model (Pa s^n)
k_B	Boltzmann constant ($1.38064852 \times 10^{-23}$ J K^{-1})
LHV	lower heating value (MJ kg^{-1})
L/G	liquid to gas ratio (–, mass basis)
m	mass (g)
$\dot{m}$	mass flow rate (kg s^{-1})
MW	molecular weight (g mol^{-1})
n	quantity of species (mol)
$\dot{n}$	molar flow rate (mol s^{-1})
n_{ind}	flow index in power-law model
N_{ag}	agitator speed (rps)
N_A	Avogadro number ($6.02214076 \times 10^{23}$ mol^{-1})
P	pressure
$P*$	equilibrium pressure
P_{el}	electric power (MW)
Q_e	electron charge (1.60219 x 10^{-8} C)
q_{mL}	saturation value of Langmuir isotherm (mol kg^{-1})
q_m, q_{90}	equilibrium or breakthrough capacity (mg g^{-1})
R	universal gas constant (8.314 kJ $kmol^{-1}$ K^{-1})
R^2	coefficient of determination
r_i	Born radius (m)
$r_{reaction}$	reaction rate (kmol kg^{-1} cat. s^{-1})
s	specific entropy (J mol^{-1} K^{-1})
t	time (s)
T	temperature
T_{ag}	agitator diameter (m)
T_b	transmittance
t_e	exposure time (s)
TIT	turbine inlet temperature (°C)
$\dot{V}$	volume flow rate (Nm^3 h^{-1})
V	volume (m^3 or L)
V_s	superficial gas velocity (m s^{-1})
v_i	stoichiometric coefficient
w	weight fraction of fuel element
w_m	moisture content of biomass

x_k	molar fraction of species *k*
y	molar fraction of gas component
z_i	ion charge

Greek letters

ε	exergy efficiency
β	statistical coefficient of biomass exergy
η	energy efficiency
α_{ij}	non-randomness parameter
ε_b	attenuation coefficient or absorptivity
ε_{dis}	energy dissipation rate (W kg^{-1})
ε_s	solvent dielectric constant
ε_w	water dielectric constant
ρ_G	gas density (kg m^{-3})
ρ_L	liquid density (kg m^{-3})
σ_{int}	interfacial tension (N m^{-1})
α	loading (mol mol^{-1})
μ	chemical potential (J mol^{-1})
ρ	closest approach parameter
σ	standard deviation
τ	binary interaction parameter
γ	activity coefficient
λ	equivalence ratio
φ	gas hold-up
ω	acentric factor

Subscripts/superscripts

0	initial, reference
∞	infinite dilution
a	anion
B	solvent molecule
biom	biomass
c	cation
C	carbon
ch	chemical
comp	compressor
daf	dry ash-free basis
db	dry basis
DB	dry biomass
dm	dry matter
el	electric
eq	equilibrium
ex	expander
exp	experiment/experimental
g	gas
ge	equilibrium state of gas phase
gs	initial state of gas phase
H	hydrogen
i, j	Component/species in mixture, number of rows, repetition index
in	inlet
L	Langmuir
lc	local composition
loss	losses
m	molecule

max	maximum
moist	moisture
N	nitrogen
O	oxygen
out	outlet
p	products
PDH	Pitzer-Debye-Hückel
ph	physical
Q	heat
r	reactants
ref	reference
S	sulfur
sol	solution
stoich	stoichiometric
t	at time t
tot	total
W	work

1 Introduction and theoretical background

1.1 Coal and biomass for energy, fuels and chemicals

1.1.1 Current status of the energy mix and future projections

Energy has always been considered to be the driving force for economic growth and improvement of living standards, especially since the start of the Industrial Revolution. According to ExxonMobil's energy outlook report [1], a country's electricity use per capita is well aligned with its income level. In 2016, half of global population had a gross domestic product (GDP) per capita of less than 20000 USD Purchasing Power Parity (PPP) and a yearly electricity consumption well below 5000 kWh per person. Developed countries such as Germany, Japan and South Korea with GDP per capita values of approx. 40000 USD PPP are responsible for annual consumptions of 5000-10000 kWh per person, while countries associated with very high GDP per capita values, such as USA, even exceeded the aforementioned consumption values. The global energy demand is projected to constantly increase in the following decades, due to the global population growth (9.2 billion people estimate for 2040). At the same time, an increase in the energy demand of rapidly-developing countries, such as China, India and other non-OECD countries, already takes place. In 2017, global primary energy consumption growth averaged 2.2%, higher than the 10-year average of 1.7% per year [2].

In 2015, fossil fuels accounted for 78.4% of global total final energy consumption [3]. According to [2], the share of coal in the global electricity production remained almost steady from 1985 to 2017 at values close to 40% (38.1% in 2017), followed closely by natural gas with a share of 23.2% in 2017. On the other hand, the share of oil in global power generation has been constantly decreasing and is below 5% during the last 5 years. This trend is counterbalanced by its larger share in terms of global primary energy consumption, which is about 35%. Concerning the latter index, coal and natural gas follow oil with shares of 27.6% and 23.4% (2017 values), respectively. The utilization of natural gas is constantly increasing during recent years and it is considered as a suitable "transition fuel" for energy decarbonization. Benefits such as its utilization in highly efficient and flexible power cycles, as well as the well-developed gas grid networks for its transportation and existing infrastructure in general, have contributed to its expansion. Of course, apart from monitoring the current fossil fuel resource consumption rates, a mapping of the future energy generation from fossil sources is necessary. The reserve-to-production (R/P) ratio is an index that can provide an indication of the potential future reliance on specific fuels. Recent estimations for the R/P ratios of oil, natural gas and coal in 2017 were presented in [2] with values of 50.2, 52.6 and 134 years, respectively. Research studies focusing on the issue of fossil resource depletion can also be found. Maggio and Cacciola [4] implemented a predictive model based on a variant of the multi-cyclic Hubbert approach to estimate the production levels of oil, coal and natural gas using extended historical data from 1857 to 2010. The authors estimated that coal and natural gas demand peak are expected to occur between 2042-2062 and 2024-2046, respectively. Based on the "business-as-usual scenarios", coal is expected to play a role in global energy production for a few years to come, mainly in emerging and rapidly-developing countries (e.g. Asia). Advantages such as low fuel cost, high capacity factors and high power density compared to renewable energy technologies further enforce this prospect.

Nevertheless, the share of fossil fuels in global energy generation will be definitely influenced by national and international targets and regulations for climate change, which have already been adopted by many countries and unions. In 2015, parties to the United Nations Framework Convention on Climate Change (UNFCCC) reached an agreement to combat climate change and to intensify their actions and investments to ensure a sustainable low-carbon future. This was the major step taken after the Kyoto Protocol in 1997. The principal aim of the Paris Agreement is to trigger action against the threat of climate change through keeping the global temperature rise this century below 2 °C above pre-industrial levels and possibly, even further to 1.5 °C. During the 2016 Opening for Signature of the Paris Agreement, 175 Parties (174 countries and the EU) signed the Agreement, while 15 States deposited instruments of ratification [5]. Within this framework, a transition from traditional fossil fuels to renewable energy sources (RES) is attempted. So far, the very high commissioning rate of new renewable energy projects (mostly solar PV and wind power) has not been translated to a significant change of the renewable energy share in terms of total final energy consumption. This fact can be attributed to the strong growth of overall energy demand. In the European Union (EU), a roadmap has been launched which sets a milestone for the reduction of carbon dioxide (CO_2) emissions by 80% until 2050 compared to 1990 [6],

which is directly associated with higher shares of RES. In this direction, a 27% renewable energy share in total final energy is a target to be met until 2030 in EU-28. A brief overview of indicative regulations and actions which relate to RES targets in the energy mix can be found in Table 1-1 (national and international level). As a basis for comparison, renewable energy provided an estimated 19.3% of global final energy consumption in 2015. Particularly in EU-28, the share of RES in final energy and electricity generation in 2015 was 16% and 28.8%, respectively.

Table 1-1: National and international regulations and actions for RES participation in the energy mix (data retrieved from [3]).

Country/region	Milestone (year)	RES target description
EU-28	2030	27% share in final energy consumption
France	2030	32% share in final energy consumption
Germany	2050	60% share in final energy consumption
Greece	2020	20% share in final energy consumption
UK	2020	15% share in final energy consumption
China	2030	20% share in primary energy consumption
Illinois (USA)	2026	25% share in electricity generation
California (USA)	2030	50% share in electricity generation
India	2030	40% share in electricity generation
Brazil	2030	23% share in electricity generation
Japan	2030	14% share in primary energy consumption
Indonesia	2025	25% share in primary energy consumption
Philippines[1]	2050	100% share in electricity generation

*Target established by the Climate Vulnerable Forum [7]

Based on current legislation, the share of RES in the energy mix will continuously increase, bringing along requirements for energy storage, expansion of electrification and new environmentally-friendly energy carriers for industry and transportation. During this transition, coal-based energy will have to adapt to the strict requirements related to climate change. Environmental benefits from coal-based heat and/or power production or processing for fuels and chemicals can arise from energy efficiency improvements in the short term and to a greater extent, from investments in Carbon Capture, Utilization and Storage (CCUS) or cleaner coal-utilization technologies. The International Renewable Energy Agency (IRENA) has prepared a roadmap (REmap) which estimates what the future participation of various RES and fossil sources could be until 2050 [8]. The REmap case study of IRENA is in line with the guidelines of the Paris Agreement to sustain a global temperature increase below 2 °C above pre-industrial levels. The study specifies directions for four key sectors i.e. transport, buildings, industry and the power sector. The major forecast is the electrification of most sectors in order to accommodate large shares of power generation from wind and solar PV. Assuming the REmap scenario, renewable electricity would account for 28% in the transport sector, while its share in the final energy consumption of buildings could be up to 48%. Moreover, in the industry sector renewable electricity will account for 36% of the total final energy consumption of the sector. Lastly, the combined share of wind and solar PV in the power sector was estimated to be as high as 58%. In all sectors, biomass was also acknowledged as an important energy source, the share of which is expected to significantly increase in the REmap 2050 scenarios. An overview of primary energy demand estimations until 2040 from BP and suggestions for low-carbon technologies until 2050 from IRENA is shown in Figure 1-1.

A few important points concerning biomass utilization by 2050 can be summarized assuming the “optimistic” REmap scenario from IRENA’s study [8].

1. In the transport sector, biogas and liquid biofuels will rise their share to 22% in final energy consumption compared to about 3% currently. This can be explained because battery electric vehicles (BEV) are known to have limitations for heavy duty transportation.
2. In the building sector, modern bioenergy systems are expected to increase their share to 14% compared to 4% currently. The term “modern bioenergy” can describe alternative technologies of biomass utilization compared to traditional cook stoves and domestic heating applications. Such applications may include

highly-efficient condensation boilers for heating, as well as micro- and small-scale combined heat and power (CHP) systems based on combustion or gasification of biomass.

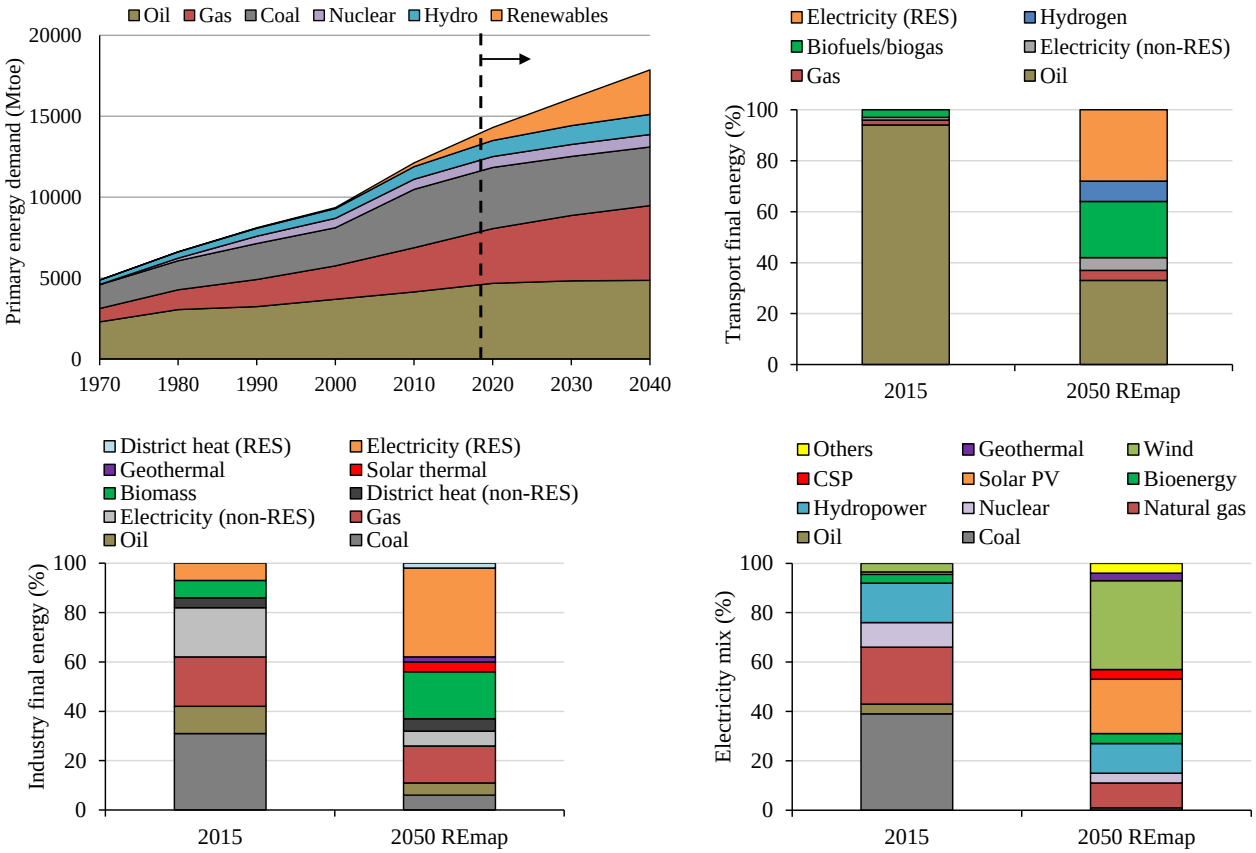

Figure 1-1:(Top left) Primary energy demand by source according to [9]. (Top right and bottom) Transport final energy, industry final energy and electricity mix by source based on the 2050 REmap scenario from [8].

3. The industrial sector is the second-largest emitter of energy-related CO_2. Particularly, the chemical, petrochemical and steel sector have the highest contribution, because they employ energy intensive and high-temperature processes which makes decarbonization more difficult. Biomass is expected to greatly contribute to the final energy consumption by almost triplicating its current share by 2050 to about 19%.
4. Concerning the power sector, the share of biomass in power generation is expected to remain almost constant. It is expected to slightly increase from 3.5% to 4.0% by 2050. However, it must be noted that a very high increase of the installed capacity of biomass plants is expected due to the increased overall energy demand (from 119 GW in 2015 to 384 GW in 2050). Electricity can be generated from biomass based on thermochemical (combustion, gasification) and biochemical (e.g. digestion) processes, as analyzed next.

Although the share of bioenergy, biogas, biofuels and other RES is forecast to significantly increase by 2050, most of the sectors will still use fossil sources, such as natural gas and oil. The share of natural gas in the transport, buildings, industry and power sectors was estimated as 4%, 7.3%, 15% and 10%, respectively, while the share of oil may still be as high as 33% in the transport sector. This fact highlights that the biomass deployment potential can be far greater when a complete elimination of fossil fuel sources will be required. As an example, Substitute Natural Gas (SNG) produced from biomass gasification and methanation could replace fossil natural gas in the future economy.

Of course, limitations related to biomass competitive applications, principally for food production, and techno-economic criteria (including optimization of biomass logistics) will formulate the extent of bioenergy penetration in the energy mix. The future potential of biomass for energy will depend on tackling challenges such as agricultural land desertification, degradation, limitless urbanization, as well as securing protection and expansion of forest areas. Yield optimization will be of great importance since this plays a major role in

increasing availability for food and fuel production. According to the World Bioenergy Association (WBA) estimates [10], about 5% of the agricultural area may be used for dedicated energy crops for biofuels and solid biomass for energy by 2035. In the next 20 years, the estimated combined energy potential of biomass from agriculture, forestry and waste sectors will be around 150 EJ. A very high percentage of the total energy potential (43%) is expected to derive from agricultural biomass such as residues, energy crops and other by-products from related activities. On the other hand, biomass from forestry operations will supply about 52% of the estimated energy. This includes both wood fuel, as well as significant quantities of forest residues and by-products of the wood processing sector. Concerning this changing situation, it must be noted that in this decade, almost 85% of the total biomass used derived from forests or trees. Table 1-2 presents medium-term predictions by WBA for the biomass potential from various sources. It is interesting to highlight that the utilization of waste biomass will have a comparable and even slightly higher share compared to that derived from dedicated crops. This is considered a very likely outcome when aiming at securing food supply especially in developing economies. Overall, as shown in Table 1-2, the future estimated potential will triplicate by 2035 assuming a) sustainable forest management practices, b) utilization of a 25% share of agricultural by-products such as rice husks, sunflower shells, etc. plus manure valorization and c) investing at high-yield crops for biofuels and solid biomass (estimated area of approx. 240 million hectares).

Table 1-2: Current and future estimates of global biomass potential in EJ [10].

Sector	Subsector	Current estimation (based on 2012 data)	Future estimated range (2035)	Future estimated average (2035)
Agriculture	Dedicated crops	3.5	26-34	30
	By-products, residues and manure	2.1	30-38	34
	Total agriculture	5.6	56-72	64
Forestry		48.9	72-84	78
Organic waste		1.7	6-10	8
Total		56.2	134-166	150

1.1.2 Solid fuel contribution to the production of transport fuels and chemicals

Valuable secondary products can be derived from coal and biomass, such as fuels and chemicals. Coal can be converted to chemicals and materials based on various strategies, several of which are described in [11]. The most appealing route is gasification followed by catalytic conversion of syngas. Application of this pathway has been a real case with the broadly applied SASOL process, which has been commercially deployed for producing paraffinic liquid fuels and chemical feedstocks through Fischer-Tropsch (FT) synthesis [12]. Another important pathway is coal conversion to liquids or coal tar, which can be done through carbonization, pyrolysis, extraction or direct liquefaction. For example, phenolic compounds can be produced through this route, derived from naphtha distillates [13, 14]. Furthermore, specific coal structures may be selectively removed to produce valuable monomers and monomer precursors. Concepts for the combined production of electricity, heat and chemicals/fuels are feasible, such as in the context of an Integrated Gasification Combined Cycle (IGCC) [15]. A few of the technologies described above also apply to biomass, either as primary thermochemical conversion steps, as well as secondary synthesis processes.

In the future economy, sustainable production of various carbon-containing products, which currently depend on fossil fuels as process inputs, will be a necessity. Two major sources of recyclable carbon which are currently investigated are atmospheric CO_2 and biomass. In general, direct CO_2 capture from air has many economic limitations due to the low CO_2 concentration (~ 400 ppm), which necessitates expensive capture units with large contact areas and the processing of large amounts of atmospheric air [16]. According to Krekel et al. [17], who performed a techno-economic investigation of direct CO_2 capture from air, the required sequestration energy is up to 4 times higher while its cost is higher by a factor of 8-13 compared to Carbon Capture and Storage (CCS) installations for large point-emitters, assuming an abatement cost of 100 \$/t CO_2 for the latter case. Consequently, biomass is acknowledged as the most promising source for obtaining a variety of carbon-containing chemicals. Biofuels, either gaseous or liquid, are typically characterized by a high market volume compared to biochemicals and biomaterials but are typically associated with comparatively lower prices.

Concerning the chemical industry, Sanders et al. [18] estimated that until 2050 at least 30% (by weight) of base chemicals will be produced from biomass. In 2050, the following market situation is expected:

- Organic base chemicals and bulk chemicals: Overall production amount estimated at 900 Mtpa (including ethylene, propylene, functionalized bulk chemicals for plastics, nylons, polyesters etc.) for an annual growth of 3%.
- Inorganic base chemicals: Overall production amount estimated at 2200 Mtpa (including sulfuric acid, lime, hydrogen, ammonia, etc.) for annual demand growth of 2%.

Reductions of fossil inputs for raw materials and energy are expected for both categories. Especially for organic base chemicals, a reduction up to 50% can be realized (combined fossil inputs for raw materials and energy), taking advantage of the (biomass) functional group properties. In 2016, the National Renewable Energy Laboratory (NREL) published a report [19] with the aim of specifying promising biomass-derived products in the short term. Several criteria were established for the evaluation and key aspects were investigated such as market volume and maturity, chemical utilization flexibility, potential economic benefits compared to fossil-based conversion pathways, as well as previous research work and funding associated with their production processes (especially by the US DOE).

The following chemicals were finally considered and evaluated, being either functional or drop-in replacements: butadiene (1, 3-), butanediol (1,4-), ethyl lactate, fatty alcohols, furfural, glycerol, isoprene, lactic acid, propanediol (1,3-), propylene glycol, succinic acid and xylene. For most of these chemicals, the overall market volume (in metric tons) and their prices as 3-5 year averages are shown in Figure 1-2. Products with high market volumes and current price levels can be identified, such as butadiene and butanediol. The report suggests the feasibility of three different production pathways depending on the type of the end-products, namely biological/biochemical conversion, thermochemical conversion and a combination of both (as in the case of syngas fermentation).

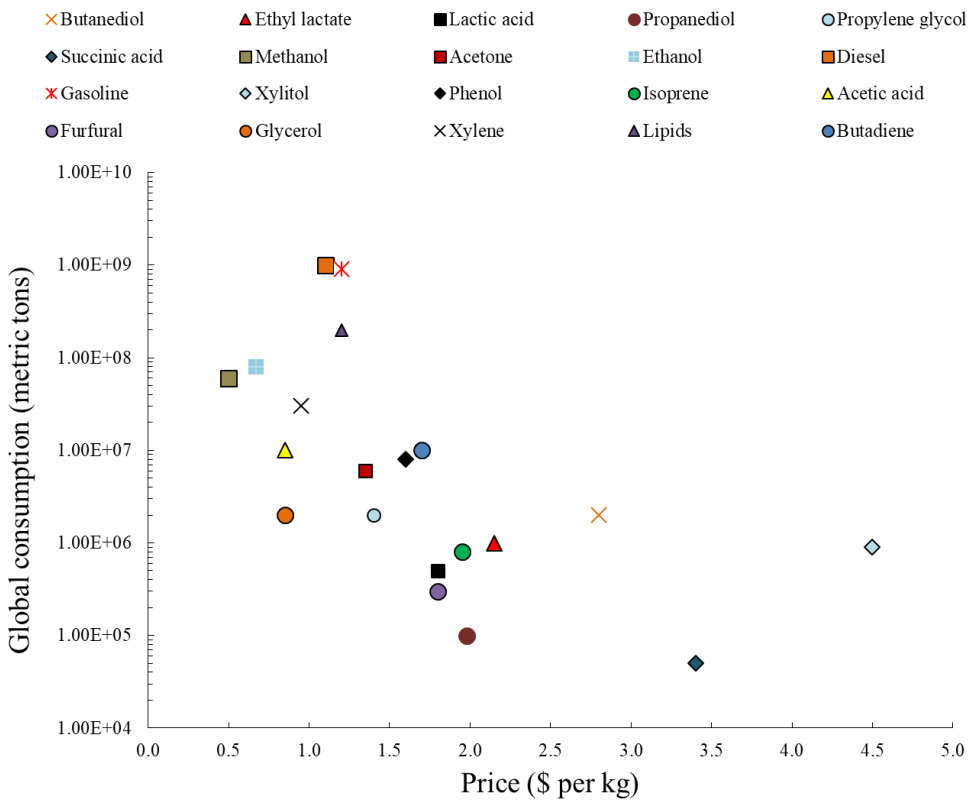

Figure 1-2: Reported 3-5 year average U.S. prices vs. global market volume for selected chemicals (modified from [19]).

In the NREL study [19], the scale of development and the Technology Readiness Level (TRL) was described as critical parameters for commercial deployment of the biomass-based syntheses processes. Xylene, isoprene and butadiene (1,3-) synthesis processes were assigned a TRL of 6, butanediol a TRL of 8 and all other chemicals were identified to be at TRL of 9, based on commodity feedstocks.

As already described, demand for biofuels will increase as dependence on fossil-based transportation fuels decreases. Similarly to chemicals, biofuels can also be derived through thermochemical and biochemical conversion routes. Gaseous biofuels are typically used for heat and power applications (domestic or centralized), while liquid biofuels are commonly applied to the transportation sector. Biomass can be used for the production of a great variety of fuels such as methanol (MeOH), ethanol (EtOH), dimethyl ether (DME), FT fuels, SNG and H_2. Biofuels can be classified into four main categories (or generations) [20]. First-generation biofuels are those directly derived from simple sugars, starch, fats and vegetable oils (methanol, ethanol, fatty acid esters, etc.). In Brazil, ethanol production from sugarcane through fermentation with yeast cells is a representative example of this route [21]. Crop utilization competition for both food and first-generation biofuel production has pushed research towards alternative conversion pathways. Lignocellulosic biomass can be used as the primary source for second-generation biofuels, based on biomass-to-liquid (BtL) processes or other concepts. The most important benefit of this option is the potential to use either waste biomass, such as agricultural and forestry residues, or energy crops which grow on non-arable, marginal land with limited or no requirement for fertilizers and pesticides. Moreover, third and fourth generation biofuels can be produced from algal biomass. Particularly, fourth-generation biofuel production processes rely on metabolic engineering and growth rate improvements of algal biomass, which results in a carbon-negative energy source [22].

In conclusion, solid fuels will play a major role in the production of energy and chemical products in the future. A high share of coal in the energy mix would probably be accompanied by the intensive application of carbon capture technologies. Biomass has the potential to decarbonize various sectors, which currently rely heavily on fossil fuels. In the next section, the main processes for the conversion of solid fuels to energy, transportation fuels and chemicals are reviewed. This literature review will subsequently focus more on biomass conversion processes since this is a field of interest in the framework of a sustainable economy. However, aspects of coal utilization are also discussed.

1.2 Biochemical and thermochemical conversion routes for energy, fuels and chemicals

This section aims to briefly present biochemical and thermochemical conversion pathways of solid fuels, with a special focus on the latter. Particularly, gasification is analyzed in detail to provide the necessary framework for the subsequent chapters.

1.2.1 Biochemical conversion pathway: an overview

In biochemical conversion processes, biomass molecules are broken into smaller ones *via* bacteria or enzymes. Fermentation and anaerobic digestion are two of the major processes which belong to this category (enzymatic conversion can also be considered). An important difference compared to thermochemical conversion processes is the fact that biochemical conversion takes place at much lower temperatures. The main steps of a biochemical conversion process are feedstock collection and supply, feedstock pretreatment, hydrolysis, biological conversion and recovery of the product(s). In fermentation, the aim of the biocatalysts is to convert the carbohydrates which are present in biomass and particularly hemicellulose and cellulose into sugars. The sugars are intermediate products that can then be fermented to produce biofuels, value-added chemicals, heat and electricity. Fermentation is a well-established, commercialized technology for producing ethanol from sugar crops and starch crops in large-scale plants [23]. More specifically, biomass grinding takes place to reduce the particle size and enzymes are employed to convert starch into sugars. During hydrolysis, polysaccharides decompose to produce pentoses (C_5 sugars e.g. xylose) and hexoses (C_6 sugars e.g. glucose), which can then be fermented by microorganisms. The fermentation of C_6 sugars to ethanol is shown in R 1-1

$$C_6H_{12}O_6(\text{glucose}) + \text{microorganisms} \xrightarrow{\text{Fermentation}} 2C_2H_6O(\text{ethanol}) + 2CO_2 \qquad \text{R 1-1}$$

The final product can be recovered through distillation, which is an energy-intensive process operation. In ethanol production plants, an ethanol purity of 95-96% is usually achieved through distillation [24]. It is important to note that broadening the utilization of biomass fractions or producing multiple products in a biorefinery concept, based on such a biochemical process, can significantly improve the profitability of the investment. Solid residues from the fermentation process can either be sold as cattle-feed or used as fuel in boilers [23]. Protein can be also coproduced and further improve the economic yield of such a plant. Possibilities for protein recovery from herbaceous energy crops have been discussed by Dale et al. [25].

Of course, the efficient utilization of low-quality, abundant lignocellulosic biomass as feedstock in biochemical conversion plants is of major importance. When lignocellulosic biomass is used, process modifications are necessary due to the complexity of the feedstock. The main difference is that prior to sugar fermentation, intensive biomass pretreatment through physical, chemical and physicochemical methods is needed to improve the accessibility of enzymes towards long-chain polysaccharide molecules. Acid or enzymatic hydrolysis is applied in order to accomplish the breakdown of cellulose into sugar. A comparative techno-economic analysis of steam explosion, dilute sulfuric acid, ammonia fiber explosion and biological pretreatments for corn stover can be found in [26]. A schematic flowsheet of an ABE (acetone-butanol-ethanol) fermentation process operating with lignocellulosic feedstock is shown in Figure 1-3.

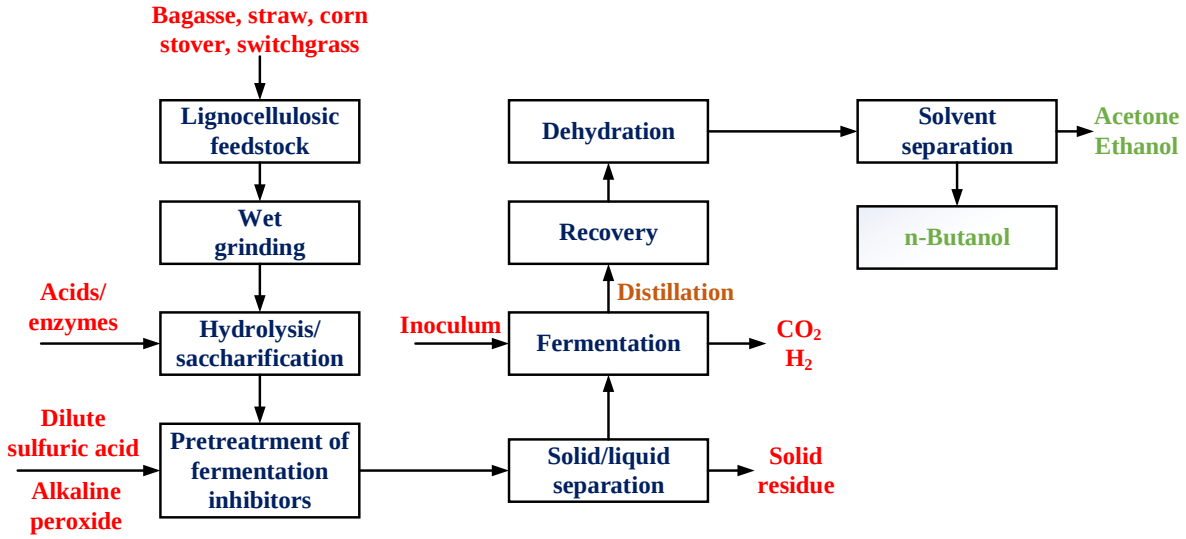

Figure 1-3: Flowsheet of ABE fermentation process from lignocellulosic biomass (adapted from [27]).

In anaerobic digestion (AD), biomass is converted to a combustible gaseous mixture which contains mainly methane (CH_4), CO_2, moisture as well as other contaminants such as H_2S and siloxanes. The process is carried out in controlled reactors or digesters where the biodegradable organic material is decomposed by bacteria in the absence of oxygen (O_2) at temperatures between 30-65 °C. The operation temperature mainly depends on the type of bacteria (mesophilic or thermophilic). The process is commercially proven and it is applied mostly for wet organic waste i.e. organic residues containing moisture contents above 80 wt.% [28]. The produced biogas has an energy content between 20-40% of the feedstock LHV and it is typically used directly in internal combustion engines (ICE) for CHP generation [23]. Biogas can also be pretreated, upgraded to remove CO_2 and fed to the natural gas grid. Moreover, other options have also emerged, such as the possibility to couple highly efficient (electrical efficiency > 50%) solid oxide fuel cells (SOFCs) with an AD process [29]. The residue from AD can be treated through processes such as composting, physicochemical treatment, solar or belt drying etc. Several of those processes are compared from an environmental perspective in [30]. The digestate can be recycled as a liquid and/or solid fertilizer since it is a material rich in nutrients. For a small to medium size biogas plant (< 500 kW_{el}), field application in the vicinity of the owner's facility is preferable. On the other hand, for higher plant capacities, transportation of the digestate is necessary in order to avoid its accumulation near farming areas and improve soil quality in areas with nutrient deficit [30]. Water can also be recovered from the AD waste stream and recycled for irrigation. The process layout of an AD plant is shown in Figure 1-4.

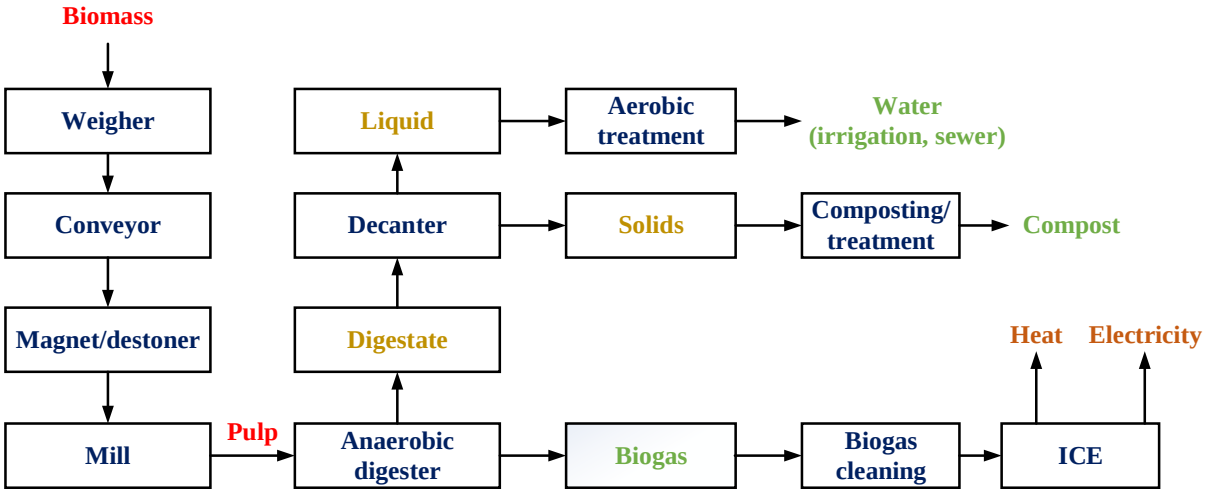

Figure 1-4: Process flowsheet of a CHP plant based on AD of biomass (adapted from [23]).

1.2.2 Thermochemical conversion pathway: an overview

Biomass thermochemical conversion processes are characterized by higher efficiencies compared to the biochemical ones. Non-fermentable lignin, which constitutes from 15% to more than 50% (daf basis) of biomass weight [31], can be decomposed through thermochemical processes. Thermochemical conversion processes operate at higher temperatures and conversion times are much lower due to improved reaction kinetics. As an order of magnitude, thermochemical conversion of biomass takes place within a few seconds or minutes, while biochemical conversion may be completed after several days or weeks [32]. Another characteristic is that the yield of gaseous, liquid or solid final products may vary depending on the process temperature. The temperature window for this conversion pathway is rather wide–operation temperatures can vary between 200 °C and 1400 °C for the various thermochemical processes. A schematic diagram of the four main conversion processes of this category is shown in Figure 1-5. Of course, one can advocate that more processes could be included, such as torrefaction, which is a mild thermal pretreatment of solid fuels at a temperature range of 200-300 °C in the absence of O_2. However, only four main routes are herein described, since most other processes can be considered as subcategories of the ones shown in Figure 1-5.

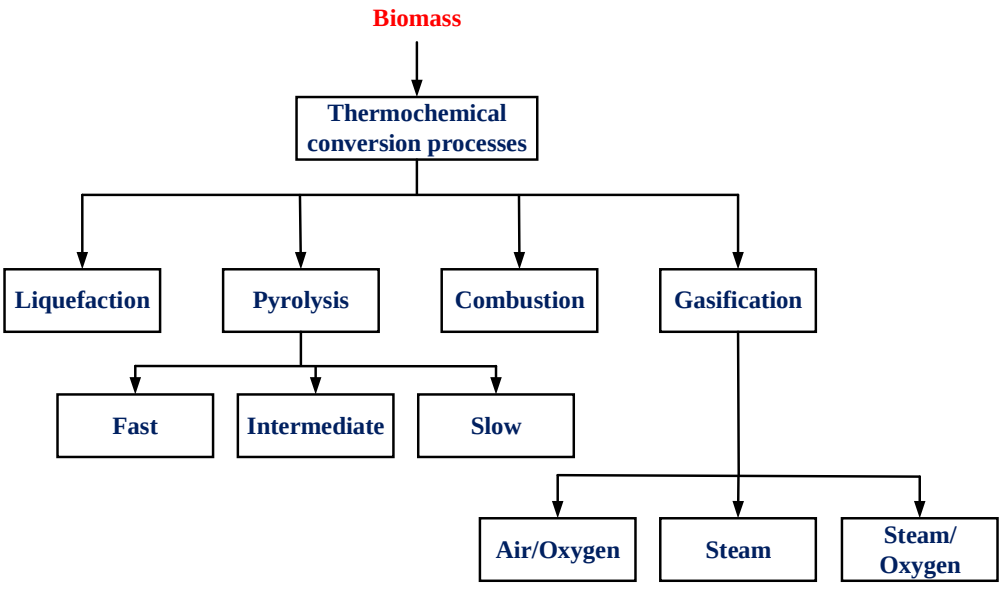

Figure 1-5: Overview of the main biomass thermochemical conversion routes.

Combustion is the oxidation of a fuel with air or pure O_2 (oxy-fuel combustion) in order to release heat. It comprises of a sequence of reactions by which carbon contained in the fuel is oxidized to CO_2 and hydrogen is oxidized to H_2O. The overall combustion process can be divided into several sub-processes such as fuel drying, pyrolysis, gasification and combustion, i.e. various thermochemical processes may take place in parallel during solid fuel conversion [33]. Initially, the fuel is heated and dried, while subsequently devolatilization occurs during which volatile organic components are released. Those volatile compounds are combusted faster compared to the carbon-rich fuel residue (char), which burns more slowly in the furnace [33]. The remaining solid waste after combustion is ideally non-combustible mineral matter (ash), although typically unburnt carbon is also collected. The overall process can be represented by the generalized reaction R 1-2 [34]

$$\begin{gathered} C_{x1}H_{x2}O_{x3}N_{x4}S_{x5}Cl_{x6}Si_{x7}K_{x8}Ca_{x9}Mg_{x10}Na_{x11}P_{x12}Fe_{x13}Al_{x14}Ti_{x15} + \\ nH_2O + n_2(1+e)(O_2 + 3.76N_2) \rightarrow n_3CO_2 + n_4H_2O + n_5O_2 + n_6N_2 + \\ n_7CO + n_8CH_4 + n_9NO + n_{10}NO_2 + n_{11}SO_2 + n_{12}HCl + n_{13}KCl + \\ n_{14}K_2SO_4 + n_{15}C + \ldots + \text{Heat} \end{gathered} \qquad \text{R 1-2}$$

Combustion is carried out with excess O_2 (compared to stoichiometric) and temperature varies between 850 °C and 1450 °C depending on the boiler technology [33, 35-38]. The combustion heat is used to generate high-enthalpy steam in a conventional water/steam Rankine cycle [39] or to evaporate an organic medium in an Organic Rankine Cycle (ORC) [40]. The working fluid then expands in a turbine and produces mechanical work and electricity through a generator. Highly-efficient, supercritical coal combustion plants are state-of-the-art technology for power and CHP generation [41]. Biomass combustion plants are also in operation worldwide, especially for CHP applications [42]. However, research is still conducted on biomass combustion in order to address ash-related issues (high-temperature chlorine corrosion, slagging, fouling, agglomeration problems, etc.) and enhance plant efficiency [43]. Co-firing of coal and biomass is another option for preserving fossil resources in existing large-scale combustion plants [44]. Typically, substitution by up to 20% of coal needs no modifications of the boiler firing system [45].

In hydrothermal liquefaction (HTL), biomass is converted into liquid components by being processed in hot, pressurized water. Temperature, pressure, residence time, feedstock and catalyst type are critical parameters that affect the process yield. Compared to pyrolysis, HTL requires both lower temperatures and lower heating rates [46]. Typically, the process takes place at temperatures in the range 250-375 °C, pressures between 40 and 220 bar and feedstock residence time of *ca*. 15 min. Both continuous and batch-type HTL processes have been reported in the literature [46, 47]. Three steps mainly occur during HTL, namely depolymerization, decomposition and recombination. Biomass decomposes into smaller compounds, which subsequently polymerize to form bio-crude or bio-oil. The resulting products from the phase separation in an HTL plant are a CO_2-rich gaseous stream, bio-oil and an aqueous phase, which can be recirculated in the system.

Bio-crude contains a wide range of organic compounds such as [46, 48]:

- Monoaromatic compounds e.g. phenol, benzene etc.
- Fatty acids e.g. myristic acid, palmitic acid, steric acid etc.
- Alkanes/alkenes e.g. hexadecane/hexadecene, heptadecane/heptadecene etc.
- Polyaromatic compounds e.g. naphthalene, indene, anthracene etc.
- Nitrogen-containing compounds e.g. indoles, pyrazines, piperidines etc.
- Oxygenated compounds e.g. esters, ketones, alcohols, acetic acid etc.

The solid byproduct of the process may be directly used as fertilizer, while the bio-oil stream usually needs further hydrotreatment processing before further utilization. The process layout of an HTL process for lignocellulosic biomass is shown in Figure 1-6. Algal biomass can also be used as feedstock for HTL with the benefit of recycling nutrients back to the cultivation [49]. The HTL aqueous phase which contains organic compounds can be treated through AD or hydrothermal gasification (HTG), indicating material, heat and power integration options. A process efficiency of ca. 85-90% can be achieved during biomass HTL [46].

Pyrolysis is thermal decomposition that takes place in the absence of O_2. Three major products are produced during biomass pyrolysis–a solid product with high carbon content (char), a gaseous product and a liquid product, which is called bio-oil. Crude bio-oil is composed of a complex mixture of oxygenated hydrocarbons (tars and heavier hydrocarbons) and water. Its water content is usually rather high (20 wt.%) due to the biomass

feedstock moisture, as well as to water produced during pyrolysis reactions. Thus, feedstock drying is carried out prior to the reactor to reduce the water content in bio-oil.

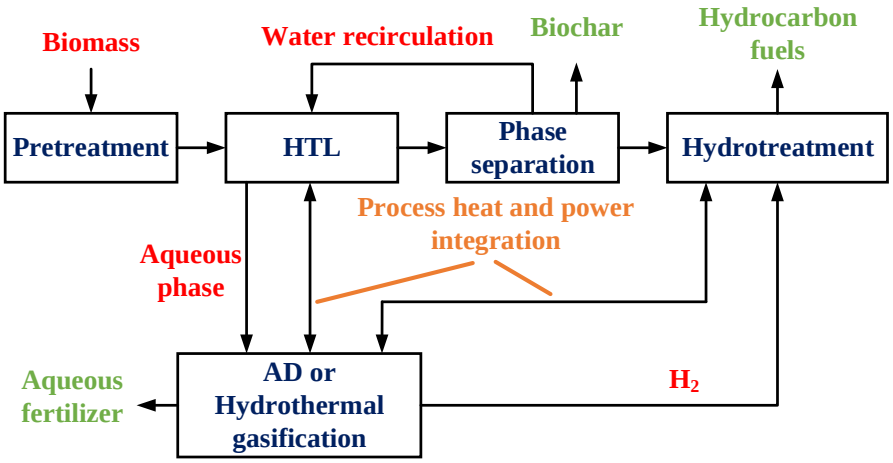

Figure 1-6: HTL process layout for lignocellulosic biomass feedstock (reproduced from [47]).

The process yield varies depending on the temperature and heating rate/residence time. Therefore, pyrolysis can be fast, intermediate and slow (carbonization). Among them, fast pyrolysis has gained particular interest due to its high bio-oil yield which can be in the range of ~75% (per dry feedstock mass as a basis). An overview of process conditions and yield depending on the operating mode/regime is shown in Table 1-3. A comparison to torrefaction has been also included, as the latter process is also termed as "slow, low-temperature pyrolysis".

Table 1-3: Wood pyrolysis product weight yields (dry fuel basis), operating conditions and comparison with torrefaction (adapted from [50]).

Mode	Operating conditions	Liquid (%)	Solid (%)	Gas (%)
Fast pyrolysis	~ 500 °C, short hot vapor residence time ~ 1 s	75 (bio-oil)	12	13
Intermediate pyrolysis	~ 500 °C, medium hot vapor residence time ~ 10-30 s	40 (2 phases)	40	20
Slow pyrolysis (carbonization)	~ 400 °C, long vapor residence time from hours to days	30	35	35
Torrefaction	~ 290 °C, solid residence time ~ 10-60 min	0 (up to 15%, if condensed)	80	20

A description of a typical fast pyrolysis plant is given by Bridgwater [50]. In a fast pyrolysis unit, the first operation stage comprises of feedstock pretreatment. Biomass is dried to below 10 wt.% and it is ground to a small particle size in order to ensure a fast reaction of the fuel in the pyrolyzer. Less than 3 mm particle size is usually needed for achieving high heat transfer rates toward the solid particles. The material is transferred to the reactor (typically, a bubbling or circulating fluidized bed reactor), where fast pyrolysis occurs [24]. The conversion reaction R 1-3 can be used to describe the pyrolysis process

$$C_nH_mO_p(\text{biomass}) \xrightarrow{\text{Heat}} \sum_{\text{liquid}} C_xH_yO_z + \sum_{\text{gas}} C_aH_bO_c + H_2O + C\ (\text{char}) \qquad \text{R 1-3}$$

Subsequently, solid char is removed from the hot vapor to suppress cracking reactions, followed by rapid cooling of the pyrolysis vapors for bio-oil recovery. The gaseous phase contains CO_2, H_2O, CO, H_2, CH_4, C_2H_2, C_2H_4, C_2H_6, C_6H_6 and other traces [24, 51]. Gas and solid char are used within the process to increase energy recovery, so flue gas and ash are the wastes. Bio-oil can be used for energy storage, as it represents an energy carrier with improved properties for transportation compared to raw biomass [52]. It is also a valuable source for producing biofuels and green chemicals. For this purpose, physical, chemical and/or catalytic upgrading processes need to be carried out for its refinement, such as filtering, emulsification, hydrotreating, catalytic vapor cracking, esterification, etc. [50, 53-55]. An overview of methods for fast pyrolysis product upgrading can be found in [56]. A schematic diagram describing possible upgrading routes is shown in Figure 1-7.

Gasification is a widely investigated technology as a first step for the conversion of solid fuels to gaseous and liquid biofuels, such as SNG and alcohols, as well as for power generation. It is a thermochemical conversion process that converts carbonaceous materials into a combustible gas (syngas), which consists mainly of carbon monoxide (CO) and hydrogen (H_2). The process is carried out at elevated temperatures, usually between 800-1500 °C depending on the gasification technology [57]. Air, pure oxygen, steam, CO_2 and mixtures of those are supplied to the reactor as gasification agents. Gasification shares similarities with combustion, for example both operate within a similar temperature range and they share common mechanisms during the first steps of fuel conversion [58]. In addition, both processes can be carried out in similar reactor design concepts (e.g. fluidized bed reactors).

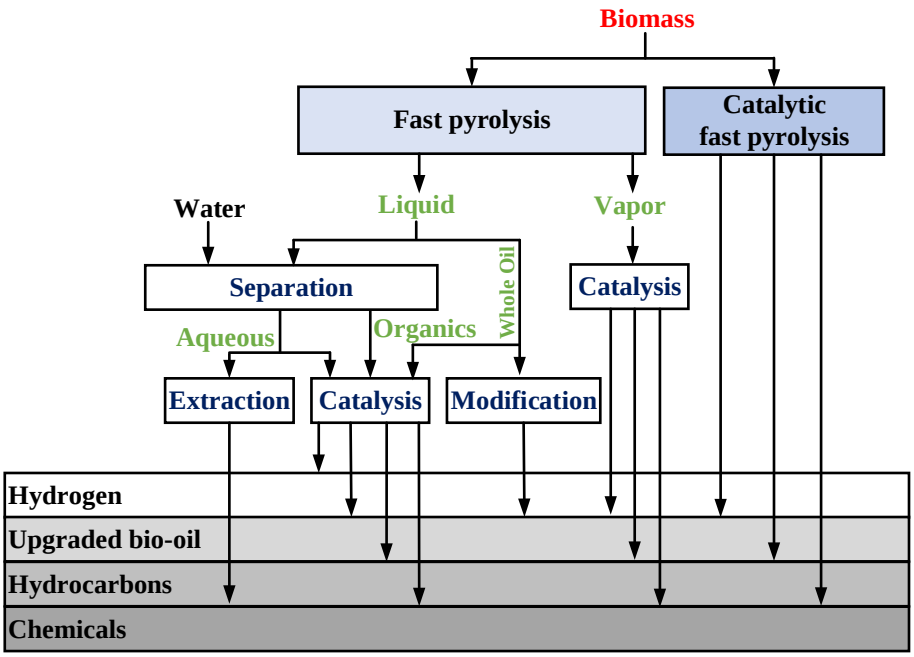

Figure 1-7: Upgrading options for fast pyrolysis products (adapted from [56]).

However, significant differences between combustion and gasification plants can be noted:

- Combustion of solid fuels aims the generation of heat for evaporating and superheating the working fluid and complete oxidation with excess O_2 is needed. During gasification with an oxidizing agent, the fuel is partially oxidized to produce enough heat for the endothermic gasification reactions. The principal output of the process is syngas, a gaseous fuel for subsequent valorization. Moreover, gasification can be carried without partial fuel oxidation inside the gasifier by supplying heat externally to the process (allothermal gasification).
- Gasification is carried out from atmospheric to high pressures (up to 70 bar) [59], while solid-fuel combustion is performed at atmospheric pressure. The main reason for high-pressure operation is the need to utilize syngas downstream of the gasifier for catalytic synthesis or in gas turbines. Storage either of the final gaseous product or other byproduct streams is another motivation for high-pressure gasification.

- The composition of the gasification product gas is essentially different compared to the flue gas derived from solid-fuel combustion. This observation does not only refer to the main gaseous components, but also to syngas contaminants. Of course, this fact necessitates the application of alternative technologies for syngas cleaning taking also into account the requirements of downstream equipment.

The following section of this chapter aims to focus more on the gasification process. Fundamental aspects concerning this thermochemical route will be described, with particular focus on the composition of the product gas and its utilization in downstream applications. This discussion will provide the basis for addressing aspects related to syngas cleanup operations in gasification-based plants.

1.3 Gasification: process mechanism, reactor technologies and syngas quality

1.3.1 Gasification mechanism and reactions

A typical gasification process follows a mechanism which consists of the following steps [58]:

1. Fuel preheating and drying
2. Fuel pyrolysis and/or oxidation
3. Char gasification

The conversion mechanism sequence is illustrated in Figure 1-8. It must be noted that although there are no clearly defined boundaries between the different process steps, solid fuel gasification is commonly described as a sequential process.

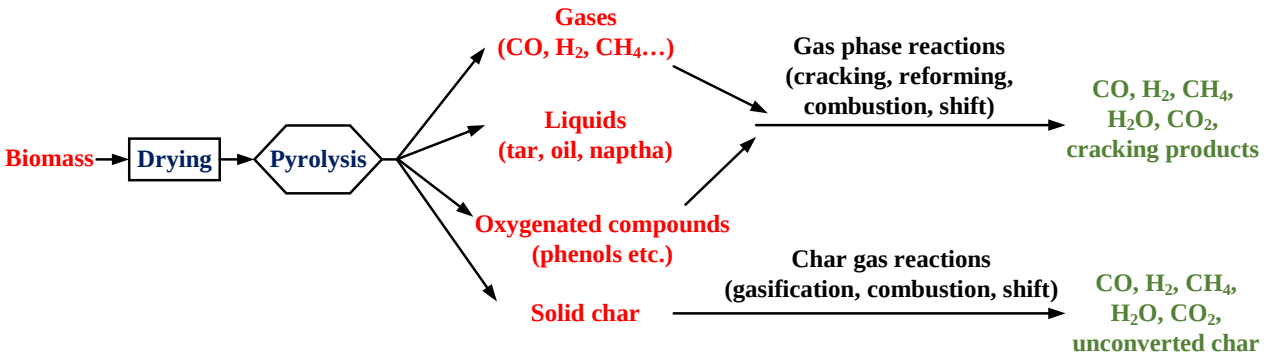

Figure 1-8: Gasification conversion steps (adapted from [24]).

Initially, the fuel enters the reactor, it is heated and moisture is released when fuel temperature increases above 100 °C. The heating of the particle continues up to a temperature of 200 °C and during this stage, volatilization of low-molecular-weight extractives occurs. In order to improve process efficiency, the fuel is pre-dried before the gasifier to moisture content in the range 10-20 wt.%. This is an important step since the moisture content of fuels such as fresh forest residues or empty fruit bunches, a solid biomass waste of palm oil production from fresh fruit bunches, can be up to 50-60 wt.% [60, 61].

As the temperature of the particles rises further, the pyrolysis of the fuel takes place. During this step, larger hydrocarbon molecules decompose to smaller ones and form condensable and non-condensable species. The pyrolysis products include gases, solid char and a wide range of condensable organic compounds, which are also called tars. Then, gas-gas and solid-gas reactions take place among the pyrolysis products themselves and among the pyrolysis products and the gasification agent, such as carbon-gas, oxidation, methanation and reforming reactions, as well as the water-gas shift (WGS) reaction. A list of reactions involving the main syngas species and their enthalpies is presented in Table 1-4.

Table 1-4: Gasification reactions and their enthalpies at 25 °C [24, 62].

Reaction type	Reaction	Enthalpy of reaction (kJ mol^{-1})
Carbon reactions		
R 1-4 (Boudouard)	$C + CO_2 \leftrightarrow 2CO$	+172
R 1-5	$C + H_2O \leftrightarrow CO + H_2$	+131
R 1-6 (Hydrogasification)	$C + 2H_2 \leftrightarrow CH_4$	-74.8
R 1-7	$C + 0.5O_2 \rightarrow CO$	-111
Oxidation reactions		
R 1-8	$C + O_2 \rightarrow CO_2$	-394
R 1-9	$CO + 0.5O_2 \rightarrow CO_2$	-284
R 1-10	$CH_4 + 2O_2 \rightarrow CO_2 + 2H_2O$	-803
R 1-11	$H_2 + 0.5O_2 \rightarrow H_2O$	-242
Water-gas shift reaction		
R 1-12	$CO + H_2O \leftrightarrow CO_2 + H_2$	-41.2
Methanation reactions		
R 1-13	$2CO + 2H_2 \leftrightarrow CH_4 + CO_2$	-247
R 1-14 (CO methanation)	$CO + 3H_2 \leftrightarrow CH_4 + H_2O$	-206
R 1-15 (CO_2 methanation/Sabatier)	$CO_2 + 4H_2 \leftrightarrow CH_4 + 2H_2O$	-165
Methane reforming reactions		
R 1-16 (steam methane reforming)	$CH_4 + H_2O \leftrightarrow CO + 3H_2$	+206
R 1-17	$CH_4 + 0.5O_2 \rightarrow CO + 2H_2$	-36

1.3.2 Gasification technologies and operating conditions

Three major gasification technologies can be identified: fixed or moving bed (FXBG), fluidized bed (FBG) and entrained flow gasifier (EFG) [57]. Those three categories are herein discussed, however, different variations may be found based on those designs. For example, one of the main variations of the FBG technology is the dual fluidized bed gasifier (DFBG), which was also installed at the biomass CHP plant in Güssing, Austria [63]. Currently, plasma-assisted gasification is another technology that is also of great interest [64]. A comparison of gasification technologies is depicted in Table 1-5.

In a FXBG, a bed of fuel is maintained at a constant depth by adding fuel from the top, which subsequently moves downward due to gravity and reacts to produce syngas, proceeding through the gasification steps described in Section 1.3.1. The design of this technology indicates that a stationary reaction zone is maintained in the reactor. In an updraft FXBG, the fuel enters at the top and the gasification agent at the bottom of the reactor. Due to the fact that the oxidation medium is supplied at the bottom, the combustion zone is placed low in the reactor and the heat which is released is consumed at the upper reaction zones to carry out endothermic reactions. Due to the fact that pyrolysis occurs as syngas ascends the reactor, a very high tar yield is usually obtained. In a downdraft FXBG, both biomass and the gasification agent flow in a concurrent way. The fuel which enters the reactor is dried and pyrolyzed. As it flows downwards, air is supplied through a smaller cross-section, also called "throat". The gas flows through a high-temperature combustion zone (1200-1400 °C), where

tar cracking reactions occur. Since a reduction zone is downstream of the combustion zone, additional cracking occurs due to the presence of char, further decreasing the tar content. The FXBG technology is commercially available for low capacities (< 10 MW_{th}) and it is common in coal gasification projects. Commercial FXBG concepts are the BGL slagging type and Lurgi dry ash [57].

FBGs are considered particularly suitable for biomass gasification compared to other technologies. The gasification agent is also used to fluidize a bed of fine particles (250-500 μm), such as sand, olivine or other material. The operation under a fluidization regime ensures improved heat and mass transfer in the reactor. This fact is associated with several advantages such as the possibility to handle diverse feedstocks and the potential to carry out *in situ* syngas cleaning (sorbents) or catalysis depending on the type of bed material. Fluidized bed reactors have proven to be appropriate for upscaling and the technology is now commercially available up to a few hundreds of MW_{th} for a wide range of biomass fuels, especially for combustion applications [65]. FBGs can mainly be categorized into bubbling fluidized bed (BFBG) and circulating fluidized bed gasifiers (CFBG). Both technologies share the same principle of bed material fluidization, however, they differ in the fact that CFBG reactors operate at higher superficial velocities and they are designed for material recirculation (through a cyclone and downcomer) for extending the solid residence time and improving fuel conversion to syngas. FBGs operate at lower temperatures (1000 °C max.) compared to other categories to avoid agglomeration due to fusible ash, a limiting parameter especially for biomass fuels [66]. The operation pressure of FBGs ranges from atmospheric up to 35 bar [67].

EFGs have been a widely adopted technology in coal gasification projects. In an EFG unit, the fuel is firstly dried and pulverized to about 75-100 μm. It is then transported to the reactor by a carrier gas flow and it is mixed with the oxidation/gasification agent. A typical EFG operates at high temperatures (~ 1400 °C) and high pressures (20-70 bar).

Table 1-5: Comparison of major gasification technologies (data from [20], [24] and [68]).

Parameter	**Fixed bed gasifier**	**Fluidized bed gasifier**	**Entrained flow gasifier**
Feed size	< 51 mm	< 6 mm	< 150 μm
Tolerance for fines	Poor	Good	Excellent
Tolerance for coarse	Very good	Good	Poor
Reactor temperature (°C)	1090	800-1000	Up to 2000
Typical feedstock type	Low-rank coal	Low-rank coal and Biomass	Coal (any type)
Oxidant requirement	Low	Moderate	High
Nature of ash	Dry	Dry	Slag
Temperature profile	High gradients	Vertically almost constant Little radial variation	Above the ash melting temperature
Tar content (g Nm^{-3})	0.015-150	4-60	0.01-4
Process flexibility	Very limited	Improved load and fuel flexibility	Very limited (especially regarding fuel properties)
Capacity (MW_{th} input)	0.01-10	2-100	50-1000
Disadvantages	-High tar (updraft) and char yield -Non-uniform temperature profile	-High particle content in syngas -Economics not favorable for small-scale units	-Energy consumption of fuel grinding -Raw gas cooling -Short gasifier refractory lifetime

Fuel particles are entrained due to the gas velocity, while fuel ash melts ("slag") because of the high reactor temperature and flows downwards on the reactor walls. Both dry- and slurry-feeding technologies have been developed for EFGs. Slurry-fed gasifiers usually require higher reactor volumes to accommodate water vapor after evaporation and they also consume more oxygen (~ 20% more than dry-fed EFGs). A few of the most

well-known technologies adopt EFGs e.g. PRENFLO, the Shell Coal Gasification Process (SCGP), E-gas, Texaco/GE, etc. [57]. The syngas tar content of EFGs is very low due to the high operating temperature. Under such conditions, mainly light tars with low molecular weights are produced.

Gasification can be carried out with various agents as already described, mostly O_2, air or steam. The term "autothermal gasification" denotes that partial oxidation of the fuel (with air or pure O_2) takes place inside the gasifier to provide heat to the process. On the other hand, the term "allothermal gasification" indicates that heat is provided by an external source to the process. This is the case when steam gasification is carried out. Combustion is usually performed in a different reactor (e.g. fluidized bed) and heat is transferred by bed material recirculation (e.g. DFBG [69]), alkali heat pipes (e.g. Heatpipe Reformer [70]) or other concepts.

The equivalence ratio (ER or λ) and the steam-to-biomass ($STBR$) or steam-to-fuel ratio are important gasification parameters which influence the process quality. The first is defined in Equation 1-1

$$\lambda = \frac{\left(\frac{\dot{m}_{air}}{\dot{m}_{fuel}}\right)_{actual}}{\left(\frac{\dot{m}_{air}}{\dot{m}_{fuel}}\right)_{stoich}} \qquad \textit{Equation 1-1}$$

where $\dot{m}_{air}$ is the mass flow rate of air (kg s^{-1}) and $\dot{m}_{fuel}$ is the mass flow rate of the fuel (kg s^{-1}).

The λ for stoichiometric combustion is by definition equal to unity. During gasification with an oxidation agent, it is usually in the range $0.2 < \lambda < 0.4$. The reactor temperature is correlated with λ, since a higher λ means that more fuel is oxidized and thus gasification temperature rises. Accordingly, $STBR$ is defined in Equation 1-2

$$STBR = \frac{\dot{m}_{steam} + \dot{m}_{moist,fuel}}{\dot{m}_{fuel}} \qquad \textit{Equation 1-2}$$

where $\dot{m}_{steam}$ is the mass flow rate of steam (kg s^{-1}) and $\dot{m}_{moist,fuel}$ is the mass flow rate of incoming fuel moisture (kg s^{-1}). The $STBR$ parameter typically varies between 0.2 and 2.0 [71].

1.3.3 Syngas composition, contaminants and gasification efficiency

Syngas generally consists of five major gaseous compounds, which are H_2, CO, CH_4, CO_2 and H_2O. Factors that principally affect syngas composition are the gasification agent type, λ (and temperature accordingly), *STBR*, fuel composition, reactor technology, operation pressure, syngas residence time and type of bed material (catalytic or not) [68]. When syngas is used in synthesis applications, gasification conditions need to be adjusted so that the composition of specific gases (or more correctly, the ratio between specific gases) is suitable for downstream utilization. Gasification with steam increases the H_2 content in syngas, which can be important when synthesis involving H_2 is carried out downstream of the gasifier. For instance, an H_2 concentration of 64 vol% was reported by Weerachanchai et al. for steam gasification of wood in a FBG [72]. Indicatively, a comparison of syngas quality from two commercial gasifier types, a CFBG fueled with biomass (air-blown) and an EFG fueled with coal (O_2/steam-blown), is shown in Table 1-6. Considering the fate of the input carbon to the process, most of it participates in gasification reactions and it ultimately migrates to the major syngas gaseous species. However, not all carbon is converted to the main gaseous compounds. Solid char and condensable tars which are produced during the pyrolysis step of gasification are also contained in syngas. Two efficiency indices are commonly applied to quantify gasification efficiency.

The carbon conversion efficiency (CCE) is an index which indicates the ratio of inlet carbon which is converted to gaseous products (condensable or not) as shown in Equation 1-3

$$CCE = \frac{\sum_{i=CO_2,CH_4,CO,C_xH_y,tar} \dot{m}_{C,i}}{\dot{m}_{C,fuel}} \cdot 100\% \qquad \textit{Equation 1-3}$$

where $\dot{m}_{C,i}$ is the carbon mass flow rate in each syngas component (kg h^{-1}) and $\dot{m}_{C,fuel}$ is the carbon mass flow rate entering the gasifier with the feedstock (kg h^{-1}).

Table 1-6: Syngas composition and specifications of commercial gasifiers (data from [24]).

Reactor type	**CFBG**	**EFG**
Feedstock	Biomass	Coal
(Syngas components are given in vol.%)		
H_2	7-20	24
CO	9-22	67
CO_2	11-16	4
CH_4	< 9	0.02
H_2O	10-14	3
Higher hydrocarbons	< 4	0
N_2	46-52	1
NH_3	~ 0	0.04
Tar	< 1	0
O_2	0	0
H_2S	< 0.1	1
H_2/CO ratio	0.6-1.0	0.36
Heating value (MJ m^{-3})	4.0-7.5	9.5
Fuel flow rate (t d^{-1})	9-108	2155
Pressure (bar)	1-19	30
Temperature (°C)	800-1000	1400
Gasification agent type	Air	O_2/steam

The second performance index which is commonly used is the cold gas efficiency (CGE) defined in Equation 1-4

$$CGE = \frac{\dot{m}_{syngas} LHV_{syngas}}{\dot{m}_{fuel} LHV_{fuel}} \cdot 100\% \qquad \textit{Equation 1-4}$$

where $\dot{m}_{syngas}$ is the syngas mass flow rate (kg h^{-1}), $\dot{m}_{fuel}$ is the fuel mass flow entering the gasifier (kg h^{-1}) and LHV_{syngas} and LHV_{fuel} are the syngas and fuel *LHV* (MJ kg^{-1}), respectively. Table 1-7 summarizes values for *CCE* and *CGE* based on thermodynamic modeling and experimental investigations in the literature. Concerning *CCE*, it typically lies between 80% and ~100%. On the other hand, *CGE* can deviate substantially depending on the technology, fuel and operating conditions–it can be as low as 40% to as high as 75-90%. Of course, deviations between various studies reported in Table 1-7 also reflect different definitions of efficiency indices. However, they provide an overview of the range of *CCE* and *CGE* values in biomass gasification.

Table 1-7: Gasification performance indices (CCE and CGE) from experimental and modeling studies.

Type	**Description**	***CCE (%)***	***CGE(%)***	**Source**
Exp.[1]	Biomass gasification in O_2/steam-blown pilot CBFG with λ: 0.33-0.47 and *STBR*: 0.81-1.52	74.0-96.6	47.0-71.5	[73]
Tm.[2]	Biomass gasification screening (80 fuels) based on thermodynamic equilibrium (λ=0.4, *P*=1 bar, air-blown)	> 84.0%	66.0-92.0	[74]
Exp.+Tm.	Wood (sawdust) gasification in pilot CFBG, T: 700-850 °C, air-blown	81.6-100.0 (Exp.)	44.2-71.4 (Exp.) Up to 95 (730 °C, Tm.)	[75]
Exp.+Tm.	O_2-blown wood gasification in EFG reactor λ: 0.25-0.50, *P*: 2 bar and 7 bar	~100.0	56.0-75.0 (Exp.) Up to 90 (Tm.) for 0.25<λ<0.35	[76]
Exp.	Steam-blown wood gasification in BFBG (lab-scale), *T*: 650-750 °C	73.6-97.7	33.4-79.6	[72]

[1]Exp.=experimental study, [2]Tm.=thermodynamic modeling

According to [56], for a conversion of 85% of inlet biomass (by mass) to gases, *ca.* 10% and 5% of inlet biomass are converted to solid (char) and condensable products (tar species), respectively. In addition, apart from the main product gas compounds, char and tar, other species containing alkali species, sulfur (S), chlorine (Cl) and nitrogen (N) are present. The proximate, ultimate and ash analyses of three biomass fuels compared to low-rank coal (lignite) are shown in Table 1-8.

As shown in Table 1-8, biomass is characterized by a much higher volatile matter content compared to lignite. In addition, while its ash content is generally lower, the elemental distribution is much different. The content of alkali species, particularly potassium (K), is higher than coal. The S content of biomass is typically low (< 0.5 wt.%, daf basis), with the exception of specific species such as black liquor, sewage sludge, animal biomass and a few kinds of grass. In addition, Cl content of agricultural residues, such as straw, can be much higher compared to coal, which raises concerns over corrosion issues at high temperatures. The concentration of these species in syngas strongly depends on their content in the feedstock. In the following section, the main contaminants in syngas derived from solid fuel gasification are briefly discussed.

Table 1-8: Proximate, ultimate and ash analyses of biomass and coal fuels (data from [77]).

Solid fuel type	Lignite	Spruce wood	Wheat straw	Switchgrass
Proximate analysis (wt.%, db)				
Volatile matter	36.7	81.2	74.8	80.4
Fixed carbon	28.7	18.3	18.1	14.5
Ash	34.6	0.5	7.1	5.1
Ultimate analysis (wt.%, daf)				
C	64.0	52.3	49.4	49.7
O	23.7	41.2	43.6	43.4
H	5.5	6.1	6.1	6.1
N	1.0	0.3	0.7	0.7
S	5.8	0.1	0.17	0.11
Cl (wt.%, db)	0.01	0.01	0.61	0.08
Ash analysis (wt.% in ash)				
SiO_2	44.87	49.30	50.35	66.25
CaO	13.11	17.20	8.21	10.21
K_2O	1.48	9.60	24.89	9.64
P_2O_5	0.20	1.90	3.54	3.92
Al_2O_3	17.11	9.40	1.54	2.22
MgO	2.50	1.10	2.74	4.71
Fe_2O3	10.80	8.30	0.88	1.36
SO_3	8.64	2.60	4.24	0.83
Na_2O	0.48	0.50	3.52	0.58
TiO_2	0.81	0.10	0.09	0.28

1.3.3.1 Tar compounds

Tar is the most abundant syngas contaminant considering the mass conversion ratio of initial feedstock. According to the definition given by experts from EU, IEA and US DOE in 1998, the term "tar" considers all syngas organic compounds with a molecular weight equal or greater than benzene [78]. The term includes oxygenated and phenolic compounds, olefins, aromatic and polyaromatic hydrocarbons (PAHs) produced during gasification. The tar formation steps (mechanism) are shown in Figure 1-9.

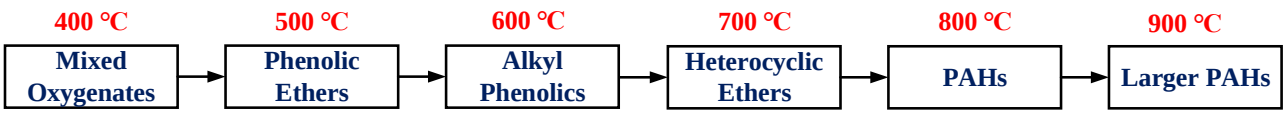

Figure 1-9:Mechanism of tar formation during gasification of solid fuels (adapted from [79]).

At low temperatures (400-500 °C), oxygenated hydrocarbons and phenolic compounds are formed. At higher temperature levels (800-900 °C) and prolonged residence time, heavy aromatic and reduced hydrocarbons are produced, however, the overall amount of tar in syngas decreases. The latter compounds are generally more stable and do not take part in further reactions. Accordingly, a grouping of tars to primary, secondary and tertiary is done based on the aforementioned mechanism. Primary tars are those which are directly released during fuel pyrolysis (e.g. furfurals). Secondary tars, such as phenolics, and tertiary tars, such as PAHs, are those which are gradually formed when temperature and residence time increase. The various tar species which are present in the product gas can be classified in five (5) categories or classes, as shown in Table 1-9. Classes 1, 4 and 5 contain tar compounds with low boiling points, which are responsible for fouling and clogging issues in biomass gasification plants, since they condense even at high temperatures (above 300 °C). Class 2 compounds are tars which are soluble in water and thus, they are collected in scrubber wastewater streams. Furthermore, Class 3 species are light tars which do not pose threats of clogging as they do not condense even at low temperature. Furthermore, they can be reformed in catalytic syngas upgrading operations. Values for the estimated tar content depending on the gasifier technology have been reported in Table 1-5.

Table 1-9: Tar classification and properties (based on [80] and [81]).

Class	Description	Properties	Representative compounds
1	GC-undetectable	Very heavy tars, undetectable by gas chromatography.	Determination: Subtracting GC-detectable tars from total gravimetric tar.
2	Heterocyclic aromatics	Tars with hetero-atoms, very soluble in water.	Pyridine (C_5H_5N), phenol (C_6H_5OH), cresols (C_7H_8O) etc.
3	Light aromatic (1 ring)	Mostly 1-ring light hydrocarbons, no condensation issues.	Toluene (C_7H_8), xylene (C_8H_{10}), styrene (C_8H_8) etc.
4	Light PAHs (2-3 rings)	2- and 3-ring species, they condense at low temperature at low concentrations.	Indene (C_9H_8), naphthalene ($C_{10}H_8$), anthracene ($C_{14}H_{10}$) etc.
5	Heavy PAHs (4-7 rings)	Larger than 3-ring compounds, they condense at high temperatures at low concentrations.	Fluoranthene ($C_{16}H_{10}$), coronene ($C_{24}H_{12}$) etc.

1.3.3.2 Sulfur compounds

Sulfur is present in syngas in inorganic and organic sulfur compounds. For both coal and biomass gasification, most of S is emitted in the form of hydrogen sulfide (H_2S), while it is also found as carbonyl sulfide (COS) and carbon disulfide (CS_2) at lower concentrations [82-84]. Jazbec et al. [85] calculated the equilibrium composition of coal gasification in a Texaco gasifier and S conversion to H_2S and COS was found to be 95% and 5%, respectively. In the aforementioned study, an H_2S concentration of ca. 950 ppmv was calculated for coal gasification at equilibrium conditions, concluding that at temperatures below 1000 °C, all S radicals are recombined to H_2S independently of the cooling rate. On the other hand, biomass gasification produces syngas with H_2S concentration in the order of 100 ppmv. According to Woolcock et al. [79], S-containing contaminants may range from 0.1 mL L^{-1} to more than 30 mL L^{-1}, depending on the S content of the feedstock. In Table 1-10, the major reactions involving S-species are shown. Reactions towards SO_3 and H_2SO_4 have not been included.

Table 1-10: Gasification reactions involving the main sulfur species [84].

Fuel devolatilization reaction		Gas-phase reactions	
$\text{Fuel} - \text{S} + \text{heat} \rightarrow \text{H}_2\text{S} + \text{COS} + \text{Char} - \text{S} + \ldots$	R 1-18	$\text{H}_2\text{S} + \frac{3}{2}\text{O}_2 \rightarrow \text{SO}_2 + \text{H}_2\text{O}$	R 1-22
Char oxidation reactions		$\text{CO}_2 + \text{H}_2\text{S} \leftrightarrow \text{COS} + \text{H}_2\text{O}$	R 1-23
$\text{Char} - \text{S} + \text{CO}_2 \rightarrow \text{COS}$	R 1-19	$\text{H}_2\text{S} + \text{CO} \leftrightarrow \text{H}_2 + \text{COS}$	R 1-24
$\text{Char} - \text{S} + \text{H}_2\text{O} \rightarrow \text{H}_2\text{S}$	R 1-20	$\text{COS} + \text{H}_2\text{S} \leftrightarrow \text{CS}_2 + \text{H}_2\text{O}$	R 1-25
$\text{Char} - \text{S} + \text{O}_2 \rightarrow \text{SO}_2$	R 1-21	$\text{CS}_2 \leftrightarrow \text{C} + \frac{2}{\text{x}}\text{S}_\text{x}$	R 1-26

Apart from H_2S, COS and CS_2, organic sulfur compounds are also found in the product gas. Common organic sulfur compounds in syngas are mercaptans or thiols (such as methanethiol, CH_3SH, and ethanethiol, C_2H_6S), thioethers, thiophenes (such as thiophene, C_4H_4S), benzothiophenes (C_8H_6S), as well as dibenzothiophenes ($C_{12}H_8S$) [82, 86-88]. Kaufman Rechulski et al. [88] quantified several organic sulfur compounds which are present in the syngas of a lab-scale BFBG. The experimental campaigns involved two fuels (wood, grass) and measurements were carried out through quench sampling and GC-SCD analysis. Organic sulfur compounds (OSCs) with boiling points between 80 °C and 300 °C were measured and it was found that thiophenes (thiophene, methyl thiophene) and benzothiophene are prevalent contaminants in the product gas. Depending on the fuel type and λ value, the sulfur concentration in organic compounds varied in the range 3.2-61.5 mg S Nm^{-3}. For a sulfur content about an order of magnitude higher in grass compared to wood, total sulfur concentration quantified by GC was also about an order of magnitude higher in the syngas of the former fuel. In another study, Cui et al. measured the thiophene and benzothiophene concentrations in a wood-fueled FBG, which corresponded to 5.6 and 0.8 mg S m^{-3}, respectively [83]. In addition, concentrations of H_2S, thiols and thiophenes in the syngas (dry basis) of the Güssing biomass gasifier have been reported to be 200 mg S m^{-3}, 20 mg S m^{-3} and 7 mg m^{-3}, respectively [89]. Although the quantification of thiophenic sulfur compounds in syngas is frequently omitted, their content in "clean" syngas can be still significant, since several of them cannot be separated by typical syngas cleaning processes, including acid gas removal (AGR) units [90]. Therefore, this is a field of research that has gained a lot of interest.

Significant effort has been made to develop processes and materials for removal of S-compounds from syngas due to several issues related to their presence:

1. Sulfur compounds are responsible for the corrosion of metal surfaces [91]. Sulfur species such as H_2S adsorb into metal surfaces. This is one of the reasons that specialized S-inert coatings for piping, storage tanks and other equipment are commercially available for accurate measurement and handling of sulfur compounds (e.g. SilcoNert® coatings [92]).
2. When syngas is burnt, sulfur compounds in syngas are oxidized to sulfur dioxide (SO_2). This is, in general, a regulated pollutant and reference documents concerning its emission levels exist (country- or union-specific), such as in EU [93].
3. More importantly, sulfur components are major catalyst poisons. They are capable of deactivating common catalyst types after a short operation time, even when present at low levels [94].

1.3.3.3 Nitrogen compounds

Nitrogen is released from proteins or heterocyclic aromatic compounds in biomass during pyrolysis of the feedstock [95]. Ammonia (NH_3) and hydrogen cyanide (HCN) are the major nitrogen contaminants in syngas and the concentration of the former is usually an order of magnitude higher (or even more) than other nitrogen species. Ammonia is produced by primary biomass decomposition reactions or from HCN in secondary reactions taking place in the gas phase. Under an H_2-rich atmosphere and for sufficient residence time, most of HCN is converted to NH_3, while the main gasification equilibrium product at specific temperature and residence time is eventually N_2 [79]. Ammonia concentration can significantly vary taking into account that N concentration in biomass can be as low as 0.1 wt.% (daf) for woody biomass to as high as 12 wt.% (daf) for meat and bone meal (MBM). Cheah et al. reported NH_3 concentration values from several biomass gasification

studies to lie in the range 500-14000 ppmv [96]. The main issues in gasification-based plants attributed to nitrogen contaminants are the following:

1. Nitrogen oxides (NO_x) are released during syngas combustion. Similarly to SO_2, NO_x compounds are regulated pollutants, a fact that necessitates their abatement.
2. Nitrogen compounds can cause problems in the syngas cleaning section itself or induce catalyst poisoning during product gas upgrading [79].

1.3.3.4 Chlorine and alkali compounds

Biomass contains alkali metal salts, which vaporize at high-temperature conditions and react with steam to produce hydrochloric acid (HCl). This is the main chlorine species in syngas and it usually varies in the range 1-200 ppmv in biomass gasification [96]. In addition, HCl participates in secondary gas-phase reactions with N and alkali species so that ammonium chloride (NH_4Cl) and sodium chloride (NaCl) are produced. The latter compounds are generally responsible for fouling and deposit formation in colder parts of the syngas pathway. Moreover, chlorine species cause corrosion of gas turbine blades due to the high operating temperature and they are known to be poisons for NH_3 and MeOH synthesis [63, 79]. Chlorine compounds such as Cl_2, HCl, CH_3Cl, C_2H_3Cl can deactivate SOFC catalysts at concentrations below 10 ppmv, due to various effects such as agglomeration and alteration of anode microstructures [97].

Alkali species can react with ash components and produce non-volatile species which are removed as bottom ash from the reactor. However, a fraction of alkalis (especially K and Na) vaporizes and it is entrained with syngas out of the gasifier at temperatures above *ca*. 600 °C. Along with the evaporation of metal and alkali catalysts used for downstream syngas processing, several problems such as fouling, corrosion, slagging and sintering in boilers, as well as catalyst poisoning can be induced [79].

1.3.3.5 Particulate matter

Particulate matter contents exceeding specific limits are associated with issues such as fouling and equipment erosion. In general, particulate matter in syngas is a mixture of solids such as:

a. Char: Solid char which was not converted to gaseous compounds through oxidation or char gasification reactions. Gómez-Barea et al. reported that the C content in fly ash collected from the main cyclone of a waste-fueled BFBG was between 9 and 20 wt.% [98], while Christodoulou et al. reported that the ratio of inlet fuel-C which was collected in fly ashes of biomass gasification in a CFBG was between 0.025 and 0.18 [99].

b. Bed material: Fines from the bed material (including catalysts) of FBGs can be entrained by the syngas flow and collected with fly ash.
c. Fuel ash species: Inorganic content such as K, Na, Mg, Si, Fe, Al and trace elements that derive from solid fuel ash are collected with the fly ash [99].

Van der Drift et al. measured dust concentrations in the range 1.7-13.1 g Nm^{-3} at the outlet of a biomass CFBG unit for different fuel types [100]. Apart from fly ash composition and content in syngas, its particle size distribution (PSD) is particularly important for the design of dust cleanup equipment. The PSD may significantly vary depending on the fuel and process. Guo et al. reported average particle sizes of 60-100 μm when sampling syngas from various ports of a lab-scale, slurry/coal-fueled EFG [101]. Gustafsson et al. [102] carried out particulate sampling in wood-fueled BFBG and CFBG reactors and found that the coarse particle content from the latter was an order of magnitude higher compared to the former. The PSD curve peaked at *ca*. 3 μm (aerodynamic diameter), while peaks at diameters < 0.1 μm were also measured, attributed to nucleation and condensation of syngas species. In most cases, particle diameters from the sub-μm scale to over 100 μm are expected [79].

Table 1-11 contains a literature review about contaminant levels in gasification product gases. Concentration values and/or ranges for the major categories which have been presented (S-species, N-species, tar compounds, Cl and alkali species) are shown.

Table 1-11: Review of contaminant concentrations in syngas (biomass- or coal-derived).

Contaminant	Description	Concentration value/range	Source
Tar species			
Total tar content	8 MW_{th} DFBG Güssing (biomass chips)	1.5-4.5 g Nm^{-3}	[63]
Total tar content	0.8 MW_{th} DFBG Milena/ECN (wood pellets)	40 g Nm^{-3}	[103]
Benzene (C_6H_6)	O_2-blown EFG reactor (forest residues)	1200 ppmv (at 1100 °C) < 100 ppmv (> 1400 °C)	[76]
Total tar content and GC analysis of tar species	Air-blown FXBG (Updraft gasifier) fueled with beechwood chips	Grav. tar: 14-16 g Nm^{-3} BTX[2]: 0.7 g Nm^{-3} Phenol: 0.4 g Nm^{-3} Acenapthene: 0.6 g Nm^{-3}	[104]
Total tar content	Air-blown CFBG fuelled with wood, sunflower and Jatropha cake residue	2.2-10.8 g Nm^{-3}	[99]
Total tar content and GC analysis of tar species	Steam-blown lab-scale FBG, tests with wood chips	Grav. tar: 3.8-5.8 g Nm^{-3} BTX: 10.2 g Nm^{-3} Naphthalene: 2.3 g Nm^{-3} Anthracene: 0.2 g Nm^{-3}	[83]
Sulfur species			
H_2S/COS (total)	O_2-blown coal EFG (Shell gasifier)	1000-10000 ppmv	[105]
H_2S/COS/CH_4S	O_2-steam blown CFBG fueled with high-sulfur biomass (dry distiller's grains with solubles, DDGS)	H_2S: 2400 ppmv COS: 40-125 ppmv CH_4S: 0.3 ppmv	[73]
H_2S	Tests in CFBG for ten (10) residual biomass fuels	50-230 ppmv	[100]
H_2S/OSCs[1]	8 MW_{th} DFBG Güssing	H_2S: 0.2 g S m^{-3} Thiols: 0.02 g S m^{-3} Thiophenes: 0.007 g S m^{-3}	[89]
H_2S/COS/OSCs	Steam-blown lab-scale FBG, tests with wood chips	H_2S: 93.3 ppmv COS: 1.7 ppmv Thiophene: 0.006 g S Nm^{-3} Benzothiophene: 0.001 g S Nm^{-3}	[83]
OSCs	10 kW BFBG fueled with grass and wood	(results for grass, all in g S Nm^{-3}) Tot. OSCs: 0.045-0.061 Thiophene: 0.036-0.046 Benzothiophene: 0.003-0.004	[88]
Nitrogen species			
NH_3/HCN	O_2-blown coal EFG (Shell gasifier)	1800-2000 ppmv	[105]
NH_3	Tests in CFBG for ten (10) residual biomass fuels	400-12500 ppmv	[100]
NH_3	Steam-blown lab-scale FBG, tests with wood chips	2134-3617 ppmv	[83]
Chlorine and alkali species			
HCl	O_2-blown coal EFG (Shell gasifier)	40-600 ppmv	[105]
HCl	CFBG tests of ten (10) residual biomass fuels	1-200 ppmv	[100]
Alkali species	Steam-blown BFBG with three biomass fuels (willow, DDGS, agrol)	Sodium (Na): up to 60 ppbv Potassium (K): 150-400 ppbv	[106]

[1]OSCs: organic sulfur compounds, [2]BTX: benzene/toluene/xylene(s)

1.4 Coupling gasification with downstream processes: syngas cleaning aspects

Syngas derived from gasification can be used as fuel in efficient engines and electrochemical devices, but it can also be upgraded through catalytic processes to produce valuable products. This section reviews indicative applications of gasification for energy, fuels and chemicals.

1.4.1 Gasification for power and CHP generation

When syngas is produced for power or CHP generation, four applications are of particular interest: co-firing in boilers, combustion in gas engines, combustion in gas turbines and utilization in high-temperature fuel cells. In the case of co-firing with renewable or non-renewable fuels in boilers (coal, heavy oil, biomass), there is the benefit of using existing infrastructure for syngas combustion, while more importantly, syngas cleanup requirements are less strict compared to other applications [107]. Regarding utilization in gas engines, the layout of the Güssing CHP plant is shown in Figure 1-10. The plant generates 2 MW_{el} and 4.5 MW_{th} district heating and it is based on allothermal gasification with steam. The hot, raw syngas from the gasifier is initially cooled in the syngas cooler and it subjected to particulate removal through a fabric filter and rape-oil-methyl-ester (RME) scrubbing for tar removal. The electrical efficiency of the Güssing CHP plant is 20-25% (the latter value being the design value). A similar thermal efficiency at 27% was reported in the thermodynamic study of Francois et al. for coupling biomass gasification with a gas engine (BGGE) [108]. Cogeneration efficiencies in the range 65-90% can be obtained by extracting heat from the gas engine cooling jackets and through flue gas cooling.

Gas turbines (GT) are highly-efficient engines that can be also fueled with syngas. Regarding process thermodynamics, electrical efficiencies of coal IGCC plants can exceed 50% without CO_2 capture [109] and *ca.* 40% with CO_2 capture ($\geq$ 90% capture efficiency) [110]. The technology involves the utilization of waste heat from the GT flue gas in a Heat Recovery Steam Generator (HRSG) to increase the plant power output through a water/steam Rankine cycle. Biomass IGCC (BIGCC) plants are investigated as an alternative technology since the 1990s [111]. For instance, the commissioning of the Värnamo plant (Sweden) was an important step for acquiring operational experience in Europe [112].

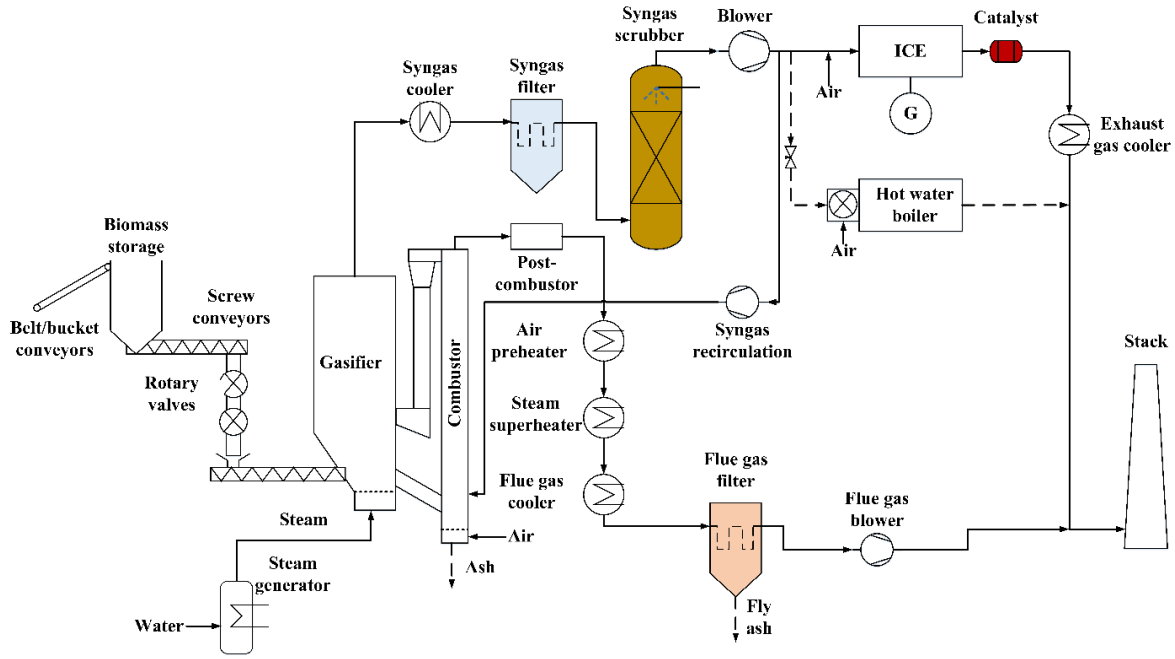

Figure 1-10: Biomass gasification CHP plant in Güssing, Austria (gas cleaning with colors, modified from [113]).

The Värnamo BIGCC CHP plant was designed to have an output of 6 MW_{el} and 9 MW_{th} district heating and a net electrical efficiency of 32%, i.e. significantly higher compared to the Güssing BGGE plant. The plant

featured a rather simplified gas cleaning section with syngas cooling and hot gas filtering prior to the gas turbine. However, the syngas cleaning system of an IGCC plant is in general complex. Process steps such as tar cracking, particulate filtration and solvent scrubbing are required, including sulfur removal for high-sulfur fuels [109, 114, 115]. Furthermore, higher capacities of 20-300 MW_{th} (fuel thermal input) apply for BIGCC plants compared to 8-50 MW_{th} for BGGE plants [116].

Among different alternatives, syngas utilization in fuel cells has the potential to achieve high electrical efficiencies even at low power capacities of 100-250 kW_e [70]. For gasification applications, molten carbonate fuel cells (MCFC) and solid oxide fuel cells (SOFC) are the most suitable technologies [117]. SOFCs benefit from several aspects of biomass gasification; steam in the syngas stream can be used to shift CO to H_2 and reform CH_4 and light hydrocarbons, while the high operating temperature (700-950 °C) offers possibilities for heat integration with the gasification process itself. The electrical efficiency of a biomass gasification SOFC (BGSOFC) plant is 35-40% [70] and it escalates above 50% for hybrid SOFC/GT configurations [118]. The syngas cleaning system preceding a high-temperature fuel cell must be capable of eliminating all major syngas contaminants. Particulate filtration, choline, sulfur and tar removal are critical aspects for the operation of a BGSOFC plant, while additional syngas conditioning may be required to avoid carbon deposition phenomena [70].

1.4.2 Gasification for fuel and/or chemical production and polygeneration

Gasification can be the base process for producing a wide variety of fuels and chemicals, as shown in Figure 1-11. Such products can be produced directly from syngas or indirectly e.g. by firstly converting syngas to MeOH, which is one of the main syngas-derived products, and then methanol to other derivatives. Hydrogen, a widely investigated energy carrier for the future economy and important feedstock for the chemical industry, can be produced by combining gasification with the WGS reaction and CO_2 separation from the WGS product [119]. Ammonia can be produced through subsequent synthesis with N_2 over a Fe catalyst. Moreover, syngas can be processed to produce fuels and chemicals such as SNG, EtOH, mixed alcohols, FT products (C_{20+} linear hydrocarbons, C_{5+} paraffins, medium weight olefins etc. and ultimately, transportation fuels) and aldehydes. A comprehensive review of the various routes and their state-of-the-art, process conditions, reactors and catalysts can be found in the NREL report by Spath and Dayton [120] and in an updated review by Sikarwar et al. [20]. Herein, SNG production based on gasification is briefly presented, being one of the most investigated synthesis processes along with the FT synthesis.

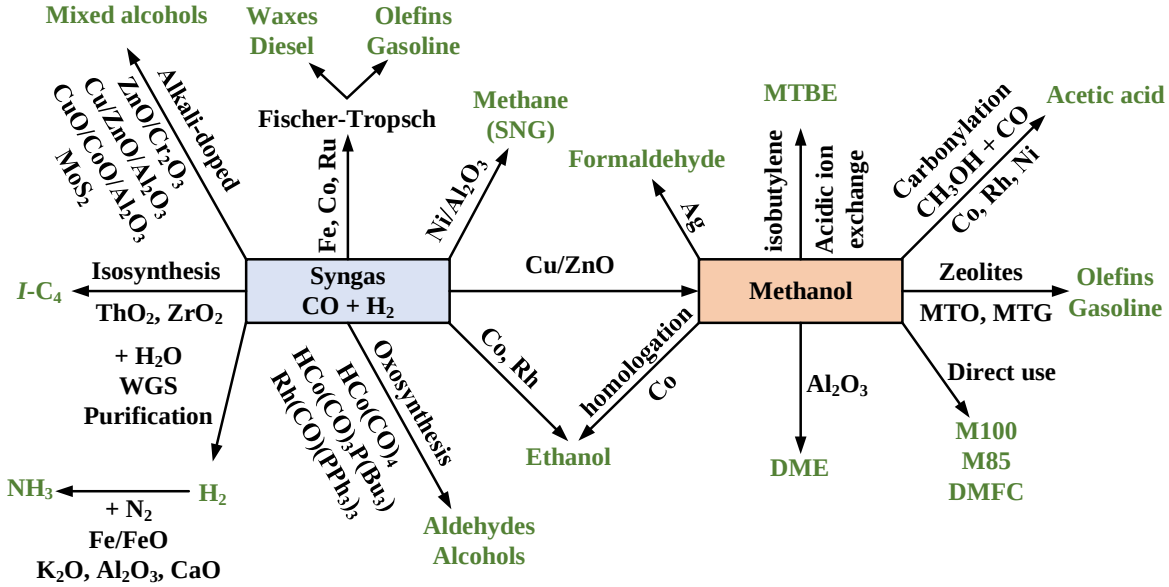

Figure 1-11: Fuel and chemical production options based on direct syngas conversion or through syngas-derived-methanol routes (modified from [20]).

Large-scale facilities for SNG based on coal are in operation or under construction worldwide. China has focused a lot on coal-to-SNG plants with several commercial projects producing 1-6 billion m^3 SNG a^{-1}. In USA, the Great Plains Synfuels Plant (North Dakota) with a capacity of 1.5 GW coal input has been in operation since 1984 [20]. In Europe, the 20 MW Bio-SNG GoBiGas project was commissioned in November 2014 in Sweden [121]. In addition, a plant upgrade up to 100 MW SNG has been under investigation for several years.

The biomass-to-SNG process layout, as developed by ECN, is shown in Figure 1-12. Biomass gasification is carried out in the steam-blown MILENA allothermal gasifier and raw syngas is produced with a high H_2 content. According to Van der Meijden et al., allothermal gasification can contribute towards an overall energy conversion efficiency above 70% [122]. Raw syngas is treated to remove contaminants and particularly ash, tars, Cl and S compounds before it can be supplied as "clean" gas to the methanation section, which comprises catalytic fixed bed reactors. During methanation, H_2 reacts with CO and CO_2 over a Ni-catalyst (typically Ni, but also Ru, Co, Fe or Mo) to produce CH_4, while the WGS reaction also takes place (see also Table 1-4).

$$CO + 3H_2 \leftrightarrow CH_4 + H_2O \qquad -173 \text{ kJ mol}^{-1} \qquad \text{R 1-27}$$

$$CO_2 + 4H_2 \leftrightarrow CH_4 + 2H_2O \qquad -164 \text{ kJ mol}^{-1} \qquad \text{R 1-28}$$

$$CO + H_2O \leftrightarrow CO_2 + H_2 \qquad -41 \text{ kJ mol}^{-1} \qquad \text{R 1-29}$$

Methanation thermodynamics indicates that the conversion process is favored at high pressure and low temperature (exothermic reactions). In addition, the Sabatier reaction for converting CO_2 to CH_4 consumes more H_2 compared to CO methanation. With the typical catalysts, CO reacts with a higher selectivity compared to CO_2. The reaction produces H_2O which is removed by cooling syngas, while heat for steam generation can be recovered after the methanation train, as well as between the fixed bed reactors. Moreover, CO_2 must be removed either prior or after the methanation reactors. In the ECN process layout, the "raw" SNG is upgraded after methanation through amine scrubbing for CO_2 removal in order to meet the specifications for injection into the natural gas grid. Methanation catalysts are subject to deactivation due to mechanical and thermal stresses, as well as due to chemical poisoning. Sulfur chemisorption on catalyst sites, carbonyl formation due to CO, tar deposition and coke formation need to be addressed [20, 123]. To avoid such issues, stringent syngas cleaning and conditioning is required, as well as accurate control of the process conditions of both gasification and methanation.

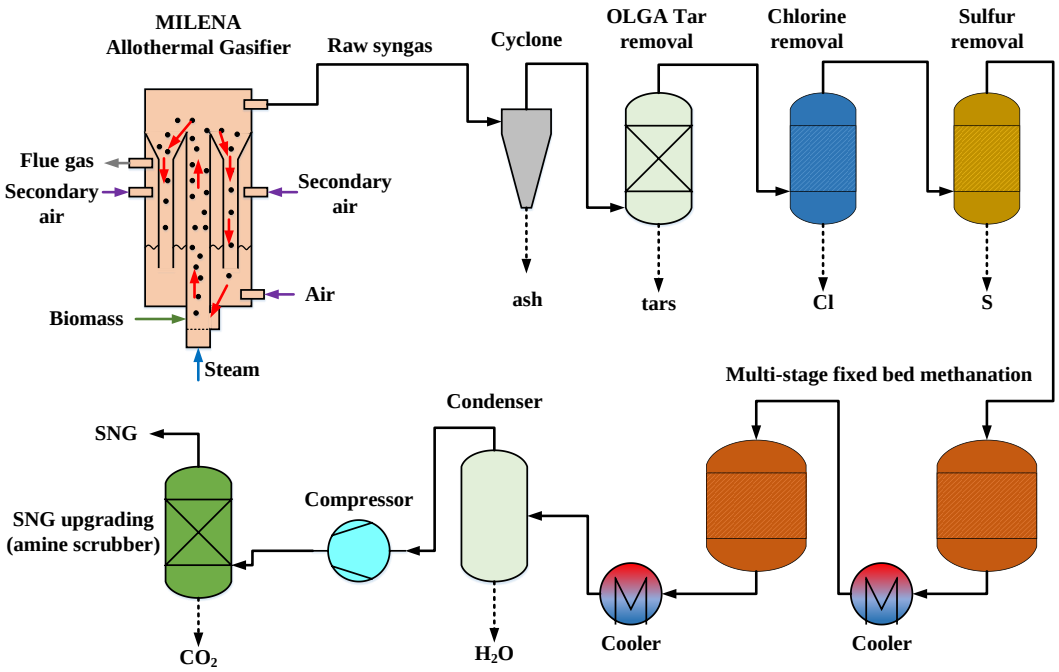

Figure 1-12: Bio-SNG production based on ECN's process layout (modified from [123]).

In FT synthesis, syngas composition is also relevant to the process reliability and catalyst protection. A comprehensive review of various deactivation mechanisms of Co and Fe catalysts can be found in [124] and [125], respectively. Sulfur and chlorine (and electronegative elements) are known poisons of Fe catalysts, while coke deposition is a phenomenon which is also reported to be a deactivation mechanism. The effect of N and alkali species is also discussed in [124]. Based on SASOL plants, decreasing the concentration of H_2S, HCl, HCN and alkalis at levels even below 10 ppb is recommended [126]. Process layouts of the syngas cleaning train of a biomass-to-liquid (BtL) plant with FT synthesis can be found in the study of Swanson et al. [127].

Gasification provides an important advantage compared to combustion in terms of plant flexibility by combining production of multiple products, such as electricity, heat, fuels and chemicals. Polygeneration schemes have been theoretically investigated and commercially employed. The Great Plains Synfuels Plant is such an example where apart from SNG, the co-products are ammonia, phenol, cresylic acid, naphtha, ammonium sulfate, tar oil, urea and CO_2, the latter utilized for Enhanced Oil Recovery (EOR) [123, 128]. On this basis, the syngas cleaning section must be designed so that the end-use application requirements are fulfilled. Such multi-product plants can have improved economic performance, as polygeneration increases the plant income and it makes it less dependent on volatile prices of a specific product (e.g. electricity). A review of polygeneration possibilities and barriers in IGCC plants can be found in [117].

1.4.3 Syngas cleaning requirements

Table 1-12 summarizes the cleaning requirements of various syngas utilization pathways, which can be coupled with biomass and/or coal gasification.

Table 1-12: Major syngas applications and associated cleaning requirements (at STP conditions unless stated otherwise) [79]. Reported values for SNG synthesis are based on ECN measurements from [129].

Contaminant	**Application**				
	ICE	**GT**	**MeOH synthesis**	**FT synthesis**	**SNG synthesis**
Particulate matter (soot, dust, char, ash)	< 50 mg m^{-3} (PM10)	< 30 mg m^{-3} (PM5)	< 0.02 mg m^{-3}	n.d.[a]	n.d.
Tars (condensable)	< 100 mg m^{-3}		< 0.1 mg m^{-3}	< d.p.[b]	< 50 mg m^{-3} (d.p.~ 100 °C)
Inhibitory species (Class 2 heteroatoms, BTX)				< 0.01 μL L^{-1} < 1 μL L^{-1}	BTX: ~ 250 ppmv
Sulfur compounds (H_2S, COS)		< 20 μL L^{-1}	< 1 mg m^{-3}	< 0.01 μL L^{-1}	< 200 ppbv
Nitrogen compounds (NH_3, HCN)		< 50 μL L^{-1}	< 0.1 mg m^{-3}	< 0.02 μL L^{-1}	< 1000 ppmv
Alkali species		< 0.024 μL L^{-1}		< 0.01 μL L^{-1}	-
Halides (mainly HCl)		1 μL L^{-1}	< 0.1 mg m^{-3}	< 0.01 μL L^{-1}	< 100 ppbv

[a] n.d.=not detectable, [b] d.p.=dew point

Syngas cleaning and conditioning is a necessary step in gasification plants designed for power and CHP generation, fuels and chemicals or polygeneration. In most power and CHP generation applications, significant reasons for raw syngas cleaning are erosion and corrosion issues, clogging due to high tar content, as well as excessive emission values of regulated pollutants, such as NO_x and SO_x. Catalytic syntheses require more stringent syngas cleaning and upgrading compared to power generation applications, which stems from two main reasons:

a. Many catalysts are extremely prone to poisoning by syngas contaminants, as already discussed above. Particularly, Ni/Al_2O_3 catalysts used in methanation for SNG production require a concentration of sulfur compounds (sum of H_2S+COS+CS_2+OSCs) below 1 ppmv [130].
b. Syngas components usually need to have a specific ratio in syngas, which is indicated by the reaction stoichiometry. Considering syngas methanation once again, the synthesis process requires a molar ratio of H_2/CO in syngas equal to 3 (assuming only H_2 and CO are present). Moreover, carbon and coke formation are possible problems that may require adjustment of syngas composition. In addition, thermal management of fixed bed reactors requires product recycling for dilution.

1.5 Gas cleaning processes: targeting CO_2, sulfur and tar compounds

In this section, the main processes applicable for removing CO_2, sulfur compounds (particularly H_2S) and tar species are discussed. It does not comprise an exhaustive presentation of available technologies, but rather an overview of a few basic concepts. For example, alternative technologies for CO_2 capture that are not presented are cryogenic methods, membranes, gas hydrates, calcium looping etc. [131].

1.5.1 Solvent-based processes

Regarding AGR technologies, they can be divided to physical and chemical absorption processes. Among the physical absorption processes, Rectisol™ and Selexol™ are state-of-the-art technologies. The layout of the Rectisol process is shown in Figure 1-13. Chilled methanol is used as a solvent at operating temperatures between -25 °C and -75 °C and high pressures up to 80 bar. At such conditions, the Henry coefficients of methanol are very high for most species present in syngas, including sulfur and C_{3+} compounds [132]. The process can achieve deep desulfurization of syngas at about 0.1 ppmv. Regeneration is achieved mainly through pressure reduction and secondly by heat supply. Due to the requirement for solvent refrigeration, the process has an increased power demand but low heat consumption.

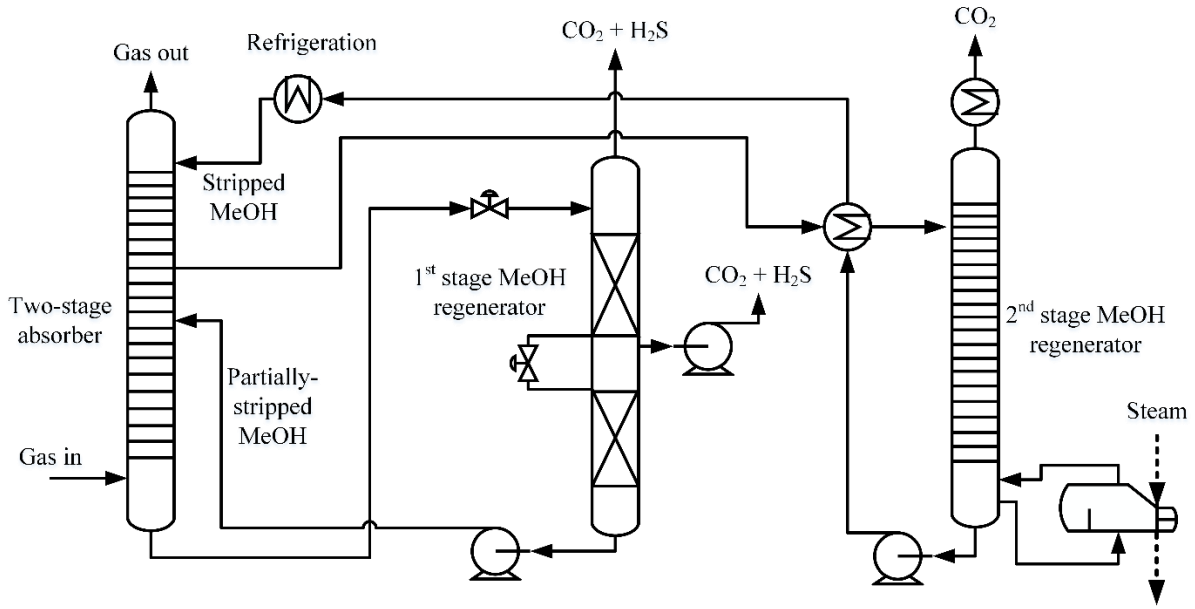

Figure 1-13: Rectisol™ physical absorption process (modified from [133]).

In contrast to Rectisol, Selexol uses dimethyl ether of polyethylene glycol as solvent. In addition, the Selexol process operates at more moderate temperature, but high-pressure conditions as well [134]. It is more selective towards sulfur species than Rectisol and it is usually applied for capturing H_2S, COS and thiols and mostly for bulk CO_2 removal. Chemical absorption processes differ in the fact that chemical reactions occur during AGR. In practice, this is translated to operation at lower pressure (~ up to 30 bar) and temperatures from ambient up to more than 100 °C. CO_2 removal by monoethanolamine (MEA) solutions at ambient pressure and temperature is the state-of-the-art technology for post-combustion CO_2 capture. As a primary amine, MEA is highly reactive with CO_2, but is has relatively small CO_2 capacity. CO_2 and H_2S can be removed at high pressure (pre-combustion AGR) through chemical absorption into MDEA and potassium carbonate (K_2CO_3) solutions. In contrast to MEA, MDEA is characterized by slower reaction kinetics but a lower regeneration duty. Further information regarding AGR by K_2CO_3 solutions are given in subsequent sections of this thesis.

Apart from CO_2 and sulfur species, solvent-scrubbing processes can be used for tar removal. Most tar removal concepts rely on physical absorption into organic liquids. In the Güssing gasification plant, biodiesel is used to clean the product gas from tar species. Another well-known tar removal process is the OLGA technology developed by ECN, which achieves tar dewpoints below -15 °C [135].

1.5.2 Solid-sorbent-based and catalytic removal processes

The most common sorbent-based process for CO_2 removal from a gas mixture is pressure swing adsorption (PSA). In PSA, a gas mixture flows through a packed bed from zeolite (e.g. ZSM-20, 5A, ZSM-5, 13X etc. [136]) under conditions of high pressure and low temperature until the sorbent is saturated with the adsorbate. The material is then regenerated by stopping the flow of the gas mixture, reducing the packed bed pressure and elutriating the adsorbed constituents with a gas having low adsorptivity [131]. A combination of two packed beds enables an alternating operation pattern by decoupling the adsorption and regeneration processes. A schematic diagram of a PSA system for CO_2 capture is shown in Figure 1-14.

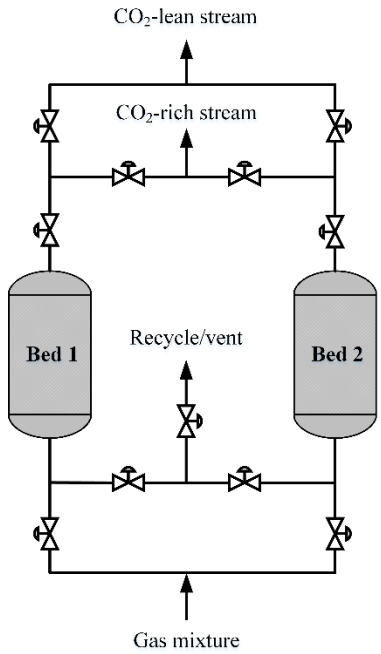

Figure 1-14: Pressure swing adsorption (PSA) process with double packed-bed configuration (reproduced from [136]).

A comprehensive review of sulfur removal by solid sorbents can be found in [84]. In bed desulfurization in a fluidized-bed gasifier can be achieved with calcium-based sorbents. Downstream desulfurization of syngas can be carried out with zeolites, mesoporous materials and metal oxide sorbents (Zn, Mn, Cu, etc.). Zinc oxide (ZnO) is one of the most common sorbents considered in the temperature range 300-500 °C. The product ZnS

can be regenerated to ZnO through oxidation at temperatures exceeding 590 °C [57]. Moreover, sulfur can be adsorbed onto activated carbons, as will be further elaborated in Chapter 3.

Apart from physical absorption and adsorption onto sorbents (e.g. activated carbon), tar species can be eliminated through thermal and catalytic cracking [137]. At sufficiently high temperatures above 1100 °C tar species decompose without the presence of a catalyst, however, the employment of a catalyst can decrease temperature to *ca*. 900 °C [138]. Tar species can be decomposed in the presence of H_2, CO_2 and H_2O to produce stable syngas components (CO, CH_4, etc.). Suitable catalysts for tar elimination include olivine, dolomite, zeolites, as well as Ni-based and Fe-based materials [137].

1.6 Scope and outline of the dissertation

AGR through K_2CO_3 solutions is considered a promising technology for gasification plants either when syngas is used for energy (power or CHP) or catalytic synthesis. The process is feasible at elevated temperature and pressure which enables the operation of the absorption and desorption step at a similar temperature, near the atmospheric boiling point of the solution. This is an advantage compared to physical absorption processes (e.g. Rectisol) in which syngas is cooled to low temperatures increasing exergy destruction in the process. In addition, K_2CO_3 is not volatile, another factor which should be considered prior to the downstream utilization of the clean gas or its disposal to the atmosphere (in case of post-combustion CO_2 capture). However, specific challenges arise due to process characteristics.

Challenge 1: The K_2CO_3-based absorption process suffers from slow kinetics of CO_2 absorption. Especially at moderate pressure conditions (< 20 bar) significant solvent improvements and screening efforts are necessary to compete with amine-based capture processes. In addition, increasing the solvent capacity is of particular interest.

Challenge 2: While CO_2 and H_2S can both be absorbed into K_2CO_3 solutions, the process is generally known to be non-selective towards H_2S removal [134] and it can be described as a process for "bulk" removal of acid gases. This arises problems when strict requirements for the operation of downstream units apply. In addition, the process cannot eliminate OSCs from syngas.

Challenge 3: Other contaminants are expected in syngas upstream of the AGR process, such as light tar species. It is of particular importance how these contaminants are treated by the process and what alternative measures need to be applied for their elimination, if necessary.

Challenge 4: Despite the fact that the heat of absorption of aqueous K_2CO_3 solutions is lower compared to amine solutions and the absorber operates at higher temperatures in the former, the process still consumes significant amounts of thermal power in the reboiler for regeneration. The effect of process parameters and the utilization of more efficient solvents needs to be evaluated in that direction as well. Regarding the overall process performance with enhanced K_2CO_3 solvents, data mostly for post-combustion plants are available.

Challenge 5: Potential benefits of the application of the AGR process in gasification-based power generation and/or fuel and chemical synthesis plants need to be evaluated. While the process has already been applied in the past for natural gas sweetening, ammonia plants etc., it is also of interest for alternative applications e.g. in biomass gasification plants towards a negative carbon footprint.

The present PhD thesis aims to contribute in addressing several of the aforementioned challenges through a combination of experimental, thermodynamic modeling and process modeling work. A general scheme of a gasification plant with hot syngas cleaning and AGR at "warm" gas cleaning conditions is shown in Figure 1-15. In this figure, the focus of the PhD thesis on different process aspects is highlighted.

In *Chapter 2*, a gasification model is developed and validated *versus* real gasification plant data from a 3 MW_{th} BFB gasifier. The model serves as a tool for identifying the effect of gasification conditions on syngas quality, which affects downstream operations, including syngas cleaning. The gasification model is used as a basis for plant-level modeling and analysis in *Chapter 7*.

In *Chapter 3*, the sorption of OSCs, H_2S and light tar species onto AC at warm gas cleaning conditions is investigated, addressing Challenge 2 shown above. The effect of a wide range of operating conditions on adsorption efficiency was investigated. Tests were carried out both with bottled gases at the laboratory, as well as with real syngas from an entrained-flow gasifier.

In *Chapter 4*, promoted K_2CO_3 aqueous solutions are compared in terms of CO_2 solubility and absorption rate, focusing on Challenge 1. The experimental study was carried out under high absorption temperatures in a pre-combustion CO_2 capture framework.

In *Chapter 5*, mixtures containing CO_2 and light tar species are treated in absorption tests with K_2CO_3 solutions. The study aims to identify possible interactions of light tar species with CO_2 absorption and tar behavior through the AGR process. In this chapter, Challenge 3 is of interest.

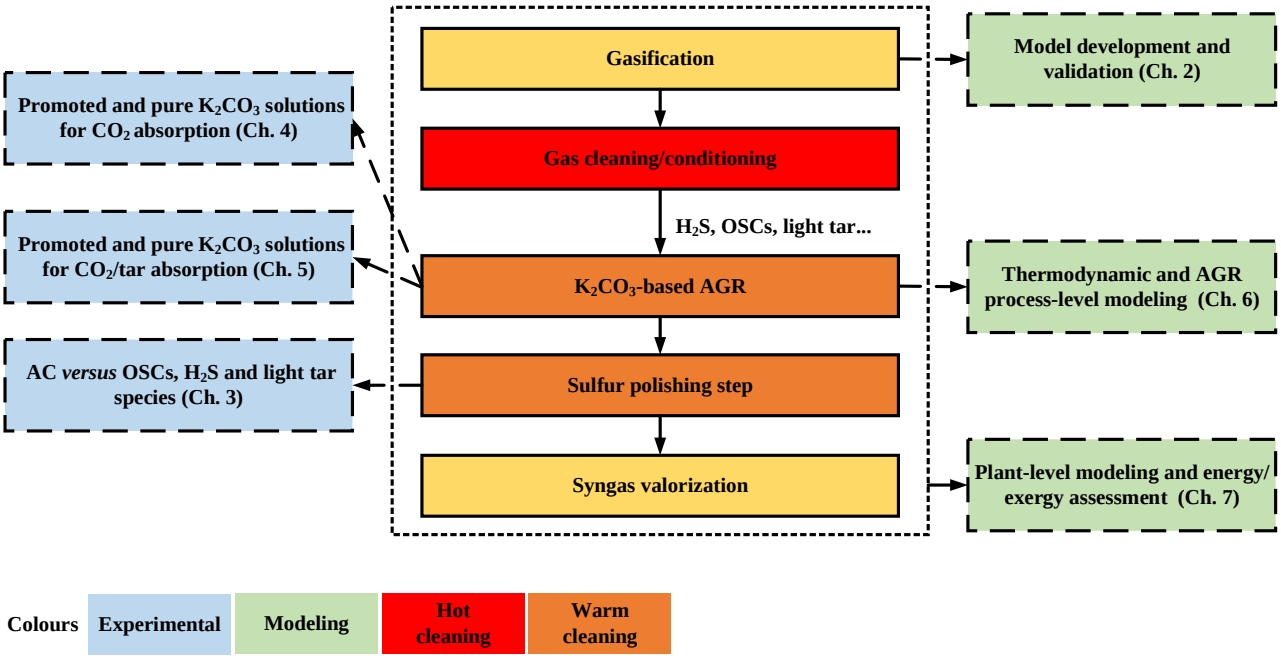

Figure 1-15: Thesis structure and distribution of experimental and modeling work.

In *Chapter 6*, Challenges 1, 2 and 4 are considered. A regressed thermodynamic electrolyte-NRTL model is coupled with rate-based column models for simulating the hot potassium carbonate AGR process (simultaneous CO_2 and H_2S removal) with pure K_2CO_3 and promoted K_2CO_3 aqueous solutions. The different solvents are compared under varying working conditions in terms of purification efficiency and regeneration energy consumption.

In *Chapter 7*, the process models are integrated into BIGCC-CCS configurations for power generation and power/MeOH cogeneration with respect to Challenge 5. The plant-level modeling is carried out in the commercial software Aspen Plus™. Based on the simulation results, energy and exergy analyses are presented, focusing on the effect of K_2CO_3-based CCS on plant efficiency.

2 Modeling and experimental investigation of syngas composition from biomass gasification

2.1 Literature review of gasification modeling and context of model development

As already presented in the first chapter, gasification can provide a useful means of utilizing solid fuels to produce a fuel gas, which can be subsequently valorized in highly-efficient engines or converted to gaseous and liquid products. Apart from its heating value, the actual syngas composition is of great interest in gasification-based processes for two main reasons. The first one is related to the subsequent synthesis reactors which require specific component ratios in the feed stream, such as the H_2/CO molar ratio [139]. Those ratios are influenced by the gasification technology, operating conditions and feedstock type, while the selection of the appropriate gasification process can also indicate the necessary syngas upgrading processes (such as CO_2 sequestration, WGS reactors, etc.). The second reason is related to the design of gas cleaning units for solid particles (char, ash) and syngas impurities which are catalyst poisons [57, 140]. Furthermore, for the many gasification projects that have been launched recently, such as the Gothenburg Biomass Gasification plant in Sweden (20 MW bio-SNG) [141], the issues of operation cost and time-consuming experimental campaigns to establish their operation under varying feedstocks are of great concern. To tackle these problems, reliable mathematical models are necessary to reduce the effort and assist towards process design and optimization. These models can be helpful also in the preceding phases of upscaling, certainly during the commissioning phase, and when changing the state of operation after that to assist operators predict the plant's new behavior.

In the literature, different gasification models have been developed which can be categorized according to the simplification adopted for fluid-dynamics computations in the following categories; computational fluid dynamics (CFD) models, fluidization models and simplified thermodynamic models [142]. The most analytical way to mathematically represent the two-phase flow, CFD models are based on solving density, momentum and enthalpy balance equations for the gas and solid phase and their sub-components. While considered very detailed and suitable for hardware design, those models lack computational speed which is an obstacle to their wider application e.g. for process thermodynamic investigations or techno-economic studies. In the case of fluidization models, simplifications to the equations solved in CFD models are applied and the momentum equation is not solved. Two phases are considered in the model, the bubble and emulsion phases, between which heat and mass transfer phenomena occur. Moreover, semi-empirical correlations are used to represent the bed hydrodynamics. In contrast to the previous two categories, simplified thermodynamic models focus on the process mass and heat balance and not on the reactor hydrodynamics. While this means that the latter models are not suitable for obtaining gas and solid distribution and temperature profiles inside the reactor, they are in fact very useful for time-efficient calculations of syngas amount, composition and heating value with regard to process conditions. Thus, thermodynamic models are considered to be very useful tools for gasification process integration studies [143] and various model structures have been presented so far. In general, equilibrium models have been developed using either an approach involving equilibrium constants or Gibbs free energy calculations. The first approach typically demands to specify chemical reactions [144]. This fact implies that specific data on chemical reactions and their exact equilibrium constant values are required which increases the model uncertainty. Concerning the second method, minimization of the Gibbs free energy has the advantage of requiring no chemical reactions to be explicitly specified.

Aspen Plus™ is considered as valuable simulation software for modeling of thermochemical processes. Doherty et al. [69] developed an Aspen Plus gasification model for a fast internally circulating fluidized bed (FICFB) gasifier which was based on Gibbs free energy minimization, zero-dimensional modeling and isothermal, steady-state operation of the reactor with a zero temperature approach at equilibrium. The model results were validated against the 8 MW Güssing gasification plant in Austria. Gasification temperature, fuel moisture, steam- and air-to-biomass ratios were investigated for the model validation. A stoichiometric reactor was also implemented by the authors for simulating the complete conversion of N_2, S and Cl_2 to NH_3, H_2S and HCl, respectively. Nikoo et al. [145] developed an Aspen Plus model in which a Gibbs minimization method was applied for combustion of volatile species and FORTRAN subroutines were coupled to simulate hydrodynamic conditions and reaction kinetics for char gasification in two continuously stirred reactor modules, for the bed and freeboard respectively. Results were validated against lab-scale experiments of pine gasification in a

fluidized bed reactor. Moreover, Pala et al. [146] presented a Gibbs free energy minimization gasification model suitable for FT synthesis and they investigated the effect of various biomass feedstocks and process parameters on syngas composition. Their results were compared to steam gasification experiments of wood residues which were carried out in a lab-scale test rig [147].

Most of the available Aspen Plus thermodynamic models in the literature have been validated with laboratory and pilot-scale gasification experiments (up to 500 kW_{th}) so far, and a good agreement has been obtained. However, investigations on their suitability to predict syngas composition in large-scale fluidized bed gasifiers are scarcer and more effort is needed to justify their implementation for this purpose. In this study, a model in Aspen Plus for wood gasification is presented and the results are compared with real plant data. For this purpose, gasification tests were carried out at the 3 MW_{th} BFB gasifier operating at the Fundación Ciudad de la Energia (CIUDEN) in Spain. The comparison focuses on syngas composition for the main components (CO, H_2, CO_2 and CH_4), C_2 hydrocarbons (modeled as ethylene) and carbon content in the fly ash, which is collected and weighted on-site. A novel aspect of the aforementioned model is the consideration of the effect of the WGS reaction on the final product composition, aiming to investigate its potential impact on gasification equilibrium products during syngas cooling.

2.2 Gasification tests and modeling methodology

2.2.1 Experimental campaigns at CIUDEN and model development

The experimental campaigns were performed in a 3 MW_{th} atmospheric, air-blown BFB gasifier which can operate with three different fuel types, specifically biomass chips, granular or pelletized biomass. For this purpose, two different fuel-supplying lines are connected to the gasifier, one for treated biomass (granular and pelletized) and one for chips. Fuel is supplied with screw feeders inside the reactor. A pressurized rotary valve is used for biomass supply, feeding biomass at two different levels located at the top and bottom of the bed. For the case of treated biomass, both feeding levels may be operated simultaneously, while for chips only one level is operated at a time. To prevent backflow of particles and syngas produced, which can cause pyrolysis in the fuel reservoirs, a minor flow of CO_2 was supplied with the fuel. For the continuous operation of the gasifier, each fuel supplying line consists of two fuel hoppers, each one with a volume sufficient for 3 h of operation. Loading of a hopper with fuel is performed while its feeding line is disconnected and therefore, the two hoppers operate independently. Moreover, the feeding mass flow rate of biomass can be measured through weight indicators (WI), which continuously record the feeding hopper weight.

A schematic representation of the gasification facility is shown in Figure 2-1. The gasifier itself is an internal refractory-lined BFB reactor with an internal diameter of 1.3 m and a total height of 5.5 m, while the freeboard section has an internal diameter of 2.0 m. The gasifier is connected to a sand feeding system which can continuously feed the required inert material for high-ash biomass operation. In addition, an additive feeding system is installed for investigating materials for tar reduction, as well as in-situ elimination of impurities. For the gasifier startup, heating of the reactor was performed with flue gas derived from natural gas combustion in a separate chamber. When biomass gasification started, a forced draft fan operated to supply air for bed fluidization. An array of 19 thermocouples, 6 differential pressure transmitters and 4 reserved ports for other measurement devices and sampling are installed across the gasifier. During the campaigns of this thesis, temperature, pressure and pressure drop at the fuel storage and feeding section, gasification reactor and gas cleaning system were continuously monitored and recorded *via* a data acquisition system. Removal of fly ash and inert solids from syngas was carried out downstream of the gasifier. Firstly, the solid particles were collected with two refractory-lined high-efficiency cyclones and they were subsequently transported to a bigger hopper with screw feeders connected to weight measuring devices. Two independent ash removal systems are used to collect the bottom and fly ash which are produced in the process, respectively. Regarding syngas composition measurements, a Tunable Diode Laser (TDL) device was used for monitoring the O_2 content in syngas, while the main gas components were measured with an on-line gas chromatograph (H_2, CO_2, CO, O_2 and CH_4).

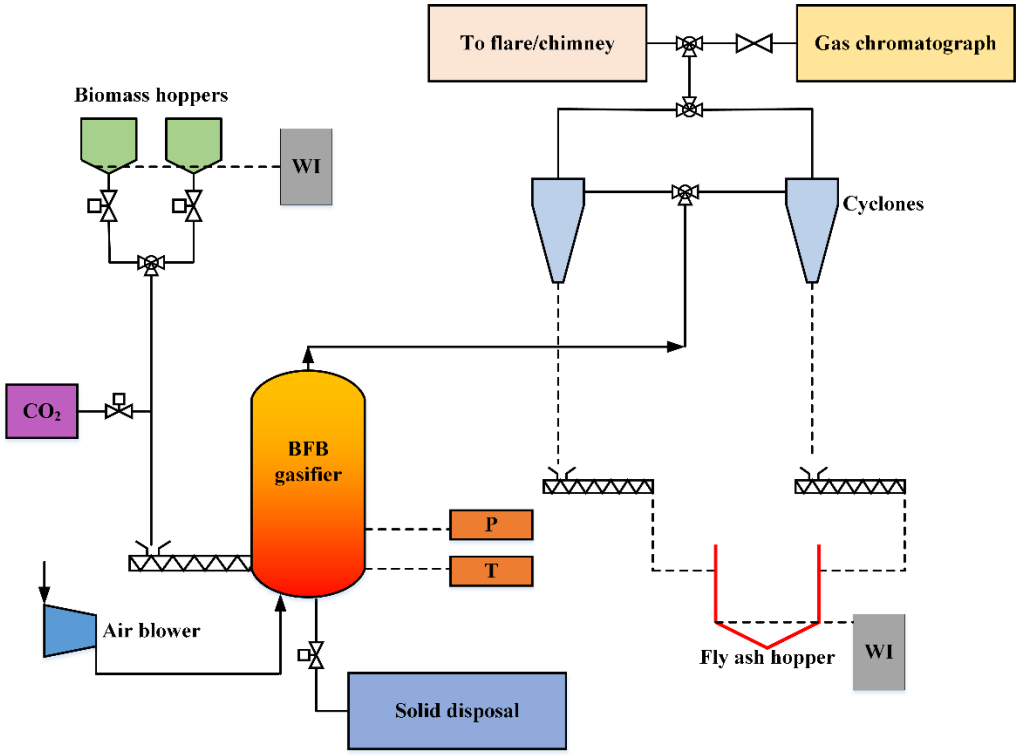

Figure 2-1: Schematic diagram of 3 MW_{th} BFB gasifier at CIUDEN.

Furthermore, dedicated sampling connections are installed in the gas duct for off-line analysis. Five experimental tests were carried out with woody biomass at a temperature of 890 °C and λ of 0.28-0.29.

2.2.2 Aspen Plus model description

The model for the prediction of syngas components is a steady-state model based on thermodynamic equilibrium through Gibbs free energy minimization. For the presented simulations hereafter, the compounds defined were N_2, O_2, C, S, H_2, CO, CO_2, CH_4, H_2O, H_2S, SO_2, SO_3, COS, HCN, C_2H_4, C_2H_6, C_6H_6, $C_{10}H_8$ as conventional components, as well as biomass and ash as non-conventional solids. Particularly, solid carbon (graphite) was selected as the component to represent solid char. For the definition of biomass properties, the HCOALGEN and DCOALIGT models were adjusted for enthalpy and density, respectively. The biomass stream was defined by the proximate, ultimate and sulfur analyses. The default Boie correlation can be used to describe the heat of combustion within the HCOALGEN model according to Equation 2-1, while a deduction for the latent heat of vaporization of water is performed to calculate the lower heating value of the fuel

$$\Delta_c h_i^{dm} = \left[a_{1i} w_{C,i}^{dm} + a_{2i} w_{H,i}^{dm} + a_{3i} w_{S,i}^{dm} + a_{4i} w_{O,i}^{dm} + a_{5i} w_{N,i}^{dm}\right] \cdot 10^2 + a_{6i} \qquad \textit{Equation 2-1}$$

where $w_{C,i}^{dm}$, $w_{H,i}^{dm}$, $w_{S,i}^{dm}$, $w_{O,i}^{dm}$, $w_{N,i}^{dm}$ denote the mass fractions of fuel elements and a_{ni} (with n = 1, 2…6) are coefficients with both positive and negative values described under the parameter name BOIEC/K in Aspen Plus (with K = 1, 2…6). For the proximate and ultimate analyses, average values from the fuel data for all five experimental campaigns were used, as provided by CIUDEN for wood and shown in Table 2-1. The model layout as developed in Aspen Plus is shown in Figure 2-2. Initially, the biomass feed decomposes in the RYield reactor. In this section, biomass is transformed from a non-conventional solid component to its elements in a molecular form, which are assumed to be C(s), H_2, N_2, S, O_2, H_2O and ash. This step is important since after decomposition the components can take part in the Gibbs free energy calculations in default Aspen Plus RGibbs modules. For this calculation, random initial values for the distribution of species at the exit of the reactor were given.

Table 2-1: Proximate and ultimate analyses of wood chips used in the experimental campaigns.

Proximate analysis	
Moisture (wt. %, wet basis)	6.06
Ash (wt.%, dry basis)	1.31
Volatile matter (wt.%, dry basis)	79.03
Fixed carbon (wt.%, dry basis)	19.66
Ultimate analysis	**(wt.%, dry basis)**
C	49.30
H	6.71
N	0.11
S	0.01
O	42.57

Afterward, the reactor block was coupled with a calculator block which calculated the composition in the outlet with a FORTRAN subroutine. The subroutine links the data provided to the software for the fuel ultimate analysis and moisture content to newly defined variables which correct the outlet mass flow of the components based on the biomass water content. The value for the moisture content is retrieved from the proximate analysis which is also provided to the software. A similar procedure for handling biomass in Aspen Plus has been described in [148]. The principal software block which performs the minimization of Gibbs free energy to obtain the syngas composition is the RGibbs reactor. Herein, a short description of the method fundamentals is given, while a more comprehensive analysis of the methodology and its numerical solution can be found in [149]. The total Gibbs free energy of the system G^{tot} can be defined based on the chemical potential of species *i* present denoted as μ_i and their quantities, n_i, according to Equation 2-2.

$$G^{tot} = \sum_{i=1}^{N} n_i \mu_i \qquad \textit{Equation 2-2}$$

The chemical potential μ_i of the species (assuming ideal gas behavior in order to simplify fugacity coefficients) can be defined as:

$$\mu_i = \Delta \bar{G}^{o}_{f,i} + RTln(y_i) \qquad \textit{Equation 2-3}$$

where $\Delta \bar{G}^{o}_{f,i}$ is the standard Gibbs free energy of formation of species, R and T are the universal gas constant and temperature, respectively, and y_i is the mole fraction of component *i* in the mixture. Based on Equation 2-2 and Equation 2-3, the total Gibbs free energy can be written as

$$G^{tot} = \sum_{i=1}^{N} n_i \, \Delta \bar{G}^{o}_{f,i} + \sum_{i=1}^{N} n_i \, RTln(y_i) \qquad \textit{Equation 2-4}$$

When the equilibrium state is established, the total Gibbs free energy of the system is minimized. Therefore, a solution for the problem can be obtained by specifying n_i values to minimize the objective function. The use of Lagrange multipliers is usually employed with the constraint of the elemental balance shown in Equation 2-5.

$$\sum_{i=1}^{N} \alpha_{ij} \, n_i = A_j \qquad \textit{with } j=1,2,3\ldots k \qquad \textit{Equation 2-5}$$

In Equation 2-5, α_{ij} denotes the number of atoms of the j^{th} element per quantity of the i^{th} species and A_j is the total number of atoms of j^{th} element in the mixture. Based on this definition, the Lagrangian function can be formulated, employing the Lagrange multipliers λ_j, as follows

$$L = G^{tot} - \sum_{j=1}^{k} \lambda_j \left(\sum_{i=1}^{N} \alpha_{ij} \, n_i - A_j \right) \qquad \textit{Equation 2-6}$$

The partial derivatives of the Lagrangian function are set equal to zero as shown in Equation 2-7. The set of equations (matrix of *i* rows) can be solved numerically (e.g. by the Newton-Raphson method) to obtain n_i which must be real numbers and satisfy the constraint of having values in the range $0 \leq n_i \leq n_{tot}$.

$$\frac{dL}{dn_i} = 0 \qquad \textit{Equation 2-7}$$

Moreover, the energy balance must be satisfied in all cases. Taking into account that inside the gasifier both exothermic and endothermic reactions take place, the heat generated from exothermic reactions is either consumed by the endothermic ones or it causes a temperature increase in the product gas temperature. The energy balance is shown in Equation 2-8

$$Q_{loss} + \sum_{reactants} n_r \, \bar{H}_r^o(T_r) = \sum_{products} n_p \, \bar{H}_p^o(T_p) + \Delta H \qquad \textit{Equation 2-8}$$

where the summation operators ("sigma") denote the enthalpy values of the reactant and product mixtures at their respective temperatures, while Q_{loss} denotes gasification heat losses. Heat losses were considered negligible in this investigation. When this term is indeed considered, it is assumed to be a small fraction of the fuel HHV value, as done by Altafini et al. [150].

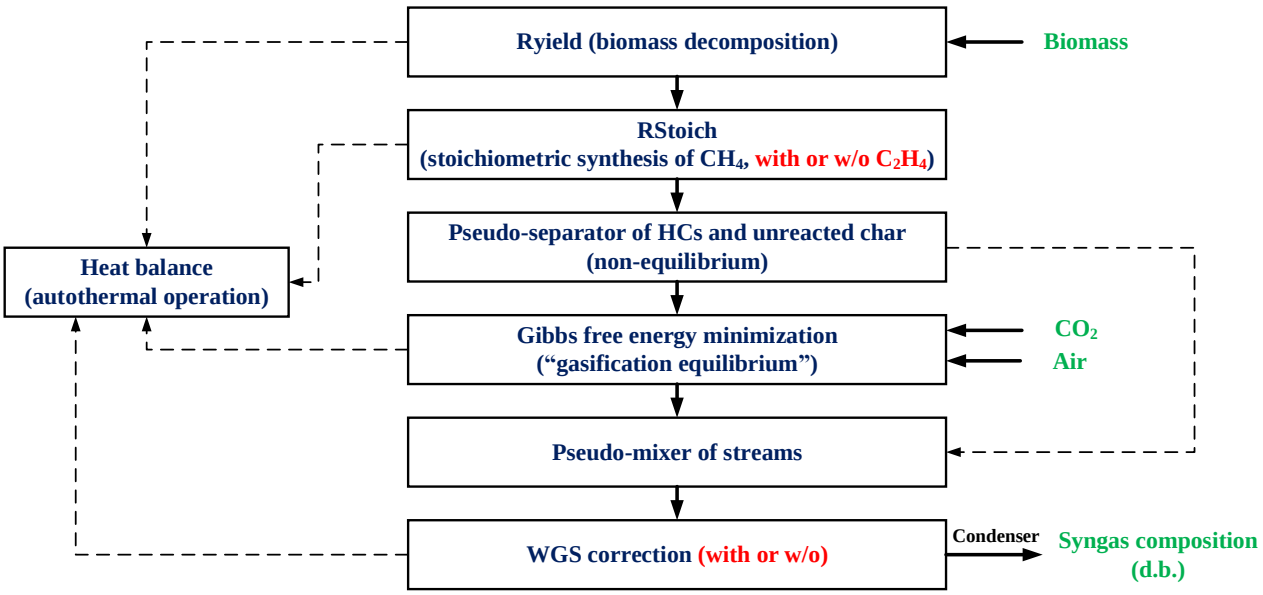

Figure 2-2: Aspen Plus gasification-equilibrium model layout.

The Gibbs minimization procedure was set to obtain products under phase and chemical equilibrium, thus excluding the specification of the temperature approach for any reaction(s). While the aforementioned methodology can adequately predict the formation of the major syngas components, non-idealities during the thermochemical conversion process lead to the underestimation of specific products that are measured during real conditions, such as char (residual carbon), CH_4 and tars [75]. For this reason, a stoichiometric reactor (RStoich) was used prior to the RGibbs reactor. In this module, an amount of CH_4 is formed from solid char and hydrogen. Initially, the molar fractional conversion of C(s) in the stoichiometric reactor was set to 12%. However, for the estimation of the final value of CH_4 composition in syngas, a design specification module was implemented in the simulation program. This feature changes the fractional conversion of solid char in the stoichiometric reactor to meet the experimental measurements for CH_4. In this specification, the final composition of CH_4 measured by the analyzer at the gasifier outlet duct was directly given as a simulation input and all calculations took into account this exit value. The CH_4 flow and the products derived from the RYield reactor are transferred to a separator block, in which a fraction of char, the total amount of methane and the total amount of ash contained in biomass are separated from the gas mixture and are further processed in a subsequent separator in the flowsheet. Based on the experimental campaigns at CIUDEN, a 6% molar fraction of the total char produced from the decomposition was subtracted from the main flow which is to be fed to the RGibbs

reactor. In the last separator, all fuel ash and the C(s) fraction that by-passed the RGibbs reactor are separated as solids from the mixture. An equilibrium reactor (REquil) is introduced after the RGibbs reactor to equilibrate the WGS reaction. To obtain the final dry gas measurement, condensation of syngas moisture is performed in a water separator. It is assumed that only moisture is removed within this block, in order to directly compare the syngas composition results from the simulations to the experimental results obtained by the gas chromatograph, which operates with dry syngas. For the RYield, RStoich and RGibbs blocks which were used to simulate the gasification process, it was assumed operation for a pressure equal to the gasifier plenum pressure. Gasification temperature for the same blocks was calculated according to manufacturer guidelines as the average temperature of the thermocouples placed at a height of 375 mm from the reactor plenum, which corresponds to an average of four (4) temperature values. The pressure in the WGS equilibrium reactor was set equal to the pressure measured at the outlet of the gasification reactor, accounting for the pressure drop through the BFB. The total heat balance of the process was calculated by combining the heat streams from the decomposition reactor (RYield), the stoichiometric reactor (RStoich) and the Gibbs free energy minimization reactor (RGibbs) blocks, including also the WGS reactor where necessary (cases with and without WGS correction were considered). A heat stream mixing block accounts for the balance between heat generation and demand of the model reactors.

2.3 Results and discussion

For all the simulated cases, the pressure and temperature values in the model reactors were altered according to the experimental data obtained from the campaigns. For the composition of the biomass feedstock, the average values of repeated ultimate and proximate analyses performed for the wood chips before each experiment were adopted in the model. The mass flow rate of biomass, CO_2 and inlet air in the system were calculated from the experimental measurements provided. The biomass feeding mass flow rate was calculated by the given weight reduction curve of the hopper. Table 2-2 provides the pressure and temperature values for the model reactors and Table 2-3 presents stream data for the Aspen Plus simulation.

Table 2-2: Pressure and temperature of the model components (blocks) for all simulated tests.

Component	**Test 1** λ**= 0.29**	**Test 2** λ **= 0.28**	**Test 3** λ **= 0.28**	**Test 4** λ **= 0.28**	**Test 5** λ **= 0.29**
RYield reactor					
Pressure (bar)	1.15	1.16	1.16	1.16	1.17
Temperature (°C)	884	884	885	885	894
RStoich reactor					
Pressure (bar)	1.15	1.16	1.16	1.16	1.17
Temperature (°C)	884	884	885	885	894
RGibbs reactor					
Pressure (bar)	1.15	1.16	1.16	1.16	1.17
Temperature (°C)	884	884	885	885	894
WGS reactor					
Pressure (bar)	1.03	1.03	1.03	1.03	1.04
Temperature (°C)	830	830	830	830	830

In the initial model developed, a significant deviation from the experimental values for syngas composition was obtained. In that preliminary model, it was assumed that only CH_4 is produced in the stoichiometric reactor to compensate for the equilibrium calculations in the Gibbs minimization reactor [70]. Under this assumption, syngas contains mainly CO, H_2, CO_2, CH_4 and N_2 as the balance gas in the moisture-free gas measured by the GC analyzer.

Table 2-3: Material stream values for wood-chip gasification modeling.

Parameter	Test 1 λ=0.29	Test 2 λ =0.28	Test 3 λ =0.28	Test 4 λ =0.28	Test 5 λ=0.29
Biomass mass flow rate (kg/h)	499.4	532.6	544.8	488.0	523.1
CO_2 hopper pressure (bar)	1.24	1.24	1.24	1.24	1.24
CO_2 temperature (°C)	25.0	25.0	25.0	25.0	25.0
CO_2 mass flow rate (kg/h)	70.7	86.4	86.4	86.4	90.3
Air pressure (bar)	1.15	1.16	1.16	1.16	1.17
Air temperature (°C)	38.8	52.2	53.1	49.6	47.3
Air mass flow rate (kg/h)	862.2	862.1	862.2	862.2	923.7

Of course, the concentration of other volatile hydrocarbons in syngas (such as C_2H_4) cannot be neglected even when not quantified, such as in the present investigation. Research studies have reported values of C_2H_4 content in syngas for air gasification under various operating conditions. Rechulski et al. [88] reported composition of 0.68 vol. % for C_2H_4 and 0.25 vol. % for C_2H_6 (C_2 hydrocarbons) for bubbling fluidized-bed gasification of wood with λ = 0.29. In another study, Mun et al. [151] reported a value of 1.1 vol. % for wood gasification with λ = 0.22 and sand as bed material. Moreover, Hurley et al. [152] reported concentrations in the range of 1.0 vol. % or higher for C_2 gases in the product gas of an air-blown, fluidized bed gasifier with woody biomass as fuel and λ = 0.30. Consequently, C_2H_4 formation was also modeled in the stoichiometric reactor block in order to improve prediction capability. The value for the fractional conversion of component C(s) to C_2H_4 was set to be 7%. The flow of C_2H_4 after the stoichiometric reactor also by-passed the RGibbs reactor, before it is mixed again with the main syngas components to account for the final product gas composition.

The first series of simulations was performed by not taking into account a WGS correction after the Gibbs module. Figure 2-3 presents a comparison between the results obtained from the model and the measurements from the BFB gasifier. Experimental values for syngas composition correspond to average measured values through GC analysis during steady-state gasification. The results refer to the first experimental test and the model results correspond to two modeling approaches, when including C_2H_4 formation (Approach a) and without C_2H_4 formation (Approach b), are shown.

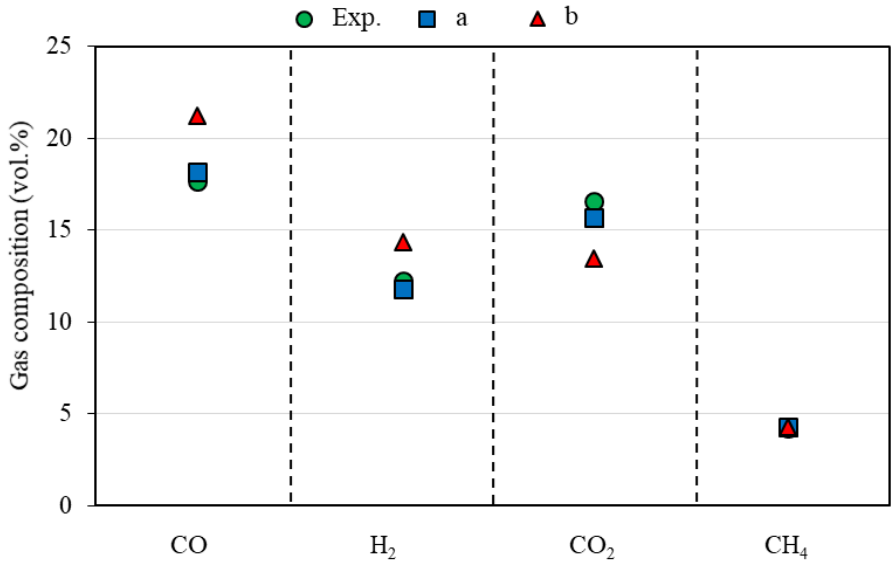

Figure 2-3: Syngas composition simulation results for two modeling approaches compared to experimental data from Test 1. Approach a: w/o WGS equilibrium, with C_2H_4 formation. Approach b: w/o WGS equilibrium, w/o C_2H_4 formation.

When modeling without WGS correction, the content of CO_2 was underestimated, while the CO content was overestimated compared to the experimental measurements. Deviations were more significant when modeling without C_2H_4 formation. On the other hand, when C_2H_4 was considered, the model performance improved and the most notable difference was in the prediction of the CO_2 content (~ 1 percentage point). As a next step, the

assumption that the WGS reaction still takes place during syngas cooling was made [153]. A WGS model reactor operating at 830 °C (~ 60 °C lower than the average gasification). This value was selected after performing a sensitivity analysis based on the equilibrium results for WGS for different temperatures compared to the experimental measurements from the BFB gasifier. For the subsequent simulations, the implementation of a pseudo-reactor for C_2H_4 formation was investigated in combination with a WGS correction. In Figure 2-4, the comparison between the model estimations and experimental data are shown for the modified Aspen Plus model and for the same experimental test (Test 1). Including C_2H_4 formation in the model with the WGS reaction improved the prediction for H_2 content in syngas and it caused both CO (~ 0.2 percentage points deviation) and CO_2 concentrations (~ 0.35 percentage points deviation) to approximate the experimental data. Based on these results, it can be concluded that the equilibrium model with WGS correction and the assumption of C_2H_4 formation is capable of predicting the composition of syngas adequately under these specific conditions.

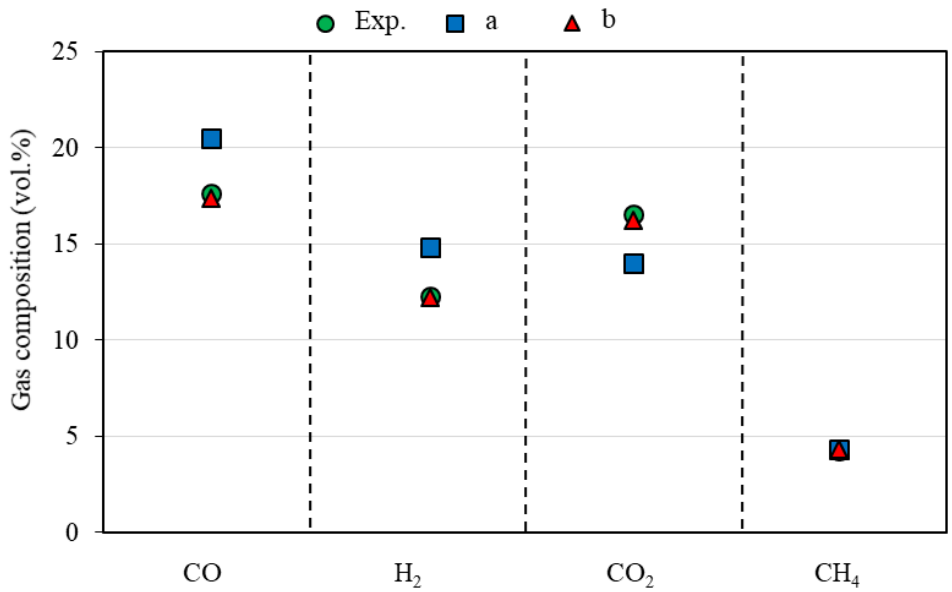

Figure 2-4: Syngas composition simulation results for two modeling approaches compared to experimental data from Test 1. Approach a: with WGS equilibrium, w/o C_2H_4 formation. Approach b: with WGS equilibrium and C_2H_4 formation.

Table 2-4 presents the syngas composition calculated from the model for the conditions of the first test. It can be noted that Gibbs free energy minimization based equilibrium calculations cannot predict the formation of minor sulfur compounds and other contaminants present in the product gas. According to model estimations, sulfur was mainly converted to hydrogen sulfide (H_2S) and to a smaller extent to COS, which is in line with published results for biomass gasification [137]. The molar conversion of incoming sulfur to hydrogen sulfide according to the model calculations was found to be approximately 93%. Such values are also in line with equilibrium product predictions for the distribution of sulfur species presented by Kuramochi et al. with the aid of FactSage software [154], who concluded that H_2S is the main sulfur species in bio-syngas followed by COS at gasification temperatures higher than 750 °C. The equilibrium model yielded approximately 25 ppmv H_2S, for which the very low sulfur concentration in the fuel should be taken into account (0.01 wt. %). The sulfur content was lower than the values reported in the literature for solid biomass, although its distribution to the main sulfur-containing products was similar. According to Aljbour et al. [155], the H_2S content in wood gasification is expected to be ca. 35-39 ppmv. However, Öhrman et al. [156] reported H_2S concentrations in the range of 15 ppmv for low-sulfur containing wood pellets and $\lambda = 0.35$. In this thesis, H_2S concentrations between 5 and 80 ppmv were measured for wood gasification with O_2, as presented next. The latter values indicate that the predicted H_2S value can be realistic for low-sulfur fuels. To account for the formation of sulfur compounds in Aspen Plus in a more explicit way, Pala et al. [146] implemented a stoichiometric reactor to convert all fuel sulfur to H_2S, neglecting conversion to other compounds. They reported an H_2S content in the range 78-2174 ppmv for fuel sulfur contents between 0.02 wt. % and 0.57 wt. % (dry basis). Although prediction of OSCs is probably equally crucial, this is rarely taken into account in steady-state equilibrium models, due to the fact that quantification of trace compounds in syngas in often omitted.

Table 2-4: Wet syngas composition for Test 1 conditions (vol. %, w.b.) calculated by the model.

Syngas component	Model results	Syngas component	Model results
CO	15.59 vol. %	H_2O	10.43 vol. %
H_2	10.97 vol. %	C_2H_4	1.23 vol. %
CO_2	14.52 vol. %	H_2S	25 ppmv
CH_4	3.86 vol. %	COS	1.79 ppmv
N_2	43.40 vol. %	HCN	86 ppb

Therefore, integration of blocks for the formation of H_2S, COS, thiophene and other sulfur species, HCl and NH_3 can result in a further improvement of the prediction capabilities of such a simulation tool. In addition, a module for predicting tar compound formation according to [70] can be integrated. The most abundant, representative and stable tar compounds which prevail at the usual operating temperature range of the gasifier are commonly selected, such as naphthalene, benzene, etc. Such an approach is presented in the seventh chapter of the present thesis for hydrocarbons, tar species and other syngas contaminants. Figure 2-5 presents a comparison of the syngas composition between the Aspen Plus model and the experimental results from Tests 1 to 5. It was found that the equilibrium model deviates as the biomass flow rate increases, especially for the second and third tests. As expected, other parameters such as hydrodynamics within the fluidized bed can influence the obtained results.

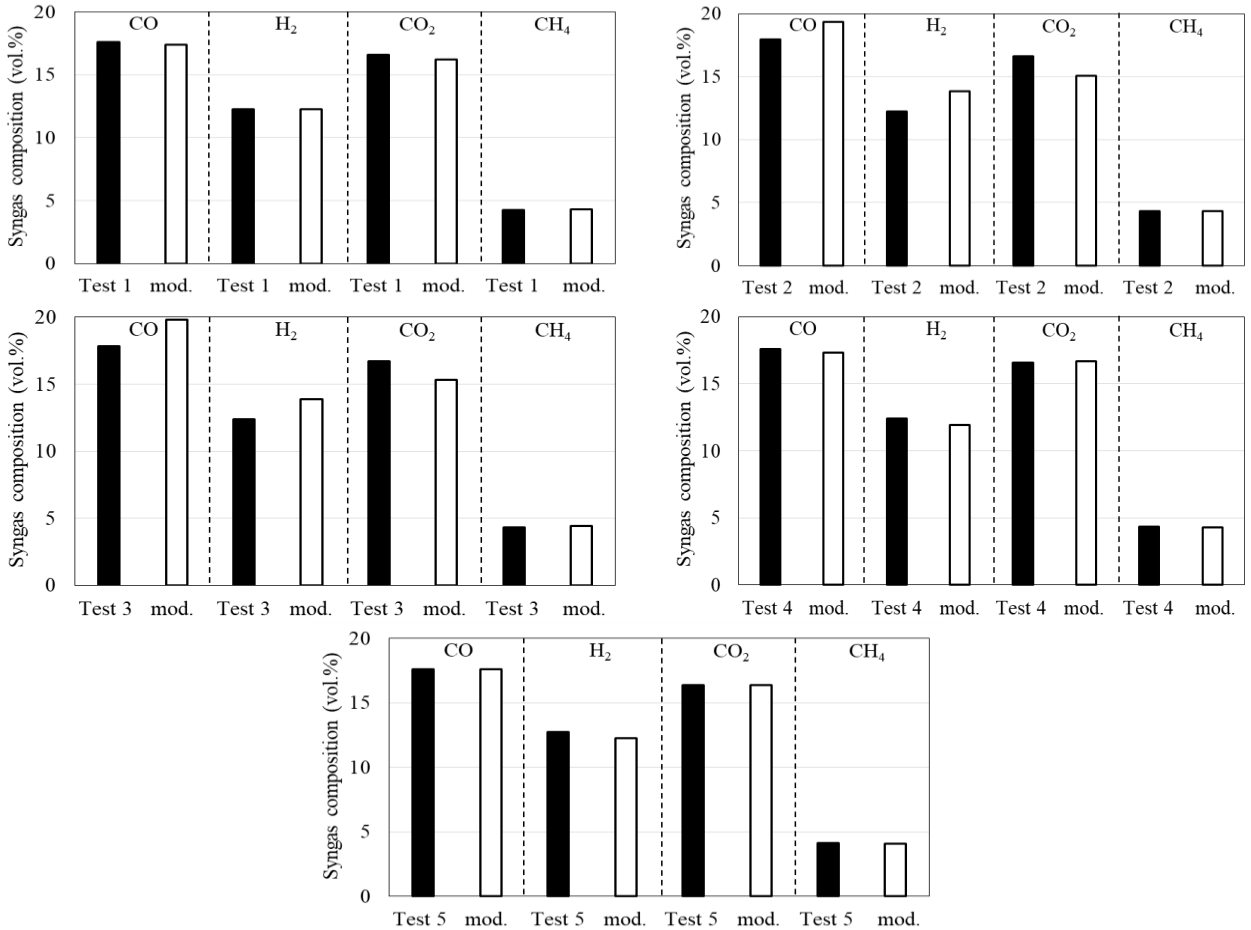

Figure 2-5: Simulation versus syngas composition results from Tests 1 to 5.

Concerning the estimations of fly ash production, Figure 2-6(a) compares the model results for char mass flow to the experimental tests 1-5. It can be noted that the assumption of a single split fraction for unreacted carbon in the proposed model fails to a certain extent to cover the effect of all gasification parameters. Finally, the results of C_2H_4 concentration, as estimated from the Aspen Plus model, are shown in Figure 2-6(b). Ethylene

composition ranged from 1.15 vol. % to 1.37 vol. %, which is consistent with the content of light hydrocarbons in wood gasification product gas.

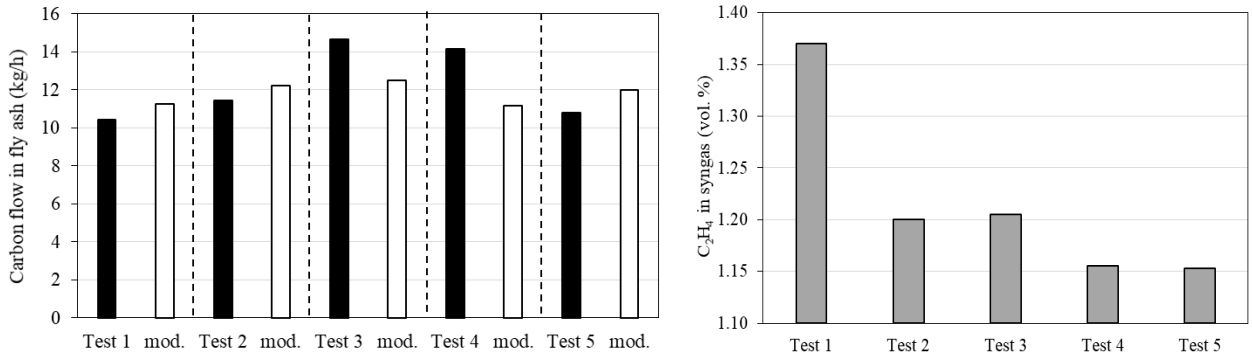

(a) (b)

Figure 2-6: (a) Model results for carbon mass flow with fly ash versus experimental results and (b) C_2H_4 content in syngas (vol.%) as estimated in Aspen Plus.

2.4 Conclusions

In this chapter, an equilibrium-based, steady-state gasification model for the prediction of syngas quality was presented, taking into account the formation of CH_4 and C_2 hydrocarbons, as well as the unconverted char in fly ash. The model was based on the minimization of Gibbs free energy for the estimation of the main product gas components, as well as on the effect of the WGS reaction equilibrium at the reactor outlet. Experimental tests were initially performed in a 3 MW_{th} air-blown BFB gasifier under nominal working conditions and the process parameters were used as inputs to the equilibrium model. The use of a WGS model reactor contributed to achieving a better agreement with the experimental data, indicating that the reaction can still be active after the gasifier outlet. When only CH_4 formation was considered, the simulation results greatly deviated from the experimental data. For this reason, the formation of C_2H_4 was integrated in the model in a stoichiometric reactor. The modified model managed to adequately predict the main syngas components. However, deviations when operating conditions such as fuel and oxidant feed rates changed were also noted. Correlations covering the production of hydrocarbons with respect to temperature, equivalence ratio and other parameters can enhance the ability of the model to predict syngas composition with higher accuracy since in the present model, data for a single temperature level (and a very narrow λ range) were used. Moreover, correlations for char conversion can further improve the model performance as the composition of the main syngas components is influenced by solid/gas reactions (e.g. Boudouard reaction). Equilibrium calculations could predict the H_2S content, which is the main sulfur compound in syngas. Nevertheless, such a simplified model is not suitable to estimate the formation of a variety of OSCs. Thus, concerning sulfur distribution, the integration of semi-empirical correlations that incorporate the main parameters influencing the OSC content in syngas (e.g. temperature, sulfur content in the fuel, etc.) are proposed as future work.

Overall, the semi-empirical equilibrium model presented in this chapter can be considered as an appropriate tool for process modeling and flowsheet development. However, it lacks accuracy when component design is of interest (gasifier, downstream cleanup equipment, etc.), where more detailed models would be required. The equilibrium model was further modified (see Chapter 7) to account for the content of various contaminants in syngas. The formation of tar and light hydrocarbons was considered there and gasification heat losses were also coupled to the Aspen Plus model.

3 Experimental study of sulfur and light tar removal by activated carbon

3.1 Literature review of sulfur and tar removal by AC sorbents and context of the study

Cleanup of coal- or biomass-derived syngas prior to catalytic synthesis requires several gas treatment steps, such as AGR and removal of contaminants present at low concentrations, such as chlorine and sulfur species. Although H_2S can be selectively removed by AGR processes [157], it is not completely eliminated [158] and it is a major contributor to noble metal catalyst poisoning, such as nickel (Ni) containing catalysts [159, 160]. Physical absorption processes (e.g. Rectisol) can remove H_2S prior down to 0.1 ppmv. However, they operate under elevated pressures and therefore, the power consumption of such units is usually high [158]. In addition, they operate at very low temperatures, which may induce undesired syngas cooling. Chemical absorption processes can operate at lower pressure and higher temperature, but thermal power is required for solvent regeneration [161]. In the context of this thesis, aqueous potassium carbonate (K_2CO_3) solvents are investigated due to the advantages of low reboiler duty and milder corrosion effects with respect to amines [162]. However, the clean, "sweet" syngas from the process still contains sulfur [163], as the process is not highly selective towards sulfur species. Particularly, OSCs such as thiophene, benzothiophene and dibenzothiophenes cannot be effectively removed by K_2CO_3 solutions [163]. Therefore, the coupling of AGR processes with guard beds with zinc oxide (ZnO) and/or activated carbon (AC) can contribute to the elimination of sulfur contaminants. ACs are promising materials for the sorption of impurities from syngas due to their high surface area, developed pore volume and competitive cost [164-166]. Surface treatment of ACs can improve their selectivity for specific syngas species and also enhance their capacity [167]. After sorption, the material can be regenerated by pressure swing or sold as fuel (it comprises, essentially, carbon) to combustion power plants equipped with $DeSO_x$ units. This constitutes an effective solution for small- to medium-scale units, for which a solvent-based selective sulfur removal process may not be financially viable. Apart from sulfur compounds, tar species can be additionally captured by ACs. Apart from the various problems that are attributed to tars such as clogging issues, potential benefits may arise when not all tar compounds are eliminated from syngas. In any case, the investigation of tar adsorption, as well as the coadsorption of sulfur and tar species on AC materials can provide important insight on the application of such materials for syngas cleaning.

Sorption of inorganic sulfur can be performed by both physical and impregnated ACs. So far, H_2S has been the most widely investigated sulfur compound, due to its high concentration in syngas and other off-gases. Xiao et al. [166] published an experimental study of H_2S sorption on Na_2CO_3-impregnated ACs derived from coal at temperatures of 30 °C and 60 °C, H_2S concentrations in the range 200-1000 ppmv and for various relative humidity (*RH*) conditions. The authors concluded that such a modification can increase the sorbent capacity under anaerobic conditions. Bandosz et al. [168] compared the performance of three different ACs, either unmodified or NaOH-impregnated, as sorbents for removing H_2S with a concentration up to 1 vol.% from off-gases. The authors concluded that unmodified ACs can be suitable materials for H_2S removal due to their catalytic activity in promoting dissociative adsorption of H_2S and its subsequent oxidation. Hervy et al. [169] produced ACs after treating pyrolysis chars by O_2/N_2 mixtures and steam but without chemical treatment. They subsequently investigated the ACs as materials for the adsorption of H_2S contained in three different, dry carrier gases (air, N_2 and syngas). They concluded that important char properties for H_2S removal are a high specific surface area and mesoporous volume, a surface with alkaline pH, the existence of mineral species on the AC surface (e.g. Ca, Al and Fe), the presence of O-containing groups, as well as a disorganized carbonaceous structure. Apart from H_2S, studies have also focused on COS and CS_2, which have significant concentrations in gasification product gases. Bak et al. [170] investigated the performance of various ACs for the adsorption of H_2S, COS and CS_2 at ambient conditions and they compared it with that of other sorbents. The authors concluded that ACs have a satisfactory affinity for the sorption of CS_2.

Regarding OSCs, Wen et al. [171] investigated the adsorption of sulfur and nitrogen organic compounds contained in model liquid fuels on ACs. Dibenzothiophene (DBT) was used as a model OSC and it was concluded that S and N compounds are adsorbed on different AC active sites. In addition, an increase in the adsorption capacity of DBT with temperature was noted and it was attributed to chemisorption on the chemically-treated AC. Another field of interest is the adsorption of OSCs which are used as odorants in NG or

SNG prior to their use in fuel cells. Cui et al. [172] investigated the performance of virgin, oxidized and impregnated ACs for removing H_2S, methyl mercaptan (MM), ethyl mercaptan (EM), dimethyl sulfide (DMS), dimethyl disulfide (DMDS), tetra hydro-thiophene (THT) and ethyl disulfide (EDS) at ambient conditions. Different modifications were found to be effective for selectively removing specific sulfur species and based on the results, optimized AC materials were proposed. Another experimental study on the adsorption of thiols and disulfides on ACs has been presented by Vega et al. [173], who focused on EM, DMS and DMDS.

Furthermore, tar compounds of various structures and with different boiling points can be removed by ACs. Many studies have focused on the adsorption of BTX compounds, while other common syngas species such as naphthalene ($C_{10}H_8$) have also been investigated as single species or in mixtures. Shin et al. [174] investigated the adsorption of benzene, toluene and ethylbenzene contained in raw landfill gas (LFG) onto ACs, addressing the effect of the water content on the breakthrough times and capacities. Lillo-Ródenas et al. [175] studied the adsorption of benzene and toluene on virgin and chemically-treated ACs at ambient temperature, while they provided an extensive literature review of benzene/toluene adsorption studies on ACs at concentration and temperature ranges of 50-800 ppmv and 24-37 °C, respectively.

Indicative studies that focused on the removal of tar species from pyrolysis and gasification product gases are those of Phuphuakrat et al. [176], Hanaoka et al. [177] and Ravenni et al. [178]. Phuphuakrat et al. [176] investigated the adsorption of various tar compounds produced from biomass pyrolysis followed by a tar reformer. It was concluded that AC can be effective in removing light aromatic hydrocarbons and light PAHs from the product gas, while a condensable tar content of 65 mg m^{-3} was measured at the AC packed bed outlet. Recently, Ravenni et al. [178] published an experimental study on the performance of carbon-based sorbents for tar removal within the temperature range 250-800 °C and tested ACs activated *via* different methods. Mixtures of toluene and naphthalene were used for tar representation and the authors noted that up to 400 °C, no decomposition/cracking reactions on ACs take place. Moreover, adsorption of naphthalene on gasification chars was found to be comparable to that of AC materials in terms of capacity at 250 °C, while the capacity of all sorbents significantly diminished at 400 °C. Hanaoka et al. [177] investigated the removal of tar and sulfur species (H_2S, COS) by AC packed beds from simulated gas and real syngas produced by a downdraft gasifier. Temperatures up to 450 °C were investigated and a sorbent system was proposed to remove sulfur gases to less than 0.1 ppmv along with three- and four-ring PAHs in the first stage, as well as one- and two-ring PAHs except for benzene in the second stage. Table 3-1 summarizes several experimental studies which have investigated the adsorption of sulfur (inorganic and OSCs) and/or tar species (light and heavy tar) onto ACs.

The following observations can be made based on the literature review which was presented:

a. Although several experimental studies have investigated the adsorption of inorganic sulfur (mainly H_2S) on ACs, research on the adsorption of OSCs in the gas phase at gasification-relevant concentrations are relatively rare. Most of them focus on adsorption of mercaptans and sulfides on virgin and modified ACs and not on less volatile S-species contained in syngas, such as thiophene (C_4H_4S). Liquid fuel desulfurization by ACs has greatly attracted research interest and thiophenes (especially thiophene, BT and/or DBT) are common model compounds [179]. In this direction, most available studies have been carried out at low temperatures, not exceeding 60 °C.

b. There is little research on the coadsorption of sulfur and tar species (light or heavy) onto ACs in real syngas matrices. Specific syngas components can affect the removal efficiency either positively or negatively (e.g. CO_2 and H_2O).

In this context, the present experimental study initially investigates the performance of AC as a material for C_4H_4S removal from a carrier gas at high temperature corresponding to "warm" syngas cleaning conditions (100-200 °C). In a next step, the simultaneous adsorption of sulfur (mainly H_2S) and light tar (mainly C_6H_6) contained in the syngas produced from a 1 MW_{th} pilot-scale, biomass-fueled EFG unit is presented. The obtained results are expected to be useful for the coupling of AC sorbents with high-temperature AGR processes, when the latter are not capable of completely eliminating sulfur downstream of the absorption column.

Table 3-1: A literature review of experimental studies dealing with sulfur and tar adsorption onto ACs.

Compounds and phase	AC type	Experimental conditions	Investigated parameters/ other remarks	Source
Sulfur compounds				
H_2S (gas phase)	Virgin[1] and Na_2CO_3-impregnated AC	C_{H_2S} : 100-1,000 ppmv T : 30 °C, 60 °C RH : 0-80% V_{tot} = 120 mL min^{-1}	– Effect of initial H_2S concentration – Effect of moisture content – Effect of AC type – Effect of temperature	[166]
H_2S (gas phase)	Virgin and NaOH-treated AC	C_{H_2S} = 1 vol.% According to Calgon TM41R method	– Effect of AC type	[168]
H_2S (gas phase)	O_2-treated and steam activated pyrolysis char	C_{H_2S} = 200 ppmv T: 21-23 °C V_{tot} = 180 mL min^{-1}	– Effect of AC type – Effect of dry gas carrier on adsorption efficiency (N_2, air, syngas)	[169]
EtSH and DMS/ C_2H_6S, DMDS /$C_2H_6S_2$ (gas phase)	Virgin and chemically treated AC by nitric acid and ozone	C_i = 4 ppmv T = 20 °C ± 2 °C V_{tot} = 250 mL min^{-1}	– Effect of S-compound type – Effect of AC type	[173]
DBT (liquid phase)	H_3PO_4-treated AC	C_i : 7.9-39.7 µmol g^{-1} T : 25, 40, 55 °C V_{tot} = 0.1 mL min^{-1} m_{ac}/m_{liq} = 1:50	– Effect of initial DBT concentration – Effect of liquid carrier type (model fuel) – Effect of temperature – Effect of coadsorption of S and N species	[171]
H_2S, MeSH, EtSH, DMS, DMDS, THT, EDS (gas phase)	Virgin AC, ACs treated with oxidizer, alkaline solutions and impregnated with Cu, Zn and Fe	C_{tot}: 5.3-9.9 ppmv T = 26 °C V_{tot} = 4.0-4.5 L min^{-1} $GHSV$ ~ 30000 h^{-1}	– Effect of AC type – Effect of S-compound type	[172]
H_2S, COS, CS_2 (gas phase)	Virgin and impregnated ACs (in comparison to other sorbents)	C_{H_2S} = 1900 ppmv C_{COS} = 100 ppmv C_{CS_2} = 100 ppmv T = 25 °C V_{tot} = 300 mL min^{-1} $GHSV$ ~ 6220 h^{-1}	– Effect of AC type For the selected material: – Effect of GHSV – Effect of inlet concentration – Effect of temperature	[170]
C_4H_4S, BT and DBT (liquid phase)	Virgin and ACs loaded with Ce/Fe	C_i : 50 ppmv (each) T : 25 °C V_{tot} = 10 L s^{-1}	– Effect of AC type and AC/Fe/Ce dosage	[179]

			– Coadsorption of thiophene, BT and DBT	

Tar compounds and coadsorption of tar/sulfur species

Compounds and phase	AC type	Experimental conditions	Investigated parameters/ other remarks	Source
Benzene/C_6H_6, Toluene/C_7H_8 (gas phase)	Virgin and KOH/NaOH- or H_3PO_4-treated AC	C_i = 200 ppmv T = 25 °C ± 1 °C V_{tot} = 90 mL min^{-1} *Sup. veloc* ~ 318 cm min^{-1}	– Effect of AC type and properties	[175]
Benzene/C_6H_6 to pyrene/$C_{16}H_{10}$ (10 compounds in gas phase)	Virgin AC	C_i : varying depending on tar species T = 25-30 °C	– Comparison of AC with other sorbent types – Integration of tar reforming and adsorption	[176]
Benzene/C_6H_6, Toluene/C_7H_8, Ethylbenzene/ C_8H_{10} (gas phase)	SGA-100, Samchonli Ltd. Korea	C_i = 400 and 600 ppmv T = 24 °C ± 2 °C *RH :* 0-90% *Sup. veloc* ~ 35.7 cm min^{-1}	– Effect of initial concentration (LFG[2] carrier gas) – Effect of moisture content – Effect of temperature	[174]
Heavy and light tars, H_2S and COS (gas phase)	Virgin and Fe-impregnated ACs	$C_{i,S}$: 7-18 ppmv C_{tar}: ~ 2.4 g Nm^{-3} T : 60-450 °C V_{H2O} *:* 0, 10 vol.% V_{tot} = 40 Nm^3 h^{-1}	– Effect of AC type – Effect of moisture content – Effect of temperature – Co-removal of tar, H_2S and COS	[177]
Toluene/C_7H_8 and naphthalene/ $C_{10}H_8$ (gas phase)	Virgin ACs or CO_2-avtivated	$C_{C_7H_8}$ = 18.3 g Nm^{-3} $C_{C_{10}H_8}$ = 1.8 g Nm^{-3} T = 250-800 °C V_{car} = 4.7 L min^{-1} *Resid. time* ~ 0.35-0.72 s	– Effect of AC type – Effect of temperature – Coadsorption and cracking of C_7H_8 and $C_{10}H_8$	[178]

[1]Virgin=steam activated, [2] LFG=landfill gas

3.2 Experimental investigation of C_4H_4S adsorption in a lab-scale test rig

3.2.1 Materials and chemicals

Argon (Ar) with a purity ≥ 99.998 % was used as a carrier gas. The model compound was supplied from a gas cylinder containing 500 ppmv C_4H_4S in helium (He). A physically activated carbon developed by CECA was the sorbent in this campaign. The material was crushed and then sieved and the 125-160 μm fraction was separated and used for the experiments. Additionally, other material properties related to the sorption behavior were measured. Particularly, the specific surface area (SSA) was obtained through the BET method and the pore size distribution through the BJH method by N_2 physisorption using a Micromeritics Tristar II. Prior to the

measurements, the sample was degassed at 150 °C for 3 h. Moreover, the skeletal density of the material was determined by a Micromeritics AccuPyc II 1340 pycnometer. The AC properties are summarized in Table 3-2.

Table 3-2: Properties of the AC material used in the experimental study.

Parameter	Values
AC type (raw material)	4 mm Extruded Mineral Steam Activated Carbon CECA ACM40-4WA
Benzene Index	40 ± 2
CCl_4 Index	>80
Average particle diameter, d_p (µm)	138
Bulk density (kg m^{-3})	497
Skeletal density (kg m^{-3})	2,450
Specific surface area, BET (m^2 g^{-1})	991
Pore radius (m)	$13 \cdot 10^{-10}$

3.2.2 *Experimental setup*

The experimental investigation was carried out at the Energy and Environment Research Division (ENE) of Paul Scherrer Institute (PSI) in Switzerland. The apparatus is divided into four sections, particularly the gas mixing, gas distribution, reactor and gas analysis sections. The test rig which was used for the lab-scale tests is depicted in Figure 3-1. The gas mixing section comprises a set of mass flow controllers (MFC, Bronkhorst EL-FLOW) to deliver defined amounts of gases. Argon, C_4H_4S and water were mixed in a heated mixing chamber to produce simulated gases with specific C_4H_4S and H_2O concentrations. Steam was produced by feeding water to a heated cross-piece by means of a syringe pump (Harvard Apparatus PHD 2000).

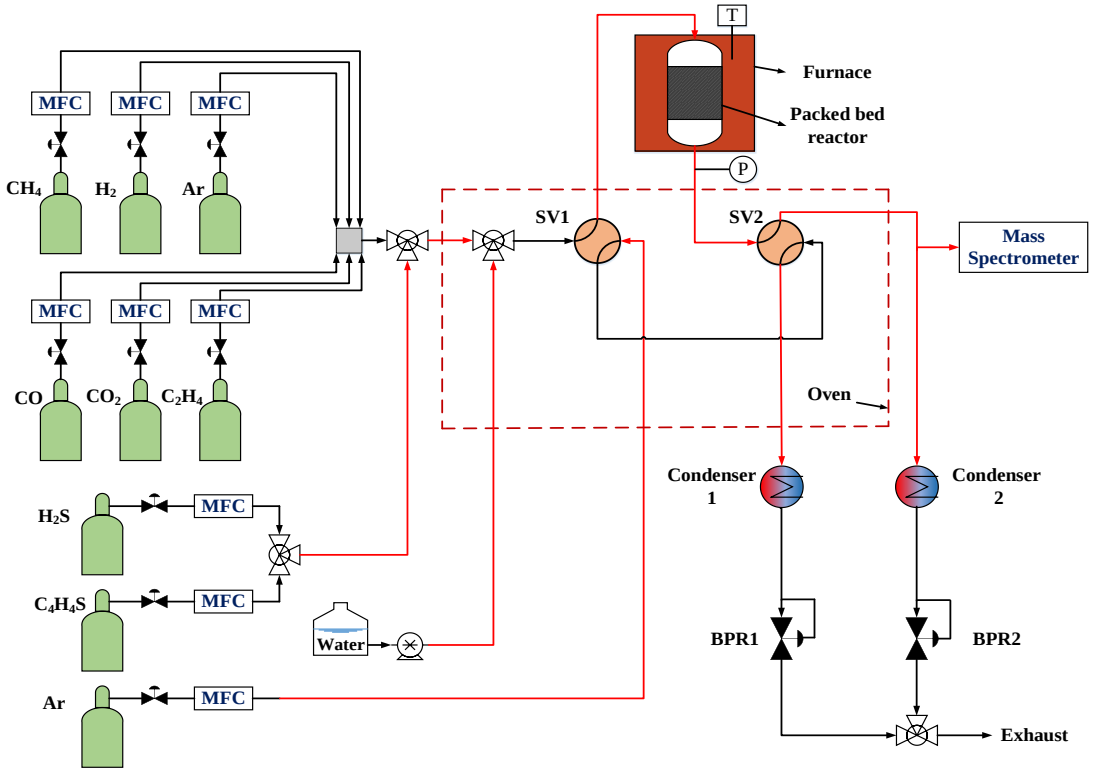

Figure 3-1: Schematic diagram of the lab-scale test rig for C_4H_4S adsorption.

All metal tubing in contact with the gas flow is coated with SiO_2 (SilcoNert® 2000) to prevent sulfur adsorption on the metal surface. The gas mixing section and the gas distribution section were both kept at 140 °C. The gas

distribution section consists of two four-port valves marked as SV1 and SV2 (VICI), which determine whether the gas mixture will flow through the reactor or through the bypass line. The switch valves also regulate the direction of the inert Ar flow which is supplied by a separate MFC. Moreover, two backpressure regulators (EL-Press, Bronkhorst), placed downstream of the reactor and in the by-pass line, respectively, control the system pressure. The quartz reactor (2 mm ID, 6 mm OD) was placed in a vertical, cylindrical-tube furnace (Carbolite MTF 12/25A) and it was operated in down-flow mode. The temperature inside the furnace is measured by a K-type thermocouple, while the sample temperature at different experimental conditions was calculated from previously recorded oven temperature profiles. The tubing was equipped with heat tracing and insulation, while the temperature was adjusted and maintained *via* PID controllers. Particularly, connecting tubes to and from the reactor were kept at temperatures above *ca.* 70 °C to prevent condensation and minimize sulfur adsorption. To prevent condensation of the moisture in the simulated gas, additional heated jackets were connected at cold spots at the input and outlet of the fixed bed reactor.

In Figure 3-2, different sections of the test rig are depicted. Particularly, the oven containing the mixing and switching valves (a), the switch valve actuators (b), the syringe pump (c), the gas mass flow controllers (d), the furnace and glass reactor with the sorbent (e), the heated inlet tubing towards the reactor (f) and the dosing syringe for water (g) are shown.

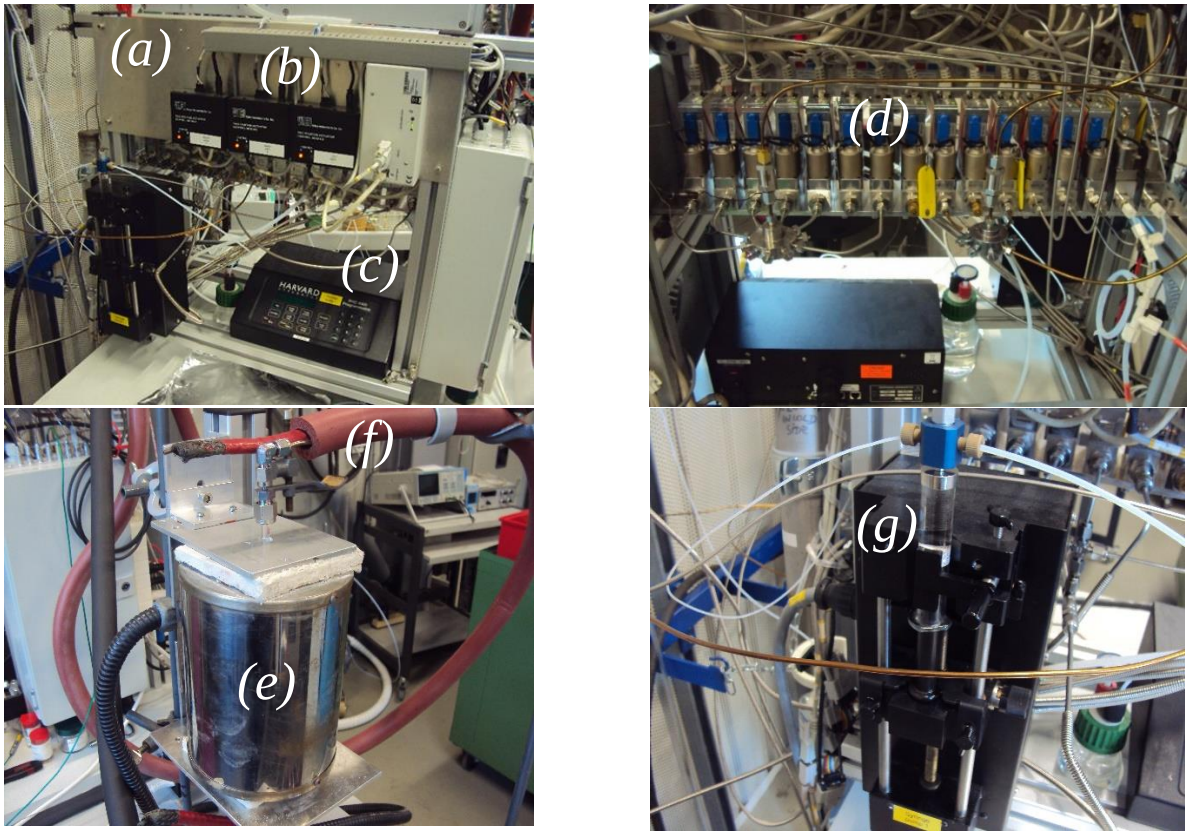

Figure 3-2: Depiction of the experimental test rig for sorbent screening.

3.2.3 Analytical Methods

Part of the gas (~ 1 NmL min^{-1}) from the second switch valve is sent to a mass spectrometer (MS) through a fused-silica column (180 μm ID) for analysis. Manufacturer specifications for this system are shown in Table 3-3. Calibration was done by measuring the inlet gas mixture fed through the bypass line to the MS analyzer. After switching to the reactor path, the gas concentration of C_4H_4S could be calculated according to Equation 3-1.

$$c_{thioph,exit} = c_{thioph,ref} \frac{I_{84,meas}}{I_{84,ref}} \qquad \textit{Equation 3-1}$$

Table 3-3: Mass spectrometer specifications [180].

Parameters/characteristics	Specifications
Type and model	Extrel Mass Spectrometer MAX300-LG
Mass spectrometer/detector	19 mm quadrupole mass filter
Mass range options	1-250 amu (standard option), 1-300 amu (available)
Component/analysis limitations	Unlimited components per analysis and analyses/sequences
Detection range	100% to 10 ppb
Mass resolving power (M/deltaM)	2,000
Accuracy	± 0.0025% on 1% Ar with no interference
Stability	± 0.005% on 1% Ar over 30 days
Response	< 400 ms
Sampling pressure conditions	Atmospheric to < 13 mbar (with ACSS inlet)
Sampling temperature conditions	Maintained at 120 °C during experiments (up to 250 °C)

The parameter *I* in Equation 3-1 refers to the measured intensities at the corresponding *m/z* and c_i refers to the gas concentration of the corresponding species in ppmv. For the applied method, the limits of detection (LOD) and quantification (LOQ) of C_4H_4S were calculated to be 0.12 ppmv and 0.39 ppmv, respectively.

3.2.4 Experimental procedure

For each experiment, 20 mg of sieved AC were weighed and transferred to the glass reactor. The sorbent was held in place by glass wool plugs. The reactor was connected to the setup and a leak test was performed at a pressure of 0.5 barg to ensure that no gas leakage could be detected at a gas flow rate of 3 NmL min^{-1}. The reactor was then heated to 150 °C under Ar atmosphere for 30 min to remove moisture at a flow rate equal to the total mass flow of simulated gas during the specific adsorption experiment. Subsequently, the temperature was set in the reactor (100, 150 or 200 °C). At the same time, the gas composition was set through the MFCs in the gas mixing section and the gas flow by-passed the reactor in order to achieve proper calibration of the MS instrument. In case a weak signal was obtained, flushing of the analyzer with higher C_4H_4S concentration was performed prior to each calibration. When a steady MS signal was obtained, switch valves were adjusted to connect the gas flow directly to the gas burner. This step was required to obtain a blank MS measurement prior to the adsorption experiment. When the signal was zero, switch valves were adjusted again to connect the gas distribution section to the reactor and initiate the experiment. Before this last step, fully steady conditions in terms of temperature in the reactor had been established. The reactor pressure was maintained at 0.5 barg in all experiments. Breakthrough curves were obtained for all tests, while breakthrough times are presented as the time required to reach 90 % of the inlet C_4H_4S concentration at the reactor exit. Accordingly, total capacities have been calculated on the same basis.

The adsorption capacity or breakthrough capacity q_m (mg C_4H_4S g^{-1} AC) was calculated based on Equation 3-2

$$q_m = \frac{MW_{thioph} C_0 \dot{V}}{1000 m_{AC}} \int_0^{t_s} \left(1 - \frac{C_t}{C_0}\right) dt \qquad \textit{Equation 3-2}$$

where MW_{thioph} is the molecular weight of C_4H_4S (84 g mol^{-1}), C_0 is the inlet C_4H_4S concentration (mol m^{-3}), C_t is the outlet C_4H_4S concentration at time t (mol m^{-3}), $\dot{V}$ is the flow rate (m^3 min^{-1}), t_s is the total saturation time (min) and m_{AC} is the mass of the AC bed (g).

The experimental conditions of the various tests are listed in Table 3-4. The effect of 4 parameters on the adsorption behavior of AC was investigated; adsorption temperature, gas flow rate, C_4H_4S concentration and H_2O concentration in the simulated gas. Concerning the H_2O content in the simulated gas, this value can be considered relatively low. In Chapter 2 (Table 2-4), the H_2O composition for air-blown gasification, as predicted from the Aspen Plus simulations, was about 10 vol.%, while this value is much higher for steam-blown gasifiers (> 35 vol.%). Operational issues for this specific campaign necessitated limiting the moisture content below 5 vol.% in the experiments. Despite this fact, the evaluation of C_4H_4S adsorption with and without H_2O addition can provide insight into the moisture effect on removal efficiency. In addition, the C_4H_4S content range (8.5-30

ppmv) in the simulated gas can be considered representative of biomass gasification. According to measurements from [88] and assuming that all OSCs can be represented by C_4H_4S, wood-derived syngas can contain 2-6 ppmv organic sulfur at typical λ conditions ($0.19 < \lambda < 0.35$), while this value increases to 31-43 ppmv for a biomass fuel with a higher sulfur content at low λ ($0.15 < \lambda < 0.20$).

Table 3-4: Test matrix of C_4H_4S adsorption onto AC.

Test	AC mass (mg)	Temperature (°C)	Gas flow rate (NmL min^{-1})	C_4H_4S concentration (ppmv)	H_2O content (vol.%)
1	19.50	100	30.0	15	0
2	20.63	150	30.0	15	0
3	20.00	200	30.0	15	0
4	20.00	100	30.0	15	3
5	20.30	150	30.0	15	3
6	20.27	150	42.5	15	0
7	19.65	150	55.0	15	0
8	20.29	150	30.0	8.5	0
9	20.31	150	30.0	23	0
10	20.11	150	30.0	30	0
11	20.46	100	30.0	8.5	0
12	20.26	100	30.0	30	0

Moreover, the value of the gas flow rate may greatly vary among different studies, since the packed bed column size and consequently, the amount of solid sorbent used, is different. In the present study a very small fixed-bed column made of glass was used (2 mm ID), which was loaded with ca. 20 mg of AC material. On the other hand, in the study of Cui et al. [172] a stainless steel reactor with 24.3 mm ID was fed with 4 g AC. Accordingly, the gas flow rates were different; a much higher flow rate was selected in the latter study. In order to better compare them, the parameter called "gas hourly space velocity" or *GHSV* (h^{-1}) can be used, as shown in Equation 3-3

$$GHSV = \frac{\dot{V}_{tot}}{V_{packed\_bed}} \qquad \textit{Equation 3-3}$$

where $\dot{V}_{tot}$ is the gas flow rate at normal conditions (Nm^3 h^{-1}) and V_{packed_bed} is the volume occupied by the sorbent in the reactor (m^3). The aforementioned parameter is particularly relevant for catalytic synthesis reactors, however, it is also used in studies related to sorbents. A definition based on sorbent mass can also be applied. The *GHSV* value which corresponds to the operating conditions of Cui et al. [172] was ~ 30000 h^{-1} for OSC adsorption on ACs. In this study, the investigated gas flow rates correspond to *GHSVs* higher than 40000 h^{-1}. However, *GHSV* values of this range have been used in other adsorption experiments as well, such as in the study of Guo et al. [181], in which chlorobenzene adsorption onto AC was investigated at a *GHSV* value of 72000 h^{-1}.

3.2.5 Results and discussion: C_4H_4S adsorption onto AC

Breakthrough time and capacity results of all experiments are summarized in Table 3-5. Among the various conditions studied, the highest C_4H_4S capacity of 11.59 mg g^{-1} AC was observed at a temperature of 100 °C, 30 NmL min^{-1} gas flow rate and a concentration of 30 ppmv C_4H_4S in the inlet gas stream. On the contrary, the lowest capacity of 0.59 mg g^{-1} was measured at 200 °C, 30 NmL min^{-1} total gas flow rate and 15 ppmv C_4H_4S in the inlet gas stream. Accordingly, sulfur breakthrough capacities ranged between 0.22 and 4.42 mg S g^{-1} AC, for the respective cases. The duration of C_4H_4S adsorption experiments varied between 10 and 152 min, before 90% of inlet concentration was measured at the fixed bed outlet by the MS analyzer. In the following subsections, the effect of the studied parameters (*i.e.* adsorption temperature, gas flow rate, C_4H_4S concentration and H_2O concentration) is analyzed. The respective breakthrough curves are given in Figure 3-3, Figure 3-4 and

Figure 3-5. Moreover, the fitting of the equilibrium capacity results to different isotherm models is presented. A sufficient agreement of the experimental results with isotherm models is important for their application for modeling AC fixed beds.

Table 3-5: Summary of breakthrough time and capacity results for all tests.

Test	Breakthrough time, t_{90} (min)	Breakthrough S capacity (mg S g^{-1} AC)	Breakthrough capacity, q_{90} (mg C_4H_4S g^{-1} AC)
1	108	3.10	8.15
2	26	0.64	1.68
3	10	0.22	0.59
4	83	2.45	6.44
5	24	0.60	1.57
6	20	0.64	1.68
7	14	0.67	1.76
8	39	0.42	1.09
9	24	0.76	2.00
10	18	1.09	2.86
11	152	2.11	5.54
12	73	4.42	11.59

3.2.5.1 Effect of temperature

Temperature has a significant effect on the AC breakthrough capacity, as well as on the shape of the breakthrough curve. A major sorbent capacity decrease by 80% was found to occur for a temperature increase from 100 °C to 150 °C, while at 200 °C the sorbent sustains 7% of its initial capacity measured at 100 °C. This trend can be attributed to the exothermic adsorption process, during which heat is released due to surface bonding. Breakthrough curves at higher temperatures had a steeper slope compared to the 100 °C curve. This shape can be affected by several factors. The increased volume flow rate through the bed, the less favourable isotherm with increasing temperature and the enhanced pore diffusion (*i.e.* reduced mass transfer resistance) contribute to the aforementioned results.

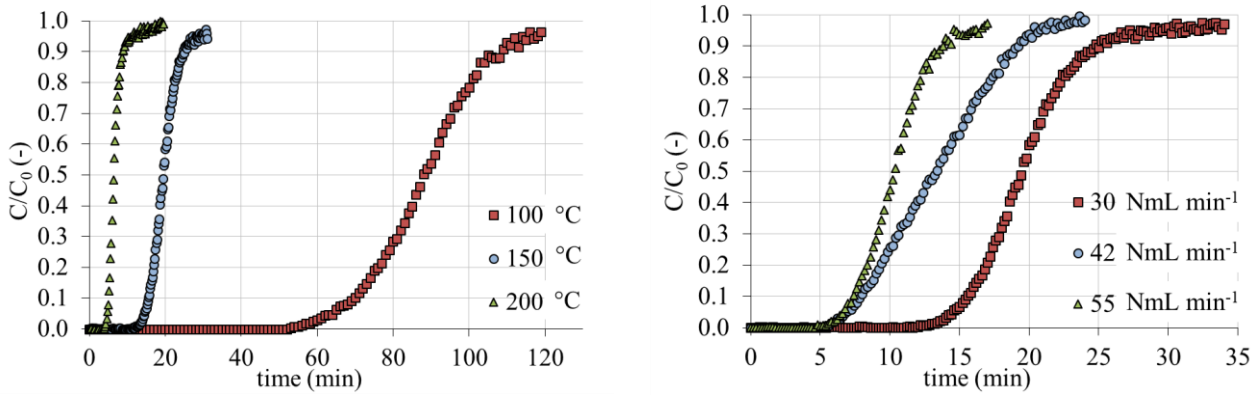

Figure 3-3: (Left) Breakthrough curves of C_4H_4S adsorption onto AC at 100, 150 and 200 °C (C_4H_4S inlet concentration: 15 ppmv, gas flow rate: 30 NmL min^{-1}, no H_2O addition) and (right) breakthrough curves of C_4H_4S adsorption onto AC for gas flow rates of 30.0, 42.5 and 55.0 NmL min^{-1} (C_4H_4S inlet concentration: 15 ppmv, temperature: 150 °C, no H_2O addition).

The effect of temperature on inorganic sulfur adsorption onto AC materials has been described to be similar by Xiao et al. [166]. The authors reported that the H_2S capacity of Na_2CO_3-promoted AC decreases by increasing temperature from 30 to 60 °C. It was proposed that temperature significantly affects H_2S physical adsorption and a decrease in the breakthrough time was also reported. Of course, it should be noted that the impregnation of solid sorbents can trigger endothermic reactions between the sorbent and the adsorbate species and in that case, a temperature increase will favor the adsorption process. For instance, Bak et al. [170] discussed that FeOOH-based sorbents involve such endothermic reactions, which induce improved chemisorption of H_2S at

higher temperatures. Moreover, Wang et al. [182] studied C_4H_4S (in *n*-octane) adsorption onto 4 different carbon-based materials. The authors calculated that the values for the heat of adsorption of C_4H_4S were as low as 14 kJ mol^{-1} for Maxsorb and as high as 24 kJ mol^{-1} for graphene. The outcome was attributed to a larger number of high-energy locations on graphene due to edge and defect sites. Between those sorbents, the heat of adsorption of AC was found to be *ca.* 17 kJ mol^{-1}. In the present study, the heat of adsorption was estimated to be higher (49.4 kJ mol^{-1}) compared to the values in [182]. Chemical modification of ACs can be a useful practice to further increase the capacity. Particularly for C_4H_4S, Wang et al. proposed that acid functional groups e.g. −COOH groups can increase the breakthrough capacity due to their affinity with the lone pair of electrons of S-atoms in C_4H_4S.

3.2.5.2 Effect of gas flow rate

The variation of the gas flow rate affects the sorbent capacity only to a minor extent since no change in the C_4H_4S partial pressure exists. While a slight increase in the capacity at the highest *GHSV* value was measured, the variations were < 3% for the flow rate range studied in the present work. However, the breakthrough time decreased significantly (approximately 50%) when the flow rate increased from 30 to 55 NmL min^{-1}. This can be attributed to the increase of the C_4H_4S molecules which enter the fixed bed cross-section per unit time. Accordingly, the concentration front moves faster due to this increase in the adsorbate flow rate. The shape of the breakthrough curve did not change significantly with the increase in the gas flow rate and a minor steepening of the breakthrough curve at 55 NmL min^{-1} was noted. If a normalized time expressed as $\tau = tu_s/L_{bed}$ is adopted in the *x*-axis, where t is the time (s), u_s is the superficial velocity (m s^{-1}) and L_{bed} is the bed length (m), the breakthrough curves are expected to flatten as the gas flow rate increases. During this flow rate increase, the residence time in each slab decreases, however, the time needed by a C_4H_4S molecule to diffuse into the AC particle remains constant which limits the adsorption rate.

Bak et al. [170] noted that the H_2S capacity of iron oxide hydroxide sorbents (IHS) is affected by *GHSV*. Particularly, the breakthrough capacity decreased asymptotically as *GHSV* increased from 1000 to 4000 h^{-1}. The fact that much higher space velocities were used in the present study must be taken into account when comparing such trends, particularly since Bak et al. reported that the effect of an increased gas flow rate diminishes for *GHSV* > 4000 h^{-1}. Better insight can be provided by a comparison with the results of Barelli et al. [183], who compared the performance of virgin AC, impregnated AC with Cu (II) and Cr (IV) salts and zeolite materials regarding H_2S and DMS adsorption. The authors found that H_2S adsorption was highly influenced by the *GHSV* conditions, which varied in the range 527-10000 h^{-1} during the experimental tests. They correlated the sorbent capacity C_{ads} with *GHSV* as shown in Equation 3-4

$$C_{ads} = a + \frac{b}{GHSV} \qquad \textit{Equation 3-4}$$

denoting an asymptotical decrease of the breakthrough capacity with an increase in *GHSV*.

When DMS was used as the adsorbate species, the authors found that the DMS adsorption is not greatly influenced by the *GHSV* conditions. In addition, it is interesting to note that while the breakthrough time significantly declined for a *GHSV* increase from 700 to 4000 h^{-1} for both AC sorbents, the breakthrough capacity of DMS remained the same or slightly increased for the maximum gas flow rate depending on the type of the AC material. Based on the results of the present work, this trend seems to apply also in the case of C_4H_4S. Overall, a weak correlation of breakthrough capacity with the gas flow rate can be attributed to a smaller affinity of the adsorbate compound with the sorbent surface. Differences between the nature of adsorbate molecules (e.g. molecule shape, charge distribution, etc.) and the pore structure (such as micropore volume) of the material itself can play an important role when determining the effect of the gas flow rate increase on the obtained capacities. Considering the requirements for developing suitable AC materials for C_4H_4S, Tang et al. [184] proposed that an AC material with big average pore size and a high ratio of micropore volume to the total pore volume can improve the adsorption of C_4H_4S contained in liquid solutions.

3.2.5.3 Effect of thiophene inlet concentration

The breakthrough curves of C_4H_4S adsorption tests under varying C_4H_4S concentration in the range 8.5-30 ppmv are shown in Figure 3-4. Increasing the inlet C_4H_4S concentration increased the sorption capacity as a result of the expected isotherm shape. However, for a favorable isotherm, the ratio of the adsorbed phase to the fluid phase concentration decreases with an increase in C_4H_4S concentration in the gas. So comparatively, a relatively

smaller degree of sorption capacity is expected when increasing the adsorbate partial pressure due to the prior adsorption of molecules, which occupy active sites on the material. At 100 °C, a concentration increase from 8.5 to 30 ppmv resulted in a breakthrough capacity increase by a factor of 2.1, while at 150 °C for the respective concentration change, a higher breakthrough capacity by a factor of 2.6 was found.

At the same time, the breakthrough time and the slope of the curves were found to be dependent on the adsorbate partial pressure. The breakthrough time decreased by *ca.* 50% for the higher C_4H_4S concentration, while the slope of the breakthrough curve gradually increased. A higher driving force along the pores is responsible for a higher adsorbate mass flux from the gas phase to the solid material. This flux relates to the product of a mass transfer coefficient k and the difference between the equilibrium and actual solid-phase concentration (linear driving force model). Film and intra-particle resistances contribute to the overall mass transfer resistance (inverse of mass transfer coefficient). Between the two, the intra-particle resistance term contributes more than 90% to the overall value of $1/k$ during C_4H_4S adsorption, as reported in [140].

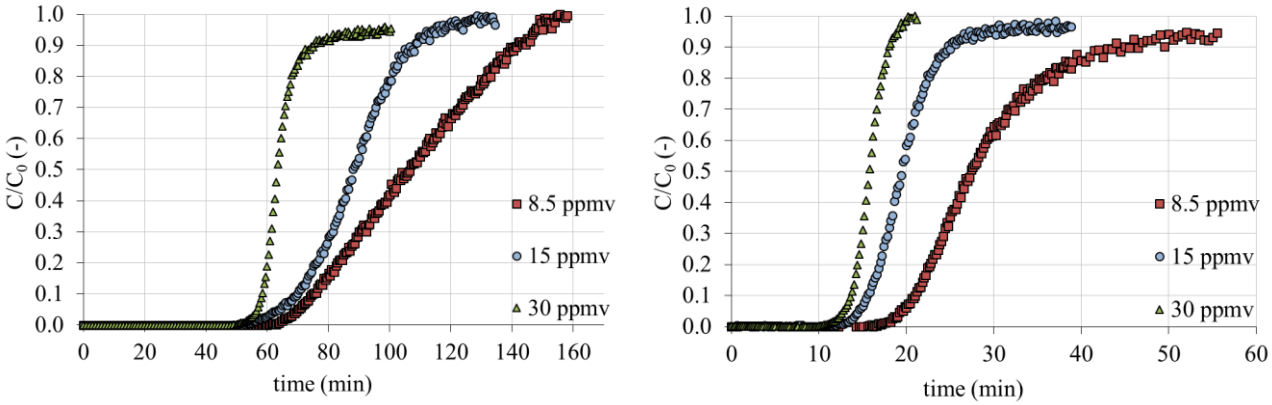

Figure 3-4: (Left) Breakthrough curves of C_4H_4S adsorption onto AC for 8.5, 15 and 30 ppmv inlet C_4H_4S concentrations (temperature: 100 °C, gas flow rate: 30 NmL min^{-1}, no H_2O addition) and (right) breakthrough curves of C_4H_4S adsorption onto AC for 8.5, 15 and 30 ppmv inlet C_4H_4S concentrations (temperature: 150 °C, gas flow rate: 30 NmL min^{-1}, no H_2O addition).

3.2.5.4 Effect of water content

The effect of H_2O addition on C_4H_4S adsorption is shown for two different temperatures in Figure 3-5. A small increase in the H_2O content was found to influence the adsorption of C_4H_4S onto activated carbon under the investigated conditions. Specifically, the breakthrough capacity decreased by 20% and 7% at 100 °C and 150 °C respectively, when 3 vol.% H_2O was added in the gas mixture. This indicates that the presence of moisture in the gas mixture can have a greater impact on sorbent capacity compared to an increase of the *GHSV* of the AC bed during C_4H_4S adsorption, especially at lower temperatures. This capacity reduction can be attributed to the co-sorption of H_2O and C_4H_4S on the AC material. Previously published research has also noted that adsorption of H_2O can decrease the affinity of AC towards organic vapor sorption [185]. In other studies, the presence of H_2O has enhanced the sorbent capacity, such as in the case of H_2S adsorption [186]. According to Xiao et al. [187], the adsorption of OSCs on the surface of ACs can be inhibited when O-containing species with electronegative oxygen are present in the mixture. The extent of such inhibitory effect is correlated with the order of the dipole moment, as well as the order of the O-atom charge. The mechanism of this adsorption is described to be different from the adsorption of OSCs. Adsorption of polar compounds takes place due to intermolecular hydrogen bonding with acidic surface functional groups present on the AC surface. Since this interaction can prevent thiophenic species from bonding on the AC surface, it has a negative effect on the capacity of target adsorbates.

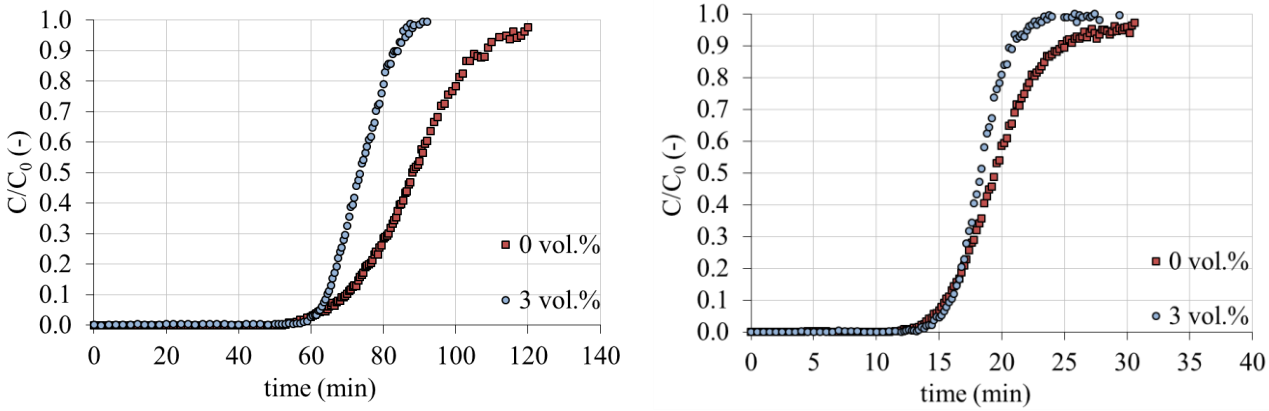

Figure 3-5: (Left) Breakthrough curves of C_4H_4S adsorption onto AC for dry carrier gas and 3.0 vol.% inlet H_2O content at 100 °C (C_4H_4S inlet concentration: 15 ppmv, gas flow rate: 30 NmL min^{-1}) and (right) breakthrough curves of C_4H_4S adsorption onto AC for dry carrier gas and 3.0 vol.% inlet H_2O content at 150 °C (C_4H_4S inlet concentration: 15 ppmv, gas flow rate: 30 NmL min^{-1}).

3.2.5.5 Isotherm fitting for breakthrough capacity prediction

An adsorption isotherm describes the correlation between the amount of an adsorbate species which has been adsorbed by a solid at a given temperature versus its partial pressure (P/P_0) or concentration C_e in the fluid phase (either gas or liquid) at equilibrium conditions. Different isotherm models have been developed in the literature. Concerning the adsorption isotherms, they are ultimately categorized into 6 groups by IUPAC, commonly denoted as Type I, II, III, IV, V or VI [188]. The shape of an isotherm can provide information regarding the adsorption mechanism and the type of bonds that are formed during the process. Models incorporating one to three parameters are commonly used for the adsorption of adsorbates onto ACs due to their simplicity. Two such models are the single-parameter Henry isotherm and the two-parameter, non-linear Langmuir isotherm. The Henry isotherm is the most simplified isotherm model to describe the correlation between the adsorbate partial pressure and the solid phase capacity. The Langmuir model is based on the assumptions that a) the adsorption process takes place on a homogeneous surface in a single layer and b) there is no interaction between the adsorbed molecules on the surface. In general, the Langmuir isotherm model is one of the most commonly applied models, which is known to provide very good agreement with available experimental data. Their expressions are given in Equation 3-5 and Equation 3-6, respectively.

Henry isotherm $$q_e = K_H C_e$$ *Equation 3-5*

Langmuir isotherm $$q_e = \frac{K_L q_{mL} C_e}{1 + K_L C_e}$$ *Equation 3-6*

In these equations, q_e is the solid-phase equilibrium C_4H_4S concentration (mol kg^{-1}), C_e is the C_4H_4S concentration in the gas phase (mol m^{-3}), K_H is the Henry constant (m^3 kg^{-1}), K_L is the Langmuir equilibrium constant (m^3 mol^{-1}) and q_{mL} is the saturation value of the Langmuir isotherm (mol kg^{-1}). The C_4H_4S gas-phase concentration C_e is correlated to the molar fraction y as shown in Equation 3-7 (P is pressure and R is the universal gas constant).

$$C_e = \frac{yP}{RT}$$ *Equation 3-7*

For the isotherm constants K_H and K_L, it is assumed that they are temperature-dependent and they are given by Equation 3-8 and Equation 3-9, respectively. In those equations, $K_{H,ref}$ (m^3 kg^{-1}) and $K_{L,ref}$ (m^3 mol^{-1}) are the Henry and Langmuir constant pre-exponential factors and ΔH_H and ΔH_L denote the heat of adsorption (J mol^{-1}) for each isotherm model, respectively. In both equation, T_{ref} denotes the reference temperature, which is assumed to be 273 K.

$$K_H = K_{H,ref} \exp\left[\frac{\Delta H_H}{RT_{ref}}\left(1 - \frac{T_{ref}}{T}\right)\right] \quad \text{Equation 3-8}$$

$$K_L = K_{L,ref} \exp\left[\frac{\Delta H_L}{RT_{ref}}\left(1 - \frac{T_{ref}}{T}\right)\right] \quad \text{Equation 3-9}$$

The isotherm constants were calculated through curve fitting in MATLAB. Their values are given in Table 3-6, while the root-mean-square error (*RMSE*) and the coefficient of determination (R^2) are also shown to compare the two models. In Figure 3-6, the experimental capacity results from the lab-scale tests are plotted against the Henry and Langmuir isotherm predictions for varying C_4H_4S gas phase concentration.

Table 3-6: Henry and Langmuir model constants and statistical results for data fitting.

Isotherm model	Parameter	Estimate
Henry	$K_{H,ref}$ (m^3 kg^{-1})	2186
	ΔH_H (J mol^{-1})	-2.58·10^4
	RMSE (mol kg^{-1})	0.016
	R^2	0.90
Langmuir	$K_{L,ref}$ (m^3 mol^{-1})	3.484·10^5
	ΔH_L (J mol^{-1})	-5.02·10^4
	q_{mL} (mol kg^{-1})	0.242
	RMSE (mol kg^{-1})	0.002
	R^2	0.99

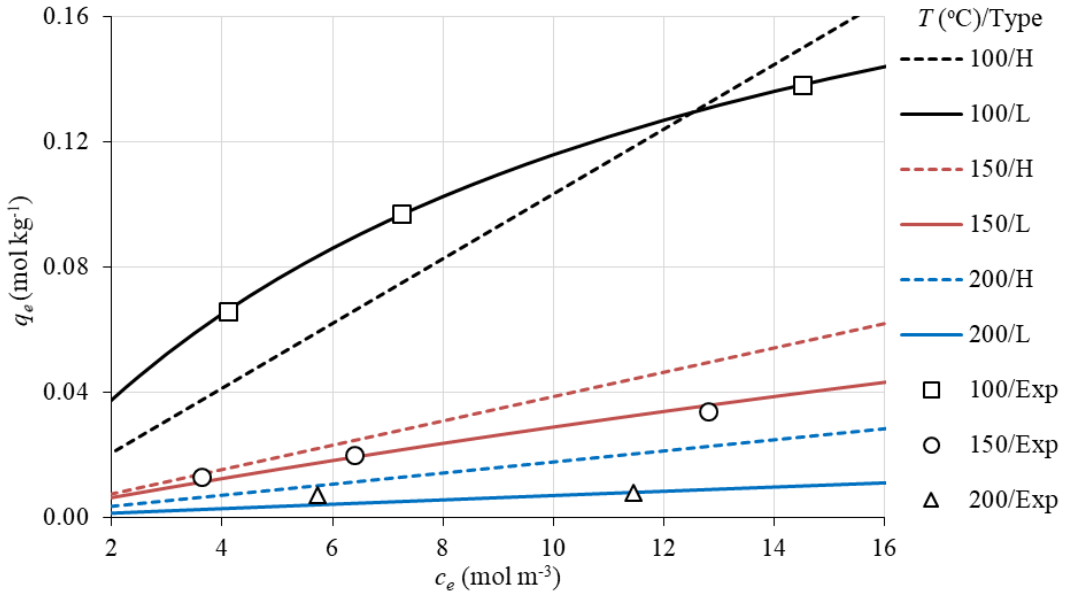

Figure 3-6: Adsorption isotherms of C_4H_4S for Henry and Langmuir models (H: Henry isotherm, L: Langmuir isotherm, Exp: Experimental data).

For the comparison of isotherm models to the experimental data at 200 °C, another test was carried out with a C_4H_4S concentration of 30 ppmv and otherwise similar conditions to Test 3. The results for this test are also shown in Figure 3-6. Parity plots comparing the experimental capacity measurements and estimates derived by the Henry and Langmuir isotherm models are depicted in Figure 3-7. The experimental tests which involved mixtures of C_4H_4S and H_2O have been excluded from these plots.

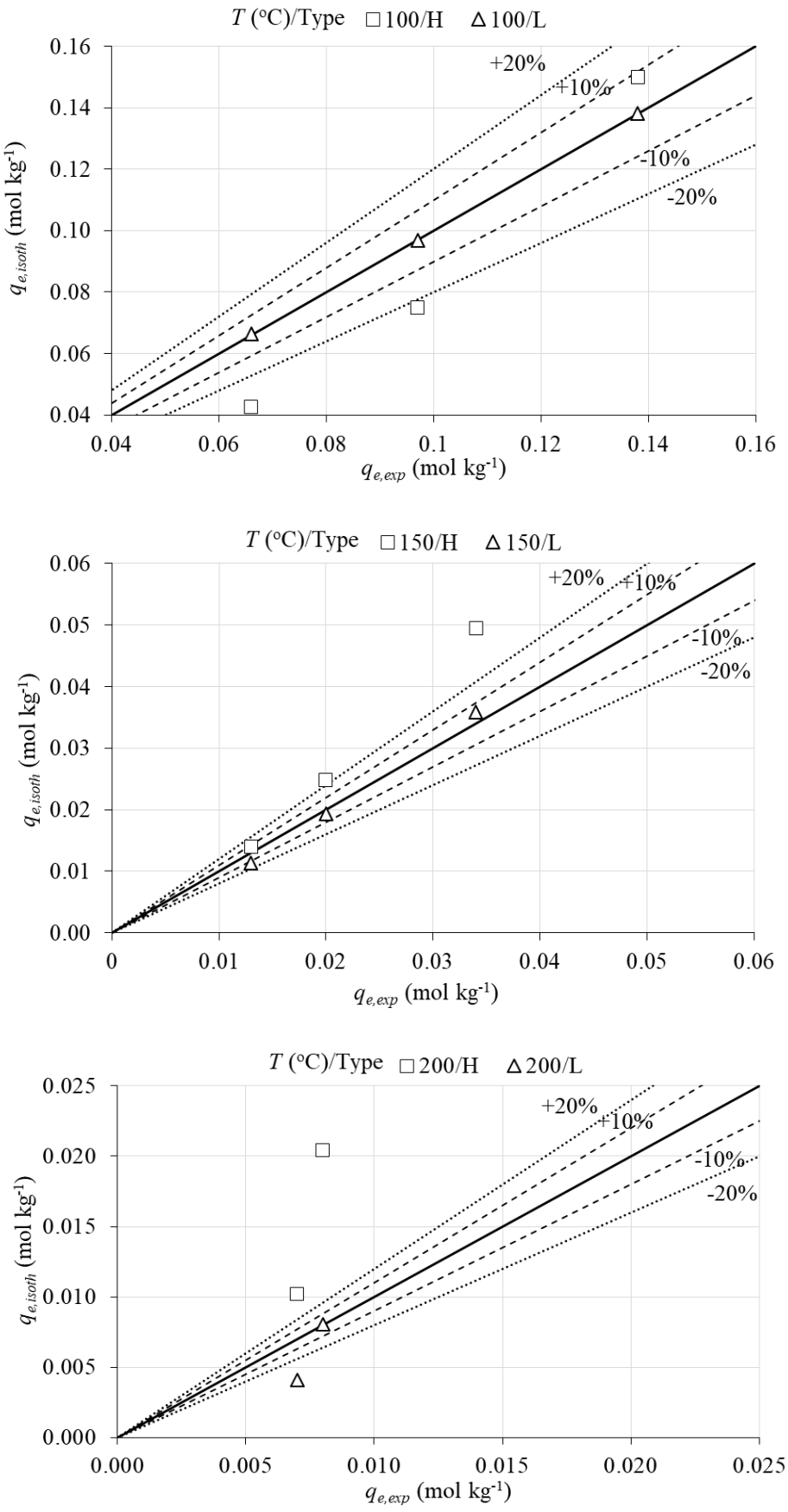

Figure 3-7: Parity plots representing AC capacities calculated from isotherm models (H: Henry, L: Langmuir isotherm) as a function of experimental data at 100 °C (top), 150 °C (middle) and 200 °C (bottom).

From Figure 3-6, it can be observed that the shape of Langmuir isotherm approaches the linear Henry model as the temperature rises and sorbent capacity decreases. The Henry model can be used only for a rough approximation of the AC capacity values, since its deviation from the experimental data exceeds in many cases the ± 20% range, as shown in Figure 3-7. On the other hand, the Langmuir model seems to be in good agreement with the experimental data, particularly at 100 °C. As the temperature increases to 150 °C, the deviation is greater, however, it is still within ± 20% at low and within ± 10% at high C_4H_4S concentration values. There was only one capacity value significantly underpredicted at 200 °C (exceeding the ± 20% range) and low C_4H_4S concentration (15 ppmv) by the Langmuir model. A better fitting of the experimental values can also be observed by the improved R^2 value, which exceeds 0.99 for the Langmuir isotherm and it is much higher compared to the Henry model (~ 0.90). Therefore, it can be suggested that the Langmuir model can adequately predict the C_4H_4S capacity values of the AC material within the investigated range of the test parameters. It is thus more suitable for implementation in kinetic models of C_4H_4S adsorption onto AC compared to the single-parameter Henry isotherm. Apart from the global sensitivity analysis study in [140], a validation of the breakthrough curves of the present work with a physical adsorption model with the Langmuir isotherm can be found in [189].

3.3 Experimental investigation of H_2S and tar removal from syngas derived from a 1 MW_{th} entrained-flow gasifier

3.3.1 Fuel and materials

Wood pellets were used as a fuel for the gasification tests. Table 3-7 presents fuel proximate and ultimate analyses. In order to be used in the gasifier, the pellets were pulverized through crushing and milling with a hammer mill (MAFA EU-4B) to obtain wood powder with *ca.* 100 μm mass median diameter (d_{50}). This corresponds to a hammer mill sieve size of 0.75 mm. A detailed PSD of the fuel for two different sieve sizes (0.75 and 1.5 mm) mounted on the aforementioned hammer mill can be found in the study of Weiland et al. [190]. The milled biomass is pneumatically transported and stored in the hoppers.

Table 3-7: Proximate and ultimate analyses of Swedish wood pellets.

Proximate analysis	
Moisture (wt. %, wet)	4.7
Ash (wt. %, dry)	0.4
Volatile matter (wt. %, dry)	80.5
Fixed carbon (wt. %, dry)	14.4
Ultimate analysis (wt.%, dry basis)	
C	50.6
H	6.3
N	0.10
S	0.006
Cl	0.02
O	42.4
LHV (MJ kg^{-1} dry biomass)	19.6

Concerning the adsorption tests, the same AC material which was used in the C_4H_4S tests was also used in the campaign with real syngas, with the exception that it was not milled prior to the tests. The AC properties were presented in Table 3-2.

3.3.2 Pilot-scale gasifier and syngas sampling system

The EFG installation, where the experiments were carried out, is located at the Energy Technology Center (ETC) in Piteå, Sweden. A schematic diagram of the pilot-scale EFG configuration is shown in Figure 3-8. The gasifier is a pressurized, entrained flow, ceramic lined (63 wt.% Al_2O_3, 31 wt.% SiO_2) reactor with 0.52 m inner

diameter and 1.67 m vertical length. The reactor is capable of operating at pressures up to 10 bar (absolute pressure) and temperatures ranging from 1200 to 1500 °C in slagging mode, while it has a nominal capacity of 1 MW_{th} fuel throughput. It was designed to operate with O_2 as a gasification agent, in concentrations varying from 100 vol.% down to 21 vol.%, when mixed with N_2. The mass flow rates of O_2 and N_2 are regulated *via* two MFCs (Bronkhorst F-203AI), while the O_2 mass flow rate is additionally measured with a Coriolis mass flow meter (Yokogawa Coriolis Rotamass RCCS31). Five (5) S-type thermocouples with ceramic encapsulation are used to monitor the temperature along the reactor height; particularly one (1) at the top of the reactor, three (3) at the middle circumference and one (1) at the lower conical part. In addition, a water-cooled, N_2-purged camera was installed at the gasifier top to visualize the reactor interior. Two biomass hopper tanks of 1 m^3 capacity each operate alternately, so that the pilot plant can run continuously. Calibration of fuel feeding mechanical devices was performed before each run. A minor flow of N_2 is mixed with the fuel supply to maintain an inert atmosphere back of the reactor burner. The accuracy of the fuel feeding system is in a ± 3% range, within a 95% confidence interval.

The syngas produced in the gasifier is transferred though the conical bottom part of the reactor to the quench section, where particles and condensable/high-boiling-point compounds are separated. Water is continuously supplied through a pump to the quenching section, which comprises 1) a two-stage/level spraying system that cools syngas down to *ca.* 100 °C followed by 2) a bubbling column section where solids and condensable species are collected. Samples from the quencher outlet are regularly collected for analysis, however, wastewater analysis was not carried out in the context of the present study. Apart from the two-stage syngas quenching/water-spraying system, a third spraying level operates for cooling and protecting the conical part of the reactor, as shown in the schematic diagram. Downstream of the gasifier, a backpressure regulator adjusts the system pressure. For the safe disposal of the gas flow to the atmosphere, the syngas outlet pipe is connected to the flare system (which is assisted by LPG combustion).

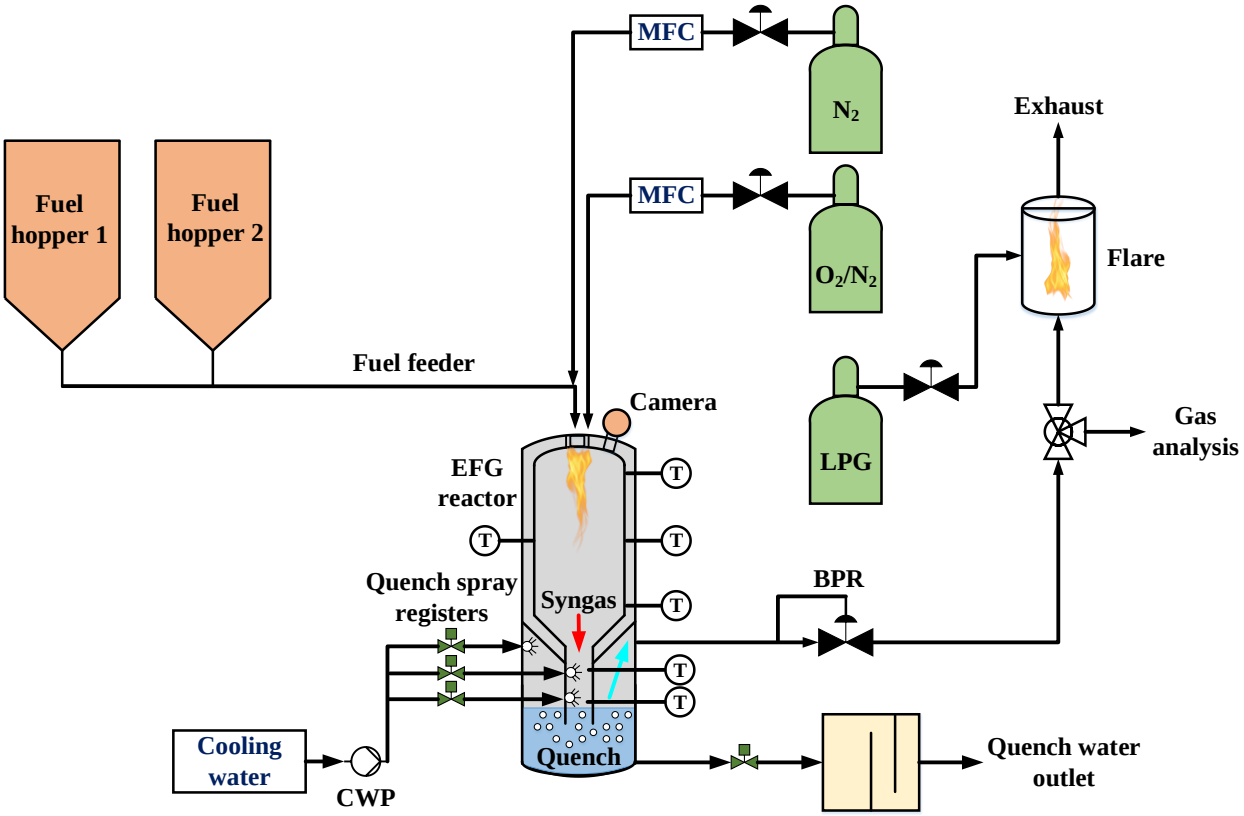

Figure 3-8: Schematic diagram of the 1 MW_{th} pressurized EFG pilot facility (reproduced from [190]).

During the start-up phase, a vertically-mounted electrical heater (Kanthal Tubothal 27 kW) operates to heat up the reactor ceramic lining to *ca.* 1000 °C. The heating phase is carried out at a slow rate (< 100 °C h^{-1}). After the desired temperature has been achieved, fuel and oxidant feeding begins and the system is pressurized. The

reactor was operated at combustion conditions for a time interval necessary to achieve a temperature of approximately 1400 °C in the cylindrical part and syngas temperatures of *ca.* 90 °C after syngas quenching. Since the EFG typically operates at λ values of 0.40-0.50, the mass flow of the oxidant was subsequently adjusted to match the target experimental conditions. For the experimental campaign which is reported, the λ values during the combustion and gasification phases were 1.29 and 0.40, respectively. A depiction of the EFG facility at ETC is shown in Figure 3-9.

Figure 3-9: Depiction of the pilot-scale 1 MW_{th} biomass-fueled PEFG unit at ETC.

The syngas sampling and analysis lines are depicted in Figure 3-10. A slipstream of syngas is sampled, filtered from particulate matter and then cooled in a water-cooled heat exchanger placed downstream of the particle filters. For removing particulate matter, a fiberglass filled trap and a glass microfiber disc filter were installed for protecting the gas analyzers. For gas analysis, four (4) analyzers are available and further details are given in Table 3-8. Syngas composition can be measured consecutively by both Fourier Transform Infrared spectroscopy (FTIR) and micro-GC analysis. Not all the equipment herein presented was used to monitor syngas composition during the gasification tests. Nevertheless, all installed devices are shown for completeness.

Table 3-8: Off-line and continuous syngas analysis equipment at ETC.

Analyzer	Model	Measured components	Remarks/other information
micro-GC	Varian 490 GC	H_2, N_2, O_2, CO, CO_2, CH_4, C_2H_4, C_2H_2	Molecular sieve 5A and PoraPlot U columns, 2 x Thermal Conductivity Detectors (TCD)
FTIR	MKS Multigas 2030 HS	CO, H_2O, CO_2 and CH_4	Continuous measurement (1 Hz sampling)
GC	Varian CP-3800	H_2, CO, CO_2, N_2, O_2, C_2H_6, C_2H_4, C_2H_2, Sulfur species (H_2S, COS, OSCs), CH_4, C_6H_6 and tars	Flame Ionization Detector (FID), Pulsed Flame Photometric Detector (PFPD) and TCD
Cascade impactor	Dekati Low-Pressure Impactor (DLPI)	Particulate matter	13-stages, 0.03-10 μm aerodynamic diameter

In the context of the present study, syngas composition measurements were carried out and recorded semi-continuously *via* the micro-GC analyzer every 3.5 min. During the campaign, neither particulate matter nor syngas analysis through FTIR were carried out. The Varian CP-3800 GC is equipped with three different types of detectors (TCD, PFPD and FID) and it can be used to measure permanent gases, hydrocarbons/tar and sulfur species in syngas. In previous campaigns, tar sampling by solid-phase adsorption (SPA) and analysis through

GC-FID were performed [156]. In the present study, syngas samples were stored in foil gas sample bags, which had been previously rinsed with N_2 in order to remove residual contaminants. The gas samples were subsequently analyzed by GC-FID and GC-PFPD analysis to quantify hydrocarbon and sulfur species in syngas, respectively.

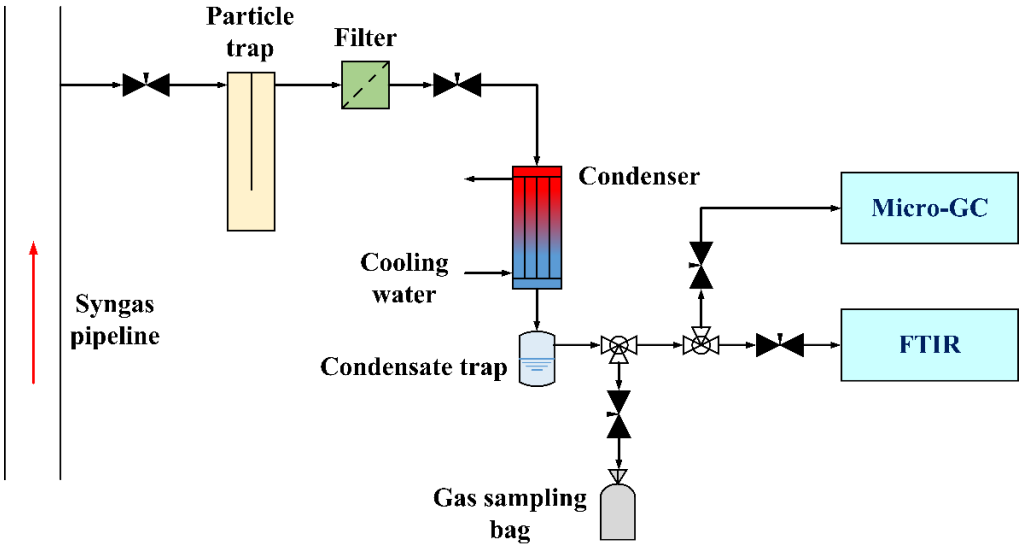

Figure 3-10: Gas sampling and analysis train for continuous and off-line measurement of syngas composition.

3.3.3 Fixed bed reactor apparatus, experimental procedure and test conditions

The adsorption experiments were carried out in a bench-scale test rig, which was initially designed for MeOH synthesis experiments. The configuration of the experimental apparatus is shown in Figure 3-11. It comprises consecutively a gas mixing station, a syngas cleaning section, the MeOH synthesis reactor, a condenser and a backpressure regulator. The gas mixing station consists of five (5) MFCs, from which the first four are connected to gas cylinders containing H_2, N_2, CO and CO_2 pure gases (> 99.9%). The fifth one is connected to the gasifier and it enables gas cleaning and synthesis tests with real syngas from the pressurized EFG. Therefore, the particular configuration of the gas mixing section enables testing of synthetic mixtures with varying H_2/CO/CO_2 composition, direct testing of gasification-derived syngas, as well as mixtures of real syngas with synthetic mixtures in order to adjust the raw syngas composition (e.g. H_2/CO stoichiometric ratio).

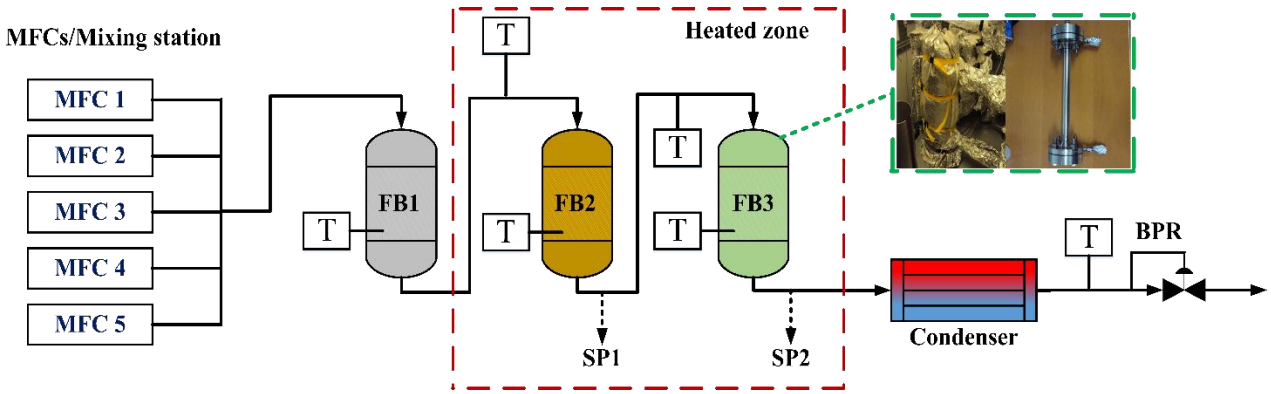

Figure 3-11: Bench-scale test rig for syngas cleaning and MeOH synthesis at ETC.

The main part of the test rig consists of three (3) stainless steel, fixed bed reactors. During MeOH synthesis tests, the first reactor (FB1) is filled with AC and kept at room temperature for removing hydrocarbons and metals from syngas. Moreover, the second one (FB2) is filled with ZnO sorbent to remove sulfur compounds from syngas, since MeOH catalysts are prone to poisoning from such species. The third reactor (FB3) is loaded with $Cu/ZnO/Al_2O_3$ catalyst, which is active for MeOH synthesis. The reactors FB2 and FB3 can be maintained at the specified temperatures through heated jackets. The FB2 and FB3 temperatures for MeOH synthesis are approximately 160 °C and 200 (inlet)/240 (outlet) °C, respectively. Electric heat tracing is also applied to the intermediate tubing and valves between the reactors. A summary of reactor specifications and experimental conditions during the tests reported in [191] is given in Table 3-9. As shown, reactors FB1 and FB3 have identical dimensions and they mainly differ in the fact that FB3 is electrically heated.

Table 3-9: Bench-scale fixed bed reactors for syngas cleaning and MeOH synthesis at ETC.

Reactor	Dimensions	Sorbent or catalyst	This investigation
FB1	19 mm (ID) 400 mm length	25 g AC material (Chemviron) at room temperature	Not used in this investigation
FB2	97 mm (ID) 900 mm length	5 kg ZnO material at 160 °C	Not used in this investigation
FB3	19 mm (ID) 400 mm length	90 g commercial $Cu/ZnO/Al_2O_3$ catalyst at 200-240 °C	Used for AC material testing at elevated temperatures

The backpressure regulator can adjust the pressure in the test rig at a constant value (MeOH synthesis at 25 bar in [191]). The temperature in different sections (fixed bed reactors, intermediate tubing, condenser outlet etc.) of the bench-scale test rig is monitored by thermocouples. During MeOH synthesis experiments, a total gas flow rate of 5 NL min^{-1} was maintained, corresponding to a *GHSV* value of *ca.* 3300 L $(kg_{cat}\ h)^{-1}$. Two available sampling ports upstream (SP1) and downstream (SP2) of FB3 were used for sampling and analysis.

Compared to the aforementioned configuration, a few adaptations were performed for testing the AC material at elevated temperatures. Reactors FB1 and FB2 were not used in the adsorption experiments and they were by-passed. Reactor FB3 was loaded with 5 g of the AC material (CECA ACM40-4WA), which was plugged with quartz wool from both sides. Adsorption tests were carried out at two different temperatures, at the same pressure and syngas mass flow rate. The reactor temperature was regulated *via* a PID controller and it was monitored with a thermocouple mounted on the upper flange of FB3. During start-up, all lines were purged with syngas derived from the gasifier to remove inert gases. Meanwhile, a N_2 flow of 4 NL min^{-1} (from the respective MFC) passed through FB3 to preheat the reactor and perform degassing and heating of the AC material. The accuracy of flow measurement was additionally validated using a 5 L capacity, wet-drum-type gas volume meter, with pressure and temperature indications. The same syngas flow rate of 4 NL min^{-1} was adjusted during the adsorption experiments, regulated by an MFC connected to the EFG reactor piping. Upon establishment of the steady-state syngas composition and a constant fixed bed reactor temperature, the syngas flow was connected to the reactor inlet. Atmospheric pressure was maintained during the tests at both temperature levels. Gas samples were collected in 10 L foil gas sample bags upstream (triplicate sampling for each test) and downstream of FB3 (6 and 8 samples per test, respectively) and analyzed through GC-FID and GC-PFPD. The duration of each sampling procedure was about 60 s. All syngas samples in the foil gas bags were analyzed within a short time interval from sampling (10-120 min) to avoid sample losses. For analysis, the samples were withdrawn through a vacuum pump in the GC systems.

A particular effort was made to reproduce the gasifier operating conditions between the two experiments (biomass mass flow rate, λ value and reactor pressure). Fluctuations on the performance of the PEFG by varying the operating conditions would cause different syngas composition and contaminant release patterns. An overview of the pressurized EFG operating conditions, given as average values during steady-state gasification, as well as the test conditions of the AC adsorption experiments are given in Table 3-10.

Table 3-10: Gasifier operating conditions, adsorption test parameters and sampling conditions.

	Gasification	
Parameter	**Test 1**	**Test 2**
Fuel type (biomass)	Swedish wood pellets (see Table 3-7)	
Gasification temperature (°C)	1274	1282
Gasification pressure (barg)	6.0	6.0
Biomass mass flow rate (kg h^{-1})	120.0	120.0
λ (–)	0.40	0.39
Quenching water inlet flow (L min^{-1})	25.5	23.0
Syngas exit temperature after quenching (°C)	96.3	107.6
Steady-state condition duration (min, approx.)	170	90
No. of syngas samples from SP1	3	3
	Fixed bed adsorption tests	
Parameter	**Test 1**	**Test 2**
AC material	CECA ACM40-4WA	
Mass of AC (g)	5.013	5.065
FB3-TC temperature (°C)	100	150
System pressure (bar)	1.1	1.1
Syngas flow rate (NL min^{-1})	4.0	4.0
Adsorption test duration (min, approx.)	110	60
No. of syngas samples from SP2	6	8

3.3.4 Results and discussion: adsorption of tar and H_2S from biomass-derived syngas

As expected and it can be noted in Table 3-10, it was not feasible to completely reproduce the gasification conditions despite the very small relative differences of the operating parameters between the tests, such as a gasification temperature relative difference of about 0.6%. The impact of such an aspect on the experimental results is further analyzed in the next sections. Firstly, the gasification results are presented and discussed, followed by the results of the AC adsorption tests carried out in the bench-scale fixed bed reactor.

3.3.4.1 Gasification and syngas composition results

A typical operation pattern in terms of λ or ER and temperature values at three different sections of the gasifier (upper reactor part, bottom conical part and syngas pipeline after quenching) during a gasification test is shown in Figure 3-12. While data acquisition and logging of one set of values per minute was carried out, the figure only depicts values between time intervals of 10 min to enhance readability. In this figure, the preheating phase (during $t < 200$ min), combustion phase (for 220 min $< t <$ 300 min) and the steady-state gasification phase (for $t > 370$ min) can be identified. After the preheating phase through electrical heating and biomass combustion with excess air, the λ is reduced from *ca.* 0.50 to 0.40. During the steady-state gasifier operation, *ER* was maintained constant causing almost steady maximum reactor temperature (1282 °C) and syngas temperature after quenching. However, other parts of the reactor still experienced a temperature increase (such as the conical reactor section) for the timespan of this campaign.

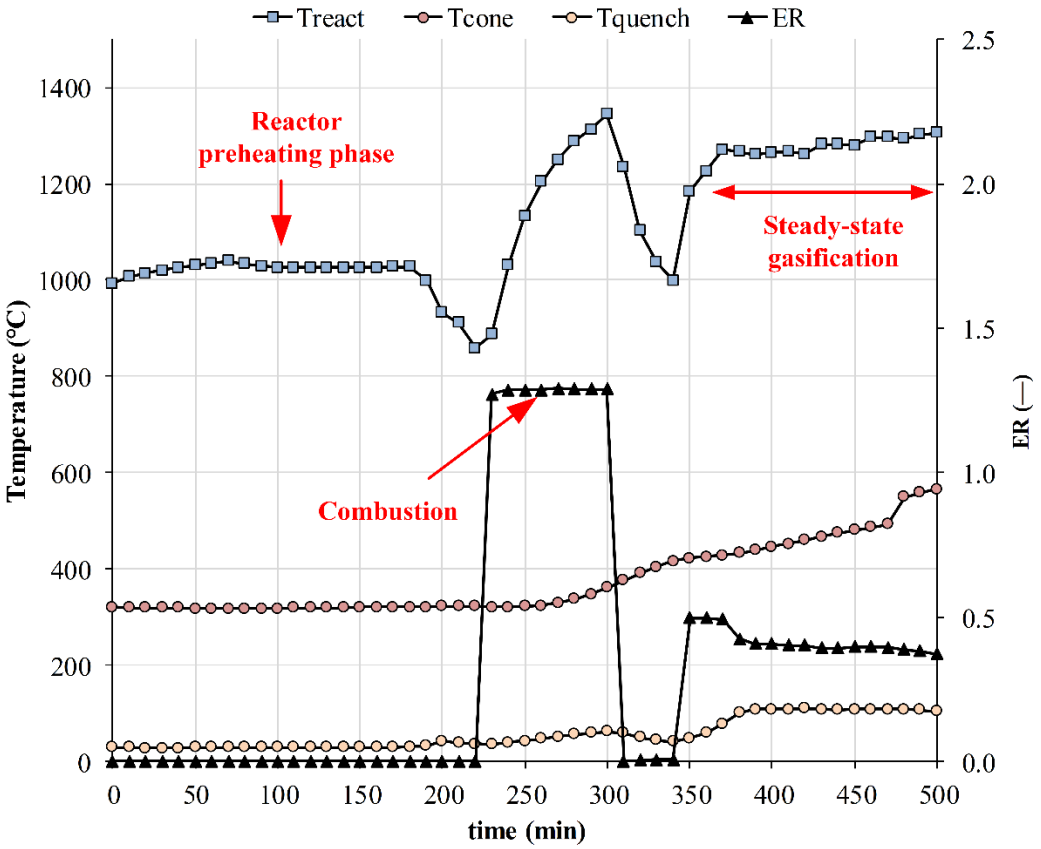

Figure 3-12: Temperature and ER versus time during PEFG startup and steady-state operation (Test 2).

Concerning syngas composition as measured by the micro-GC, deviations between the two tests were small albeit not negligible. In addition, it was confirmed that the syngas composition in terms of permanent gases was nearly constant through the course of each gasification test. Standard deviation (σ) values for the concentration of CO, H_2, CO_2, CH_4 and C_2H_4 in syngas as measured during each test are given in Table 3-11.

Table 3-11: Syngas composition (average and σ values for main gases) for Tests 1 and 2.

	Test 1		Test 2	
Syngas component	**Content (vol.%, dry)**	**σ (vol.%)**	**Content (vol.%, dry)**	**σ (vol.%)**
CO	49.02	0.40	47.38	0.85
H_2	28.98	0.34	28.15	0.59
CO_2	13.98	0.32	15.50	0.21
CH_4	1.83	0.25	1.25	0.10
C_2H_4	0.04	0.01	0.02	~0.00

Moreover, the syngas composition over the steady-state gasification interval is shown in Figure 3-13. The PEFG reactor produces syngas with H_2/CO ratio of 0.6, while H_2 and CO constituted nearly 80% of the syngas volume (db). The content of CH_4 in the syngas of the pressurized EFG was below 2.2 vol%, which can be attributed to the high operating temperature. In addition, only small concentrations of light hydrocarbons were measured by the micro-GC analyzer. Ethylene was the main species with a concentration of up to 0.06 vol.% in syngas. Furthermore, much lower values were measured for acetylene at 0.01 vol.%.

Sampling of syngas from the gasifier outlet during adsorption experiments was carried out at the start, middle and ending of the sorption experiments. Analysis of the samples revealed that C_6H_6 and H_2S were the main contaminant species representing tar and sulfur compounds in syngas, since the operating conditions of entrained flow gasification promote the thermal cracking of species with higher boiling points (OSCs and PAHs).

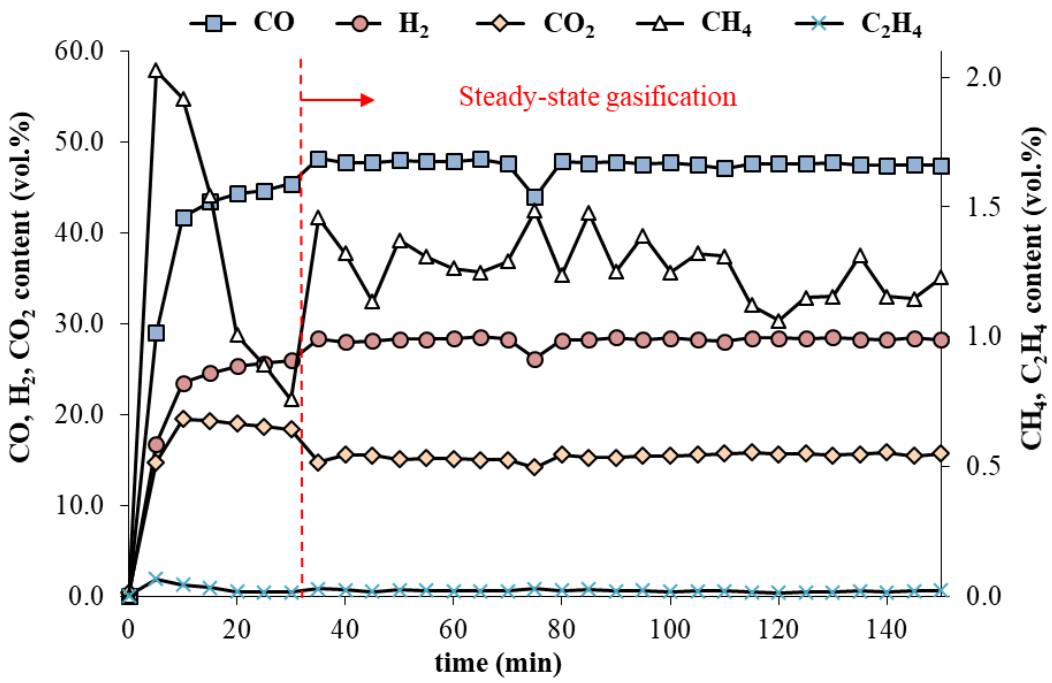

Figure 3-13: Dry syngas composition versus time during steady-state gasification (Test 2).

Table 3-12 summarizes the concentration of those species in syngas as measured upstream of reactor FB3, normalized for the N_2 content in the gas sample. According to the measurements from the gasifier outlet, the H_2S and C_6H_6 content varied between the two tests. Specifically, the H_2S content increased from around 5 ppmv to 80 ppmv, whereas the C_6H_6 content decreased from 170 ppmv to 77 ppmv. Such an outcome confirms the difficulty of repeatedly producing syngas of the same quality in terms of tar and sulfur contaminants, even from the same fuel under identical gasification conditions. Small deviations on fuel quality and quenching system operating conditions can also affect the obtained results. For instance, H_2S solubility in the bubbling column aqueous solution is temperature-dependent and the syngas exit temperature during the first test was 10-11 °C lower than the second one.

Table 3-12: H_2S and C_6H_6 concentration in raw syngas for Tests 1 and 2.

Test 1/Sample No.	**H_2S (ppmv)**	**C_6H_6 (ppmv)**
1	3.8	146.8
2	5.8	186.1
3	5.6	176.5
Average	5.1	169.8
σ	0.9	16.7
Test 2/Sample No.	**H_2S (ppmv)**	**C_6H_6 (ppmv)**
1	78.5	62.8
2	76.7	87.6
3	85.7	80.2
Average	80.3	76.9
σ	3.9	10.4

The measured values are in line with previous gasification tests with wood pellets at the same unit [156], during which H_2S and C_6H_6 concentrations were 2-20 ppmv and 50-300 ppmv, respectively, for similar gasification conditions. Of course, the concentration of H_2S is highly dependent on the content of S in biomass and previous experiments with lignin (0.3 wt.% S) resulted in values of *ca.* 350 ppmv. In order to validate the concentrations of C_6H_6 in syngas, as measured through GC-FID analysis, the existence of a correlation with the content of CH_4 was investigated. Such correlations for the content of light and higher molecular weight hydrocarbons have been found for the typical operating λ range 0.35-0.5 (0.4 in the present study) of the PEFG facility and they are also reported in [156]. Correlations among the concentrations of hydrocarbons are depicted in Figure 3-14.

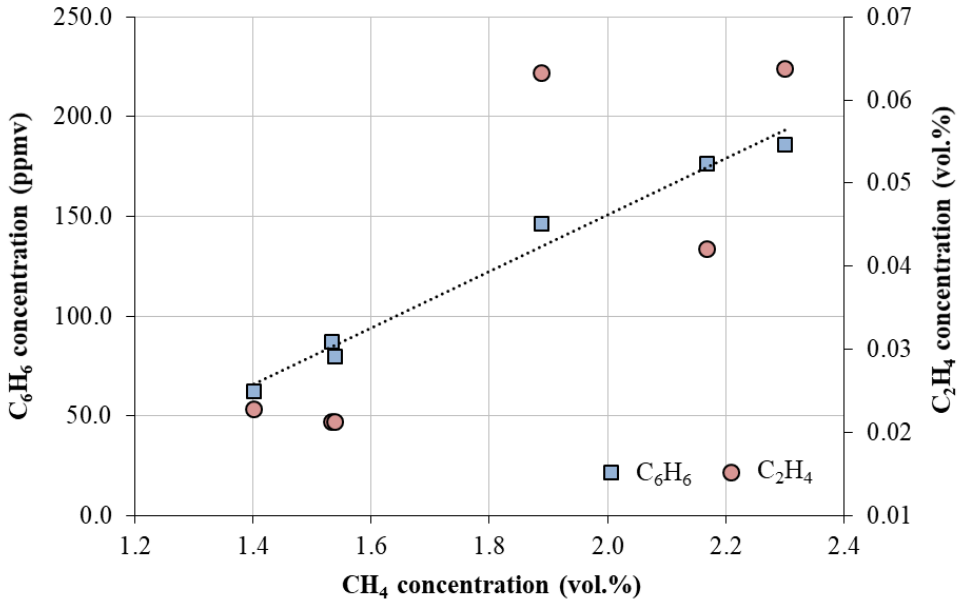

Figure 3-14: Correlation of CH_4, C_2H_4 and C_6H_6 concentrations (N_2-free and dry basis) in the PEFG raw syngas samples (Values for CH_4 and C_6H_6 were obtained through GC-FID analysis, while values for C_2H_4 through micro-GC/TCD analysis).

In order to compare the values on a similar basis, the CH_4 and N_2 contents were measured through GC-FID and GC-TCD respectively. The CH_4 concentration values as obtained by the Varian CP-3800 GC analyzer were 1.8-2.15 vol.% (Test 1) and 1.25-1.4 vol.% (Test 2), which are in agreement with the micro-GC measurements. As shown in Figure 3-14, an almost linear correlation between the concentrations of C_6H_6 and CH_4 in syngas exists. Moreover, a higher CH_4 content in the raw syngas of Test 1 coincided with higher C_2H_4 concentrations as well.

3.3.4.2 AC adsorption results: H_2S and tar adsorption from biomass-derived syngas

The breakthrough curves of H_2S adsorption onto AC at 100 and 150 °C are presented in Figure 3-15 in a similar manner as for the lab-scale tests of C_4H_4S adsorption *i.e.* through the ratio of outlet to inlet feed H_2S concentration C/C_0. In addition, the C_6H_6 breakthrough curves are shown in Figure 3-16. During Test 2, eight (8) gas samples were collected in total to quantify the sorbent capacity. The GC-PFPD analysis of the 8th sample indicated that the H_2S concentration in syngas corresponded to a C/C_0 ratio of 0.7. Despite the fact that the saturation for all other cases exceeded C/C_0= 0.9, a value of 0.7 was considered as the breakthrough point for the comparison of breakthrough time and capacity between the adsorbates. Similarly to the temperature effect during the lab-scale tests for C_4H_4S, the curve at 150 °C shifted to the left of the respective one at 100 °C, indicating a shorter breakthrough time (*ca.* 30% reduction). The curve steepening and the shorter breakthrough time can also be attributed to the higher H_2S concentration during Test 2. A consistent trend was observed for the C_4H_4S adsorption tests with an increase in adsorbate concentration, as analyzed in Section 3.2.5.3. Two more parameters that influence the breakthrough curve shape and adsorption capacity are herein analyzed.

1. *Concentration of H_2S*: Apart from the substantial difference of H_2S average concentration between Tests 1 and 2 (5.1 and 80.3 ppmv), a variability of H_2S concentration within the course of a single gasification run was noted. Particularly during Test 2, the inlet H_2S concentration ranged between 76.7 ppmv and 85.7 ppmv. Such a deviation causes an alteration of the adsorption driving force. Moreover, it must be pointed out that the COS content at the packed bed outlet was found to be higher than the inlet, which suggests that reactions involving the conversion of H_2S towards COS could also take place (see also Table 1-10), particularly reactions with CO and CO_2 (reverse of COS-hydrolysis reaction). Such an aspect could have an influence on the reported H_2S capacity values up to a certain extent. The reactions are shown in R 3-1 and R 3-2.

$$H_2S + CO \leftrightarrow COS + H_2 \quad \text{R 3-1}$$

$$H_2S + CO_2 \leftrightarrow COS + H_2O \quad \text{R 3-2}$$

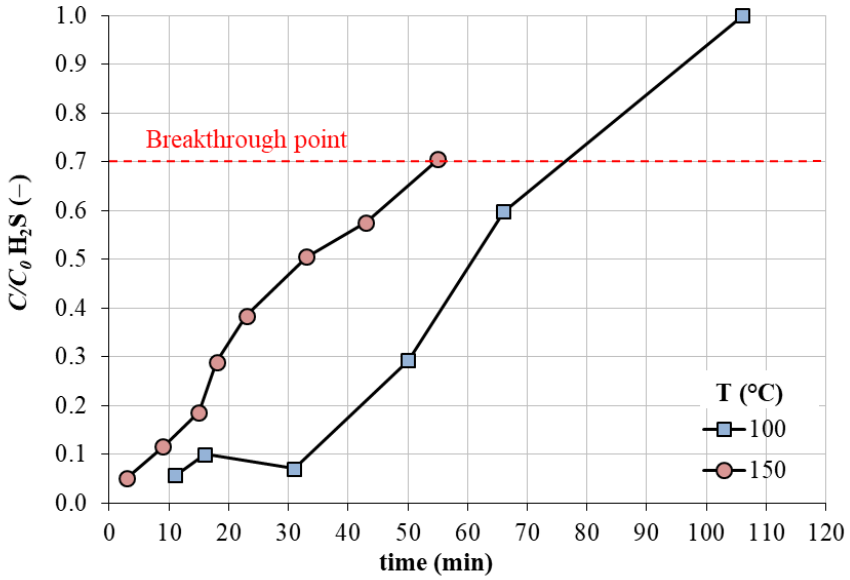

Figure 3-15: Breakthrough curves of H_2S adsorption onto AC at 100 and 150 °C (biomass-derived syngas tests).

2. *Co-adsorption of adsorbates onto the AC material*: Benzene was one of the main co-adsorbates of H_2S in the present study, and thus, the selectivity of the AC material under the investigated conditions is another point of interest. The partial pressure of the co-adsorbate affects the obtained results especially when it is comparable or higher than that of a target compound. In this study, the measured C_6H_6 concentration in syngas was significantly higher than the H_2S levels in Test 1, while in Test 2, similar concentration values were measured for both adsorbates in raw syngas. In addition, the co-adsorption of other compounds was not considered and other minor species were not quantified upstream and downstream of the AC bed. Since other contaminants or metals in syngas can also be adsorbed onto the AC surface, tracking the fate of those species could provide further information. Furthermore, H_2O is another syngas component that can alter the sorbent performance *i.e.* breakthrough time and capacity. During the bench-scale C_4H_4S adsorption tests, it was found that the breakthrough capacity and time decreased when H_2O was added in the gas mixture at a concentration of 3 vol.% (see also Table 3-5). Possible mechanisms that affect the adsorption of C_4H_4S, as well as OSCs in general, onto ACs when H_2O is contained in the feed gas were discussed in Section 3.2.5.4. On the contrary, the presence of H_2O in the gas matrix has been found to be beneficial for H_2S adsorption onto ACs in previous studies. Xiao et al. [166] noted an increase of AC capacity by a factor of 3 for an increase in *RH* from 0 to 80% at 30 °C, while Sitthikhankaew et al. [186] also noted a positive impact of H_2O on H_2S adsorption. The aforementioned effect has been explained through the phenomenon of H_2O capillary condensation in the AC pores followed by transportation and dissolution of H_2S molecules to H^+ and HS^- ions in the water film. While the H_2O content in the product gas was not quantified in this study, continuous FTIR measurements of H_2O concentration in syngas derived from the PEFG unit at ETC were reported by Weiland et al. [192]. For pulverized wood pellets as fuel (as in this work), it was reported that the measured H_2O concentration (4-6 vol.%) corresponds to saturated syngas after the quenching section of the PEFG. Thus, a similar H_2O concentration can be assumed in the syngas that was fed into the AC bed in this work.

The present investigation of H_2S/C_6H_6 adsorption onto AC from a syngas matrix revealed that C_6H_6 was adsorbed with a higher selectivity compared to H_2S, which can be seen from the sorbent capacity results summarized in Table 3-13. The breakthrough time of C_6H_6 adsorption was influenced by both temperature and concentration and it decreased by more than 50% when temperature increased from 100 to 150 °C.

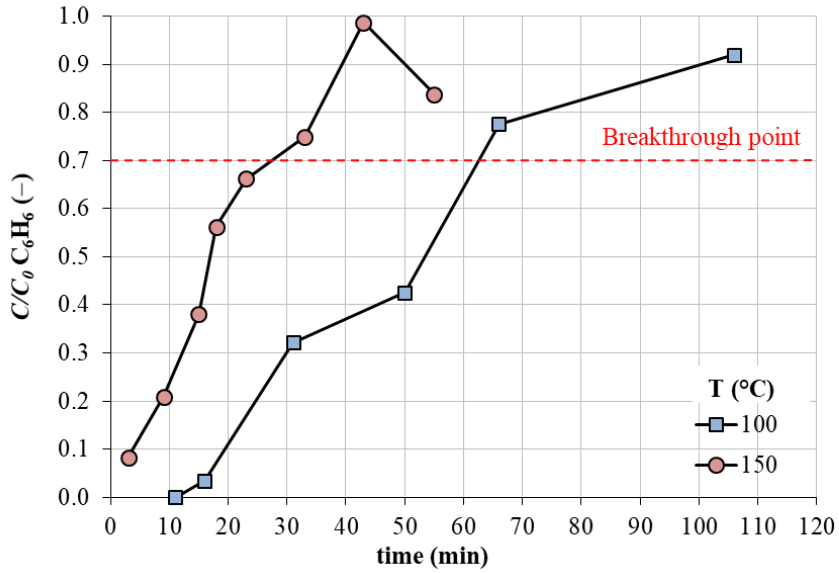

Figure 3-16: Breakthrough curves of C_6H_6 adsorption onto AC at 100 and 150 °C (biomass-derived syngas tests).

A breakthrough time of *ca.* 27 min was required to achieve a saturation level of 70% for C_6H_6 at 150 °C. The fact that the H_2S concentration in the feed gas increased by a factor of 16 from Test 1 to Test 2 also contributed to a decrease in the breakthrough time, as well as sorbent capacity towards C_6H_6 adsorption.

The sulfur capacity of the sorbent varied between 0.53 and 2.95 mg S g^{-1}, it was thus comparatively lower than the maximum value measured in the C_4H_4S tests (4.42 mg S g^{-1}). At 100 °C and under the lowest C_4H_4S concentration (8.5 ppmv), a breakthrough capacity of 2.11 mg S g^{-1} AC was measured, which corresponds to a decrease by a factor of 4 for the H_2S experiments. On the other hand, the highest capacity value measured at 150 °C for C_4H_4S was 1.09 mg S g^{-1}, which is significantly lower compared to the experiments performed under a real syngas atmosphere. Of course, a fair comparison would require identical test conditions, which was not the case between the two campaigns at PSI and ETC.

Table 3-13: Summary of breakthrough time and capacity results for H_2S and C_6H_6 adsorption onto AC.

Parameter / **Test No.**	**1**		**2**	
Compound	H_2S	C_6H_6	H_2S	C_6H_6
C/C_0 (–) breakthrough assumption	0.70	0.70	0.70	0.70
Breakthrough time (min)	76	63	55	27
AC capacity (mg g^{-1})	0.57	18.76	3.14	9.18
Sulfur capacity (mg S g^{-1})	0.53	–	2.95	–

However, the simultaneous decrease of C_6H_6 and increase in H_2S partial pressure in syngas well above that of the C_4H_4S experiments can justify this outcome. The adsorption capacity of C_6H_6 was comparable to the values reported by Chiang et al. for different types of AC materials at a maximum temperature of 80 °C [193]. The authors reported capacities in the range 15-55 mg g^{-1} AC for single-adsorbate tests at 400 ppmv, *i.e.* a significantly higher concentration than the one used in this work. For H_2S with a concentration of 200 ppmv and under ambient conditions, a capacity value around 65 mg H_2S g^{-1} AC was found to be the maximum by Hervy et al. [169]. Finally, it is interesting to note that Marchelli et al. [194] and Itaya et al. [195] reported that increasing temperature may influence H_2S adsorption in a different manner compared to OSCs. Marchelli et al. [194] reported that increasing the temperature from ambient to 90 °C can increase both the adsorption breakthrough time and the H_2S capacity for char samples derived from commercial gasification plants. Itaya et al. [195] investigated H_2S adsorption onto activated coke under "warm" gas cleaning conditions through thermogravimetric tests and suggested that there is an optimum for the process at *ca.* 150 °C. On the other hand, the adsorption performance was found to deteriorate at higher temperatures. This observation seems to be

inconsistent with the fact that physical adsorption is hindered by a temperature increase. Although in this work a higher H_2S capacity was measured at 150 °C, this outcome cannot be herein attributed to the temperature increase. Co-sorption effects and different adsorbate partial pressures between Tests 1 and 2 must be considered and thus, a more systematic study with a consistent syngas composition would be necessary.

3.4 Conclusions

In this chapter, the adsorption of organic and inorganic sulfur onto physically-activated carbon at high-temperature conditions was experimentally investigated. Initially, laboratory tests were carried out with C_4H_4S as model species and inert balance gas. The effect of four parameters (temperature, *GHSV*, adsorbate concentration and moisture content) on sorption capacity and breakthrough curve results was investigated. It was found that, within the investigated parameter ranges, temperature has the most pronounced effect on the reduction of breakthrough capacity of C_4H_4S, since at a temperature of 200 °C the material sustains less than 10% of its capacity measured at 100 °C. An increase in C_4H_4S concentration was also found to affect the material capacity, being the second most important parameter after temperature. At higher temperatures and adsorbate concentrations, the breakthrough curve slope steepened. When increasing temperature, this trend can be attributed to higher volume flow rate through the bed, less favorable isotherms and enhanced pore diffusion, while an increase of C_4H_4S concentration improves the adsorption driving force. A minor H_2O concentration in the gas stream (3 vol.%) was found to deteriorate the breakthrough capacity, which suggests that a further investigation of H_2O/C_4H_4S coadsorption is necessary. This is considered of particular importance when the AC guard bed is installed as a polishing step downstream of a pre-combustion AGR process at high temperature since the product gas exiting the AGR unit will not be moisture-free. Furthermore, in this study high *GHSV* values were applied and it was found that a change in the gas flow rate does not have an impact on the C_4H_4S capacity of the material at high temperature, apart from a reduction in the breakthrough time for saturation. It seems, therefore, that the sorption of C_4H_4S shares similar characteristics regarding the *GHSV* effect with reported trends for DMS adsorption onto ACs. The Langmuir isotherm model can describe the effect of temperature and adsorbate concentration on sorbent capacity adequately ($R^2 > 0.99$). On the other hand, the Henry single-parameter isotherm model was just capable of providing a rough approximation of the measured values.

Following the investigation with the single OSC adsorbate, the same material was tested for the simultaneous adsorption of sulfur and tar present in real syngas. Gasification tests were carried out in an EFG fueled with woody biomass. The syngas from the O_2-blown EFG was rich in CO and H_2, while a low content of hydrocarbons was measured. The latter outcome is attributed to the high operating temperatures of the gasifier (> 1200 °C), which promoted hydrocarbon cracking reactions. The content of light hydrocarbons and tars was found to be correlated with the CH_4 content in syngas. GC-FID and GC-PFPD analyses of syngas samples indicated that C_6H_6 and H_2S were the main tar and sulfur compounds, respectively. One of the peculiarities of those tests was the variation of contaminant concentrations, despite the consistent reproduction of gasification operating conditions. Although this observation makes direct comparisons more difficult, useful information can be obtained regarding material performance under representative working conditions. The tests indicated that the sulfur capacity may decline due to co-sorption effects with light tar (C_6H_6) in syngas, particularly when the C_6H_6 concentration in syngas exceeded 150 ppmv (vol. ratio H_2S:C_6H_6 =1:30). On the other hand, the specific sulfur uptake dramatically increased when the volume ratio of H_2S and C_6H_6 in syngas was approximately 1:1 (80 ppmv each) at 150 °C. Under these conditions, higher sulfur capacities compared to the lab-scale C_4H_4S tests (at 30 ppmv though) were measured, which translates to roughly the same total mass uptake for both sulfur species. Overall, it can be concluded that AC materials can be utilized for syngas desulfurization from H_2S and OSCs at "warm" gas cleaning conditions downstream of an AGR process. Nevertheless, the effect of syngas matrix and particularly, light tar species not captured in the AGR step and moisture, should be taken into account during process design. However, in the specific case that light tar species are meant to be converted in downstream processes, sulfur-selective materials need to be evaluated since a high affinity for benzene has been shown at elevated temperatures.

4 Carbon dioxide absorption into pure and promoted hot potassium carbonate solutions

4.1 Literature review of CO_2 capture with K_2CO_3 solutions and context of the study

As previously presented in the thesis introduction, CO_2 separation processes based on absorption have gained interest over the last decades due to climate change future projections [196]. Apart from post-combustion applications, CO_2 can be captured from gas streams prior to syngas-based power generation or production of synthetic fuels [134, 197]. During SNG production, intermediate process steps, such as methanation, require CO_2 removal from syngas after gasification to reduce the hydrogen requirement for syngas conversion to CH_4, while inorganic and organic sulfur removal is needed for catalyst protection [94, 140]. Furthermore, the SNG content in acidic gases (such as CO_2 and H_2S) must be low before the gas is fed to the grid. The state-of-the-art option for AGR is by liquid solvents [134], which is carried out by gas-liquid contacting equipment. In chemical absorption processes, two separation columns are necessary, one for acid gas absorption and one for acid gas recovery. In the absorber, CO_2 is transferred from the gas to the liquid phase, while in the desorption column, CO_2 is stripped out of the solution as a result of providing heat to the reboiler and/or due to pressure reduction. Solvent screening and evaluation is essential in order to determine the suitability of different liquid solvents with respect to a number of criteria, such as solvent capacity, absorption rate, required reboiler duty for regeneration, toxicity, corrosion potential, cost and thermochemical stability [198]. Specific types of amines are considered for their enhanced solvent capacity and increased absorption rates [199]. However, the utilization of amine solutions is associated with certain drawbacks such as high reboiler duty, material corrosion and solvent degradation issues. Aqueous solutions of K_2CO_3 can overcome several of these problems. Operation at elevated temperatures, i.e. close to the atmospheric boiling point, is beneficial for reduced energy requirement for regeneration [200], while K_2CO_3 is thermochemically stable and non-volatile [201]. In addition, K_2CO_3 solutions are characterized by a low corrosion potential [202]. On the other hand, one of their major drawbacks is the low CO_2 absorption rate compared to primary amines [203].

Measurements of CO_2 equilibrium solubility in concentrated aqueous K_2CO_3 solutions at temperatures ranging from 110-140 °C and 70-110 °C have been published for a conversion of K_2CO_3 to bicarbonate ($KHCO_3$) from 0 to more than 80 % [204, 205]. Water vapor pressure was found to be nearly constant, except when the temperature exceeded 120 °C, which caused an initial increase and a sharp decrease for conversions higher than 40 %. A sharper increase in CO_2 partial pressure for more concentrated mixtures was noted, while equilibrium constants were found to be nearly constant for more dilute solutions for each pair of concentration and temperature. Recently, experimental test rigs such as stirred reactors [206] and wetted-wall columns [207] have been used in studies dealing with CO_2 absorption into liquid solvents. Studies of CO_2 absorption into aqueous K_2CO_3 [208, 209] and aqueous amine solutions [210, 211] can be found, while recent investigations greatly focus on mixtures of amines, amine/K_2CO_3 or amino acid/K_2CO_3 blends in order to seek favorable characteristics such as low heat duty for regeneration, fast absorption rates and high solvent capacity [212]. The maximum concentration of K_2CO_3 is typically limited to 50 wt.% or about 5.5 M based on published density measurements [213]. A higher concentration must be avoided due to the low $KHCO_3$ solubility, which can cause precipitation and fouling problems. In practice, moderate concentrations of 20-40 wt.% or maximum molar concentrations up to 4 M K_2CO_3 are considered more appropriate. Promoter concentrations for amines are usually in the 1-10 wt.% range [202, 203], while for amino acid promoters, experimental investigations have also targeted a wide concentration range [214].

According to Thee et al. [207], the addition of 1.1 M and 2.2 M MEA in an aqueous solution of 30 wt.% K_2CO_3 at 63 °C can increase the absorption rate by a factor of 16 and 45 respectively. It is also stated that the effect of primary amines is more significant compared to secondary or tertiary amines. In a recent study, Ramazani et al. [215] measured the solubility of CO_2 in MEA-promoted K_2CO_3 solutions with three molar ratios and a total concentration of 2.5 M at 40 °C and concluded that a high molar ratio of MEA to K_2CO_3 is not beneficial for CO_2 solubility (expressed as the ratio of CO_2 molecules in the liquid phase divided by the total solvent molecules in the solution). However, this molar ratio increase was found to positively influence the CO_2 absorption rate. On the other hand, it was concluded that the addition of 2-(1-piperazinyl)-ethylamine (PZEA), piperazine (PZ) and tetraethylenepentamine (TEPA) in aqueous potassium carbonate solutions results to an increase in CO_2

specific absorption capacity. TEPA was proposed as the most efficient promoter for increasing both solubility and CO_2 absorption rate at ambient temperature. Concerning PZ as a promoter, Cullinane and Rochelle [216] presented a vapor-liquid equilibrium (VLE) study to demonstrate the effect of potassium to piperazine ratio on CO_2 solubility. For the promoted solvent, they found that the trend of the solubility curves is similar to the one obtained for aqueous PZ and aqueous K_2CO_3, however, PZ addition to the potassium carbonate solution induces a depression of the CO_2 equilibrium partial pressure. Kim et al. [217] carried out a study on CO_2 solubility in PZ- and 2-methylpiperazine (2-MPZ)-promoted K_2CO_3 aqueous solutions over a temperature range of 40-80 °C in a batch stirred reactor. Increasing the promoter concentration had a greater impact on CO_2 solubility compared to increasing potassium ions in the mixture. Over the investigated temperature range, the absorption rate of CO_2 was similar for aqueous K_2CO_3-2-MPZ and K_2CO_3-PZ.

Glycine ($C_2H_5NO_2$) and other amino acids have not been studied extensively as promoters of potassium-containing solvents. For glycine as a promoter, laboratory-scale results for the kinetics of absorption at 40 °C, 60 °C and 80 °C can be found in Thee et al. [214] and results from a small-scale pilot plant have been published by Smith et al. [218]. Moreover, studies on different types of amino acids in potassium-containing solutions are those published by Aronu et al. [219] and Shen et al. [220]. For the case of MDEA, measurements at inlet CO_2 partial pressures in the range 0-20 kPa and at ambient temperature were published by Nii and Takeuchi [221].

From the aforementioned literature, it can be concluded that further research is needed for the application of promoted aqueous K_2CO_3 solutions at "warm" gas cleaning conditions (i.e. at higher temperatures). Since K_2CO_3 solutions are particularly suitable for high-temperature absorption [222], the suitability of amines for long-term operation needs particular attention. Oxidative degradation may be observed in the absorber column when flue gas is processed, while thermal degradation usually occurs in the stripper section. According to Rochelle [223], thermal degradation is rapid in the 120-150 °C temperature range for most amines. Thus, the upper-temperature limit for the current investigation was set to 120 °C, which is known to be an acceptable value for units operating with MEA, taking into account the amine make-up requirement. A short overview of studies related to amine thermal degradation for various temperature ranges is provided in Table 4-1. Corrosion, toxicity and other major issues that need to be addressed for the safe and reliable operation of absorption units containing amines are discussed by Hu et al. [202].

Table 4-1: Thermal degradation studies of investigated amines.

Compound	Temperature (°C)	Thermal degradation potential	Source
MEA	111-125	First order rate constant k_1=2.9·10^{-8} s^{-1}	[224]
Piperazine	162	First order rate constant k_1=2.9·10^{-8} s^{-1}	[225]
MDEA	119-129	First order rate constant k_1=2.9·10^{-8} s^{-1}	[223]
Glycine (Na salts)	125-145	More than an order of magnitude higher than MEA	[226]

In this chapter, the effect of four additives on CO_2 solubility and absorption rate into aqueous K_2CO_3 solutions is presented (the results have been published in [227]). A first experimental campaign was performed with 1.81 M and 2.53 M aqueous K_2CO_3 solutions (corresponding to 25 g and 35 g K_2CO_3 per 100 mL of solution, respectively) at 80-120 °C in a stirred cell reactor and the results were compared and validated with VLE results obtained through thermodynamic modeling of the CO_2-H_2O-K_2CO_3-$KHCO_3$ system with the electrolyte-NRTL model in Aspen Plus™ software. After assessing these preliminary results, which were also used as a reference for comparison, the effect of a primary amine (Monoethanolamine, MEA), a tertiary amine (Methyl diethanolamine, MDEA), a diamine (Piperazine, PZ) and an amino acid (Glycine, Gly) on CO_2 solubility was evaluated at elevated temperatures (100 °C and 120 °C). Because most existing studies have investigated such mixtures at lower temperatures [202, 207, 214, 215, 217, 221, 228, 229], the present investigation focused on higher temperatures for which solubility results are scarce for those promoters [216], while this could be an advantage for the integration of a K_2CO_3-based absorption process in a hot gas cleaning configuration. Furthermore, the current investigation provides experimental results for CO_2 solubility in Gly-promoted K_2CO_3 solutions for which very few studies are available [230]. Absorption rates are also compared among promoted solutions to propose efficient mixtures for high-temperature CO_2 absorption.

4.2 Reaction mechanisms

4.2.1 Reaction mechanism for CO_2 absorption into aqueous pure K_2CO_3 solutions

The overall chemical reaction of the aqueous pure K_2CO_3 solution with CO_2 takes place according to R 4-1.

$$K_2CO_{3(l)} + H_2O_{(l)} + CO_{2(aq)} \rightleftharpoons 2KHCO_{3(aq)} \quad \text{R 4-1}$$

The mechanism is described through the physical solubility of CO_2 and hydrolysis, K_2CO_3 dissolution in water, carbonate hydrolysis, carbonate and bicarbonate formation, as well as water ionization [203]. Since K_2CO_3 and $KHCO_3$ are both strong electrolytes, the metal is present only in the form of potassium ions. The carbonate ion reacts with water to generate hydroxyl ions, which then react with CO_2. A list of these reactions is presented in Table 4-2. For a pH value higher than 9, the reaction shown in R 4-6 is the rate-limiting step, while the chemical reaction R 4-5 is instantaneous.

Table 4-2: Chemical reactions for CO_2 absorption into H_2O-K_2CO_3 solutions.

Reactions	
$CO_{2(g)} \rightleftharpoons CO_{2(aq)}$	R 4-2
$CO_{2(aq)} + 2H_2O_{(l)} \rightleftharpoons HCO^-_{3(aq)} + H_3O^+_{(aq)}$	R 4-3
$K_2CO_{3(s)} \rightleftharpoons 2K^+_{(aq)} + CO^{2-}_{3(aq)}$	R 4-4
$CO^{2-}_{3(aq)} + H_2O_{(l)} \rightleftharpoons HCO^-_{3(aq)} + OH^-_{(aq)}$	R 4-5
$OH^-_{(aq)} + CO_{2(aq)} \rightleftharpoons HCO^-_{3(aq)}$	R 4-6
$2H_2O_{(l)} \rightleftharpoons H_3O^+_{(aq)} + OH^-_{(aq)}$	R 4-7

4.2.2 Reaction mechanisms for CO_2 absorption into promoted K_2CO_3 solutions

Despite the diverse physical and chemical properties of additives, there are also similarities such as having OH− or O− groups or acting as Lewis bases with CO_2 being a Lewis acid [231, 232]. Previous studies have suggested a variety of promotion mechanisms and one of the principal conclusions drawn is that promoters can influence the reaction between CO_2 and H_2O [202]. Astarita et al. [233] presented a generalized model to explain the effect of specific amines or inorganic promoters through the formation of an intermediate species due to the reaction of the promoter with CO_2.

Concerning the additives used in this study, reaction mechanisms have been studied and proposed in the literature. Monoethanolamine (MEA, $NH_2CH_2CH_2OH$) can react with CO_2 to form a zwitterion intermediate which subsequently loses a proton to form a carbamate. The reaction mechanism consists of reactions in R 4-8 to R 4-10 with the addition of R 4-5 to R 4-7, as well as the deprotonation of the zwitterion intermediate with free MEA or other compounds which act as bases in the solution. Rate-limiting reaction steps (kinetic reactions) are R 4-6 and R 4-8. Further details can be found in the study of Thee et al. [207].

$$CO_2 + RNH_2 \rightleftharpoons RNH_2^+COO^- \quad \text{R 4-8}$$

$$RNHCOO^- + H_2O \rightleftharpoons RNH_2 + HCO_3^- \quad \text{R 4-9}$$

$$RNH_3^+ + H_2O \rightleftharpoons RNH_2 + H_3O^+ \quad \text{R 4-10}$$

The promotion mechanism for piperazine (PZ, $C_4H_{10}N_2$) can similarly be described through carbamate formation. However, PZ is a diamine and thus both forms, $PZCOO^-$ and $PZ(COO^-)_2$, are present. The reactions for CO_2 absorption into PZ-promoted K_2CO_3 solutions are given in R 4-11 to R 4-14 with the addition of R 4-5 to R 4-7. In this case, R 4-6, R 4-11and R 4-13 are rate-limiting steps [196]. Further details can be found in the study of Cullinane and Rochelle [228].

$$PZ + H_2O + CO_2 \rightleftharpoons PZCOO^- + H_3O^+ \quad \text{R 4-11}$$

$$PZH^+ + H_2O \rightleftharpoons PZ + H_3O^+ \quad \text{R 4-12}$$

$$PZCOO^- + H_2O + CO_2 \rightleftharpoons PZ(COO^-)_2 + H_3O^+ \quad \text{R 4-13}$$

$$H^+PZCOO^- + H_2O \rightleftharpoons PZCOO^- + H_3O^+ \quad \text{R 4-14}$$

When Glycine (Gly, NH_2CH_2COOH) is added in aqueous solutions, it can be present in a protonated (Gly^+), zwitterionic ($^-Gly^+$) and anionic form (^-Gly) [214]. At sufficiently high pH values, the concentration of the protonated form is very low. The reaction mechanism can be described through the protonation of the anionic form, the formation of a carbamate and the carbamate hydrolysis to bicarbonate, as shown in R 4-15, R 4-16 and R 4-17, respectively. The reaction mechanism when glycine is used with aqueous K_2CO_3 is further analyzed in [229].

$$^-Gly + H_3O^+ \rightleftharpoons {}^-Gly^+ + H_2O \quad \text{R 4-15}$$

$$^-Gly + CO_2 + H_2O \rightleftharpoons {}^-GlyCOO^- + H_3O^+ \quad \text{R 4-16}$$

$$^-GlyCOO^- + H_2O \rightleftharpoons {}^-Gly + HCO_3^- \quad \text{R 4-17}$$

The CO_2 reaction mechanism with MDEA ($CH_3N(CH_2CH_2OH)_2$) differs in that no carbamate formation takes place as in the previous cases. Instead, it is based on the generation of hydroxyl anions through MDEA hydrolysis and the kinetic reaction of MDEA with CO_2 and water, as shown in R 4-18 and R 4-19, in addition to R 4-5 to R 4-7. The rate-limiting reactions are shown in R 4-6 and R 4-19. A more thorough description of the chemistry in aqueous K_2CO_3 solutions with MDEA, as well as aqueous solutions with MDEA, is given in [234] and [235], respectively.

$$MDEA + H_2O \rightleftharpoons MDEAH^+ + OH^- \quad \text{R 4-18}$$

$$MDEA + CO_2 + H_2O \rightleftharpoons MDEAH^+ + HCO_3^- \quad \text{R 4-19}$$

4.3 Experimental apparatus and procedure

4.3.1 Materials and solvent preparation

Nitrogen (N_2) with a purity higher than 99.8 % and CO_2 with a purity higher than 99.7 % were supplied by Air Liquide Hellas SAGI. Potassium carbonate (K_2CO_3, anhydrous, ≥ 99.0 % purity), Piperazine (PZ, anhydrous, ≥ 99.0 % purity), Monoethanolamine (MEA, ≥ 99.0 % purity), Glycine (Gly, anhydrous, ≥ 99.0 % purity) and Methyl diethanolamine (MDEA, ≥ 99.0 % purity) were supplied by Merck Hellas SA. All gases and chemicals were used "as-received", i.e. without further purification. Deionized water was used for the preparation of mixtures and volumetric measurements were performed with a graduated cylinder (± 0.5 mL accuracy). Moreover, a precision balance (Kern-ALJ 220-5DNM) with an accuracy of ± 0.0001 g was used. The total solution volume was constant (400 mL) for all experiments. Mixtures of PZ/K_2CO_3 and MEA/K_2CO_3 were tested at 100 °C and 120 °C, while MDEA- and Gly-containing mixtures were evaluated at 100 °C. The test matrix for pure K_2CO_3 and promoted solutions is shown in Table 4-3.

Table 4-3:Test matrix of CO_2 absorption in pure and promoted K_2CO_3 solutions.

K_2CO_3 concentration (M)	**Promoter type/concentration (M)**	**Promoter/K_2CO_3 molar ratio (-)**	**Temperature (°C)**
1.81	No/-	-	80, 100, 120
2.53	No/-	-	80, 100, 120
1.81	PZ/0.58	0.32	100, 120
1.81	PZ/1.16	0.64	100, 120
1.81	MEA/0.82	0.45	100, 120
1.81	MDEA/0.25	0.14	100
1.81	MDEA/0.84	0.46	100
1.81	Gly/0.67	0.37	100

4.3.2 Experimental test rig and measurement equipment

The experimental campaigns were conducted in the laboratory-scale test rig depicted in Figure 4-1, which was constructed in the framework of the present thesis at the Laboratory of Steam Boilers and Thermal Plants of NTUA. Moreover, a more detailed drawing of the experimental apparatus showing the component configuration and measurement equipment is given in Figure 4-2. The apparatus mainly consists of two pressure vessels, the preheating and the equilibrium cell, which are made of 316L stainless steel. Both cells are cylindrical and have a diameter of 100 mm and a height of 195 mm. Electrically heated jackets were designed to fit the vessels and preserve a constant temperature with an accuracy of ± 0.1 K with PID temperature control. Electric heat tracing was additionally installed for flange and tube heating. The pressure was measured with two WIKA S-10 pressure transmitters (0-6 bar abs, accuracy ± 0.03 bar), one for each cell. The temperature was measured with K-type thermocouples, previously calibrated with a Pt100 temperature sensor in boiling water. In the equilibrium cell, where gaseous and liquid phases co-exist, the temperature was measured with two thermocouples, one for each phase.

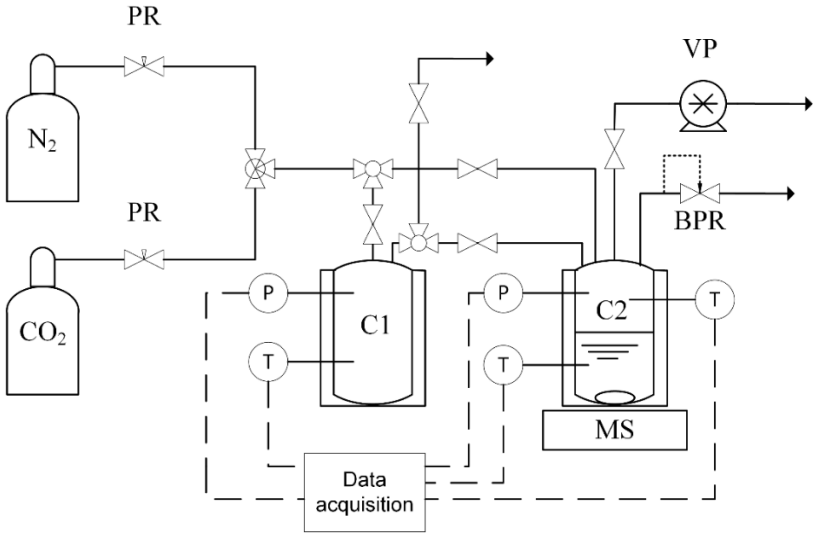

Figure 4-1: Schematic diagram of the apparatus for solvent screening (C1: preheating cell, C2: equilibrium cell, PR: pressure regulator, BPR: back pressure regulator, VP: diaphragm vacuum pump, MS: magnetic stirrer, P: pressure transmitter, T: thermocouple).

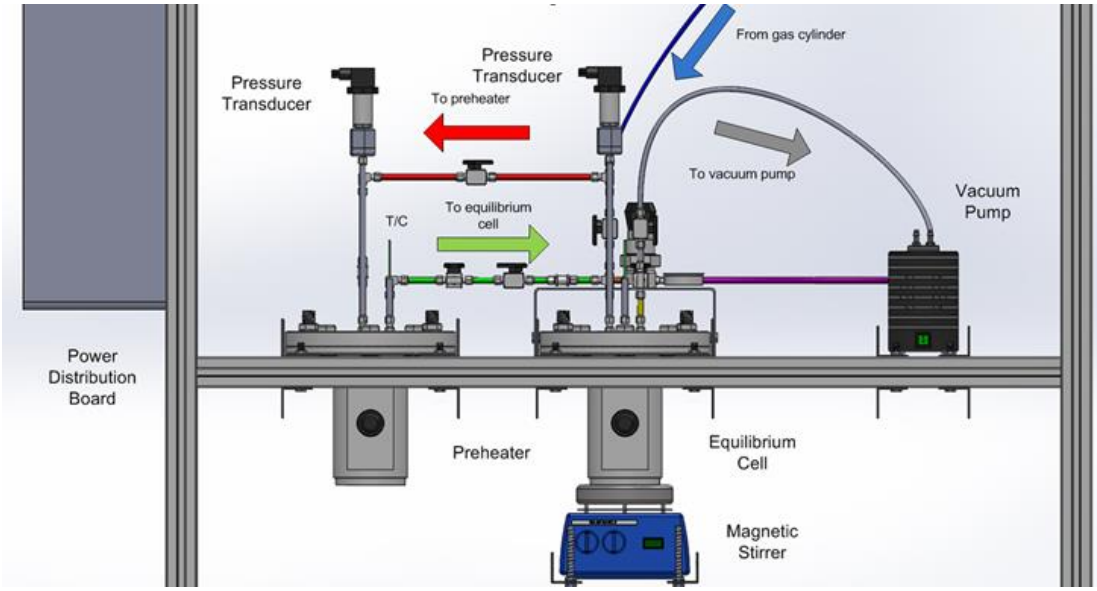

Figure 4-2: Drawing of the batch experimental apparatus for gas solubility measurement.

A diaphragm vacuum pump (KNF Laboport N86 KT.18), which is capable of establishing *ca.* 160 mbar pressure (absolute), was connected to the piping system for residual gas removal. Furthermore, a magnetic hotplate stirrer was used in order to ensure a uniform temperature distribution in the liquid phase and simultaneously reduce the time interval to equilibrium. A back pressure regulator was installed at the pipeline exit for pressure adjustment and safety purposes. Pressure and temperature values were continuously monitored and recorded by a data acquisition system.

4.3.3 Experimental procedure

Initially, the solvent was transferred to the equilibrium cell and the vacuum pump was used to evacuate it at about 400 mbar (absolute pressure) and remove air contaminants and oxygen. While still at ambient conditions, nitrogen was added to slightly pressurize the equilibrium cell in order to avoid boiling in the vessel at higher temperatures. Pressurization at 1.2 bar and 2.0 bar was applied for 100 °C and 120 °C experiments, respectively, while no additional nitrogen was added for experiments at 80 °C. The stirring rotational speed was constant at 180 rpm for all tests. Afterward, the heating phase began and lasted about 3 h in order to ensure that pressure and temperature had stabilized and an initial VLE state had been achieved. During the heating of both cells, the preheating vessel was purged with CO_2 in order to remove atmospheric air. After purging for 2 min, CO_2 was stored in the preheating cell under pressure (8 bar maximum storage pressure) and it was heated at the desired temperature level for at least 30 min. Subsequently, the valve to the equilibrium cell opened and CO_2 was transferred from the preheating to the equilibrium cell within about 1 s, causing a peak in cell pressure at the beginning of each injection. The CO_2 solubility was measured by the pressure decay method. After the pressure inside the equilibrium cell reached a maximum value, a pressure decrease followed, characterized by an initial sharper drop which gradually became smoother until the pressure stabilized. The sequence of injections continued until the desired partial pressure range was scanned. Pressure values were recorded every 2 s. An equilibrium state was assumed to occur when the pressure measurement deviation from the average value recorded was not greater than 0.01 bar for a time interval of 40 min. All the major steps of the experimental procedure are highlighted in Figure 4-3, which presents a typical pressure profile recorded inside the equilibrium cell.

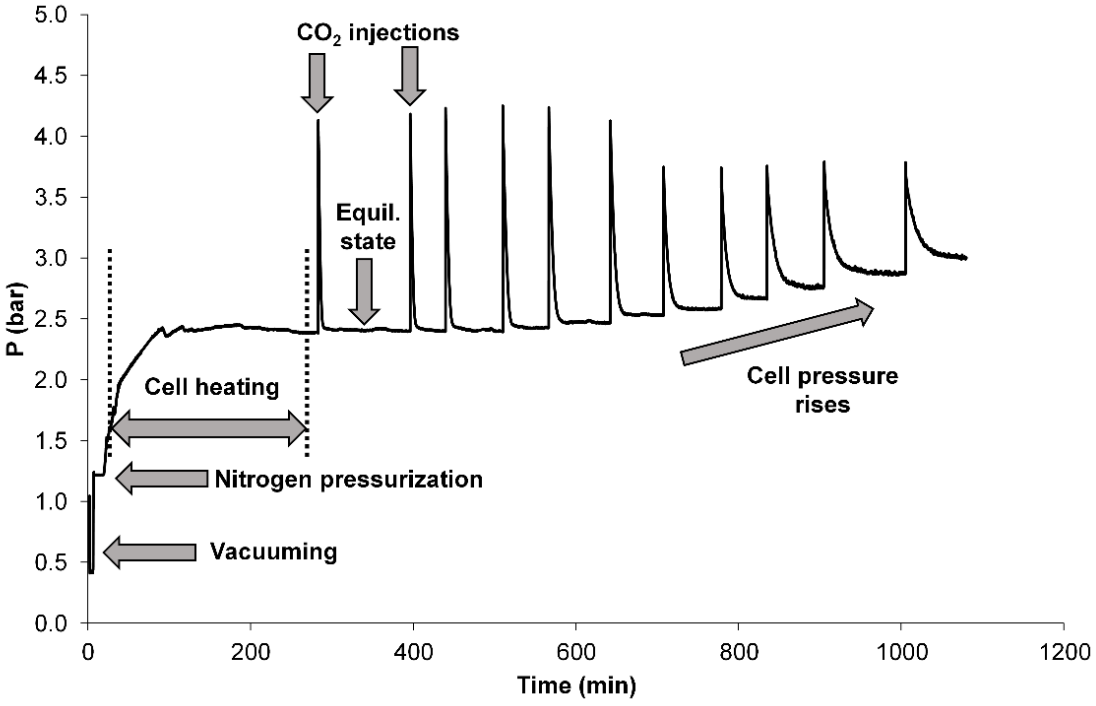

Figure 4-3: Pressure profile and experimental procedure for CO_2 solubility measurement.

4.3.4 CO_2 solubility calculation and error analysis

The CO_2 solubility in a liquid solvent can be derived by continuously or semi-continuously analyzing the CO_2 content of the gaseous or liquid phase [220, 236]. If an analyzer is not to be used, the solubility can be derived by comparing the initial to the equilibrium pressure in a batch feeding mode [215, 237]. After sufficient time after the injection of CO_2 into the absorption cell (which contains the liquid under study) has elapsed, an equilibrium state is achieved. The CO_2 equilibrium pressure ($P^*_{CO_2}$) can be derived according to Equation 4-1

$$P^*_{CO_2} = P_{eq} - P_s \qquad \textit{Equation 4-1}$$

where P_{eq} is the total equilibrium cell pressure after a CO_2 injection *j* and P_s is the total equilibrium cell pressure before the first CO_2 injection. The value of this residual pressure P_s was assumed to remain constant throughout the course of each experiment that adds consecutive amounts of CO_2.

The quantity of CO_2 contained in the solution after each injection *j* is described by Equation 4-2.

$$n_{CO_2,j,sol} = n_{CO_2,j-1,sol} + n_{CO_2,gs} - n_{CO_2,ge} \qquad \textit{Equation 4-2}$$

It is, therefore, the sum of the existing amount in solution, $n_{CO_2,j-1,sol}$ after the *(j-1)* injection and equilibrium state, and the current difference between the CO_2 quantity initially present in the gas phase, $n_{CO_2,gs}$ and the final equilibrated gas-phase CO_2 quantity, denoted as $n_{CO_2,ge}$.

The expression for the transferred CO_2 moles from the preheating to the equilibrium cell, $n_{CO_2,t}$, can be formulated as shown in Equation 4-3

$$n_{CO_2,t} = \frac{P_b V_{pre}}{RT_b} - \frac{P_a V_{pre}}{RT_a} \qquad \textit{Equation 4-3}$$

where V_{pre} is the total volume of the preheater cell, P_b, T_b are the pressure and temperature of the preheater before the valve opens and P_a, T_a are the pressure and temperature of the preheater after the valve has been closed and indications have stabilized. For the $n_{CO_2,gs}$ calculation on intermediate points, the remaining CO_2 moles from the previous injection are also considered.

When equilibrium is achieved, the quantity of CO_2 in the gas phase of the equilibrium cell ($n_{CO_2,ge}$) is given by Equation 4-4

$$n_{CO_2,ge} = \frac{P^*_{CO_2} V_{g,eq}}{RT_{eq}} \qquad \textit{Equation 4-4}$$

where $V_{g,eq}$ is the gas-phase volume of the equilibrium cell and T_{eq} is the temperature recorded at equilibrium conditions.

For the interpretation of results, CO_2 solubility denoted as C_{CO_2} (mol CO_2/L of initial solvent) is used since it provides a comparative measure of solvent capacity per unit volume. It is defined as the ratio of the amount of CO_2 absorbed, $n_{CO_2,j,sol}$, to the initial solvent volume V_s, as shown in Equation 4-5

$$C_{CO_2} = \frac{n_{CO_2,j,sol}}{V_s} \qquad \textit{Equation 4-5}$$

For the solution loading definition, different formulas can be found in the literature [208, 217]. In this experimental study, solution loading (α) is defined as the ratio of the CO_2 quantity absorbed (in moles) to the sum of the equivalent K_2CO_3 quantity (in moles), $n_{K_2CO_3}$, and the amount of promoter (in moles), $n_{promoter}$, if any.

$$a = \frac{n_{CO_2,j,sol}}{n_{K_2CO_3} + n_{promoter}} \qquad \textit{Equation 4-6}$$

In order to estimate the uncertainty of solubility values which are reported in this work, an error propagation analysis was carried out taking into account available uncertainties of volume, pressure and temperature measurements for the preheating and equilibrium cell, as well as volume measurement accuracy for the liquid solvent. The uncertainty estimation expression given by Moffat [238] was used, which is shown in Equation 4-7

$$\delta C_{CO_2} = \left\{ \sum_{i=1}^{N} \left(\frac{\partial C_{CO_2}}{\partial u_i} \delta u_i \right)^2 \right\}^{\frac{1}{2}} \qquad \textit{Equation 4-7}$$

where N is the number of all u_i variables subject to measurements and δu_i is the measurement uncertainty for each variable. The solubility measurement uncertainty was calculated to be ± 4 % arising from the accuracy of the equipment used. Pressure measurement accuracy significantly contributed to the overall uncertainty result, as also noted in other studies [208].

4.4 Results and discussion

4.4.1 Test rig reliability evaluation: comparison with default and regressed electrolyte-NRTL model results

The reliability of the experimental test rig was evaluated by measuring CO_2 solubility in pure K_2CO_3 aqueous solutions. The results were compared against solubility predictions from the electrolyte-NRTL model coupled with the Soave-Redlich-Kwong (SRK) equation of state. This model was developed for liquid solutions that contain electrolytes and describes the excess Gibbs energy by taking into account long-range ion-ion interactions, mixed solvent composition (Born correction) and local interactions according to the NRTL theory [239, 240]. The model adjustable parameters can either be set to default values available in the Aspen Plus database or be modified through data regression analysis [234]. More details about the thermodynamic model development are presented in Chapter 6 of this dissertation. Figure 4-4 indicates that the experimental results in this study are in good agreement with the model results for the pure K_2CO_3 aqueous solution when the default Aspen Plus databank parameters are used. The relative deviation between the model and experimental results was particularly small for the lower solution concentration (1.81 M K_2CO_3).

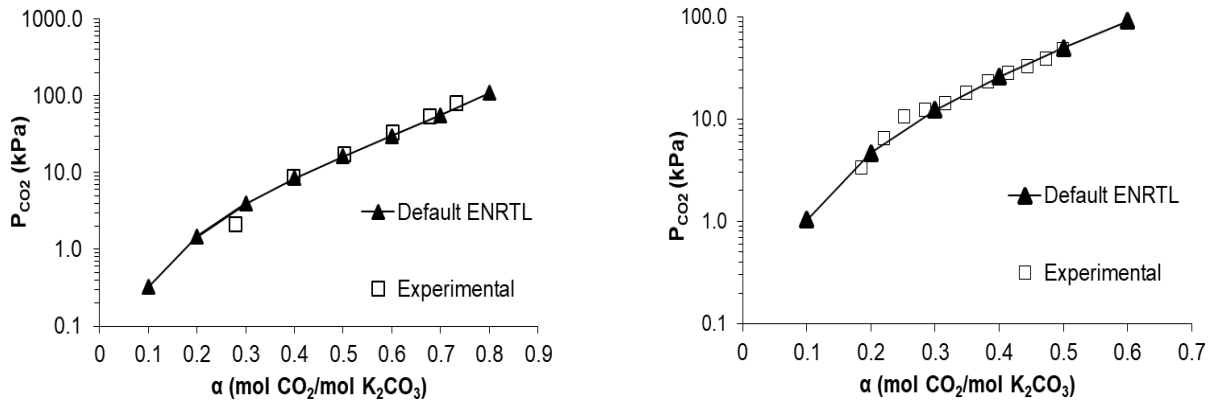

(a) (b)

Figure 4-4: Experimental results and electrolyte-NRTL model predictions with default pair interaction parameters for the 1.81 M K_2CO_3 aqueous solution at (a) 80 ℃ and (b) 120 ℃.

In the case of 2.53 M K_2CO_3 aqueous solution, the relative deviation between predicted electrolyte-NRTL and experimental results was more pronounced and thus, a regression procedure was performed to adjust the molecule-electrolyte binary parameters of the activity coefficient model based on experimental data from the literature. Apart from its importance for predicting VLE curves with a higher accuracy, this methodology is widely used when modeling absorption columns with detailed reaction kinetics, mass transfer correlations and comprehensive thermodynamic models for the liquid and gaseous phases [234, 241]. Therefore, the adjustable

parameters of the model were determined through data regression in Aspen Plus software according to the methodology and experimental data sets described by Hilliard [242]. Apart from CO_2 solubility data from Tosh et al. [204], the regressed model includes experimental data for the mean ionic activity coefficient, vapor pressure depression and heat capacity of the solution. As shown in Figure 4-5, the experimental results of CO_2 solubility in the 2.53 M K_2CO_3 aqueous solution agree better with the regressed electrolyte-NRTL model.

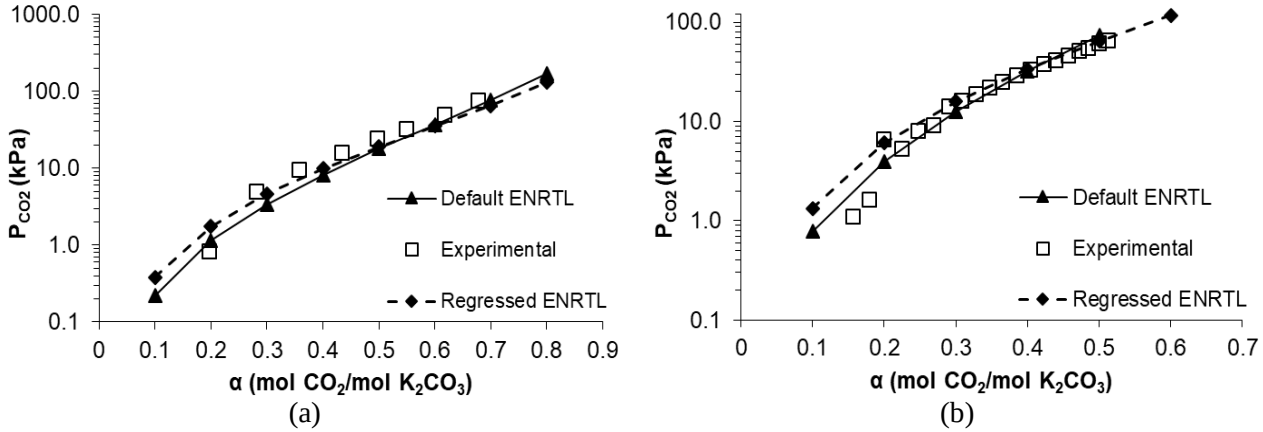

Figure 4-5: Experimental results and electrolyte-NRTL model predictions with regressed binary interaction parameters for 2.53 M K_2CO_3 aqueous solution at (a) 80 °C and (b) 120 °C.

The relative deviations were smaller compared to those obtained with the default Aspen Plus parameters, which was more evident when α ranged between 0.2 mol CO_2/mol K_2CO_3 and 0.4 mol CO_2/mol K_2CO_3 in Figure 4-5(a), where the regressed model curve fits better the experimental results. The aforementioned comparison validated that the experimental apparatus and measurement methodology can be considered reliable for the solvent screening procedure of pure and promoted K_2CO_3 mixtures.

4.4.2 CO_2 solubility in pure K_2CO_3 aqueous solutions

The experimental results for the aqueous K_2CO_3 solutions are presented in Table 4-4 as pairs of equilibrium CO_2 partial pressure and CO_2 solubility values, represented as the quantity of CO_2 absorbed per liquid solution volume. The solvent capacity increased when K_2CO_3 concentration increased from 1.81 M to 2.53 M for the similar equilibrium CO_2 partial pressure and temperature.

On the other hand, when solution loading was used (Figure 4-6), defined as the ratio of CO_2 amount in the liquid phase (in moles) to the amount of K_2CO_3 (in moles), the loading declined for a higher solution concentration. A similar trend was described by Bohloul et al. [208]. In the aforementioned study, the effect of CO_2 physical solubility in water was compared to the solubility in the K_2CO_3 aqueous solution and it was concluded that the chemical reaction dominates CO_2 absorption into the liquid phase. For the same K_2CO_3 concentration, an increase in temperature negatively influenced CO_2 solubility in all cases. In Figure 4-6(a), increasing temperature from 80 °C to 100 °C for 1.81 M K_2CO_3 and CO_2 partial pressure equal to 10 kPa caused a decrease in CO_2 loading by about 24 %, while the reduction between 80 °C and 120 °C was 33 %, respectively. For the higher K_2CO_3 concentration, Figure 4-6(b) shows a similar trend with a slightly weaker effect of temperature. An analogous behavior was also reported by Tosh et al. [204] for potassium carbonate concentrations of 1.7 M and 2.8 M. In their study, a temperature increase from 70 °C to 110 °C resulted in a loading reduction of about 34 % and 29 %, respectively. This effect can be attributed both to the exothermic overall reaction in R 4-1, as well as to the effect of higher temperatures on CO_2 physical solubility. Figure 4-6 also shows that at 80 °C and for a constant partial pressure, the resulting loading reduction between 1.81 M and 2.53 M K_2CO_3 solutions was about 14 %. This decrease was even lower at higher temperatures.

Table 4-4: Experimental results of CO_2 solubility in pure K_2CO_3 aqueous solutions.

1.81 M K_2CO_3/80 °C		**1.81 M K_2CO_3/100 °C**		**1.81 M K_2CO_3/120 °C**	
$P^*_{CO_2}$ (kPa)	C_{CO_2} (mol CO_2/L)	$P^*_{CO_2}$ (kPa)	C_{CO_2} (mol CO_2/L)	$P^*_{CO_2}$ (kPa)	C_{CO_2} (mol CO_2/L)
2.1	0.50	4.2	0.35	3.3	0.33
8.8	0.72	7.0	0.49	6.5	0.40
17.5	0.91	13.1	0.64	10.5	0.46
33.6	1.09	20.4	0.76	12.3	0.52
55.4	1.27	27.7	0.85	14.4	0.57
81.3	1.32	32.4	0.91	18.2	0.63
				23.3	0.69
				28.2	0.75
				32.7	0.80
				38.9	0.86
				48.0	0.90
2.53 M K_2CO_3/80 °C		**2.53 M K_2CO_3/100 °C**		**2.53 M K_2CO_3/120 °C**	
$P^*_{CO_2}$ (kPa)	C_{CO_2} (mol CO_2/L)	$P^*_{CO_2}$ (kPa)	C_{CO_2} (mol CO_2/L)	$P^*_{CO_2}$ (kPa)	C_{CO_2} (mol CO_2/L)
5.1	0.71	4.1	0.48	5.4	0.57
9.6	0.91	7.3	0.63	8.1	0.63
16.0	1.10	11.8	0.75	9.4	0.68
24.7	1.26	15.0	0.85	14.3	0.74
32.2	1.39	17.8	0.92	16.5	0.78
50.7	1.56	27.3	1.08	18.9	0.83
75.6	1.71	39.2	1.22	22.4	0.88
		55.3	1.36	25.1	0.92
		77.3	1.49	29.3	0.97
				33.6	1.02
				38.4	1.07
				42.2	1.11
				46.7	1.15
				52.3	1.19
				55.9	1.23
				61.7	1.24
				66.3	1.30

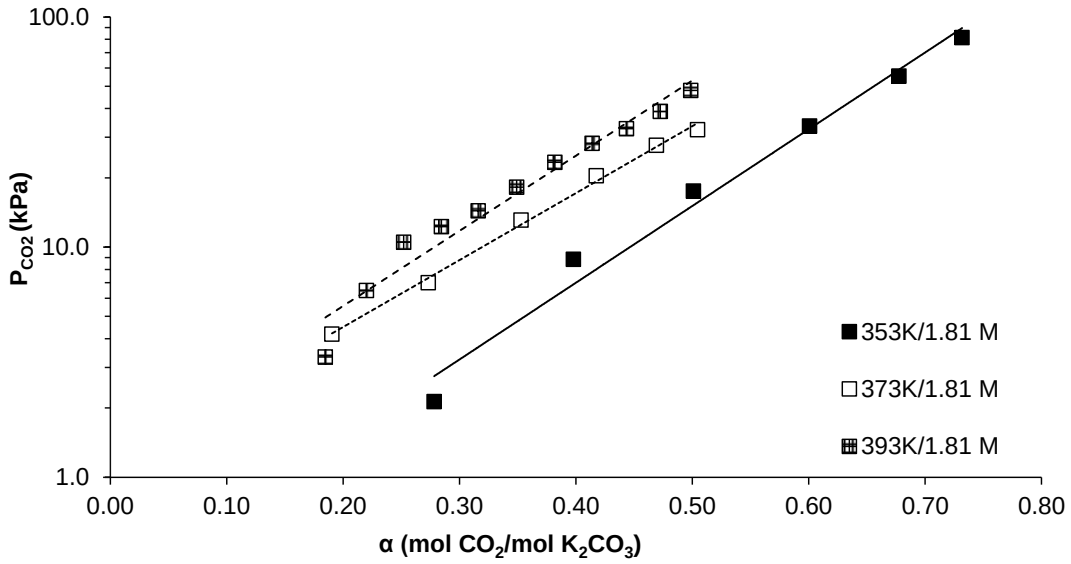

(a)

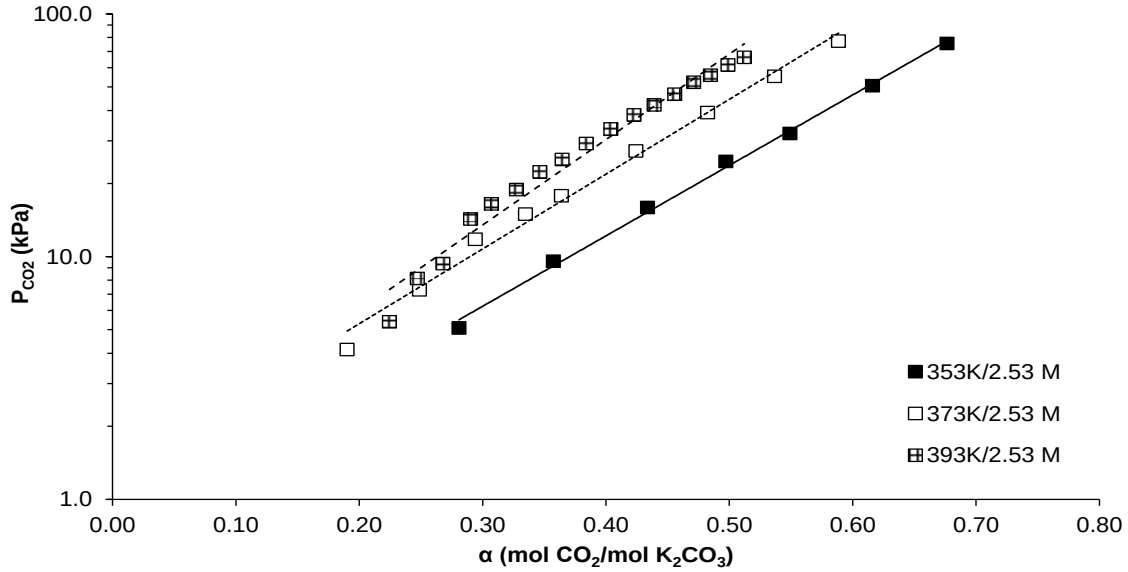

(b)

Figure 4-6: Effect of temperature on CO_2 solubility in (a) 1.81 M and (b) 2.53 M pure K_2CO_3 aqueous solutions.

4.4.3 CO_2 solubility in promoted K_2CO_3 aqueous solutions

The results for the promoted solutions are similarly presented in a logarithmic scale for CO_2 partial pressure in the vertical axis. Exponential curves are fitted to all VLE data series to better visualize their slopes. From Figure 4-7 and Figure 4-8, it can be seen that C_{CO_2} increases as CO_2 partial pressure increases. It is important to note that additives did not influence CO_2 solubility in the same way, but differences were found based on additive type, concentration and temperature.

The additives that do not contribute favorably to CO_2 solubility compared to pure K_2CO_3 solvents at 100 °C can be identified from Figure 4-7. Glycine addition into the solution caused a shift of the solubility curve to the left, indicating a decrease in solubility compared to the 1.81 M K_2CO_3 case. In addition, the slope of the solubility curve was found to be steeper compared to the reference K_2CO_3 solvent and the mixture only achieved a solubility of 0.88 mol CO_2/L solvent at a maximum CO_2 equilibrium partial pressure of 89 kPa.

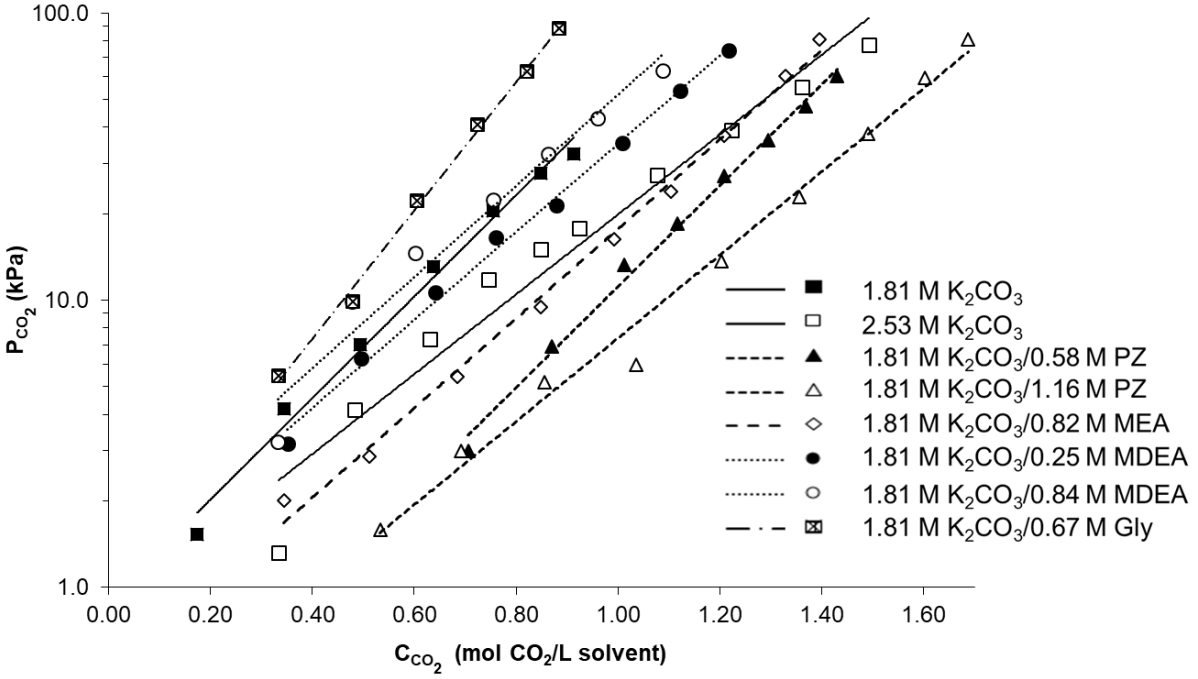

Figure 4-7: Effect of additives on CO_2 solubility in 1.81 M K_2CO_3 solutions at 100 °C.

However, CO_2 solubility was comparable for pure 1.81 M K_2CO_3 and Gly-promoted solutions at partial pressures below 10 kPa. A similar amino acid (arginine) was studied by Shen et al. who found that, while its effect on capacity was positive at partial pressures below 1 kPa and low solution loadings, it greatly diminished when loading increased to $\alpha > 0.3$ [220]. The behavior was attributed to bicarbonate formation from carbonate and carbamate formation from active promoters in the solution. For potassium glycinate used as a promoter, Lee et al. measured a CO_2 partial pressure decrease when glycine concentration increased and proposed that this can be attributed to the fact that the additive acts as an additional mode of CO_2 capture in the solution. It must be noted however that a different range of solution loadings was evaluated and that glycine was deprotonated by mixing with potassium hydroxide [230]. MDEA exhibited a different behavior as an additive based on its concentration: a) for the case of 1.81 M K_2CO_3/0.25 M MDEA, the solubility curve was found to be placed between those of 1.81 M K_2CO_3 and 2.53 M K_2CO_3, thus slightly improving capacity compared to the 1.81 M K_2CO_3 reference case, while b) the solubility of CO_2 decreased when the MDEA concentration increased to 0.84 M. This can be attributed to the different chemical reaction mechanism in the system [234], in comparison with the one governing the interaction of primary amines with CO_2 which is described through carbamate formation.

On the other hand, MEA and PZ promoters were both found to significantly contribute to the CO_2 solubility increase at 100 °C compared to 1.81 M K_2CO_3. The solubility curves obtained for 0.82 M MEA, 0.58 M PZ and 1.16 M PZ in 1.81 M K_2CO_3 were found to be shifted on the right of the curve of 1.81 M K_2CO_3 (without promoter addition). Moreover, CO_2 solubility in these mixtures was found to be also higher than that of the 2.53 M K_2CO_3 solution. Among these mixtures, 1.81 M K_2CO_3/1.16 M PZ yielded the highest solubility results, followed by 1.81 M K_2CO_3/0.58 M PZ and finally 1.81 M K_2CO_3/0.82 M MEA. When comparing the solutions 1.81 M K_2CO_3 and 1.81 M K_2CO_3/1.16 M PZ, a C_{CO_2} value equal to 0.85 mol CO_2/L was obtained for CO_2 partial pressures of 28 kPa and 5 kPa respectively, corresponding to more than an 80 % relative decrease in equilibrium partial pressure. Concerning the effect of PZ as an additive, Cullinane et al. [216] reported that increasing PZ concentration in a solution of constant K^+ concentration can benefit CO_2 solubility and this is reflected through a less steep solubility curve. The increased solubility can be attributed to the conversion of active PZ to $PZCOO^-$ at low/medium loadings and $PZ(COO^-)_2$ at higher loadings (see also R 4-11 to R 4-14). For the case of MEA, the improved CO_2 absorption efficiency can be attributed to the increased OH^- ions, which increase the solution pH as measured in [207], as well as to the zwitterion mechanism for carbamate formation between MEA and CO_2 shown in R 4-8 to R 4-10.

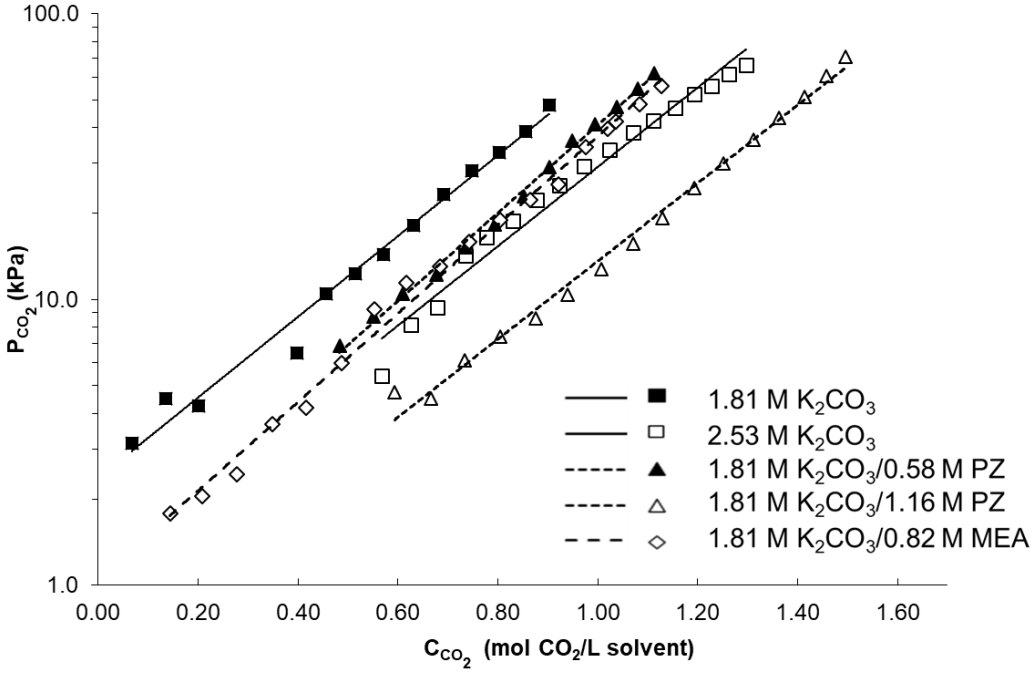

Figure 4-8: Effect of additives on CO_2 solubility in 1.81 M K_2CO_3 solutions at 120 °C.

At 120 °C, the 1.81 M K_2CO_3/1.16 M PZ solution was again found to contribute to a higher CO_2 solubility compared to the rest of the mixtures. Glycine and MDEA were excluded from investigations at 120 °C. From Figure 4-8, it can be concluded that 1.81 M K_2CO_3 solutions with 0.58 M PZ and 0.82 M MEA exhibit similar results to those measured for the 2.53 M K_2CO_3 aqueous solution. An outcome of this comparison at 120 °C is the fact that MEA performs slightly better in terms of capacity compared to the 1.81 M K_2CO_3/0.58 M PZ mixture at higher partial pressures, which was not the case at 100 °C. When solution loading values (α) are to be compared between pure K_2CO_3 solutions and promoted mixtures, the addition of MEA seems to have a detrimental effect on solution loading compared to the reference pure 1.81 M K_2CO_3 solution, already at CO_2 partial pressures above 10 kPa at 100 °C. The equilibrium curve at 120 °C is positioned above that of the pure K_2CO_3 aqueous solutions at the partial pressure range investigated. A similar effect was described by Ramazani et al. [215], for molar ratios of MEA promoter to K_2CO_3 between 0.25 and 1.5 at 40 °C.

4.4.4 Effect of additives on CO_2 absorption rate

In order to compare the absorption rates for the promoted solutions, results are reported for a similar initial CO_2 loading, as well as similar partial pressure at the beginning of the pressure decay curve. Results for fresh solvents and for intermediate points of $\alpha = 0.3$ are discussed, since a typical absorption/desorption process operates with only partially stripping the absorbed acid gas so as to lower the reboiler heat duty [207, 243]. While for the current experimental method this entails that not all starting loading and partial pressure values are identical for the intermediate loading points, the comparison can provide a good insight on the suitability of different promoters for enhancing the overall reaction rate. For a more accurate quantification of reaction kinetics, experiments with a device which ensures a measurable surface area for mass transfer are required to determine the CO_2 flux [244]. Absorption rate results for different solvents are shown in Figure 4-9 and Figure 4-10.

For a starting α value of about 0.3 at 100 °C, a time duration between 18-20 min was needed to reach equilibrium for the 1.81 M K_2CO_3 solution, while a shorter time interval was required to attain equilibrium state for the first CO_2 injection (~14 min), which is anticipated due to faster reaction kinetics for the fresh solvent compared to the loaded one. This is caused by a higher availability of OH^- to react with CO_2, as shown in the kinetic reaction R 4-6.

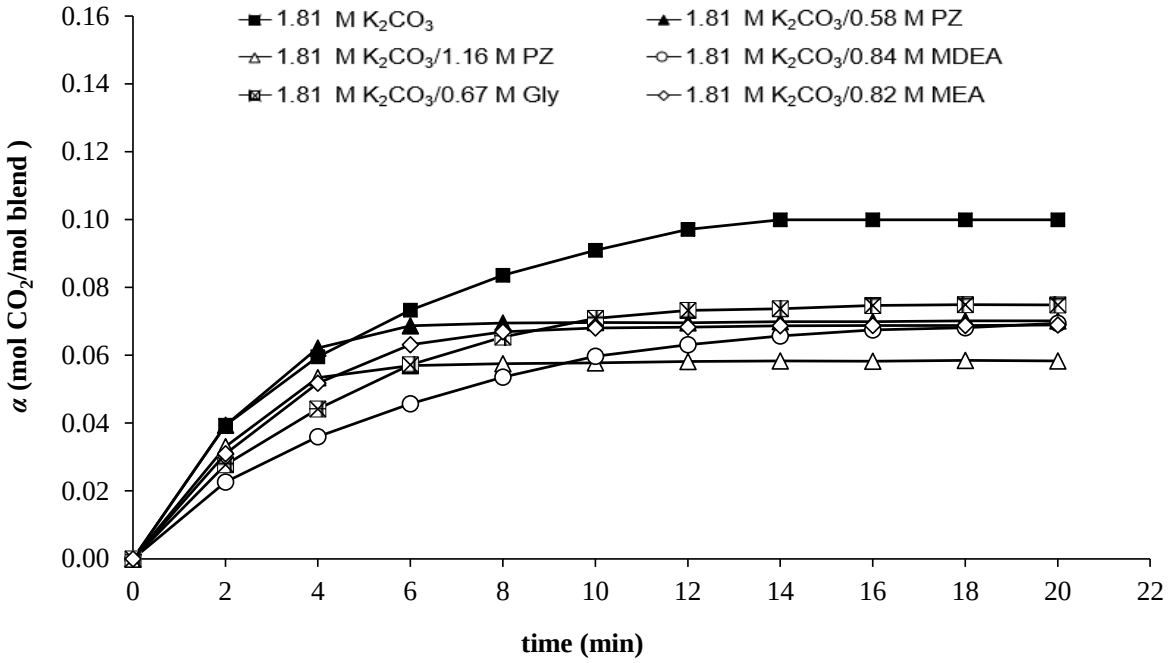

Figure 4-9: Effect of additives on CO_2 absorption rate for fresh solvents ($P_{CO_2,gs}$=180 kPa for promoted solutions, $P_{CO_2,gs}$=200 kPa for the pure K_2CO_3 aqueous solution, T=100 °C).

A similar observation on the effect of increasing solution loading on absorption rate was made for the promoted solutions independently of their type and concentration. The high absorption rate for 1.81 M K_2CO_3 at both temperatures is attributed to a higher CO_2 partial pressure at the beginning of the pressure decay process. Addition of PZ and MEA was found to greatly improve the absorption rate compared to the other promoters used. As shown in Figure 4-9 and Figure 4-10., the solution promoted with 1.16 M PZ performed better and it was followed by the mixtures 1.81 M K_2CO_3/0.58 M PZ and 1.81 M K_2CO_3/0.82 M MEA. At 100 °C, the average absorption rate over the entire time interval towards the equilibrium point for a starting loading equal to 0.3 mol CO_2/mol blend was 0.0047 mol/min for the mixture 1.81 M K_2CO_3/1.16 M PZ. This value was about 11% higher compared to the mixture promoted with 0.82 M MEA. For the fresh solvents at 100 °C, those containing PZ (both concentrations), MEA, Gly and MDEA (at its higher concentration) equilibrated after 7, 10, 15 and 20 min respectively, while at $\alpha = 0.3$, the promotion effect of a higher PZ concentration was more prominent compared to the lower concentration, mainly due to a higher amount of free amine molecules which can react with CO_2 molecules. At this loading level, MEA followed PZ promoted solutions with equilibration times in the order of 14 min for the former and 10 min for the latter. The structure of PZ molecules, comprising two amino groups, and a high pK_a value has been proposed to be responsible for its performance in terms of absorption rate [215, 216]. For the mixture containing MDEA as an additive, no particular enhancement effect on the absorption rate was noted. Taking into account the solubility results for the MDEA/K_2CO_3 mixture of this study, MDEA is not recommended as a promoter for CO_2 absorption at this temperature range, which is in agreement with the conclusions of Borhani et al. [234] in the framework of a simulation analysis for MDEA promoted K_2CO_3. Moreover, according to Nii and Takeuchi [221], MDEA can only slightly improve the CO_2 flux compared to other amines in aqueous solutions of K_2CO_3 and the enhancement factor was found to be much smaller compared to other amines at ambient temperature conditions.

The absorption rate for Gly-promoted solutions was found to be comparable to the reference case solution and similar to the solution promoted with MDEA. Pure Gly seems to have no remarkable impact on CO_2 absorption at high solution loadings and a slight improvement for the fresh solvents can be pointed out based on Figure 4-9. According to Thee et al., the pretreatment of glycine towards a deprotonated amino acid can establish a reaction mechanism similar to the one described for alkanolamines with the formation of a carbamate intermediate [214]. The K_2CO_3 solution with the deprotonated amino acids was found to exhibit improved reaction kinetics compared to primary amines and it is therefore suggested for future investigation. A strong

base must be used in this case, such as KOH, and the reaction for deprotonation of the zwitterions is represented by R 4-20

$$^{+}NH_2R_1R_2COO^- + OH^- \rightleftharpoons NHR_1R_2COO^- + H_2O \qquad \text{R 4-20}$$

The absorption rate curves for PZ and MEA at 120 °C were compared to the one obtained for K_2CO_3 without additives. As shown in Figure 4-10 for the fresh solvents, the time to equilibrium after the first injection of CO_2 was in a range of 6-7 min for the promoted solutions and 11-12 min for the pure K_2CO_3 aqueous solution. Piperazine promoted solutions were found to enhance the absorption rate to a greater extent at this higher temperature, similarly to the observations made at 100 °C. However, at this higher temperature level, similar absorption rates for MEA and PZ were observed and thus both promoters may be used for high-temperature CO_2 absorption. According to [207], the apparent reaction rate constant of CO_2 in a MEA-promoted K_2CO_3 solution can be increased by increasing both MEA concentration and solution temperature.

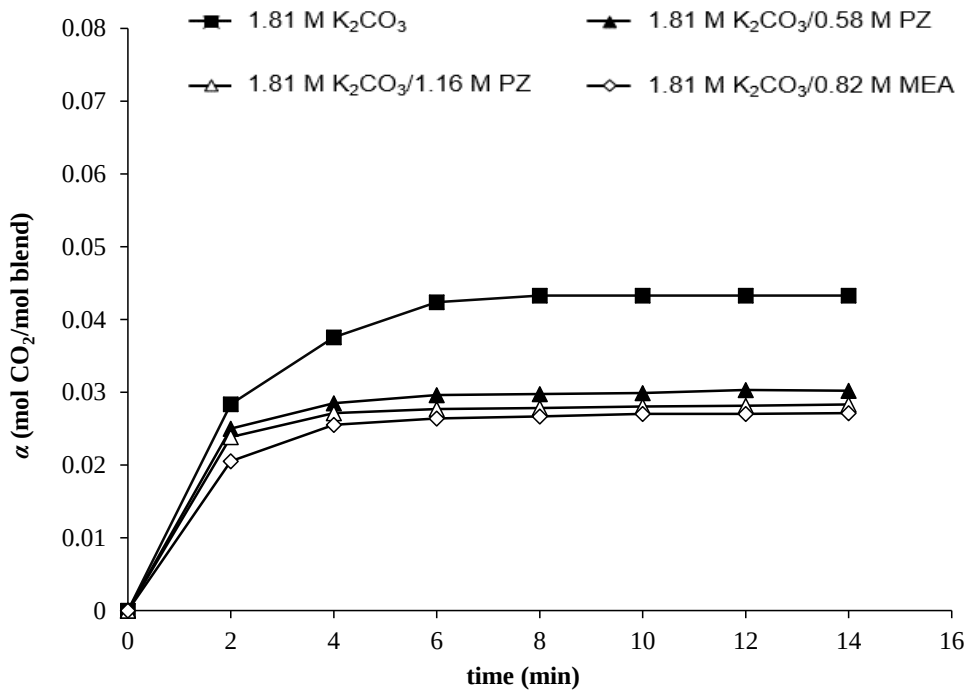

Figure 4-10: Effect of additives on CO_2 absorption rate for fresh solvents ($P_{CO_2,gs}$=80 kPa for promoted solutions, $P_{CO_2,gs}$=90 kPa for the pure K_2CO_3 aqueous solution, T=120 °C).

4.5 Conclusions

In this chapter, an experimental investigation of CO_2 solubility and its absorption rate into pure and promoted K_2CO_3 solvents was presented. For K_2CO_3 aqueous solutions without promoters, tests were carried out at 80 °C, 100 °C and 120 °C with two different K_2CO_3 concentrations and experimental results were successfully validated against simulation results obtained with the electrolyte-NRTL model fitted with default electrolyte pair parameters in Aspen Plus™, as well as regressed parameters based on experimental data from previous studies in order to improve the accuracy of the activity coefficient model. Glycine, MDEA, MEA and PZ were tested at 100 °C as additives, while the latter two promoters were also tested at 120 °C. As far as K_2CO_3 solvents are concerned, solubility increases with a decrease in temperature or with a denser solvent. Regarding the addition of promoters, the use of PZ greatly improves CO_2 solubility and absorption rate at the same time. The use of MEA is also beneficial for both solubility and absorption rate, but to a lesser extent compared to PZ. On the other hand, MDEA can potentially improve solubility results when added in lower quantities, however, when used at higher concentrations, it lowers CO_2 solubility. Taking into account that also no remarkable effect on CO_2 absorption rate was measured, MDEA is not recommended as a promoter for aqueous K_2CO_3 solutions. Finally, pure Glycine addition, even at a low molarity, deteriorates CO_2 solubility.

Based on the solvent screening study presented in this chapter, the best performing promoters during those high-temperature absorption tests, *i.e.* PZ and MEA, were considered for further investigation. Those two promoters can improve the solubility and absorption rate of CO_2 absorption and thus, they are potential additives to an AGR process based on hot K_2CO_3 solutions. In Chapter 5, the absorption of CO_2 and light tar mixtures into pure K_2CO_3 and MEA-promoted K_2CO_3 aqueous solutions is experimentally investigated, as such species are expected in the syngas of biomass- or coal-fuelled gasifiers. In Chapter 6, process modeling of the hot potassium process with and without additives is carried out in Aspen Plus. The aim is to compare pure K_2CO_3 aqueous solutions to PZ-promoted K_2CO_3 solutions for the simultaneous removal of CO_2 and H_2S from gasification product gas under elevated temperature and pressure conditions.

5 Absorption of carbon dioxide/light tar mixtures into potassium carbonate solutions

5.1 Scope of study

In this chapter, the solubility of CO_2 and light tar species in K_2CO_3 aqueous solutions (either pure K_2CO_3 or promoted) is presented. When light tar compounds are maintained in syngas downstream of an AGR unit, they can be converted to non-condensable gases e.g. toluene can be converted towards CO and CH_4 in the presence of $NiO/MgO/Al_2O_3$ catalysts [245]. Coll et al. investigated the steam reforming potential of different aromatic compounds, typically found in gasification product gases, over Ni-based catalysts [246]. They concluded that the reactivity of benzene and toluene was higher compared to other aromatics and they reported that this also applies to compounds with a smaller number of aromatic rings in their molecule.

A benefit of the application of K_2CO_3 solutions is that they can are expected to be less selective for absorbing BTX and tar species, especially those with small polarity. On the other hand, physical absorption processes have been reported to have a high affinity for BTX, C_{3+} hydrocarbons, heavy tar and moisture [134]. This study aims to quantify solvent capacities for C_6H_6 and C_7H_8 as two of the major species which can be converted downstream of the AGR unit in an SNG plant. In addition, the present study explores the effect of MEA content on the absorption process.

5.2 Experimental apparatus and procedure

5.2.1 Chemicals and preparation of aqueous solutions

All gases used in this experimental study were supplied by Air Liquide Hellas SAGI. For the preparation of the gas mixtures which were fed to the reactor, N_2 with a purity higher than 99.8%, CO_2 with a purity higher than 99.7% and CH_4 with a purity higher than 99.995% were used. In addition, N_2 with a purity higher than 99.999% was purchased and used for all analyzer operations that required a carrier gas of high purity *i.e.* for purging and cleaning, for zero calibration and for acquiring calibration spectra at various concentrations. All other chemicals were purchased by Fisher Chemical, Lach-Ner (Tech-Line SA) and Merck Hellas SA. Potassium carbonate (K_2CO_3, anhydrous, 99.6% purity) and Monoethanolamine (MEA, 99.5 % purity) were mixed with deionized water to obtain solutions of a specific composition. Benzene (C_6H_6) and toluene (C_7H_8) of analytical reagent grade were used during the tests (> 99.9% purity). All gases and chemicals were used "as-received", *i.e.* without further purification or pretreatment. A precision balance (Kern-ALJ 220-5DNM) with an accuracy of ± 0.0001 g was used for preparing the aqueous solutions. In this experimental campaign, the solution mass was constant (500 g) at the start of each test.

5.2.2 Experimental apparatus

The experimental investigation of C_6H_6/C_7H_8 and CO_2 absorption into MEA-promoted and pure K_2CO_3 aqueous solutions was carried out at the Laboratory of Steam Boilers and Thermal Plants of NTUA. A basic design parameter of the apparatus was the requirement of evaluating the multicomponent absorption of compounds at different partial pressures. The experimental procedure in which CO_2 solubility was determined by pressure decay was not applied in this investigation. Useful information regarding potential modifications for the experimental methodology of Chapter 4 for multicomponent mixtures may be found in the study of Vopička et al. [247], who investigated the sorption of gas mixtures into a solid membrane with a pressure-decay method through its combination with gas chromatography. A pressure-decay method for solubility measurements of binary mixtures with GC analysis can also be found in [248]. Instead of the batch-type method, the measurements can be done in a semi-continuous or continuous manner with gas- and/or liquid-phase analysis. In such cases, the gas can be either absorbed into a constant mass solution without liquid recirculation but with a continuous gas flow rate through it or a continuous supply of both liquid and gas phases can be established

e.g. *via* an absorption column for contacting the two phases. For the present study, the former methodology was selected and the test rig was modified accordingly. A schematic diagram of the experimental setup is shown in Figure 5-1.

The experimental test rig consists of the support frame, gas mixing section, reactor, piping network, heating systems, pressure and temperature measurement equipment, sampling line, FTIR analyzer and all necessary auxiliary devices for signal processing, data acquisition and power supply (either AC or DC). The gas mixing section has the purpose to supply gas mixtures with specific composition to the reactor containing the liquid absorbent. For supplying CO_2, CH_4 and N_2, pressure regulators were installed at the outlet of the gas cylinders with an adjustable pressure up to 8 barg, which are subsequently connected to the mass flow controllers (MFCs) through PTFE tubing. Four (4) thermal MFCs were installed to regulate and measure the mass flow rates of the gases, each with a different nominal operation range from 0 up to 2 NL min^{-1}. Their working principle is based on using the fluid heat conductivity (gas or liquid), which makes their measurement relatively independent to fluctuations in temperature or pressure. In this experimental study, only three of the four MFCs were employed for adjusting the mass flow rates of gases (Omega FMA 5400 with 0-2000 NmL min^{-1} flow range for N_2 regulation, Tylan FC-280s with 0-700 NmL min^{-1} flow range for CO_2 regulation and Aalborg GFC 17 with 0-200 NmL min^{-1} flow range for CH_4 regulation). The MFC device which controlled the mass flow rate of N_2 (carrier gas) had been initially calibrated with the same gas, whereas correction factors were used for the other MFCs. Using such a correction factor that is different for each gas, the mass flow controller ensures accuracy of 5-10% over the range of the measurement scale. On the other hand, for the MFC that operated with the calibration gas, an accuracy of ± 1.5% applies according to the manufacturer.

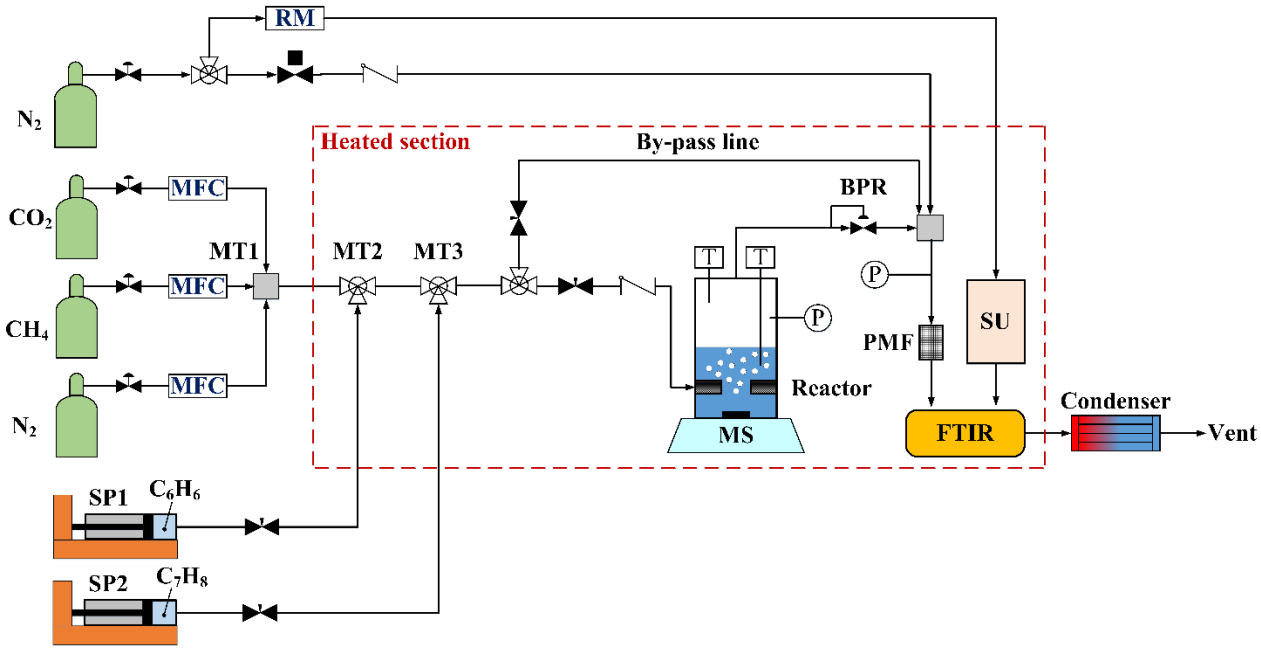

Figure 5-1: Sparged stirred reactor apparatus for gas absorption studies into liquid solvents (RM: rotameter, MFC: mass flow controller, MT: mixing tee, SP: syringe pump, MS: magnetic stirrer, BPR: backpressure regulator, PMF: Particulate matter filter, SU: sampling unit).

There are three main mixing tees in the assembly, which are used to either mix gases or gases with liquid compounds. In MT1, the main gases comprising the simulated stream can be mixed, herein, CO_2, CH_4 and N_2 as the carrier gas. Although not depicted in Figure 5-1, a tubing coil was installed downstream of MT1 with an internal diameter of 1.755 mm in order to increase turbulence and residence time. This is followed by the second and third mixing tees (MT2 and MT3) in which liquid compounds (at room temperature) are added to the gas stream, which may be water, liquid hydrocarbons, etc. Each MT is connected to a separate syringe pump which can supply such small quantities to the point of mixing. It was selected to install two different syringe pumps (New Era NE-300 and NE-1000 supplied by Metrolab SA), so that the flow rate of each species can be set independently through a) adjusting different flow rate settings and b) using different syringe sizes from sub-mL

up to 60 mL. Moreover, the mixing tees MT2 and MT3 are trace-heated so that the liquid species are mixed at higher concentrations. The heat tracing is controlled *via* a PID controller, in which temperature measurements are provided through a Pt100 sensor. Inside MT2 and MT3, the fluid fed by the syringe pump is forced to go through a metallic needle which is installed in the pathway of the main gas flow in such a way that the liquid is entrained by the gas mixture. Downstream of MT3, there is another heated tubing coil to extend the residence time of the gas mixture. Initially, the MTs were immersed in an oil bath, however, a severe mixing instability was encountered. In addition, this configuration excluded the possibility of independently adjusting the mixing point temperature if necessary. A depiction of the mixing tee configuration, where the fluid flow rate from the syringe pumps is mixed with the main gases, is shown in Figure 5-2.

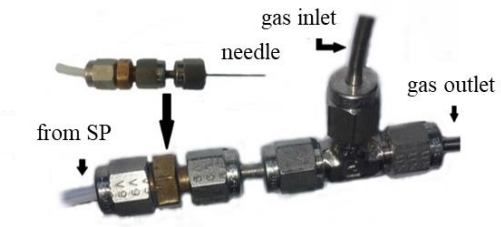

Figure 5-2: Depiction of the mixing tee (MT2 and MT3) configuration for injection from SP1 and SP2.

Regarding particularly the gas syringes, the injection rate depends on the diameter of the syringe to be mounted on the pump and the speed at which the plunger moves. The speed of the piston is adjusted by a screw-nut drive and the rotational movement of the motor is converted to a linear one. The specifications of the three SGE gas-tight glass syringes which were used in this study for tar injection are shown in Table 5-1. It can be noted that although a wide range of flow rate conditions can be achieved from below 1 μL h^{-1} up to tenths or hundreds mL h^{-1}, the flow rate setpoint has a direct impact on the time needed until the syringe is completely discharged from the liquid. A syringe was filled at the start of an experiment and it could not be filled up during the syringe pump operation without disrupting it. This arises an optimization problem also because the selection of the syringe type influences other parameters, such as the liquid flow rate accuracy and stability at a specific set point. A syringe pump was also used during the investigation of AC sorbents (see Chapter 3), therefore such aspects are herein discussed in more detail, as well as the solutions adopted for the operation of the syringe pumps in the framework of the present study.

Table 5-1: Syringe specifications for C_6H_6 and C_7H_8 injection through the syringe pumps.

Syringe No.	Barrel material	Internal diameter (mm)	Volume (mL)	Max. pressure, temperature (bar/°C)	Flow rate range (μL h^{-1})
1	Borosilicate glass	3.3	0.5	27.6/70	0.7-91800
2	Borosilicate glass	4.6	1	27.6/70	1.4-183600
3	Borosilicate glass	10.3	5	27.6/70	7.0-918000

One of the main issues encountered during this investigation was their oscillatory behavior especially at low flow rates of the syringe operation range. This problem can be partially addressed by the use of small-diameter syringes, as well as the use of "damping" hoses made of elastic materials e.g. PVC. The choice of syringe diameter in the pump is related to the displacement rate of the piston for infusion of the liquid. As the device is equipped with a stepper motor for its movement, a smaller syringe diameter involves a higher speed of rotation of the stepper motor and consequently a reduction in the periodic effects caused by its continuous rotation. In addition, the use of a specific syringe influences the pressure P of the liquid supply from the correlation $P = F/A$, where F is the linear force applied on the syringe plunger and A is the cross-section area of the syringe. This implies that a smaller cross-section for a specific linear force results in an increase in the maximum fluid discharge pressure. This is an aspect that may pose a constraint when selecting a suitable combination between the syringe pump and syringe size.

In order to evaluate the reliability and stability of the liquid dosing system of the current study, the following aspects were investigated:

a. The effect of syringe size (1 and 5 mL syringes) on dosing H_2O to achieve 5 vol.% and 10 vol.% concentration in the gas mixture using N_2 carrier gas.

b. The effect of adding elastic PVC tubing to dampen the pressure-induced effects during liquid supply.

The results from the different SP settings and configurations are shown in Figure 5-3. The diagram demonstrates how the pump's supply stability changes by using syringes of different diameters or by using an elastic hose. From left to right, a decrease in the oscillatory behavior of the pump by reducing the syringe cross-section can be noted for a H_2O content of 5 vol.% in the gas mixture. After about 30 min, the syringe pump flow rate is increased and the injection stability of the syringe pump among different cases is compared for 10 vol.% H_2O. It can be noted again that the amplitude of the oscillation of the H_2O flow rate decreases as the syringe's internal diameter and volume decrease. Additionally, the use of a PVC hose along with a 5 mL syringe significantly eliminates oscillations and the injection stability resembles that of the 1 mL syringe. In order to quantify the impact of each configuration and obtain metrics for comparison, a statistical analysis was carried out and the results are shown in Table 5-2. At each concentration level, the mean value corresponds to the FTIR measurement prior to the calibration process, which explains a higher relative difference between the adjusted and the measured composition especially at 10 vol.%. The main indices used for comparison are the standard deviation (σ) and the coefficient of variation (CV) defined in Equation 5-1 and Equation 5-2, respectively. In those equations, N is the number of data values, x_i is the individual composition value at each point i and $\bar{x}$ is the mean value of H_2O concentration in the gaseous mixture.

$$\sigma = \sqrt{\frac{1}{N-1}\sum_{i=1}^{N}(x_i - \bar{x})^2} \qquad \textit{Equation 5-1}$$

$$CV = \frac{\sigma}{\bar{x}} \qquad \textit{Equation 5-2}$$

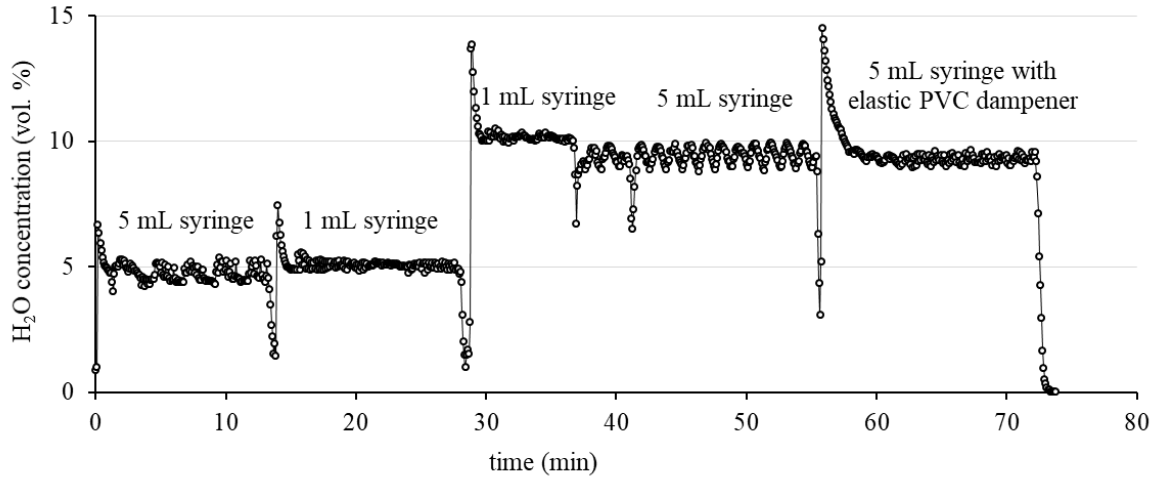

Figure 5-3: Syringe pump injection stability: effect of syringe size and elastic "dampener" tube.

From the results shown in Table 5-2, it can be concluded that the replacement of a larger syringe with a smaller one has the greatest effect on reducing σ and CV of the measured concentration values. Therefore, the 1-mL-syringe test resulted in a much lower CV compared to the 5-mL test at 5 vol.% H_2O, while using the same 5-mL syringe at 10 vol.% H_2O decreased the CV by 50% compared to Test 1. Thus, it is recommended that, when possible, smaller size syringes be used. When this is not possible, it was found that the use of a PVC dampener indeed reduced the oscillatory behavior. While the benefits of this measure were not as evident as those of the syringe size, it was found that a reduction in the CV by more than 45% can be achieved. In this study, a PVC tubing was not applied due to the nature of the organic species under study. Particularly, PVC tubing is not suitable for C_6H_6 and C_7H_8 as these species can permeate through the walls [249]. Herein, no other tube materials

were investigated or tested as alternatives to PVC dampeners, but this is recommended for future studies. Instead, PTFE tubing was used to transfer the hydrocarbons from the syringe pumps to MT2 and MT3. Moreover, the smallest possible syringe size was used so that smoother dosing is ensured in each case and the selection was based on the estimated duration of the test.

Table 5-2: Comparison of syringe pump performance with different syringe sizes and tubing.

Test	**1**	**2**		**3**	**4**	
Dampener	No PVC	No PVC		No PVC	With PVC	
Syringe volume (mL)	5	1		5	5	
H_2O content (vol.%)	5	5	**Rel. diff. (%)**	10	10	**Rel. diff. (%)**
$\bar{x}$ (vol.%)	4.73	5.07	+6.7	9.47	9.29	-1.9
σ (vol.%)	0.28	0.10	-64.2	0.31	0.16	-48.6
CV (-)	0.06	0.02	-66.7	0.03	0.02	-47.6

At this point, two more important design factors influencing the stability of liquid dosing must be included. Firstly, the temperature at the mixing point was found to influence the stability of dosing at low concentrations and small liquid dosing flow rates, accordingly. This can be attributed to the vaporization of the sample inside the needle and thus, no heating was applied when such an issue was encountered. Secondly, the mixing concept can also affect the oscillations which are measured. Initially, the injection of the hydrocarbons was carried out directly by connecting the PTFE hose to the mixing tee. However, very large deviations of the concentration were measured indicating that such an effect could be due to the formation of bigger droplets. This issue was tackled through the use of the injection needle at the mixing tee as described above.

The stirred reactor is made of 316 L stainless steel. It has an inner diameter of 102 mm and a height of 192 mm. Its peripheral walls are 6 mm thick, while its base is 8 mm thick. The flanges at its top have a diameter of 220 mm and a thickness of 20 mm. Four ports can be found at the upper flange where the gas inlet tube, outlet tube and measurement devices (pressure and temperature sensors) are mounted. A fifth port is sealed and used only for loading and unloading the liquid solutions. Reactor sealing is achieved by a Viton O-ring mounted on a groove of the lower flange. A hot-plate magnetic stirrer (IKA RH Basic 2, stirring speed: 100-2400 rpm, temperature: ambient to 320 °C), which was also used during the batch experiments (see Chapter 4), was used for liquid-phase stirring. The reactor is first loaded with the liquid solution under study and the gas is dispersed into the liquid. The gas mixture enters close to the lower section of the reactor and is released into the solvent mass in the form of bubbles. The saturation rate of the solution depends on the mass transfer rate of CO_2 by physical and chemical absorption. The design of a sparged stirred reactor for an efficient mass transfer from the gaseous to the liquid phase is, therefore, an important aspect that has to be considered. In the study of Garcia-Ochoa and Gomez [250], the main parameters influencing the volumetric mass transfer coefficient of sparged stirred reactors are discussed. According to Higbie's penetration theory, the mass transfer coefficient can be defined as

$$k_L = 2\sqrt{\frac{D_L}{\pi t_e}} \qquad \textit{Equation 5-3}$$

where D_L is the liquid diffusion coefficient and t_e is the contact or exposure time for mass transfer. Different theories give the mass transfer coefficient for a different description of the flow phenomena. For non-Newtonian fluids according to Ostwald- de Waele's theory, the coefficient is given as

$$k_L = \frac{2}{\sqrt{\pi}}\sqrt{D_L}\left(\frac{\varepsilon_{dis}\rho}{k_{ind}}\right)^{\frac{1}{2(1+n_{ind})}} \qquad \textit{Equation 5-4}$$

where ε_{dis} is the energy dissipation rate, ρ is the density, k_{ind} is the consistency index in the power-law model and n_{ind} is the flow index in a power-law model (dimensionless). The rate of energy dissipation is influenced by several parameters, such as the stirring speed. An increase in the work input per unit volume of fluid can lead to an improvement of k_L. In addition, it is necessary to maximize the specific interfacial area a, which can be calculated by the average bubble size inside the reactor d_b and the gas hold-up φ

$$a = \frac{6\varphi}{d_b} \qquad \textit{Equation 5-5}$$

Therefore it is important to reduce the average diameter d_b of the bubbles to enhance mass transfer. The gas hold-up φ was expressed by Garcia-Ochoa and Gomez according to a semi-empirical (see Equation 5-6), which is based on the isotropic turbulence theory

$$\frac{\varphi}{1-\varphi} = 0.819 \frac{V_s^{\frac{2}{3}} N_{ag}^{\frac{2}{5}} T_{ag}^{\frac{4}{15}}}{g^{\frac{1}{3}}} \left(\frac{\rho_L}{\sigma_{int}}\right)^{\frac{1}{5}} \left(\frac{\rho_L}{\rho_L - \rho_G}\right) \left(\frac{\rho_L}{\rho_G}\right)^{-\frac{1}{15}} \qquad \textit{Equation 5-6}$$

where V_s is the superficial gas velocity, N_{ag} the agitator speed, T_{ag} the agitator diameter, ρ_L and ρ_G the liquid and gas density and σ_{int} the interfacial tension. Various types of gas diffusers have been evaluated in the literature as components to carry out the mass transfer into the liquid phase. Factors such as the relative position between the stirrer (or multiple stirrers) and the position of the sparger, as well as the ratio of the diameter of the vessel to that of the agitator (D/T_{ag}) can affect the mass transfer coefficient. A D/T_{ag} ratio of about 2 can have a positive effect on increasing the interfacial area as discussed in [250]. A stirrer diameter of $T_{ag} = 50$ mm was used in this experimental campaign.

Three (3) different gas diffusers were evaluated before the final selection of the sparger, particularly a) a vertical 1/4 inch tube with an ID of 4.57 mm, b) a circular diffuser (ring) consisting of 21 holes with a diameter of 0.3 mm each and c) a porous gas sparger with 2 μm pore size (all made of SS). This investigation was carried out as a "trial-and-error" procedure in order to achieve sufficient mass transfer inside the reactor rather than as a comprehensive comparison of the hydrodynamic performance of different designs. The comparison of the three sparger types is shown in Figure 5-4. This study was carried out under identical CO_2 partial pressure, solution composition and mass, gas flow rate, reactor temperature and N_2 as the carrier gas.

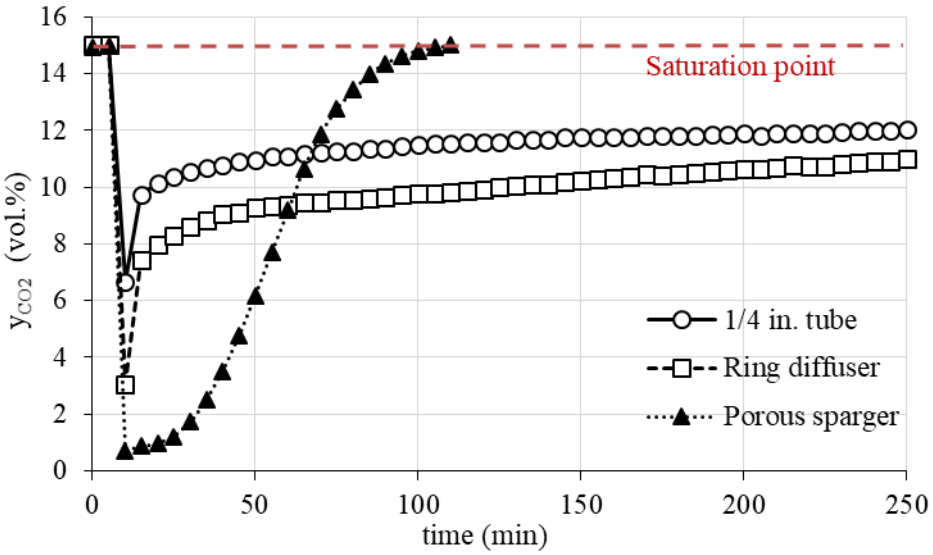

Figure 5-4: CO_2 concentration in outlet gas (vol.%) versus time with different gas diffusers.

The order of mass transfer performance for the different configurations was *porous sparger* > *ring diffuser* > *vertical SS tube*. The replacement of the vertical tube with the ring diffuser improved the CO_2 transfer to the liquid phase, however, it remained very low to ensure the completion of the experiments within a reasonable time duration. In the case of these two dispersing systems, the CO_2 capture rate did not exceed 30% at rotational speeds of 500-1000 rpm, often resulting in equilibrium conditions after 10-12 h. On the other hand, when they were replaced by the sintered-metal stainless steel sparger, an improved mass transfer performance was achieved. For the latter case, the CO_2 capture rate was higher than 98%. By adopting this configuration, the time required to saturate the aqueous solutions was around 1.5-2 h for the experimental conditions of this campaign, which are presented in detail later.

After the mixing tees MT1, MT2 and MT3 and before the stirred reactor, there are a by-pass line and two ball valves for regulating the flow direction. Two of the main purposes of this configuration are a) to measure the gas composition at the start of each test and b) directly supply gas mixtures to the FTIR analyzer for calibration. In addition, with such a configuration, the gas mixing station can be operated independently to supply gas mixtures for other applications and test facilities. This line may be also used when an alternative pathway for gases is required e.g. in the event of a reactor blockage due to particles, sediments, etc. In addition, the reactor requires a check valve to avoid suction due to overpressure from the sparger to the inlet pipe. Downstream of the reactor, there is a backpressure regulator (BPR) for controlling the absorption pressure from ambient up to 7 bar. After the backpressure regulator and before the FTIR analyzer, the gas flow is directed to a porous filter (0.5 μm) for the protection of downstream equipment from solids and aerosols, denoted as PMF in Figure 5-1.

For all lines with heat tracing, SS 1/4 in tubing was installed. In fact, the maximum operating temperature was around 200 °C and initially, PTFE tubing was used to a greater extent for connecting the different components. However, failures that can be attributed to heating and cooling cycles and temperature overshooting were encountered and thus, the tubing was replaced. Smaller size tubing was used for the SS tube coils (1/8 in) and for the PTFE tubing, which transfers C_6H_6 or C_7H_8 from the syringe pumps to the mixing tees (1/16 in). In addition, for lines at ambient temperature, PTFE 1/4 in tubing was used (e.g. tubing from the gas cylinders to the MFCs). Flexible heated cables insulated with quartz yarn (Horst HSQ) were installed over metal tubing for heat tracing and they were operated well below their temperature limit (900 °C). The reactor outlet and inlet lines are heated independently and their temperatures are regulated by separate PID controllers with Pt100 sensors. This is due to the different requirements in each case: the inlet gas flow rate was preheated at the reactor temperature, while the outlet flow rate was heated to a much higher temperature, as this is necessary for the operation of the FTIR spectrometer. In addition, the reactor is heated with a 2 kW tailor-made, PID-controlled heating jacket, which can operate up to 300 °C (Mica Electric Heaters). Electric heating was also installed at the reactor flange (Thermon HPT 10-2 heating tape) in order to ensure that no condensation occurs due to a lower temperature at the upper part of the reactor. This heating zone was also PID-controlled and it was typically adjusted about 2-3 °C above the reactor temperature. Apart from the Pt100 sensors of the PID controllers, temperature inside the reactor is measured by two K-type thermocouples (UTECO, 3 mm diameter), one for the liquid (20 cm long) and one for the gas phase (8 cm long), similarly to Chapter 4. In addition the pressure sensors which were used during the batch tests were also used in this new configuration for pressure measurements (WIKA S-10 pressure transmitters, 0-6 bar, accuracy ± 0.03 bar). Those pressure transmitters were placed upstream (i.e. reactor pressure) and downstream of the BPR.

For data acquisition and logging, ADAM signal processing modules were installed (Advantech SA). Particularly, signals from thermocouples, pressure transmitters and MFCs are delivered to two (2) ADAM-4019+ analog input modules. In addition, signals to the MFCs are provided *via* an ADAM-4024 analog output module. All input data for pressure, temperature and mass flow rates were continuously monitored and recorded by a data acquisition system, which also enabled the remote adjustment of gas flow values. Gas analysis measurements are logged through another data acquisition software, as discussed next. A depiction of the experimental apparatus for the investigation of CO_2/light tar absorption into liquid solvents is shown in Figure 5-5.

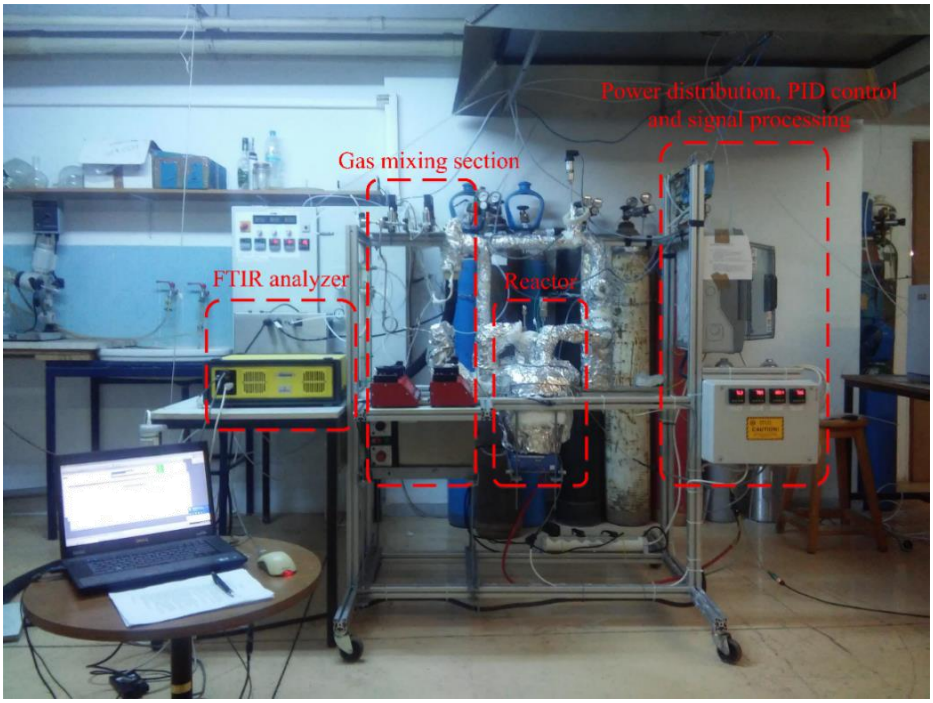

Figure 5-5: Depiction of sparged stirred reactor apparatus for gas absorption studies into liquid solvents.

5.2.3 Gas-phase analysis through FTIR spectroscopy

5.2.3.1 Principles of FTIR spectroscopy

In general, IR spectroscopy is a method of identifying molecules based on their characteristic frequencies of rotation and vibration when they absorb IR and move towards higher energy states. Due to the fact that different molecules absorb IR at different wavelengths, a unique IR absorption spectrum results for each compound. With this method, all gas species apart from O_2, N_2, H_2, Cl_2, F_2, H_2S and noble gases can be measured. The particular benefit of the Fourier transform method compared to alternatives is that a full spectrum over the IR wavelengths is produced and multiple components can be analyzed within a single measurement. The quantification of the concentration of a species is based on the Beer-Lambert-Bouguer law shown in Equation 5-7.

$$A = \log\left(\frac{I_0}{I}\right) = \log\left(\frac{1}{T_b}\right) = \varepsilon_b l c \qquad \textit{Equation 5-7}$$

where A is the absorbance, I_0 is the initial radiation intensity, I is the radiation intensity after contact with the sample, T_b is the transmittance, ε_b is the attenuation coefficient or absorptivity of the attenuating species, l is the optical path length and c is the sample concentration. The molecular absorptivity can vary at conditions of very high concentration or when the absorption intensity of particular wavelengths is significant. When the influence of the concentration is not high, it can be stated that for a certain optical path length, there is a linear correlation between the IR absorbance and the species concentration in the sample. Changes in temperature and pressure can also influence the IR absorbance and it is, therefore, necessary to carry out calibrations and sample analyses under specific conditions.

The main operation of an FTIR spectrometer is carried out by the interferometer. It is an optical modulator, which modulates the radiation emitted by an IR source resulting in an "optical Fourier Transform" on the IR. The Michelson interferometer is one of the simplest and more common interferometer configurations, consisting of a beam splitter for splitting the incoming radiation and two mirrors, a stationary and a moving one. The movement of the mirror at a constant velocity changes the optical path difference (*OPD*) between the beams *i.e.* the distance traveled by the beam heading to the stationary mirror minus the distance of the beam traveling to the moving mirror. The beams at the detector interfere constructively for *OPD*s equal to integer multiples of

wavelength λ and destructively for integer multiples of $\lambda/2$. Consequently, for a single wavelength and a moving mirror at constant velocity, the detector signal varies as a cosine function with maxima at zero *OPD* and integer multiples of λ. The result of the superposition of those cosine functions for all radiation wavelengths results to an "interferogram" which is the measured intensity *versus* the *OPD*. At this point, it should be noted that an IR interferogram has a center burst at zero *OPD* and complex wave patterns around it. Its form can be simplified by installing a laser source which also results in improved accuracy for tracking the mirror position and consequently the *OPD*. A laser interferogram can be produced by a He-Ne laser beam traveling through the interferometer into a special detector at a constant wavelength (632.8 nm). In contrast to the IR interferogram, the laser interferogram is an almost ideal cosine wave.

In order to produce IR absorption spectra (function of *frequency* or *wavelength*) from interferograms (a function of *OPD* or *time*), Fourier transform can be applied as shown in Equation 5-8 and Equation 5-9.

Fourier Transform $$F(\omega) = \int_{-\infty}^{+\infty} f(t) e^{-i\omega t} dt$$ *Equation 5-8*

Inverse Fourier Transform $$f(t) = \frac{1}{2\pi} \int_{-\infty}^{+\infty} F(\omega) e^{i\omega t} d\omega$$ *Equation 5-9*

In this form, the Fourier transform allows a transformation from a time domain (t) to a frequency domain (ω) or reversely. This procedure is performed through algorithms, such as the Fast Fourier Transform-FFT algorithm applied by Gasmet Technologies.

5.2.3.2 FTIR system description and analysis methodology

In this study, the gas-phase analysis was carried out by a portable Gasmet DX4000 FTIR analyzer. It incorporates an FTIR spectrometer, a temperature-controlled sample cell and auxiliary electronics for signal processing. The measurements are logged to a PC through Calcmet software, which can visualize results in real-time and save them as ASCII files for further processing. Table 5-3 briefly summarizes the analyzer specifications. Herein, wavenumber is the inverse of wavelength.

Table 5-3: Gasmet DX4000 FTIR analyzer specifications [251].

Parameter	**Values/description**
Spectrometer resolution (cm^{-1})	8 or 4
Scan frequency (scans s^{-1})	10
Detector type	Peltier-cooled Mercury-Cadmium-Telluride
Source type	SiC, 1550 K
Beam splitter type	Zn-Se
Wavenumber range (cm^{-1})	900–4,200
Optical path length (m)	5
Sample/cell temperature (°C)	180
Sample pressure (kPa)	Ambient
Sample cell volume (L)	0.4
Sample gas flow rate (NL h^{-1})	120-600
Temperature drift	< 2% of measuring range per 10 °C change
Pressure influence	1% measurement change per 1% pressure change

The analyzer can be used for the analysis of wet off-gases. An auxiliary sampling unit (denoted as SU in Figure 5-1) can be connected to the FTIR analyzer for flue gas sampling. The SU contains a heated particulate filter (2 μm), a heated sample pump at 180 °C and all necessary valves, PID controllers and power supply auxiliaries. In this case, heated lines (4 mm, PTFE) are used to transfer the sample from the sampling point to the SU and next to the FTIR analyzer. Due to the sufficient overpressure downstream of the sparged reactor, the SU was not used during the course of a test, but the heated PTFE line was directly connected at the FTIR analyzer inlet instead. The SU was only used for performing daily zero point calibration with ultra-pure N_2, as well as for regulating the heated line temperature at a constant value of 180 °C. Bypassing the SU has another implication.

The FTIR analyzer becomes susceptible to wear from aerosols in the gas sample. In this case, a heated filter was installed downstream of the BPR and all outlet tubing from the reactor to the FTIR analyzer was also kept at 180 °C since the sample gas temperature should be the same as the sample cell temperature to avoid temperature drift issues or condensation.

Reference spectra are needed for the analyses of gas samples. Gasmet Technologies suggests a regular recalibration of H_2O for maintaining the instrument accuracy. In this work, reference spectra for all species, apart from CO_2, were produced. For CO_2, existing reference spectra from the FTIR databank were used covering a range between 3 and 30 vol.%. Table 5-4 presents all the concentration values used for the generation of reference spectra for the single components. No reference spectra existed for MEA in the databanks. However, it is a volatile compound and therefore it is expected to be present in the gas phase. In other cases, they were available for a narrow concentration range or much lower levels, such as for hydrocarbons (e.g. CH_4 and C_6H_6), since this analyzer is mostly used for wet flue gas analysis.

Table 5-4: Selected concentration points (vol.% or ppmv) for reference IR absorption spectra generation.

Component	Concentration values
H_2O	0.1, 0.2, 0.5, 1.0 and 2.0−40.0 vol.% with 2 vol.% step
CO_2	3.0, 5.97, 10.0, 15.0, 20.0, 25.0 and 29.9 vol.%
CH_4	50, 100, 200, 500, 700, 1000 ppmv and 0.5, 1.0, 1.5, 2.0, 2.5, 3.0, 3.5, 4.25, 5.0, 7.0 vol%
MEA	200, 500 and 1000 ppmv
C_6H_6	50, 100, 200, 400, 600, 800, 1000, 1200, 1400, 1600, 1800 and 2000 ppmv
C_7H_8	50, 100, 200, 400, 600, 800, 1000, 1200, 1400, 1600, 1800 and 2000 ppmv

For the calibration procedure, N_2 was used as the carrier gas and it was regulated through the OMEGA FMA5516 MFC (± 1% of setpoint). All liquid compounds at ambient conditions, *i.e.* MEA, H_2O, C_6H_6 and C_7H_8, were supplied by syringe pumps and the resulting gas mixtures were transferred to the FTIR analyzer through the reactor bypass line.

For the analysis of multiple compounds, appropriate wavelength analysis areas must be selected depending on the species. Calcmet software enables up to three (3) analysis areas for each compound. Simpler compounds in small concentration areas require only a few reference spectra since their molecular absorption remains nearly constant, however other compounds (e.g. H_2O and CO_2) require more as they exhibit changes in IR absorption at different wavelengths. An absorbance value of 1.0 corresponds to 10% permeability, which means that the component molecules absorb 90% of the incident radiation. In general, the signal-to-noise ratio must be 3. For the GASMET DX4000 analyzer, the noise level should be about 2% or a maximum of 1.2 absorption units. During FTIR analysis, the absorption peaks can overlap and it is necessary to determine any interferences from other compounds. For instance, H_2O has two large absorption areas that extend nearly throughout the IR spectrum. Those interferences can be defined in the Calcmet software for each component. While the procedure of selection of the analysis areas is generally intensive and a subject of further optimization, an effort has been made in this work to select the most suitable wavenumber regions. Table 5-5 summarizes the analysis regions selected for each component and the interferences defined in each case for the CO_2/C_6H_6 tests. In addition, the shape of the absorbance curve and the areas for FTIR multicomponent analysis are depicted in Figure 5-6 for a typical gas sample obtained during an absorption test.

Table 5-5: Specifications for gas-phase analysis based on FTIR spectroscopy with Gasmet DX4000.

Component	Analysis area (cm^{-1})	Interferences	Absorption limit (−)	Analysis options
H_2O	3200−3500	CO_2, MEA, C_6H_6	1.0	DRF[1]
CO_2	926−1150	H_2O, MEA, C_6H_6	1.0	−
CH_4	2650−2950	H_2O, CO_2, MEA, C_6H_6	0.8	−
MEA	1500−2000	H_2O, CO_2, CH_4, C_6H_6	1.0	SC[2]
C_6H_6	1700−2000	H_2O, CO_2, MEA	1.0	SC

[1] DRF: double-reference fitting, [2] SC: slope correction function

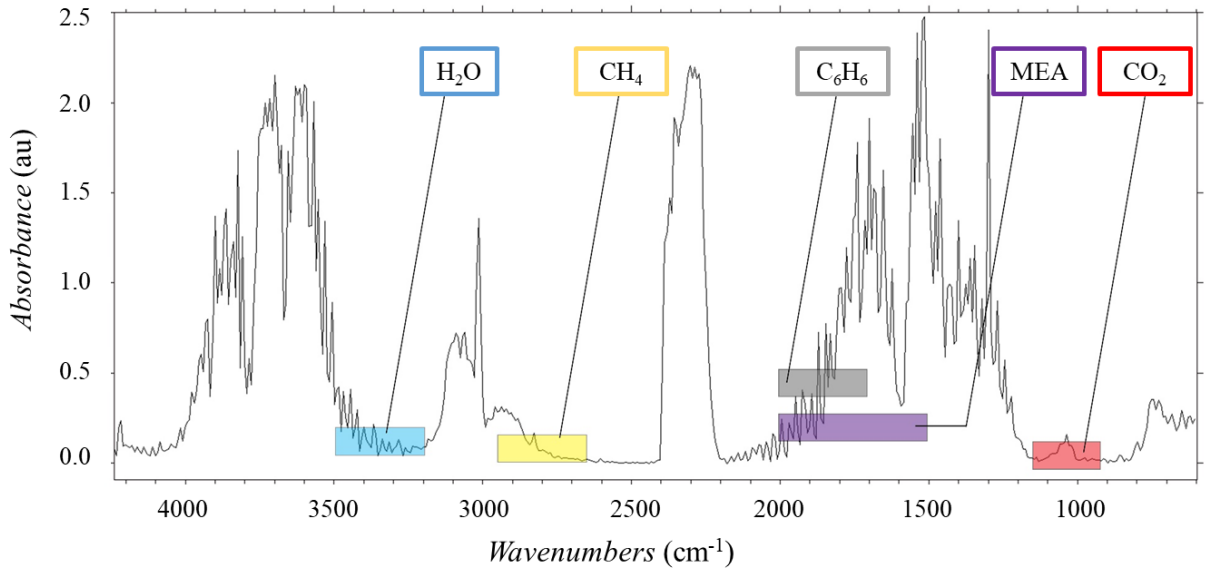

Figure 5-6: Component analysis areas for FTIR spectroscopy. Measurements depicted from CO_2/C_6H_6 absorption test with MEA-promoted aqueous K_2CO_3 solution.

Next, the methods and constraints applied for the determination of multicomponent FTIR analysis parameters are briefly presented. They are based on manufacturer guidelines [252] and general practice.

1. The spectral range selected must have evident peaks for the component of interest.
2. In the case of a mixture: when peaks from other species in the same wavenumber region exist (e.g. in the range of 0.8 au), this area must be preferably excluded if possible.
3. If the concentration of a single species is such that its highest absorption peaks are very intense, such analysis areas must be preferably excluded. Instead, it is preferable to select areas with smaller peaks and a more linear behavior *versus* concentration changes.
4. The analysis area should not be too narrow and a wavenumber range of at least 200 cm^{-1} must be selected. Moreover, it is not exactly the peak itself that should be defined, but a region that includes the absorption area of the compound in the vicinity of the peak.
5. A general rule dictates the use of more data points in the areas of analysis than the interferences listed. For instance, if the analysis region extends for 200 cm^{-1} and the resolution is 8 cm^{-1}, there are only 25 data points in that domain. If there were 20 or more interferences, the analysis would become practically impossible.
6. In large analysis areas and when two (2) or three (3) separate analysis areas are defined, the use of the "*slope correction*" function is suggested by the manufacturer. Similarly, for large analysis areas and when these separate areas are far away, the "*curve correction*" function is recommended. Such corrections were also applied in this study where relevant (e.g. for MEA).
7. Additionally, Gasmet DX4000 and Calcmet offer the possibility of a function named "*double-reference fitting*". This option uses the two nearest reference spectra of a compound for better fitting. This is recommended when the concentration of that compound is high and it changes in a non-linear way relative to other components. In the present work, it was enabled for improving the accuracy of H_2O measurements.

5.2.4 Experimental methodology and solubility calculation

Figure 5-7 depicts a simplified flowchart of the experimental procedure which was applied, while Table 5-6 presents the test matrix of the experimental investigation. Initially, the FTIR analyzer is preheated for *ca.* 45 min until the interferometer, cell and system electronics reach their steady-state temperature values, according to the manufacturer specifications. At the same time, the data acquisition starts for recording measurements from MFCs, pressure transmitters and thermocouples, as well as FTIR gas measurements (Calcmet software). Heating of the reactor and tubing also starts, which is completed in two (2) steps to suppress thermal stresses. During all those preliminary steps, the inlet port of the FTIR analyzer is connected to the SU device.

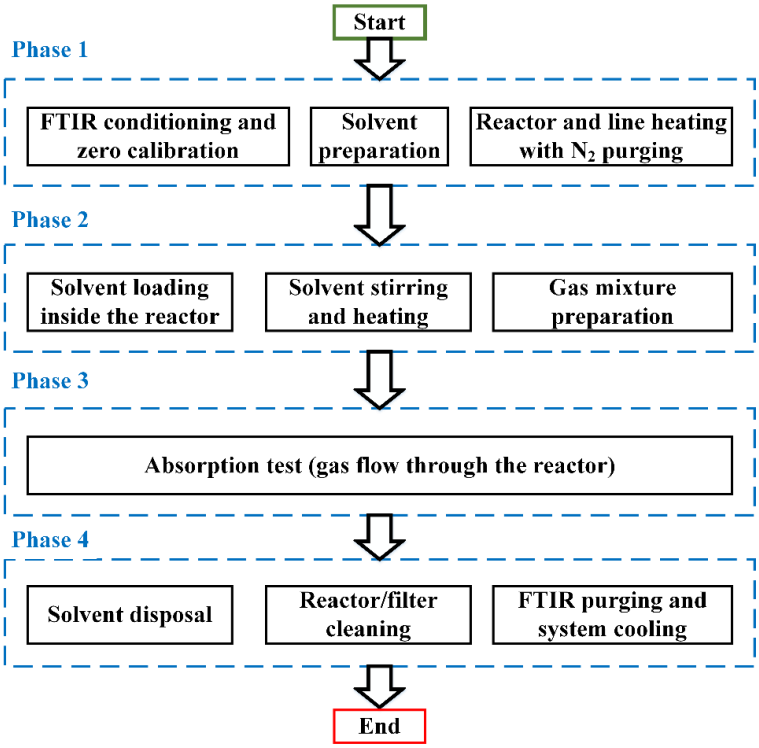

Figure 5-7: Flowchart of the experimental procedure for investigating gas absorption into liquid solvents.

After 45 min, ambient air was sampled and sent to the analyzer through the SU for O_2 calibration for 90 min and subsequently, valves were switched to allow N_2 with 99.999% purity into the analyzer. At this stage, zero calibration (10 min) and measurement of the "background" reference spectrum (3 min) were also carried out. After the solution has been prepared, it is loaded into the reactor from the reactor upper port. When the reactor is filled, the magnetic stirrer is set at a constant speed of 1300 rpm throughout the test. The heated line of the FTIR system was connected to the reactor outlet tubing and during this heating phase, a constant N_2 flow was sent to the analyzer through the bypass line (the minimum sample flow rate required by the FTIR manufacturer). A few minutes before the solution reaches the desired temperature, a gas mixture is simulated with 3 vol.% CH_4, 15 vol.% CO_2 and tar type/concentration according to Table 5-6. Industrial-purity N_2 was used as the carrier gas and the total gas flow rate was 2 NL min^{-1} for all tests. The mixture was sent to the FTIR analyzer through the bypass line and the gas composition was measured and recorded. The analyzer was adjusted to carry out measurements with a 1-min step through Calcmet.

When the reactor temperature and gas composition reached their steady-state values, the gas flow was switched to the sparged reactor for starting the absorption test. During this study, experiments were carried out with the BPR fully-open. However, a slight overpressure (~ 0.4-0.6 barg) was monitored during the tests, which can be attributed to pressure losses particularly due to the sparger and the 0.5-μm particulate filter. The experiment proceeds until the solution is saturated and the CO_2 composition has values in the range $C/C_0 = 0.99$ (db). After saturation, the gas flow is switched again to the bypass line and then, the MFCs and syringe pumps are stopped, apart from the N_2 flow. The N_2 flow rate is maintained for purging the FTIR analyzer before it is connected to the SU, which is then supplied with atmospheric air and finally with ultra-pure N_2. Single measurements with a 2-min step are carried out for the last 10-15 min to confirm that the sample cell of the FTIR analyzer does not contain contaminants. The reactor is filled with deionized water two (2) times to dissolve any remaining species prior to the next run. During the preliminary tests, no filter inspection was performed. However, a pressure increase in the range of 0.2-0.3 bar was monitored at the start of the following test, caused by deposits probably due to aerosol entrainment.

Table 5-6: Test matrix for the absorption of C_6H_6/CO_2 and C_7H_8/CO_2 mixtures into pure and MEA-promoted K_2CO_3 solutions.

Test No.	K_2CO_3 concentration (wt.%)	MEA concentration (wt.%)	Temperature (°C)	Tar type/ concentration (ppmv)
1	25	–	60	–
2	25	–	70	–
3	25	–	60	C_6H_6/1000
4	25	–	60	C_6H_6/2000
5	25	–	70	C_6H_6/1000
6	25	–	70	C_6H_6/2000
7	25	–	60	C_7H_8/1000
8	25	–	60	C_7H_8/2000
9	25	–	70	C_7H_8/1000
10	25	–	70	C_7H_8/2000
11	25	1	60	–
12	25	1	70	–
13	25	5	60	–
14	25	5	70	–
15	25	1	60	C_6H_6/1000
16	25	1	60	C_6H_6/2000
17	25	1	70	C_6H_6/1000
18	25	1	70	C_6H_6/2000
19	25	1	60	C_7H_8/1000
20	25	1	60	C_7H_8/2000
21	25	1	70	C_7H_8/1000
22	25	1	70	C_7H_8/2000
23	25	5	60	C_6H_6/1000
24	25	5	60	C_6H_6/2000
25	25	5	70	C_6H_6/1000
26	25	5	70	C_6H_6/2000
27	25	5	60	C_7H_8/1000
28	25	5	60	C_7H_8/2000
29	25	5	70	C_7H_8/1000
30	25	5	70	C_7H_8/2000

Since such an issue affects the partial pressure of the gaseous components, cleaning of the particulate filter with hot water was performed after each test followed by mild heating inside a furnace. Four parameters were varied in this study, particularly the solution composition (MEA concentration), the type of tar species, the concentration of tar species and the solution temperature. A lower temperature (60-70 °C) was applied compared to the batch experiments, due to ambient pressure conditions. Herein, it has been assumed that the removal of CH_4 at low partial pressures is negligible. Paolini et al. [253] demonstrated that the CH_4 slip during CO_2 absorption from biogas with K_2CO_3 solutions is < 0.1%, which is in line with the assumption. For this reason, the CH_4 concentration in the reactor outlet gas was used to quantify the solubility of CO_2, C_6H_6 and C_7H_8 in this study. However, it is suggested that a mass flow measurement device would be required for more precise estimation. The solubility (mol kg^{-1}) of a species i was calculated from the difference of reactor inlet and outlet concentration curves for that species according to Equation 5-10.

$$solubility = \frac{\dot{n}_{i,in} t_{exp} - \sum_{k=1}^{k=j-1} \left[\Delta t_m \frac{\dot{n}_{i,out}(k) + \dot{n}_{i,out}(k+1)}{2} \right]}{m_{sol,in}} \qquad \textit{Equation 5-10}$$

In this equation, $\dot{n}_{i,in}$ (mol min^{-1}) denotes the molar flow rate of species i measured prior to the absorption test, $\dot{n}_{i,out}(k)$ is the molar flow rate for the k measurement, Δt_m is the analysis step (1-min measurements), t_{exp} is the total saturation time (min) and $m_{sol,in}$ is the initial solution mass (kg) in the sparged reactor.

5.3 Results and discussion

5.3.1 CO_2 solubility and absorption rate results

The experimental results for CO_2 solubility under different conditions of temperature, tar concentration and additive content are shown in Figure 5-8. In this experimental campaign, the CO_2 partial pressure was around 22 kPa for all tests. It can be noted that within the ranges that the parameters varied, CO_2 solubilities at saturation were found in the range 1.02-1.43 mol kg^{-1} solvent. Temperature has a detrimental effect on CO_2 solubility, however, its effect seems to be rather negligible when no MEA is added into the solution. When the MEA content increases though, the effect of temperature is more important, which can be attributed to the increased heat of absorption due to carbamate formation. At 70 °C, higher solubilities were found in certain cases for the pure K_2CO_3 solution compared to that promoted by 1 wt.% MEA. This outcome can be partially be attributed to MEA losses which were found to occur even at this temperature range. Increasing the MEA concentration in the promoted K_2CO_3 solution to 5 wt.%, significantly improved CO_2 solubility yielding the highest capacity values measured during the tests.

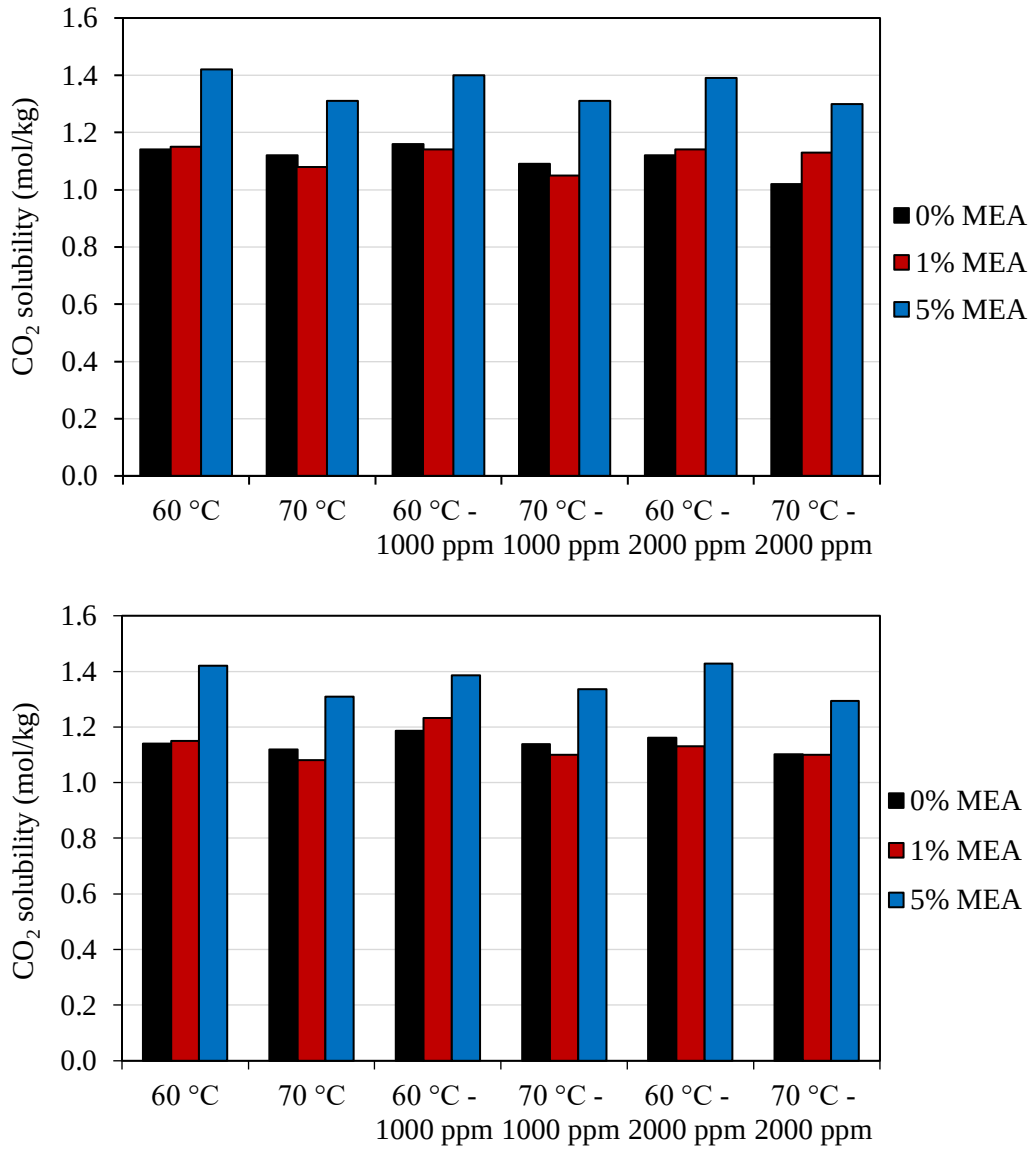

Figure 5-8: Effect of MEA additive concentration on CO_2 solubility in the case of $CO_2/C_6H_6/CH_4$ mixtures (top) and $CO_2/C_7H_8/CH_4$ gas mixtures (bottom).Concentrations of light tar species denoted in ppm.

No statistically important effect of the tar content on CO_2 solubility was found since similar or even higher solvent capacities were measured when C_6H_6 and C_7H_8 were added in the gas mixture. It can thus be concluded that the process can sufficiently handle light tar species without penalizing the AGR process performance. Of course, the rich solvent may require some treatment process if condensable tars are present in syngas.

The effect of MEA addition on the CO_2 absorption rate under constant stirring speed is shown in Figure 5-9. The addition of MEA increases the concentration of reactive species in the solution and improves the reaction rate with CO_2. Increasing temperature from 60 to 70 °C improves the absorption rate, which can be clearly noted from the 5 wt.% MEA curve. Adding a slight amount of MEA (1 wt.%) has almost no effect on the slope of the saturation curve, in contrast to the 5 wt.% case. In general, the effect of promoter addition became evident when the liquid-phase concentration increased to values higher than 0.8 mol kg^{-1}. This value corresponds to a loading of 0.44 mol CO_2 mol^{-1} K_2CO_3 for the pure K_2CO_3 aqueous solution.

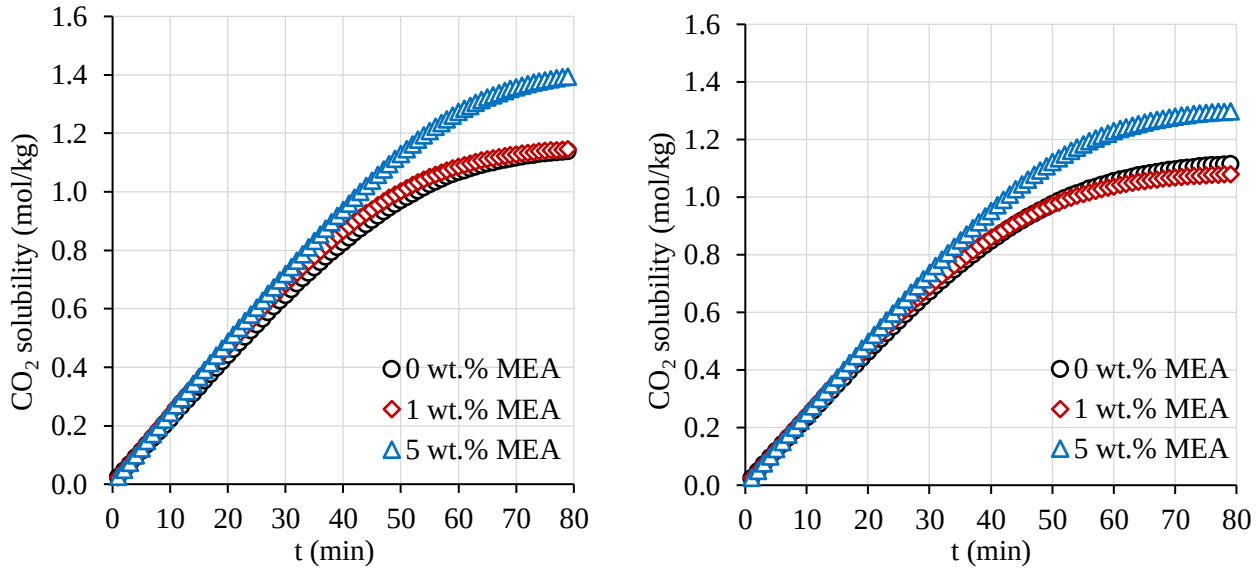

Figure 5-9: Effect of MEA concentration on CO_2 absorption (no BTX in inlet gas) rate into promoted K_2CO_3 solutions at 60 °C (left) and 70 °C (right) and comparison with 25 wt.% pure K_2CO_3 aqueous solution.

5.3.2 Light tar absorption results

Results for C_6H_6 and C_7H_8 solubility in pure K_2CO_3 and MEA-promoted solutions are shown in Table 5-7. It can be noted that very low solubility values were found for both compounds, with the highest values at 1.65 and 1.72 mmol kg^{-1} for C_6H_6 and C_7H_8, respectively. Tar solubility values were thus three orders of magnitude lower than the amount of CO_2 in the liquid phase. The limited C_6H_6 and C_7H_8 affinity of the K_2CO_3 aqueous solutions demonstrates that their application in AGR processes at high temperatures will enable the recovery of those species downstream. On the other hand, when the elimination of those species is desired, an alternative solvent must be used. Polyethylene glycols, phthalates, adipates and silicon oils have been considered as suitable for the absorption of C_7H_8 by Heymes et al. [254]. Properties that affect the absorption of light tar species are liquid density, liquid viscosity and polarity of solvent and organic compounds, as described in [255]. The high polarity of aqueous solutions is a factor that contributes to the results reported in the present work. Ozturk and Yilmaz [255] found that very small BTX removal efficiencies were feasible in absorption experiments in a lab-scale bubble column when water was used as the solvent, which is line with the results in the present study for the aqueous solutions.

Table 5-7: C_6H_6 and C_7H_8 solubility in pure and MEA-promoted K_2CO_3 aqueous solutions.

Solution concentration K_2CO_3/MEA (wt.%/wt.%)	**T (°C)**	**Tar content (ppmv)**	**C_7H_8 solubility (mmol kg^{-1})**	**C_6H_6 solubility (mmol kg^{-1})**
25/−	60	1000	1.40	1.01
25/−	60	2000	1.72	1.65
25/−	70	1000	1.13	0.52
25/−	70	2000	1.25	1.24
25/1	60	1000	0.78	0.35
25/5	60	1000	1.26	0.80
25/1	60	2000	1.00	1.01
25/5	60	2000	1.59	1.50
25/1	70	1000	0.53	0.77
25/5	70	1000	0.31	0.60
25/1	70	2000	0.77	0.82
25/5	70	2000	0.52	1.14

5.4 Conclusions

In this chapter, an extension of the work carried out in Chapter 4 was presented. The focus was on the investigation of the performance of aqueous K_2CO_3 solutions (without promoters and promoted by MEA) towards the simultaneous absorption of CO_2 and light tar species which are present in syngas. Two model compounds were studied, particularly C_6H_6 and C_7H_8. The tests were carried out in a semi-continuous absorption apparatus with gas-phase analysis through FTIR spectroscopy. The effect of temperature, MEA concentration and tar content on the absorption of gas mixtures was investigated.

The study revealed that the addition of a small concentration of MEA in the range of 1 wt.% has no notable impact on CO_2 solubility compared to the case pure K_2CO_3 is added exclusively in the aqueous solution. Temperature deteriorates the solubility of CO_2 in all solvents, however, a more evident effect was found for the 5 wt.% MEA promoted solution. On the other hand, a temperature increase by 10 °C has a very small impact on the solution capacity for smaller promoter concentrations or only K_2CO_3. In Chapter 4, it was shown that MEA addition can improve the absorption rate of CO_2 into aqueous solutions of K_2CO_3 at elevated temperatures (≥ 100 °C). In this chapter, it was shown that MEA added at 5 wt.% in the solution can improve the CO_2 absorption rate especially when the liquid-phase CO_2 concentration increases above ~ 0.8 mol kg^{-1}. On the other hand, very low C_6H_6 and C_7H_8 capacities (< 2 mmol kg^{-1}) were measured. This was attributed to the discrepancy between VOC and solvent polarities. Nevertheless, this outcome can be considered desirable when downstream utilization of light tar species is intended (such as tar reforming downstream of the AGR process e.g. over Ni catalysts). Finally, no significant impact on CO_2 solubility was observed when tar species were added in the gas mixture.

6 Thermodynamic and process modeling study of AGR based on hot potassium carbonate solutions

6.1 Literature review of thermodynamic and process modeling of AGR by aqueous K_2CO_3 solutions and scope of the present study

In Chapter 4, the fundamentals of CO_2 absorption into hot K_2CO_3 solutions have been analyzed especially regarding the reaction mechanisms of pure K_2CO_3 or promoted aqueous solutions with different additives. In this chapter, the focus is on the thermodynamic and process modeling of CO_2 and H_2S absorption into aqueous K_2CO_3 solutions as an important aspect of process design and optimization. In order to achieve this goal, the study was carried out in two steps. Firstly, thermodynamic models were developed with parameters representative of the systems under study. Subsequently, rate-based models with kinetic and mass transfer expressions were implemented for the absorption/desorption process in order to investigate the performance of the AGR unit. In this section, a literature review regarding the theoretical background of thermodynamic and process modeling is given.

6.1.1 Literature review: thermodynamic modeling of CO_2 absorption into K_2CO_3 solutions

One of the early attempts for modeling the VLE of an electrolyte system was the single-equation model of McCoy for the CO_2-Na_2CO_3-H_2O system [256]. Over the course of the last 50 years, significant research has been carried out in developing accurate thermodynamic models for electrolyte systems. Particularly, semi-empirical Gibbs energy expressions have been suggested, which model the system through two contribution terms. The first term describes long-range interactions caused by electrostatic forces between ions in the solution and it is usually based on the Debye-Hückel theory. The second term describes short-range or local interactions of different types and it is based on expressions for non-electrolyte systems. Among the models which have been proposed, the model of Pitzer [257] and the electrolyte-NRTL model of Chen et al. [258] have been widely used in research studies and industrial practice [240]. Both models generally provide a thermodynamic framework for the calculation of properties of electrolyte solutions (e.g. mean ionic activity coefficients, fugacities etc.), as well as for estimating vapor-liquid equilibrium (VLE), liquid-liquid equilibrium (LLE) and salt solubility. The Pitzer model is mostly used for modeling dilute aqueous electrolyte solutions, while on the other hand, the electrolyte-NRTL model has been used for both aqueous and mixed-solvent electrolyte systems and over a much more wide concentration range. Various applications of the electrolyte-NRTL model are given in the study of Chen and Song [240], such as calculations of phase behavior and ionic activity coefficients of strong and weak electrolyte systems, aqueous or organic, etc. The Pitzer and electrolyte-NRTL models, as well as their extensions, have been used for modeling the CO_2-K_2CO_3-H_2O system (with promoters or not) as discussed next. Other models have also been used, such as the extended-UNIQUAC model in the study of Fosbøl et al. [259]. However, this review will only focus on the two most common thermodynamic models.

An extended Pitzer model applicable in the temperature range of 70–140 °C and K_2CO_3 concentration up to 40 wt.% was developed to describe the CO_2-K_2CO_3-H_2O ternary system by Chen et al. [260]. A good agreement with experimental VLE data was reported. More recent studies applying the Pitzer model are in chronological order those of Kamps et al. [261], Imle et al. [262] and Bohloul et al. [263]. Kamps et al. [261] studied the VLE prediction capability of the Pitzer model through comparison with in-house experimental measurements within a temperature range of 40–120 °C, pressures of 2.7–92 bar, CO_2 loadings in the range 0.7–3.6 and K_2CO_3 concentrations (molality) between 0.43 and 1.7 m. In addition, the authors compared the deviation of their model with experimental studies from the literature covering a wider range of conditions (e.g. temperature, K_2CO_3 concentrations etc.). While a small deviation was found compared to their experimental results ($\Delta p/p = 7\%$), higher deviations were found for more relevant K_2CO_3 concentrations to the Benfield process (~ 28%). From a comparison of the model results with experimental measurements from 8 different studies, deviations in the range of 6–65% were reported. An extended Pitzer equation was used by Imle et al. [262] to model CO_2 solubility in K_2CO_3 solutions activated by boron and vanadium. The authors carried out measurements at two temperatures (70 and 110 °C), a single K_2CO_3 concentration of 26 wt.%, CO_2 loading range of 0.4–1.0 and

various additive concentrations. The deviations between the Pitzer model and the experimental results were found to be in the range 5–19%. Moreover, the Pitzer model of Bohloul et al. was evaluated by comparison with experimental data in a temperature range of 40-60 °C, K_2CO_3 concentrations of 15, 20 and 30 wt.%, CO_2 loadings in the range of 0.4–1.25 and pressures up to 12 bar [263]. The authors found a consistency between the VLE measurements and the thermodynamic model. For the optimized model parameters, the average absolute relative deviation (AARD) between the experimental and the predicted values of the Pitzer model were reported to be < 3%.

Significant work has been carried out on the thermodynamic modeling of the CO_2-K_2CO_3-H_2O system through the electrolyte-NRTL model. The work of Hilliard [242] has been one of the most comprehensive studies on the field of thermodynamic modeling of K_2CO_3 solutions through the aforementioned model. The author developed a regressed electrolyte-NRTL model based on experimental data from various sources and CO_2 solubility from Tosh et al. [204]. The model applicability covers a temperature range of 40-130 °C and the K_2CO_3 concentrations tested in [204], *i.e.* 20, 30 and 40 wt.%. Hilliard reported that the overall AARD for the properties of the H_2O-K_2CO_3/H_2O-$KHCO_3$ systems and the CO_2 solubility of the CO_2-K_2CO_3-H_2O was < 4%. Particularly for CO_2 solubility, a relative error of ± 11% was found for the optimum model with a maximum AARD value of 33%. Additionally, thermodynamic modeling with MEA and PZ as promoters was applied in the same study, extending also previous work from Cullinane and Rochelle [216]. In the latter study, the authors implemented the electrolyte-NRTL model for the CO_2-K_2CO_3-H_2O-PZ system for CO_2 loadings of 0.3-0.7, temperatures in the range 40-110 °C, PZ and K_2CO_3 solution concentrations in the range 0.6-2.6 m and 2.5-6.2 m, respectively. An overall AARD of 15.5% was reported in [242] for the thermodynamic model of the CO_2-K_2CO_3-H_2O-PZ system. Following those studies, Endo et al. [264] evaluated the accuracy of the electrolyte-NRTL models of Hilliard and Cullinane and Rochelle for predicting the VLE of the boron-promoted CO_2-K_2CO_3-H_2O system and reported a better accuracy of the regressed models compared to the default electrolyte-NRTL parameters of Aspen Plus™ software. Complementary to the work of Hilliard, Thee et al. [244] published a thermodynamic and process modeling study for the system CO_2-K_2CO_3-H_2O-MEA in a temperature range of 40-80 °C and various MEA concentrations in a 30 wt.% K_2CO_3 solution. The authors used a combination of the default parameters of Aspen Plus™ and the binary parameters from [216] for their electrolyte-NRTL model. Moreover, Lee et al. [229] reported that a regressed electrolyte-NRTL model can sufficiently describe the thermodynamics of a Gly-promoted K_2CO_3 solution. Recently, Kaur and Chen [265] used the electrolyte-NRTL model to simulate a wide range of operational conditions of CO_2 capture (absorption and desorption) by K_2CO_3 solutions. The model is valid in a temperature of 0-200 °C, K_2CO_3 concentrations up to saturation and CO_2 loadings in a range of 0-3.6. Average relative deviation values for osmotic coefficients, mean ionic activity coefficients, salt solubility and heat capacity were within ± 10% for the systems K_2CO_3-H_2O and $KHCO_3$-H_2O. The CO_2 solubility predictions of the model were found to be accurate with an error in the range ± 5.7-33.9%, depending on the experimental datasets that were used for the VLE of the CO_2-K_2CO_3-H_2O system. Overall, the results published by Kaur and Chen demonstrated that the electrolyte-NRTL model can accurately describe the thermodynamics of the CO_2-K_2CO_3-H_2O ternary system and K_2CO_3-H_2O and $KHCO_3$-H_2O binary systems. Based on its proven suitability for the thermodynamic modeling of promoted and unpromoted K_2CO_3 solutions, the electrolyte-NRTL model was also chosen in this work.

6.1.2 Literature review: process modeling of CO_2 absorption/desorption by K_2CO_3 solutions

A summary of selected modeling studies found in the literature employing CO_2 capture systems with K_2CO_3 solvents is given in Table 6-1. It can be noted that the technology has drawn particular interest and studies either focusing on its core components, particularly the absorber and the desorber, or the overall capture process have been published. A great deal of work has been done regarding the modeling, design and optimization of various absorber types operating with promoted or pure K_2CO_3 aqueous solutions, while fewer studies are available regarding stripper configurations and their optimization. Concerning the integration of the process to other facilities, a number of studies have focused on the application of the Benfield process for post-combustion CO_2 capture especially with promoted solutions. However, other modeling studies have dealt with pre-combustion CO_2 capture from various sources. For example, Borhani et al. [234] and Berrouk et al. [266] modelled an industrial absorber and a CO_2 capture plant for NG sweetening based on the Benfield process, respectively.

Table 6-1: Process and/or component modeling studies involving CO_2 absorption into K_2CO_3 solutions.

Model type	System(s)	Process description	Source
EQM (FORTRAN)	CO_2-K_2CO_3-H_2O-DEA	Industrial packed absorber modeling for CO_2 capture in ammonia plants	[267]
e-NRTL/RBM (FORTRAN)	CO_2-K_2CO_3-H_2O	Sieve-tray absorber modeling for CO_2 capture	[268]
RBM (FORTRAN)	CO_2-K_2CO_3-H_2O-DEA CO_2-K_2CO_3-H_2O-MEA CO_2-K_2CO_3-H_2O-MAE	Split-flow absorber tower modeling with packing for CO_2 capture	[269]
Pitzer/RBM (FORTRAN/ChemCAD)	CO_2-K_2CO_3-H_2O CO_2-KOH-H_2O	Modeling of packed absorber and desorber columns for coke oven gas cleaning	[270]
e-NRTL/EQM (Aspen Plus™)	CO_2-K_2CO_3-H_2O CO_2-K_2CO_3-H_2O-PZ	Absorption/desorption process modeling for post-combustion CO_2 capture	[271]
RBM (Aspen Plus™)	CO_2-K_2CO_3-H_2O-BA	Industrial packed absorber modeling for CO_2 capture	[272]
e-NRTL/RBM (Aspen Plus™ and Aspen Custom Modeler)	CO_2-K_2CO_3-H_2O-PZ	Modeling of packed vacuum- and normal-pressure stripper for CO_2 capture plants	[273]
Unit activity coefficient numerical model (Matlab)	CO_2-K_2CO_3-H_2O-DEA	Modeling of rotating packed bed for CO_2 capture	[274]
e-NRTL/RBM (Aspen Plus™)	CO_2-K_2CO_3-H_2O	Absorption/desorption process modeling for post-combustion CO_2 capture	[275]
2D-RBM (COMSOL)	H_2S-CO_2-K_2CO_3-H_2O	Modeling of CO_2 and H_2S absorption through hollow fiber membrane contactor	[276]
e-NRTL/RBM (Aspen Plus™)	CO_2-K_2CO_3-H_2O CO_2-K_2CO_3-H_2O-BA	Absorption/desorption process modeling for pre-combustion CO_2 capture from syngas	[277]
KLG numerical model	CO_2-K_2CO_3-H_2O-PZ	Absorption/desorption process modeling for CO_2 capture	[278]
e-NRTL/RBM (Aspen Plus™)	CO_2-K_2CO_3-H_2O-MEA	Absorption/desorption process modeling for post-combustion CO_2 capture	[207]
e-NRTL/RBM (Aspen Plus™)	CO_2-K_2CO_3-H_2O-DEA	Modeling of absorber for NG sweetening	[234]
n.a./MOO (Aspen Plus™)	CO_2-K_2CO_3-H_2O	Absorption/desorption process modeling for post-combustion CO_2 capture	[279]
EQM/Electrolytic ELR-PR (ProMax™)	CO_2-K_2CO_3-H_2O-DEA	Absorption/desorption process modeling for NG sweetening (Benfield-HiPure)	[266]

EQM: equilibrium model, RBM: rate-based model, MAE: methyl amino ethanol, BA: boric acid, KLG: Karhunen–Loève Galerkin, MOO: multi-objective optimization

According to Honeywell UOP, which provides the Benfield technology on the market, NG sweetening is one of its main applications along with syngas cleaning in ammonia plants, coke oven gas treatment (steel industry) and recycle gas purification in ethylene oxide units [280]. However, very few studies have been dedicated on modeling the overall absorption/desorption process into K_2CO_3-based solvents with CO_2 capture from syngas [277].

Modeling of the absorber and desorber columns is a crucial part during the process model development. Two main approaches exist for modeling a reactive absorption (or desorption) column: the equilibrium-stage and non-equilibrium-stage models. Those approaches are schematically depicted in Figure 6-1, where a stage corresponds to a tray in a tray column or a packing section in a packed column.

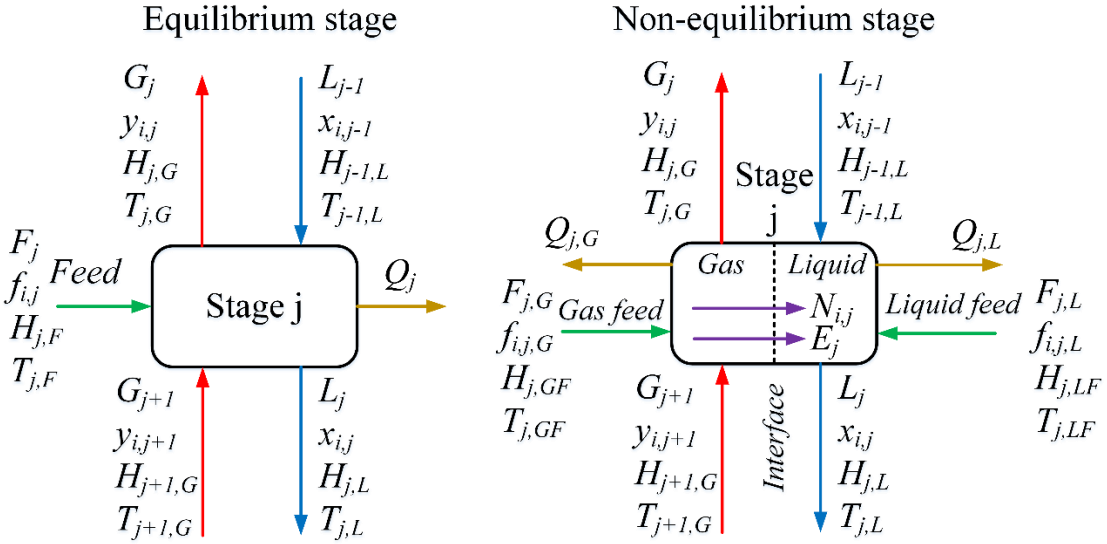

Figure 6-1: Schematic depictions of e*quilibrium (left) and non-equilibrium (right) stages (reproduced from [234]).*

In the equilibrium-stage approach, vapor and liquid phases enter the stage and they exit the stage under equilibrium conditions after exchanging energy and matter between them. Thermodynamic equilibrium is assumed to exist at the outlet of the stage and balance equations can be written for the overall stage. Those equations are described with the abbreviation MESH *i.e.* Mass balance, Equilibrium, Summation and enthalpy/Heat balance equations. When modeling distillation or absorption processes, a stage efficiency is introduced (tray efficiency or height equivalent to a theoretical plate, HETP) to increase the accuracy of the model. An equilibrium-stage model is generally suitable for non-reactive systems and in this case, a decent accuracy be achieved [203]. However, for units where reactive distillation or absorption, multicomponent mass transfer, etc. occur, a more detailed model is generally required.

For reactive systems with mass transfer constraints, a more accurate representation can be achieved through the implementation of a rate-based, non-equilibrium approach. In a non-equilibrium stage, vapor and liquid enter a tray or packed section and material and energy transfer occurs between the two across a fluid-fluid interface layer. In such a rate-based model, mass transfer resistance is considered for each phase, while chemical and thermodynamic equilibrium is assumed only at the interface between the phases. In this case, separate balance equations are written for each phase. No resistance for heat or mass transfer is assigned to the interface but a comprehensive description of rates of mass transfer, heat transfer and chemical reactions in each phase is included in the model. Compared to the equilibrium-stage model, the rate-based approach equation set is defined as MERQ *i.e.* Mass balance, Energy (or heat) balance, Rate (or transfer) and eQuilibrium equations. It can be considered an extension of the MESH equations including additional expressions for material/heat transfer, chemical reaction rates, column hydrodynamics and phase equilibria. Since they are more detailed and include equipment design parameters, non-equilibrium models can be applied for optimizing the design and operating conditions of reactive absorption or desorption columns.

Due to their higher accuracy, rate-based models have been used to simulate the operation of pilot or industrial facilities with K_2CO_3 solutions and are herein adopted for modeling absorption and desorption components as well. The CO2CRC Research Center (Australia) has developed non-equilibrium models to simulate a post-combustion capture pilot plant with K_2CO_3 coupled to a 1600 MW brown-coal-fired power station [275] and a pilot pre-combustion capture plant operating with CO_2-K_2CO_3-H_2O-BA mixtures [277]. In addition, a multi-objective optimization (MOO) study on the optimal integration of a K_2CO_3 absorption/desorption process in a coal-fired plant was been published by the same institute in [279], aiming to define the optimal selection of plant and CCS unit operating conditions to minimize the reboiler heat duty and increase the power plant energy efficiency. In addition to the studies mentioned, Oexmann et al. [271] published a techno-economic study aided by process modeling in Aspen Plus™ and EbsilonProfessional™ for the integration of chemical absorption into a coal-fired combustion plant. The authors reported that a chemical absorption unit based on the CO_2-K_2CO_3-H_2O-PZ system has energetic and economic benefits compared to a reference MEA-based CO_2 capture unit. Studies for the integration of the K_2CO_3 absorption/desorption process for pre-combustion CO_2 capture from NG (NGCC plant) and syngas (coal-fired IGCC plant) have been published by Lambert et al. [281] and Li et al. [282], respectively.

6.1.3 Scope of the absorption/desorption process modeling study

Isa et al. have noted in their review paper [283] that there is a need for comparative process modeling studies that will address the effect of various operating parameters on the heat and electricity demand of CO_2 capture units with promoted-K_2CO_3 solutions. In fact, while some work is available in the literature as case studies for post-combustion CO_2 capture as already presented, further work is required for pre-combustion capture from syngas. To the author's knowledge, no process modeling study is available on the effect of operating parameters on the energy (reboiler, condenser, electricity consumption) and AGR efficiency (H_2S and CO_2) of PZ-promoted K_2CO_3 solutions for a high-temperature capture unit fed with syngas. In addition, it is important to note that the study conducted herein has another feature in the fact that H_2S is considered as a species for removal along with CO_2. Two modeling studies were found dealing with H_2S absorption into K_2CO_3 solutions, those of Dindore et al. [284] and Faiz and Al-Marzouqi [276]. The following contribution is further provided in the present work compared to the aforementioned studies:

1. Process modeling of the overall absorption/desorption process was carried out and not limited to the absorption device. The process energetic efficiency (mainly, reboiler duty) is of particular interest in this study.
2. A detailed electrolyte-NRTL model with regressed parameters is developed for liquid phase modeling in contrast to the more simplified models for calculating CO_2 and H_2S solubility.

The aim of the present chapter is to implement modified/regressed electrolyte-NRTL thermodynamic models for all promoted or pure K_2CO_3 aqueous solutions and combine them with absorber/desorber models with detailed rate expressions. Based on those models, the components of the carbon capture unit can be accurately simulated. In a next step, case studies for different solvents are investigated and sensitivity analyses of the effect of operating conditions on system performance are presented. This study is performed in the framework of pre-combustion AGR, therefore aspects related to the process integration into gasification-based plants are also discussed.

6.2 Thermodynamic modeling and system chemistry

6.2.1 Electrolyte-NRTL model

The electrolyte-NRTL model is suitable for the calculation of activity coefficients of low to high-concentration solutions. The model implements binary molecular interaction parameters and electrolyte-electrolyte or molecule-electrolyte interaction parameters (pair parameters) to model electrolyte systems. When the electrolyte concentrations are zero, the model is converted to the Non-Random Two-Liquid (NRTL) activity-coefficient model. The infinite dilution aqueous solution is used as the asymmetric reference state of the ions. Water must be contained in the electrolytic system for the conversion to the ion reference state. In this study, Aspen Plus™ is used for the implementation of the electrolyte-NRTL model due to the advantage of extensive property databanks for liquid and vapor mixtures in the software.

The model is based on two fundamental assumptions:

i. Like-ion repulsion assumption: The local concentration of cations around cations (or anions around anions) is zero due to strong repulsive forces between ions of the same charge.
ii. Local electro-neutrality assumption: The distribution of cations and anions in the region around a central solvent molecule is such that the net local charge is zero.

The asymmetric Pitzer-Debye-Hückel model is used for describing long-range interactions between ions and the NRTL model is used to express local interactions. The model of local interactions is symmetric and is based on pure solvent and pure dissolved liquid electrolyte reference states. This model is normalized through infinite dilution activity coefficients and converted to asymmetric. As a result, the overall combination of those equations leads to the formulation of the excess Gibbs energy expression shown in Equation 6-1.

$$\frac{G_m^{*E}}{RT} = \frac{G_m^{*E,PDH}}{RT} + \frac{G_m^{*E,Born}}{RT} + \frac{G_m^{*E,lc}}{RT} \qquad \textit{Equation 6-1}$$

where G_m^{*E}, $G_m^{*E,PDH}$, $G_m^{*E,Born}$ and $G_m^{*E,lc}$ are the total excess Gibbs energy and the terms related to the contribution of long-range interactions, Born correction and local interactions attributed to Van der Waals forces. The star (*) symbol denotes the asymmetric reference state. Equation 6-1 can be converted to an expression with activity coefficients as in Equation 6-2.

$$ln\gamma_i^* = \frac{G_m^{*E}}{RT} = \left[\frac{\partial(n \cdot G_m^{*E})}{\partial n_i}\right] \qquad \textit{Equation 6-2}$$

Particularly, the Pitzer-Debye-Hückel contribution term, expressed through molar fractions, is given in Equation 6-3.

$$\frac{G_m^{*E,PDH}}{RT} = -\sum_k (x_k)\left(\frac{100}{M_B}\right)^{\frac{1}{2}}\left(\frac{4A_\varphi I_x}{\rho}\right) ln\left(1 + \rho I_x^{\frac{1}{2}}\right) \qquad \textit{Equation 6-3}$$

where x_k is the molar fraction of a species k, M_B is the molecular weight of solvent B, ρ is the closest-approach parameter, A_φ is the Debye-Hückel parameter and I_x is the ionic strength on a molar fraction basis. The latter two parameters are given by the following equations

$$A_\varphi = \frac{1}{3}\left(\frac{2\pi N_A d_s}{1000}\right)^{1/2}\left(\frac{{Q_e}^2}{\varepsilon_w k_B T}\right)^{3/2} \qquad \textit{Equation 6-4}$$

$$I_x = \frac{1}{2}\sum_i (x_i z_i^2) \qquad \textit{Equation 6-5}$$

where N_A is the Avogadro number, d_s is the solvent density, Q_e is the electron charge, ε_w is the water dielectric constant, k_B is the Boltzmann constant and z_i is the charge of the ion i.

The Born equation is used for Gibbs free energy with respect to the conversion of ions from the infinite dilution state of a solvent mixture to the infinite dilution state of aqueous phase. In Equation 6-6, r_i is the Born radius.

$$\frac{G_m^{*E,Born}}{RT} = \frac{Q_e^2}{2k_BT}\left(\frac{1}{\varepsilon_s} - \frac{1}{\varepsilon_w}\right)\left(\frac{\sum_i(x_i z_i^2)}{r_i}\right)10^{-2} \qquad \textit{Equation 6-6}$$

For the local interactions, the NRTL model is employed as mentioned already. Its basic assumption is that the non-ideal entropy of mixing is negligible compared to the enthalpy of mixing. The effective local mole fractions of i and j species in the vicinity of i are correlated with Equation 6-7.

$$\frac{X_{ji}}{X_{ii}} = \left(\frac{X_j}{X_i}\right)G_{ji} \qquad \textit{Equation 6-7}$$

where $X_j = x_j C_j$ with $C_j = z_j$ for ions and $C_j = 1$ for molecules. In this equation, $G_{ji} = e^{-\alpha_{ji}\tau_{ji}}$ and $\tau_{ji} = \frac{g_{ji}-g_{ii}}{RT}$, where α_{ji} is the non-randomness factor and the symbols g_{ji} and g_{ii} denote the interaction energy between two species $j-i$ or $i-i$. Similarly to the symmetric convention of the NRTL model, the values of α_{ji} and g_{ji} are symmetric regarding i and j, therefore $\alpha_{ji} = \alpha_{ij}$ and $g_{ji} = g_{ij}$. The τ_{ji} denotes a binary interaction parameter for the species pair $j-i$.

The contribution of local interactions on the excess Gibbs energy is given in Equation 6-8.

$$\frac{G_m^{E,lc}}{RT} = \sum_B X_B \frac{\sum_j(X_j\, G_{jB}\tau_{jB})}{\sum_k(X_k G_{kB})} + \sum_c X_c \sum_{a'}\left(\frac{X_\alpha}{\sum_{a''}(X_{a''})}\right)\frac{\sum_j(X_j\, G_{jc,a'c}\tau_{jc,a'c})}{\sum_k(X_k G_{kc,a'c})} + \sum_a X_a \sum_{c'}\left(\frac{X_{c'}}{\sum_{c''}(X_{c''})}\right)\frac{\sum_j(X_j\, G_{ja,c'a}\tau_{ja,c'a})}{\sum_k(X_k G_{ka,c'a})} \qquad \textit{Equation 6-8}$$

where j and k may be any species such as cation (c), anion (a) or solvent molecule (B).

In electrolyte-NRTL, adjustable parameters are the dielectric constants of pure compounds (non-aqueous solvent), the Born ion radius and the interaction parameters. The interaction parameters in electrolyte-NRTL comprise the non-randomness factor α_{ji} and the energy interaction parameters τ_{ji}. The parameters τ_{ji} can be of three (3) types, particularly molecule-molecule ($\tau_{m,m'}$ and $\tau_{m',m}$), molecule-electrolyte ($\tau_{m,ca}$ and $\tau_{ca,m}$) and electrolyte-electrolyte ($\tau_{ca,ca'}$ and $\tau_{ca',ca}$). In the electrolyte-electrolyte pair, there must be a common ion, whether it is anion or cation. The non-randomness factors are symmetric, while the binary energy interaction parameters are asymmetric.

It should be noted that energy interaction parameters are temperature-dependent and their dependence with temperature is given below, from Equation 6-9 to Equation 6-13, where T^{ref} is taken as 298.15 K.

molecule-molecule

$$\tau_{BB'} = A_{BB'} + \frac{B_{BB'}}{T} + F_{BB'}\ln(T) + G_{BB'}\,T \qquad \textit{Equation 6-9}$$

electrolyte-molecule

$$\tau_{ca,B} = C_{ca,B} + \frac{D_{ca,B}}{T} + E_{ca,B}\left[\frac{T^{ref}-T}{T} + ln\left(\frac{T}{T^{ref}}\right)\right] \qquad \textit{Equation 6-10}$$

$$\tau_{B,ca} = C_{B,ca} + \frac{D_{B,ca}}{T} + E_{B,ca}\left[\frac{T^{ref}-T}{T} + ln\left(\frac{T}{T^{ref}}\right)\right] \qquad \textit{Equation 6-11}$$

electrolyte-electrolyte

$$\tau_{c'a,c''a} = C_{c'a,c''a} + \frac{D_{c'a,c''a}}{T} + E_{c'a,c''a}\left[\frac{T^{ref}-T}{T} + ln\left(\frac{T}{T^{ref}}\right)\right] \qquad \textit{Equation 6-12}$$

$$\tau_{ca',ca''} = C_{ca',ca''} + \frac{D_{ca',ca''}}{T} + E_{ca',ca''}\left[\frac{T^{ref}-T}{T} + ln\left(\frac{T}{T^{ref}}\right)\right] \qquad \textit{Equation 6-13}$$

6.2.2 Gas phase model, Henry components and reaction chemistry

For gas-phase modeling, various equations of state (EOS) can be considered. In Aspen Plus, the default vapor EOS to be coupled with the electrolyte-NRTL model is the Redlich-Kwong equation. However, this EOS is more accurate at low pressure (< 10 bar), where non-ideality effects are negligible for the vapor phase, as also suggested by AspenTech. On the other hand, the hot potassium carbonate process operates at pressures above the suggested limit for the application of Redlich-Kwong EOS. Therefore, in the present study the Redlich-Kwong-Soave (RKS) EOS was applied for the vapor phase with the general form given in Equation 6-14. In this equation, α is a function of temperature (T) and molecule sphericity represented by the acentric factor (ω).

$$P = \frac{RT}{V_m - b} - \frac{a\alpha(T,\omega)}{V_m(V_m + b)} \qquad \textit{Equation 6-14}$$

Supercritical gases and non-condensable species are defined as Henry components in the model. The reference state of a Henry component is calculated at infinite dilution as $x_i \to 0$. The liquid-phase fugacity coefficient f_i^{*l} becomes the Henry coefficient H_i and the activity coefficient γ_i is converted to an infinite dilution reference state according to Equation 6-15.

$$\gamma_i^* = \left(\frac{\gamma_i}{\gamma_i^\infty}\right) \textit{ for } i=h \qquad \textit{Equation 6-15}$$

where γ_i^∞ is the activity coefficient of the Henry component at infinite dilution. The phase equilibrium expression is written as

$$f_i^v \, y_i \, p = x_i \, \gamma_i^* \, H_i = x_i \, \gamma_i \left(\frac{H_i}{\gamma_i^\infty}\right) \qquad \textit{Equation 6-16}$$

In Aspen Plus™, the solubility of a Henry component is calculated through a volume-weighted mixing rule. For molecular solutes, infinite dilution in a mixed or aqueous solvent can be selected. The former option which is the default Aspen Plus setting was used in the present work.

Equilibrium constants K for the system reactions were calculated in Aspen Plus according to Equation 6-17

$$K = (x_w \gamma_w)^{\nu_w} \prod_i (x_i \gamma_i^*)^{\nu_i} \qquad \textit{Equation 6-17}$$

where x_w is the water mole fraction, γ_w is the water activity coefficient, x_i is the mole fraction of a non-water component, γ_i^* is the activity coefficient of a non-water component and ν_i is the stoichiometric coefficient. The reactions for the most complicated H_2S-CO_2-K_2CO_3-H_2O-PZ system are shown next. It was assumed that K_2CO_3 completely dissociates resulting in the formation of two potassium ions (K^+) and one carbonate ion (CO_3^{-2}). When the solution is not promoted by PZ, reactions R 6-4 to R 6-7 can be omitted.

$$2\,H_2O \leftrightarrow H_3O^+ + OH^- \qquad \text{R 6-1}$$

$$CO_2 + 2H_2O \leftrightarrow H_3O^+ + HCO_3^- \qquad \text{R 6-2}$$

$$HCO_3^- + H_2O \leftrightarrow H_3O^+ + CO_3^{2-} \qquad \text{R 6-3}$$

$$PZH^+ + H_2O \leftrightarrow PZ_{(l)} + H_3O^+ \qquad \text{R 6-4}$$

$$PZ_{(l)} + HCO_3^- \leftrightarrow PZCOO^- + H_2O \qquad \text{R 6-5}$$

$$PZCOO^- + HCO_3^- \leftrightarrow PZ(COO^-)_2 + H_2O \qquad \text{R 6-6}$$

$$H^+PZCOO^- + PZ_{(l)} \leftrightarrow PZCOO^- + PZH^+ \qquad \text{R 6-7}$$

$$H_2O + H_2S \leftrightarrow H_3O^+ + HS^- \qquad \text{R 6-8}$$

$$H_2O + HS^- \leftrightarrow H_3O^+ + S^{2-} \qquad \text{R 6-9}$$

$$K_2CO_3 \rightarrow 2\,K^+ + CO_3^{2-} \qquad \text{R 6-10}$$

In addition, the temperature dependence is included in Aspen Plus for the equilibrium constants as shown in Equation 6-18

$$\ln(K) = a + \frac{b}{T} + c\ln(T) + dT \qquad \textit{Equation 6-18}$$

where a, b, c and d are coefficients. Default values were used for all chemical reactions except for those involving PZ species. For those reactions, the coefficients from [285] were used and which are shown in Table 6-2. Moreover, power-law expressions for kinetically-controlled reactions (forward and reverse) are required in Aspen Plus, which were taken from [286] and [287].

Table 6-2: Temperature-dependence coefficients for equilibrium constants of reactions involving PZ species used in this work [285].

Reaction	***a***	***b***	***c***	***d***
R 6-4	481.945	-33448.7	-69.783	0
R 6-5	-609.969	36511.7	87.075	0
R 6-6	-251.395	14080.2	36.782	0
R 6-7	-488.753	27752.8	69.783	0

6.2.3 Thermodynamic modeling of pure and PZ-promoted K_2CO_3 solvents

All missing thermodynamic and physicochemical properties of piperazine ions (PZH^+, $PZCOO^-$, $PZ(COO^-)_2$ and H^+PZCOO^-) which are not included in the Aspen Plus databanks were retrieved from [285]. For the thermodynamic modeling of aqueous K_2CO_3 solutions through the electrolyte-NRTL model, the default Aspen Plus™ pair parameters can be implemented. However, a more accurate system representation can be achieved through experimental data regression. Regressed electrolyte-NRTL models for the systems CO_2-K_2CO_3-H_2O and CO_2-PZ-K_2CO_3-H_2O were published in [285]. The Hilliard's data regression analysis focused on adjusting the values of electrolyte-molecule interaction parameters C, D and E (see also Section 6.2.1). This regressed model was used as a basis for the electrolyte-NRTL models of the present work. Electrolyte-electrolyte pair parameters can be important when dealing with salt precipitation, however, the salt concentrations considered in this work did not necessitate the inclusion of the respective salt precipitation equilibrium reactions. Thus, the electrolyte-electrolyte interactions were ignored and the corresponding parameters were assumed to be zero. A list of all experimental data introduced for data regression analysis is given in Table 6-3. While CO_2 solubility data from Tosh et al. [204] were regressed in [285], data regression considering the experimental results of this thesis (see Chapter 4) for the CO_2-K_2CO_3-H_2O and CO_2-PZ-K_2CO_3-H_2O systems can also be carried out.

The parameters C, D, E and the non-randomness factor are represented in the electrolyte-NRTL model of Aspen Plus as *GMELCC*, *GMELCD*, *GMELCE* and *GMELCN*, respectively, and the values for the cases where only CO_2 absorption is considered can be found in [285]. However, the regressed model in [285] did not take into account the simultaneous absorption of CO_2 and H_2S, basically due to the fact that it was developed for CO_2 capture from flue gas. This work extends that model to include the adjustment of the H_2S solubility in K_2CO_3 solutions. By correcting the VLE curves for both acidic gases (CO_2, H_2S), the model can be applied for syngas cleaning. Equilibrium pressures of CO_2 and H_2S over solutions of K_2CO_3 were measured in [288]. Experimental data from that study were used for data regression. The specific experimental data are referring to H_2O-K_2CO_3-CO_2-H_2S system and include the partial pressure of H_2S and CO_2 over aqueous K_2CO_3-$KHCO_3$ solutions as a function of the equivalent H_2S content, fractional conversion of K_2CO_3 to $KHCO_3$ and KHS, equivalent K_2CO_3 concentration and temperature. The ranges of the experimental data for the regression analysis are as follows:

- temperature range of 70–130 °C,
- equivalent K_2CO_3 content in a range 20–40 wt. %,
- fractional conversion of K_2CO_3 at equilibrium due to H_2S and CO_2 in a range 7–68% and
- equivalent H_2S content in a range 10–1500 mol m^{-3}.

The term "equivalent H_2S content" describes the number of H_2S moles which react with a unit solution volume to form $KHCO_3$ and KHS.

Table 6-3: Experimental data for the development of regressed electrolyte-NRTL models for CO_2-K_2CO_3-H_2O and CO_2-PZ-K_2CO_3-H_2O mixtures.

System	Data type	Data points	Temperature and concentration ranges	Source
K_2CO_3-H_2O	Mean ionic activity coefficient	53	25 °C 0.014–50 wt.% K_2CO_3	[289]
	Vapor pressure depression	543	25–130 °C 2–50 wt.% K_2CO_3	[290]
	Vapor pressure depression	42	25–90 °C 0.048–0.51 wt.% K_2CO_3	[291]
	Heat capacity of solution	298	25–130 °C 2–50 wt.% K_2CO_3	[289]
$KHCO_3$-H_2O	Vapor pressure depression	10	25 °C 2–25 wt.% K_2CO_3	[290]
	Heat capacity of solution	214	5–130 °C 4–20 wt.% K_2CO_3	[289]
CO_2-K_2CO_3-H_2O	CO_2 solubility	113	70–140 °C 20, 30, 40 wt.% K_2CO_3	[204]
CO_2-PZ- H_2O	Total pressure	30	60–120 °C 2–4 m PZ Loading 0.5–1.0	[292]
	CO_2 solubility	14	40–70 °C 0.62 m PZ Loading 0.2–1.0	[293]
	^{1}H NMR	101	10–60 °C 0.1–1.5 m PZ Loading 0.15–0.97	[294]
CO_2-PZ-K_2CO_3-H_2O	CO_2 solubility	38	39–110 °C 2.5–6.2 m K^+ 0.6–3.6 m PZ Loading 0.37–0.74	[216]
	^{1}H NMR	41	27–70 °C 3.4–6.2 m K^+ 0.6–3.6 m PZ Loading 0.38–0.65	[216]

In this work, the pure component dielectric constant coefficients of non-aqueous solvents and the Born radius of ionic species were left as default since their modification is required only for mixed-solvent electrolyte systems. The adjustable NRTL parameters were determined by the Data Regression System (DRS) of Aspen Plus using the maximum likelihood principle of Britt and Luecke [295]. The objective function f shown in Equation 6-19 is minimized through the use of Lagrange multipliers to adjust the measurable variables and the model parameters within vapor-liquid equilibrium constraints and parameter bounds

$$f = \sum_{k=1}^{n} W_{U_k} \left[\frac{\left(U_{k,adj} - U_{k,obs}\right)^2}{\sigma_{U_k}^2} \right] + \sum_{k=1}^{n} W_{P_k} \left[\frac{\left(P_{k,adj} - P_{k,obs}\right)^2}{\sigma_{P_k}^2} \right] \qquad \textit{Equation 6-19}$$

where U_k denotes state variables and P_k denotes property variables.

The key interaction molecule-electrolyte pairs affecting the H_2S VLE are the H_2O–(K^+,HS^-) and H_2O–(K^+,S^{2-}). For these pairs the *GMELCC*, *GMELCD* and *GMELCE* parameters were adjusted during the regression. The ions H_3O^+ and OH^- were not taken into consideration, since their concentration is negligible compared to other ions. Also, the H_2S concentration is insignificant in relation to the concentration of H_2O. During the regression procedure, 94 data points were used, while the number of regressed parameters ranged from 0 to 12, depending on the parameter set. Before introducing the experimental data to the software, conversions to liquid mole

fractions were necessary. For instance, the H_2S equivalent concentrations were given in grains gal^{-1} of solution in [288]. The resulting data points were entered in Aspen Plus applying the constraint by which the vapor phase contains only H_2S, similarly to the methodology followed in the literature [296]. In Aspen Plus DRS, standard errors associated with the temperature, pressure and liquid component mole fractions were set to 0.1 °C, 5% and 0.1%, respectively. Standard errors for the mole fractions of the other vapor components apart from H_2S were set to zero.

A series of regression runs was performed resulting in the optimum set of adjustable parameter values. Initially, the investigated parameters were set to Aspen Plus databank values, if available, otherwise they are set to the default values. By regressing the full set of adjustable parameters (12 in this case), the "full set" of parameters is recorded. The regression analysis procedure which was carried out in this work to derive the different models and ultimately determine the optimum set of binary interaction parameters is described in steps. For simplicity, *GMELCC*, *GMELCD* and *GMELCE* pair parameters are herein referred to as C, D and E.

1. Initially, a regression analysis of all system parameters was carried out resulting in the full model.
2. One E parameter was excluded from the regression procedure and its value was set to its default in Aspen Plus. The new submodel that did not include the first E parameter was named "E1". Then, another E parameter was excluded from the regression in a similar manner and the new model was called "E2". The procedure continues until all single E parameters have been excluded from the regression.
3. In a third step, the first two E parameters are simultaneously excluded from the regression analysis and this results in a submodel named "E12". The procedure continues until all possible combinations have been excluded.
4. Subsequently, a progressive exclusion of three E parameters is carried out for all possible combinations.
5. A submodel named "E" was obtained by excluding all four parameters.
6. While all E parameters are excluded, steps 2–5 are repeated for the four D parameters.
7. While all E and D parameters are excluded, steps 2–5 are repeated for the four C parameters.

After obtaining all the submodels, the optimum set is determined through an F-test which compares the reliability of the simplified set against the full. The corresponding one-tail p-value was calculated to determine the probability of observing the F-test value if the null hypothesis was true. The null hypothesis assumes that the simplified set fits better the data than the full, where F≈1 and p > 0.05. The probability value was calculated through the function "*FDIST*" in Excel. The functions for the F-test are shown in the following equations.

$$F = \frac{\frac{WSSQ_{simpl} - WSSQ_{full}}{df_{simpl} - df_{full}}}{\frac{WSSQ_{full}}{df_{full}}} \qquad \textit{Equation 6-20}$$

$$df = N_{data} - N_{param} \qquad \textit{Equation 6-21}$$

$$p = f(F, df_{simpl} - df_{full}, df_{full}) \qquad \textit{Equation 6-22}$$

where $WSSQ_{full}$ is the weighted sum of squares for the full model (all parameters included), $WSSQ_{simpl}$ is the weighted sum of squares of the submodel under study, df_{full} and df_{simpl} denote the degrees of freedom of the full and submodel respectively, N_{data} is the number of experimental data points that were used in the analysis and N_{param} is the number of regressed parameters.

The simplified sets that passed the F-test were sorted according to their calculated *WSSQ* value and a logic test was performed in order to tabulate the number of parameters in each set with a standard deviation greater than the estimated value. Finally the set with the lowest logic-test result and *WWSQ* value was labeled as the optimum set resulting in the final regressed electrolyte-NRTL model. The full set had 7 out of the 12 estimates lower than their standard deviation. However, the optimum set had all estimates larger than their standard deviation. The calculated parameters for the interactions of H_2S ions in the liquid mixture are shown in Table 6-4. Standard deviations as calculated by Aspen Plus DRS have been included.

Table 6-4: Optimum H_2S-related interaction parameters of the regressed electrolyte-NRTL model.

Interaction parameter	Interaction pair		Estimate	σ
$C_{m,ca}$	H_2O	(K^+,HS^-)	9.90	1.28
$C_{ca,m}$	(K^+,HS^-)	H_2O	-4.65	0.41
$C_{m,ca}$	H_2O	(K^+,S^{2-})	4.39	1.01
$C_{ca,m}$	(K^+,S^{2-})	H_2O	-5.36	0.20
$D_{m,ca}$	H_2O	(K^+,HS^-)	-494.66	323.05
$D_{m,ca}$	H_2O	(K^+,S^{2-})	3138.90	288.57
			$WSSQ$: 1666.2	$RRMSQE$ [1]: 4.38

[1] *RRMSQE*: residual root mean square error

The regressed electrolyte-NRTL model estimations est_i are compared to the experimental data points $\exp_i$ by means of $AARD$, as defined in Equation 6-23.

$$AARD(\%) = \frac{100}{N}\sum_i \frac{|\exp_i - est_i|}{\exp_i} \qquad \textit{Equation 6-23}$$

6.3 Process modeling methodology

A model was developed in Aspen Plus™ software for the AGR process fed with syngas. The regressed electrolyte-NRTL model as described in Section 6.2.3 and coupled with the RKS EOS was the applied method for the simulation. The syngas is assumed to be derived from coal allothermal gasification [134], produced in a 50 MW_{th} coal-to-SNG plant. The characteristics of the utilized coal and the composition of the syngas, which was used in this work, are shown in Table 6-5. Herein, two important points regarding the fuel and the gasification technology should be discussed.

1. Coal was considered as the gasification feedstock, as coal-derived syngas has typically a higher H_2S content. It can be seen that the product gas, which was assumed in this process modeling study, has a sulfur concentration > 500 ppmv. It is considered that the application of a hot potassium carbonate process for the bulk removal of both acid gases is particularly relevant for such an SNG plant.
2. With an allothermal Heat-pipe gasification technology, the H_2/CO molar ratio in syngas is favorable for subsequent methanation. Therefore, in this study it is assumed that no WGS reactor is required prior to the AGR unit and only contaminant removal and cooling take place.

Table 6-5: Coal composition (proximate/ultimate analyses) and syngas properties.

Coal composition			
Proximate analysis (as received)		**Ultimate analysis (as received)**	
Volatiles (wt.%)	42.0	C (wt.%)	53.6
Fixed carbon (wt.%)	35.5	H (wt.%)	3.9
Ash (wt.%)	3.5	O (wt.%)	19.2
Moisture (wt.%)	19.0	N (wt.%)	0.6
Heating value (MJ kg^{-1})	19.8	S (wt.%)	0.35
Syngas properties			
H_2O (mole %)	36.39	Pressure (bar)	20
CO_2 (mole %)	12.66	Temperature (°C)	800
H_2 (mole %)	34.85	Mass flow rate (kg s^{-1})	3.5
N_2 (mole %)	0.13		
CH_4 (mole %)	3.29		
CO (mole %)	11.62		
H_2S (mole %)	0.06		

A simplified process configuration was investigated with the absorber and stripper at a similar temperature. The advantage of this configuration is the reduced capital investment since the heat exchanger for heating the rich

solvent and cooling the lean solvent is eliminated. The process layout is depicted in Figure 6-2. Of course, various alternative configurations are available for the hot potassium carbonate process aiming to decrease the regeneration heat duty and/or increase the product purity. Such processes are the Benfield LoHeat with internal steam generation or steam ejectors and mechanical vapor compression, Benfield Hi-pure, the split-flow absorption and two-pressure level regeneration Giammarco-Vetrocoke process, the Catacarb process and its modifications, etc. A detailed presentation of those configurations and processes can be found in [163].

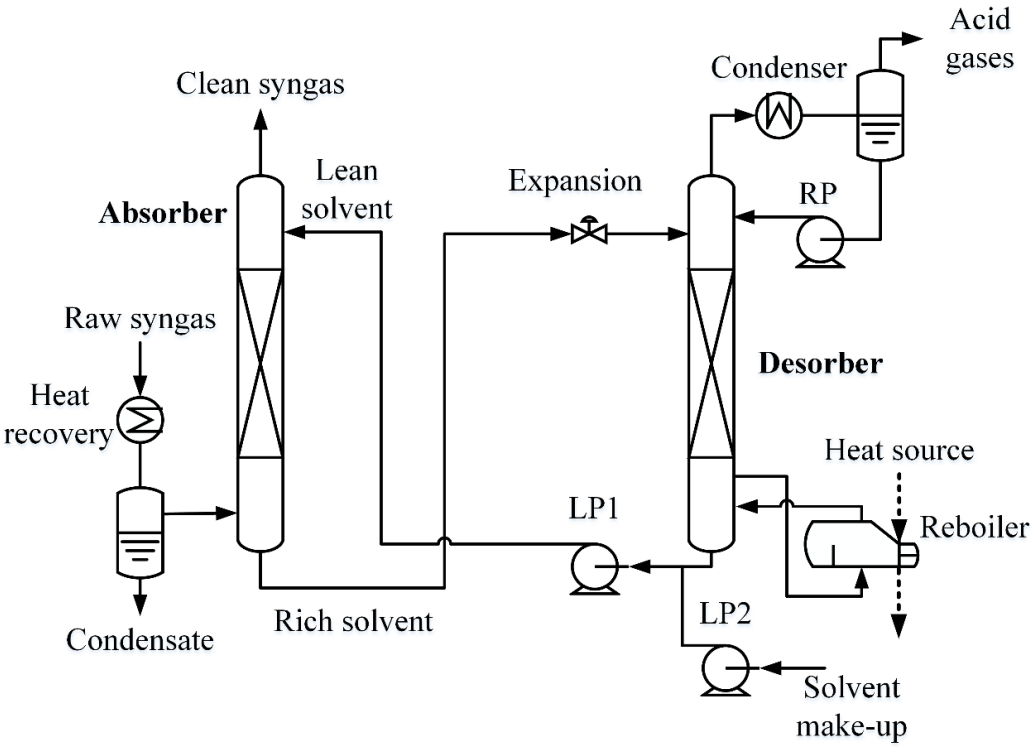

Figure 6-2: Configuration of the hot potassium carbonate process modeled in Aspen Plus.

Hot syngas with high water content is cooled down through a Heater block and is adiabatically flashed to separate the condensate. If other contaminants have been captured upstream of the AGR, this condensate stream which comprises almost entirely H_2O and it is available at high temperature, can be used to replenish solvent losses. Water removal from the syngas stream is advantageous, because the CO_2 and H_2S partial pressures increase, enhancing the absorption driving force. The mole fractions of CO_2 and H_2S both increase by ~50% downstream of the Flash model, while the mass flow rate of the stream decreases due to condensation. The "warm" syngas enters from the lower part of the absorber with a temperature of 100 °C and pressure of 19.5 bar. In the absorber, CO_2 and H_2S are absorbed into the liquid solvent, which flows counter-currently. The clean gas exits at the top of the absorber and the solvent which is loaded with the acid gases (rich solvent) leaves at the bottom. The rich solvent leaving the absorber is regenerated in the desorber column, where the acidic gases are stripped due to a lower pressure (atmospheric in this work) and countercurrent contact and heating with steam produced in the reboiler. A heat source supplies the thermal energy which is necessary for solvent regeneration. Although the heat exchange was not explicitly modeled in this study, saturated steam at low pressure (< 10 bar) is typically used. The regenerated, lean solvent is pumped at 18 bar through LP1 (70% pump efficiency) and it enters at the upper part of the absorber near its boiling temperature at ambient pressure conditions. The CO_2-rich gas stream leaving at the top of the stripper is cooled at 50 °C in the condenser and the condensate is recirculated to the washing section at the top of the column through the reflux pump (RP). Compression of CO_2 and off-gas treatment were not included in the model.

Absorption and desorption columns were modeled with rate-based RadFrac modules in Aspen Plus with five (5) and six (6) stages, respectively, and a fixed packing height of 1.5 m for every stage. The absorber was modeled as a column without reboiler and condenser components, while the stripper column was modeled with an integrated reboiler (corresponding to the 6^{th} stage) and an external condenser. Random packing of 1-inch

INTALOX Metal Tower Packing (IMTP) type was used and the pressure drop was estimated by the correlation of Stichlmair et al [297]. The column diameter was sized according to the theoretical stage that shows the largest gas and liquid mass flow values having 75% fractional approach to flood. The Onda et al. and Chilton and Colburn correlations were used for calculating the mass and heat transfer coefficients [298]. The flowsheet model was built as an "open-loop" for achieving a better convergence and decreasing the computational time. In order to model the "closed-loop" operation of the real process, the implementation of various design specifications in Aspen Plus was necessary. The "closed-loop" condition is fulfilled when the solvent stream downstream of the desorber has the same temperature, pressure, mass flow rate and composition with the inlet absorber stream. This input stream was specified prior to the simulation in a stream block (base-case model) and case studies for the sensitivity analyses were defined in a "Sensitivity" operation block in Aspen Plus. A summary of the design specifications that were integrated in the process flowsheet of Aspen Plus is given in Table 6-6 (for the names of streams and blocks, see also the Appendix of the present thesis). The equations were provided to the software through FORTRAN expressions.

Table 6-6: Design specifications for the "open-loop" modeling of the hot potassium carbonate process.

Design specification	Varying parameter	Target variable	Expression	Description
ABSORBER	$\dot{m}_{ABS-LEAN}$	$\dot{n}_{CO2,ABS-G-OUT}$	$\dot{n}_{CO2,ABS-G-OUT} = (1-0.95)\dot{n}_{CO2,ABS-G-OUT}$	Defines the CO_2 capture rate which in this work was kept constant at 95%.
STRIP	$\dot{Q}_{REBOILER}$	$\dot{n}_{CO2,CO2-2}$	$\dot{n}_{CO2,CO2-2} = \dot{n}_{CO2,ABS-G-IN} - \dot{n}_{CO2,ABS-G-OUT}$	Defines the stripped CO_2 yield and therefore the CO_2 lean loading.
T-BALANC	$\dot{Q}_{T-REGUL}$	T_{LEAN3}	$T_{LEAN3} = T_{LEAN}$	A heat exchanger "T-REGUL" is used to investigate the effect of lean solvent cooling.
M-BALANC	$\dot{m}_{W1}$	$\dot{m}_{LEAN2}$	$\dot{m}_{LEAN2} = \dot{m}_{ABS-LEAN}$	The W1 stream coming from the moisture removal flash unit is used for solvent make-up.
H2S	$\dot{n}_{H2S,H2S}$	$\dot{n}_{H2S,ABS-G-OUT}$	$\dot{n}_{H2S,ABS-G-OUT} = \dot{n}_{H2S,ABS-G-IN} - \dot{n}_{H2S,CO2-2}$	The H_2S mass balance in the system was defined by varying the H_2S molar flow of the lean solvent.

The solvent mass balance is maintained by the implementation of a design specification (M-BALANC) by which the solvent mass loss is replenished from the condensate stream, which is available upstream of the absorber. The solvent mass loss was mainly attributed to the water entrained at the gas outlet streams of the two columns. The solvent loss is mainly water, since K_2CO_3 is not volatile and PZ losses were considered minimal. This latter assumption will be further discussed in the results section and values for PZ losses will be presented. A second design specification (T-BALANC) varies the heat duty of the heater block which adjusts the lean solvent temperature and is active during sensitivity analyses of lean solvent cooling. Regarding the solvent composition, this is adjusted by two design specs, named "STRIP" and "H2S", which define the CO_2 and H_2S lean loadings respectively. Although the composition concerns the liquid streams, the design specs were applied to the inlet and outlet gas streams of the overall absorption/desorption, due to the difficulty in expressing the mole flows of CO_2 and H_2S in the liquid phase. The reason for this is that the "true-component" approach of

electrolyte-NRTL used in this work calculates and expresses the liquid phase in molecules and ions based on the system chemistry. As a result, the CO_2 and H_2S absorption into aqueous potassium carbonate solution involves five molecular "apparent" components (CO_2, H_2S, K_2CO_3, H_2O and PZ) from which 9 ions and one zwitterion are produced. Eventually, if the CO_2 and H_2S mass balances are fulfilled in the inlet and outlet gas streams of the overall absorption/desorption process, then the same applies to the recirculated solvent. The design specification "STRIP" tracks the user's input at the lean stream regarding the CO_2 loading and varies the reboiler duty so as to meet this loading value downstream of the solvent pump. However, the design spec "*H2S*" acts backward: it exploits the H_2S loading results from the desorber outlet as input for varying the H_2S mole flow of a "pseudo-stream", which is mixed with the lean solvent entering the packed absorber. For all the simulated cases, a carbon capture rate of 95% was considered. An overview of the base-case modeling assumptions and parameters is provided in Table 6-7 (see also Appendix for stream names).

Table 6-7: Base-case modeling assumptions for the hot potassium carbonate process.

Stream (S) / Block model (B)	**Parameter**	**Value**
FEED (S: raw syngas)	Pressure (bar)	20
	Temperature (°C)	100
	Composition (mole%)	(see Table 6-5)
ABS-LEAN (S: lean solvent)	Pressure (bar)	18
	Temperature (°C)	102
	Composition	30 wt.% K_2CO_3
	Lean loading (–)	0.3/0.4
FLASH (B: condensate removal)	Pressure (bar)	19.5 bar (before absorber) 1 bar (after desorber)
	Heat duty (kW)	Adiabatic
ABS (B: absorber)	Number of stages (–)	5
	Pressure (bar)	17
	Packing material	1-inch IMTP
	Packed height per stage (m)	1.5
	Fractional approach to flood	0.75
STR (B: desorber)	Number of stages (–)	6
	Pressure (bar)	1
	Packing material	1-inch IMTP
	Packed height per stage (m)	1.5
	Fractional approach to flood	0.75
	Reboiler type	Kettle
CNDSR (B: stripped gas condenser)	Pressure (bar)	1
	Outlet temperature (°C)	50
PUMP (B: lean solvent pump)	Pressure (bar)	18
	Pump efficiency (%)	70
	Driver efficiency (%)	96
MX1 and MX2 (B: mixers)	Pressure drop (bar)	0
SPLIT (B: condensate splitter)	Pressure drop (bar)	0
	Split fraction (–)	Design spec M-BALANC
T-REGUL (B: lean solvent heater/cooler)	Pressure (bar)	18
	Heat duty (kW)	Design spec T-BALANC

For the column simulation with the RadFrac models of Aspen Plus, the film diffusion resistance was accounted for through the "Discrxn" and "Film" models for the liquid and gas phases, respectively. For both phases, the film non-ideality was taken into account through the implementation of fugacity coefficient corrections. Concerning the composition of the K_2CO_3 solutions, a few general remarks for the equivalent K_2CO_3

concentration range have already been made previously. In this work, the equivalent K_2CO_3 concentration was assumed to be 30 wt.%, which is in agreement with the suggestions in [163] as a measure to eliminate erosion problems in impellers and other components. According to the findings from the batch experiments (see Section 4.4), PZ is an effective promoter for increasing the solvent capacity and absorption rate compared to the pure K_2CO_3 aqueous solution. Three promoter concentration values were investigated (given as molality below), resulting in three different promoter/K_2CO_3 molar ratios:

- 6.5m K^+/0.65 m PZ with a PZ/K^+ molar ratio of 0.1 (named "PZ0.1"),
- 6.5 m K^+/1.3 m PZ with a PZ/K^+ molar ratio of 0.2 (named "PZ0.2") and
- 6.5 m K^+/1.95 m PZ with a PZ/K^+ molar ratio of 0.3 (named "PZ0.3").

The 6.5 m K^+ concentration roughly corresponds to a 30 wt.% K_2CO_3 solution. It must be emphasized that the molar ratio values refer to the ratio of PZ to the potassium ions in the liquid phase. When the equivalent K_2CO_3 amount is considered, the molar ratio values change to 0.2, 0.4 and 0.6, respectively. Those values are comparable to the PZ concentration range studied in Chapter 4 (0.32-0.64 molar ratio).

Furthermore, a few definitions regarding certain parameters are given here. The capture rates CR for CO_2 and H_2S are given in Equation 6-24 and Equation 6-25, respectively

$$CR_{CO_2}(\%) = \frac{\dot{n}_{CO_2,in} - \dot{n}_{CO_2,out}}{\dot{n}_{CO_2,in}}\ 100\% \qquad \textit{Equation 6-24}$$

$$CR_{H_2S}(\%) = \frac{\dot{n}_{H_2S,in} - \dot{n}_{H_2S,out}}{\dot{n}_{H_2S,in}}\ 100\% \qquad \textit{Equation 6-25}$$

where the symbol $\dot{n}_{j,in/out}$ describes the inlet or outlet molar flow rate (mol s^{-1}) of the species j (CO_2 or H_2S) in the absorber.

The ratio of the liquid solvent to the syngas flow rate (L/G) in the absorber is another important parameter for the column sizing and operation. In this thesis, it is calculated on a mass basis and defined in Equation 6-26

$$L/G = \frac{\dot{m}_{solvent,in}}{\dot{m}_{syngas,in}} \qquad \textit{Equation 6-26}$$

where $\dot{m}_{solvent,in}$ and $\dot{m}_{syngas,in}$ denote the mass flow rate (kg s^{-1}) of the solvent and syngas in the absorber column, respectively. Definitions for the loading (a) of the liquid phase have been previously given in Chapter 4. However, the "true-component" approach used in Aspen Plus necessitated a different definition for the loading calculation. For the CO_2-K_2CO_3-H_2O system, loading was defined according to Equation 6-27

$$a = \frac{[\mathrm{CO_2}] + [\mathrm{CO_3^{2-}}] + [\mathrm{HCO_3^-}] - \frac{[\mathrm{K^+}]}{2}}{\frac{[\mathrm{K^+}]}{2}} \qquad \textit{Equation 6-27}$$

while for the CO_2-PZ-K_2CO_3-H_2O system, loading was defined according to Equation 6-28.

$$a = \frac{[\mathrm{CO_2}] + [\mathrm{CO_3^{2-}}] + [\mathrm{HCO_3^-}] + [\mathrm{HPZCOO}] + [\mathrm{PZCOO^-}] + 2[\mathrm{PZ(COO^-)_2}] - \frac{[\mathrm{K^+}]}{2}}{\frac{[\mathrm{K^+}]}{2} + [\mathrm{PZ}] + [\mathrm{PZH^+}] + [\mathrm{HPZCOO}] + [\mathrm{PZCOO^-}] + [\mathrm{PZ(COO^-)_2}]} \qquad \textit{Equation 6-28}$$

6.4 Results and discussion

6.4.1 Thermodynamic modeling results for pure and PZ-promoted K_2CO_3 solutions

Figure 6-3 compares experimental VLE data with electrolyte-NRTL estimations for the CO_2-K_2CO_3-H_2O system. VLE curves were obtained in Aspen Plus through a simplified model with a Flash2 module. The liquid composition at a specific α value was defined at the inlet stream and under the flash options, the option "liquid-only" was specified.

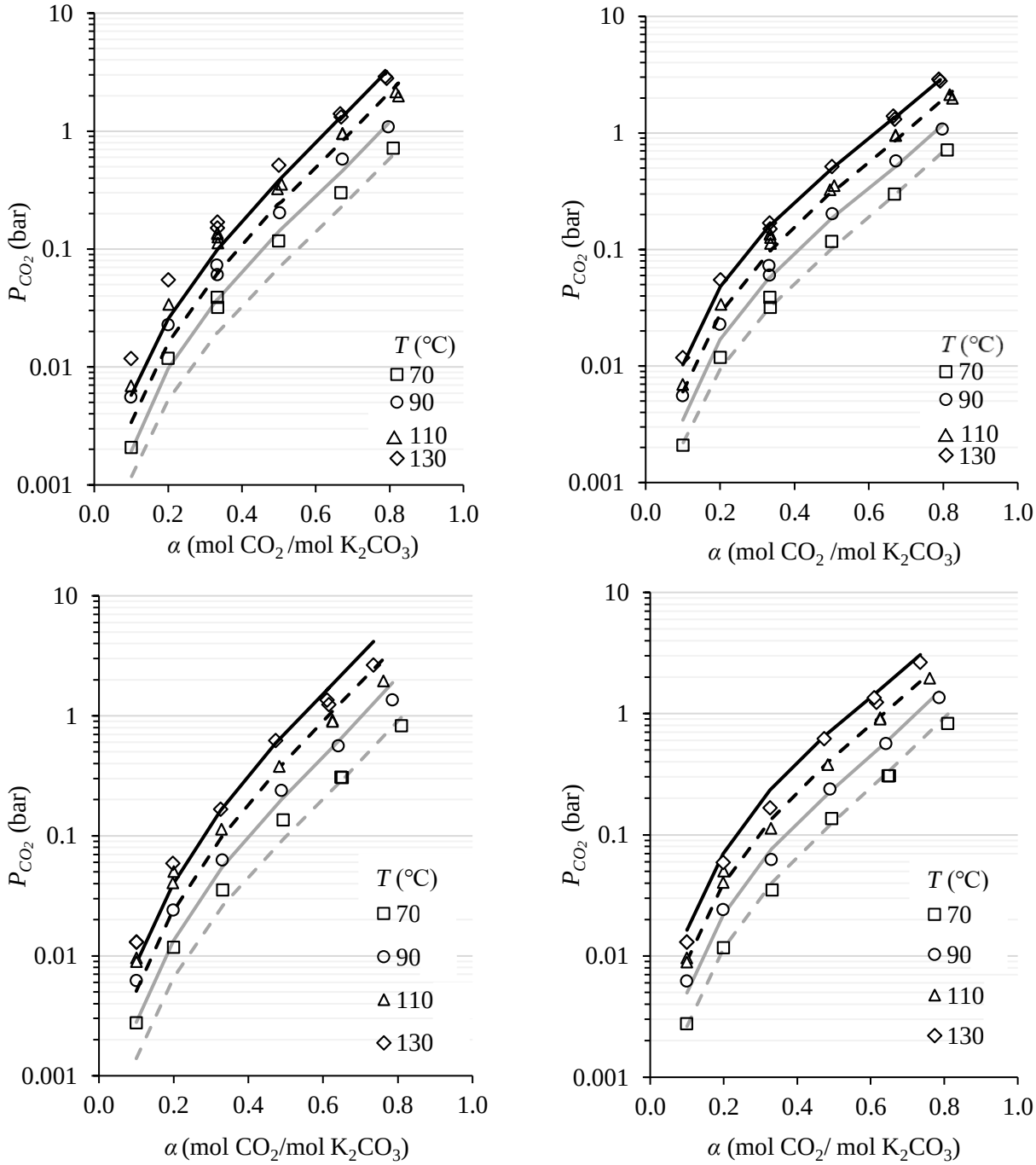

Figure 6-3: CO_2 partial pressure estimations (solid and dashed lines) over 20 wt.% (top) and 30 wt.% equivalent K_2CO_3 aqueous solutions (bottom) at 70, 90, 110 and 130 °C with default Aspen Plus (left column) and regressed electrolyte-NRTL (right column) interaction parameters. Markers represent experimental data from [204].

In the Flash2 module, temperature and a small vapor fraction (0.0001) were defined, so that the compositions of the inlet and outlet liquid streams remain unaffected. The partial pressure of a component could be subsequently calculated based on the available results for the pressure and vapor stream composition. It can be seen that a moderate deviation between the experimental data and "default" electrolyte-NRTL estimations exists for the pure K_2CO_3 aqueous solution. *AARD* exceeded 40% in the case of the most concentrated solution studied in [204] (not shown is Figure 6-3). It can be confirmed that the electrolyte-NRTL model can sufficiently reproduce the trend of the VLE curves across a wide temperature and concentration range for this particular system. A better agreement with experimental data was found for the regressed model used in this study. In addition, a validation of the regressed electrolyte-NRTL model with the experimental data of the present work for the CO_2-K_2CO_3-H_2O system was presented in Section 4.4.1. Figure 6-4 compares experimental VLE data with electrolyte-NRTL estimations for the H_2S-CO_2-K_2CO_3-H_2O system regarding the H_2S partial pressure.

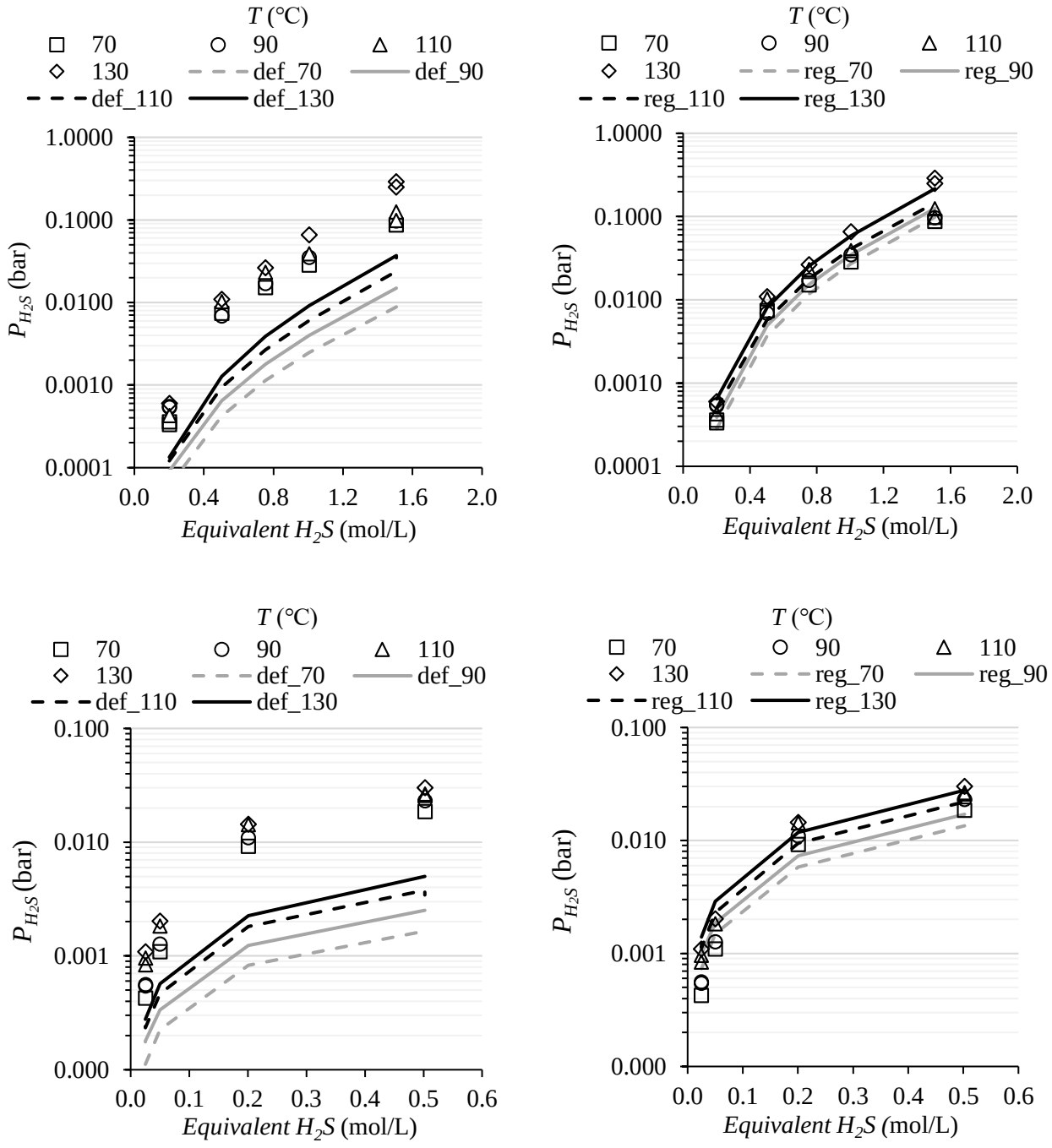

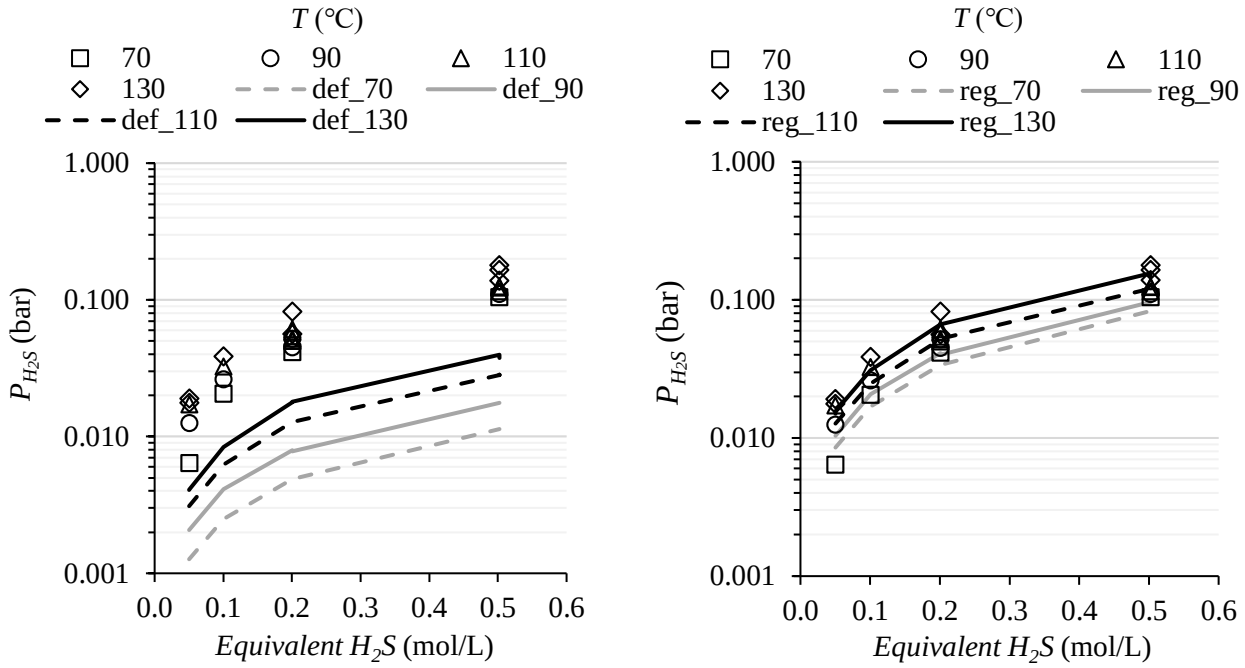

Figure 6-4: H_2S partial pressure estimations (solid and dashed lines) over 30 wt.% equivalent K_2CO_3 aqueous solutions at 70, 90, 110 and 130 °C with default Aspen Plus (left column) and regressed electrolyte-NRTL (right column) interaction parameters. Upper row: conversion occurs exclusively due to H_2S. Middle row: 33% conversion to ($KHCO_3$+KHS) due to CO_2 and H_2S. Bottom row: 66% conversion to ($KHCO_3$+KHS) due to CO_2 and H_2S. Markers represent experimental data from [288].

From the figures above, it is clear that the default interaction parameters of the electrolyte-NRTL model significantly underestimate the H_2S partial pressure in a 30 wt.% K_2CO_3 aqueous solution. The *AARD* of H_2S partial pressures compared to the experimental data was found to exceed 80%. It is interesting to note that the selected conversions in the experimental study of Tosh et al. [288] correspond to representative solution compositions in a hot potassium carbonate plant. Apart from the first case, in which it was assumed that all the conversion of K_2CO_3 is due to the presence of H_2S, the two other cases represent a lean (33% conversion) and a rich solution (66% conversion) at the inlet and outlet of the absorber, respectively. The regressed electrolyte-NRTL model was in better agreement with the experimental results. Regression analysis can, therefore, be important when mixtures of CO_2 and H_2S are treated in the process. The regression procedure also included a concentration of 40 wt.% K_2CO_3 (not shown in Figure 6-4). However, results regarding the deviation of experimental data [288] from the default and regressed electrolyte-NRTL model are presented for both K_2CO_3 concentrations next.

In addition, the validation of the regressed electrolyte NRTL model with experimental data for the solutions containing PZ is presented in Figure 6-5 and Figure 6-6. Particularly, a comparison regarding the model estimations for the solubility of CO_2 and the speciation of PZ species in the liquid phase is depicted. In Figure 6-5, VLE estimations (regressed model) for a 0.625 m PZ solution at 2 temperatures (left) and 5 m K^+/2.5 m PZ solution at 5 temperatures (right) are compared to experimental data. In Figure 6-6, PZ speciation estimations are compared for two aqueous solutions, one with a concentration of 1 m PZ at 25 °C (top) and one with a concentration of 5 m K^+/2.5 m PZ at 60 °C (bottom). While for the aqueous PZ solution, the regressed electrolyte-NRTL model seems to capture the ^{1}H NMR results accurately, a greater deviation regarding the estimation of PZ species in the PZ/K_2CO_3 aqueous solution can be observed. In the latter case, the *AARD* values for the PZ species varied in a range of 9-20%. From Figure 6-6, it can be noted that with an increase of the quantity of CO_2, PZ is consumed and converted to $PZCOO^-$ and $PZ(COO^-)_2$. According to [216], the reactive PZ concentration increases with total PZ for a constant K^+ amount, which is investigated in the process model by varying the promoter composition.

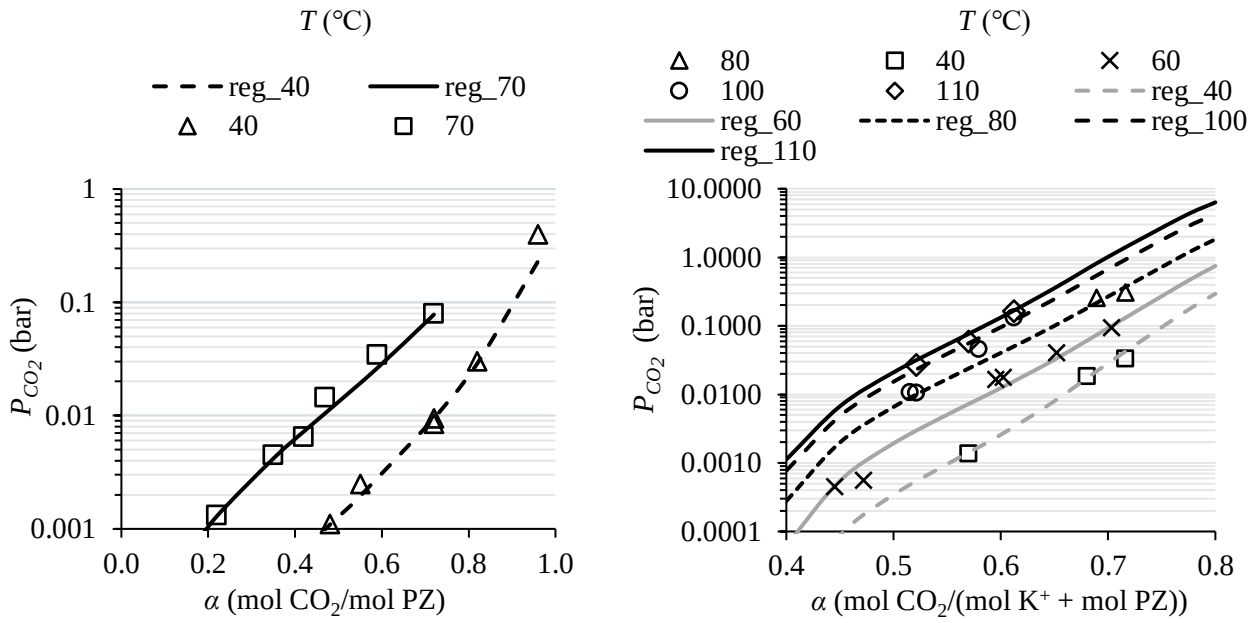

Figure 6-5: CO_2 solubility in aqueous PZ (left) and aqueous PZ/K_2CO_3 (right) solutions as predicted through the regressed electrolyte-NRTL versus experimental data from [293] and [216].

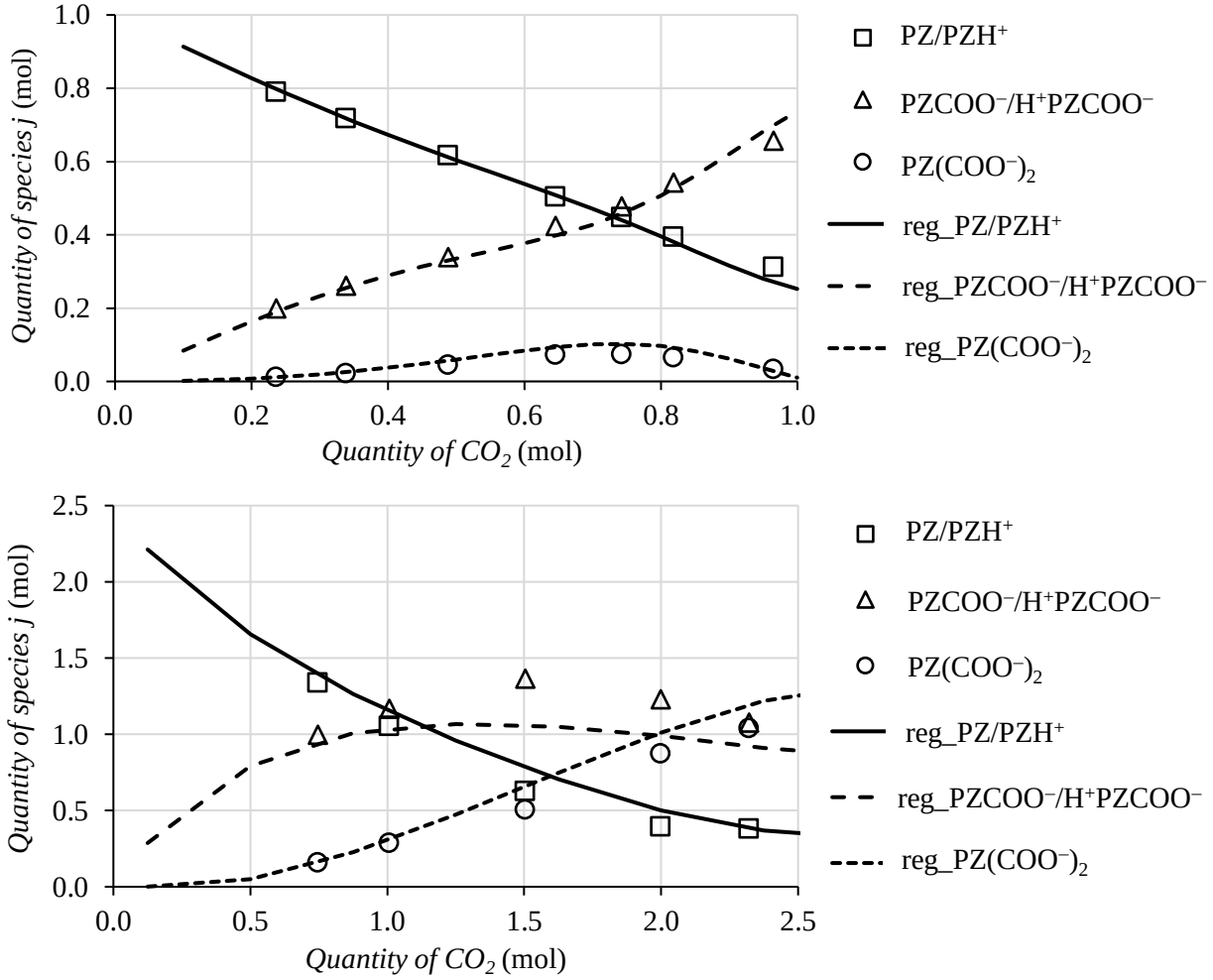

Figure 6-6: PZ speciation as predicted through the regressed electrolyte-NRTL model versus experimental data from [294] (top, aqueous PZ) and [216] (bottom, PZ/K_2CO_3 mixture).

A summary of the average absolute relative deviations between the default or regressed electrolyte-NRTL and the experimental data for the solutions without promoter is given in Table 6-8. In addition, a summary of the average absolute relative deviations between the regressed electrolyte-NRTL compared and the experimental data for the solutions promoted by PZ is given in Table 6-9. Due to fact that the regressed electrolyte-NRTL model had significantly lower *AARD* values, the process modeling study was carried out with this model.

Table 6-8: Average absolute relative deviation values between experimental data and estimations of default and regressed electrolyte-NRTL models (only K^+).

Source	Data type	Composition (wt.%)	Data points	Default eNRTL *AARD* (%)	Regressed eNRTL *AARD* (%)
[204]	CO_2 solubility	20	31	33.9	9.6
[204]	CO_2 solubility	30	26	24.2	9.2
[204]	CO_2 solubility	40	67	41.6	14.7
Total			**124**	**35.3**	**11.9**
[288]	H_2S solubility	30	63	82.8	20.0
[288]	H_2S solubility	40	31	86.8	15.9
Total			**94**	**84.1**	**18.6**

Table 6-9: Average absolute relative deviation values between experimental data and estimations of regressed electrolyte-NRTL model (PZ/K^+ solutions).

Source	Data type/species	Data points	Regressed eNRTL *AARD* (%)
[216]	CO_2 solubility	38	13.9
	^{1}H NMR for PZ/PZH^+	41	12.0
	^{1}H NMR for $PZCOO^-$/H^+PZCOO^-		9.2
	^{1}H NMR for $PZ(COO^-)_2$		19.7
Total		**130***	**12.9***

*Total number of data points and total *AARD* are reported including the experimental results for aqueous PZ solutions.

6.4.2 Process modeling results for CO_2 and H_2S capture from coal-derived syngas

Initially, preliminary sensitivity analyses were carried out for the pure K_2CO_3 aqueous solution in order to determine fundamental parameters of the process modeling study. As a next step, the performance of the processes involving PZ-promoted solutions was compared to that of a "reference" hot potassium carbonate pre-combustion capture plant with a 30 wt.% K_2CO_3 solution. The aim of this section is not to present an optimization of the process parameters, but rather explore their effect on the process performance. However, the findings of this work can be useful for specifying the basis for a multi-objective optimization study of a PZ-promoted, hot potassium carbonate process for pre-combustion AGR.

The comparison of the 4 solutions was performed through the variation of 3 process parameters and their effect regarding the L/G ratio, specific reboiler heat duty and H_2S removal efficiency for a constant 95% CO_2 capture. Those parameters are discussed below.

- Absorber pressure: Values in a range of 10-18 bar were studied in this work. The range was chosen according to the features of the coal-to-SNG plant, in which gasification was assumed to take place in a fluidized bed heat-pipe reformer, which operates up to 20 bar. In Chapter 6, an absorption pressure above 20 bar is considered for a hot potassium carbonate process integrated to a BIGCC plant for power and MeOH cogeneration.
- Desorber pressure: Values in a range of 0.4-5.3 bar were studied in this work. Vacuum strippers have been proposed for the promoted hot potassium process, in which desorption takes place at lower temperatures [273]. The desorption process usually operates at pressures close to ambient. Of course, this results in higher power consumption of the CO_2 compressors downstream of the stripper.

- Lean solvent loading: Values in a range of 0.24-0.44 were studied in this work. In the hot potassium carbonate process, the rich solvent is not completely regenerated and the lean solvent enters the absorber with a loading of 0.2 or above [288, 299].

For the selection of absorber and stripper stages, sensitivity analyses were carried out to determine optimum values based on the reboiler duty and L/G requirements. For the absorber, a fixed number of stripper stages was set (N=6) and all other parameters were defined according to Table 6-7. The sensitivity analysis results are shown in Figure 6-7.

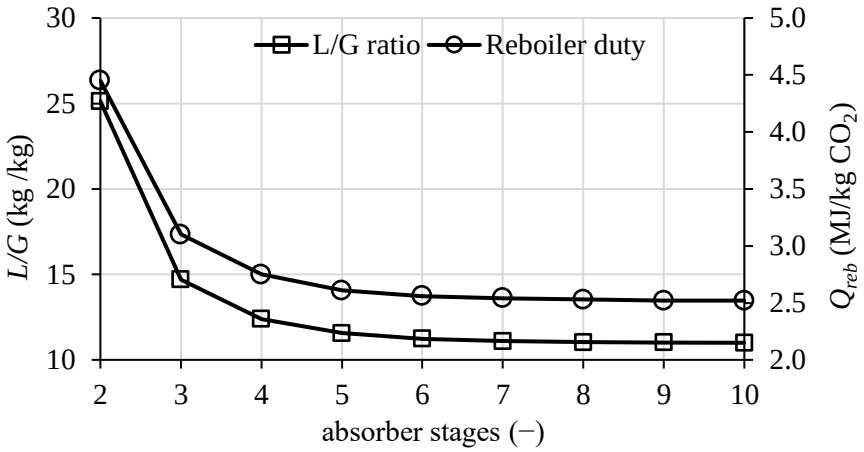

Figure 6-7: Effect of absorber stages on specific reboiler duty and L/G ratio.

It can be seen that an increase of absorber stages has a great impact on the liquid circulation rate and reboiler duty. This is attributed to the fact that a shorter residence time in the absorber necessitates a higher liquid flow rate to achieve the same CO_2 capture level. Of course, it must be noted here that a higher number of stages increases the capital and maintenance cost, while a shorter column will increase the operational expenditure due to the higher energy consumption and liquid circulation rate. An increase of absorber stages from 2 to 5 resulted in a decrease of reboiler duty and L/G by 41% and 54%, respectively. A further increase from 5 to 6 stages resulted in a minor further decline by 2% and 3%, respectively. Almost no change was observed for a number of absorber stages exceeding 7 and eventually, 5 absorber stages were selected for all subsequent simulations. The diameter of the desorber was found to be more sensitive to the number of absorber stages compared to the absorber. An increase of absorber stages from 2 to 5 stages resulted in a decrease of absorber diameter by only 5%, while it caused a decrease in the desorber diameter by around 22%. This difference can be justified by the nature of the desorption process. A significant increase in the liquid circulation rate means that a larger amount of solvent will have to be evaporated in the reboiler to supply steam for the desorption process. The increasing volume of vapor phase in the desorber results in a larger column diameter. Finally, a similar analysis for the stripper column maintaining a fixed number of absorber stages (N=5) indicated that 6 stages will result in an acceptable compromise between the desorber size and the energy consumption for solvent regeneration.

A comparison regarding the effect of absorber pressure on L/G and reboiler duty for the pure K_2CO_3 and PZ-promoted aqueous solutions is shown in Figure 6-8. In these diagrams, a similar lean loading of 0.4 has been considered for all solvents, while the inlet temperature of syngas to the column was constant at 100 °C. Minimum reboiler duties in the range of 1.85-2.0 MJ_{th} kg^{-1} CO_2 captured were calculated at the highest absorber pressure investigated in this study (18 bar). It can be observed that an increase in the absorber pressure results in the simultaneous decrease of reboiler heat duty and L/G for all solvents. A higher PZ content shifts the pressure range of this decrease to lower values. Particularly, when the process operates with the solvents PZ0.2 and PZ0.3, reboiler duty values of around 2.5 MJ kg^{-1} CO_2 can be achieved at absorber pressures of 11-12 bar. On the contrary, such values can be achieved by the pure K_2CO_3 aqueous solvent when the pressure increases to *ca.* 15 bar. As the pressure increases at values higher than 15 bar, the promoted solutions become less favorable. In this case, the energy consumption, as well as the liquid circulation rate of the K_2CO_3 aqueous solvent substantially decrease. At 18 bar, L/G approaches values of 15-16 (mass basis) for all 4 solvents. The PZ0.3 solvent results in lower reboiler duty and L/G ratios for the pressure range covered in this sensitivity analysis, which can be attributed to a higher solvent capacity and a higher concentration of reactive species,

thus an improved absorption rate. This outcome is in agreement with the results of the batch experiments presented in Chapter 4.

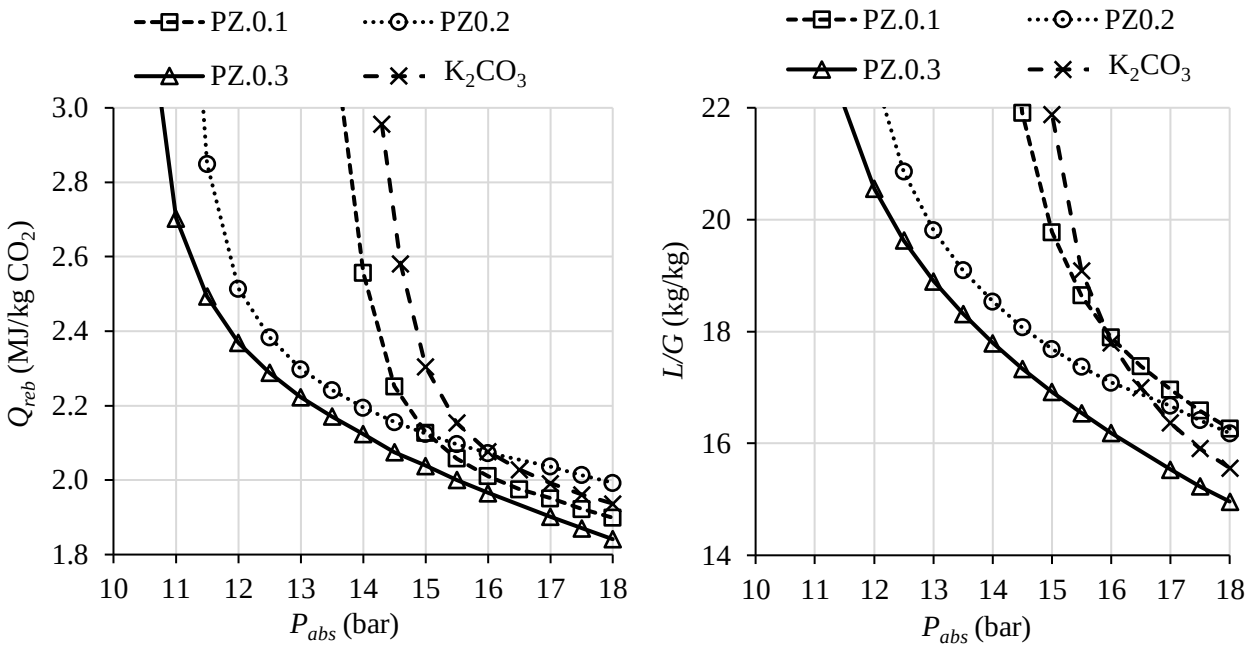

Figure 6-8: Effect of absorber pressure on specific reboiler heat duty (left) and L/G ratio (right).

The H_2S removal rate, CR_{H_2S}, with varying absorption pressure for a fixed CR_{CO_2}=95% is shown in Figure 6-9. In general, the capture efficiency of H_2S was found to be slightly better than that of CO_2 (in a range of 95-97%). Particularly, it can be observed that an increase in absorption pressure resulted in an improvement of removal efficiency attributed to the increase of H_2S partial pressure. However, this increase was almost negligible, a fact which can be attributed to small L/G values at higher pressures. This factor seems to counterbalance the pressure increase as the reduction in liquid circulation affects the H_2S hydrolysis in the column. Moreover, CR_{H_2S} values that correspond to 50, 20 and 1 ppmv H_2S concentration in the clean syngas have been drawn in Figure 6-9.

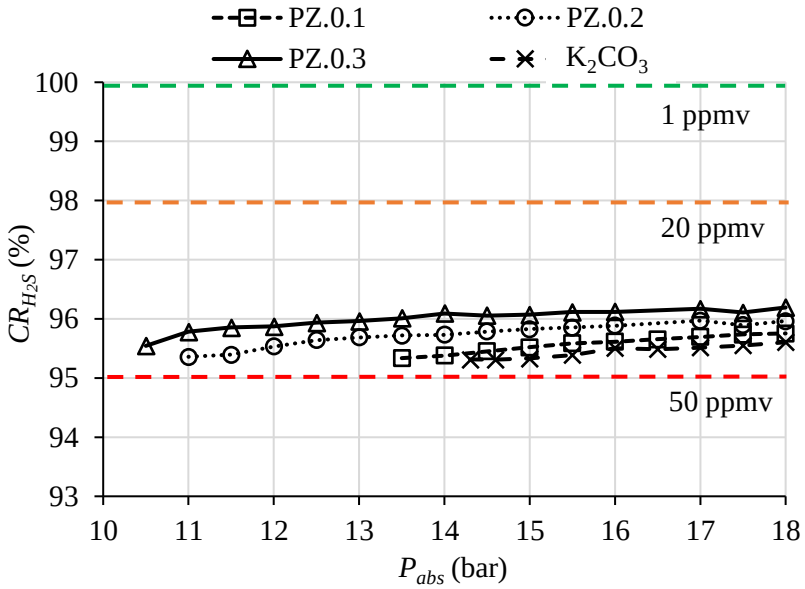

Figure 6-9: Effect of absorber pressure on the capture rate of H_2S from syngas.

It is evident from this figure that the process can efficiently remove the bulk of H_2S along with CO_2. The H_2S concentration decreases from around 900 ppmv in the raw syngas stream to values below 50 ppmv in the clean gas. However, it can be noted that such a configuration is not effective for completely eliminating the sulfur

content in syngas, as 1 ppmv or below is needed for certain catalysts. Field et al. [300] reported CR_{H_2S} values of around 97% during the combined absorption of CO_2 and H_2S in a pilot plant, which is close to the estimated values of the rate-based model. Using a cooled (10-30 °C lower temperature than the main lean solvent flow) split lean stream entering at a higher section of the absorber combined with 2-stage regeneration was found to improve CR_{H_2S}. Particularly, values up to 99% were reported for split stream temperatures of around 70 °C. In any case, it is expected that a polishing step for capturing organic sulfur and remaining sulfur-containing acid gases would be necessary upstream of reactors with non-tolerant catalysts e.g. for SNG synthesis. On the other hand, the achieved degree of H_2S capture by the hot potassium carbonate process alone can be adequate for syngas utilization for power generation.

The effect of lean solvent loading on specific reboiler duty and L/G is shown in Figure 6-10 for a constant absorber pressure of 17 bar and solvent regeneration at ambient conditions. It can be observed that an increase of lean solvent loading decreases the reboiler duty, while on the other hand, this causes an increase in L/G ratios. A higher CO_2 concentration in the liquid phase facilitates stripping in the desorber due to its elevated partial pressure over the liquid solution. On the other hand, this benefit is accompanied by a higher liquid flow rate demand to achieve 95% CO_2 removal in the absorber. For most solvents, minimum heat duties close to 2 MJ kg^{-1} CO_2 were estimated at $a = 0.4$. Of course, those values consider only the process heat of desorption without taking into account heat losses in columns and pipes, as well as heat transfer losses in the reboiler. At low loading values ($a < 0.36$) and elevated absorber pressure, it seems that the pure K_2CO_3 aqueous solution is advantageous with reboiler duties below 3 MJ kg^{-1} CO_2 captured. On the other hand, the PZ-promoted solvents exhibit higher heat duties, a fact that can be attributed to a higher heat of absorption ΔH_{abs}. For a low fraction of PZ, ΔH_{abs} is almost constant however while a higher amount is added in the solution (or similarly, more reactive PZ species are present), ΔH_{abs} increases sharply and it is representative of aqueous amine solutions [216]. As the lean loading is increased above 0.36, the reboiler heat duties of the PZ-promoted cases approach the values of the pure K_2CO_3 aqueous solution Ultimately, reboiler duties for PZ-promoted solvents become equal or lower than that of the reference solvent when $a \geq 0.4$. Particularly when $a \geq 0.42$, PZ0.3 results in the lowest reboiler duty and L/G. From Figure 6-10 (right), it seems that thermodynamic and kinetic limitations become important when loading exceeds 0.36, resulting in a larger slope of L/G values in the order PZ0.3 < PZ0.2 < PZ0.1 < K_2CO_3.

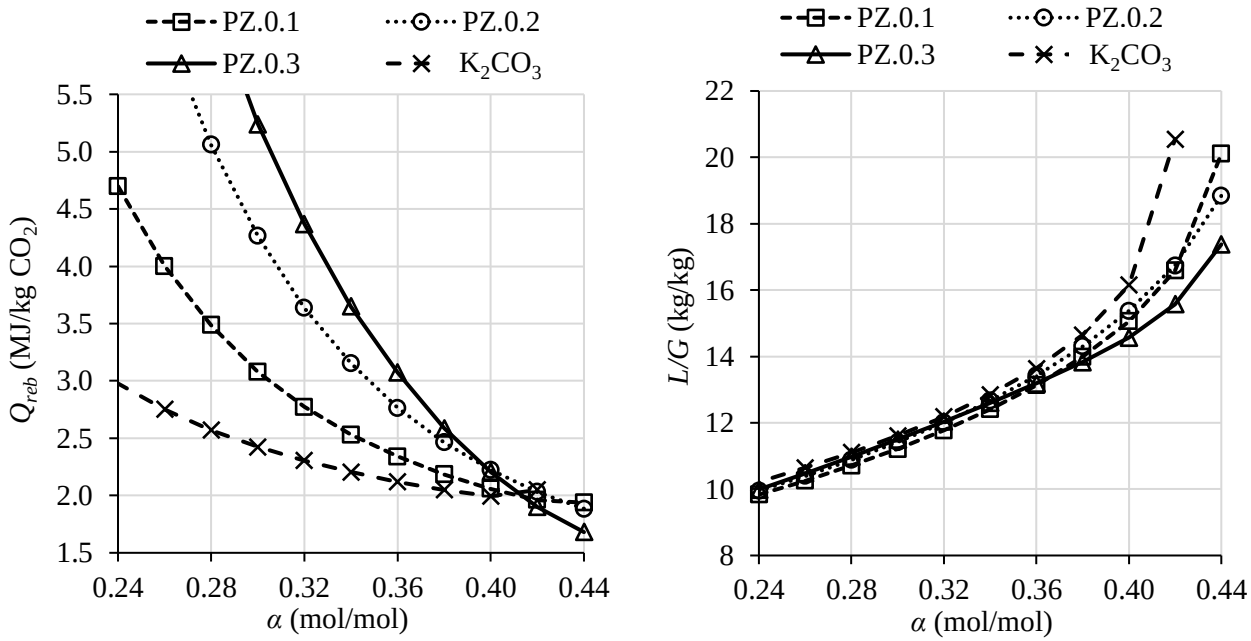

Figure 6-10: Effect of lean loading on specific reboiler heat duty (left) and L/G ratio (right).

Moreover, the effect of lean solvent loading on CR_{H_2S} is depicted in Figure 6-11 (left). It would be expected that the increase of L/G would result in a higher CR_{H_2S}. However, the loading increase from 0.24 to 0.44 slightly deteriorates the capture efficiency by *ca.* 1 percentage point as the H_2S solubility is affected by the K_2CO_3 conversion degree according to the overall reaction R 6-11.

$$H_2S + CO_3^{2-} \leftrightarrow HS^- + HCO_3^- \qquad R\ 6\text{-}11$$

Thus, in terms of maximizing CR_{H_2S}, a lower lean solvent loading can be advantageous. A sensitivity analysis for the effect of lean solvent temperature on CR_{H_2S} is also shown in Figure 6-11 (right). In this case, higher L/G values as temperature increased resulted in an improvement of H_2S purification efficiency for a constant loading of $a = 0.4$. This effect can be attributed to the enhanced hydrolysis of H_2S, which is separated from the syngas mixture. Moreover, the desorber operation pressure is another process parameter which is of major importance. In Figure 6-12, the effect of desorption pressure on reboiler heat duty is shown.

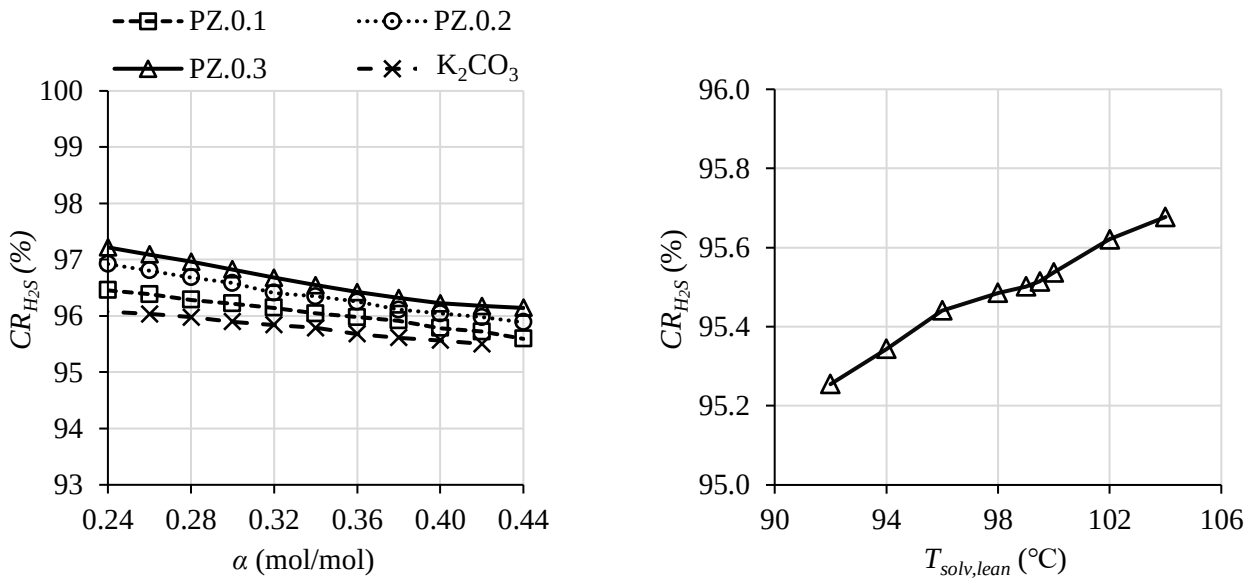

Figure 6-11: (Left) Effect of lean loading on the capture rate of H_2S from syngas. (right) Effect of lean solvent inlet temperature on the capture rate of H_2S from syngas (pure K_2CO_3 aqueous solution).

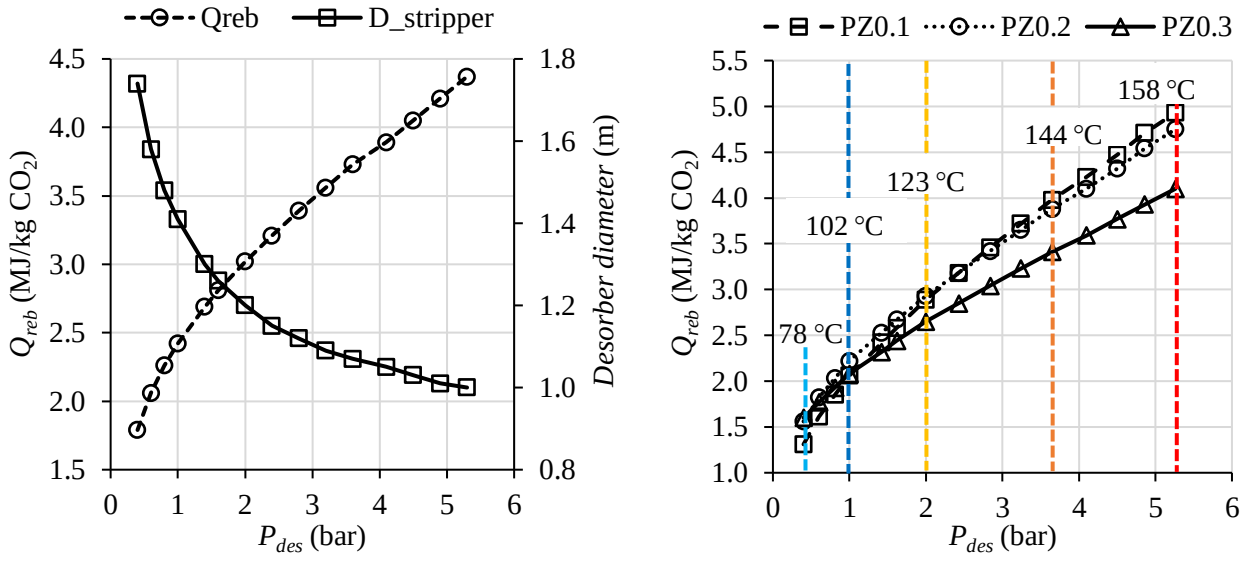

Figure 6-12: (Left) Effect of desorption pressure on specific reboiler duty and desorber diameter for aqueous K_2CO_3 solvent with a=0.3 and constant L/G in the absorber. (Right) Effect of desorption pressure on specific reboiler duty for PZ0.1, PZ0.2 and PZ0.3 solvents with a=0.4 and constant L/G in the absorber. Temperature values denote solvent boiling points at the indicated pressure.

On the left side, the effect of desorption pressure on reboiler duty and desorber diameter is depicted for the reference case where no promoter is used. For this analysis, the heater block coupled with the "T-BALANC" design specification in Aspen Plus was used to adjust the lean solvent temperature at a constant value of 100 °C. An increase of desorption pressure increases the specific reboiler duty, which approximately doubles for an increase of desorber pressure by a factor of 5. Operation under vacuum conditions seems to be beneficial for the hot potassium carbonate process, as the reboiler duty falls sharply between 1 bara and 400 mbara. At the same time, the column diameter increases significantly due to the increased volume of the vapor phase. Operation under vacuum has also a positive effect on reducing the specific reboiler duty of PZ0.1, PZ0.2 and PZ0.3 solvents. It was found that vacuum operation is preferable when the solvent contains a small concentration of PZ. For a pressure reduction from 1 bara to 400 mbara, the specific reboiler duty decreases by 36%, 30% and 23% for PZ0.1, PZ0.2 and PZ0.3 solvents, respectively. Vacuum stripping has advantages for solvents with a low heat of desorption due to a smaller production of water vapor relative to ambient pressure operation [271]. On the contrary, solvents with higher heat of desorption benefit when the desorber operates at higher pressure, a strategy to increase the partial pressure of CO_2 relative to the partial pressure of H_2O in the vapor phase. This can be noted in Figure 6-12 (right), where the PZ0.3 solvent exhibits lower specific reboiler duty compared to PZ0.1 and PZ0.2 as the pressure increases from ambient to 5 bar. In this diagram, the solvent boiling points at different pressure levels of the desorber are also given. It is interesting to note that for typical desorber pressure (up to 2 bar), low-pressure steam at a pressure of 2-3 bar can be extracted to supply heat for regeneration. Increasing the desorber pressure at 5 bar would require higher quality steam to be extracted from the plant turbine. When operating under vacuum conditions, on the other hand, waste heat (< 100 °C) can be exploited to drive the regeneration process.

Finally, amine losses is an important issue when operating the AGR process at elevated temperatures. Based on data from pilot-scale plants, amine emissions have been measured as vapor and aerosols at the absorber outlet, with concentrations even exceeding 1000 ppmv in a few cases [301]. Akinpelumi et al. [301] reported PZ emissions from a pilot-scale plant with concentrated PZ for post-combustion CO_2 capture. For absorber operation with a lean solvent at 43-54 °C, PZ emissions varied between 12-66 ppmv. Those values are in agreement with the findings of Freeman et al. [236], who quantified PZ volatility from concentrated aqueous PZ solutions at ambient pressure and 40 °C to be in a range of 10-21 ppmv. Significant reductions were achieved by upstream control of SO_3 and a two-stage water wash at the absorber exit. Particularly for PZ/K_2CO_3 mixtures, Hilliard reported that the volatility of PZ varied between 4 and 54 ppmv at 40 °C, while an increase of temperature from 40 to 80 °C was found to increase the PZ partial pressure by an order of magnitude [242]. The results for PZ emissions as estimated in the present study are shown in Figure 6-13.

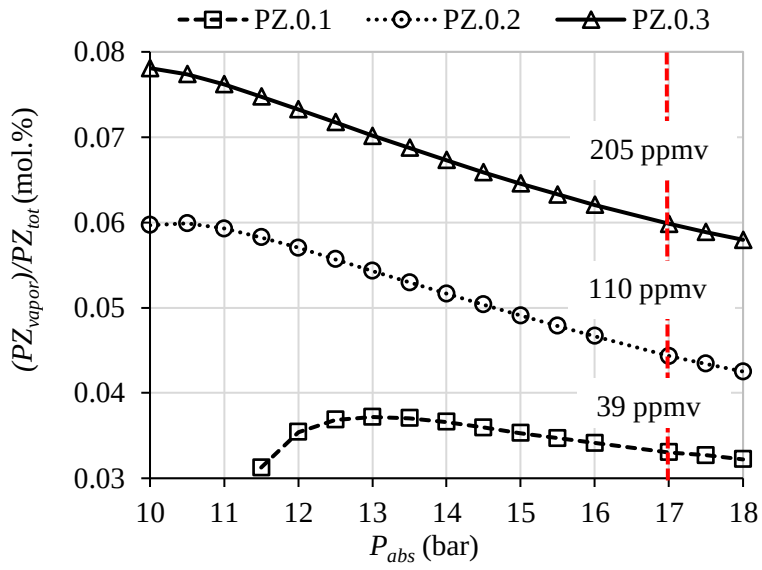

Figure 6-13: Effect of absorption pressure on PZ emissions from the absorber (no water wash section).

PZ losses are expressed as the molar ratio of PZ in the outlet vapor to the total PZ entering the absorber, while the concentration of PZ in the clean gas for all PZ-promoted solvents is given in the figure (at a pressure of 17 bar). Operation at higher absorption pressure leads to a decrease of amine losses while increasing the PZ fraction in the solvent has an adverse effect on emissions (an increase from 39 to 205 ppmv). Based on the estimated losses, it is suggested that PZ make-up and emission control would be required in the case of integration into a gasification plant for SNG synthesis. PZ emission control could be accomplished through a washing section or selective sorption of PZ volatile species downstream of the absorber. In addition, an investigation on possible interactions of the PZ vapor with methanation catalysts would be necessary.

6.5 Conclusions

In this chapter, an Aspen Plus™ model for the hot potassium carbonate process aiming at the simultaneous capture of CO_2 and H_2S from coal-derived syngas (coal-to-SNG plant) was developed in order to investigate the effect of additives and operating parameters on process efficiency. Particularly, pure K_2CO_3 and PZ-promoted aqueous solutions with varying PZ fractions were evaluated as promising solvents. While process modeling studies on post-combustion CO_2 capture with PZ/K_2CO_3 mixtures are available in the literature, the present study focused on the pre-combustion capture at elevated temperature and pressure. Adjustment of electrolyte-NRTL parameters was performed through experimental data regression as default Aspen Plus™ parameters did not accurately model the thermodynamics of the liquid solution. A regressed thermodynamic model with experimental data for mean ionic activity coefficients, vapor pressure depression, solution heat capacity, CO_2 and H_2S solubility and PZ speciation can result in a more accurate system description compared to the default electrolyte-NRTL parameters in Aspen Plus. Average relative deviation for the pure K_2CO_3 aqueous solutions was found to be less than 12% when only CO_2 is the absorbate, while it increased to 18.6% for the H_2S-CO_2-K_2CO_3-H_2O system. The average relative deviation during the prediction of CO_2 solubility and PZ speciation in PZ-promoted solutions is found to be between those two extremes.

The regressed thermodynamic model was implemented in detailed rate-based models in Aspen Plus to describe the absorption and desorption columns. The variation of absorption pressure, desorption pressure and lean solvent loading affected the process performance and in particular, the liquid-to-gas ratio, the heat consumption of the reboiler and the purification efficiency of H_2S. It was found that when the process operates with PZ-promoted solutions, similar reboiler duties to the pure K_2CO_3 solvents can be achieved at lower absorber pressure. The operation of the absorber at higher pressure generally benefits both promoted and pure K_2CO_3 aqueous solutions, which indicates its particular suitability as pre-combustion CO_2 capture technology. A higher lean solvent loading is required when PZ is used as additive to the process, attributed to a higher heat of desorption. PZ volatility in the promoted solutions was found to be higher compared to emissions reported for concentrated aqueous PZ at ambient conditions. Thus, PZ interactions with catalysts downstream of the AGR process should be taken into account. It was found that when the lean loading exceeds values of ca. 0.42, the required L/G values sharply increased for most solvents. Furthermore, operation of the desorber column at elevated pressure was found to benefit solvents with a higher PZ fraction. Finally, H_2S removal efficiency was consistently above the CO_2 capture level (set to 95% in all cases). Strategies for further reducing the H_2S content in clean syngas were also discussed, especially in the case in which the AGR process is located upstream of a reactor with a catalyst that can be poisoned by sulfur compounds.

7 Energy and exergy analyses of a gasification plant for power/MeOH cogeneration with CCS

In the previous chapters, experimental and modeling work regarding syngas cleaning by K_2CO_3 solutions has been included. Particularly, a modeling study of the AGR process alone for the investigation of operation parameters on process efficiency was presented in Chapter 6. In Chapter 7, the integration of the hot potassium carbonate process in two different biomass IGCC (BIGCC) plant configurations is analyzed (electricity-only and electricity/MeOH cogeneration). In the next section, a brief literature review on the background and the scope of the study are described.

7.1 Literature review and scope of study

As already discussed in Chapter 1, the gasification process provides a major benefit compared to solid fuel combustion, which is the potential to produce energy (electricity, heat), fuels and chemicals from the same intermediate process stream (i.e. syngas). Regarding electricity generation, IGCC plants are of particular interest, since syngas is utilized in a highly efficient combined-cycle increasing the overall plant efficiency. In an IGCC plant, gasification can be carried out at elevated pressure for supplying syngas to the GT combustor. Pressurized gasification can be coupled with pre-combustion AGR in the context of CCS/CCUS systems. Bhave et al. [302] presented a screening and techno-economic assessment of biomass power generation technologies with CCS. A time horizon from 2010's until 2050 was considered. In that study, various research organizations and companies were involved in the framework of TESBiC project. It was concluded that BIGCC-CCS plants can achieve higher energy efficiencies compared to alternative power generation technologies such as biomass oxy-fuel combustion, biomass chemical looping combustion and biomass combustion with amine-based CO_2 capture. At the same time, the levelised cost of electricity (LCOE) for the different technologies was reported for the 2010-2050 timeframe and for a reference plant capacity of 50 MW_e. Lower LCOE values were predicted for the BIGCC-CCS technology compared to oxy-fuel combustion and biomass combustion with amine-based CO_2 capture. Apart from energy efficiency and cost-related benefits, application of CCS in biomass gasification plants has the feature that it can achieve negative CO_2 emissions per unit energy delivered. Oreggioni et al. [303] reported that the climate change potential of power generation *via* biomass gasification plants with CCS varies between -151 $g\,CO_{2,eq}\,kWh_e^{-1}$ and -340 $g\,CO_{2,eq}\,kWh_e^{-1}$ depending on the CCS technology and CO_2 capture rate. Consequently, BIGCC-CCS plants are expected to be a competitive future technology for power generation and polygeneration, considering that decarbonization of the energy mix will take place.

Studies on the thermodynamic and economic performance of BIGCC-CCS plants can be found in the literature. Rhodes and Keith [114] published a techno-economic assessment of a large-scale BIGCC plant with glycol-based CO_2 capture. The system featured the BCL/FERCO indirect gasifier and net plant efficiencies in the range 25-28% (HHV basis) were reported. Erlach et al. [304] studied a BIGCC-CCS configuration based on a wood-fuelled, steam/O_2 blown fluidized-bed gasifier with hot gas desulfurization and low-temperature CO_2 capture by Rectisol AGR. This configuration was compared to the case of a BIGCC-CCS plant fuelled with biomass treated by hydrothermal carbonization (HTC). It was concluded that the case of bio-coal leads to a lower overall process efficiency due to losses and auxiliary energy consumption during the HTC pretreatment step. Recent studies on BIGCC-CCS plants are those of Dinca et al. [305] and Zang et al. [306]. Dinca et al. [305] investigated the performance of a BIGCC-CCS plant with chemical absorption into an aqueous MEA solution. The authors reported net efficiencies between 25 and 32% depending on the steam extraction pressure for covering the regeneration heat duty. Zang et al. [306] compared various configurations of BIGCC and BIGCC-CCS plants with steam/O_2 mixtures and either post-combustion (MEA) or pre-combustion CO_2 capture (Selexol™) in terms of exergetic efficiency. It was found that BIGCC plants with pre-combustion CO_2 capture with Selexol coupled to steam/O_2 gasification can achieve improved efficiency compared to the MEA case. Although most studies have focused on physical solvents, pre-combustion chemical absorption at elevated pressure can be a viable alternative. Urech et al. [299] reported that the integration of MDEA-CCS results in similar energy efficiency with a Selexol-CCS unit in a coal IGCC plant. Moreover, the authors reported that a CCS unit based on aqueous

K_2CO_3 solutions operating at high pressure and temperature can increase the energy efficiency by 1-3 percentage points. A major part of the investigation in this chapter aims to investigate this coupling in a BIGCC plant.

MeOH (CH_3OH) is among the most widely traded chemicals globally and it is used for energy (internal combustion engines, fuel cells, etc.), adhesives, pharmaceuticals, silicones, paints, screens and in many other applications [307]. For this reason, a great deal of work has been lately dedicated to the production of MeOH from captured CO_2 [308, 309], which can be carried out with electrolysis-derived H_2. Such a conversion requires a higher stoichiometric amount of H_2 compared to the more efficient pathway of syngas catalytic conversion. Ptasinski et al. [310] presented a process for MeOH production based on sewage sludge gasification through the catalytic reaction of CO and CO_2 with H_2 in syngas and selective sulfur removal prior to the synthesis reactor. In a recent publication, Puig-Gamero et al. [311] presented an Aspen Plus model of an integrated process for MeOH production from wood gasification and evaluated the effect of different process parameters. In addition, studies on the production of gasoline and olefins from biomass-derived MeOH through gasification are those of Phillips et al. [312] and Xiang et al. [313], respectively.

Apart from stand-alone plants, MeOH can be co-produced with electricity in a BIGCC plant. Mass and energy integration between the BIGCC plant and a synthesis process can allow improved energy efficiency and reductions on equipment investment and CO_2 capture cost [314]. As an example of polygeneration in IGCC plants, Cormos et al. [315] investigated the co-production of power, H_2, SNG and FT-fuels through coal/biomass co-firing from a techno-economic perspective. Liu et al. [314] and Heinze et al. [316] investigated the possibility of integrating MeOH synthesis in a coal-fuelled IGCC plant. In the former study, stand-alone and integrated configurations were compared. They reported that when the same output of electricity and methanol is considered for the stand-alone and cogeneration configurations, a fuel exergy saving ratio of around 7% can be achieved with an integrated system. In the study of Heinze et al. [316], different operation modes of a coal IGCC-CCS plant producing MeOH independently from electricity were evaluated.

In this chapter, the impact of K_2CO_3-based CCS integration on the energy and exergy efficiency of BIGCC plants with and without MeOH cogeneration is investigated. Case studies with varying parameters such as gasification agent, CO_2 capture rate and MeOH cogeneration rate were evaluated. One of the particular contributions of this work is to identify the efficiency penalty of a future BIGCC-CCS plant with hot gas cleaning and AGR at "warm" gas cleaning conditions of elevated pressure and temperature. Since differences between the configurations of coal-fired IGCC and BIGCC plants can be significant (e.g. different gasification technology, syngas composition, GT and steam cycle specifications, etc.), differences are also expected on the obtained results. The second contribution of this study is to investigate potential benefits in terms of energy/exergy efficiency in the case when MeOH cogeneration is carried out in parallel with power generation in an integrated system. The scope of the study additionally includes a comprehensive analysis and comparison of the exergy destruction rates among the plant components. The obtained results can provide useful information for further optimizing the process design.

7.2 System configuration and process modeling methodology

7.2.1 Description of BIGCC-CCS configurations and Aspen Plus modeling

The BIGCC configurations considered in this study were modeled in Aspen Plus™ software and all include the following sections: biomass drying, air separation unit (ASU), gasification, syngas cleaning and conditioning, gas turbine (GT) and a Rankine steam cycle (SC). In each configuration, a network of heat exchangers for heat recovery has been integrated. The scenarios with CCS additionally include WGS reactors and a hot potassium carbonate AGR unit (see also Chapter 6) with compressors for CO_2 transportation and storage. Moreover, in the cogeneration flowsheets, a MeOH-synthesis process has been integrated into the flowsheet. Other variations among the different configurations studied in this work do exist and they are discussed next. The three BIGCC configurations that were studied in this work are shown in Figure 7-1. Simplified layouts are depicted in this figure. For instance, the heat exchanger network, multiple turbine stages, sub-process configurations, etc. are not shown. However, detailed flowsheets for the three scenarios can be found in the Appendix of this thesis.

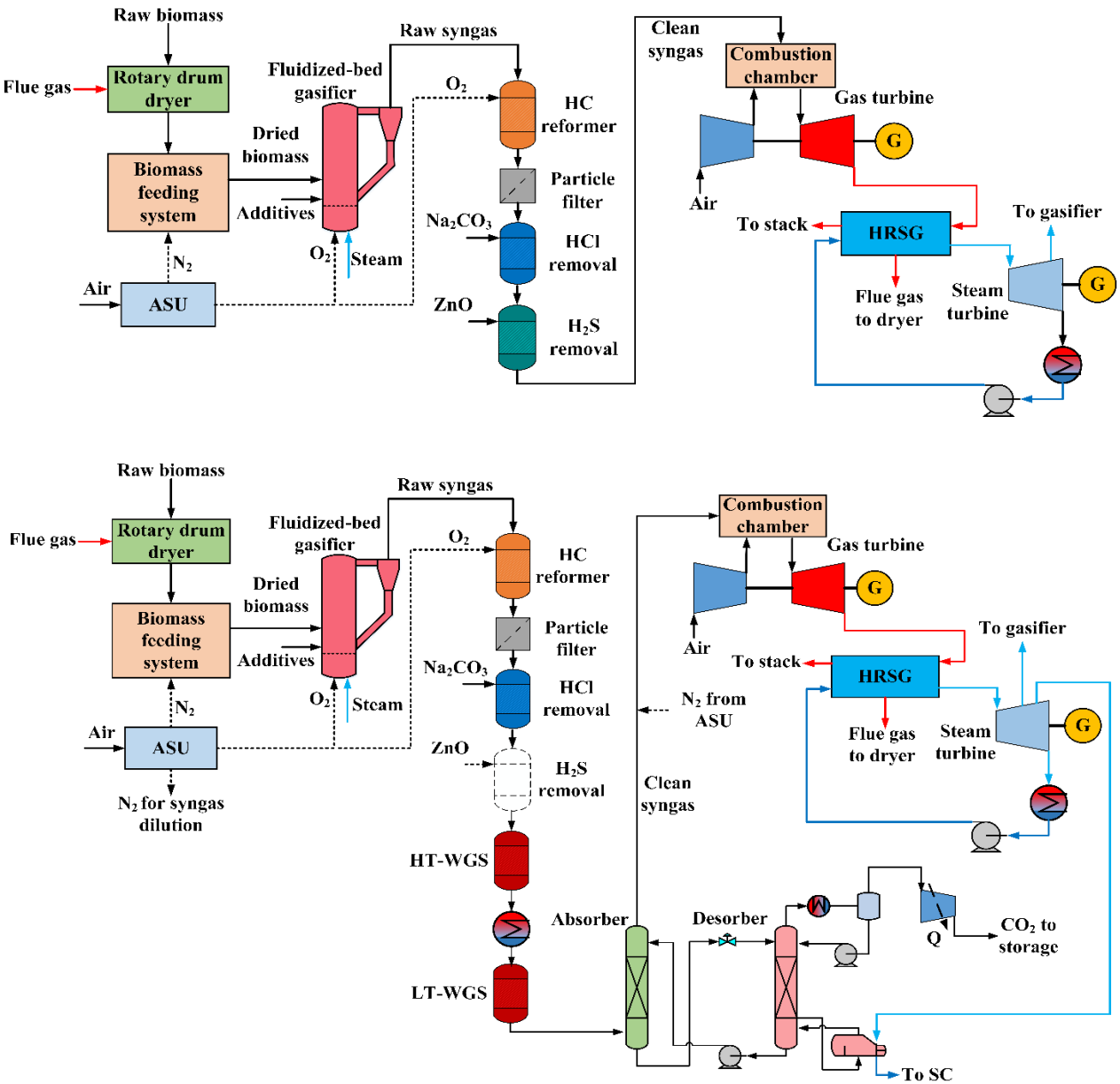

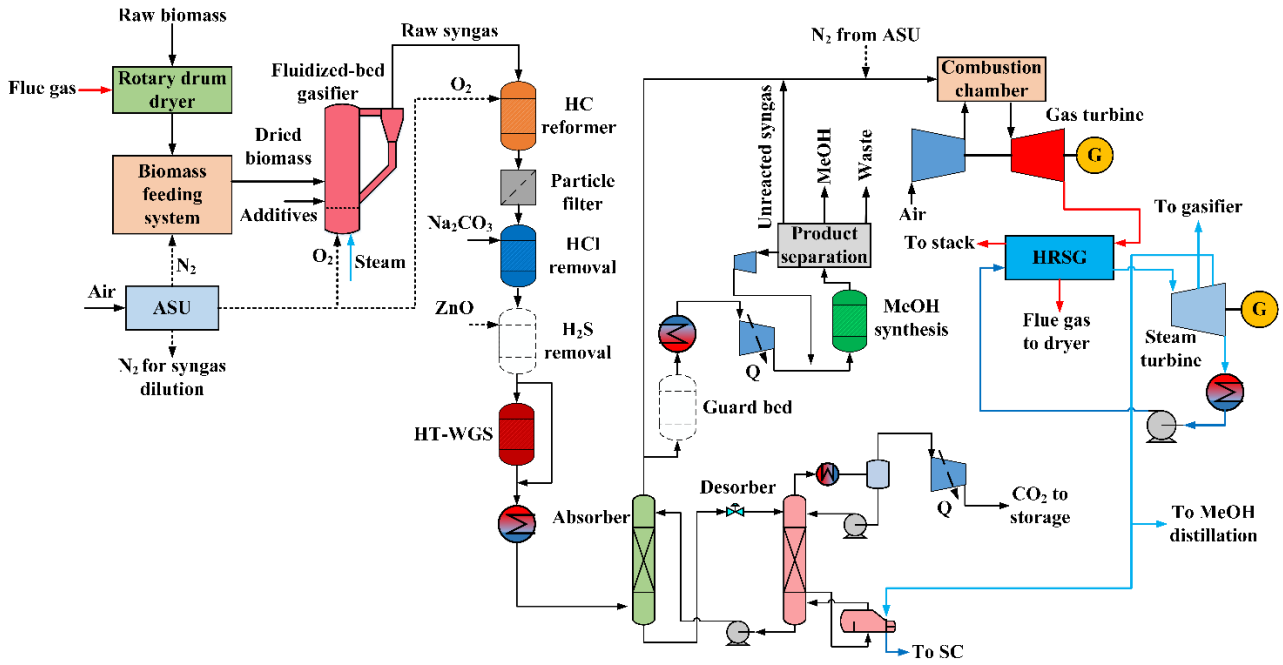

Figure 7-1: BIGCC configurations modelled in this study. (Top) Reference electricity-only BIGCC plant w/o CCS (Scenario I), (middle) electricity-only BIGCC plant with CCS (Scenario II), (bottom) MeOH and electricity cogeneration BIGCC plant with CCS (Scenario III).

For all scenarios, the biomass thermal input to the BIGCC plant was assumed equal to 126 MW_{th} (LHV). Taking into account issues of biomass supply and logistics, this is considered a realistic plant size. This capacity is within the range considered by Difs et al. [116] for a BIGCC plant (20-300 MW_{th}). Wood residues were considered as a fuel for the BIGCC plant and composition data regarding the proximate and ultimate analyses were retrieved from Vassilev et al. [77]. The biomass moisture at the plant gate was assumed at 30 wt.%. No biomass comminution was considered to occur within the BIGCC plant and any power consumption related to it has been excluded from the analysis. Nevertheless, this could be necessary depending on the size of raw biomass which is delivered. Biomass is dried to 10 wt.% moisture by flue gas in a rotary dryer [317]. Modeling of the drying operation is carried out through a pseudo-stoichiometric reactor and a flash block in Aspen Plus.

Gasification takes place at 900 °C and 29 bar in a fluidized-bed gasifier, with O_2 entering at 200 °C and H_2O at 350 °C. The technology design and performance were presented in [318] by the Institute of Gas Technology (IGT). The gasifier is O_2/H_2O blown and it has been operated up to approximately 1000 °C. In the present work, a more moderate gasification temperature was considered to avoid any agglomeration potential. The utilization of a non-woody fuel with a lower ash-melting temperature would necessitate a further decrease of gasification temperature. In Aspen Plus, the gasifier model was based on the steady-state, Gibbs free energy minimization model presented in Chapter 2 with a few modifications. A restricted-equilibrium approach was set in the Gibbs minimization module with the reactions specified in [146]. Further modifications are summarized below.

- *HC formation and CCE*: In the stoichiometric reactor prior to the RGibbs module, fractions of solid carbon are converted to CH_4 (0.2), C_2H_6 (0.02), C_6H_6 (0.0028) and $C_{10}H_8$ (0.0061) to account for the formation of HCs and tar. Fraction values were based on syngas measurements from [318] and on the assumption that catalytic gasification with olivine/dolomite is carried out to reduce the tar content [304, 319]. In a separator block, 2% of C(s) bypasses the RGibbs reactor (*CCE*=98%).
- *In-bed desulfurization and other contaminants*: For simplification, all S in fuel is assumed to be converted to H_2S, all N to NH_3 and all Cl to HCl. In bed desulfurization (Ca-based sorbent) takes place in order to capture 60% of S prior to the stoichiometric reactor, which is modeled in Aspen Plus according to Hannula and Kurkela [320].
- *Heat losses*: Heat losses in the gasifier were simulated as 1% of biomass HHV input to the process.

Table 7-1: Proximate and ultimate analyses of wood residue fuel.

Proximate analysis		**Ultimate analysis (d.b.)**	
Volatile matter (wt.%, d.b.)	78.0	C (wt.%)	48.62
Fixed carbon (wt.%, d.b.)	16.6	H (wt.%)	5.77
Ash (wt.%, d.b.)	5.4	O (wt.%)	39.64
Moisture (wt.%, a.r.)	30	N (wt.%)	0.47
HHV (MJ kg^{-1}, d.b.)	19.32	S (wt.%)	0.08
		Cl (wt.%)	0.02

The ASU unit was based on the cryogenic distillation technology [321, 322] and it is depicted in Figure 7-2. Ambient air is filtered and compressed in a two-stage compressor with intercooling slightly above the pressure of the high-pressure (HP) distillation column. A minor air flow (20% of total) is further compressed to 30 bar, cooled and expanded before sent to the distillation columns (RadFrac distillation models). The HP distillation column operating at 5.5 bar achieves a first separation of the air stream, which has been cooled and partially liquefied through heat exchange with the products of the process (AMHX). The O_2-rich bottom product and the N_2-rich product from the top of the HP column are expanded and sent to a low-pressure (LP) distillation column operating at 1.6 bar. An O_2 purity of at least 95% vol.% is achieved in the LP-column bottom product, which is considered acceptable in the context of O_2/H_2O blown gasification. In the two-column distillation process, the heat duty in the LP column reboiler is covered by the condenser duty in the HP column. The two distillation columns are thus under tight heat integration (2-5 K). The liquid, O_2 product of the LP column is pumped to 30 bar to be fed to the gasifier, while the gaseous N_2-rich product is compressed to various pressure levels depending on its downstream utilization. Part of N_2 is used for the pressurization of biomass hoppers, while the major flow is utilized for the dilution of syngas in the GT combustor (H_2 content ≤ 50 vol.%) in the CCS scenarios. The N_2-rich stream that is not exploited is released in the atmosphere. Nevertheless, it can be sold as a valuable by-product of the plant.

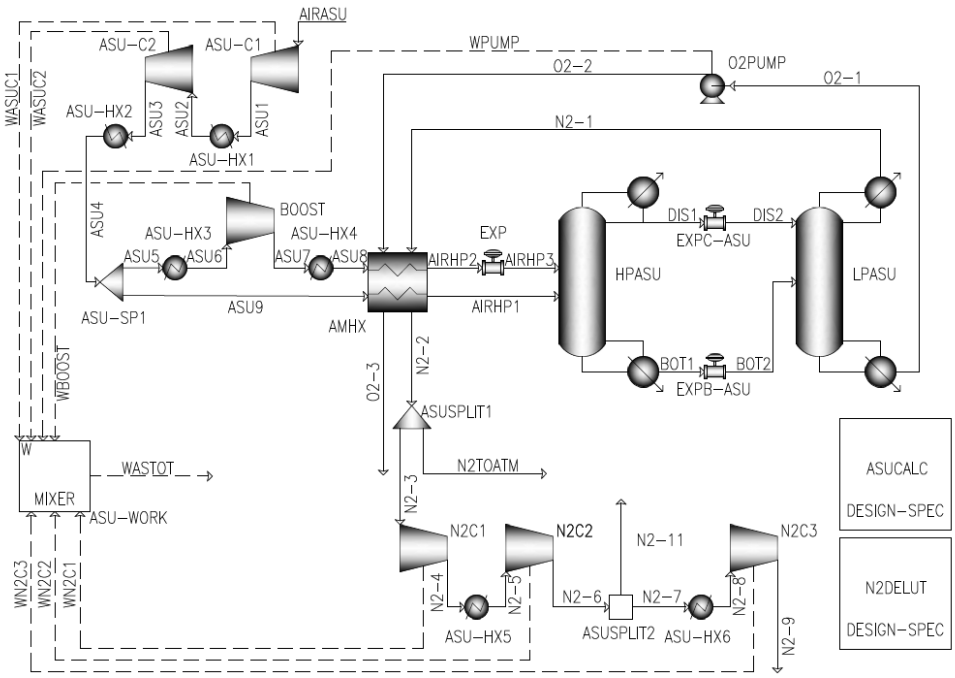

Figure 7-2: ASU model based on cryogenic air distillation with HP/LP column configuration.

An autothermal catalytic reformer downstream of the gasifier is adopted for the reforming of HCs and NH_3 in raw syngas. Catalysts based on Ni/Al_2O_3 or modified catalysts with precious metals are known to be active for steam reforming. The reformer concept is based on [323] and the model is based on Gibbs free energy minimization, similarly to [320]. Instead of the temperature-dependent conversion expressions, fixed values for the extent of reforming were given. Conversions of 99% for C_2H_6, C_6H_6 and $C_{10}H_8$, 90% for NH_3 and 70% for CH_4 were defined based on the studies [320, 324, 325]. Oxygen from the ASU is supplied to the autothermal

reformer, the flow rate of which is regulated to maintain a reforming temperature of 910 °C at the reactor outlet. The reactions occurring during tar steam reforming are given in R 7-1, R 7-2 and R 7-3.

$$C_nH_m + nH_2O \leftrightarrow nCO + \left(n + \frac{m}{2}\right)H_2 \qquad R\ 7\text{-}1$$

$$CO + H_2O \leftrightarrow CO_2 + H_2 \qquad R\ 7\text{-}2$$

$$CO + 3H_2 \leftrightarrow CH_4 + H_2O \qquad R\ 7\text{-}3$$

After heat is recovered by cooling to 420 °C, particulate matter is removed from syngas with a high-temperature filter. At this temperature, it is expected that alkali species also condense and collected along with the solid matter. The particulate-free syngas enters a fixed-bed reactor, in which HCl is removed by a low-cost, dry Na_2CO_3 sorbent according to the reaction R 7-4, as proposed in [70].

$$2HCl + Na_2CO_3 \leftrightarrow 2NaCl + CO_2 + H_2O \qquad R\ 7\text{-}4$$

Syngas is further cooled at 350 °C and desulfurization is achieved in a single ZnO sorbent bed, so that the sulfur-tolerance specifications of GT are fulfilled. Higher temperatures were found to deteriorate the H_2S removal efficiency, a phenomenon which depends on the moisture content of syngas. The chemical reaction for H_2S removal is given in R 7-5. Both HCl and H_2S removal were modelled with adiabatic, equilibrium reactors in Aspen Plus software. It should be noted HCl can interact with ZnO sorbents, so its removal must precede syngas desulfurization [326].

$$ZnO + H_2S \leftrightarrow ZnS + H_2O \qquad R\ 7\text{-}5$$

Clean syngas at a temperature of 200 °C is delivered to the GT combustor, which operates with a pressure ratio of 15. In Aspen Plus, the GT is modelled as a combination of compressor/turbine blocks, RGibbs reactor and splitters/mixers to model the cooling of turbine blades. In the GT combustor, 4% pressure losses are assumed. The GT sub-model is coupled to an optimization block in Aspen Plus in order to maximize the net power by varying the air flow rate and the by-pass split ratio. In the optimization model, two constraints that apply are that the turbine inlet temperature (*TIT*) must not exceed 1230 °C and the flue gas outlet temperature must be up to 550 °C. The flue gas stream is then sent to the heat recovery steam generator (HRSG), where heat is recovered through a Rankine steam cycle. The HRSG has HP/LP levels of 110/4.2 bar and a live steam temperature of 520 °C entering the high pressure turbine (HPT). Steam is extracted at 30 bar: a fraction of it is reheated to 350 °C and supplied as agent to the gasifier and the rest is reheated to 520 °C and expanded in a medium pressure turbine (MPT). The exiting steam flow is expanded until a pressure of 0.06 bar in the low pressure turbine (LPT), unless a fraction is extracted at 2.5 bar and sent to the reboilers of AGR and MeOH units. Flue gas is also extracted from the HRSG at a temperature of 220 °C for biomass drying. The flue gas stream at the exit of the HRSG has a temperature of 75 °C. The flue gas stream from the dryer exits at 95 °C and no further heat recovery was considered.

In Scenario II (BIGCC-CCS), it is assumed that the ZnO reactor is eliminated and H_2S is captured along with CO_2 in the AGR unit. After HCl removal, two WGS reactors at high (WGSHT) and low temperature (WGSLT) increase the CO_2 partial pressure upstream of the AGR process. The reactors were modelled in Aspen Plus as adiabatic equilibrium reactors operating at inlet temperatures of 350 and 200 °C, respectively. The reactions are exothermic, so excess heat was recovered in the WGS section for steam generation. No process steam injection was required upstream of the reactors, as excess steam was provided in the gasifier ($H_2O/CO > 2$). In the case that sulfur is removed in the AGR unit, Cu-based WGSLT catalysts must be excluded, since they are prone to deactivation at sulfur contents < 0.1 ppmv [327]. According to Haldor Topsøe [328], a combination of sulfur-resistant MoS_2 (WGSLT) and Fe-based catalysts (WGSHT) would be more appropriate for the proposed configuration. A variation in Scenario III regarding the WGS configuration can be noted in Figure 7-1. A single WGSHT reactor is employed in this case, while a fraction of the total syngas flow rate completely bypasses the unit. The reason for this change is the fact that only a minor adjustment of syngas composition is necessary in order to meet the specifications of the MeOH synthesis process.

The AGR unit has the same configuration as the process layout studied in Chapter 6. In order to reduce the computational time and improve flowsheet convergence, equilibrium models were used for the absorber and desorber columns in the plant process model (instead of rate-based models in Chapter 6). A 30 wt.% aqueous K_2CO_3 solution without promoters was assumed for the chemical absorption process. Syngas enters the hot potassium carbonate process with a temperature of 122 °C. A design specification regulates L/G for a constant lean loading value of 0.3, so that a certain CO_2 capture rate can be achieved. For Scenario II, the base-case CO_2 capture rate was assumed to be 90%, while for Scenario III, CO_2 capture was fixed at 95%. The effect of CO_2 capture rate on process performance was also investigated through sensitivity analysis. Absorber and desorber columns operate at 25 and 1.5 bar, respectively. The reboiler heat duty is supplied by low-pressure saturated steam extracted from the steam turbine island at a pressure of 2.5 bar. The desorber off-gas, which is CO_2-rich, is cooled and compressed to 100 bar *via* a 3-stage intercooled compressor for storage [299].

The configuration of the MeOH synthesis unit is shown in Figure 7-3. The core of the process is a $Cu/ZnO/Al_2O_3$ catalytic reactor which operates at moderate pressure and temperature (52.5 bar/234 °C). A fraction of the purified syngas from the AGR unit is completely purified from sulfur species and any remaining contaminants in a guard bed (e.g. activated carbon, see Chapter 3) downstream of the AGR unit. It is cooled, compressed and heated to the reactor temperature, where MeOH synthesis occurs. For synthesis, a ratio of H_2/CO ~ 2.5 was adjusted, while further constraints for the molar ratios between H_2, CO and CO_2 were considered according to [311].

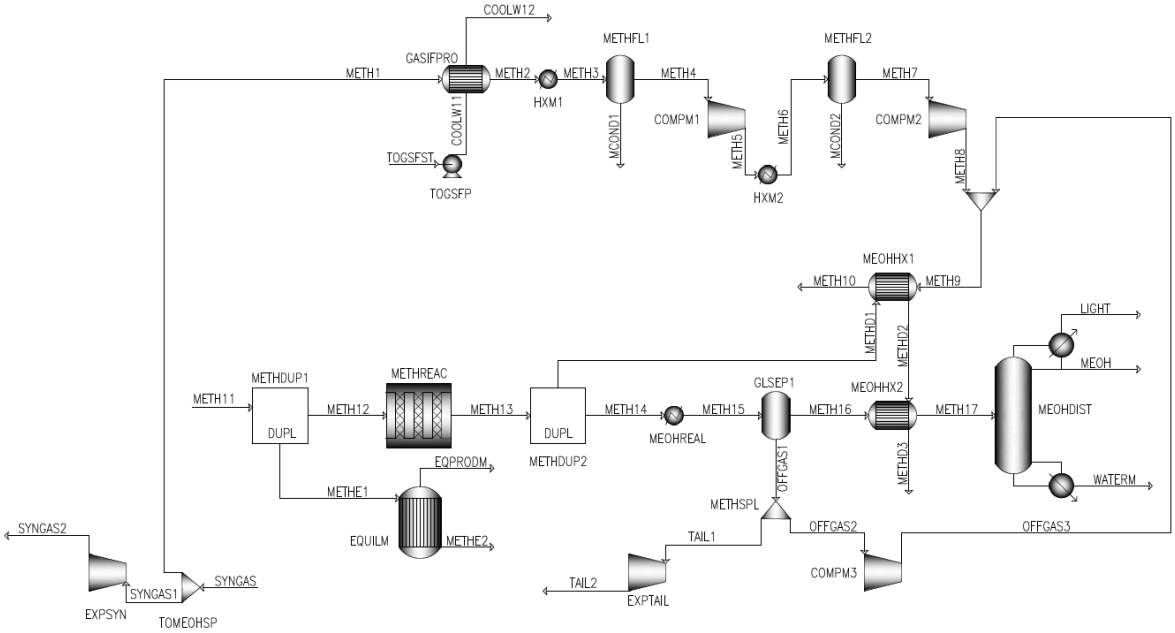

Figure 7-3: MeOH synthesis unit layout (incl. compressors, catalytic reactor, heat exchange equipment and product recovery equipment).

A reaction model describing the kinetics of synthesis was implemented in Aspen Plus RPlug according to the generalized Langmuir-Hinshelwood-Hougen-Watson (LHHW) model. The system is described through the reactions for hydrogenation of CO, hydrogenation of CO_2 and reverse WGS, while the process is exothermic. All three reactions are not independent and in this work, the conversion is described based on the latter two, as shown in R 7-6 and R 7-7.

$$CO_2 + 3H_2 \leftrightarrow MeOH + H_2O \qquad R\ 7\text{-}6$$

$$CO_2 + H_2 \leftrightarrow CO + H_2O \qquad R\ 7\text{-}7$$

Their kinetic expressions are given in Equation 7-1 and Equation 7-2

$$r_{CH_3OH} = \frac{k_1\, P_{CO_2}\, P_{H_2} - k_6\, P_{H_2O}\, P_{CH_3OH}\, {P_{H_2}}^{-2}}{\left(1 + k_2\, P_{H_2O}\, {P_{H_2}}^{-1} + k_3\, {P_{H_2}}^{0.5} + k_4\, P_{H_2O}\right)^3} \quad \left[\frac{\text{kmol}}{\text{kg}_{\text{cat}}\text{s}}\right] \qquad \textit{Equation 7-1}$$

$$r_{RWGS} = \frac{k_5\, P_{CO_2} - k_7\, P_{H_2O}\, P_{CO}\, {P_{H_2}}^{-1}}{1 + k_2\, P_{H_2O}\, {P_{H_2}}^{-1} + k_3\, {P_{H_2}}^{0.5} + k_4\, P_{H_2O}} \quad \left[\frac{\text{kmol}}{\text{kg}_{\text{cat}}\text{s}}\right] \qquad \textit{Equation 7-2}$$

where the kinetic constants k_i are expressed according to Equation 7-3.

$$lnk_i = A_i + \frac{B_i}{T} \qquad \textit{Equation 7-3}$$

Temperature is handled in Aspen Plus in K, while partial pressures in Pa. This issue necessitates a conversion before kinetic expressions are implemented in the software, when constants are available with different units. In this work, the modified constants from the study of Van-Dal and Bouallou were used [329] and they are given in Table 7-2.

Table 7-2: A_i and B_i parameters of the rearranged kinetic model [329].

i	A_i	B_i
1	-29.87	4811.2
2	8.147	0
3	-6.452	2068.4
4	-34.95	14928.9
5	4.804	-11797.5
6	17.55	-2249.8
7	0.1310	-7023.5

The Lurgi-type reactor was assumed to operate isothermally: saturated water (30 bar) is evaporated for maintaining the temperature at a constant level. This steam flow is then superheated in the HRSG and supplied to the gasifier. The reactor is considered as a tubular-type, where the catalyst is placed inside multiple tubes and the boiling water surrounds the tubes in the reactor shell. The MeOH reactor contains tubes with a length of 10 m and a diameter of 0.05 m. The number of reactor tubes was specified based on a constant *GHSV* value of 4000 h^{-1} according to experimental results from Yang et al. [330]. An equilibrium model reactor was modelled in parallel to the RPlug model (through stream duplication) to obtain the maximum potential MeOH yield under chemical equilibrium conditions at the specified temperature and pressure of the synthesis process. Downstream of the reactor, the product is cooled through heat exchange with the syngas feed stream and flashed in an adiabatic separator. A fraction of the gas by-product (60% of unreacted syngas) is recompressed and mixed with the syngas feed, while the rest of it is partially expanded and mixed with the syngas flow which is supplied to the GT combustor. The liquid, crude-MeOH stream is reheated to 80 °C and sent to a distillation column to recover the purified MeOH product (with purity ≥ 99.0 wt.%). The distillation column has 50 theoretical stages, a reflux ratio equal to 1.4 and a condenser pressure of 1.2 bar. Heat for the distillation reboiler is supplied by saturated steam of the same quality (2.5 bar) as the steam supplied to the desorber column reboiler of the AGR process.

In contrast to Scenarios I and II, a steam reheat was not applied in the SC of Scenario III due to the smaller thermal input to the HRSG. In all scenarios, heat recovery in the BIGCC plant is carried out through a heat exchanger network for recovering heat in the SC and exchanging heat between process streams (e.g. gasification agent preheating). Heat exchangers along the syngas cleaning and conditioning path were modelled for evaporating saturated water from the SC at two HRSG pressure levels. A minor flow of water at 2.5 bar is also recirculated and evaporated in a syngas cooler to supply latent heat to the plant reboilers as in [282]. Minimum temperature approach and all other major process modeling assumptions are summarized in Table 7-3.

Table 7-3: Summary of main process modeling assumptions of the present study.

Component	Process parameter	Value
ASU	HP column/LP column/booster pressure (bar)	5.5/1.6/30
	Booster split fraction (−)	0.2
	O_2 product specification (vol.%)	≥ 95.0
	HP/LP distillation column stages (−)	30/35
Biomass dryer	Inlet/outlet flue gas temperature (°C)	220/95
Gasifier	Temperature/pressure (°C/bar)	900/29
	O_2 inlet temperature (°C)	200
	Steam inlet temperature (°C)	350
	Carbon conversion efficiency (%)	98
	In-bed desulfurization (as % of fuel S)	60
	Heat losses (% of input biomass HHV)	1
Autothermal catalytic reformer	Outlet syngas temperature (°C)	910
	Tar and C_{2+} conversion (%)	99
	CH_4 conversion (%)	70
	NH_3 conversion (%)	90
HCl removal (Na_2CO_3 sorbent)	Inlet syngas temperature (°C)	420
H_2S removal (ZnO sorbent)	Inlet syngas temperature (°C)	350
WGS reactors	WGSHT inlet temperature (°C)	350
	WGSLT inlet temperature (°C)	200
AGR unit	K_2CO_3 concentration (wt.%)	30
	Absorber pressure (bar)	25
	Desorber pressure (bar)	1.5
	Lean solvent loading (−)	0.3
	Syngas inlet temperature (°C)	122
CO_2 storage	Compressor type, storage pressure (bar)	3-stage, 100 bar
Gas turbine	Pressure ratio	15
	Combustor pressure loss (% of inlet)	4
	TIT_{max} (°C)	1230
	Compressor polytropic efficiency (−)	0.90
	Turbine isentropic efficiency (−)	0.88
	Flue gas temperature at the GT exit (°C)	550
HRSG	Flue gas temperature to the stack (°C)	75
	HP/RH/LP levels (bar)	110/30/4.2
	HP turbine inlet temperature (°C)	520
	Minimum temperature approach in HRSG (°C)	20
Steam turbine	Isentropic efficiency, all stages (−)	0.82
	Condenser pressure (bar)	0.06
MeOH synthesis	MeOH synthesis temperature/pressure (°C/bar)	234/52.5
	Unreacted syngas recirculation rate (%)	60
	H_2/CO ratio at reactor inlet (−)	2.5
	$GHSV$ (h^{-1})	4000
	MeOH product purity (wt.%)	≥ 99.0
Heat exchangers	Minimum temperature approach, gas/liquid (K)	10
	Minimum temperature approach, gas/gas (K)	20
Compressors	Polytropic efficiency (−)	0.8
	Intercooling temperature (°C)	35
Pumps	Pump efficiency (−)	0.78
Expanders	Isentropic efficiency (−)	0.88
Other	Pressure drop* (as % of inlet pressure)	1
	Mechanical efficiency for compressors, pumps etc. (−)	0.99
	Generator efficiency (−)	0.98

*considered for all heat exchangers and reactors

Different thermodynamic property methods were used for the process simulation in Aspen Plus. The general property method applied was Peng-Robinson with Boston–Mathias alpha function (PR–BM), while MeOH synthesis was modelled with RKS method. In addition, STEAMNBS was used for the water/steam properties. Furthermore, the electrolyte-NRTL model with the SRK EOS was applied for modeling the hot potassium carbonate process. Finally, the effect of the following parameters was investigated in the context of the present investigation:

- *STBR*: In Scenario I, the steam-to-biomass ratio defined as the ratio between the total H_2O (steam and biomass moisture) mass flow rate to the mass flow rate of dry biomass into the gasifier was adjusted to values of 0.60, 0.87 (base-case Scenario I) and 1.09. Those values cover the wide operation range of the IGT pressurized gasifier [318]. In the section of results, these are described as Scenarios I-LS, I-MS and I-HS, respectively. An *STBR* value of 0.87 was kept constant in Scenarios II and III.
- *CO_2 capture rate*: In Scenario II, the CO_2 capture rate was varied with values of 50, 70 and 90% (base-case Scenario II). In the section of results, these are described as Scenarios II-50%, II-70% and II-90%, respectively.
- *Syngas split to MeOH synthesis*: In Scenario III, the split fraction of syngas flow rate for MeOH synthesis to the syngas flow rate to the GT combustor downstream of the AGR unit was varied with values of 25% and 50%. In the section of results, these are described as Scenarios III-25% MeOH and III-50% MeOH (base-case Scenario III), respectively.

7.2.2 Performance indices and exergy analysis methodology

Regarding gasification performance and operation, definitions for the main indices, namely *STBR*, *λ*, *CGE* and *CCE* have been presented in Chapter 1. In this study, the energy efficiency of the BIGCC configurations is calculated on a LHV basis as shown in Equation 7-4

$$\eta = \frac{\dot{m}_{MeOH} LHV_{MeOH} + P_{el,net}}{\dot{m}_{biom} LHV_{biom}} \qquad \textit{Equation 7-4}$$

where $P_{el,net}$ is the net electric power (MW), $\dot{m}_{biom}$ is the biomass mass flow rate (kg s^{-1}), LHV_{biom} the LHV of biomass (MJ kg^{-1}), $\dot{m}_{MeOH}$ the mass flow rate of CH_3OH product (kg s^{-1}) and LHV_{MeOH} is the LHV of CH_3OH (MJ kg^{-1}). The net electric power is calculated as

$$P_{el,net} = P_{el,net,GT} + P_{el,SC} + P_{el,ex} - P_{el,comp} - P_{el,pumps} \qquad \textit{Equation 7-5}$$

However, energy balances do not provide information about the internal losses of a process. In addition, they treat all forms of energy as equal without differentiating the quality of different energy flows which are exchanged across the system boundaries. In order to achieve this differentiation, it is necessary to include the 2nd Law of Thermodynamics in the analysis and introduce the term “exergy”. Exergy is the maximum work that can be produced when a material or heat stream is brought to equilibrium relatively to a reference environment. This reference environment is made of specific chemical species and it has constant temperature and pressure (reference conditions). An exergy balance for a single process or a whole plant shows us how much of the usable work input (exergy) provided to the process is consumed by the process itself. This “consumed exergy” is described as irreversibility (I).

The exergy of a material stream, E_i (W), comprises four (4) terms and it is defined as

$$E_i = E_{i,k} + E_{i,p} + E_{i,ph} + E_{i,ch} \qquad \textit{Equation 7-6}$$

where $E_{i,k}$ is the kinetic exergy, $E_{i,p}$ the dynamic exergy, $E_{i,ph}$ the physical exergy and $E_{i,ch}$ the chemical exergy. In the framework of this investigation, the kinetic and dynamic exergy terms are considered negligible and exergy is calculated as the sum of physical and chemical exergy terms as in Equation 7-7

$$E_i = N_i(e_{i,ph} + e_{i,ch}) \qquad \textit{Equation 7-7}$$

where $e_{i,ph}$ is the specific physical exergy (J mol^{-1}), $e_{i,ch}$ the specific chemical exergy (J mol^{-1}) and N is the total molar flow rate (mol s^{-1}).

The specific (molar) physical exergy $e_{i,ph}$ of a material stream is calculated with respect to the reference conditions as

$$e_{i,ph} = (h_i - h_0) - T_0(s_i - s_0) \qquad \textit{Equation 7-8}$$

In Equation 7-8, h_i is the enthalpy (J mol^{-1}) and s_i the entropy (J mol^{-1} K^{-1}) of a stream i at the current thermodynamic state, while h_0 and s_0 are the enthalpy and entropy at reference conditions. In this work, the reference conditions for exergy calculations were defined as (T_0, P_0)=(298 K, 1 bar). Moreover, the specific chemical exergy $e_{i,ch}$ of a gas stream equals the sum of the exergy of its k components reduced by the compression work as shown in Equation 7-9

$$e_{i,ch} = \sum_k x_k e_{0,k} + RT_0 \sum_k x_k \ln(x_k) \qquad \textit{Equation 7-9}$$

where x_k is the mole fraction and $e_{0,k}$ the specific chemical exergy of a species k in the mixture at reference conditions (J mol^{-1}), while R denotes the ideal gas constant (8.314 J mol^{-1} K^{-1}). The second term of the right-hand part in Equation 7-9 is always a negative number, which means that the chemical exergy of a multicomponent mixture is always smaller than the sum of exergy values of its individual species at the specified temperature and pressure. For the same reference conditions as those used in this work, the values of $e_{0,k}$ were taken from tables available in [331]. Moreover, it has been assumed that the ambient temperature is the same as the reference temperature for the exergy calculations. Thus, no correction of chemical exergy values is necessary.

For liquid mixtures, chemical exergy is calculated according to the generalized Equation 7-10.

$$e_{i,ch} = \sum_k x_k e_{0,k} + RT_0 \sum_k x_k \ln(\gamma_k x_k) \qquad \textit{Equation 7-10}$$

The activity coefficients γ_k are generally different than unity for real solutions, while they are always equal to unity in an ideal solution. In the latter case, Equation 7-10 can be simplified and converted to Equation 7-9, which has been also adopted in this study.

The values required to calculate the exergy of each material stream (enthalpy, entropy, molar fraction and molar flow) are calculated within the model developed in Aspen Plus. To calculate the reference enthalpy and entropy, transfer blocks were used to reproduce all process streams and their copies were linked to "heater" modules adjusted for the reference conditions (T_0, P_0). Nevertheless, the calculation of solid fuel exergy (biomass) requires a different methodology as discussed next. According to Szargut et al. [332, 333], the specific chemical exergy of biomass $\varepsilon_{ch,biom}$ (MJ kg^{-1}) can be calculated as

$$e_{ch,biom} = \beta(LHV_{biom} + w_m h_w) \qquad \textit{Equation 7-11}$$

where LHV_{biom} is the lower heating value of biomass (MJ kg^{-1}), w_m is the biomass moisture content (wt.%) and h_w is the enthalpy of water evaporation (2.442 MJ kg^{-1}). The coefficient β is derived through statistical correlations and it depends on biomass composition. For woody biomass, which was the case in this investigation, it is calculated according to Equation 7-12.

$$\beta = \frac{1.0412 + 0.216\frac{H}{C} - 0.2499\frac{O}{C}\left(1 + 0.7884\frac{H}{C}\right) + 0.045\frac{N}{C}}{1 - 0.3035\frac{O}{C}} \qquad \textit{Equation 7-12}$$

The terms $\left(\frac{H}{C}\right)$, $\left(\frac{O}{C}\right)$ and $\left(\frac{N}{C}\right)$ describe the mass ratios of H, C, O and N in biomass. A review of available correlations for the calculation of biomass chemical exergy can be found in [334].

The exergy balance equation for a process is given in Equation 7-13 and it was applied to calculate process irreversibilities I.

$$\sum_{in} E_j + \sum_{in} E_{T_{in}}^{Q} + \sum_{in} E^{w} = \sum_{out} E_k + \sum_{out} E_{T_{out}}^{Q} + \sum_{out} E^{w} + I \qquad \textit{Equation 7-13}$$

The terms $\sum_{in} E_j$ and $\sum_{out} E_k$ denote the total exergy flow of inlet and outlet material streams in the process, respectively. The terms $\sum_{in} E^{w}$ and $\sum_{out} E^{w}$ express the exergy of mechanical power supplied and produced in the process, respectively (equal to the mechanical power itself). The total exergy flow of inlet and outlet heat stream to the process are described as $\sum_{in} E_{T_{in}}^{Q}$ and $\sum_{out} E_{T_{out}}^{Q}$, respectively. Particularly, the exergy of a heat stream Q to or from the process is calculated according to Equation 7-14 [335]

$$E_T^Q = Q\left(1 - \frac{T_0}{T}\right) \qquad \textit{Equation 7-14}$$

where T is the temperature that the heat stream is available (K).

The exergy efficiency ε of the BIGCC plant is described by Equation 7-15

$$\varepsilon = \frac{\dot{m}_{MeOH} e_{MeOH} + P_{el,net}}{\dot{m}_{biom} e_{ch,biom} + E_{air,ASU} + E_{air,GT} + E_w} \qquad \textit{Equation 7-15}$$

where e_{MeOH} is the specific chemical exergy of CH_3OH (MJ kg^{-1}), $E_{air,ASU}$ is the exergy flow of air supplied to the ASU (MW), $E_{air,GT}$ is the exergy flow of air supplied to the GT (MW) and E_w is the exergy flow of make-up water to the plant (MW).

Finally, the exergy efficiency of a subsystem k of the plant is defined as

$$\varepsilon_k = 1 - \frac{I_k}{E_k^{in}} \qquad \textit{Equation 7-16}$$

where I_k is the irreversibility of the process and E_k^{in} is the total exergy flow into the process.

7.3 Results and discussion

7.3.1 Gasification performance, syngas composition and conditioning

As the thermochemical conversion step is a core part of the process, the gasification results, as derived by the Aspen Plus simulation, are firstly discussed. The variations of $STBR$ in Scenarios I-LS and I-HS corresponded to a change of the base-case value by -25% and +25%, respectively. It was found that the $STBR$ reduction decreases the H_2, CO_2 and CH_4 concentration in syngas, while it causes an increase in the CO concentration. From Figure 7-4, it can be seen that the $STBR$ change has a more notable effect on CO and CO_2 rather than H_2. On the other hand, it was found that the CH_4 content is weakly correlated with $STBR$. Its high composition in syngas (> 10 vol.%) can be attributed to the high gasification pressure of the IGT fluidized-bed gasifier. According to the experimental measurements of Evans et al. [318], an increase in $STBR$ within a range of 0.69 to 1.44 led to an increase in the percentages of H_2 and CO_2, while the levels of CO and CH_4 were reduced. During their original campaigns, it was suggested that the WGS reaction is favored under conditions of excess H_2O in the gasifier, resulting in a simultaneous increase in CO_2 and a decrease in CO concentration. In all cases, there was still an increase in the H_2O content in syngas due to incomplete consumption of the gasification agent, leading to an accumulation in the raw product gas. The composition values for the CO, H_2, CO_2 and CH_4 constituents as predicted by the Aspen Plus model are in agreement with the values in [318] for the gasification of woody biomass with H_2O/O_2 mixtures (CO: 10-20 vol.%, H_2: 15-35 vol.%, CO_2: 35-40 vol.%, CH_4: 13-18

vol.%). The trends are also in agreement with the experimental data published by Turn et al. [336], who attributed the effects of higher $STBR$ values to the WGS and steam reforming reactions. Differences compared to the latter study (e.g. increased CO_2 concentration in syngas) can be attributed to the presence of the oxidative agent in the present work for autothermal gasification.

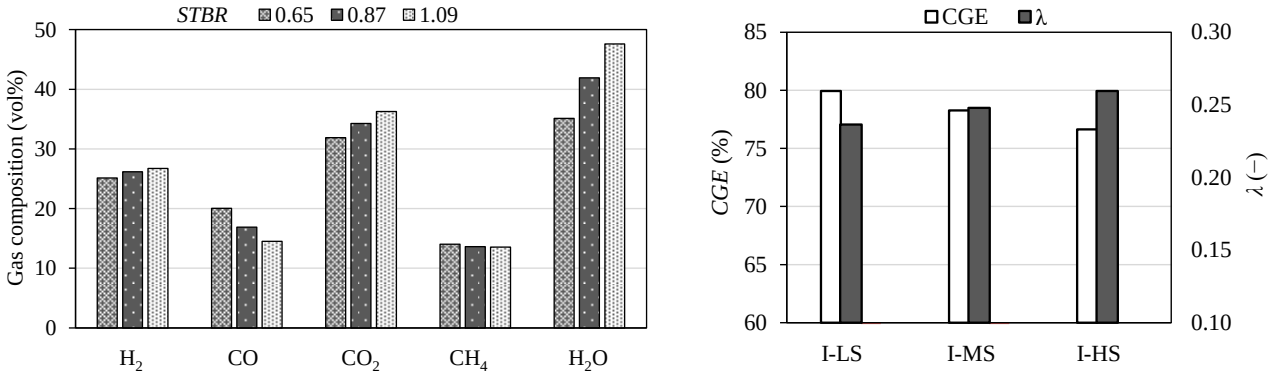

Figure 7-4: (Left) Effect of STBR on raw syngas composition (db apart from H_2O) and (Right) effect of STBR on λ and CGE for Scenarios I-LS (low STBR), I-MS (medium STBR) and I-HS (high STBR).

At this point, it is worth commenting on some parameters related to the downstream treatment and utilization of the syngas produced. At temperatures above 800 °C, the following four reactions can lead to carbon deposition and catalyst deactivation.

$$C_nH_m \rightarrow nC(s) + \frac{m}{2}H_2 \qquad R\ 7\text{-}8$$

$$C_nH_m \rightarrow \text{olefins} \rightarrow \text{char} \qquad R\ 7\text{-}9$$

$$CH_4 \leftrightarrow C(s) + 2H_2 \qquad R\ 7\text{-}10$$

$$CH_4 \leftrightarrow C(s) + 2H_2 \qquad R\ 7\text{-}11$$

The ratio H_2O/C_{ref} expresses the ratio of H_2O molar flow rate to the molar flow rate of C in the carbon-containing compounds in syngas, which are subject to steam reforming reactions. Particularly, it may be expressed for the compounds CH_4, C_2H_4, C_2H_6, C_6H_6 and $C_{10}H_8$ of the present model as

$$\frac{H_2O}{C_{ref}} = \frac{\dot{n}_{H_2O}}{\dot{n}_{CH_4} + 2\dot{n}_{C_2H_4} + 2\dot{n}_{C_2H_6} + 6\dot{n}_{C_6H_6} + 10\dot{n}_{C_{10}H_8}} \qquad R\ 7\text{-}12$$

Protection of the catalyst downstream of the gasifier requires a ratio of $H_2O/C_{ref} > 4$, according to experimental tests by Kaisalo et al. [323]. As noted in that work, the formation and deposition of carbon depends on additional factors such as the ratio of oxygen-to-carbon, the composition of hydrocarbons in syngas and the type of catalyst. For Scenarios I-LS ($STBR$ = 0.65), I-MS ($STBR$ = 0.87) and I-HS ($STBR$ = 1.09) of the present work, the ratio H_2O/C_{ref} in the synthesis gas was found to be 3.4, 4.8 and 5.9, respectively. Although in no case did thermodynamically solid C(s) formation occur within the model reforming unit, the $STBR$ parameter was fixed at 0.87 in all cases of Scenarios II and III. In addition, for scenarios considering cogeneration of MeOH (Scenarios III-25% MeOH and III-50% MeOH), the H_2/CO ratio is required to be greater than 2. When increasing the $STBR$ parameter from the minimum (I-LS) to the maximum value (I-HS), the ratio increases from 1.25 to 1.84. These values are particularly high compared to gasification solely with O_2. Thus, this technology is appropriate in cases where syngas utilization for catalytic synthesis through hydrogenation reactions is foreseen. The minimum H_2O/CO molar ratio for the WGS section is required to be greater than 2 and it is typically recommended to operate with a ratio even 50% higher than the minimum value [337]. The gasification parameters selected in this work lead to a H_2O/CO ratio of 2.4 upstream of the WGSHT reactor in all cases of Scenarios II and III.

Furthermore, the effect of $STBR$ on gasification efficiency and O_2 consumption can also be observed in Figure 7-4. For all scenarios, high CGE values over 75% were calculated and a maximum value of 79.9%. However, an increase in $STBR$ causes a decrease in CGE. This outcome indicates that operation of H_2O/O_2 gasification with reduced H_2O supply is beneficial in terms of energy conversion efficiency. This is similar to the outcome of operating allothermal gasification at higher $STBR$ values [70]. An explanation is that as the steam ratio increases, so does the thermal energy requirement to maintain the gasification temperature. During conditions of high $STBR$ operation, heat is consumed to heat the inert steam which is not consumed in the process. This can be verified by the λ increase as the steam flow rate increases: the necessary amount of O_2 agent increases to maintain gasification temperature at 900 °C.

7.3.2 Comparative energetic assessment of BIGCC configurations

The basis for the energetic and exergetic assessment was the detailed simulation of BIGCC configurations. Based on the simulation results, it was possible to obtain mass and energy balances and determine process stream properties. Selected results illustrating the thermodynamic state and composition of syngas, flue gas and other process streams are presented in Table 7-4, Table 7-5 and Table 7-6. Mass flow rates of all process streams are given divided by the mass flow of dry biomass (DB) entering the process.

Table 7-4: Selected process stream results of Scenario I (LS, MS and HS denote low, medium and high STBR cases, respectively).

		$\dot{m}/\dot{m}_{DB}$	T	P	H_2	CO	CO_2	CH_4	H_2O	O_2	N_2	C_2+ HCs
		(–)	(°C)	(bar)	Concentration (mol.%)							
A	I-LS	2.04	900	29.00	16.28	13.01	20.69	9.07	35.07	0.00	4.97	0.50
	I-MS	2.27	900	29.00	15.23	9.83	19.92	7.95	41.87	0.00	4.41	0.44
	I-HS	2.50	900	29.00	14.03	7.61	19.02	7.09	47.58	0.00	3.97	0.39
B	I-LS	2.16	909	28.71	25.96	19.47	16.69	2.34	30.88	0.00	4.61	0.00
	I-MS	2.39	909	28.71	24.47	15.56	16.87	2.09	36.81	0.00	4.15	0.00
	I-HS	2.63	909	28.71	22.91	12.68	16.72	1.89	41.97	0.00	3.79	0.00
C	I-LS	2.16	200	21.00	25.96	19.47	16.69	2.34	30.89	0.00	4.61	0.00
	I-MS	2.39	200	21.00	24.47	15.56	16.87	2.09	36.82	0.00	4.15	0.00
	I-HS	2.63	200	21.00	22.91	12.68	16.73	1.89	41.97	0.00	3.79	0.00
D	I-LS	8.57	75	1.01	0.00	0.00	7.34	0.00	12.63	12.47	66.70	0.00
	I-MS	8.38	75	1.01	0.00	0.00	7.57	0.00	15.20	11.82	64.59	0.00
	I-HS	8.18	75	1.01	0.00	0.00	7.80	0.00	17.93	11.13	62.34	0.00

A: Gasifier outlet, B: Catalytic autothermal reformer outlet, C: Syngas inlet to GT, D: Flue gas from HRSG

Figure 7-5 depicts the electric power balance considering the GT, steam turbine island and total electric power consumption of plant components, while in Figure 7-6, the breakdown of the electricity self-consumption of each scenario is analyzed. Firstly, Scenario I variants show a slight increase in GT power generation (including upstream syngas expansion) due to the increased syngas flow rate as $STBR$ increases (see Table 7-4). On the other hand, the generated electric power in the SC decreases, since as $STBR$ increases, so does the demand of steam from the gasifier, which is provided through extraction from an intermediate steam turbine pressure level. Moreover, the total power consumption within the BIGCC plant increases from Scenario I-LS to Scenario I-HS. As the demand for O_2 in the gasifier increases (higher λ value), so does the ASU consumption, as well as the pumps' power consumption in the SC. ASU occupies the largest share of total power consumption in Scenario I by far, accounting for a share of 85%. The specific power consumption to produce pure O_2 in the present work was found to be 1.14 MW_e $(kg\text{-}O_2\ s^{-1})^{-1}$. This value is slightly higher than the reference cryogenic air distillation units, which is ca. 1.0 MW_e $(kg\text{-}O_2\ s^{-1})^{-1}$ [338]. Reductions in ASU power consumption can occur through optimization of operating conditions and extraction of compressed air from the GT (ASU-GT integration), as described by Jones et al. [322]. In addition, the low-enthalpy heat discharged through intercooling between the ASU compressors in the present model can be recovered. In this case, an ORC unit can convert part of the recovered heat into electric power, thereby reducing ASU consumption by an estimated 10% [321].

Table 7-5: Selected process stream results of Scenario II (percentages in different cases denote the CO_2 capture rate).

		$\dot{m}/\dot{m}_{DB}$ (–)	T (°C)	P (bar)	H_2	CO	CO_2	CH_4	H_2O	O_2	N_2
					Concentration (mol.%)						
A	II-50%	2.39	909	28.71	24.47	15.56	16.87	2.09	36.81	0.00	4.15
	II-70%	2.39	909	28.71	24.47	15.56	16.87	2.09	36.81	0.00	4.15
	II-90%	2.39	909	28.71	24.47	15.56	16.87	2.09	36.81	0.00	4.15
B	II-50%	2.39	350	27.58	24.47	15.56	16.87	2.09	36.82	0.00	4.15
	II-70%	2.39	350	27.58	24.47	15.56	16.87	2.09	36.82	0.00	4.15
	II-90%	2.39	350	27.58	24.47	15.56	16.87	2.09	36.82	0.00	4.15
C	II-50%	2.39	200	26.76	34.81	5.22	27.21	2.09	26.47	0.00	4.15
	II-70%	2.39	200	26.76	34.81	5.22	27.21	2.09	26.47	0.00	4.15
	II-90%	2.39	200	26.76	34.81	5.22	27.21	2.09	26.47	0.00	4.15
D	II-50%	2.09	122	25.45	45.91	0.80	37.05	2.44	8.92	0.00	4.85
	II-70%	2.09	122	25.45	45.91	0.80	37.05	2.44	8.92	0.00	4.85
	II-90%	2.09	122	25.45	45.91	0.80	37.05	2.44	8.92	0.00	4.85
E	II-50%	1.25	134	25.00	57.16	0.97	23.09	2.47	10.27	0.00	6.04
	II-70%	0.90	133	25.00	64.29	1.08	15.59	2.53	9.72	0.00	6.79
	II-90%	0.54	163	25.00	73.84	1.24	5.97	2.62	8.52	0.00	7.80
F	II-50%	1.58	200	21.00	50.00	0.85	20.19	2.16	8.92	0.04	17.83
	II-70%	1.47	200	21.00	50.00	0.84	12.12	1.97	7.48	0.07	27.52
	II-90%	1.37	200	21.00	50.00	0.84	4.04	1.78	5.67	0.10	37.57
G	II-50%	8.60	75	1.01	0.00	0.00	4.27	0.00	12.52	12.46	69.89
	II-70%	7.92	75	1.01	0.00	0.00	2.79	0.00	12.28	12.46	71.61
	II-90%	7.38	75	1.01	0.00	0.00	1.27	0.00	11.97	12.46	73.43

A: Catalytic autothermal reformer outlet, B: WGSHT reactor inlet, C: WGSLT reactor inlet, D: Absorber column inlet (syngas), E: Absorber column outlet (syngas), F: Syngas inlet to GT, G: Flue gas from HRSG

Table 7-6: Selected process stream results of Scenario III (percentages in different cases denote the syngas split for MeOH cogeneration).

		$\dot{m}/\dot{m}_{DB}$ (–)	T (°C)	P (bar)	H_2	CO	CO_2	CH_4	H_2O	O_2	N_2	CH_3OH
					Concentration (mol.%)							
A	III-25%	2.39	909	28.71	24.47	15.56	16.87	2.09	36.81	0.00	4.15	0.00
	III-50%	2.39	909	28.71	24.47	15.56	16.87	2.09	36.81	0.00	4.15	0.00
B	III-25%	0.72	350	27.58	24.47	15.56	16.87	2.09	36.82	0.00	4.15	0.00
	III-50%	0.72	350	27.58	24.47	15.56	16.87	2.09	36.82	0.00	4.15	0.00
C	III-25%	1.68	350	27.58	24.47	15.56	16.87	2.09	36.82	0.00	4.15	0.00
	III-50%	1.68	350	27.58	24.47	15.56	16.87	2.09	36.82	0.00	4.15	0.00
D	III-25%	1.82	122	25.45	37.90	17.13	27.45	2.87	8.89	0.00	5.71	0.00
	III-50%	1.82	122	25.45	37.90	17.13	27.45	2.87	8.89	0.00	5.71	0.00
E	III-25%	0.76	124	25.00	55.04	24.15	2.00	2.95	7.56	0.00	8.30	0.00
	III-50%	0.76	124	25.00	55.04	24.15	2.00	2.95	7.56	0.00	8.30	0.00
F	III-25%	0.77	200	21.00	50.00	21.31	2.11	3.22	6.20	0.03	17.06	0.07
	III-50%	0.62	200	21.00	50.00	20.37	2.56	4.02	5.19	0.02	17.65	0.19
G	III-25%	0.29	234	52.50	55.49	22.01	3.12	4.97	0.09	0.00	14.05	0.27
	III-50%	0.58	234	52.50	55.49	22.02	3.12	4.97	0.09	0.00	14.04	0.27
H	III-25%	0.29	234	52.50	40.43	12.50	4.18	6.66	0.12	0.00	18.82	17.37
	III-50%	0.58	234	52.50	40.37	12.52	4.17	6.66	0.15	0.00	18.81	17.34
I	III-25%	0.29	40	1.20	0.00	0.00	0.53	0.02	0.00	0.00	0.01	99.43
	III-50%	0.17	40	1.20	0.00	0.00	0.53	0.02	0.00	0.00	0.01	99.43
J	III-25%	5.60	75	1.01	0.00	0.00	3.29	0.00	8.66	13.95	73.17	0.00
	III-50%	4.00	75	1.01	0.00	0.00	3.27	0.0	8.59	13.92	73.28	0.00

A: Catalytic autothermal reformer outlet, B: WGSHT reactor inlet, C: Bypass syngas stream of WGSHT, D: Absorber column inlet (syngas), E: Absorber column outlet (syngas), F: Syngas inlet to GT, G: MeOH reactor inlet, H: MeOH reactor outlet, I: MeOH product stream, J: Flue gas from HRSG

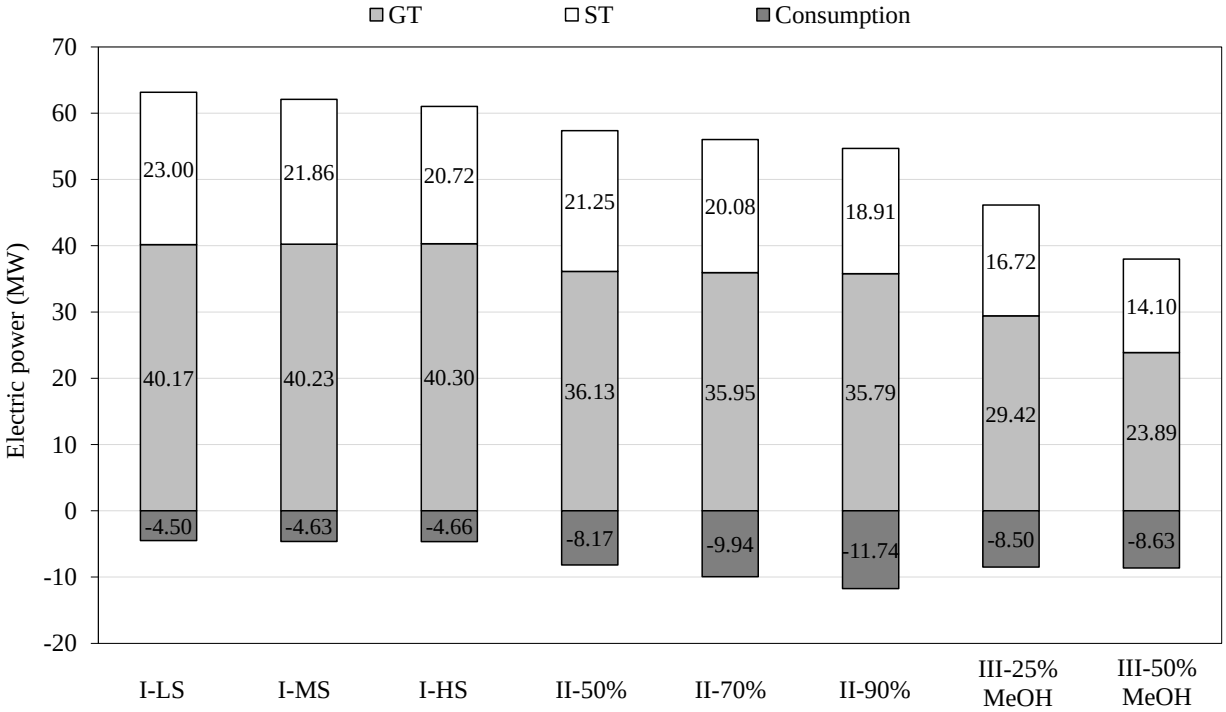

Figure 7-5: Electric power generation and consumption balance of Scenarios I (gasification steam amount variation), II (CO_2 capture rate variation) and III (MeOH cogeneration rate variation).

The variants of Scenario II show a decrease in the power output of the GT, which is due to a reduction in the syngas supply to the combustor (see Table 7-5). In addition, the power in the SC is significantly reduced, as the CO_2 desorption reboiler requires a significant amount of thermal power in the form of saturated steam. By increasing the CO_2 capture rate from 50% to 70% and then 90%, the heat duty requirement for solvent regeneration accordingly increases. Moreover, the total electricity consumption increases with increasing the CO_2 capture rate. As CO_2 capture increases, the product gas becomes richer in H_2 (even > 70 vol.% H_2). In order to respect the maximum allowable H_2 content upstream of the GT, an increased N_2 supply for syngas dilution is necessary. This limitation increases the power consumption of N_2 compressors downstream of the ASU. Furthermore, an increase in the CO_2 capture rate also results in an increase in the desorber off-gas flow rate for storage, which induces a higher power consumption of the CO_2 compressors. For a fairer comparison between different BIGCC-CCS scenarios in the present work, it was assumed that the lean loading into the absorption column was constant in each case (a = 0.3), as were the column stages. Therefore, as the required CO_2 capture rate increases, so does the ratio of the liquid solvent to the syngas flow rate (L/G). Thus, there is also an increase in the required pump power, as it is necessary to circulate a higher flow rate of the K_2CO_3 aqueous solution from the desorber to the absorber. Finally, the ASU's electricity consumption, as a share of the total plant power consumption, ranges from 33 to 48%, from 15 to 23% for N_2 compressors and from 28 to 35% for the CO_2 compressors (CCS unit).

From Figure 7-6 it can be observed that the CCS power consumption for the case II-90% is greater than that of Scenario III (both cases), in which CO_2 capture is fixed at 95%. In Scenario II, there is a two-stage WGS process upstream of the absorption column with the aim of increasing the carbon capture in the BIGCC plant. In Scenario III though, a single WGSHT reactor is implemented to adjust the ratio between H_2 and CO, so that syngas can be converted to MeOH. Based on this criterion, the mass flow rate to the WGS unit is also adjusted, while the remaining syngas flow bypasses the WGS reactor. As a result, the total CO_2 mass flow at the absorber inlet significantly varies between the two cases.

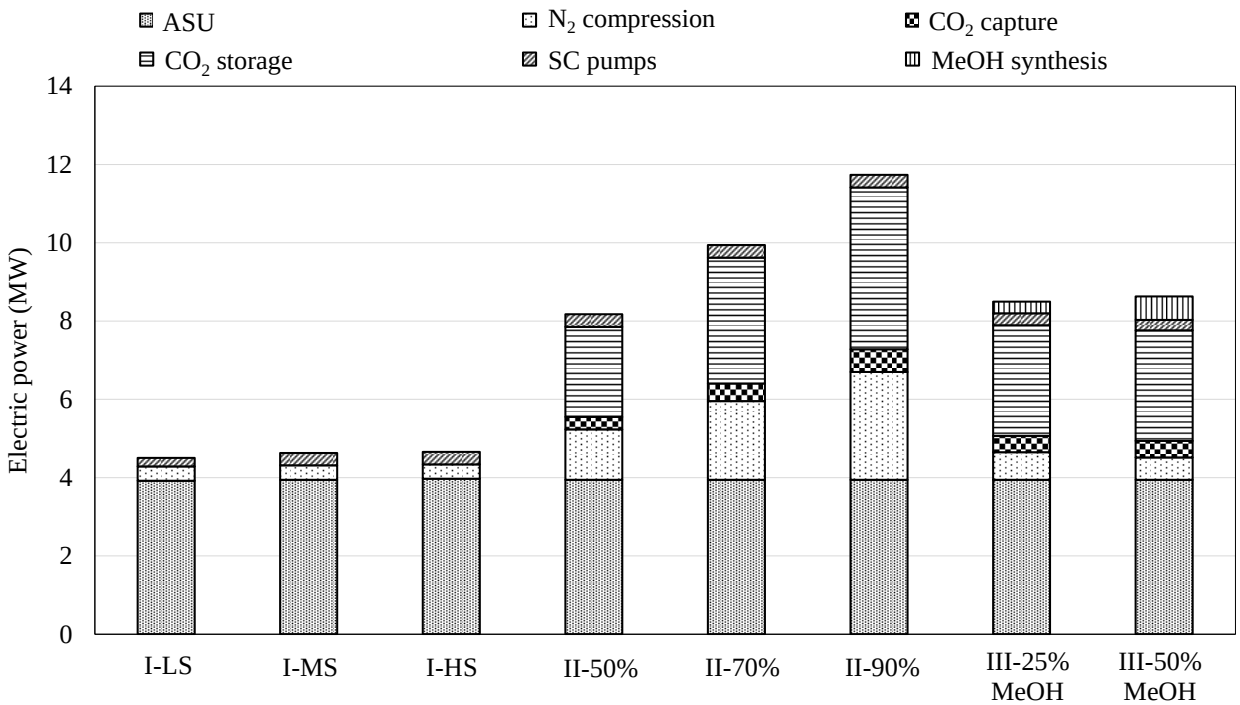

Figure 7-6: Electricity consumption per process of Scenarios I (gasification steam amount variation), II (CO_2 capture rate variation) and III (MeOH cogeneration rate variation).

The energy efficiency of the various BIGCC configurations is shown in Figure 7-7. The results indicate that achieving high energy efficiency is feasible in BIGCC plants integrated with a hot gas cleanup system and biomass drying. As expected, Scenario I has the highest energy efficiency due to the lack of a CCS unit.

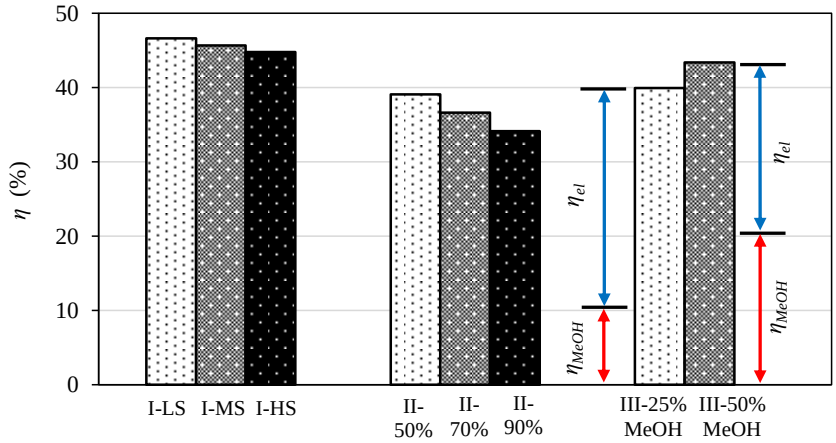

Figure 7-7: Energy efficiency comparison for BIGCC configurations of Scenarios I (gasification steam amount variation), II (CO_2 capture rate variation) and III (MeOH cogeneration rate variation).

The gradual increase in *STBR* reduces the plant efficiency by 1.8 percentage points, while a significantly lower energy efficiency compared to the reference non-CCS scenario can be noted for Scenarios II-50%, II-70% and II-90%. For CO_2 capture of 50, 70 and 90%, the energy efficiency declines by 6.5, 9.0 and 11.5 percentage points, respectively. In the case of electricity and MeOH cogeneration, energy efficiency is improved compared to Scenario II. As the syngas split ratio for MeOH synthesis increases from 25% to 50%, the BIGCC plant energy efficiency increases by 3.5 percentage points, only slightly below the values of Scenario I. Power and methanol energy efficiencies are 29.91% and 10.02% for Scenario IIIa, respectively, and for IIIb 23.33% and 20.04%.

Regarding the MeOH synthesis unit, the CO conversion in the catalytic reactor was found to be 57.5%. On the other hand, the equilibrium MeOH reactor predicted a theoretical maximum CO conversion for the given conditions at about 65.8%. Experimental measurements for the conversion of CO-rich syngas to MeOH over a Cu/ZnO catalyst have been published by Inui et al. [339] and Yang et al. [330]. Inui et al. [339] found that the conversion efficiency of CO can reach up to 60% at 80 bar, *GHSV* values in the range 18,000-38,000 h^{-1} (significantly higher compared to the present work) and a temperature of about 250 ℃. Yang et al. [330] reported that the maximum CO conversion (~ 50%) occurs at temperatures between 240-250 ℃ for *GHSV* = 4000 h^{-1}. Differences between tests influence the final results, such as the H_2/CO and CO/CO_2 ratios in each study and the specific catalyst type. The kinetic model used in this work can be considered reliable under the specified operating conditions in the context of a process modeling study. However, a sensitivity analysis would be useful in order to verify its accuracy for variable process conditions (syngas composition, temperature, pressure, *GHSV* etc.).

7.3.3 Comparative exergetic assessment of BIGCC configurations

Figure 7-8 shows a comparison of exergy efficiency among the BIGCC configurations. The highest exergy efficiency was found for Scenario I-LS (38.35%). In Scenario II, exergy efficiency decreases with increasing the CO_2 capture rate. Between the base-case Scenarios I-MS and II-90%, an exergy efficiency decline by 9.4 percentage points was found. It is worth noting that the integration of the hot potassium carbonate process seems to marginally mitigate the exergy efficiency reduction of the BIGCC-CCS configuration compared to Selexol technology (reduction 9.6 percentage points) and more significantly compared to the integration of post-combustion chemical absorption with MEA (13 percentage points) [306]. Moreover, it must be noted that in the present work, a simplified CO_2 absorption process was modelled.

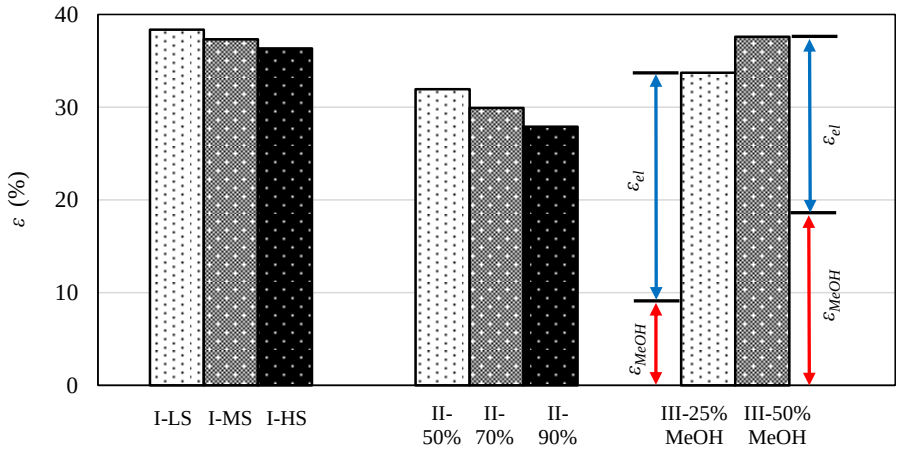

Figure 7-8: Exergy efficiency comparison for BIGCC configurations of Scenarios I (gasification steam amount variation), II (CO_2 capture rate variation) and III (MeOH cogeneration rate variation).

The model comprised an absorption column, desorption column and pump for solvent circulation, and it was assumed that the total flow is regenerated in the desorber before it is pumped to the absorber. Optimization of operating conditions or alternative configurations (e.g. UOP LoHeat™ technology for Benfield units) can induce further reduction in reboiler heat consumption. Implementing innovative desorption processes, such as crystallization, can greatly reduce the specificity heat consumption required for solvent regeneration even below 1.5 MJ kg^{-1} CO_2 according to Zhang et al. [340]. Moreover, as shown in Chapter 6, operation of desorber under vacuum conditions (400 mbar) or the utilization of PZ as a promoter can further reduce the specific heat consumption calculated here (~ 2.25 MJ kg^{-1} CO_2) by approximately 20%. Finally, in contrast with the energy efficiency results, Scenario III-50% MeOH achieves higher exergy efficiency compared to the reference Scenario I-MS.

In order to identify the processes that contribute more to the total exergy destruction (as well as exergy losses with waste streams) of the BIGCC plants, detailed exergy balances for all components and scenarios were

carried out. Figure 7-9 presents the exergy balance results for the base-case Scenarios I, II and III, as well as the distribution of the total exergy destruction to the plant components/processes. It can be observed that the cogeneration of MeOH decreases the share of exergy destruction in the BIGCC plant. This is expected because the exergy efficiency of a biomass-to-MeOH process exceeds the exergy efficiency of an electricity-only BIGCC plant [314]. It is therefore possible to achieve a reduction of the exergy destruction share by ca. 9 percentage points compared to the base-case Scenario II-90%. Moreover, it can also be noted that the major exergy losses from the plant are due to flue gas emissions, CO_2 effluent to storage (accounted as product in certain studies) and the waste N_2-rich stream from the ASU.

As seen in the exergy destruction diagrams, a grouping of certain processes has been performed to simplify the presentation of the results and comparisons among them. The largest exergy destruction is located in the GT of the BIGCC plant for Scenarios I and II, with shares of 45% and 40% of total exergy destruction, respectively. The significant contribution of the GT is mainly caused by the combustion process, since the efficiency of the compression and expansion components is significantly higher [341]. A reduction of the exergy destruction penalty in the GT can be achieved by increasing the maximum *TIT*, which was considered low (1230 °C) in the present study. This decision was based on the fuel nature and in line with values from [306] for an SGT-600 gas turbine. The gasification unit is the second largest source of exergy destruction for the electricity-only BIGCC configurations, while it becomes the major one when electricity and MeOH are cogenerated. For the BIGCC plants without CCS technology, the steam turbine island and the hot gas purification and heat recovery system along the syngas path account for about 5% each of the total exergy destruction in the plant. Their contribution decreases in the variants of Scenario II, since CO_2 capture induces a more significant penalty in the CCS unit. The exergy destruction share for the baseline BIGCC plant with 90% CO_2 capture is in the order of 10%, while taking into account the exergy losses with the CO_2 stream to storage, the overall exergy destruction percentage on the basis of incoming exergy is 14%, a value slightly lower than CO_2 absorption by Selexol process [306].

When comparing Scenarios I-LS, I-MS and I-HS, it can be concluded that an increase in the value of *STBR* leads to an increase in exergy destruction of the gasifier and the hot syngas cleanup system. This higher exergy destruction at the gasification stage is associated with the dilution of the product gas with the H_2O agent and with the increased exergy input required to complete the gasification process. A significant exergy destruction (2.5-3.2 MW) was calculated for the high-temperature heat exchanger downstream of the reforming unit. Among Scenarios II-50%, II-70% and II-90%, it can be noted that increasing the CO_2 capture rate from 50% to 90% causes a two-fold increase of the exergy destruction ratio of the CCS unit. Interestingly, the exergy destruction ratios in the HRSG and ASU are relatively small (< 5% of total). The highest exergy destruction ratio of ASU for Scenario II compared to Scenario I can be attributed to the relatively smaller thermal power transferred to the bottoming cycle and the increased power consumption of N_2 compression unit. Particularly, large exergy efficiency values exceeding 97% were calculated for the HRSG. This is consistent with the HRSG efficiency reported by Atsonios et al. for a combined-cycle plant fuelled with H_2 [342]. On the other hand, the exergy efficiency of the ASU was found to be low (ca. 58%). The exergy destruction in the MeOH synthesis unit was equal to 0.7 MW (Scenario III-50% MeOH), which is much smaller compared to the exergy destruction in the gasification section (29.4 MW). In Scenario III-50% MeOH, the exergy destruction values for the AGR and CO_2 compression sections of the CCS unit are 4.9 and 1.3 MW, respectively. The exergy efficiency of the gasifier in this work was ca. 82%, slightly lower than that of allothermal gasification at ambient pressure and low-to-moderate *STBR* [343].

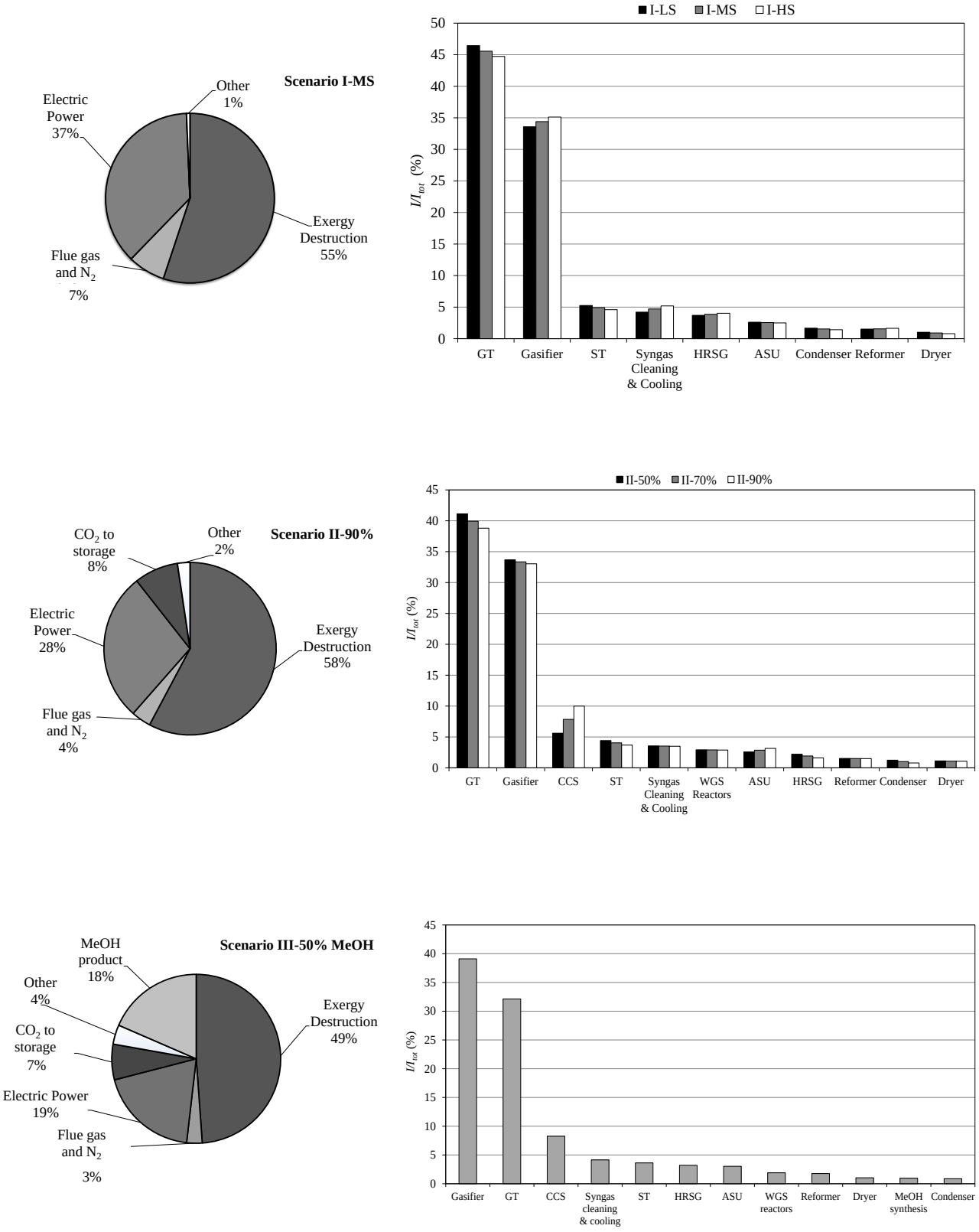

Figure 7-9: (Left column) Overall exergy balance of BIGCC base-case Scenarios I-MS (top/left), II-90% (middle/left) and III-50 % MeOH (bottom/left) with respect to the total exergy input. (Right column) Exergy destruction distribution per process for Scenarios I-LS, I-MS, I-HS (top/right), Scenarios II-50%, II-70%, II-90% (middle/right) and Scenario III-50% MeOH (bottom/right).

7.3.4 CO_2 purity aspects for CCS application

An important aspect related to the transportation of the off gas from the AGR unit through pipelines (as part of a CCS system) is the composition of the CO_2 stream. Its quality and specifications are associated with technical and economic implications as noted in [344]. Therefore, it is considered useful to identify the feasibility to integrate the proposed AGR unit with a broad CCS scheme/network. The Dynamis study has provided allowable specifications for the CO_2-rich off gas, taking into account various constraints such as safety and toxicity limits, infrastructure durability and transport efficiency [345]. A comparison of the off gas quality as derived from the present study (Scenario II-90%) and the Dynamis study pipeline specifications is shown in Table 7-7.

Table 7-7: CO_2 stream composition compared to specifications from the Dynamis study [345].

Component	Simulation results	Dynamis specification
CO_2	96.9 vol.%	> 95.5 vol.%
H_2O	3000 ppmv	< 500 ppmv
H_2S	25 ppmv	< 200 ppmv
CO	816 ppmv	< 2000 ppmv
CH_4	2.3 vol.%	< 4.0 vol.%
Non-condensable gases	< 3 vol.%	< 4.0 vol.%

It can be noted that the compressed CO_2 stream satisfies the pipeline specifications apart from the moisture content, which was found to exceed the Dynamis limit. Therefore, further cooling of the desorber effluent prior to the compressors could be a solution to reduce the H_2O content. In addition, the low H_2S content can be attributed to the in-bed desulfurization and the low sulfur content in wood. However, it is expected that further off gas treatment may be necessary for high-sulfur biomass, when no desulfurization occurs upstream of the AGR unit (either in-bed or through guard bed system downstream of the gasifier).

7.4 Conclusions

In this chapter, energy and exergy analyses of various biomass-fuelled IGCC configurations were presented, aided by process modeling in Aspen Plus software. Emphasis was put on the integration of hot syngas cleanup processes and CO_2 capture at high temperature and pressure conditions *via* aqueous K_2CO_3 solutions (pre-combustion capture). For the BIGCC-CCS plant and in the direction of partial independence from electricity price fluctuations, MeOH cogeneration by using up to and 50% of the product gas was investigated. Regarding the gasification process, a higher *STBR* value decreased the gasification efficiency and increased the required λ for the autothermal process due to steam dilution of the syngas mixture. Although the lowest *STBR* value is preferable in terms of process efficiency, a compromise is necessary in order to ensure the required excess steam in syngas. This is necessary for the operation of the downstream catalytic tar reformer and WGS reactors in the IGCC-CCS scenarios. For the cases without CCS application, it was found that the combination of biomass gasification with O_2/H_2O mixtures, hot gas purification and biomass drying can provide a high energy efficiency for power generation (> 46%).

An overwhelming share of the total electric consumption within the plant is occupied by the ASU, which significantly declines though when CCS is applied. In the latter case, the shares of N_2 compression for syngas dilution and CO_2 compression for storage become comparable to that of ASU for 90% CO_2 capture. Pre-combustion chemical absorption technology *via* K_2CO_3 solutions induces an energy efficiency penalty in the range of 6.5-11.5 pct. points, depending on the CO_2 capture rate. This exergy efficiency penalty is found to be similar and slightly lower than physical absorption through Selexol technology and significantly lower compared to BIGCC-CCS plants with post-combustion capture with MEA. For the BIGCC-CCS cases where MeOH and power are cogenerated, the overall energy efficiency approached the efficiency results of the electricity-only BIGCC configurations without CCS. A substantial decrease of exergy destruction was found for the MeOH/electricity cogeneration scenarios in the order of 9 pct. points compared to the reference BIGCC-CCS configuration. The GT and gasifier contribute to the greatest extent to the total exergy destruction in the BIGCC configurations. For the electricity-only BIGCC-CCS scenarios, it was found that the CCS unit is responsible for 5-10% of the total exergy destruction depending on the capture rate, while it is ca. 8% for the

base MeOH/electricity cogeneration scenario. The steam turbine island and syngas cleanup (including heat recovery) of syngas follow the aforementioned processes in terms of irreversibility.

8 Conclusions and future work

In the first section of this chapter, the main conclusions of the present thesis are summarized, followed by its innovative aspects. In the third section, recommendations for future work are provided.

8.1 Main conclusions of the thesis

The research was carried out in two major directions in the present thesis. The first direction comprised the experimental investigation of K_2CO_3 aqueous solutions and AC sorbents regarding their application for CO_2, H_2S, OSCs and light tar removal from syngas. The second direction comprised the thermodynamic and process modeling of K_2CO_3-based AGR process and its integration into an IGCC plant for power/MeOH cogeneration. The major conclusions are summarized below.

8.1.1 Conclusions from experimental tests of solvents and sorbents

The adsorption of organic (single-OSC tests with balance gas) and inorganic sulfur (real syngas tests) onto physically-activated carbon at elevated temperature conditions were experimentally investigated in Chapter 3, as a mitigation measure to decrease the sulfur content in syngas when downstream catalytic synthesis takes place. Within the investigated parameter ranges of the single-OSC adsorption tests, temperature has the most pronounced effect on the reduction of breakthrough capacity of the model OSC (C_4H_4S). At the highest temperature under study (200 °C), the AC material sustains less than 10% of its capacity measured at 100 °C. The variation of inlet OSC concentration was also found to affect the sorbent capacity, being the second most important parameter after temperature. Breakthrough curve steepening was also noted, attributed to higher volume flow rate through the bed, less favorable isotherms and enhanced pore diffusion (for temperature increase), as well as improvement of adsorption driving force (for a concentration increase). The adsorption of the model OSC species at high-temperature conditions was found to be inhibited by the presence of moisture even at low concentration (3 vol.%) in the gas mixture. This moisture content in the simulated gas mixture during the lab-scale experiments resulted in a decrease of breakthrough time and capacity. This can be of major importance when the AC guard bed is installed as a polishing step downstream of a pre-combustion AGR process since the product gas exiting the AGR unit will not be moisture-free. The role of moisture on OSC adsorption can be downplayed when operating at higher temperature, however, the impact of this strategy on the OSC capacity should also be considered. On the other hand, the *GHSV* effect on sorbent capacity was found to be negligible and it only affects the measured breakthrough time, which seems to agree with observations regarding the sorption of OSCs other than C_4H_4S in the literature. Moreover, a statistical analysis dictated that a Langmuir-type isotherm model describes adequately the equilibrium capacity of C_4H_4S.

In order to investigate the efficiency of the sorbent for sulfur removal from real syngas, pilot-scale tests were carried out in a biomass-fuelled 1 MW_{th} EFG unit. The major contaminants in syngas were H_2S and C_6H_6, while organic compounds with larger molecules were almost eliminated due to the high gasification temperature exceeding 1250 °C. The content of light hydrocarbons and tars (mainly C_6H_6) was found to be correlated with the CH_4 content in syngas. While direct adsorption from quenched syngas was carried out, the low sulfur content in wood pellets can justify that only slightly lower sulfur concentrations would be measured downstream of an AGR process. A difficulty that was encountered during the tests under real syngas produced on-site was the fact that syngas composition variation was measured despite the replication of gasification conditions in each test. Therefore, the utilization of a preheated buffer tank (or another solution that will avoid contaminant losses) could be suggested to reproduce experiments with a consistent syngas composition. The tests indicated that the sulfur capacity declined due to co-sorption effects with C_6H_6 in syngas, particularly when the C_6H_6 concentration in syngas far exceeds the sulfur content. On the other hand, the specific sulfur uptake dramatically increased when the volume ratio of H_2S and C_6H_6 in syngas was approximately 1:1 even at high adsorption temperatures. Overall, it can be concluded that AC materials can be utilized for syngas desulfurization from H_2S and OSCs at "warm" gas cleaning conditions downstream of an AGR process. Nevertheless, the effect of syngas matrix and particularly, light tar species not captured in the AGR step and moisture, should be taken into

account during process design. In the specific case that light tar species are to be converted in downstream processes, alternative sulfur-selective materials need to be evaluated.

The absorption of CO_2 into aqueous K_2CO_3 solutions at high-temperature conditions was studied through experimental tests in Chapter 4, as the (promoted−) hot potassium carbonate process was acknowledged as a process suitable for pre-combustion AGR in gasification plants. The experimental investigation focused on pure and promoted K_2CO_3 solvents. The first part of the study concerned CO_2 absorption into pure K_2CO_3 aqueous solutions without promoters in a batch-type stirred reactor and the experimental data were used to successfully validate the measurement procedure with simulation-derived results. For this comparison, a thermodynamic model based on the electrolyte-NRTL theory was used (its development was analyzed in Chapter 6). As far as K_2CO_3 solvents are concerned, solubility increases with a decrease in temperature or with a denser solvent. Four different promoters glycine, MDEA, MEA and PZ were tested as additives at high-temperature conditions. Regarding the addition of promoters, the use of PZ was found to simultaneously improve CO_2 solubility and absorption rate. The use of MEA indicated benefits for both solubility and absorption rate as well, but to a lesser extent compared to PZ. On the contrary to the former promoters, MDEA can potentially improve solubility results when added in lower quantities, but it lowers CO_2 solubility at high concentration in the solution. Considering the performance of MDEA and pure glycine addition in aqueous K_2CO_3 solutions, those additives are not recommended as absorption promoters. Instead, based on the solvent screening study, the best performing promoters during those high-temperature absorption tests, i.e. PZ and MEA, were considered for further investigation in the framework of this dissertation.

As a next step, the absorption of CO_2 and light tar mixtures into pure K_2CO_3 and MEA-promoted K_2CO_3 aqueous solutions was experimentally investigated as a follow-up study in Chapter 5. In that study, C_6H_6 and C_7H_8 were used as model compounds. The tests were carried out in a semi-continuous absorption apparatus with gas-phase analysis through FTIR spectroscopy. The study revealed that the addition of a small concentration of MEA in the range of 1 wt.% has no notable impact on CO_2 solubility compared to the case pure K_2CO_3 is added exclusively in the aqueous solution. Temperature deteriorates the solubility of CO_2 in all solvents, however, a more evident effect was found when increasing the MEA concentration in the promoted solution. On the other hand, a temperature increase by 10 °C has a very small impact on the solution capacity for smaller promoter concentrations or only K_2CO_3. MEA added at 5 wt.% in the solution can improve the CO_2 absorption rate especially when the liquid-phase CO_2 concentration increases above ~0.8 mol kg^{-1}. On the other hand, very low C_6H_6 and C_7H_8 capacities were measured, which can be attributed to the difference between VOC and solvent polarities. Nevertheless, this outcome can be considered desirable when valorization of light tar species is intended. Finally, no impact on CO_2 solubility was observed when tar species were added in the gas mixture.

8.1.2 Conclusions from thermodynamic and process modeling studies

Starting with the equilibrium gasification modeling (Chapter 2), a Gibbs minimization model was developed in Aspen Plus and experimental measurements were carried out in an air-blown, wood-fuelled 3 MW_{th} BFB gasifier for its validation. The use of a WGS model reactor contributed to achieving a better agreement with the experimental data, indicating that the reaction can be still active during syngas cooling. Considering only CH_4 as a non-equilibrium product originating from the biomass pyrolysis step seems to be inappropriate, as the simulation results and the experimental data were not in agreement. A modified model including C_2H_4 formation and the effect of WGS reaction during cooling successfully estimated the main product gas components. Deviations when operating conditions, such as fuel and oxidant feed rates changed were also noted, which indicates that the model cannot simulate the complex hydrodynamics of a fluidized bed gasifier. More semi-empirical correlations involving the fuel type and gasification parameters on syngas quality need to be implemented in order to improve the model accuracy. However, the semi-empirical equilibrium model developed in Chapter 2 can be considered as a flexible tool for process modeling and flowsheet development. Based on the reported results, the equilibrium model was further modified to account for the content of various contaminants in syngas for the process modeling task of Chapter 7.

In Chapter 6, a process model for the hot potassium carbonate process was developed in Aspen Plus targeting the simultaneous capture of CO_2 and H_2S from coal-derived syngas (applicable to a coal-to-SNG process). The investigation focused on the effect of additives and operating parameters on process efficiency. Particularly,

pure K_2CO_3 and PZ-promoted aqueous solutions with varying PZ fractions were evaluated, based on the results derived from the solvent screening tests in Chapter 4. It was shown that significant deviations between experimental data and default electrolyte-NRTL model estimations can be expected. Thus, the adjustment of electrolyte-NRTL parameters through experimental data regression is necessary. A regressed thermodynamic model with experimental data for mean ionic coefficients, vapor pressure depression, solution heat capacity, CO_2 and H_2S solubility and PZ speciation resulted in a more accurate system description compared to the default electrolyte-NRTL parameters in Aspen Plus. Average relative deviation for the pure K_2CO_3 aqueous solutions was found to be less than 12% when only CO_2 is the absorbate, increasing to ± 19 % for the H_2S-CO_2-K_2CO_3-H_2O system (to be compared to ± 84 % with default binary interaction parameters). Moreover, the average relative deviation during the prediction of CO_2 solubility and PZ speciation in PZ-promoted solutions is found to be ± 13 %. Nevertheless, further improvement of the developed model is necessary to decrease deviations to a suggested ± 10 %. The regressed electrolyte-NRTL model was implemented in detailed rate-based models (mass/heat transfer and kinetics) in Aspen Plus to simulate the AGR process. When the process operates with PZ-promoted solutions, similar reboiler duties to the pure K_2CO_3 solvents can be achieved at lower pressure of the absorber. Increasing absorption pressure was advantageous for both promoted and pure K_2CO_3 aqueous solutions, which indicates its particular suitability as pre-combustion CO_2 capture technology. A higher lean solvent loading for PZ-promoted solutions can counterbalance a higher heat of desorption. However, when the lean loading exceeded values of ~ 0.42, the required *L/G* values sharply increased for most solvents. The investigation of desorber pressure effect on process efficiency concluded than an elevated desorption pressure can benefit processes with solvents with a higher PZ fraction (smaller reboiler duty increase with pressure). On the other hand, near-ambient or even vacuum stripping is preferable for K_2CO_3 solutions with low heat of desorption. Despite the fact that the H_2S removal efficiency was consistently above the CO_2 capture level (which was set to 95% in all cases), the sulfur content in the purified gas could not meet the requirements for catalytic synthesis. This issue further highlights the need for a polishing process (e.g. AC in this thesis) when low sulfur levels are to be achieved.

In Chapter 7, the AGR process of Chapter 6 was integrated in BIGCC configurations with hot gas cleaning. Cases of power generation and power/MeOH cogeneration with CCS were evaluated and BIGCC configurations were modeled in Aspen Plus. The simulation results were used to assess the energy and exergy efficiency, as well as exergy destruction in different process steps. Regarding the gasification process, a higher *STBR* value during O_2/H_2O gasification decreases gasification efficiency and increases the required λ for the autothermal process. Although the lowest *STBR* value is preferable in terms of process efficiency, a compromise must be considered as necessary in order to ensure the required excess steam in syngas for the downstream catalytic tar reformer and WGS reactors (BIGCC-CCS scenarios). Reference BIGCC efficiencies without CCS application exceeded 46%, with the main share of the total electric consumption within the plant occupied by the ASU. On the other hand, when the K_2CO_3 AGR process is installed upstream of the GT (90% CO_2 capture), electric consumption shares of N_2 compressors for syngas dilution and CO_2 compressors for storage become comparable to that of ASU. The thermodynamic assessment concluded that, depending on the CO_2 capture level (50 to 90%), pre-combustion chemical absorption technology *via* hot K_2CO_3 solutions induces an energy efficiency penalty in the range of 6.5-11.5 pct. points. In addition, the exergy efficiency penalty is similar and slightly lower than physical absorption through Selexol technology and significantly lower compared to BIGCC-CCS plants with MEA-based chemical absorption. A significant decrease in total exergy destruction was found for the MeOH/electricity cogeneration scenarios in the order of 9 pct. points compared to the reference BIGCC-CCS configuration. The greatest part of the total exergy destruction occurs within the GT and gasifier. For the electricity-only BIGCC-CCS scenarios, it was found that the K_2CO_3-based CCS unit (including CO_2 compression) is responsible for 5-10% of the total exergy destruction depending on the capture rate, while it is *ca*. 8% for the MeOH/electricity cogeneration scenario.

8.2 Innovative aspects

The aspects of the thesis that contribute to knowledge are summarized below.

- Gasification tests in medium-scale gasification plants with woody biomass: in a 3 MW_{th} BFB gasifier and a 1 MW_{th} EFG gasifier. Those scales far exceed capacities of current laboratory and pilot installations, which are typically limited to 500 kW_{th}.
- Investigation of the effect of C_2 hydrocarbon formation and WGS reaction (and their combination) on the capability of a simplified gasification model to estimate syngas composition.
- Experimental data for CO_2 solubility were reported for promoted K_2CO_3 solutions (4 promoters) at conditions relevant to high-temperature pre-combustion CO_2 capture (CO_2 partial pressure up to 100 kPa and temperatures up to 120 °C).
- Experimental study of AC performance towards OSC and H_2S adsorption from syngas at "warm" gas cleaning conditions. Apart from common adsorption parameters (e.g. temperature, partial pressure), the effect of H_2O and light tar (in simulated and real syngas, respectively) on the adsorption efficiency was reported.
- A study on the combined removal of CO_2/light tar mixtures by K_2CO_3 solutions was presented. This demonstrates a new possible direction for solvent screening studies (when pre-combustion AGR processes are considered).
- AGR process modeling based on a regressed electrolyte-NRTL model for aqueous K_2CO_3 and K_2CO_3/PZ mixtures for integration in a coal-to-SNG plant. Process performance study (e.g. reboiler duty), not limited to absorption column performance.
- Development of process models with integrated K_2CO_3-based AGR in BIGCC plants with hot gas cleaning. Evaluation of energy/exergy efficiency of configurations with K_2CO_3-based CCS and MeOH cogeneration.

8.3 Future work

Based on the conclusions of the present thesis, indicative suggestions for future work are given below.

1. *AGR process modeling*: In this PhD thesis, a simplified solvent regeneration scheme was modeled and emphasis was given on the effect of promoted solvent type on process performance. Alternative AGR process configurations operating with improved K_2CO_3-based solvents can lead to further efficiency improvements. Such improved solvents comprise, for example, amino acid salts which are currently investigated at laboratory and pilot scale.
2. *Process modeling and techno-economics/thermo-economics:* In the present thesis, energy and exergy analyses of a cogeneration plant based on biomass gasification with hot gas cleaning and K_2CO_3 pre-combustion AGR process were presented. As a follow-up, a thermo-economic optimization of the proposed layouts can be carried out including also promoted solvents. In such a way, the impact of the optimized AGR process on electricity and MeOH costs can be identified and minimized.
3. *Solvent screening studies:* As future work, solubility studies with CO_2/H_2S mixtures could be carried out. Most studies have focused so far solely on CO_2 absorption. This is of particular importance when promoted solutions are considered for CO_2/H_2S absorption. The obtained results can be used to develop regressed thermodynamic models to accurately describe VLE behavior.
4. *AC sorbent studies:* Experimental efforts can be allocated to the improvement of solid sorbent selectivity towards OSCs and H_2S, when light tar species are present in syngas. This aspect is important when light tar species (e.g. benzene, toluene) can be utilized downstream of the AGR process. Chemical modification and pore network optimization can be applied to seek such favorable characteristics. In addition, a minimized effect of the H_2O content is required, as it was found to affect OSC adsorption even at high-temperature conditions in the present thesis.
5. *Life Cycle Assessment (LCA)*: The environmental impact of the K_2CO_3 process as part of a pre-combustion CCS scheme can be evaluated through combining mass and energy balance results from Aspen Plus, inventory databases from commercial software (e.g. ecoinvent in SimaPro™ software) and other relevant data from the literature and industry experts. A comparison of environmental indices with other major pre-combustion capture technologies can also be suggested. A study on the LCA impact of K_2CO_3 AGR process for post-combustion CO_2 capture can be found in [346] and it could be used as a guide to the proposed task.

References

1. ExxonMobil, Outlook for Energy: A view to 2040. 2018.
2. BP, Statistical review of world energy, 67th Edition. 2018.
3. REN21, Renewables 2017: Global status report. 2017.
4. Maggio, G. and G. Cacciola, When will oil, natural gas, and coal peak? Fuel, 2012. **98**: p. 111-123.
5. UN. United Nations Climate Change: 175 States Sign Paris Agreement, available at: https://unfccc.int/news/175-states-sign-paris-agreement. 2016.
6. European Commission, The roadmap for transforming the EU into a competitive, low-carbon economy by 2050.
7. CVF, Climate Vulnerable Forum (CVF) Countries Forging Ahead with Implementing the Marrakech Vision on 100% Renewable Energy. 2018: New York (USA).
8. IRENA, Global Energy Transformation: A roadmap to 2050, International Renewable Energy Agency, Abu Dhabi. 2018.
9. BP, BP Energy Outlook: 2019 Edition.
10. WBA, World Biomass Association fact sheet: Global Biomass Potential Towards 2035. 2013.
11. Schobert, H.H. and C. Song, Chemicals and materials from coal in the 21st century. Fuel, 2002. **81**(1): p. 15-32.
12. Van Dyk, J., M. Keyser, and M. Coertzen, Syngas production from South African coal sources using Sasol–Lurgi gasifiers. International Journal of Coal Geology, 2006. **65**(3-4): p. 243-253.
13. Kodera, Y., A. Matsumura, and K. Ukegawa, Continuous extraction of phenolic compounds from coal liquids. Sekitan ekikayuchu phenol rui no renzoku chushutsu. 1992.
14. Yoshida, T., et al., Study on separation of heteroatomic compounds.(III).; Extraction of phenols in naphthas with sodium alkylbenzenesulfonate aqueous solution. Hetero kagobutsu no bunri ni kansuru kenkyu.(III).; Alkylbenzenesulfon san natoriumu suiyoeki ni yoru sekitan ekika naphtha no phenol rui no chushutsu bunri. 1991.
15. Hoya, R. and C. Fushimi, Thermal efficiency of advanced integrated coal gasification combined cycle power generation systems with low-temperature gasifier, gas cleaning and CO2 capturing units. Fuel Processing Technology, 2017. **164**: p. 80-91.
16. Koytsoumpa, E.I., C. Bergins, and E. Kakaras, The CO2 economy: Review of CO2 capture and reuse technologies. The Journal of Supercritical Fluids, 2018. **132**: p. 3-16.
17. Krekel, D., et al., The separation of CO 2 from ambient air–A techno-economic assessment. Applied Energy, 2018. **218**: p. 361-381.
18. Sanders, J., et al., Process intensification in the future production of base chemicals from biomass. Chemical engineering and processing: process intensification, 2012. **51**: p. 117-136.
19. Biddy, M.J., C. Scarlata, and C. Kinchin, Chemicals from biomass: a market assessment of bioproducts with near-term potential. 2016, National Renewable Energy Lab.(NREL), Golden, CO (United States).
20. Sikarwar, V.S., et al., Progress in biofuel production from gasification. Progress in Energy and Combustion Science, 2017. **61**: p. 189-248.
21. Basso, L.C., T.O. Basso, and S.N. Rocha, Ethanol production in Brazil: the industrial process and its impact on yeast fermentation, in Biofuel production-recent developments and prospects. 2011, InTech.
22. Lü, J., C. Sheahan, and P. Fu, Metabolic engineering of algae for fourth generation biofuels production. Energy & Environmental Science, 2011. **4**(7): p. 2451-2466.
23. McKendry, P., Energy production from biomass (part 2): conversion technologies. Bioresource technology, 2002. **83**(1): p. 47-54.
24. Basu, P., Biomass gasification, pyrolysis and torrefaction: practical design and theory. 2018: Academic press.
25. Dale, B.E., et al., Protein feeds coproduction in biomass conversion to fuels and chemicals. Biofuels, bioproducts and biorefining, 2009. **3**(2): p. 219-230.
26. Baral, N.R. and A. Shah, Comparative techno-economic analysis of steam explosion, dilute sulfuric acid, ammonia fiber explosion and biological pretreatments of corn stover. Bioresource technology, 2017. **232**: p. 331-343.
27. Kumar, M., et al., Comparative economic assessment of ABE fermentation based on cellulosic and non-cellulosic feedstocks. Applied Energy, 2012. **93**: p. 193-204.

28. Rabaçal, M., et al., Biorefineries: targeting energy, high value products and waste valorisation. Vol. 57. 2017: Springer.
29. Papurello, D., et al., Waste to energy: Exploitation of biogas from organic waste in a 500 Wel solid oxide fuel cell (SOFC) stack. Energy, 2015. **85**: p. 145-158.
30. Rehl, T. and J. Müller, Life cycle assessment of biogas digestate processing technologies. Resources, Conservation and Recycling, 2011. **56**(1): p. 92-104.
31. Demirbaş, A., Relationships between lignin contents and heating values of biomass. Energy conversion and management, 2001. **42**(2): p. 183-188.
32. Bridgwater, A., Thermal conversion of biomass and waste: the status. Birmingham (UK): Bio-Energy Research Group, Aston University, 2001.
33. Basu, P., Combustion and gasification in fluidized beds. 2006: CRC press.
34. Saidur, R., et al., A review on biomass as a fuel for boilers. Renewable and sustainable energy reviews, 2011. **15**(5): p. 2262-2289.
35. Avagianos, I., et al., Thermal Simulation and Economic Study of Predried Lignite Production Retrofit of a Greek Power Plant for Enhanced Flexibility. Journal of Energy Engineering, 2019. **145**(2): p. 04019001.
36. Hajebzadeh, H., A.N. Ansari, and S. Niazi, Mathematical modeling and validation of a 320 MW tangentially fired boiler: A case study. Applied Thermal Engineering, 2019. **146**: p. 232-242.
37. Wu, H., et al., Impact of coal fly ash addition on ash transformation and deposition in a full-scale wood suspension-firing boiler. Fuel, 2013. **113**: p. 632-643.
38. Chi, H., et al., An investigation of lime addition to fuel as a countermeasure to bed agglomeration for the combustion of non-woody biomass fuels in a 20kWth bubbling fluidised bed combustor. Fuel, 2019. **240**: p. 349-361.
39. Han, X., et al., Exergy analysis of the flue gas pre-dried lignite-fired power system based on the boiler with open pulverizing system. Energy, 2016. **106**: p. 285-300.
40. Karellas, S. and K. Braimakis, Energy–exergy analysis and economic investigation of a cogeneration and trigeneration ORC–VCC hybrid system utilizing biomass fuel and solar power. Energy conversion and management, 2016. **107**: p. 103-113.
41. Guan, G., Clean coal technologies in Japan: A review. Chinese journal of chemical engineering, 2017. **25**(6): p. 689-697.
42. Salomón, M., et al., Small-scale biomass CHP plants in Sweden and Finland. Renewable and Sustainable Energy Reviews, 2011. **15**(9): p. 4451-4465.
43. Biofficiency project: Highly-efficient biomass CHP plants by handling ash-related problems-EU Horizon 2020 research and innovation programme under grant agreement No 727616. Available at: https://www.biofficiency.eu/.
44. Gil, M.V. and F. Rubiera, Coal and biomass cofiring: fundamentals and future trends, in New Trends in Coal Conversion. 2019, Elsevier. p. 117-140.
45. Stam, A.F. and G. Brem, Fouling in coal-fired boilers: Biomass co-firing, full conversion and use of additives–A thermodynamic approach. Fuel, 2019. **239**: p. 1274-1283.
46. Gollakota, A., N. Kishore, and S. Gu, A review on hydrothermal liquefaction of biomass. Renewable and Sustainable Energy Reviews, 2018. **81**: p. 1378-1392.
47. Biller, P. and A. Ross, Production of biofuels via hydrothermal conversion, in Handbook of biofuels production. 2016, Elsevier. p. 509-547.
48. Toor, S.S., L. Rosendahl, and A. Rudolf, Hydrothermal liquefaction of biomass: a review of subcritical water technologies. Energy, 2011. **36**(5): p. 2328-2342.
49. Guo, Y., et al., A review of bio-oil production from hydrothermal liquefaction of algae. Renewable and Sustainable Energy Reviews, 2015. **48**: p. 776-790.
50. Bridgwater, A., Biomass conversion technologies: fast pyrolysis liquids from biomass: quality and upgrading, in Biorefineries. 2017, Springer. p. 55-98.
51. Fu, P., et al., Comparative study on fast pyrolysis of agricultural straw residues based on heat carrier circulation heating. Bioresource technology, 2019. **271**: p. 136-142.
52. Braimakis, K., et al., Economic evaluation of decentralized pyrolysis for the production of bio-oil as an energy carrier for improved logistics towards a large centralized gasification plant. Renewable and Sustainable Energy Reviews, 2014. **35**: p. 57-72.
53. Ikura, M., M. Stanciulescu, and E. Hogan, Emulsification of pyrolysis derived bio-oil in diesel fuel. Biomass and bioenergy, 2003. **24**(3): p. 221-232.

54. Elliott, D. and E. Baker, Hydrotreating biomass liquids to produce hydrocarbon fuels. 1986, Pacific Northwest Lab., Richland, WA (USA).
55. Huber, G.W. and A. Corma, Synergies between bio-and oil refineries for the production of fuels from biomass. Angewandte Chemie International Edition, 2007. **46**(38): p. 7184-7201.
56. Bridgwater, A.V., Review of fast pyrolysis of biomass and product upgrading. Biomass and bioenergy, 2012. **38**: p. 68-94.
57. Mondal, P., G. Dang, and M. Garg, Syngas production through gasification and cleanup for downstream applications—Recent developments. Fuel Processing Technology, 2011. **92**(8): p. 1395-1410.
58. Basu, P., Biomass gasification and pyrolysis: practical design and theory. 2010: Academic press.
59. Seyitoglu, S., I. Dincer, and A. Kilicarslan, Energy and exergy analyses of hydrogen production by coal gasification. International Journal of Hydrogen Energy, 2017. **42**(4): p. 2592-2600.
60. Stichnothe, H. and F. Schuchardt, Comparison of different treatment options for palm oil production waste on a life cycle basis. The International Journal of Life Cycle Assessment, 2010. **15**(9): p. 907-915.
61. Phanphanich, M. and S. Mani, Impact of torrefaction on the grindability and fuel characteristics of forest biomass. Bioresource technology, 2011. **102**(2): p. 1246-1253.
62. Higman, C. and M. van der Burgt, Chapter 1 - Introduction, in Gasification (Second Edition), C. Higman and M. van der Burgt, Editors. 2008, Gulf Professional Publishing: Burlington. p. 1-9.
63. Göransson, K., et al., Review of syngas production via biomass DFBGs. Renewable and Sustainable Energy Reviews, 2011. **15**(1): p. 482-492.
64. Pang, Y., et al., Plasma-assisted biomass gasification with focus on carbon conversion and reaction kinetics compared to thermal gasification. Energies, 2018. **11**(5): p. 1302.
65. Valmet: HYBEX boilers - using BFB technology, https://www.valmet.com/energyproduction/bfb-boilers/ (accessed on 05.04.2019).
66. Christodoulou, C., et al., Attempts on cardoon gasification in two different circulating fluidized beds. Case Studies in Thermal Engineering, 2014. **4**: p. 42-52.
67. Tijmensen, M.J., et al., Exploration of the possibilities for production of Fischer Tropsch liquids and power via biomass gasification. Biomass and Bioenergy, 2002. **23**(2): p. 129-152.
68. Ruiz, J.A., et al., Biomass gasification for electricity generation: Review of current technology barriers. Renewable and Sustainable Energy Reviews, 2013. **18**: p. 174-183.
69. Doherty, W., A. Reynolds, and D. Kennedy, Aspen Plus simulation of biomass gasification in a steam blown dual fluidised bed. Materials and Processes for Energy: Communicating Current Research and Technological Developments, 2013: p. 212-220.
70. Panopoulos, K., et al., High temperature solid oxide fuel cell integrated with novel allothermal biomass gasification: Part I: Modelling and feasibility study. Journal of Power Sources, 2006. **159**(1): p. 570-585.
71. Parthasarathy, P. and K.S. Narayanan, Hydrogen production from steam gasification of biomass: influence of process parameters on hydrogen yield–a review. Renewable energy, 2014. **66**: p. 570-579.
72. Weerachanchai, P., M. Horio, and C. Tangsathitkulchai, Effects of gasifying conditions and bed materials on fluidized bed steam gasification of wood biomass. Bioresource Technology, 2009. **100**(3): p. 1419-1427.
73. Meng, X., et al., Biomass gasification in a 100 kWth steam-oxygen blown circulating fluidized bed gasifier: Effects of operational conditions on product gas distribution and tar formation. Biomass and Bioenergy, 2011. **35**(7): p. 2910-2924.
74. Vaezi, M., et al., On a methodology for selecting biomass materials for gasification purposes. Fuel Processing Technology, 2012. **98**: p. 74-81.
75. Li, X., et al., Biomass gasification in a circulating fluidized bed. Biomass and bioenergy, 2004. **26**(2): p. 171-193.
76. Weiland, F., et al., Influence of process parameters on the performance of an oxygen blown entrained flow biomass gasifier. Fuel, 2015. **153**: p. 510-519.
77. Vassilev, S.V., et al., An overview of the chemical composition of biomass. Fuel, 2010. **89**(5): p. 913-933.
78. Devi, L., K.J. Ptasinski, and F.J. Janssen, A review of the primary measures for tar elimination in biomass gasification processes. Biomass and bioenergy, 2003. **24**(2): p. 125-140.
79. Woolcock, P.J. and R.C. Brown, A review of cleaning technologies for biomass-derived syngas. Biomass and bioenergy, 2013. **52**: p. 54-84.

80. Li, C. and K. Suzuki, Tar property, analysis, reforming mechanism and model for biomass gasification—an overview. Renewable and Sustainable Energy Reviews, 2009. **13**(3): p. 594-604.
81. Bergman, P.C., S.V. van Paasen, and H. Boerrigter. The novel "OLGA" technology for complete tar removal from biomass producer gas. in Pyrolysis and gasification of biomass and waste, expert meeting, Strasbourg, France. 2002.
82. Attar, A., Chemistry, thermodynamics and kinetics of reactions of sulphur in coal-gas reactions: A review. Fuel, 1978. **57**(4): p. 201-212.
83. Cui, H., et al., Contaminant estimates and removal in product gas from biomass steam gasification. Energy & Fuels, 2010. **24**(2): p. 1222-1233.
84. Meng, X., et al., In bed and downstream hot gas desulphurization during solid fuel gasification: A review. Fuel Processing Technology, 2010. **91**(8): p. 964-981.
85. Jazbec, M., K. Sendt, and B.S. Haynes, Kinetic and thermodynamic analysis of the fate of sulphur compounds in gasification products. Fuel, 2004. **83**(16): p. 2133-2138.
86. Khan, M.R., Prediction of sulphur distribution in products during low temperature coal pyrolysis and gasification. Fuel, 1989. **68**(11): p. 1439-1449.
87. Ma, R.P., R.M. Felder, and J.K. Ferrell, Evolution of hydrogen sulfide in a fluidized bed coal gasification reactor. Industrial & Engineering Chemistry Research, 1989. **28**(1): p. 27-33.
88. Rechulski, M.K., et al., Sulfur containing organic compounds in the raw producer gas of wood and grass gasification. Fuel, 2014. **128**: p. 330-339.
89. Rauch, R., Latest developments in FT synthesis and methanation at the Güssing biomass CHP plant. IEA Bioenergy, Task 33 meeting. 2009.
90. Materazzi, M., et al., Reforming of tars and organic sulphur compounds in a plasma-assisted process for waste gasification. Fuel processing technology, 2015. **137**: p. 259-268.
91. Lovell, R., S. Dylewski, and C. Peterson, Control of sulfur emissions from oil shale retorts. Final report Jul 79-Jul 80. 1982, IT-Enviroscience, Knoxville, TN (USA).
92. SilcoNert: The Ultimate Inert Coating for Supercharged Analytical Flowpath Performance. Available at: https://www.silcotek.com/silcod-technologies/silconert-inert-coating (accessed on 21.05.2019).
93. Lecomte, T., et al., Best Available Techniques (BAT) Reference Document for Large Combustion Plants. 2017, EUR.
94. Neubert, M., et al., Influence of hydrocarbons and thiophene on catalytic fixed bed methanation. Fuel, 2017. **207**: p. 253-261.
95. Hansson, K.-M., et al., Formation of HNCO, HCN, and NH3 from the pyrolysis of bark and nitrogen-containing model compounds. Combustion and Flame, 2004. **137**(3): p. 265-277.
96. Cheah, S., D.L. Carpenter, and K.A. Magrini-Bair, Review of mid-to high-temperature sulfur sorbents for desulfurization of biomass-and coal-derived syngas. Energy & Fuels, 2009. **23**(11): p. 5291-5307.
97. Li, T.S., et al., Chlorine contaminants poisoning of solid oxide fuel cells. Journal of Solid State Electrochemistry, 2011. **15**(6): p. 1077-1085.
98. Gómez-Barea, A., et al., Plant optimisation and ash recycling in fluidised bed waste gasification. Chemical Engineering Journal, 2009. **146**(2): p. 227-236.
99. Christodoulou, C., et al., Circulating fluidized bed gasification tests of seed cakes residues after oil extraction and comparison with wood. Fuel, 2014. **132**: p. 71-81.
100. Van der Drift, A., J. Van Doorn, and J. Vermeulen, Ten residual biomass fuels for circulating fluidized-bed gasification. Biomass and Bioenergy, 2001. **20**(1): p. 45-56.
101. Guo, Q., et al., Particulate matter properties in a bench-scale entrained-flow coal water slurry gasifier. Powder technology, 2014. **254**: p. 125-130.
102. Gustafsson, E., L. Lin, and M. Strand, Characterization of particulate matter in the hot product gas from atmospheric fluidized bed biomass gasifiers. Biomass and bioenergy, 2011. **35**: p. S71-S78.
103. Van der Meijden, C., et al. Scale-up of the Milena biomass gasification technology. in 17th European Biomass Conference & Exhibition, Hamburg, Germany. 2009.
104. Neubert, M., et al., Experimental comparison of solid phase adsorption (SPA), activated carbon test tubes and tar protocol (DIN CEN/TS 15439) for tar analysis of biomass derived syngas. Biomass and bioenergy, 2017. **105**: p. 443-452.
105. Mitchell, S.C., Hot gas cleanup of sulphur, nitrogen, minor and trace elements. 1998: IEA Coal Research.
106. Erbel, C., et al., Continuous in situ measurements of alkali species in the gasification of biomass. Proceedings of the Combustion Institute, 2013. **34**(2): p. 2331-2338.

107. Molino, A., S. Chianese, and D. Musmarra, Biomass gasification technology: The state of the art overview. Journal of Energy Chemistry, 2016. **25**(1): p. 10-25.
108. François, J., et al., Detailed process modeling of a wood gasification combined heat and power plant. Biomass and bioenergy, 2013. **51**: p. 68-82.
109. Giuffrida, A., M.C. Romano, and G. Lozza, Efficiency enhancement in IGCC power plants with air-blown gasification and hot gas clean-up. Energy, 2013. **53**: p. 221-229.
110. Shi, B., et al., Novel design of integrated gasification combined cycle (IGCC) power plants with CO2 capture. Journal of cleaner production, 2018. **195**: p. 176-186.
111. Bridgwater, A., The technical and economic feasibility of biomass gasification for power generation. Fuel, 1995. **74**(5): p. 631-653.
112. Ståhl, K. and M. Neergaard, IGCC power plant for biomass utilisation, Värnamo, Sweden. Biomass and Bioenergy, 1998. **15**(3): p. 205-211.
113. Hermann, H., et al. Biomass CHP Plant Güssing–a success story. in Expert meeting on pyrolysis and gasification of biomass and waste. 2002.
114. Rhodes, J.S. and D.W. Keith, Engineering economic analysis of biomass IGCC with carbon capture and storage. Biomass and Bioenergy, 2005. **29**(6): p. 440-450.
115. Jin, H., E.D. Larson, and F.E. Celik, Performance and cost analysis of future, commercially mature gasification-based electric power generation from switchgrass. Biofuels, Bioproducts and Biorefining, 2009. **3**(2): p. 142-173.
116. Difs, K., et al., Biomass gasification opportunities in a district heating system. Biomass and Bioenergy, 2010. **34**(5): p. 637-651.
117. Parraga, J., K.R. Khalilpour, and A. Vassallo, Polyfeed and Polyproduct Integrated Gasification Systems, in Polygeneration with Polystorage for Chemical and Energy Hubs. 2019, Elsevier. p. 175-212.
118. Toonssen, R., et al., Alternative system designs of biomass gasification SOFC/GT hybrid systems. International journal of hydrogen energy, 2011. **36**(16): p. 10414-10425.
119. Roumpedakis, T., et al., Hydrogen Production and Storage. Renewable Energy Engineering: Solar, Wind, Biomass, Hydrogen and Geothermal Energy Systems., 2018. **3**: p. 272-323.
120. Spath, P.L. and D.C. Dayton, Preliminary screening--technical and economic assessment of synthesis gas to fuels and chemicals with emphasis on the potential for biomass-derived syngas. 2003, National Renewable Energy Lab., Golden, CO.(US).
121. Thunman, H., GoBiGas demonstration –a vital step for a large-scale transition from fossil fuels to advanced biofuels and electrofuels. Available at: https://research.chalmers.se/publication/503260. (accessed on 29.05.2019). 2018: Chalmers University of Technology.
122. van der Meijden, C.M., H.J. Veringa, and L.P. Rabou, The production of synthetic natural gas (SNG): A comparison of three wood gasification systems for energy balance and overall efficiency. Biomass and bioenergy, 2010. **34**(3): p. 302-311.
123. Kopyscinski, J., T.J. Schildhauer, and S.M. Biollaz, Production of synthetic natural gas (SNG) from coal and dry biomass–A technology review from 1950 to 2009. Fuel, 2010. **89**(8): p. 1763-1783.
124. Tsakoumis, N.E., et al., Deactivation of cobalt based Fischer–Tropsch catalysts: a review. Catalysis Today, 2010. **154**(3-4): p. 162-182.
125. de Smit, E. and B.M. Weckhuysen, The renaissance of iron-based Fischer–Tropsch synthesis: on the multifaceted catalyst deactivation behaviour. Chemical Society Reviews, 2008. **37**(12): p. 2758-2781.
126. Leibold, H., A. Hornung, and H. Seifert, HTHP syngas cleaning concept of two stage biomass gasification for FT synthesis. Powder Technology, 2008. **180**(1-2): p. 265-270.
127. Swanson, R.M., et al., Techno-economic analysis of biomass-to-liquids production based on gasification. Fuel, 2010. **89**: p. S11-S19.
128. Dittus, M. and D. Johnson, The hidden value of lignite coal. Available at: https://www.globalsyngas.org/uploads/eventLibrary/GTC01010.pdf (accessed on 28.05.2019), in Gasification Technologies Conference. 2001.
129. Zwart, R., et al., Production of synthetic natural gas (SNG) from biomass. Report for Energy Research Center of the Netherlands. Available at: https://pdfs.semanticscholar.org/777d/354091e7cbd4f70032c288090a2ce53285c2.pdf (accessed on 3 June 2013), 2006.
130. Boerrigter, H. and R. Rauch, Review of applications of gases from biomass gasification. ECN Biomassa, Kolen en Milieuonderzoek, 2006. **20**.

131. Mondal, M.K., H.K. Balsora, and P. Varshney, Progress and trends in CO2 capture/separation technologies: a review. Energy, 2012. **46**(1): p. 431-441.
132. Bell, D.A., B.F. Towler, and M. Fan, Coal gasification and its applications. 2010: William Andrew.
133. Speight, J.G., Natural gas: a basic handbook. 2018: Gulf Professional Publishing.
134. Koytsoumpa, E.-I., et al., Modelling and assessment of acid gas removal processes in coal-derived SNG production. Applied Thermal Engineering, 2015. **74**: p. 128-135.
135. Boerrigter, H., et al. Tar removal from biomass product gas; development and optimisation of the OLGA tar removal technology. in Proceedings of the 14th European Biomass Conference & Exhibition. 2005.
136. Wiheeb, A., et al., Pressure swing adsorption technologies for carbon dioxide capture. Separation & Purification Reviews, 2016. **45**(2): p. 108-121.
137. Abdoulmoumine, N., et al., A review on biomass gasification syngas cleanup. Applied Energy, 2015. **155**: p. 294-307.
138. Simell, P., et al., Catalytic hot gas cleaning of gasification gas. Catalysis Today, 1996. **27**(1-2): p. 55-62.
139. Vitasari, C.R., M. Jurascik, and K.J. Ptasinski, Exergy analysis of biomass-to-synthetic natural gas (SNG) process via indirect gasification of various biomass feedstock. Energy, 2011. **36**(6): p. 3825-3837.
140. Edinger, P., et al., Adsorption of thiophene by activated carbon: A global sensitivity analysis. Journal of Environmental Chemical Engineering, 2017. **5**(4): p. 4173-4184.
141. Haro, P., F. Johnsson, and H. Thunman, Improved syngas processing for enhanced Bio-SNG production: A techno-economic assessment. Energy, 2016. **101**: p. 380-389.
142. Gómez-Barea, A. and B. Leckner, Modeling of biomass gasification in fluidized bed. Progress in Energy and Combustion Science, 2010. **36**(4): p. 444-509.
143. He, J. and W. Zhang, Techno-economic evaluation of thermo-chemical biomass-to-ethanol. Applied Energy, 2011. **88**(4): p. 1224-1232.
144. Zainal, Z., et al., Prediction of performance of a downdraft gasifier using equilibrium modeling for different biomass materials. Energy conversion and management, 2001. **42**(12): p. 1499-1515.
145. Nikoo, M.B. and N. Mahinpey, Simulation of biomass gasification in fluidized bed reactor using ASPEN PLUS. Biomass and Bioenergy, 2008. **32**(12): p. 1245-1254.
146. Pala, L.P.R., et al., Steam gasification of biomass with subsequent syngas adjustment using shift reaction for syngas production: An Aspen Plus model. Renewable Energy, 2017. **101**: p. 484-492.
147. Fremaux, S., et al., An experimental study on hydrogen-rich gas production via steam gasification of biomass in a research-scale fluidized bed. Energy Conversion and Management, 2015. **91**: p. 427-432.
148. Michailos, S. and A. Zabaniotou, Simulation of olive kernel gasification in a bubbling fluidized bed pilot scale reactor. Journal of Sustainable Bioenergy Systems, 2012. **2**(4): p. 145.
149. Jarungthammachote, S. and A. Dutta, Equilibrium modeling of gasification: Gibbs free energy minimization approach and its application to spouted bed and spout-fluid bed gasifiers. Energy Conversion and Management, 2008. **49**(6): p. 1345-1356.
150. Altafini, C.R., P.R. Wander, and R.M. Barreto, Prediction of the working parameters of a wood waste gasifier through an equilibrium model. Energy Conversion and Management, 2003. **44**(17): p. 2763-2777.
151. Mun, T.-Y., J.-W. Kim, and J.-S. Kim, Air gasification of railroad wood ties treated with creosote: Effects of additives and their combination on the removal of tar in a two-stage gasifier. Fuel, 2012. **102**: p. 326-332.
152. Hurley, S., et al., Catalytic gasification of woody biomass in an air-blown fluidized-bed reactor using Canadian limonite iron ore as the bed material. Fuel, 2012. **91**(1): p. 170-176.
153. Higman, C. and M. van der Burgt, Chapter 6-Practical Issues. Gasification (Second Edition), 2008: p. 193-255.
154. Kuramochi, H., W. Wu, and K. Kawamoto, Prediction of the behaviors of H2S and HCl during gasification of selected residual biomass fuels by equilibrium calculation. Fuel, 2005. **84**(4): p. 377-387.
155. Aljbour, S.H. and K. Kawamoto, Bench-scale gasification of cedar wood–Part II: Effect of Operational conditions on contaminant release. Chemosphere, 2013. **90**(4): p. 1501-1507.
156. Öhrman, O.G., et al., Analysis of trace compounds generated by pressurized oxygen blown entrained flow biomass gasification. Environmental Progress & Sustainable Energy, 2014. **33**(3): p. 699-705.
157. Mondal, P., G.S. Dang, and M.O. Garg, Syngas production through gasification and cleanup for downstream applications — Recent developments. Fuel Processing Technology, 2011. **92**(8): p. 1395-1410.

158. Koytsoumpa, E.I., et al., Modelling and assessment of acid gas removal processes in coal-derived SNG production. Applied Thermal Engineering, 2015. **74**(0): p. 128-135.
159. Kopyscinski, J., T.J. Schildhauer, and S.M.A. Biollaz, Production of synthetic natural gas (SNG) from coal and dry biomass – A technology review from 1950 to 2009. Fuel, 2010. **89**(8): p. 1763-1783.
160. Lebarbier, V.M., et al., Sorption-enhanced synthetic natural gas (SNG) production from syngas: A novel process combining CO methanation, water-gas shift, and CO2 capture. Applied Catalysis B: Environmental, 2014. **144**(0): p. 223-232.
161. Yildirim, Ö., et al., Reactive absorption in chemical process industry: A review on current activities. Chemical Engineering Journal, 2012. **213**(0): p. 371-391.
162. Lee, A., et al., A study of the vapour–liquid equilibrium of CO2 in mixed solutions of potassium carbonate and potassium glycinate. International Journal of Greenhouse Gas Control, 2015. **36**(0): p. 27-33.
163. Kohl, A.L. and R.B. Nielsen, Chapter 5 - Alkaline Salt Solutions for Acid Gas Removal, in Gas Purification (Fifth Edition), A.L. Kohl and R.B. Nielsen, Editors. 1997, Gulf Professional Publishing: Houston. p. 330-414.
164. Chen, W., et al., Arsenic removal by iron-modified activated carbon. Water Research, 2007. **41**(9): p. 1851-1858.
165. Parette, R. and F.S. Cannon, The removal of perchlorate from groundwater by activated carbon tailored with cationic surfactants. Water Research, 2005. **39**(16): p. 4020-4028.
166. Xiao, Y., et al., Experimental and simulation study of hydrogen sulfide adsorption on impregnated activated carbon under anaerobic conditions. Journal of Hazardous Materials, 2008. **153**(3): p. 1193-1200.
167. Mohammed, J., et al., Adsorption of benzene and toluene onto KOH activated coconut shell based carbon treated with NH3. International Biodeterioration & Biodegradation, 2015. **102**(0): p. 245-255.
168. Bandosz, T.J., et al., Unmodified versus caustics-impregnated carbons for control of hydrogen sulfide emissions from sewage treatment plants. Environmental science & technology, 2000. **34**(6): p. 1069-1074.
169. Hervy, M., et al., H2S removal from syngas using wastes pyrolysis chars. Chemical Engineering Journal, 2018. **334**: p. 2179-2189.
170. Bak, C.-u., et al., Removal of sulfur compounds and siloxanes by physical and chemical sorption. Separation and Purification Technology, 2019. **209**: p. 542-549.
171. Wen, J., et al., A critical study on the adsorption of heterocyclic sulfur and nitrogen compounds by activated carbon: equilibrium, kinetics and thermodynamics. Chemical Engineering Journal, 2010. **164**(1): p. 29-36.
172. Cui, H., S.Q. Turn, and M.A. Reese, Removal of sulfur compounds from utility pipelined synthetic natural gas using modified activated carbons. Catalysis Today, 2009. **139**(4): p. 274-279.
173. Vega, E., et al., Adsorption of volatile sulphur compounds onto modified activated carbons: effect of oxygen functional groups. Journal of hazardous materials, 2013. **258**: p. 77-83.
174. Shin, H.-C., et al., Removal characteristics of trace compounds of landfill gas by activated carbon adsorption. Environmental Pollution, 2002. **119**(2): p. 227-236.
175. Lillo-Ródenas, M., D. Cazorla-Amorós, and A. Linares-Solano, Behaviour of activated carbons with different pore size distributions and surface oxygen groups for benzene and toluene adsorption at low concentrations. Carbon, 2005. **43**(8): p. 1758-1767.
176. Phuphuakrat, T., T. Namioka, and K. Yoshikawa, Tar removal from biomass pyrolysis gas in two-step function of decomposition and adsorption. Applied Energy, 2010. **87**(7): p. 2203-2211.
177. Hanaoka, T., et al., Hot and dry cleaning of biomass-gasified gas using activated carbons with simultaneous removal of tar, particles, and sulfur compounds. Catalysts, 2012. **2**(2): p. 281-298.
178. Ravenni, G., et al., Adsorption and decomposition of tar model compounds over the surface of gasification char and active carbon within the temperature range 250–800° C. Applied Energy, 2019. **241**: p. 139-151.
179. Danmaliki, G.I. and T.A. Saleh, Effects of bimetallic Ce/Fe nanoparticles on the desulfurization of thiophenes using activated carbon. Chemical Engineering Journal, 2017. **307**: p. 914-927.
180. Quantitative Gas Analyzer MAX300-LG Brochure, Extrel Core Mass Spectrometers. Available at: https://www.extrel.com/Module/Catalog/CatalogDocFileFile/mobile/Gas_Analysis_Systems/MAX300-LG_High-Performance_Laboratory_Gas_Analyzer/MAX300-LG_Quantitative_Brochure_IPLG102A/MAX300-LG_Product_Note_IPLG102A.pdf?id=181

(accessed on 30.05.2019).

181. Guo, Y., et al., Effects of activated carbon properties on chlorobenzene adsorption and adsorption product analysis. Chemical Engineering Journal, 2014. **236**: p. 506-512.
182. Wang, L., R.T. Yang, and C.L. Sun, Graphene and other carbon sorbents for selective adsorption of thiophene from liquid fuel. AIChE Journal, 2013. **59**(1): p. 29-32.
183. Barelli, L., et al., Dimethyl sulfide adsorption from natural gas for solid oxide fuel cell applications. Fuel processing technology, 2015. **140**: p. 21-31.
184. Tang, X.-l., et al., Adsorption of thiophene on Pt/Ag-supported activated carbons prepared by ultrasonic-assisted impregnation. Industrial & Engineering Chemistry Research, 2011. **50**(15): p. 9363-9367.
185. Qi, S., K.J. Hay, and M.P. Cal, Predicting humidity effect on adsorption capacity of activated carbon for water-immiscible organic vapors. Advances in Environmental Research, 2000. **4**(4): p. 357-362.
186. Sitthikhankaew, R., et al., Effects of humidity, O2, and CO2 on H2S adsorption onto upgraded and KOH impregnated activated carbons. Fuel processing technology, 2014. **124**: p. 249-257.
187. Xiao, J., et al., Effects of aromatics, diesel additives, nitrogen compounds, and moisture on adsorptive desulfurization of diesel fuel over activated carbon. Industrial & Engineering Chemistry Research, 2012. **51**(8): p. 3436-3443.
188. Snoussi, Y., et al., Surface Analysis of Clay–Polymer Nanocomposites, in Clay-Polymer Nanocomposites. 2017, Elsevier. p. 363-411.
189. Ortiz, F.J.G., M.B. Rodríguez, and R.T. Yang, Modeling of fixed-bed columns for gas physical adsorption. Chemical Engineering Journal, 2019: p. 121985.
190. Weiland, F., et al., Pressurized oxygen blown entrained-flow gasification of wood powder. Energy & Fuels, 2013. **27**(2): p. 932-941.
191. Häggström, C., et al., Catalytic methanol synthesis via black liquor gasification. Fuel processing technology, 2012. **94**(1): p. 10-15.
192. Weiland, F., et al., Online characterization of syngas particulates using aerosol mass spectrometry in entrained-flow biomass gasification. Aerosol Science and Technology, 2014. **48**(11): p. 1145-1155.
193. Chiang, Y.-C., P.-C. Chiang, and C.-P. Huang, Effects of pore structure and temperature on VOC adsorption on activated carbon. Carbon, 2001. **39**(4): p. 523-534.
194. Marchelli, F., et al., Experimental study ON H2S adsorption on gasification char under different operative conditions. Biomass and Bioenergy, 2019. **126**: p. 106-116.
195. Itaya, Y., et al., Dry gas cleaning process by adsorption of H2S into activated cokes in gasification of carbon resources. Fuel, 2009. **88**(9): p. 1665-1672.
196. Sreedhar, I., et al., Carbon capture by absorption–path covered and ahead. Renewable and Sustainable Energy Reviews, 2017. **76**: p. 1080-1107.
197. Atsonios, K., et al., Plant design aspects of catalytic biosyngas conversion to higher alcohols. Biomass and Bioenergy, 2013. **53**: p. 54-64.
198. Dawodu, O.F. and A. Meisen, Degradation of alkanolamine blends by carbon dioxide. The canadian journal of chemical engineering, 1996. **74**(6): p. 960-966.
199. Wang, M., et al., Post-combustion CO2 capture with chemical absorption: A state-of-the-art review. Chemical Engineering Research and Design, 2011. **89**(9): p. 1609-1624.
200. Ye, X. and Y. Lu, Kinetics of CO 2 absorption into uncatalyzed potassium carbonate–bicarbonate solutions: effects of CO 2 loading and ionic strength in the solutions. Chemical Engineering Science, 2014. **116**: p. 657-667.
201. Kothadaraman, A., Carbon Dioxide Capture by Chemical Absorption: A Solvent Comparison Study, in Chemical Engineering. 2010, MIT: Massachuchetts Institute of Technology.
202. Hu, G., et al., Carbon dioxide absorption into promoted potassium carbonate solutions: A review. International Journal of Greenhouse Gas Control, 2016. **53**: p. 28-40.
203. Borhani, T.N.G., et al., CO2 capture with potassium carbonate solutions: A state-of-the-art review. International Journal of Greenhouse Gas Control, 2015. **41**: p. 142-162.
204. Tosh, J.S., et al., Equilibrium study of the system potassium carbonate, potassium bicarbonate, carbon dioxide, and water. 1959, Bureau of Mines, Pittsburgh, Pa.(USA).
205. Benson, H., Improved Process for CO_2 Absorption Used Hot Carbonate Solutions. Chem. Eng. Progr., 1956. **52**: p. 433-438.
206. Mazinani, S., et al., Equilibrium solubility, density, viscosity and corrosion rate of carbon dioxide in potassium lysinate solution. Fluid Phase Equilibria, 2015. **396**: p. 28-34.

207. Thee, H., et al., A kinetic and process modeling study of CO 2 capture with MEA-promoted potassium carbonate solutions. Chemical engineering journal, 2012. **210**: p. 271-279.
208. Bohloul, M.R., et al., Experimental and analytical study of solubility of carbon dioxide in aqueous solutions of potassium carbonate. International Journal of Greenhouse Gas Control, 2014. **29**: p. 169-175.
209. Park, S.-B., et al., Solubilities of carbon dioxide in the aqueous potassium carbonate and potassium carbonate/poly (ethylene glycol) solutions. Fluid phase equilibria, 1997. **134**(1): p. 141-149.
210. Li, H., et al., CO 2 solubility measurement and thermodynamic modeling for 1-methylpiperazine/water/CO 2. Fluid Phase Equilibria, 2015. **394**: p. 118-128.
211. Singh, P., D.W. Brilman, and M.J. Groeneveld, Evaluation of CO 2 solubility in potential aqueous amine-based solvents at low CO 2 partial pressure. International Journal of Greenhouse Gas Control, 2011. **5**(1): p. 61-68.
212. Cullinane, J.T., Thermodynamics and Kinetics of Aqueous Piperazine with Potassium Carbonate for Carbon Dioxide Absorption, in Chemical Engineering. 2005, The University of Texas at Austin: Texas, USA.
213. Knuutila, H., O. Juliussen, and H.F. Svendsen, Density and N2O solubility of sodium and potassium carbonate solutions in the temperature range 25 to 80 C. Chemical Engineering Science, 2010. **65**(6): p. 2177-2182.
214. Thee, H., et al., A kinetic study of CO 2 capture with potassium carbonate solutions promoted with various amino acids: glycine, sarcosine and proline. International Journal of Greenhouse Gas Control, 2014. **20**: p. 212-222.
215. Ramazani, R., et al., Experimental investigation of the effect of addition of different activators to aqueous solution of potassium carbonate: Absorption rate and solubility. International Journal of Greenhouse Gas Control, 2016. **45**: p. 27-33.
216. Cullinane, J.T. and G.T. Rochelle, Thermodynamics of aqueous potassium carbonate, piperazine, and carbon dioxide. Fluid Phase Equilibria, 2005. **227**(2): p. 197-213.
217. Kim, Y.E., et al., CO2 absorption capacity using aqueous potassium carbonate with 2-methylpiperazine and piperazine. Journal of Industrial and Engineering Chemistry, 2012. **18**(1): p. 105-110.
218. Smith, K., et al., Pilot plant results for a precipitating potassium carbonate solvent absorption process promoted with glycine for enhanced CO2 capture. Fuel Processing Technology, 2015. **135**: p. 60-65.
219. Aronu, U.E., H.F. Svendsen, and K.A. Hoff, Investigation of amine amino acid salts for carbon dioxide absorption. International Journal of Greenhouse Gas Control, 2010. **4**(5): p. 771-775.
220. Shen, S., X. Feng, and S. Ren, Effect of arginine on carbon dioxide capture by potassium carbonate solution. Energy & Fuels, 2013. **27**(10): p. 6010-6016.
221. Nii, S. and H. Takeuchi, Removal of CO2 and/or SO2 from gas streams by a membrane absorption method. Gas separation & purification, 1994. **8**(2): p. 107-114.
222. Kohl, A.L. and R. Nielsen, Gas purification. 1997: Gulf Professional Publishing.
223. Rochelle, G.T., Thermal degradation of amines for CO2 capture. Current Opinion in Chemical Engineering, 2012. **1**(2): p. 183-190.
224. Davis, J., Thermal degradation of aqueous amines used for carbon dioxide capture, in Chemical Engineering. 2009, The University of Texas at Austin: Texas, USA.
225. Freeman, S., Thermal degradation and oxidation of aqueous piperazine for carbon dioxide capture, in Chemical Engineering. 2011, The University of Texas at Austin: Texas, USA.
226. Huang, Q., et al., Thermal degradation of amino acid salts in CO2 capture. International Journal of Greenhouse Gas Control, 2013. **19**: p. 243-250.
227. Grimekis, D., et al., Experimental investigation of CO2 solubility and its absorption rate into promoted aqueous potassium carbonate solutions at elevated temperatures. International Journal of Greenhouse Gas Control, 2019. **81**: p. 83-92.
228. Cullinane, J.T. and G.T. Rochelle, Carbon dioxide absorption with aqueous potassium carbonate promoted by piperazine. Chemical Engineering Science, 2004. **59**(17): p. 3619-3630.
229. Lee, A., et al., Understanding the vapour–liquid equilibrium of CO2 in mixed solutions of potassium carbonate and potassium glycinate. International Journal of Greenhouse Gas Control, 2016. **47**: p. 303-309.
230. Lee, A., et al., A study of the vapour–liquid equilibrium of CO2 in mixed solutions of potassium carbonate and potassium glycinate. International Journal of Greenhouse Gas Control, 2015. **36**: p. 27-33.

231. Dennard, A. and R. Williams, The catalysis of the reaction between carbon dioxide and water. Journal of the Chemical Society A: Inorganic, Physical, Theoretical, 1966: p. 812-816.
232. Phan, D.T., et al., Catalysis of CO2 absorption in aqueous solution by inorganic oxoanions and their application to post combustion capture. Environmental science & technology, 2014. **48**(8): p. 4623-4629.
233. Astarita, G., D.W. Savage, and J.M. Longo, Promotion of CO2 mass transfer in carbonate solutions. Chemical Engineering Science, 1981. **36**(3): p. 581-588.
234. Borhani, T.N.G., et al., Rate-based simulation and comparison of various promoters for CO2 capture in industrial DEA-promoted potassium carbonate absorption unit. Journal of Industrial and Engineering Chemistry, 2015. **22**: p. 306-316.
235. Pacheco, M.A. and G.T. Rochelle, Rate-based modeling of reactive absorption of CO2 and H2S into aqueous methyldiethanolamine. Industrial & engineering chemistry research, 1998. **37**(10): p. 4107-4117.
236. Freeman, S.A., et al., Carbon dioxide capture with concentrated, aqueous piperazine. International Journal of Greenhouse Gas Control, 2010. **4**(2): p. 119-124.
237. Li, J., et al., Measurement and modelling of the solubility of carbon dioxide in aqueous 1, 8-p-menthane-diamine solution. The Journal of Chemical Thermodynamics, 2014. **71**: p. 64-70.
238. Moffat, R.J., Describing the uncertainties in experimental results. Experimental thermal and fluid science, 1988. **1**(1): p. 3-17.
239. Chen, C.C. and L.B. Evans, A local composition model for the excess Gibbs energy of aqueous electrolyte systems. AIChE Journal, 1986. **32**(3): p. 444-454.
240. Chen, C.C. and Y. Song, Generalized electrolyte-NRTL model for mixed-solvent electrolyte systems. AIChE Journal, 2004. **50**(8): p. 1928-1941.
241. Koronaki, I., L. Prentza, and V. Papaefthimiou, Modeling of CO2 capture via chemical absorption processes− An extensive literature review. Renewable and Sustainable Energy Reviews, 2015. **50**: p. 547-566.
242. Hilliard, M., A Predictive Thermodynamic Model for an Aqueous Blend of Potassium Carbonate, Piperazine, and Monoethanolamine for Carbon Dioxide Capture from Flue Gas, in Chemical Engineering department. 2008, The University of Texas at Austin: Texas, USA.
243. Moioli, S. and L.A. Pellegrini, Improved rate-based modeling of the process of CO 2 capture with PZ solution. Chemical Engineering Research and Design, 2015. **93**: p. 611-620.
244. Thee, H., et al., Carbon dioxide absorption into unpromoted and borate-catalyzed potassium carbonate solutions. Chemical Engineering Journal, 2012. **181**: p. 694-701.
245. Yue, B., et al., Catalytic reforming of model tar compounds from hot coke oven gas with low steam/carbon ratio over Ni/MgO–Al2O3 catalysts. Fuel Processing Technology, 2010. **91**(9): p. 1098-1104.
246. Coll, R., et al., Steam reforming model compounds of biomass gasification tars: conversion at different operating conditions and tendency towards coke formation. Fuel Processing Technology, 2001. **74**(1): p. 19-31.
247. Vopička, O., M.G. De Angelis, and G.C. Sarti, Mixed gas sorption in glassy polymeric membranes: I. CO2/CH4 and n-C4/CH4 mixtures sorption in poly (1-trimethylsilyl-1-propyne)(PTMSP). Journal of membrane science, 2014. **449**: p. 97-108.
248. Kastanidis, P., et al., Solubility of Methane and Carbon Dioxide in the Aqueous Phase of the Ternary (Methane+ Carbon Dioxide+ Water) Mixture: Experimental Measurements and Molecular Dynamics Simulations. Journal of Chemical & Engineering Data, 2018. **63**(4): p. 1027-1035.
249. Mao, F., J.A. Gaunt, and S.K. Ong, Permeation of organic contaminants through PVC pipes. Journal-American Water Works Association, 2009. **101**(5): p. 128-136.
250. Garcia-Ochoa, F. and E. Gomez, Theoretical prediction of gas–liquid mass transfer coefficient, specific area and hold-up in sparged stirred tanks. Chemical engineering science, 2004. **59**(12): p. 2489-2501.
251. Gasmet Technologies. Gasmet DX4000 Technical Data. Available at: https://www.gasmet.com/products/category/portable-gas-analyzers/dx4000/ (accessed 14.09.2019).
252. Gasmet Technologies Oy. Calcmet for Windows: User's Guide and Reference Manual. 2009; Available at: http://www.gasmet.fi.
253. Paolini, V., et al., CO2/CH4 separation by hot potassium carbonate absorption for biogas upgrading. International Journal of Greenhouse Gas Control, 2019. **83**: p. 186-194.
254. Heymes, F., et al., A new efficient absorption liquid to treat exhaust air loaded with toluene. Chemical Engineering Journal, 2006. **115**(3): p. 225-231.

255. Ozturk, B. and D. Yilmaz, Absorptive removal of volatile organic compounds from flue gas streams. Process Safety and Environmental Protection, 2006. **84**(5): p. 391-398.
256. McCoy, H.N., Equilibrium in the system composed of sodium carbonate, sodium bicarbonate, carbon dioxide, and water. 1904: University of Chicago Press.
257. Pitzer, K.S., Thermodynamics of electrolytes. I. Theoretical basis and general equations. The Journal of Physical Chemistry, 1973. **77**(2): p. 268-277.
258. Chen, C.C., et al., Local composition model for excess Gibbs energy of electrolyte systems. Part I: Single solvent, single completely dissociated electrolyte systems. AIChE Journal, 1982. **28**(4): p. 588-596.
259. Fosbøl, P.L., B. Maribo-Mogensen, and K. Thomsen, Solids modelling and capture simulation of piperazine in potassium solvents. Energy Procedia, 2013. **37**: p. 844-859.
260. Chen, C.C., et al., Extension and application of the pitzer equation for vapor-liquid equilibrium of aqueous electrolyte systems with molecular solutes. AIChE Journal, 1979. **25**(5): p. 820-831.
261. Pérez-Salado Kamps, Á., et al., Solubility of CO2 in aqueous solutions of KCl and in aqueous solutions of K2CO3. Journal of Chemical & Engineering Data, 2007. **52**(3): p. 817-832.
262. Imle, M., et al., Solubility of carbon dioxide in activated potash solutions in the low and high gas loading regions. Industrial & Engineering Chemistry Research, 2013. **52**(37): p. 13477-13489.
263. Bohloul, M., et al., CO2 absorption using aqueous solution of potassium carbonate: Experimental measurement and thermodynamic modeling. Fluid Phase Equilibria, 2017. **447**: p. 132-141.
264. Endo, K., et al., The effect of boric acid on the vapour liquid equilibrium of aqueous potassium carbonate. Fluid Phase Equilibria, 2011. **309**(2): p. 109-113.
265. Kaur, H. and C.-C. Chen, Thermodynamic modeling of CO2 absorption in aqueous potassium carbonate solution with electrolyte NRTL model. Fluid Phase Equilibria, 2020. **505**: p. 112339.
266. Berrouk, A.S. and R. Ochieng, Improved performance of the natural-gas-sweetening Benfield-HiPure process using process simulation. Fuel processing technology, 2014. **127**: p. 20-25.
267. Sanyal, D., N. Vasishtha, and D.N. Saraf, Modeling of carbon dioxide absorber using hot carbonate process. Industrial & engineering chemistry research, 1988. **27**(11): p. 2149-2156.
268. Al-Ramdhan, H.A., A rate-based model for the design and simulation of a carbon dioxide absorber using the hot potassium carbonate process. 2002.
269. Rahimpour, M. and A. Kashkooli, Enhanced carbon dioxide removal by promoted hot potassium carbonate in a split-flow absorber. Chemical Engineering and Processing: Process Intensification, 2004. **43**(7): p. 857-865.
270. Thiele, R., et al., Design of industrial reactive absorption processes in sour gas treatment using rigorous modelling and accurate experimentation. Chemical Engineering Research and Design, 2007. **85**(1): p. 74-87.
271. Oexmann, J., C. Hensel, and A. Kather, Post-combustion CO2-capture from coal-fired power plants: Preliminary evaluation of an integrated chemical absorption process with piperazine-promoted potassium carbonate. International journal of greenhouse gas control, 2008. **2**(4): p. 539-552.
272. Ahmadi, M., V. Gomes, and K. Ngian, Advanced modelling in performance optimization for reactive separation in industrial CO2 removal. Separation and Purification Technology, 2008. **63**(1): p. 107-115.
273. Oyenekan, B.A. and G.T. Rochelle, Rate modeling of CO2 stripping from potassium carbonate promoted by piperazine. International Journal of Greenhouse Gas Control, 2009. **3**(2): p. 121-132.
274. Yi, F., et al., Modeling and experimental studies on absorption of CO2 by Benfield solution in rotating packed bed. Chemical Engineering Journal, 2009. **145**(3): p. 377-384.
275. Mumford, K.A., et al., Post-combustion capture of CO2: results from the solvent absorption capture plant at Hazelwood power station using potassium carbonate solvent. Energy & fuels, 2011. **26**(1): p. 138-146.
276. Faiz, R. and M. Al-Marzouqi, Insights on natural gas purification: Simultaneous absorption of CO2 and H2S using membrane contactors. Separation and purification technology, 2011. **76**(3): p. 351-361.
277. Smith, K.H., et al., Pre-combustion capture of CO2—Results from solvent absorption pilot plant trials using 30 wt% potassium carbonate and boric acid promoted potassium carbonate solvent. International Journal of Greenhouse Gas Control, 2012. **10**: p. 64-73.
278. Park, H., Reduced-order modeling of carbon dioxide absorption and desorption with potassium carbonate promoted by piperazine. International Journal of Heat and Mass Transfer, 2014. **73**: p. 600-615.
279. Harkin, T., A. Hoadley, and B. Hooper, Using multi-objective optimisation in the design of CO2 capture systems for retrofit to coal power stations. Energy, 2012. **41**(1): p. 228-235.

280. Echt, W. Technologies for Efficient Purification of Natural and Synthesis Gases, available at: https://www.uop.com/technologies-for-efficient-purification-of-natural-and-synthesis-gases/ (accessed 20.10.2019). 2013.
281. Lambert, T., A. Hoadley, and B. Hooper, Process integration of solar thermal energy with natural gas combined cycle carbon capture. Energy, 2014. **74**: p. 248-253.
282. Li, S., et al., Energy and exergy analyses of an integrated gasification combined cycle power plant with CO2 capture using hot potassium carbonate solvent. Environmental science & technology, 2014. **48**(24): p. 14814-14821.
283. Isa, F., et al., CO2 removal via promoted potassium carbonate: A review on modeling and simulation techniques. International Journal of Greenhouse Gas Control, 2018. **76**: p. 236-265.
284. Dindore, V., D.W.F. Brilman, and G. Versteeg, Modelling of cross-flow membrane contactors: mass transfer with chemical reactions. Journal of membrane science, 2005. **255**(1-2): p. 275-289.
285. Hilliard, M., Thermodynamics of Aqueous Piperazine/Potassium Carbonate/Carbon Dioxide Characterized by the Electrolyte NRTL Model within Aspen Plus. 2005, The University of Texas at Austin: Texas, USA.
286. Pinsent, B., L. Pearson, and F. Roughton, The kinetics of combination of carbon dioxide with hydroxide ions. Transactions of the Faraday Society, 1956. **52**: p. 1512-1520.
287. Chen, E., Carbon dioxide absorption into piperazine promoted potassium carbonate using structured packing. 2007.
288. Tosh, J.S., et al., Equilibrium pressures of hydrogen sulfide and carbon dioxide over solutions of potassium carbonate. Vol. 5622. 1960: US Department of the Interior, Bureau of Mines.
289. Aseyev, G. and I. Zaytsev, translated from Russian by Yu. A. Gorshkov. Volumetric Properties of Electrolyte Solutions: Estimation Methods and Experimental Data, 1996.
290. Aseyev, G., Electrolytes: equilibria in solutions and phase equilibria. Calculation of Multicomponent Systems and Experimental Data on the Activities of Water, Vapor Pressures, and Osmotic Coefficients, Begell House, New York, 1999.
291. Puchkov, L. and V. Kurochkina, Saturated Vapor Pressure Over Aqueous Solutions of Potassium Carboonate. Zhur. Prikland. Khim, 1970. **43**(1): p. 181-183.
292. Kamps, Á.P.S., J. Xia, and G. Maurer, Solubility of CO2 in (H2O+ piperazine) and in (H2O+ MDEA+ piperazine). AIChE Journal, 2003. **49**(10): p. 2662-2670.
293. Bishnoi, S., Carbon dioxide absorption and solution equilibrium in piperazine activated methyldiethanolamine. 2002.
294. Ermatchkov, V., Á.P.-S. Kamps, and G. Maurer, Chemical equilibrium constants for the formation of carbamates in (carbon dioxide+ piperazine+ water) from 1H-NMR-spectroscopy. The Journal of Chemical Thermodynamics, 2003. **35**(8): p. 1277-1289.
295. Britt, H. and R. Luecke, The estimation of parameters in nonlinear, implicit models. Technometrics, 1973. **15**(2): p. 233-247.
296. Ooi, S.M.P., Development and demonstration of a new non-equilibrium rate-based process model for the hot potassium carbonate process. 2009.
297. Stichlmair, J., J. Bravo, and J. Fair, General model for prediction of pressure drop and capacity of countercurrent gas/liquid packed columns. Gas Separation & Purification, 1989. **3**(1): p. 19-28.
298. Onda, K., H. Takeuchi, and Y. Okumoto, Mass transfer coefficients between gas and liquid phases in packed columns. Journal of chemical engineering of Japan, 1968. **1**(1): p. 56-62.
299. Urech, J., et al., An assessment of different solvent-based capture technologies within an IGCC–CCS power plant. Energy, 2014. **64**: p. 268-276.
300. Field, J.H., et al., Removing hydrogen sulfide by hot potassium carbonate absorption. Vol. 5660. 1960: United States Dept. of the Interior, Bureau of Mines.
301. Akinpelumi, K., C. Saha, and G.T. Rochelle, Piperazine aerosol mitigation for post-combustion carbon capture. International Journal of Greenhouse Gas Control, 2019. **91**: p. 102845.
302. Bhave, A., et al., Screening and techno-economic assessment of biomass-based power generation with CCS technologies to meet 2050 CO2 targets. Applied energy, 2017. **190**: p. 481-489.
303. Oreggioni, G.D., et al., Environmental assessment of biomass gasification combined heat and power plants with absorptive and adsorptive carbon capture units in Norway. International Journal of Greenhouse Gas Control, 2017. **57**: p. 162-172.

304. Erlach, B., B. Harder, and G. Tsatsaronis, Combined hydrothermal carbonization and gasification of biomass with carbon capture. Energy, 2012. **45**(1): p. 329-338.
305. Dinca, C., et al., CO2 capture from syngas generated by a biomass gasification power plant with chemical absorption process. Energy, 2018. **149**: p. 925-936.
306. Zang, G., et al., A comparative study of biomass integrated gasification combined cycle power systems: performance analysis. Bioresource technology, 2018. **255**: p. 246-256.
307. Verhelst, S., et al., Methanol as a fuel for internal combustion engines. Progress in Energy and Combustion Science, 2019. **70**: p. 43-88.
308. Atsonios, K., K.D. Panopoulos, and E. Kakaras, Investigation of technical and economic aspects for methanol production through CO2 hydrogenation. International Journal of Hydrogen Energy, 2016. **41**(4): p. 2202-2214.
309. Kiss, A.A., et al., Novel efficient process for methanol synthesis by CO2 hydrogenation. Chemical engineering journal, 2016. **284**: p. 260-269.
310. Ptasinski, K., C. Hamelinck, and P. Kerkhof, Exergy analysis of methanol from the sewage sludge process. Energy Conversion and Management, 2002. **43**(9-12): p. 1445-1457.
311. Puig-Gamero, M., et al., Three integrated process simulation using aspen plus®: Pine gasification, syngas cleaning and methanol synthesis. Energy conversion and management, 2018. **177**: p. 416-427.
312. Phillips, S.D., et al., Gasoline from woody biomass via thermochemical gasification, methanol synthesis, and methanol-to-gasoline technologies: A technoeconomic analysis. Industrial & engineering chemistry research, 2011. **50**(20): p. 11734-11745.
313. Xiang, Y., et al., Exergetic evaluation of renewable light olefins production from biomass via synthetic methanol. Applied energy, 2015. **157**: p. 499-507.
314. Liu, G.-j., et al., Energy savings by co-production: a methanol/electricity case study. Applied Energy, 2010. **87**(9): p. 2854-2859.
315. Cormos, A.-M., C. Dinca, and C.-C. Cormos, Multi-fuel multi-product operation of IGCC power plants with carbon capture and storage (CCS). Applied Thermal Engineering, 2015. **74**: p. 20-27.
316. Heinze, C., et al., Techno-economic assessment of polygeneration based on fluidized bed gasification. Fuel, 2019. **250**: p. 285-291.
317. Fagernäs, L., et al., Drying of biomass for second generation synfuel production. Biomass and Bioenergy, 2010. **34**(9): p. 1267-1277.
318. Evans, R., et al., Development of biomass gasification to produce substitute fuels. 1988, Pacific Northwest Lab., Richland, WA (USA).
319. Christodoulou, C., et al., Comparing calcined and un-treated olivine as bed materials for tar reduction in fluidized bed gasification. Fuel processing technology, 2014. **124**: p. 275-285.
320. Hannula, I. and E. Kurkela, A parametric modelling study for pressurised steam/O2-blown fluidised-bed gasification of wood with catalytic reforming. Biomass and Bioenergy, 2012. **38**: p. 58-67.
321. Aneke, M. and M. Wang, Potential for improving the energy efficiency of cryogenic air separation unit (ASU) using binary heat recovery cycles. Applied Thermal Engineering, 2015. **81**: p. 223-231.
322. Jones, D., et al., Optimal design and integration of an air separation unit (ASU) for an integrated gasification combined cycle (IGCC) power plant with CO2 capture. Fuel processing technology, 2011. **92**(9): p. 1685-1695.
323. Kaisalo, N., et al., Reforming solutions for biomass-derived gasification gas–experimental results and concept assessment. Fuel, 2015. **147**: p. 208-220.
324. Anis, S. and Z. Zainal, Tar reduction in biomass producer gas via mechanical, catalytic and thermal methods: A review. Renewable and sustainable energy reviews, 2011. **15**(5): p. 2355-2377.
325. Xu, C.C., et al., Recent advances in catalysts for hot-gas removal of tar and NH3 from biomass gasification. Fuel, 2010. **89**(8): p. 1784-1795.
326. Hein, K., et al., Joule II-Programme. Clean Coal Technology R&D. 2nd phase. Volume IV. Integrated hot fuel gas cleaning for advanced gasification combined cycle processes. 1998.
327. Carbo, M., et al., Steam demand reduction of water–gas shift reaction in IGCC power plants with pre-combustion CO2 capture. International Journal of Greenhouse Gas Control, 2009. **3**(6): p. 712-719.
328. Andersson, K.J., M.S.-S. Rasmussen, and P.E.H. Nielsen, Industrial-scale gas conditioning including Topsoe tar reforming and purification downstream biomass gasifiers: An overview and recent examples. Fuel, 2017. **203**: p. 1026-1030.

329. Van-Dal, É.S. and C. Bouallou, Design and simulation of a methanol production plant from CO2 hydrogenation. Journal of Cleaner Production, 2013. **57**: p. 38-45.
330. Yang, C., et al., Methanol synthesis from CO2-rich syngas over a ZrO2 doped CuZnO catalyst. Catalysis Today, 2006. **115**(1-4): p. 222-227.
331. Kotas, T.J., The exergy method of thermal plant analysis. 2013: Elsevier.
332. Szargut, J., D.R. Morris, and F.R. Steward, Exergy analysis of thermal, chemical, and metallurgical processes. 1987.
333. Szargut, J. and T. Styrylska, Approximate evaluation of the exergy of fuels. Brennst. Wärme Kraft, 1964. **16**(12): p. 589-596.
334. Qian, H., et al., Prediction models for chemical exergy of biomass on dry basis from ultimate analysis using available electron concepts. Energy, 2017. **131**: p. 251-258.
335. Kalogirou, S.A., et al., Exergy analysis of solar thermal collectors and processes. Progress in Energy and Combustion Science, 2016. **56**: p. 106-137.
336. Turn, S., et al., An experimental investigation of hydrogen production from biomass gasification. International journal of hydrogen energy, 1998. **23**(8): p. 641-648.
337. Chu, H., et al., Investigation of hydrogen production from model bio-syngas with high CO2 content by water-gas shift reaction. International Journal of Hydrogen Energy, 2015. **40**(11): p. 4092-4100.
338. Andersson, J., J. Lundgren, and M. Marklund, Methanol production via pressurized entrained flow biomass gasification–Techno-economic comparison of integrated vs. stand-alone production. Biomass and bioenergy, 2014. **64**: p. 256-268.
339. Inui, T., et al., Structure and function of Cu-based composite catalysts for highly effective synthesis of methanol by hydrogenation of CO2 and CO. Catalysis today, 1997. **36**(1): p. 25-32.
340. Zhang, S., X. Ye, and Y. Lu, Development of a Potassium Carbonate-Based Absorption Process with Crystallization-Enabled High-Pressure Stripping for CO2 Capture: Vapor–Liquid Equilibrium Behavior and CO2 Stripping Performance of Carbonate/Bicarbonate Aqueous Systems. Energy Procedia, 2014. **63**: p. 665-675.
341. Ebadi, M.J. and M. Gorji-Bandpy, Exergetic analysis of gas turbine plants. International Journal of Exergy, 2005. **2**(1): p. 31-39.
342. Atsonios, K., et al., Exergy analysis of a hydrogen fired combined cycle with natural gas reforming and membrane assisted shift reactors for CO2 capture. Energy conversion and management, 2012. **60**: p. 196-203.
343. Panopoulos, K., et al., High temperature solid oxide fuel cell integrated with novel allothermal biomass gasification: Part II: Exergy analysis. Journal of Power Sources, 2006. **159**(1): p. 586-594.
344. Wetenhall, B., J. Race, and M. Downie, The effect of CO2 purity on the development of pipeline networks for carbon capture and storage schemes. International Journal of Greenhouse Gas Control, 2014. **30**: p. 197-211.
345. De Visser, E., et al., Dynamis CO2 quality recommendations. International journal of greenhouse gas control, 2008. **2**(4): p. 478-484.
346. Grant, T., C. Anderson, and B. Hooper, Comparative life cycle assessment of potassium carbonate and monoethanolamine solvents for CO2 capture from post combustion flue gases. International Journal of Greenhouse Gas Control, 2014. **28**: p. 35-44.

Appendix-I: Figures

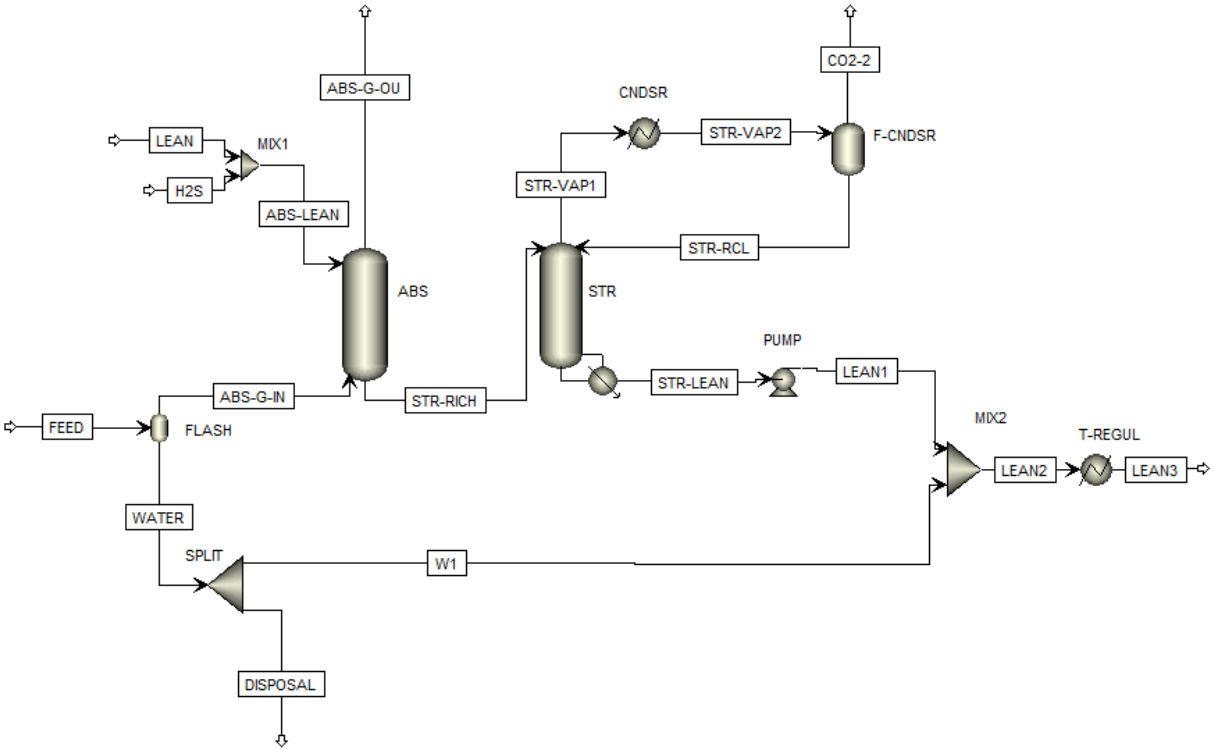

Figure A1: Flowsheet of AGR process for both PZ-promoted and pure K_2CO_3 solutions in Aspen Plus™ (Chapter 6)

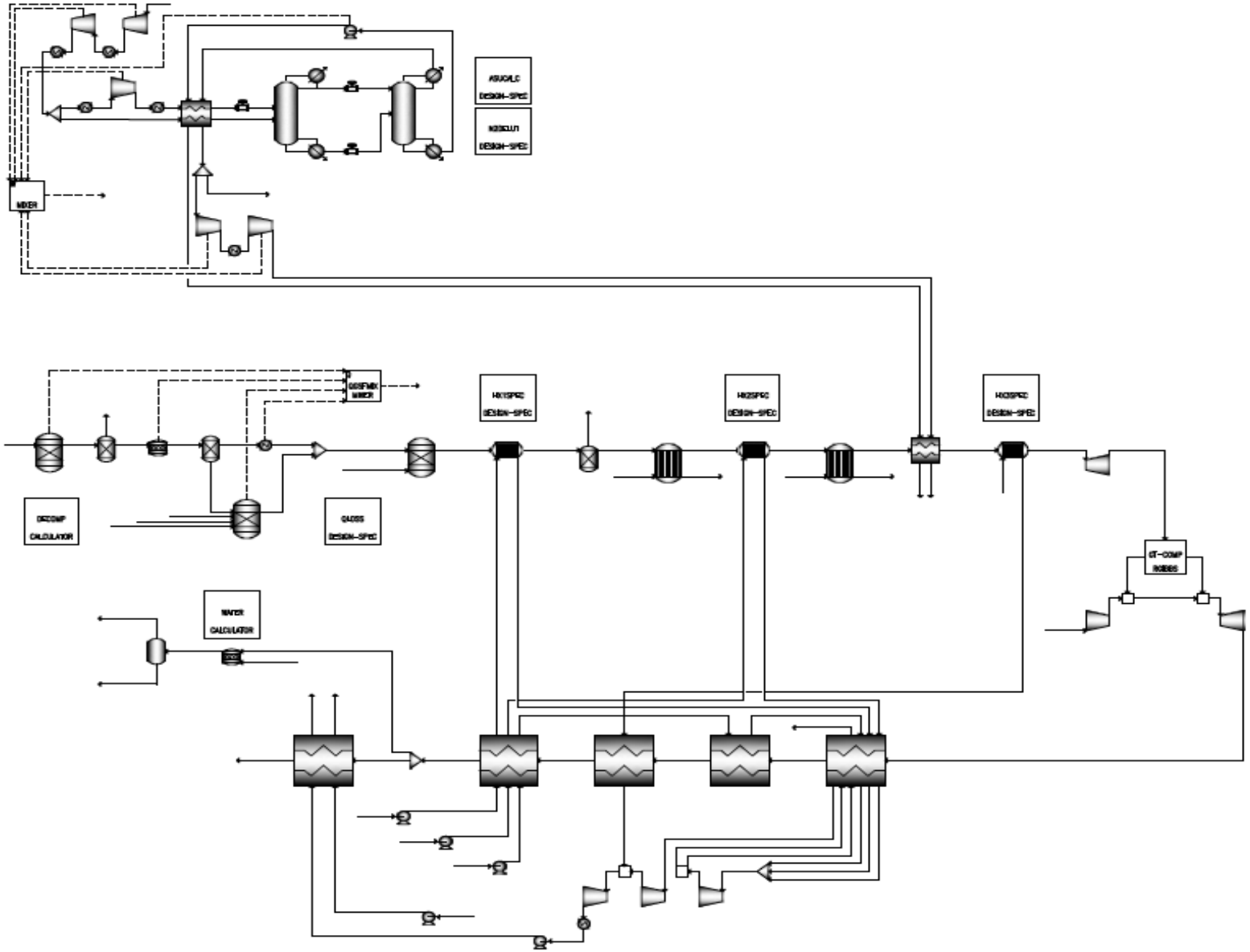

Figure A2: Flowsheet of BIGCC plant without CCS for electricity generation (Scenario I, Chapter 7) in Aspen Plus™

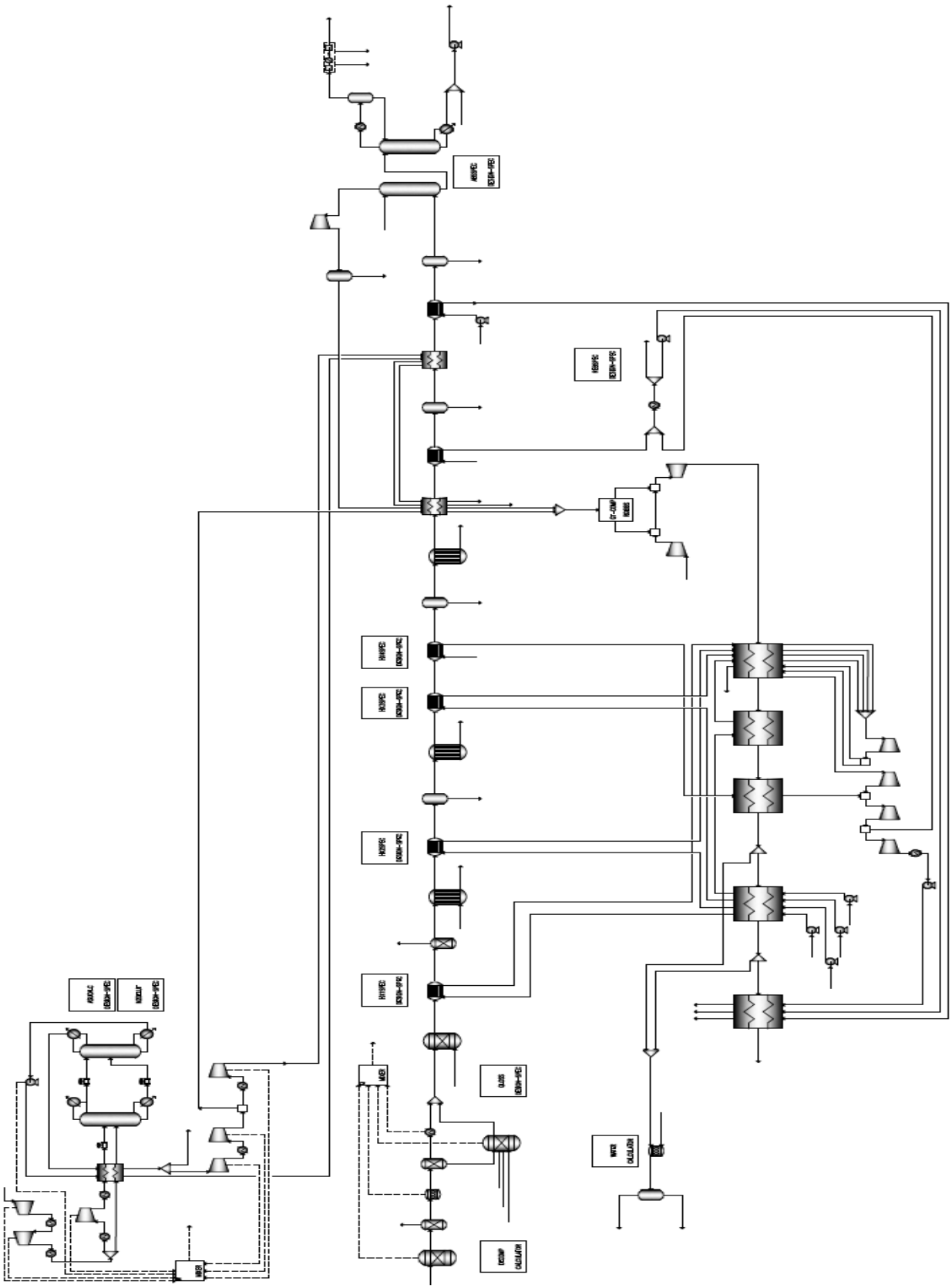

Figure A3: Flowsheet of BIGCC plant with K_2CO_3 AGR for electricity generation (Scenario II, Chapter 7) in Aspen Plus™

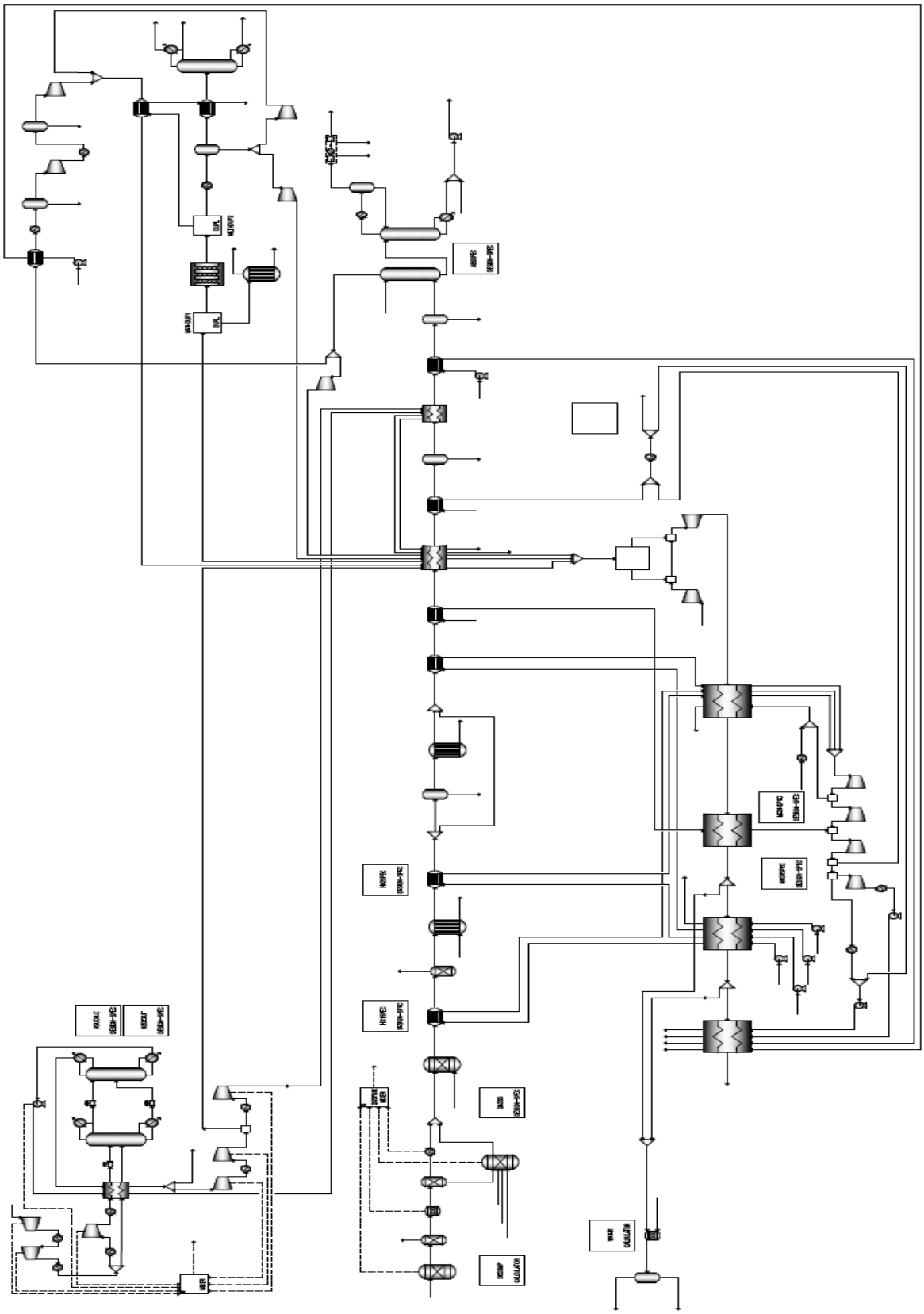

Figure A4: Flowsheet of BIGCC plant with K_2CO_3 AGR for electricity/MeOH cogeneration (Scenario III, Chapter 7) in Aspen Plus™

Appendix-II: List of author publications

Diploma Thesis (School of Mechanical Engineering, NTUA):

- Experimental study of agricultural residues as feedstock for fluidized bed gasification compared to woody biomass and calcined olivine as bed material for the process (NTUA, in Greek).

Book Chapter:

- Roumpedakis, T., Vlavakis, P., Braimakis, K., Grimekis, D., & Karellas, S. (2018). Hydrogen Production and Storage. Renewable Energy Engineering: Solar, Wind, Biomass, Hydrogen and Geothermal Energy Systems., 3, 272-323.

Journal articles (peer-reviewed):

- Grimekis, D., Giannoulidis, S., Manou, K., Panopoulos, K. D., & Karellas, S. (2019). Experimental investigation of CO_2 solubility and its absorption rate into promoted aqueous potassium carbonate solutions at elevated temperatures. International Journal of Greenhouse Gas Control, 81, 83-92.
- Edinger, P., Grimekis, D., Panopoulos, K., Karellas, S., & Ludwig, C. (2017). Adsorption of thiophene by activated carbon: A global sensitivity analysis. Journal of environmental chemical engineering, 5(4), 4173-4184.
- Christodoulou, C., Grimekis, D., Panopoulos, K. D., Vamvuka, D., Karellas, S., & Kakaras, E. (2014). Circulating fluidized bed gasification tests of seed cakes residues after oil extraction and comparison with wood. Fuel, 132, 71-81.
- Christodoulou, C., Grimekis, D., Panopoulos, K. D., Pachatouridou, E. P., Iliopoulou, E. F., & Kakaras, E. (2014). Comparing calcined and un-treated olivine as bed materials for tar reduction in fluidized bed gasification. Fuel processing technology, 124, 275-285.
- Roumpedakis, T., Kallis G., Magiri-Skouloudi, D., Grimekis, D. & Karellas, S. Life Cycle Analysis of ZEOSOL solar cooling and heating system (2019, submitted in Renewable Energy journal, Elsevier).
- Braimakis, K., Magiri-Skouloudi, D., Grimekis, D. & Karellas, S. Energy-exergy analysis and CO_2 footprint evaluation of ultra-supercritical biomass-fuelled steam power plants for industrial CHP, district heating and cooling (2019, submitted in Renewable Energy journal, Elsevier).
- Grimekis, D., Pavlis, C., Panopoulos, K. D., & Karellas, S. Energy and exergy analyses of a biomass gasification plant for power/MeOH cogeneration with CCS (manuscript under preparation for submission).
- Grimekis, D., Manou, K., Panopoulos, K. D., & Karellas, S. Thermodynamic and process modeling study of AGR from syngas based on pure and promoted K_2CO_3 aqueous solutions (manuscript under preparation for submission).

Conference papers (peer-reviewed):

- Grimekis, D., Delgado Calvo, M. A., Panopoulos, K. D., & Karellas, S. Modelling of a 3 MW_{th} BFB gasifier in Aspen Plus. European Biomass Conference and Exhibition 2018, Copenhagen, Denmark.
- Magiri-Skouloudi, D., Dimiropoulos, V., Grimekis, D. & Karellas, S. Environmental evaluation of highly efficient large scale biomass-fuelled cogeneration plants. ECOS 2019, Wrocław, Poland.
- Braimakis, K., Magiri-Skouloudi, D., Grimekis, D. & Karellas, S. Optimization of supercritical biomass-fueled steam power plants for industrial CHP, district heating and cooling. ECOS 2019, Wrocław, Poland.
- Hysenj, S., Grimekis, D., Doukelis, A., Panopoulos, K.D. & Karellas, S. Modeling of a large scale, biomass fired combined heat and power plant coupled with an alumina/aluminium production process. ECOS 2018, Guimaraes, Portugal.
- Christodoulou, C., Grimekis, D., Tsiotas, K., Papamichail, I., Panopoulos, K. D., Vamvuka, D., Karellas, S. & Kakaras, E. Circulating fluidized bed gasification of 1st and 2nd generation biofuel seed cakes after oil extraction. In Proceedings of the 21st European Biomass Conference 2013, Copenhagen, Denmark.

ΕΚΤΕΤΑΜΕΝΗ ΠΕΡΙΛΗΨΗ ΤΗΣ ΔΙΔΑΚΤΟΡΙΚΗΣ ΔΙΑΤΡΙΒΗΣ ΣΤΗΝ ΕΛΛΗΝΙΚΗ ΓΛΩΣΣΑ

1 Εισαγωγή και θεωρητικό υπόβαθρο εργασίας

1.1 Το ενεργειακό μίγμα και ο ρόλος των στερεών καυσίμων για την παραγωγή ενέργειας, καυσίμων και χημικών

Η ενέργεια αποτελεί κινητήρια δύναμη για την οικονομική ανάπτυξη και τη βελτίωση του βιοτικού επιπέδου, κυρίως από την εποχή της Βιομηχανικής Επανάστασης και μέχρι σήμερα. Σύμφωνα με την έκθεση της ExxonMobil για το ενεργειακό τοπίο [1], η κατά κεφαλήν κατανάλωση ηλεκτρικής ενέργειας σε μια χώρα φαίνεται να είναι εναρμονισμένη με το κατά κεφαλήν εισόδημα. Στο πλαίσιο αυτό, η ζήτηση ενέργειας αναμένεται να αυξηθεί συνεχώς τις επόμενες δεκαετίες, λόγω της πληθυσμιακής αύξησης (9.2 δισεκατομμύρια πληθυσμός μέχρι το 2040). Ταυτόχρονα, έχει ήδη σημειωθεί αύξηση της καταναλισκόμενης ενέργειας σε χώρες με ταχείς ρυθμούς ανάπτυξης, όπως η Κίνα, η Ινδία και άλλες χώρες εκτός ΟΟΣΑ. Το 2017, η παγκόσμια αύξηση της κατανάλωσης πρωτογενούς ενέργειας ήταν κατά μέσο όρο 2.2%, υψηλότερη από τον μέσο όρο 10 ετών, με αύξηση 1.7% ετησίως [2].

Το 2015, τα ορυκτά καύσιμα αντιπροσώπευαν το 78.4% της παγκόσμιας τελικής κατανάλωσης ενέργειας [3]. Σύμφωνα με την πηγή [2], το ποσοστό του ορυκτού άνθρακα στην παγκόσμια παραγωγή ηλεκτρικής ενέργειας παρέμεινε σχεδόν σταθερό μεταξύ 1985 και 2017 με τιμές κοντά στο 40% (38.1% το 2017), ακολουθούμενη από το φυσικό αέριο με ποσοστό 23.2% το 2017. Το ποσοστό του πετρελαίου στην παγκόσμια παραγωγή ηλεκτρικής ενέργειας μειώνεται συνεχώς και είναι κάτω από 5% κατά την τελευταία πενταετία. Η τάση αυτή αντισταθμίζεται από το μεγαλύτερο μερίδιο του στην παγκόσμια κατανάλωση πρωτογενούς ενέργειας (περίπου 35%). Επιπλέον, η χρήση του φυσικού αερίου αυξάνεται συνεχώς τα τελευταία χρόνια και θεωρείται ως ένα κατάλληλο «μεταβατικό» καύσιμο για την μείωση των εκπομπών CO_2. Οφέλη όπως η αξιοποίησή του σε πολύ αποδοτικούς και ευέλικτους κύκλους παραγωγής ηλεκτρικής ισχύος, καθώς και η διαθεσιμότητα ανεπτυγμένου δικτύου μεταφοράς και η υπάρχουσα υποδομή για τη διαχείρισή του γενικότερα εκτιμάται πως θα συμβάλουν στην περαιτέρω διάδοσή του. Ο λόγος αποθέματος προς παραγωγή (R/P) αποτελεί ένα χρήσιμο δείκτη που μπορεί να παράσχει ενδείξεις για την πιθανή μελλοντική εξάρτηση από συγκεκριμένα καύσιμα. Πρόσφατες εκτιμήσεις (2017) για τους δείκτες R/P πετρελαίου, φυσικού αερίου και άνθρακα παρουσιάστηκαν από την BP [2] με τιμές 50.2, 52.6 και 134 έτη, αντίστοιχα. Ερευνητικές μελέτες που εστιάζουν στο ζήτημα της εξάντλησης των ορυκτών πόρων έχουν επίσης δημοσιευτεί. Οι Maggio και Cacciola [4] εκτίμησαν ότι ο ορυκτός άνθρακας και το φυσικό αέριο αναμένεται να παρουσιάσουν την αιχμή της ζήτησής τους μεταξύ 2042-2062 και 2024-2046, αντίστοιχα. Με βάση τα σενάρια αναφοράς, ο ορυκτός άνθρακας αναμένεται να διαδραματίσει σημαντικό ρόλο στην παγκόσμια παραγωγή ενέργειας κατά τις επόμενες δεκαετίες, κυρίως σε αναδυόμενες και ταχέως αναπτυσσόμενες χώρες (π.χ. στην Ασία). Η ExxonMobil εκτιμά πως το ποσοστό του ορυκτού άνθρακα στην πρωτογενή κατανάλωση ενέργειας κατά το 2040 θα είναι της τάξεως του 20% [1]. Πλεονεκτήματα όπως το χαμηλό κόστος, η υψηλή διαθεσιμότητα των σταθμών παραγωγής ενέργειας και η υψηλή πυκνότητα ισχύος σε σύγκριση με τεχνολογίες ανανεώσιμων πηγών ενέργειας (ΑΠΕ) ενισχύουν περαιτέρω αυτή την προοπτική.

Φυσικά, το ποσοστό των ορυκτών καυσίμων στην παγκόσμια παραγωγή ενέργειας θα επηρεαστεί σίγουρα από εθνικούς και διεθνείς στόχους και πολιτικές για την κλιματική αλλαγή, οι οποίοι έχουν ήδη υιοθετηθεί ή βρίσκονται υπό επεξεργασία από κράτη και συνασπισμούς κρατών. Το 2015, τα συμβαλλόμενα μέρη του Οργανισμού Ηνωμένων Εθνών για την κλιματική αλλαγή (UNFCCC) συμφώνησαν σε δράσεις στην κατεύθυνση της καταπολέμησης της κλιματικής αλλαγής και σε εντατικοποίηση των επενδύσεων για ένα βιώσιμο μέλλον με χαμηλές εκπομπές άνθρακα («Συμφωνία του Παρισιού»). Βασικό σημείο αναφοράς ορίστηκε ο περιορισμός της αύξησης της θερμοκρασίας του πλανήτη κάτω από 1.5 °C σε σχέση με τα προ-βιομηχανικά επίπεδα. Στο πλαίσιο αυτό επιχειρείται η μετάβαση από τα παραδοσιακά ορυκτά καύσιμα στις ΑΠΕ. Η Ευρωπαϊκή Ένωση (ΕΕ) δημοσίευσε έναν οδικό χάρτη για τη μείωση των εκπομπών CO_2 άνω του 80% μέχρι το 2050 σε σύγκριση με το 1990 [6], η οποία συνδέεται άμεσα με υψηλότερα ποσοστά ΑΠΕ. Ωστόσο, μέχρι στιγμής, ο υψηλός ρυθμός ολοκλήρωσης νέων έργων ΑΠΕ (κυρίως φωτοβολταϊκών και αιολικών πάρκων) δεν έχει μεταφραστεί σε μια σημαντική μεταβολή του ποσοστού τους όσον αφορά τη ολική τελική κατανάλωση ενέργειας. Το γεγονός αυτό μπορεί να αποδοθεί στην έντονη αύξηση της συνολικής ζήτησης ενέργειας.

Είναι επομένως σαφές πως η χρήση ορυκτών καυσίμων συμπεριλαμβανομένου του ορυκτού άνθρακα θα πρέπει να συνδυαστεί με αποδοτικότερες τεχνολογίες ενεργειακής αξιοποίησης καθώς και τεχνολογίες δέσμευσης, αξιοποίησης και αποθήκευσης CO_2 (Carbon Capture, Utilization and Storage-CCUS). Ο Διεθνής Οργανισμός για τις Ανανεώσιμες Πηγές Ενέργειας (IRENA) δημοσίευσε έναν οδηγό με κατευθυντήριες γραμμές, ο οποίος εκτιμά ποια θα είναι η μελλοντική συμμετοχή διαφόρων ΑΠΕ και ορυκτών πηγών ενέργειας έως το 2050 [8]. Η συγκεκριμένη μελέτη του IRENA είναι σύμφωνη με τα βασικά σημεία της Συμφωνίας του Παρισιού (σενάριο REmap). Συγκεκριμένα, η μελέτη καθορίζει κατευθύνσεις για τέσσερις βασικούς τομείς: τις μεταφορές, τα κτήρια, τη βιομηχανία και τον τομέα της ηλεκτροπαραγωγής. Η σημαντικότερη εκτίμηση είναι η ηλεκτροδότηση των περισσότερων τομέων προκειμένου να αφομοιωθεί το υψηλό ποσοστό συμμετοχής της αιολικής και ηλιακής ενέργειας στο ενεργειακό μίγμα. Η βιομάζα αναγνωρίζεται ως μια σημαντική πηγή ενέργειας προς την κατεύθυνση της απεξάρτησης από τα ορυκτά καύσιμα στη μελέτη του IRENA. Συγκεκριμένα, στον τομέα των μεταφορών εκτιμάται αύξηση του ποσοστού συμμετοχής του βιοαερίου και των υγρών βιοκαυσίμων στην τελική κατανάλωση ενέργειας από 3% σήμερα σε 22% μέχρι το 2050. Στον κτηριακό τομέα, αναμένεται αντίστοιχη αύξηση του ποσοστού της βιοενέργειας από 4% σε 14%, ενώ στο βιομηχανικό τομέα αναμένεται τριπλασιασμός του ποσοστού συμμετοχής της βιομάζας (19% στην τελική κατανάλωση ενέργειας το 2050). Τέλος, στον τομέα της ηλεκτροπαραγωγής αναμένεται σχετικά μικρότερη αύξηση του ποσοστού συμμέτοχής της βιομάζας, η οποία ωστόσο συνδέεται με σημαντική αύξηση της συνολικά εγκατεστημένης ισχύος των σταθμών βιομάζας (από 119 GW το 2015 σε 384 GW το 2050). Το μέγιστο διαθέσιμο δυναμικό αναμένεται να καθορίσει το τελικό ποσοστό συμμετοχής, ενώ η βελτιστοποίηση των αλυσίδων μεταφοράς και η αύξηση του ποσοστού των αξιοποιούμενων βιογενών παραπροϊόντων (π.χ. υπολειμμάτων της αγροτικής παραγωγής, λοιπών απορριμμάτων κλπ.) αποτελούν βασικές κατευθύνσεις για την εντατικότερη αξιοποίηση των πηγών βιομάζας. Το Σχήμα 1 παρουσιάζει διάφορες εκτιμήσεις σχετικά με την συμμετοχή των ορυκτών καυσίμων, αλλά και των ΑΠΕ, μέχρι το 2050.

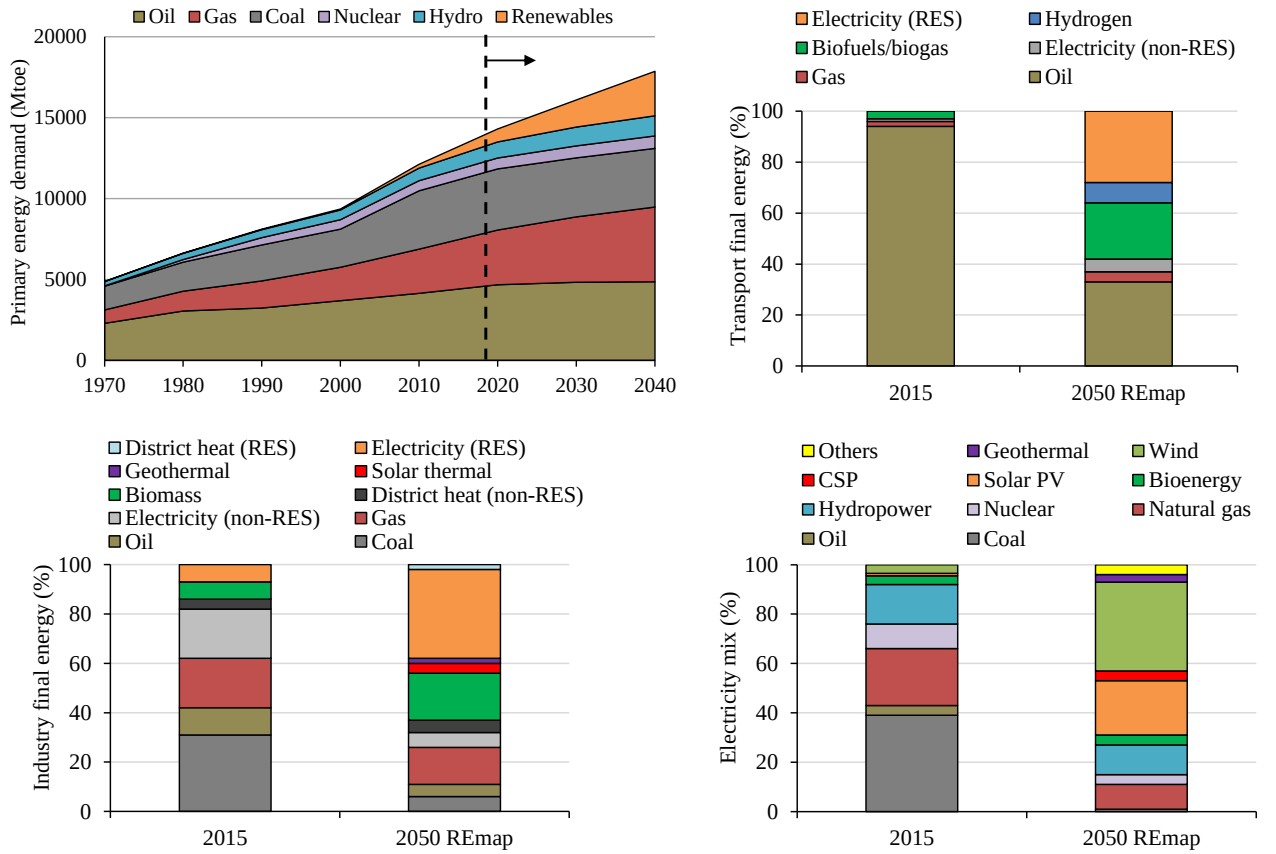

Σχήμα 1:(Άνω αριστερά) Πρωτογενής κατανάλωση ενέργειας ανά πηγή σύμφωνα με την [9]. (Άνω δεξιά και κάτω) Τελική κατανάλωση ενέργειας στις μεταφορές και στο βιομηχανικό κλάδο και μίγμα ηλεκτροπαραγωγής σύμφωνα με το Σενάριο REmap του IRENA [8].

Ιδιαίτερο σημείο αναφοράς αποτελεί η δυνατότητα αξιοποίησης βιομάζας για την παραγωγή αερίων και υγρών βιοκαυσίμων, αλλά και χημικών. Σχετικά με τη χημική βιομηχανία, οι Sanders et al. [18] εκτίμησαν πως μέχρι το 2050, τουλάχιστον 30% κ.β. των βασικών χημικών ουσιών θα παράγονται από βιομάζα. Ειδικά για τις οργανικές βασικές χημικές ουσίες εκτιμήθηκε πως μπορεί να επιτευχθεί μείωση των εισροών ορυκτών καυσίμων για πρώτες ύλες και ενέργεια κατά 50% αξιοποιώντας τις ιδιότητες διαφορετικών ειδών βιομάζας. Επιπλέον, μια μελέτη του ινστιτούτου NREL κατά το 2016 [19] διερεύνησε την παραγωγή διαφόρων χημικών ουσιών με βάση τη βιομάζα μέσω θερμοχημικών και βιοχημικών διεργασιών μετατροπής. Η μελέτη συμπεριλάμβανε μια σειρά κριτηρίων αξιολόγησης και κατέληξε σε μια λίστα χημικών στην οποία συμπεριλαμβάνονταν τα ξυλόλιο, (1, 3-) βουταδιένιο, γαλακτικό οξύ, ισοπρένιο κ.α. Επιπλέον, όπως ήδη περιεγράφηκε, η ζήτηση για βιοκαύσιμα θα αυξηθεί καθώς η εξάρτηση από τα ορυκτά καύσιμα μεταφοράς μειώνεται. Ομοίως με τις χημικές ουσίες, τα βιοκαύσιμα μπορούν επίσης να ληφθούν μέσω θερμοχημικών και βιοχημικών διεργασιών μετατροπής. Τα βιοκαύσιμα μπορούν να διακριθούν σε 4 κατηγορίες ή γενιές: η 1η γενιά περιλαμβάνει τα βιοκαύσιμα που παράγονται άμεσα από σάκχαρα, άμυλο κλπ. όπως μεθανόλη, αιθανόλη κλπ, η 2η γενιά βιοκαύσιμα που παράγονται από λιγνοκυτταρινική βιομάζα, ενώ τα βιοκαύσιμα 3ης και 4ης γενιάς σχετίζονται με την αξιοποίηση φυκών.

1.2 Βιοχημικές και θερμοχημικές διεργασίες μετατροπής για ενέργεια, καύσιμα και χημικά

Όπως ήδη αναφέρθηκε, βιοχημικές και θερμοχημικές οδοί μπορούν να χρησιμοποιηθούν για την παραγωγή ενέργειας, καυσίμων και χημικών από ορυκτό άνθρακα και βιομάζα. Στις βιοχημικές διεργασίες μετατροπής, τα μακρομόρια της βιομάζας διασπώνται σε μικρότερα μέσω βακτηρίων ή ενζύμων. Η ζύμωση (fermentation) και η αναερόβια χώνευση (anaerobic digestion) είναι δύο από τις κύριες διεργασίες που ανήκουν στην κατηγορία αυτή (μπορεί επίσης να συμπεριληφθεί η ενζυματική μετατροπή). Μια σημαντική διαφορά σε σχέση με τις θερμοχημικές διεργασίες μετατροπής είναι το γεγονός ότι η βιοχημική μετατροπή λαμβάνει χώρα σε σημαντικά χαμηλότερες θερμοκρασίες. Τα κύρια στάδια μιας διεργασίας βιοχημικής μετατροπής είναι η συλλογή και προμήθεια πρώτων υλών, η προκατεργασία, η υδρόλυση, η βιολογική μετατροπή και η ανάκτηση των προϊόντων. Οι διεργασίες θερμοχημικής μετατροπής χαρακτηρίζονται από υψηλότερες αποδόσεις σε σύγκριση με τις βιοχημικές. Η λιγνίνη, η οποία αποτελεί από 15% έως περισσότερο από 50% του βάρους (daf) της βιομάζας [31], μπορεί να αποσυντεθεί μέσω θερμοχημικών διεργασιών. Οι θερμοχημικές διεργασίες μετατροπής πραγματοποιούνται σε υψηλότερες θερμοκρασίες και οι χρόνοι μετατροπής είναι πολύ χαμηλότεροι λόγω της βελτιωμένης κινητικής των αντιδράσεων. Ως τάξη μεγέθους, η θερμοχημική μετατροπή της βιομάζας πραγματοποιείται μέσα σε λίγα δευτερόλεπτα ή λεπτά, ενώ η βιοχημική μετατροπή μπορεί να ολοκληρωθεί μετά από αρκετές ημέρες ή εβδομάδες [32]. Ένα ακόμη χαρακτηριστικό είναι ότι η απόδοση των αερίων, υγρών ή στερεών τελικών προϊόντων μπορεί να ποικίλει ανάλογα με τη θερμοκρασία της διεργασίας. Το θερμοκρασιακό εύρος των θερμοχημικών διεργασιών είναι ιδιαίτερα ευρύ καθώς οι θερμοκρασίες λειτουργίας μπορεί να κυμαίνονται μεταξύ 200 °C και 1400 °C. Ένα σχηματικό διάγραμμα των τεσσάρων κύριων θερμοχημικών διεργασιών μετατροπής παρουσιάζεται στο Σχήμα 2.

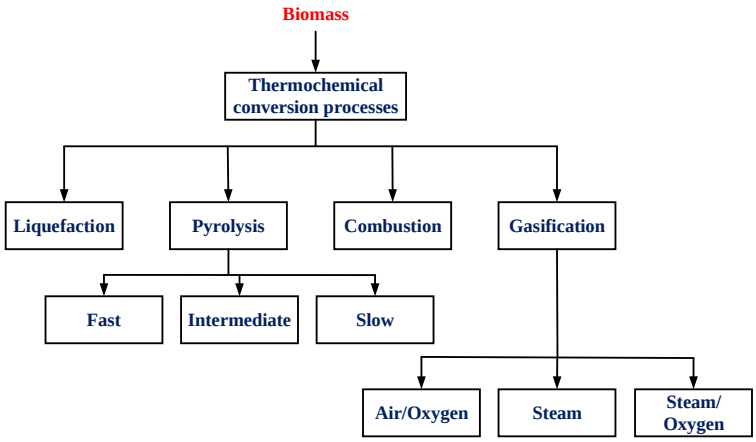

Σχήμα 2: Κυριότερες θερμοχημικές διεργασίες μετατροπής της βιομάζας.

Η αεριοποίηση είναι μια ευρέως εξεταζόμενη τεχνολογία ως πρώτο βήμα για τη μετατροπή των στερεών καυσίμων σε αέρια και υγρά βιοκαύσιμα, καθώς και για την παραγωγή ενέργειας. Πρόκειται για μια θερμοχημική διεργασία που μετατρέπει τα ανθρακούχα υλικά σε καύσιμο αέριο (αέριο σύνθεσης ή syngas), το οποίο αποτελείται κυρίως από μονοξείδιο του άνθρακα (CO) και υδρογόνο (H_2). Η διεργασία πραγματοποιείται σε υψηλές θερμοκρασίες, συνήθως μεταξύ 800-1500 °C ανάλογα με την τεχνολογία αεριοποίησης [57]. Αέρας, καθαρό οξυγόνο, ατμός, CO_2 και μείγματα αυτών τροφοδοτούνται στον αντιδραστήρα ως μέσο αεριοποίησης. Η διεργασία παρουσιάζει ομοιότητες με την καύση, καθώς για παράδειγμα και οι δύο λειτουργούν εντός παραπλήσιου εύρους θερμοκρασιών και εμφανίζουν κοινούς μηχανισμούς κατά τα πρώτα στάδια της μετατροπής του στερεού καυσίμου [58]. Επιπλέον, αμφότερες μπορούν να διεξαχθούν σε αντιδραστήρες παραπλήσιου σχεδιασμού (π.χ. αντιδραστήρες ρευστοποιημένης κλίνης).

Εντούτοις, μπορούν να παρατηρηθούν σημαντικές διαφορές μεταξύ των δύο διεργασιών:

- Η καύση στερεών καυσίμων στοχεύει στη παραγωγή θερμικής ενέργειας για την ατμοποίηση και υπερθέρμανση του εργαζόμενου ρευστού απαιτώντας περίσσεια O_2. Αντίθετα, στην αεριοποίηση με οξειδωτικό παράγοντα, το καύσιμο οξειδώνεται μερικώς ώστε να παραχθεί επαρκής θερμότητα για τις ενδοθερμικές αντιδράσεις της αεριοποίησης. Επιπλέον, η διεργασία μπορεί να πραγματοποιηθεί χωρίς μερική οξείδωση του καυσίμου εντός του αεριοποιητή παρέχοντας θερμότητα εξωτερικά στη διεργασία (αλλοθερμική αεριοποίηση).
- Η αεριοποίηση πραγματοποιείται από ατμοσφαιρικές συνθήκες έως υψηλές πιέσεις (μέχρι 70 bar) [59], ενώ η καύση στερεών καυσίμων πραγματοποιείται συνήθως σε ατμοσφαιρική πίεση. Ο κύριος λόγος για τη λειτουργία σε υψηλότερη πίεση είναι η απαίτηση χρήσης του αερίου σύνθεσης κατάντη του αεριοποιητή για καταλυτική σύνθεση ή για καύση σε αεριοστρόβιλο. Η αποθήκευση του τελικού αερίου προϊόντος αλλά και ο διαχωρισμός διαφόρων παραπροϊόντων (π.χ. CO_2) αποτελούν επιπρόσθετο κίνητρο για λειτουργία σε αυξημένη πίεση.
- Η σύσταση του αερίου προϊόντος της αεριοποίησης είναι διαφορετική σε σχέση με τα καυσαέρια που προέρχονται από την καύση στερεών καυσίμων. Η διαφοροποίηση δεν περιορίζεται μόνο στα κύρια αέρια συστατικά, αλλά και στους μολυσματικούς παράγοντες στο αέριο σύνθεσης. Το γεγονός αυτό απαιτεί την εφαρμογή διαφορετικών τεχνολογιών καθαρισμού του παραγόμενου αερίου.

1.3 Αεριοποίηση: μηχανισμός διεργασίας, τεχνολογίες μετατροπής και ποιότητα αερίου

Μια τυπική διεργασία αεριοποίησης ακολουθεί έναν μηχανισμό που αποτελείται από τα στάδια της προθέρμανσης και ξήρανσης του καυσίμου, πυρόλυσης και μερικής οξείδωσης και αεριοποίησης του εξανθρακώματος και των αντιδράσεων μεταξύ των αερίων προϊόντων. Τα στάδια της αεριοποίησης φαίνονται στο Σχήμα 3. Όπως φαίνεται στο σχήμα, κατά το στάδιο της πυρόλυσης, η βιομάζα διασπάται σε αέρια, υγρά και στερεά προϊόντα (εξανθράκωμα). Ακολουθούν στη συνέχεια αντιδράσεις μεταξύ των συστατικών της αέριας φάσης ή μεταξύ των αερίων συστατικών και του στερεού εξανθρακώματος. Για μια μετατροπή της βιομάζας κατά 85% σε αέριο σύνθεσης (κ.β.), περίπου 10% και 5% μετατρέπεται σε στερεό εξανθράκωμα και συμπυκνώσιμα οργανικά προϊόντα (αρωματικές και πολυαρωματικές ενώσεις, φαινόλες κλπ.), αντίστοιχα [56].

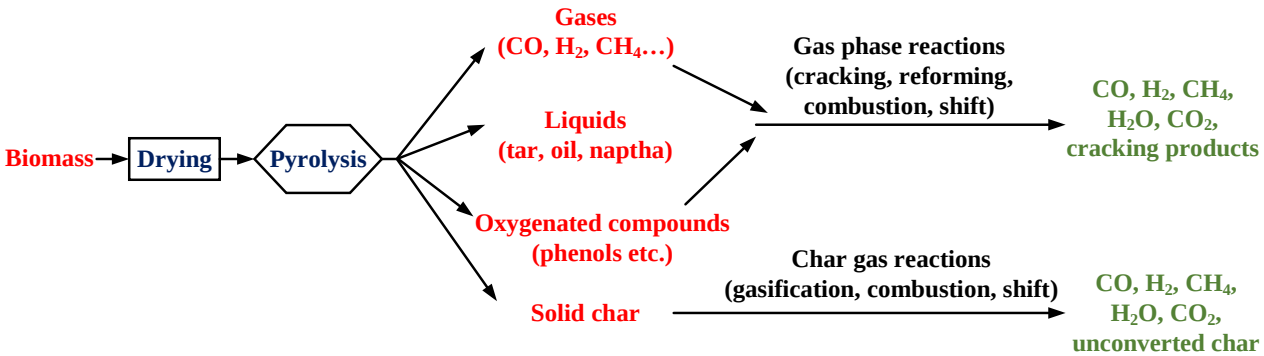

Σχήμα 3: Στάδια θερμοχημικής μετατροπής της βιομάζας μέσω αεριοποίησης [24].

Διαφορετικές τεχνολογίες είναι διαθέσιμες για την αεριοποίηση των στερεών καυσίμων, όπως ρευστοποιημένες ή σταθερές κλίνες, αεριοποιητές κονιοποιημένου καυσίμου κ.α. [57]. Δύο σημαντικοί δείκτες που χαρακτηρίζουν την ποιότητα της αεριοποίησης είναι η απόδοση μετατροπής άνθρακα (*CCE*) και ο βαθμός απόδοσης ψυχρού αερίου (*CGE*). Ο πρώτος δείκτης λαμβάνει τιμές συνήθως πάνω από 80%, ενώ ο δεύτερος μπορεί να λάβει τιμές στο εύρος 40-90% ανάλογα με τα χαρακτηριστικά και την τεχνολογία της αεριοποίησης. Τα κύρια συστατικά του αερίου σύνθεσης είναι τα CO, H_2, CO_2, CH_4 και H_2O, ενώ στο αέριο σύνθεσης περιλαμβάνονται επιπλέον διάφορες προσμίξεις.

Οι πίσσες αποτελούν τις προσμίξεις που συναντώνται στο αέριο σύνθεσης με την υψηλότερη συγκέντρωση. Ο όρος περιλαμβάνει οργανικές ενώσεις με μοριακό βάρος ίσο ή μεγαλύτερο του βενζολίου σύμφωνα με την πηγή [78]. Στις πίσσες περιλαμβάνεται έτσι μια ευρεία γκάμα ενώσεων, όπως ενώσεις με υψηλό σημείο βρασμού που σχετίζονται με προβλήματα επικαθίσεων λόγω συμπύκνωσης σε θερμοκρασίες της τάξης των 300 °C, καθώς και ελαφρύτερες ενώσεις (π.χ. BTX), οι οποίες μπορούν να αξιοποιηθούν σε καταλυτικούς αντιδραστήρες κατάντη του αεριοποιητή και δεν συμπυκνώνονται παρά μόνον σε πολύ χαμηλή θερμοκρασία [80, 81].

Το θείο (S) συναντάται στο αέριο σύνθεσης σε ανόργανες και οργανικές θειούχες ενώσεις. Κατά την αεριοποίηση του άνθρακα και της βιομάζας, το μεγαλύτερο μέρος του S εκπέμπεται με τη μορφή υδρόθειου (H_2S), ενώ συναντάται επίσης ως καρβονυλοσουλφίδιο (COS) και δισουλφίδιο του άνθρακα (CS_2) σε χαμηλότερες συγκεντρώσεις [82-84]. Ακόμη, ανάλογα με τις συνθήκες και την τεχνολογία αεριοποίησης, οργανικές θειούχες ενώσεις (OSCs) συναντώνται στο αέριο όπως θειόλες, θειοφαίνιο (C_4H_4S) κλπ. Σύμφωνα με τους Woolcock et al. [79], η συγκέντρωση των θειούχων ενώσεων μπορεί να κυμαίνεται από 0.1 mL L^{-1} μέχρι και πάνω από 30 mL L^{-1}, ανάλογα με το ποσοστό θείου στο καύσιμο. Επιπλέον, προσμίξεις όπως σωματίδια, αζωτούχες ενώσεις, αλκάλια, ενώσεις χλωρίου κ.α. συναντώνται στο αέριο σύνθεσης.

1.4 Συνδυασμός αεριοποίησης με κατάντη διεργασίες: καθαρισμός αερίου σύνθεσης

Ο καθαρισμός και η προετοιμασία του αερίου σύνθεσης προς χρήση αποτελούν απαραίτητα στάδια για τις μονάδες αεριοποίησης που έχουν σχεδιαστεί για παραγωγή ηλεκτρικής ενέργειας, καυσίμων και χημικών ή πολυπαραγωγή. Στους σταθμούς παραγωγής ηλεκτρικής ενέργειας και συμπαραγωγής ηλεκτρισμού και θερμότητας μέσω αεριοποίησης, σημαντικοί λόγοι για τον καθαρισμό του αερίου σύνθεσης είναι ζητήματα μηχανικής φθοράς και διάβρωσης, η συμπύκνωση των πισσών σε σχετικά υψηλή θερμοκρασία και οι εκπομπές ελεγχόμενων ρύπων όπως NO_x και SO_x. Οι διεργασίες καταλυτικής σύνθεσης χαρακτηρίζονται από αυστηρότερες προδιαγραφές καθαρισμού, οι οποίες οφείλονται σε δύο επιπλέον λόγους:

α. Πολλοί καταλύτες είναι εξαιρετικά ευαίσθητοι σε δηλητηρίαση από μολυσματικούς παράγοντες. Για παράδειγμα, οι καταλύτες Ni/Al_2O_3 που χρησιμοποιούνται στη μεθανοποίηση για την παραγωγή SNG απαιτούν συγκέντρωση ενώσεων θείου (άθροισμα H_2S + COS + CS_2 + OSCs) κάτω από 1 ppmv [130].

β. Τα συστατικά του αερίου σύνθεσης απαιτείται συχνά να έχουν μια συγκεκριμένη αναλογία, η οποία υποδεικνύεται από τη στοιχειομετρία των αντιδράσεων σύνθεσης. Θεωρώντας ξανά ως παράδειγμα τη σύνθεση SNG, η διεργασία απαιτεί μοριακή αναλογία H_2/CO στο αέριο σύνθεσης ίση με 3 (υποθέτοντας ότι υπάρχουν μόνο H_2 και CO). Επιπλέον, ο σχηματισμός και η εναπόθεση άνθρακα είναι πιθανά προβλήματα που μπορεί να απαιτούν ρύθμιση της σύστασης (π.χ. διατήρηση υγρασίας σε συγκεκριμένα επίπεδα). Επιπλέον, η θερμική διαχείριση των αντιδραστήρων σταθερής κλίνης απαιτεί συχνά ανακύκλωση για αραίωση.

Στη σύνθεση FT, η σύσταση και η ποιότητα του αερίου σύνθεσης παίζει επίσης σημαντικό ρόλο. Χαρακτηριστικά, μια γενική ανασκόπηση διαφόρων μηχανισμών απενεργοποίησης καταλυτών Co και Fe μπορεί να βρεθεί στις πηγές [124] και [125]. Οι ενώσεις θείου και χλωρίου αποτελούν προσμίξεις που οδηγούν σε δηλητηρίαση των καταλυτών Fe, ενώ η εναπόθεση εξανθρακώματος αποτελεί έναν επιπρόσθετο μηχανισμό απενεργοποίησης. Επομένως, συνολικά, διάφορα στάδια καθαρισμού για την δέσμευση όξινων αερίων (AGR), πισσών, λοιπών ενώσεων οργανικού και ανόργανου θείου, ενώσεων χλωρίου, σωματιδίων κλπ. απαιτούνται κατάντη της μονάδας αεριοποίησης. Στον Πίνακα 1 φαίνονται οι απαιτήσεις καθαρισμού από προσμίξεις για τις κυριότερες εφαρμογές αξιοποίησης αερίων σύνθεσης.

Πίνακας 1: Κύριες εφαρμογές αξιοποίησης αερίου σύνθεσης και σχετικές απαιτήσεις καθαρισμού (σε συνθήκες STP εκτός αν αναφέρεται διαφορετικά) [79]. Οι τιμές που αναφέρονται για τη σύνθεση SNG βασίζονται σε μετρήσεις του ECN από την πηγή [129].

Τύπος προσμίξεων	**Εφαρμογές**				
	Αεριομηχανή	**Αεριοστρόβιλος**	**Σύνθεση MeOH**	**Σύνθεση FT**	**Σύνθεση SNG**
Σωματίδια	< 50 mg m^{-3} (PM10)	< 30 mg m^{-3} (PM5)	< 0.02 mg m^{-3}	n.d.[a]	n.d.
Πίσσες	< 100 mg m^{-3}		< 0.1 mg m^{-3}	< d.p.[b]	< 50 mg m^{-3} (d.p.~ 100 °C)
Ετεροάτομα Κλάσης 2, BTX				< 0.01 μL L^{-1} < 1 μL L^{-1}	BTX: ~ 250 ppmv
Θειούχες ενώσεις (H_2S, COS)		< 20 μL L^{-1}	< 1 mg m^{-3}	< 0.01 μL L^{-1}	< 200 ppbv
Αζωτούχες ενώσεις (NH_3, HCN)		< 50 μL L^{-1}	< 0.1 mg m^{-3}	< 0.02 μL L^{-1}	< 1000 ppmv
Αλκάλια		< 0.024 μL L^{-1}		< 0.01 μL L^{-1}	-
Αλογονούχα (κυρίως HCl)		1 μL L^{-1}	< 0.1 mg m^{-3}	< 0.01 μL L^{-1}	< 100 ppbv

[a] n.d.=μη ανιχνεύσιμο, [b]d.p.= σημείο δρόσου

1.5 Διεργασίες καθαρισμού αερίου: CO_2, θειούχες ενώσεις και πίσσες

Όσον αφορά τις διεργασίες AGR για απομάκρυνση των CO_2 και H_2S, αυτές διακρίνονται κυρίως σε διεργασίες φυσικής και χημικής απορρόφησης σε διαλύτες. Κύριες διεργασίες φυσικής απορρόφησης είναι οι Rectisol™ και Selexol™. Οι διεργασίες φυσικής απορρόφησης λειτουργούν τυπικά σε χαμηλές θερμοκρασίες και υψηλή πίεση. Σε τέτοιες συνθήκες, οι συντελεστές Henry των διαλυτών για τις ενώσεις ενδιαφέροντος (π.χ. CO_2, θειούχες ενώσεις, C_{3+} κ.α.) λαμβάνουν μεγάλες τιμές και είναι δυνατόν να επιτύχουν πλήρη αποθείωση του αερίου σύνθεσης [134]. Αναγέννηση επιτυγχάνεται πρωτίστως με τη μείωση της πίεσης και ακολούθως με την πρόσδοση θερμότητας. Οι διεργασίες χημικής απορρόφησης διαφέρουν στο γεγονός ότι εμπλέκουν χημικές αντιδράσεις. Στην πράξη, αυτό μεταφράζεται σε λειτουργία σε χαμηλότερη πίεση (~ μέχρι 30 bar) και θερμοκρασίες μεταξύ συνθηκών περιβάλλοντος έως και πάνω από 100 °C. Η δέσμευση CO_2 από τα διαλύματα μονοαιθανολαμίνης (MEA) σε πίεση και θερμοκρασία περιβάλλοντος αποτελεί τεχνολογία αιχμής για τη δέσμευση CO_2 από καυσαέρια (δηλ. σε χαμηλή μερική πίεση CO_2). Ως πρωτοταγής αμίνη, η MEA είναι εξαιρετικά αντιδραστική ως προς το CO_2. Τα CO_2 και H_2S μπορούν να απομακρυνθούν σε υψηλή πίεση (AGR προ-καύσης) μέσω χημικής απορρόφησης σε διαλύματα MDEA ή ανθρακικού καλίου (K_2CO_3). Σε αντίθεση με τη MEA, η MDEA χαρακτηρίζεται από βραδύτερη κινητική αντίδρασης, αλλά και ταυτόχρονα χαμηλότερη ενέργεια αναγέννησης σε σχέση με τη MEA. Εκτός από τη δέσμευση CO_2 και θειούχων ενώσεων, διαλύτες (συνήθως οργανικοί) μπορούν να χρησιμοποιηθούν για τη δέσμευση πισσών από το αέριο σύνθεσης. Στην κατηγορία αυτή, μια ευρέως γνωστή διεργασία δέσμευσης πισσών είναι η τεχνολογία OLGA που αναπτύχθηκε από το ECN και η οποία επιτυγχάνει θερμοκρασία συμπύκνωσης των πισσών κάτω από -15 °C [135].

Εκτός από τις διεργασίες καθαρισμού με βάση διαλύτες, η απομάκρυνση CO_2, θειούχων ενώσεων και πισσών μπορεί να επιτευχθεί με ρόφηση σε στερεά υλικά ή σε καταλυτικούς αντιδραστήρες με στερεούς καταλύτες. Χαρακτηριστικά παραδείγματα σε κάθε περίπτωση είναι η διεργασία προσρόφησης CO_2 με εναλλαγή πίεσης (PSA) [136], η δέσμευση θειούχων ενώσεων σε κλίνη από ZnO [84] και η μετατροπή πισσών με ολιβίνη, δολομίτη, καταλύτες Ni κ.α. [137].

1.6 Πλαίσιο και δομή διδακτορικής διατριβής

Η δέσμευση όξινων αερίων μέσω διαλυμάτων K_2CO_3 αποτελεί μια πολλά υποσχόμενη τεχνολογία για τις μονάδες αεριοποίησης είτε κατά την αξιοποίηση του αερίου σύνθεσης για παραγωγή ενέργειας (ηλεκτρική ισχύς ή CHP) είτε για καταλυτική σύνθεση. Η διεργασία είναι εφικτή σε υψηλή θερμοκρασία και πίεση, καθιστώντας δυνατή τη λειτουργία του σταδίου απορρόφησης και εκρόφησης σε παρόμοια θερμοκρασία (κοντά στο ατμοσφαιρικό σημείο βρασμού του διαλύματος). Αυτό αποτελεί πλεονέκτημα σε σύγκριση με τις διεργασίες φυσικής απορρόφησης (π.χ., Rectisol) στις οποίες το αέριο ψύχεται σε χαμηλές θερμοκρασίες, αυξάνοντας την καταστροφή της εξέργειας. Επιπλέον, το K_2CO_3 δεν είναι πτητικό, ένας άλλος παράγοντας που πρέπει να ληφθεί υπόψη πριν από την κατάντη αξιοποίηση του καθαρού αερίου. Ωστόσο, διάφορες προκλήσεις πρέπει να αντιμετωπιστούν λόγω των χαρακτηριστικών της διεργασίας.

Πρόκληση 1: Η διεργασία απορρόφησης με βάση διαλύματα K_2CO_3 χαρακτηρίζεται από αργή κινητική αντίδρασης με το CO_2. Ειδικά σε συνθήκες πίεσης < 20 bar είναι απαραίτητες σημαντικές βελτιώσεις των διαλυτών για να είναι ανταγωνιστική με διεργασίες αμινών ή διεργασίες φυσικής απορρόφησης. Επιπλέον, η βελτίωση της χωρητικότητας του διαλύτη παρουσιάζει ιδιαίτερο ενδιαφέρον.

Πρόκληση 2: Ενώ τα CO_2 και H_2S μπορούν αμφότερα να απορροφηθούν από υδατικά διαλύματα K_2CO_3, η διεργασία είναι γενικά μη επιλεκτική προς την απομάκρυνση H_2S [134]. Το γεγονός αυτό δημιουργεί προβλήματα όταν ισχύουν αυστηρές προδιαγραφές αποθείωσης για τη λειτουργία του κατάντη εξοπλισμού. Επιπλέον, η διεργασία δεν μπορεί να εξαλείψει τις οργανικές θειούχες ενώσεις (OSCs) από το αέριο σύνθεσης.

Πρόκληση 3: Επιπρόσθετες προσμείξεις αναμένονται στο αέριο σύνθεσης πριν από τη διεργασία AGR, όπως ενώσεις πισσών χαμηλού σημείου βρασμού (π.χ. BTX). Είναι ιδιαίτερα σημαντικό το πώς αντιμετωπίζονται αυτές οι ενώσεις από τη διεργασία και ποια εναλλακτικά μέτρα πρέπει να εφαρμοστούν για την εξάλειψή τους, εφόσον κάτι τέτοιο απαιτείται.

Πρόκληση 4: Παρά το γεγονός ότι η θερμότητα εκρόφησης CO_2 των υδατικών διαλυμάτων K_2CO_3 είναι χαμηλότερη σε σύγκριση με τα διαλύματα αμινών, η διεργασία απαιτεί σε κάθε περίπτωση σημαντική θερμική ισχύ κατά το στάδιο της αναγέννησης. Η επίδραση των παραμέτρων των διεργασίας και η χρήση αποδοτικότερων διαλυτών πρέπει να αξιολογηθεί προς αυτή την κατεύθυνση. Όσον αφορά τη συνολική απόδοση της διεργασίας με ενισχυμένα διαλύματα K_2CO_3, δεδομένα από εγκαταστάσεις δέσμευσης CO_2 μετά την καύση είναι κυρίως διαθέσιμα (σημαντική διαφοροποίηση συνθηκών λειτουργίας και σύστασης αερίου).

Πρόκληση 5: Κρίνεται απαραίτητη η αξιολόγηση πιθανών οφελών που προκύπτουν κατά την εφαρμογή της διεργασίας σε μονάδες παραγωγής ηλεκτρισμού και/ή διεργασίες σύνθεσης καυσίμων και χημικών με βάση την αεριοποίηση. Έτσι, ενώ η τεχνολογία έχει ήδη εφαρμοστεί στο παρελθόν σε μονάδες επεξεργασίας φυσικού αερίου, μονάδες αμμωνίας κλπ., παρουσιάζει επιπλέον ενδιαφέρον για εναλλακτικές εφαρμογές με βάση την αεριοποίηση.

Η παρούσα διδακτορική διατριβή στοχεύει σε αρκετές από τις προαναφερθείσες προκλήσεις μέσω ενός συνδυασμού πειραματικής μελέτης, θερμοδυναμικής μοντελοποίησης, αλλά και μοντελοποίησης και ενεργειακής/εξεργειακής αξιολόγησης διεργασιών. Ένα απλοποιημένο σχήμα μιας μονάδας αεριοποίησης με θερμό καθαρισμό αερίου σύνθεσης και μονάδα AGR με K_2CO_3 παρουσιάζεται στο Σχήμα 4. Στο σχήμα αυτό επισημαίνονται τα σημεία στα οποία επικεντρώνεται η διδακτορική διατριβή στο επίπεδο του καθαρισμού, αλλά και στο επίπεδο ενός ολοκληρωμένου σταθμού με βάση την αεριοποίηση. Στον πυρήνα της διατριβής βρίσκεται ο συνδυασμός των τεχνολογιών δέσμευσης όξινων αερίων από διαλύματα K_2CO_3 και προσρόφησης προσμίξεων σε ενεργό άνθρακα για την πλήρη αποθείωση του αερίου σύνθεσης.

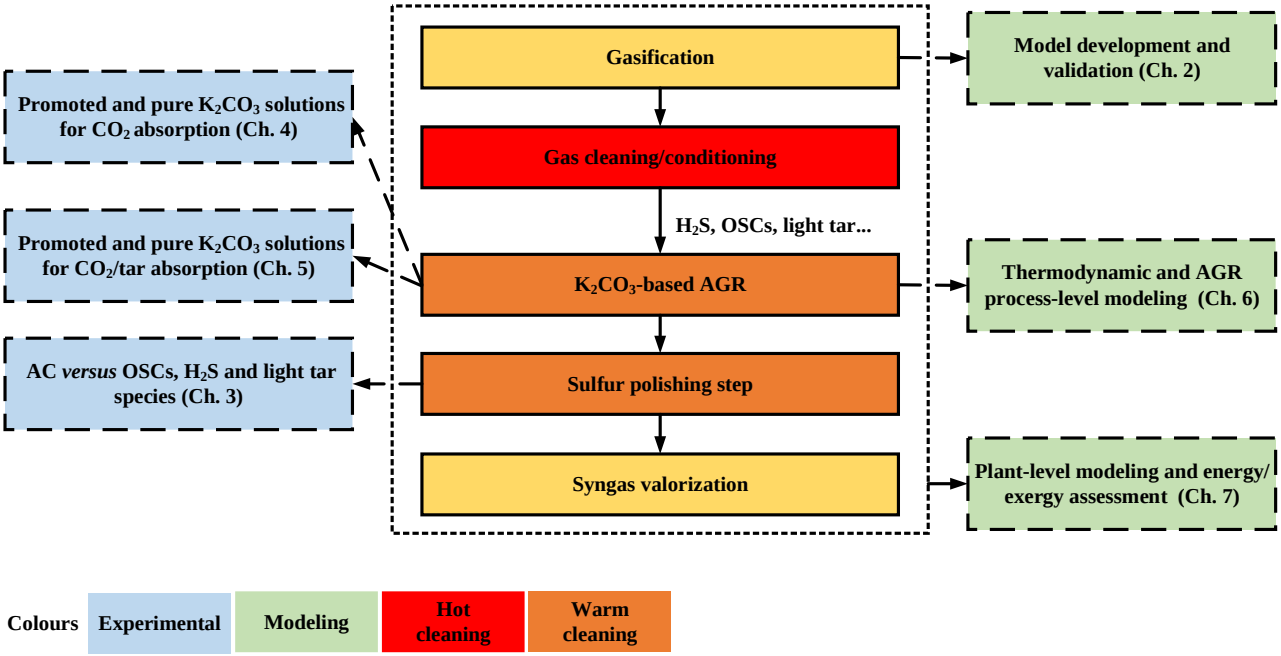

Σχήμα 4: Δομή διατριβής και κατανομή πειραματικής εργασίας και μοντελοποίησης ανά κεφάλαιο.

2 Μοντελοποίηση και πειραματική διερεύνηση της σύστασης αερίου σύνθεσης από αεριοποίηση βιομάζας

2.1 Βιβλιογραφική ανασκόπηση και πλαίσιο ανάπτυξης του μοντέλου αεριοποίησης

Όπως αναλύθηκε και στην εισαγωγή της εργασίας, η αεριοποίηση αποτελεί μια χρήσιμη οδό για την αξιοποίηση στερεών καυσίμων για την παραγωγή αερίου σύνθεσης, το οποίο στη συνέχεια μπορεί να αξιοποιηθεί σε μηχανές υψηλής απόδοσης ή να μετατραπεί σε χημικά προϊόντα. Η σύσταση του αερίου σύνθεσης παρουσιάζει μεγάλο ενδιαφέρον για διεργασίες που βασίζονται στην αεριοποίηση. Καταρχάς η σύσταση του αερίου σύνθεσης παίζει σημαντικό ρόλο για την επακόλουθη αξιοποίηση του σε καταλυτικούς αντιδραστήρες που απαιτούν συγκεκριμένες αναλογίες συστατικών στο ρεύμα τροφοδοσίας, όπως η αναλογία των H_2 και CO [139]. Αυτές οι αναλογίες επηρεάζονται από την τεχνολογία αεριοποίησης, τις συνθήκες λειτουργίας και τον τύπο της καυσίμου, ενώ η επιλογή της τεχνολογίας αεριοποίησης υποδεικνύει τις απαραίτητες διεργασίες καθαρισμού και αναβάθμισης του αερίου (π.χ. δέσμευση όξινων αερίων, αντιδραστήρες WGS κ.λπ.). Η γνώση της σύστασης του ακάθαρτου αερίου σύνθεσης παρέχει χρήσιμη πληροφορία για το σχεδιασμό μονάδων καθαρισμού για στερεά σωματίδια (εξανθράκωμα, τέφρα) και προσμίξεις που μπορούν να αποτελέσουν παράγοντες δηλητηρίασης καταλυτών [57, 140]. Επιπλέον, για τα διάφορα έργα αεριοποίησης που έχουν παραδοθεί πρόσφατα, όπως ο σταθμός αεριοποίησης βιομάζας για την παραγωγή SNG στο Γκέτεμποργκ της Σουηδίας (20 MW bio-SNG) [141], το κόστος λειτουργίας και οι ασύμφορες, χρονοβόρες πειραματικές δοκιμές για τη διερεύνηση της λειτουργίας τους αποτελούν ένα ακόμη σημαντικό ζήτημα. Στην κατεύθυνση της αντιμετώπισης τέτοιων προβλημάτων μπορούν να συνδράμουν αξιόπιστα μαθηματικά μοντέλα που να εκτιμούν τη σύσταση του αερίου σύνθεσης υπό μεταβαλλόμενες συνθήκες αεριοποίησης. Τα μοντέλα αυτά μπορούν να βοηθήσουν κατά τις φάσεις της μελέτης κλιμάκωσης και έναρξης λειτουργίας, αλλά και κατά την αλλαγή της κατάστασης λειτουργίας της μονάδας, βοηθώντας τους χειριστές να προβλέψουν τη συμπεριφορά της.

Διάφορα μοντέλα αεριοποίησης έχουν αναπτυχθεί που ανήκουν σε διαφορετικές κατηγορίες. Για αντιδραστήρες αεριοποίησης ρευστοποιημένης κλίνης, τα κυριότερα μοντέλα διακρίνονται σε μοντέλα υπολογιστικής ρευστοδυναμικής (CFD), μοντέλα ρευστοποίησης και απλοποιημένα θερμοδυναμικά μοντέλα [142]. Τα μοντέλα CFD παρέχουν την πλέον αναλυτική περιγραφή της διεργασίας καθώς βασίζονται σε ισοζύγια πυκνότητας, ορμής και ενθαλπίας τόσο για την αέρια όσο και για τη στερεή φάση. Στην περίπτωση των μοντέλων ρευστοποίησης, εφαρμόζονται απλουστεύσεις στις εξισώσεις που επιλύονται στα μοντέλα CFD και η εξίσωση της ορμής δεν επιλύεται. Τα συγκεκριμένα μοντέλα ενσωματώνουν ημι-εμπειρικές σχέσεις για την περιγραφή των υδροδυναμικών φαινομένων στην κλίνη. Για την περαιτέρω απλοποίηση και μείωση του υπολογιστικού χρόνου χρησιμοποιούνται μοντέλα θερμοδυναμικής ισορροπίας, τα οποία βασίζονται είτε σε σταθερές ισορροπίας αντιδράσεων είτε στην εφαρμογή μεθόδων ελαχιστοποίησης της ελεύθερης ενέργειας Gibbs.

Τα περισσότερα από τα διαθέσιμα θερμοδυναμικά μοντέλα στη βιβλιογραφία έχουν αναπτυχθεί στο λογισμικό Aspen Plus κι έχουν επικυρωθεί με δοκιμές αεριοποίησης σε εργαστηριακή και πιλοτική κλίμακα (έως 500 kW_{th}). Ωστόσο, μελέτες σχετικά με την καταλληλότητά τους για την πρόβλεψη της σύστασης του αερίου σύνθεσης από αεριοποιητές ρευστοποιημένης κλίνης μεγαλύτερης κλίμακας είναι ελάχιστες και απαιτούνται περισσότερες εργασίες προς την κατεύθυνση αυτή προκειμένου να δικαιολογηθεί η εφαρμογή τους. Στο κεφάλαιο αυτό, παρουσιάζεται ένα μοντέλο αεριοποίησης βασισμένο στην ελαχιστοποίηση της ελεύθερης ενέργειας Gibbs, το οποίο αναπτύχθηκε στο λογισμικό Aspen Plus. Για την επικύρωση του μοντέλου, πραγματοποιήθηκαν δοκιμές αεριοποίησης ξύλου σε αεριοποιητή ρευστοποιημένης κλίνης φυσαλίδων (BFBG) ισχύος 3 MW_{th} στο ινστιτούτο Fundación Ciudad de la Energia (CIUDEN) στην Ισπανία. Η σύγκριση επικεντρώνεται στα κύρια συστατικά του αερίου σύνθεσης (CO, H_2, CO_2 και CH_4) και την περιεκτικότητα άνθρακα στην ιπτάμενη τέφρα. Ένα από τα σημεία καινοτομίας του προαναφερθέντος μοντέλου είναι η μελέτη της επίδρασης της αντίδρασης WGS στη σύσταση του τελικού αερίου προϊόντος, με στόχο τη διερεύνηση της δυνητικής επίπτωσής της κατά τη διάρκεια της ψύξης του σύνθεσης. Ακόμη, μελετάται η σύγκλιση μεταξύ πειραματικών και θεωρητικών αποτελεσμάτων όταν συμπεριλαμβάνεται ο σχηματισμός C_2 υδρογονανθράκων (αιθυλένιο στην παρούσα μελέτη) στο μοντέλο αεριοποίησης, ώστε να αντισταθμιστούν αποκλίσεις από τις συνθήκες θερμοδυναμικής ισορροπίας.

2.2 Δοκιμές αεριοποίησης και μεθοδολογία μοντελοποίησης

Οι πειραματικές δοκιμές διεξήχθησαν σε έναν αεριοποιητή ισχύος 3 MW_{th} τεχνολογίας ρευστοποιημένης κλίνης φυσαλίδων που βρίσκεται στο ινστιτούτο CIUDEN της Ισπανίας και ο οποίος μπορεί να λειτουργήσει με τρεις διαφορετικούς τύπους καυσίμου, συγκεκριμένα τσιπ, κοκκώδη και πελετοποιημένη βιομάζα. Για το σκοπό αυτό, δύο διαφορετικές γραμμές τροφοδοσίας καυσίμου συνδέονται με τον αεριοποιητή, μία για την επεξεργασμένη βιομάζα (κοκκώδη και πελετοποιημένη) και μία για τα τσιπ. Το καύσιμο παρέχεται μέσω κοχλία τροφοδοσίας μέσα στον αντιδραστήρα. Για την παροχή βιομάζας χρησιμοποιείται μια περιστροφική βαλβίδα σε πίεση, η οποία τροφοδοτεί βιομάζα σε δύο διαφορετικά επίπεδα που βρίσκονται στην κορυφή και στο κάτω μέρος της κλίνης. Για την περίπτωση επεξεργασμένης βιομάζας, και τα δύο επίπεδα τροφοδοσίας μπορούν να λειτουργούν ταυτόχρονα, ενώ για τα τσιπ λειτουργεί μόνο ένα επίπεδο κάθε φορά. Για την αποφυγή της αντίστροφης διαδρομής σωματιδίων και αερίου, το στερεό καύσιμο τροφοδοτείται μαζί με μια μικρή παροχή CO_2. Για τη συνεχή λειτουργία του αεριοποιητή, κάθε γραμμή τροφοδοσίας καυσίμου αποτελείται από δύο σιλό τροφοδοσίας. Η φόρτωση ενός σιλό με καύσιμο πραγματοποιείται όταν η γραμμή τροφοδοσίας είναι αποσυνδεδεμένη και συνεπώς, οι δύο δεξαμενές λειτουργούν ανεξάρτητα. Επιπλέον, ο η παροχή μάζας της τροφοδοτούμενης βιομάζας μετράται με αισθητήρες βάρους, οι οποίοι καταγράφουν συνεχώς το βάρος του σιλό τροφοδοσίας συναρτήσει του χρόνου.

Μια σχηματική αποτύπωση της εγκατάστασης του CIUDEN παρουσιάζεται στο Σχήμα 5. Ο αεριοποιητής φέρει επένδυση από πυρίμαχο υλικό και έχει εσωτερική διάμετρο 1.3 m και συνολικό ύψος 5.5 m, ενώ το τμήμα της ελεύθερης επιφάνειας έχει εσωτερική διάμετρο 2 m. Για την εκκίνηση του αεριοποιητή, η θέρμανση του αντιδραστήρα πραγματοποιήθηκε με καυσαέρια από την καύση φυσικού αερίου σε ξεχωριστό θάλαμο καύσης. Κατά την εκκίνηση της αεριοποίησης βιομάζας, ένας φυσητήρας αέρα χρησιμοποιείται για τη ρευστοποίηση της κλίνης. Ο αεριοποιητής εξοπλίζεται με 19 θερμοστοιχεία, 6 μετρητικά διαφορικής πίεσης και 4 θύρες για άλλες συσκευές μέτρησης ή δειγματοληψία. Κατά τη διάρκεια των δοκιμών αεριοποίησης, η θερμοκρασία και η πτώση πίεσης στο τμήμα αποθήκευσης και τροφοδοσίας καυσίμου, στον αντιδραστήρα και στο σύστημα καθαρισμού παρακολουθούνταν συνεχώς και καταγράφονταν μέσω συστήματος συλλογής δεδομένων. Κατάντη του αεριοποιητή, τα στερεά σωματίδια συλλέγονται σε δύο κυκλώνες υψηλής απόδοσης και στη συνέχεια μεταφέρονται σε σιλό αποθήκευσης τα οποία είναι συνδεδεμένα με συσκευές μέτρησης βάρους. Δύο ανεξάρτητα συστήματα χρησιμοποιήθηκαν κατά τη διάρκεια των δοκιμών για τη συλλογή της τέφρας από τον πυθμένα του αντιδραστήρα και της ιπτάμενης τέφρας, αντίστοιχα. Όσον αφορά τις μετρήσεις σύστασης του αερίου, μια συσκευή TDL κι ένας αέριος χρωματογράφος χρησιμοποιούνται για τη μέτρηση του ποσοστού O_2 και των κύριων συστατικών του αερίου σύνθεσης (H_2, CO_2, CO και CH_4), αντίστοιχα. Πέντε (5) πειραματικές δοκιμές πραγματοποιήθηκαν συνολικά χρησιμοποιώντας ξυλώδη βιομάζα, θερμοκρασία αεριοποίησης ~ 890 °C και λόγο αέρα καύσης λ στο εύρος 0.28-0.29. Η σύσταση του καυσίμου δίνεται στον Πίνακα 2.

Το μοντέλο για την πρόβλεψη της σύστασης του αερίου σύνθεσης είναι βασισμένο στη θερμοδυναμική ισορροπία μέσω ελαχιστοποίησης της ελεύθερης ενέργειας Gibbs. Για τις προσομοιώσεις που παρουσιάζονται στη συνέχεια, οι ενώσεις που ορίστηκαν ήταν οι N_2, O_2, C(s), S, H_2, CO, CO_2, CH_4, H_2O, H_2S, SO_2, SO_3, COS, HCN, C_2H_4, C_2H_6, C_6H_6, $C_{10}H_8$, καθώς και η βιομάζα και η τέφρα ως μη συμβατικά στερεά. Συγκεκριμένα, το στερεό εξανθράκωμα C(s) που προκύπτει κατά το στάδιο της πυρόλυσης μοντελοποιήθηκε ως γραφίτης. Οι ιδιότητες της βιομάζας εκφράστηκαν μέσω των μοντέλων ενθαλπίας και πυκνότητας HCOALGEN και DCOALIGT, αντίστοιχα. Επειδή το Aspen Plus δεν μπορεί να χειριστεί μη συμβατικά στερεά, προ της ελαχιστοποίησης της ελεύθερης ενέργειας Gibbs η βιομάζα αποσυντίθεται «εικονικά» σε έναν αντιδραστήρα RYield σε C(s), H_2, N_2, S, O_2, H_2O και τέφρα. Το ισοζύγιο μάζας διατηρείται μέσω ενός υπολογιστικού εργαλείου σε γλώσσα FORTRAN, το οποίο τροφοδοτείται από την προσεγγιστική και στοιχειακή ανάλυση της βιομάζας. Επιπλέον, πραγματοποιείται ισολογισμός ενθαλπίας στον αντιδραστήρα RYield, ο οποίος αξιοποιείται για να καταστρωθεί το ολικό ισοζύγιο ενέργειας της διεργασίας. Ανάντη του αντιδραστήρα RGibbs στον οποίο πραγματοποιείται ελαχιστοποίηση της ενέργειας Gibbs υπάρχει στοιχειομετρικός αντιδραστήρας RStoich, στον οποίο ένα μέρος του στερεού άνθρακα (12%) αντιδρά με το H_2 προς σχηματισμό CH_4. Η τιμή αυτή διορθώνεται βάσει των πειραματικών μετρήσεων από το σύστημα αέριας χρωματογραφίας μέσω ενός μπλοκ «Design specification» στο Aspen Plus. Η ενσωμάτωση του συγκεκριμένου αντιδραστήρα κρίνεται σημαντική καθώς είναι γνωστό πως το CH_4 στο αέριο σύνθεσης προέρχεται κυρίως από το στάδιο της πυρόλυσης και δεν προβλέπεται στις συνθήκες χημικής και θερμοδυναμικής ισορροπίας ενός αεριοποιητή. Ακόμη, ένα μπλοκ διαχωρισμού χρησιμοποιείται για τη μοντελοποίηση της ροής του στερεού εξανθρακώματος που δεν μετέχει σε αντιδράσεις με αέριες ενώσεις στο μίγμα και συλλέγεται με την ιπτάμενη τέφρα.

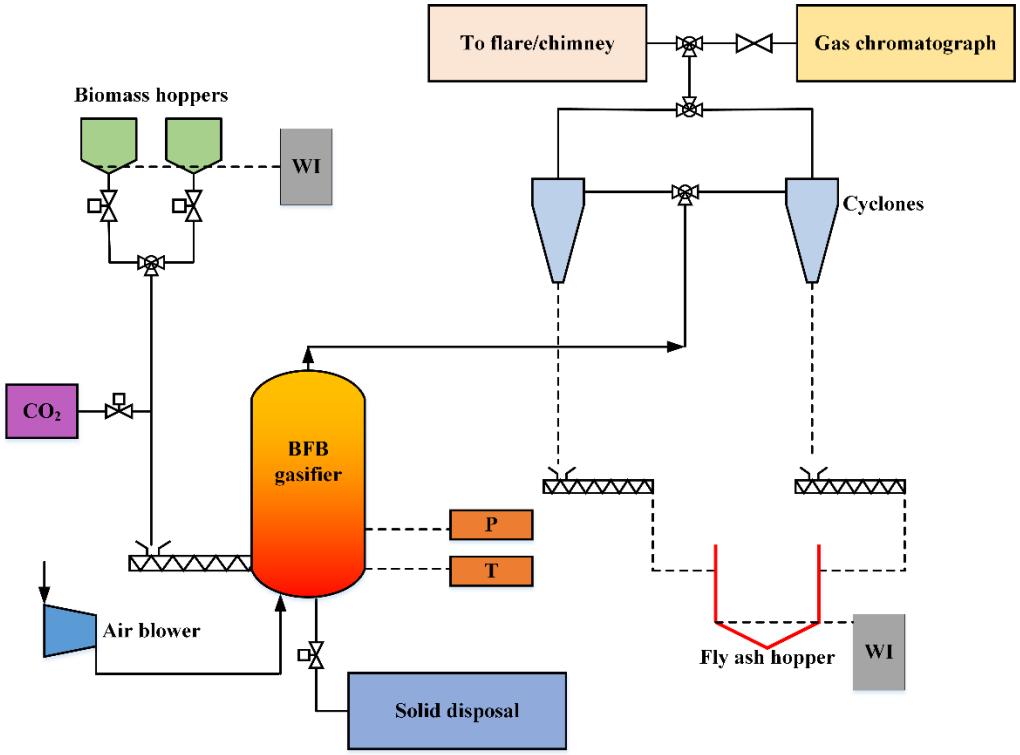

Σχήμα 5: Σχηματική απεικόνιση του αεριοποιητή ισχύος 3 MW_{th} τεχνολογίας BFB (CIUDEN).

Πίνακας 2: Προσεγγιστική και στοιχειακή ανάλυση ξυλώδους βιομάζας.

Προσεγγιστική ανάλυση	
Υγρασία (κ.β. %, επί υγρής βάσης)	6.06
Τέφρα (κ.β. %, επί ξηρού)	1.31
Πτητικά (κ.β. %, επί ξηρού)	79.03
Μόνιμος άνθρακας (κ.β. %, επί ξηρού)	19.66
Στοιχειακή ανάλυση	**(κ.β. %, επί ξηρού)**
C	49.30
H	6.71
N	0.11
S	0.01
O	42.57

Η ολική ενέργεια Gibbs εκφράζεται σύμφωνα με την Εξ. 1α

$$G^{tot} = \sum_{i=1}^{N} n_i \, \Delta\bar{G}^{o}_{f,i} + \sum_{i=1}^{N} n_i \, RTln(y_i) \qquad \textit{Εξ. 1α}$$

όπου $\Delta\bar{G}^{o}_{f,i}$ είναι η ελεύθερη ενέργεια Gibbs σχηματισμού των ενώσεων i, R και T η σταθερά ιδανικών αερίων και η θερμοκρασία αντίστοιχα και y_i είναι το γραμμομοριακό κλάσμα του συστατικού i στο μίγμα. Η διαδικασία υπολογισμού της σύστασης των προϊόντων βασίζεται στο μηδενισμό των μερικών παραγώγων της συνάρτησης Lagrange L, η οποία δίνεται στην Εξ. 1β.

$$L = G^{tot} - \sum_{j=1}^{k} \lambda_j \left(\sum_{i=1}^{N} \alpha_{ij} \, n_i - A_j \right) \qquad \textit{Εξ. 1β}$$

Ως θερμοκρασία αεριοποίησης ορίστηκε ο μέσος όρος των μετρήσεων 4 θερμοστοιχείων σε ύψος 375 mm από το διασκορπιστή, ενώ ως πίεση του αεριοποιητή ορίστηκε ο μέσος όρος των τιμών της πίεσης που μετρήθηκαν στο διασκορπιστή. Οι τιμές αυτές ορίστηκαν σε όλες τις συνιστώσες του θερμοδυναμικού μοντέλου ανάντη του διορθωτικού αντιδραστήρα (REquil) μετατόπισης WGS, η οποία φαίνεται στην αντίδραση A1.

$$CO + H_2O \leftrightarrow CO_2 + H_2 \qquad A1$$

Η θερμοκρασία του αντιδραστήρα REquil ορίστηκε βάσει μιας αρχικής ανάλυσης ευαισθησίας 60 °C χαμηλότερα σε σχέση με τα μπλοκ του βασικού μοντέλου αεριοποίησης, ενώ η πίεση ορίστηκε ίση με την πίεση στην έξοδο του αεριοποιητή. Η ιδέα πίσω από τη διόρθωση της αντίδρασης WGS έγκειται στην πιθανή συμμετοχή της στον καθορισμό της τελικής σύστασης του αερίου σύνθεσης κατά το στάδιο της ψύξης στην έξοδο του αεριοποιητή. Τέλος, το ενεργειακό ισοζύγιο της διεργασίας προκύπτει συνδυάζοντας όλες τις ροές θερμικής ισχύος της εγκατάστασης σε μπλοκ ανάμιξης στο λογισμικό Aspen Plus.

2.3 Αποτελέσματα και συζήτηση

Στο αρχικό μοντέλο που αναπτύχθηκε πραγματοποιήθηκε η θεώρηση ότι σχηματίζεται μόνο CH4 ως αντιπροσωπευτική ένωση υδρογονανθράκων στο αέριο σύνθεσης οδηγώντας σε σημαντικές αποκλίσεις για τα CO, H_2 και CO_2 συγκριτικά με τα πειραματικά δεδομένα, όπως φαίνεται και στο Σχήμα 6. Υπό την παραδοχή αυτή, το αέριο σύνθεσης περιέχει CO, H_2, CO_2, CH_4 και N_2 (επί ξηρής βάσης), τα οποία είναι και τα αέρια συστατικά που αναλύονται στο σύστημα αέριας χρωματογραφίας.

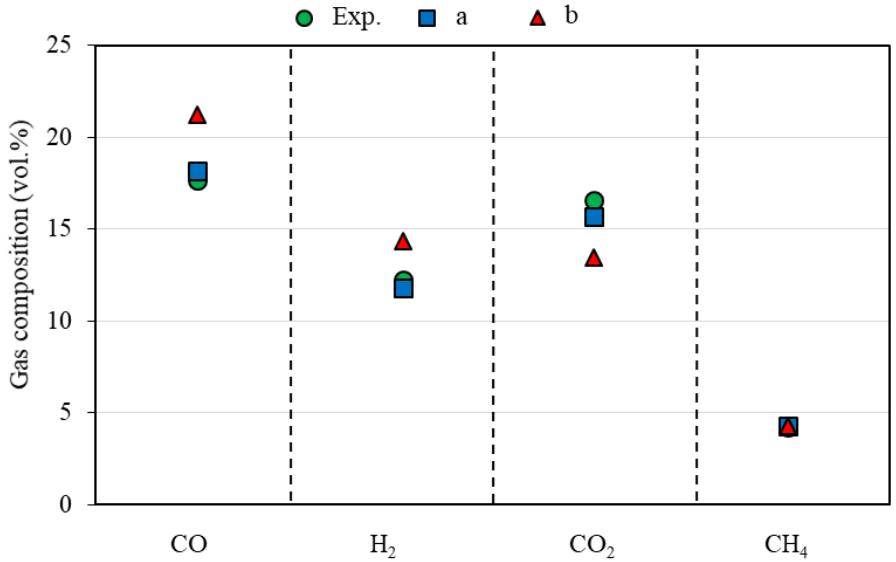

Σχήμα 6: Αποτελέσματα μοντελοποίησης για τη σύσταση του αερίου σύνθεσης για δύο διαφορετικές προσεγγίσεις σε σχέση με τα πειραματικά δεδομένα από τη Δοκιμή 1. Προσέγγιση a: χωρίς διόρθωση WGS, με σχηματισμό C_2H_4. Προσέγγιση b: χωρίς διόρθωση WGS, χωρίς σχηματισμό C_2H_4.

Ωστόσο, αν και στο πλαίσιο των δοκιμών που πραγματοποιήθηκαν στο CIUDEN δεν μετρήθηκαν λοιπές ενώσεις υδρογονανθράκων στο αέριο σύνθεσης, η παρουσία άλλων ενώσεων όπως υδρογονανθράκων C_{2+} στο αέριο προϊόν ενός αεριοποιητή ρευστοποιημένης κλίνης θεωρείται δεδομένη. Χαρακτηριστικά, οι Rechulski et al. [88] και Mun et al. [151] ανέφεραν πως δύο από τις κύριες ενώσεις που εντοπίστηκαν στο αέριο σύνθεσης από την αεριοποίηση βιομάζας είναι οι C_2H_4 και C_2H_6 με συγκέντρωση στο αέριο στο εύρος 0.2-1.1 vol.%. Επομένως, πραγματοποιήθηκε τροποποίηση του θερμοδυναμικού μοντέλου ως προς το σχηματισμό υδρογονανθράκων, μοντελοποιώντας το σχηματισμό C_2H_4 στον ίδιο στοιχειομετρικό αντιδραστήρα στον οποίο πραγματοποιείται η εικονική σύνθεση του CH_4, το οποίο δεν προβλέπεται από τη χημική ισορροπία μέσω ελαχιστοποίησης της ελεύθερης ενέργειας Gibbs.

Κατά τη μοντελοποίηση χωρίς διόρθωση WGS, η περιεκτικότητα σε CO_2 βρέθηκε να υποεκτιμάται, ενώ η περιεκτικότητα CO να υπερεκτιμάται σε σύγκριση με τις πειραματικές μετρήσεις. Οι αποκλίσεις ήταν πιο σημαντικές κατά τη μοντελοποίηση χωρίς σχηματισμό C_2H_4. Από την άλλη πλευρά, όταν συμπεριλήφθηκε ο σχηματισμός C_2H_4, η σύγκλιση βελτιώθηκε και η πιο αξιοσημείωτη διαφορά ήταν στην πρόβλεψη της περιεκτικότητας του CO_2 (~ 1 vol.% απόκλιση).

Σε επόμενο στάδιο εξετάστηκε η επίδραση της διόρθωσης της αντίδρασης WGS στην πρόβλεψη της σύστασης του αερίου σύνθεσης και τα αποτελέσματα φαίνονται στο Σχήμα 7. Η θεώρηση διόρθωσης της WGS χωρίς το σχηματισμό C_2H_4 φαίνεται να οδηγεί εκ νέου σε μεγάλη απόκλιση μεταξύ θεωρητικών και πειραματικών αποτελεσμάτων (Προσέγγιση a). Ωστόσο, βρέθηκε πως ο συνδυασμός της διόρθωσης WGS με στοιχειομετρικό σχηματισμό C_2H_4 (σταθερό ποσοστό σχηματισμού C σε C_2H_4 ίσο με 7%) μπορεί να βελτιώσει περαιτέρω τη συμφωνία μεταξύ των αποτελεσμάτων μοντελοποίησης και των πειραματικών αποτελεσμάτων.

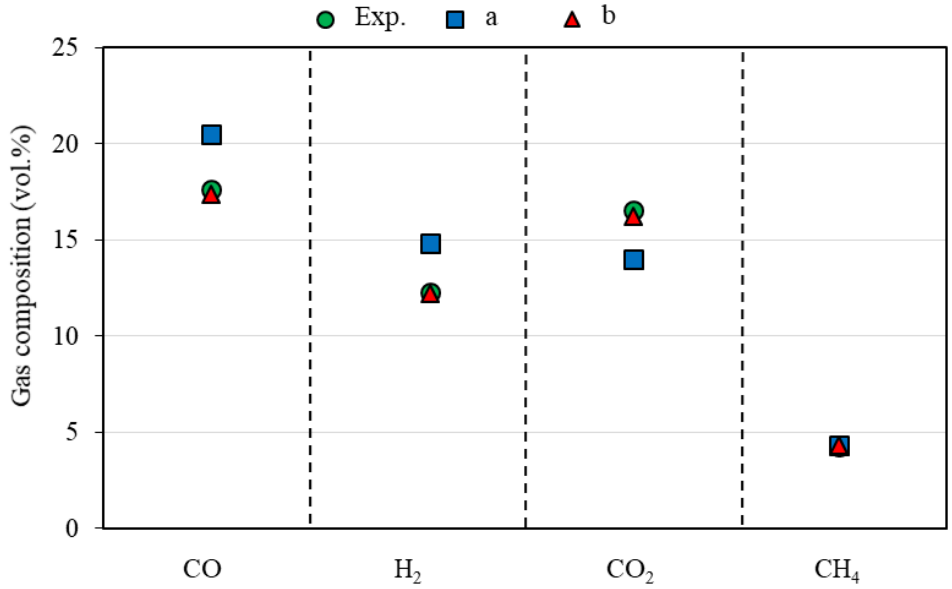

Σχήμα 7: Αποτελέσματα μοντελοποίησης για τη σύσταση του αερίου σύνθεσης για δύο διαφορετικές προσεγγίσεις σε σχέση με τα πειραματικά δεδομένα από τη Δοκιμή 1. Προσέγγιση a: με διόρθωση WGS, χωρίς σχηματισμό C_2H_4. Προσέγγιση b: με διόρθωση WGS και σχηματισμό C_2H_4.

Επιπλέον, το μοντέλο παρουσιάζει ικανοποιητική προσέγγιση των τιμών του εξανθρακώματος C(s) που διαφεύγει με την ιπτάμενη τέφρα, όπως διακρίνεται και στο Σχήμα 8. Ωστόσο, αποκλίσεις βρέθηκαν επίσης τόσο ως προς την εκτίμηση του εξανθρακώματος όσο και της σύστασης των κύριων αερίων του αερίου σύνθεσης κατά τη λειτουργία του σταθμού σε διαφορετικές συνθήκες (π.χ. Δοκιμή 3).

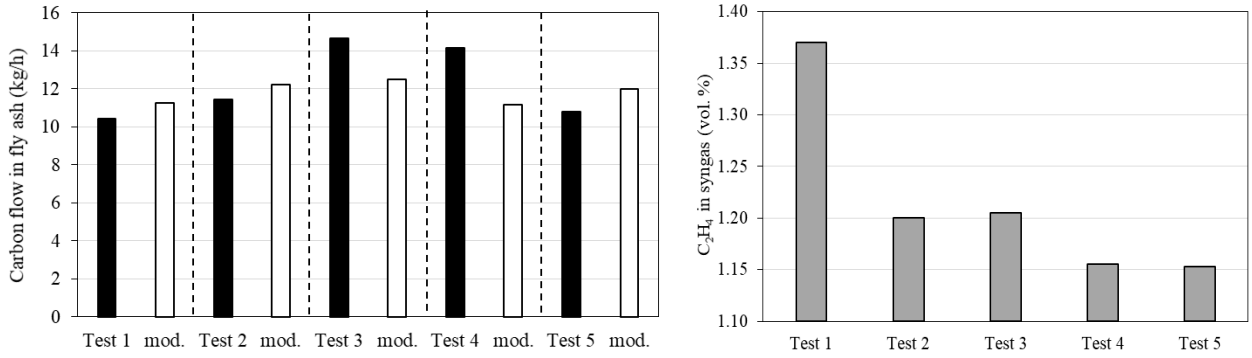

(a) (b)

Σχήμα 8: (a) Σύγκριση πειραματικών και αποτελεσμάτων μοντελοποίησης για την παροχή μάζας C(s) στην ιπτάμενη τέφρα και (b) σύσταση C_2H_4 στο αέριο σύνθεσης (vol.%) σύμφωνα με το θερμοδυναμικό μοντέλο.

Το γεγονός αυτό μπορεί να αποδοθεί σε διαφορετικές υδροδυναμικές συνθήκες εντός του αεριοποιητή που οφείλονται σε μεταβολή των παραμέτρων λειτουργίας, όπως της παροχής μάζας καυσίμου. Σχετικά με την εκτίμηση του ποσοστού του C_2H_4 στο αέριο, οι εκτιμώμενες τιμές βρίσκονται εντός του αναμενόμενου εύρους βάσει της βιβλιογραφίας. Η συγκέντρωση του H_2S στο αέριο βρέθηκε να είναι της τάξης των 25 ppmv, ενώ η μετατροπή του εισερχόμενου S σε H_2S αντιστοιχεί σε περίπου 93%. Η τιμή αυτή βρίσκεται σε συμφωνία με εκτιμήσεις των Kuramochi et al. [154]. Ένας σημαντικός περιορισμός του μοντέλου βρέθηκε να είναι η εκτίμηση του σχηματισμού OSCs και πισσών, καθώς για τα προϊόντα αυτά απαιτείται η ενσωμάτωση περισσότερων ημι-εμπειρικών σχέσεων στο μοντέλο εξαρτώμενων από παραμέτρους της διεργασίας.

2.4 Συμπεράσματα

Σε αυτό το κεφάλαιο παρουσιάστηκε ένα μοντέλο σταθερής κατάστασης για την πρόβλεψη της ποιότητας του αερίου σύνθεσης κατά την αεριοποίηση ξυλώδους βιομάζας, το οποίο αναπτύχθηκε στο λογισμικό Aspen Plus. Στο συγκεκριμένο μοντέλο λήφθηκε υπόψη ο σχηματισμός υδρογονανθράκων (CH_4 και C_2), καθώς και η διαφυγή μέρος του στερεού εξανθρακώματος μαζί με την ιπτάμενη τέφρα. Το μοντέλο βασίστηκε στην ελαχιστοποίηση της ελεύθερης ενέργειας Gibbs για την εκτίμηση των κύριων συστατικών του αερίου προϊόντος, ενώ ακόμη αξιολογήθηκε η επίδραση της ισορροπίας της αντίδρασης WGS στη σύγκλιση μεταξύ πειραματικών αποτελεσμάτων και μοντελοποίησης. Οι πειραματικές δοκιμές διεξήχθησαν σε αεριοποιητή τεχνολογίας BFB ισχύος 3 MW_{th} με μέσο αεριοποίησης αέρα, ενώ οι λειτουργικές παράμετροι των δοκιμών χρησιμοποιήθηκαν ως εισροές στο μοντέλο ισορροπίας. Η ενσωμάτωση ενός μοντέλου διόρθωσης της WGS συνέβαλε στην επίτευξη καλύτερης συμφωνίας με τα πειραματικά δεδομένα, υποδεικνύοντας ότι η αντίδραση μπορεί να παραμείνει ενεργή κατά την ψύξη του αερίου σύνθεσης. Όταν εξετάστηκε αποκλειστικά ο σχηματισμός CH_4 (αντιπροσωπευτική ένωση των υδρογονανθράκων που προκύπτουν κατά το στάδιο της πυρόλυσης στον αεριοποιητή), τα αποτελέσματα της προσομοίωσης απέκλιναν σημαντικά από τα πειραματικά δεδομένα. Για το λόγο αυτό, ενσωματώθηκε επιπλέον ο σχηματισμός του C_2H_4 στο μοντέλο ως αντιπροσωπευτική ένωση ελαφρών υδρογονανθράκων στο αέριο σύνθεσης. Το τροποποιημένο μοντέλο κατόρθωσε να προβλέψει επαρκώς τα κύρια συστατικά του αερίου σύνθεσης. Εντούτοις, σημειώθηκαν αποκλίσεις με αλλαγή των συνθηκών λειτουργίας, όπως των παροχών τροφοδοσίας καυσίμου και οξειδωτικού. Συσχετίσεις που περιγράφουν την παραγωγή υδρογονανθράκων σε σχέση με τις παραμέτρους της αεριοποίησης μπορούν να βελτιώσουν την ικανότητα του μοντέλου να προβλέψει τη σύσταση του παραγόμενου αερίου, καθώς στο παρόν μοντέλο, χρησιμοποιήθηκαν δεδομένα για ένα μόνο θερμοκρασιακό επίπεδο. Επιπλέον, σχέσεις για τη μετατροπή του στερεού εξανθρακώματος μπορούν να βελτιώσουν περαιτέρω τις επιδόσεις του μοντέλου, καθώς η περιεκτικότητα των κύριων συστατικών του παραγόμενου αερίου επηρεάζεται από αντιδράσεις στερεών/αερίων (π.χ. αντίδραση Boudouard). Οι υπολογισμοί θερμοδυναμικής ισορροπίας μπορούν να προβλέψουν ικανοποιητικά τη συγκέντρωση του H_2S, η οποία είναι η κύρια ένωση θείου στο αέριο σύνθεσης. Παρόλα αυτά, ένα τέτοιο απλοποιημένο μοντέλο δεν είναι κατάλληλο για την εκτίμηση του σχηματισμού των OSCs. Έτσι, όσον αφορά την κατανομή θείου στα αέρια συστατικά, προτείνεται ως μελλοντική εργασία η ενσωμάτωση ημι-εμπειρικών σχέσεων που τροφοδοτούνται με τις κυριότερες παραμέτρους που επηρεάζουν την περιεκτικότητα και τον τύπο των OSCs (π.χ. θερμοκρασία, *λ*, περιεκτικότητα βιομάζας σε θείο κ.λπ.).

Συνολικά, το ημι-εμπειρικό μοντέλο ισορροπίας που παρουσιάστηκε στο παρόν κεφάλαιο μπορεί να θεωρηθεί ως κατάλληλο εργαλείο για τη μοντελοποίηση της αεριοποίησης βιομάζας, καθώς και πιο σύνθετων διεργασιών που βασίζονται σε αυτήν. Ωστόσο, χαρακτηρίζεται από πεπερασμένη ακρίβεια όταν αντικειμενικός σκοπός είναι η ακριβής διαστασιολόγηση εξοπλισμού, όπου απαιτούνται και λεπτομερέστερα μοντέλα (π.χ. CFD). Το συγκεκριμένο μοντέλο ισορροπίας τροποποιήθηκε περαιτέρω (βλ. Κεφάλαιο 7) για να συμπεριληφθεί σε αυτό η συγκέντρωση διαφόρων ρύπων στο αέριο σύνθεσης. Στο πλαίσιο αυτό θεωρήθηκε ο σχηματισμός πισσών και ελαφρών υδρογονανθράκων, καθώς και απώλειες θερμότητας κατά τη διεργασία.

3 Πειραματική διερεύνηση της δέσμευσης θειούχων ενώσεων και ελαφρών πισσών από ενεργό άνθρακα

3.1 Βιβλιογραφική ανασκόπηση και πλαίσιο μελέτης

Στο πλαίσιο της εργασίας, διερευνώνται τεχνολογίες AGR που βασίζονται σε υδατικά διαλύματα ανθρακικού καλίου (K_2CO_3) εξαιτίας των πλεονεκτημάτων τους, όπως η μειωμένη θερμική κατανάλωση αναγέννησης και η μειωμένη διάβρωση σε σχέση με τις αμίνες [162]. Ωστόσο, το καθαρό αέριο σύνθεσης εξακολουθεί να περιέχει θείο [163], καθώς η διεργασία δεν είναι ιδιαίτερα επιλεκτική έναντι των ενώσεων θείου. Συγκεκριμένα, OSCs όπως το θειοφαίνιο, το βενζοθειοφαίνιο κ.α. δεν απομακρύνονται αποτελεσματικά με διαλύματα K_2CO_3 [163]. Επομένως, η σύζευξη των διεργασιών AGR με κλίνες οξειδίου του ψευδαργύρου (ZnO) και/ή ενεργό άνθρακα (AC) μπορεί να συμβάλει στην περαιτέρω δέσμευση των θειούχων ενώσεων. Οι ACs αποτελούν υποσχόμενα υλικά για την προσρόφηση προσμίξεων από το αέριο σύνθεσης λόγω της μεγάλης επιφάνειας τους, του αυξημένου όγκου πόρων και του ανταγωνιστικού τους κόστους [164-166]. Η επιφανειακή επεξεργασία των ACs μπορεί να βελτιώσει την επιλεκτικότητα τους για συγκεκριμένες ενώσεις στο αέριο σύνθεσης και επίσης να ενισχύσει την χωρητικότητά τους [167]. Μετά τη ρόφηση, το υλικό είναι εφικτό να αναγεννηθεί μέσω εναλλαγής πίεσης ή να πωληθεί ως καύσιμο (αποτελείται ουσιαστικά από άνθρακα) σε μεγάλης κλίμακας μονάδες καύσης εξοπλισμένες με σύστημα $DeSO_x$. Αυτή είναι μια αποτελεσματική λύση για μονάδες μικρής έως μέσης κλίμακας, για τις οποίες μια επιλεκτική διεργασία απομάκρυνσης του θείου με βάση υγρούς διαλύτες μπορεί να μην είναι οικονομικά βιώσιμη. Παράλληλα με τις θειούχες ενώσεις, διάφορα είδη πισσών μπορούν να συλλεχθούν. Εκτός από τα διάφορα προβλήματα που αποδίδονται στις πίσσες, πιθανά οφέλη μπορεί να προκύψουν όταν δεν εξαλειφθούν πλήρως από το αέριο σύνθεσης. Σε κάθε περίπτωση, η διερεύνηση της προσρόφησης πισσών, καθώς και η συνδυασμένη προσρόφηση ενώσεων θείου και πισσών από ACs, μπορεί να προσφέρει χρήσιμες πληροφορίες σχετικά με την εφαρμογή τέτοιων υλικών για καθαρισμό του αερίου σύνθεσης σε συνδυασμό με διεργασίες AGR που χρησιμοποιούν διαλύματα K_2CO_3.

Οι ακόλουθες παρατηρήσεις μπορούν να γίνουν με βάση την ανασκόπηση της βιβλιογραφίας:

- Αν και αρκετές πειραματικές μελέτες έχουν διερευνήσει την προσρόφηση ανόργανων ενώσεων θείου (κυρίως H_2S) σε ACs [166], οι σχετικές εργασίες με την προσρόφηση των OSCs από την αέρια φάση σε συγκεντρώσεις που αντιστοιχούν στην αεριοποίηση στερεών καυσίμων είναι πολύ σπανιότερες. Οι περισσότερες από αυτές επικεντρώνονται στην προσρόφηση μερκαπτανών και σουλφιδίων σε μη επεξεργασμένους ή τροποποιημένους ACs [172] και όχι σε λιγότερο πτητικές θειούχες ενώσεις που περιέχονται στο αέριο σύνθεσης, όπως το θειοφαίνιο (C_4H_4S). Η αποθείωση υγρών καυσίμων μέσω ACs έχει προσελκύσει το ερευνητικό ενδιαφέρον και ενώσεις με βάση το θειοφάινιο (π.χ. θειοφαίνιο, BT και/ή DBT) χρησιμοποιούνται ως μοντέλα [179]. Σε αυτή την κατεύθυνση, οι διαθέσιμες μελέτες έχουν διεξαχθεί σε χαμηλές θερμοκρασίες, που δεν υπερβαίνουν τους 60 °C.
- Υπάρχουν λίγες μελέτες σχετικά με την ταυτόχρονη προσρόφηση ενώσεων θείου και πισσών σε ACs όταν οι ενώσεις περιέχονται σε πραγματικό αέριο σύνθεσης. Συγκεκριμένα συστατικά του αερίου μίγματος μπορούν να επηρεάσουν την απόδοση της δέσμευσης είτε θετικά είτε αρνητικά (π.χ. CO_2 και H_2O).

Σε αυτό το πλαίσιο, η παρούσα πειραματική μελέτη αρχικά διερευνά την απόδοση του AC ως υλικού για την δέσμευση του C_4H_4S από ένα φέρον αέριο σε υψηλή θερμοκρασία που αντιστοιχεί σε συνθήκες θερμού (warm) καθαρισμού του αερίου σύνθεσης. Σε επόμενο στάδιο παρουσιάζεται η ταυτόχρονη προσρόφηση θείου (κυρίως H_2S) και ελαφρών πισσών (κυρίως C_6H_6) που περιέχονται στο αέριο σύνθεσης αεριοποιητή τεχνολογίας κονιοποιημένου καυσίμου ισχύος 1 MW_{th} τροφοδοτούμενου από βιομάζα.

3.2 Πειραματική διερεύνηση της προσρόφησης θειοφαινίου σε εργαστηριακή κλίμακα

3.2.1 Υλικά, πειραματική εγκατάσταση και μεθοδολογία μετρήσεων

Τα χαρακτηριστικά του AC που χρησιμοποιήθηκε κατά τη διάρκεια των δοκιμών φαίνονται στον Πίνακα 3. Το υλικό υπέστη αρχικά κονιοποίηση και επιλέχθηκε το κλάσμα με εύρος διαμέτρων σωματιδίων μεταξύ 125 και 160 μm. Επιπλέον, προσδιορίστηκαν ιδιότητες όπως η ειδική επιφάνεια (μεθοδολογία BET), η κατανομή των πόρων (μεθοδολογία BJH) και η πυκνότητα του υλικού μέσω αναλυτικών οργάνων διαθέσιμων στο PSI. Τέλος, πριν από κάθε δοκιμή το υλικό υπεβλήθη σε θέρμανση για 3 h στους 150 °C. Για τις πειραματικές δοκιμές χρησιμοποιήθηκε υπερκάθαρο Ar (≥ 99.998 %) και 500 ppmv C_4H_4S σε He.

Πίνακας 3: Ιδιότητες ενεργού άνθρακα που χρησιμοποιήθηκε στις πειραματικές δοκιμές.

Παράμετρος	**Τιμή**
Τύπος AC (αρχικό υλικό)	CECA ACM40-4WA
Αριθμός C_6H_6	40 ± 2
Αριθμός CCl_4	>80
Μέση διάμετρος σωματιδίων, d_p (μm)	138
Χύδην πυκνότητα (kg m^{-3})	497
Πυκνότητα (kg m^{-3})	2,450
Ειδική επιφάνεια, BET (m^2 g^{-1})	991
Ακτίνα πόρων (m)	$13 \cdot 10^{-10}$

Η πειραματική διάταξη (ινστιτούτο PSI, Ελβετία) στην οποία πραγματοποιήθηκαν οι πειραματικές δοκιμές της προσρόφησης C_4H_4S φαίνεται στο Σχήμα 9. Το τμήμα ανάμιξης αερίων περιλαμβάνει ένα σύνολο ελεγκτών ροής μάζας (MFC, Bronkhorst EL-FLOW) για την παροχή καθορισμένων ποσοτήτων αερίων. Τα Ar, C_4H_4S και νερό αναμίχθηκαν σε ένα θερμαινόμενο θάλαμο ανάμιξης για την παραγωγή προσομοιωμένων αερίων με συγκεκριμένες συγκεντρώσεις. Η προσθήκη υγρασίας στο μίγμα πραγματοποιήθηκε με τροφοδοσία νερού σε ένα θερμαινόμενο κόμβο μέσω αντλίας σύριγγας (Harvard Apparatus PHD 2000). Ο γυάλινος αντιδραστήρας στον οποίο τοποθετείται το προσροφητικό υλικό έχει κυλινδρική μορφή με εσωτερική διάμετρο 2 mm και τοποθετείται σε κατακόρυφη διάταξη εντός ενός θερμοστατούμενου κλιβάνου (Carbolite MTF 12/25A). Δύο αυτόματες ρυθμιστικές βάνες 4 θυρών (SV1 και SV2) χρησιμοποιούνται για την ρύθμιση της κατεύθυνσης της ροής των αερίων. Η ανάλυση της αέριας φάσης πραγματοποιείται μέσω φασματοσκοπίας μάζας (Extrel Mass Spectrometer MAX300-LG). Όλες οι μεταλλικές σωληνώσεις που έρχονται σε επαφή με τη ροή του αερίου επικαλύπτονται με SiO_2 (SilcoNert® 2000) ώστε να αποφευχθεί η προσρόφηση θείου στην επιφάνεια του μετάλλου. Η πίεση της προσρόφησης ελέγχεται μέσω των ρυθμιστών BPR1 και BPR2 (βλ. Σχήμα 9).

Σε κάθε δοκιμή, 20 mg AC ζυγίστηκαν και τοποθετήθηκαν στον γυάλινο αντιδραστήρα. Στη συνέχεια, πραγματοποιήθηκε έλεγχος διαρροών με μια μικρή παροχή αερίου ίση με 3 NmL min^{-1} και πίεση ίση με την πίεση των πειραματικών δοκιμών (0.5 barg). Κατόπιν ρυθμίζεται η παροχή των αερίων και εξακριβώνεται η σύσταση του μίγματος στον αναλυτή πριν οδηγηθεί στην κλίνη προσρόφησης. Επιπλέον, μια ροή Ar περνάει από τον αντιδραστήρα πριν τη δοκιμή προσρόφησης και επιπλέον ρυθμίζεται η θερμοκρασία στην επιθυμητή τιμή. Το πέρας κάθε δοκιμής ορίζεται από τον κορεσμό του προσροφητικού υλικού με C_4H_4S, ενώ ο χρόνος διαρροής και η χωρητικότητα του υλικού υπολογίστηκαν με αναφορά το σημείο κατά το οποίο η συγκέντρωση εξόδου αντιστοιχεί στο 90% της συγκέντρωσης του C_4H_4S στην είσοδο της κλίνης. Ακολούθως, η χωρητικότητα του υλικού στο σημείο διαρροής υπολογίζεται όπως φαίνεται στην Εξ. 2

$$q_m = \frac{MW_{thioph} C_0 \dot{V}}{1000 m_{AC}} \int_0^{t_s} \left(1 - \frac{C_t}{C_0}\right) dt \qquad \textit{Εξ. 2}$$

όπου MW_{thioph} το μοριακό βάρος του C_4H_4S (84 g mol^{-1}), C_0 η συγκέντρωση εισόδου του C_4H_4S (mol m^{-3}), C_t η συγκέντρωση εξόδου του C_4H_4S τη χρονική στιγμή t (mol m^{-3}), $\dot{V}$ η παροχή όγκου του αερίου (m^3 min^{-1}), t_s ο συνολικός χρόνος κορεσμού (min) και m_{AC} η μάζα της κλίνης του ενεργού άνθρακα (g).

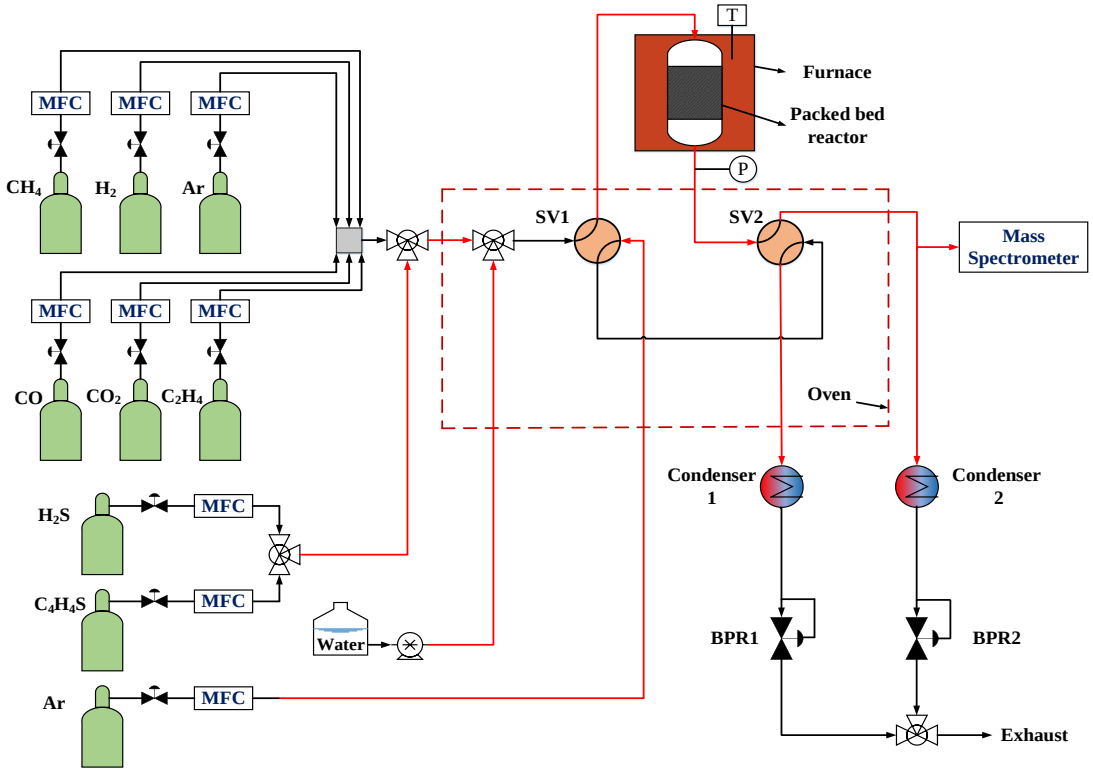

Σχήμα 9: Σχηματική απεικόνιση της πειραματικής διάταξης για την προσρόφηση του C_4H_4S.

Στον Πίνακα 4 φαίνονται οι δοκιμές προσρόφησης που πραγματοποιήθηκαν. Τέσσερις (4) παράμετροι της διεργασίας μεταβλήθηκαν κατά τη διάρκεια της συγκεκριμένης μελέτης και συγκεκριμένα η θερμοκρασία (100-200 °C), η παροχή του αερίου (30-55 NmL min^{-1}) και η συγκέντρωση των C_4H_4S (8.5-30 ppmv) και H_2O (0, 3 vol.%).

Πίνακας 4: Πίνακας δοκιμών προσρόφησης C_4H_4S σε AC.

Δοκιμή	**Μάζα AC (mg)**	**Θερμοκρασία (ºC)**	**Παροχή αερίου (NmL min^{-1})**	**Συγκέντρωση C_4H_4S (ppmv)**	**Συγκέντρωση H_2O (vol.%)**
1	19.50	100	30.0	15	0
2	20.63	150	30.0	15	0
3	20.00	200	30.0	15	0
4	20.00	100	30.0	15	3
5	20.30	150	30.0	15	3
6	20.27	150	42.5	15	0
7	19.65	150	55.0	15	0
8	20.29	150	30.0	8.5	0
9	20.31	150	30.0	23	0
10	20.11	150	30.0	30	0
11	20.46	100	30.0	8.5	0
12	20.26	100	30.0	30	0

3.2.2 Αποτελέσματα προσρόφησης C_4H_4S σε AC

Μια σύνοψη των αποτελεσμάτων χρόνου διαρροής και χωρητικότητας του υλικού AC για όλες τις δοκιμές προσρόφησης δίνεται στον Πίνακα 5. Στη συνέχεια αναλύεται η επίδραση των παραμέτρων της διεργασίας για στα αποτελέσματα, ενώ επιπλέον δίνονται οι καμπύλες διαρροής για την προσρόφηση του C_4H_4S. Η μέγιστη χωρητικότητα του υλικού μετρήθηκε σε θερμοκρασία 100 °C (ελάχιστη θερμοκρασία δοκιμής) και συγκέντρωση 30 ppmv C_4H_4S (μέγιστη συγκέντρωση δοκιμής), ενώ η ελάχιστη χωρητικότητα μετρήθηκε στη μέγιστη θερμοκρασία των 200 °C.

Πίνακας 5: Αποτελέσματα χρόνου διαρροής και χωρητικότητας AC για όλες τις δοκιμές προσρόφησης C_4H_4S.

Δοκιμή	**Χρόνος διαρροής, t_{90} (min)**	**Χωρητικότητα S (mg S g^{-1} AC)**	**Χωρητικότητα C_4H_4S, q_{90} (mg C_4H_4S g^{-1} AC)**
1	108	3.10	8.15
2	26	0.64	1.68
3	10	0.22	0.59
4	83	2.45	6.44
5	24	0.60	1.57
6	20	0.64	1.68
7	14	0.67	1.76
8	39	0.42	1.09
9	24	0.76	2.00
10	18	1.09	2.86
11	152	2.11	5.54
12	73	4.42	11.59

Η επίδραση της θερμοκρασίας και της παροχής αερίου στη μορφή των καμπυλών διαρροής για την προσρόφηση του C_4H_4S φαίνεται στο Σχήμα 10. Η αύξηση της θερμοκρασίας έχει τη σημαντικότερη επίδραση στη χωρητικότητα του AC, αφού το υλικό στους 200 °C διατηρεί μόνο το 7% της αρχικής χωρητικότητας που μετρήθηκε στους 100 °C. Επιπλέον, παρατηρείται μια πιο απότομη κλίση της καμπύλης διαρροής με αύξηση της θερμοκρασίας η οποία αποδίδεται στη μεγαλύτερη παροχή όγκου στην κλίνη και στη βελτιωμένη διάχυση στους πόρους του υλικού. Το αποτέλεσμα της παρούσας μελέτης φαίνεται να βρίσκεται σε συμφωνία με τις μετρήσεις των Xiao et al. για AC εμποτισμένο με Na_2CO_3 [166]. Η επίδραση της θερμοκρασίας είναι άμεσα συνδεδεμένη με τον εξώθερμο χαρακτήρα της φυσικής προσρόφησης, ενώ η επιλογή ενός ροφητικού υλικού που εισάγει ενδόθερμες αντιδράσεις με την ένωση που προσροφάται μπορεί να αντιστρέψει την τάση που βρέθηκε για τον AC [170].

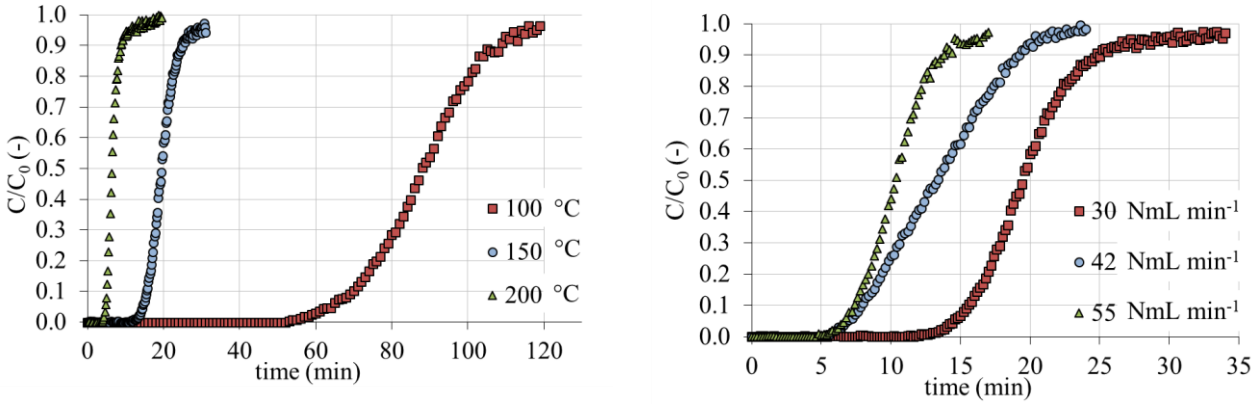

Σχήμα 10: (Αριστερά) Καμπύλες διαρροής για την προσρόφηση C_4H_4S σε AC στους 100, 150 και 200 °C (συγκέντρωση εισόδου C_4H_4S: 15 ppmv, παροχή αερίου: 30 NmL min^{-1}, χωρίς προσθήκη H_2O) και (δεξιά) καμπύλες διαρροής για την προσρόφηση C_4H_4S σε AC για παροχή αερίου 30.0, 42.5 και 55.0 NmL min^{-1} (συγκέντρωση εισόδου C_4H_4S: 15 ppmv, θερμοκρασία: 150 °C, χωρίς προσθήκη H_2O).

Από την άλλη πλευρά, η μεταβολή της παροχής του αερίου επηρεάζει την ικανότητα απορρόφησης του AC σε πολύ μικρό βαθμό, εφόσον δεν υπάρχει μεταβολή στη μερική πίεση του C_4H_4S. Έτσι, παρά το γεγονός ότι μετρήθηκε μια ανεπαίσθητη αύξηση της χωρητικότητας του υλικού στην υψηλότερη τιμή *GHS*V, οι μεταβολές ήταν < 3% για το εύρος της παροχής που μελετήθηκε στην παρούσα εργασία. Φαίνεται επομένως πως η μεταβολή της παροχής του αερίου επηρεάζει την προσρόφηση του C_4H_4S κατά αντίστοιχο τρόπο με την προσρόφηση του DMS σύμφωνα με τους Barelli et al. [183].

Η επίδραση της μερικής πίεσης του C_4H_4S στις καμπύλες διαρροής της προσρόφησης φαίνεται στο Σχήμα 11. Αύξηση της μερικής πίεσης οδηγεί σε μείωση του χρόνου διαρροής και αύξηση της χωρητικότητας του AC. Αντίστοιχα, η επίδραση της προσθήκης υγρασίας σε σύσταση 3 vol.% φαίνεται στο Σχήμα 12, όπου διακρίνεται πως η παρουσία υγρασίας οδηγεί σε μείωση του χρόνου διαρροής, ενώ μετρήθηκε επίσης μείωση της χωρητικότητας του AC. Παρά το γεγονός ότι η προσρόφηση του H_2O (δεσμοί υδρογόνου) είναι διαφορετικής φύσης σε σχέση με την προσρόφηση του C_4H_4S [187], δυσχεραίνει την προσρόφηση των μορίων του θειοφαινίου στην επιφάνεια του AC.

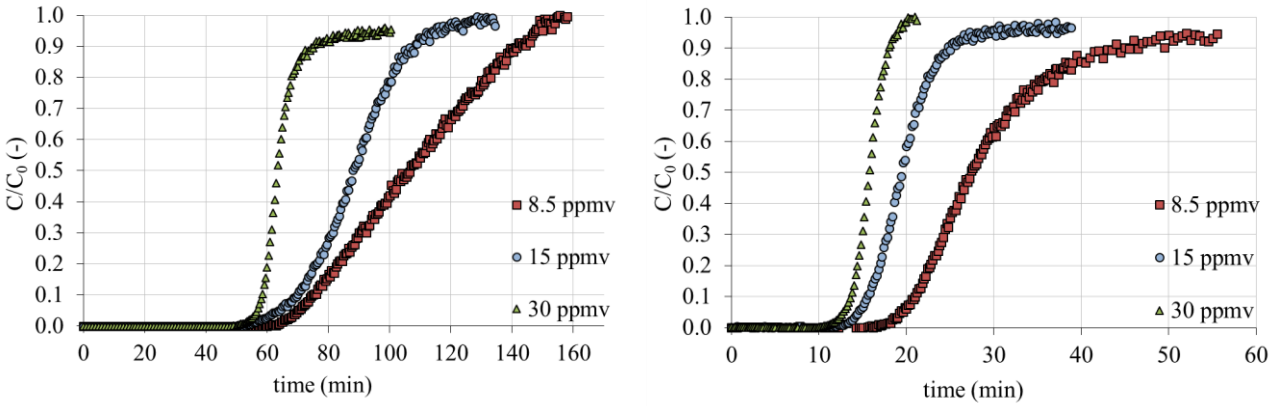

Σχήμα 11: (Αριστερά) Καμπύλες διαρροής για την προσρόφηση C_4H_4S σε AC για 8.5, 15 και 30 ppmv συγκέντρωση εισόδου (θερμοκρασία: 100 °C, παροχή αερίου: 30 NmL min^{-1}, χωρίς προσθήκη H_2O) και (δεξιά) καμπύλες διαρροής για την προσρόφηση C_4H_4S σε AC για 8.5, 15 και 30 ppmv συγκέντρωση εισόδου (θερμοκρασία: 150 °C, παροχή αερίου: 30 NmL min^{-1}, χωρίς προσθήκη H_2O).

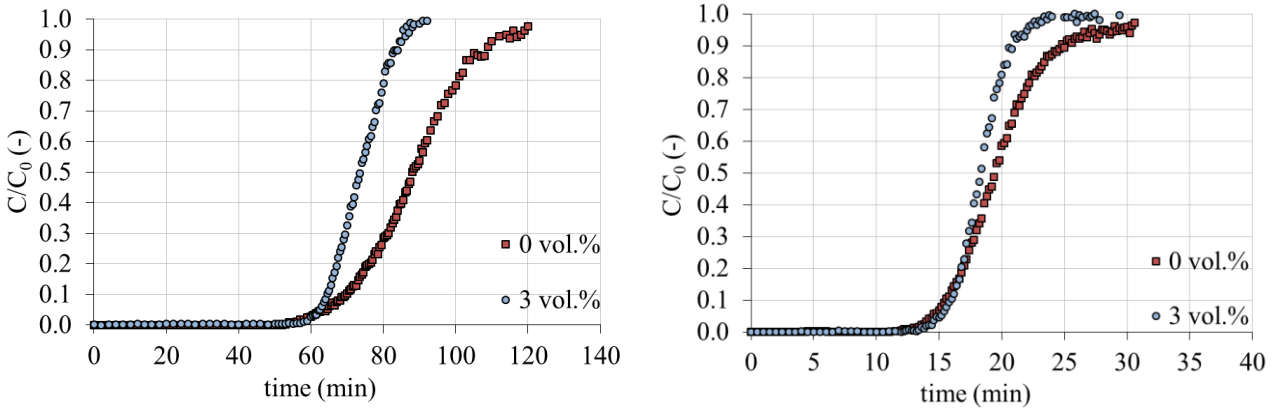

Σχήμα 12: (Αριστερά) Καμπύλες διαρροής για την προσρόφηση C_4H_4S σε AC για ξηρό φέρον αέριο και για 3.0 vol.% H_2O στους 100 °C (συγκέντρωση εισόδου C_4H_4S: 15 ppmv, παροχή αερίου: 30 NmL min^{-1}) και (δεξιά) καμπύλες διαρροής για την προσρόφηση C_4H_4S σε AC για ξηρό φέρον αέριο και για 3.0 vol.% H_2O στους 150 °C (συγκέντρωση εισόδου C_4H_4S: 15 ppmv, παροχή αερίου: 30 NmL min^{-1}).

Με βάση τα πειραματικά αποτελέσματα εξετάστηκαν δύο μοντέλα ισόθερμων για την περιγραφή της προσροφητικής ικανότητας του ενεργού άνθρακα, ένα μονοπαραμετρικό μοντέλο (Henry) και ένα μοντέλο 2 παραμέτρων (Langmuir). Η ανάλυση έδειξε πως με ένα μοντέλο τύπου Langmuir μπορεί να επιτευχθεί σαφώς καλύτερη σύγκλιση των πειραματικών αποτελεσμάτων και θεωρητικών εκτιμήσεων (± 20% και $R^2 > 0.99$). Τα μοντέλα Henry και Langmuir που χρησιμοποιήθηκαν για την μοντελοποίηση φαίνονται στις Εξ. 3 και Εξ. 4, αντίστοιχα. Οι σταθερές των ισόθερμων όπως προέκυψαν στην παρούσα εργασία δίνονται στον Πίνακα 6, ενώ οι μορφές τους σε σχέση με τα πειραματικά δεδομένα φαίνονται στο Σχήμα 13.

$$q_e = K_H C_e \qquad \textit{Εξ. 3}$$

$$q_e = \frac{K_L q_{mL} C_e}{1 + K_L C_e} \qquad \textit{Εξ. 4}$$

Πίνακας 6: Σταθερές μοντέλων Henry και Langmuir και αποτελέσματα στατιστικής ανάλυσης.

Μοντέλο ισόθερμης	**Παράμετρος**	**Τιμή**
Henry	$K_{H,ref}$ ($m^3\ kg^{-1}$)	2186
	ΔH_H ($J\ mol^{-1}$)	$-2.58 \cdot 10^4$
	RMSE ($mol\ kg^{-1}$)	0.016
	R^2	0.90
Langmuir	$K_{L,ref}$ ($m^3\ mol^{-1}$)	$3.484 \cdot 10^5$
	ΔH_L ($J\ mol^{-1}$)	$-5.02 \cdot 10^4$
	q_{mL} ($mol\ kg^{-1}$)	0.242
	RMSE ($mol\ kg^{-1}$)	0.002
	R^2	0.99

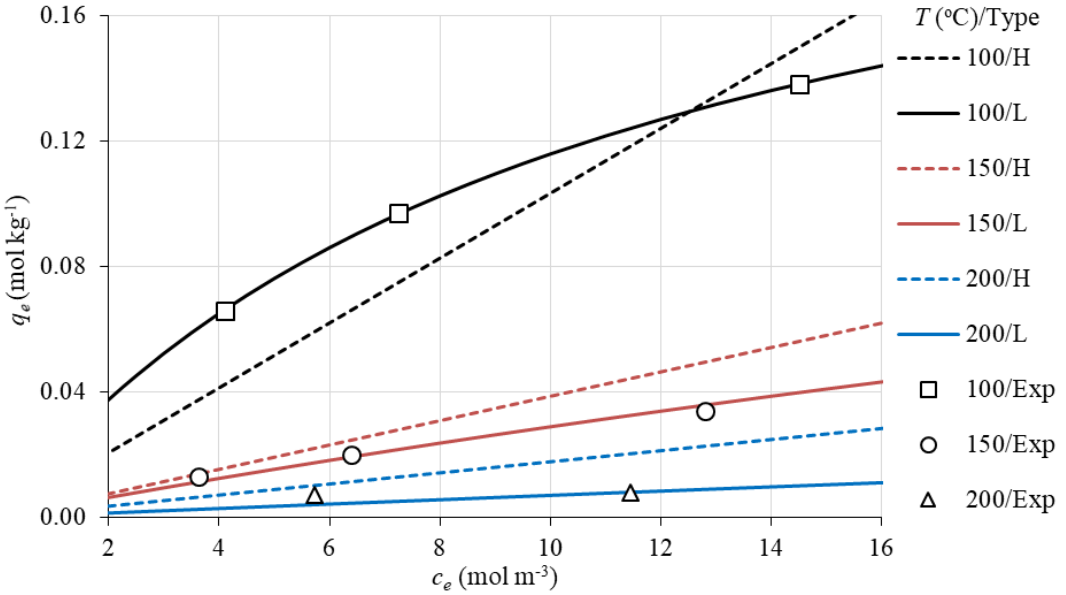

Σχήμα 13: Ισόθερμες προσρόφησης του C_4H_4S για τα μοντέλα Henry και Langmuir (H: Henry, L: Langmuir, Exp: πειραματικά αποτελέσματα μελέτης).

3.3 Πειραματική διερεύνηση της προσρόφησης θείου και πισσών από πραγματικό αέριο σύνθεσης

3.3.1 Υλικά, πειραματική εγκατάσταση και μεθοδολογία μετρήσεων

Οι πειραματικές δοκιμές αεριοποίησης και προσρόφησης με πραγματικό αέριο σύνθεσης πραγματοποιήθηκαν στο ινστιτούτο ETC στη Σουηδία. Η πιλοτική διάταξη αεριοποίησης φαίνεται στο Σχήμα 14. Αποτελείται από το σύστημα κονιοποίησης και τροφοδοσίας καυσίμου/οξειδωτικού, τον αντιδραστήρα (ID=0.52 m, ύψος=1.67 m, κεραμική επίστρωση), το σύστημα κατακράτησης συμπυκνώσιμων και σωματιδίων (quench), έναν ρυθμιστή για τη διατήρηση της πίεσης αεριοποίησης ανάντη, το φλόγιστρο (flare) για την καύση του προϊόντος, καθώς και εξοπλισμό για τη μέτρηση λειτουργικών παραμέτρων (θερμοκρασία, πίεση, παροχή μάζας κ.α.). Οι δοκιμές αεριοποίησης πραγματοποιήθηκαν με καύσιμο πελέτες ξύλου, ενώ ως υλικό προσρόφησης χρησιμοποιήθηκε το ίδιο με τις εργαστηριακές δοκιμές που πραγματοποιήθηκαν στο PSI. Η ανάλυση του καύσιμου για τις συγκεκριμένες δοκιμές δίνεται στον Πίνακα 7.

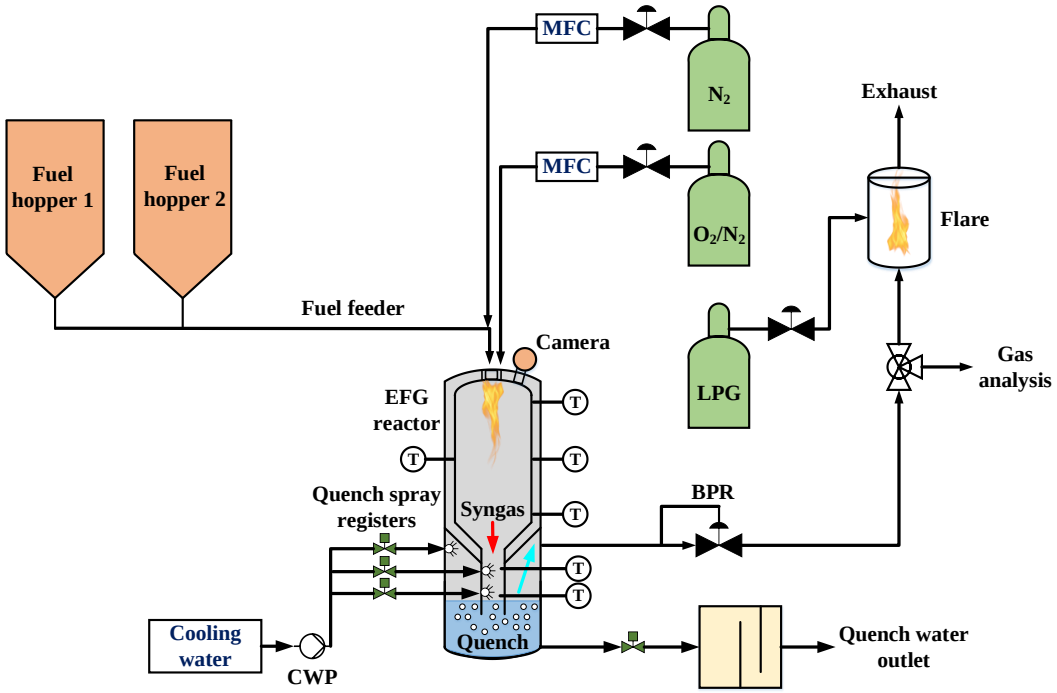

Σχήμα 14: Σχηματική απεικόνιση του αεριοποιητή ισχύος 1 MW_{th} στο ETC (με βάση την [190]).

Πίνακας 7: Προσεγγιστική και στοιχειακή ανάλυση πελετών ξύλου από τη Σουηδία.

Προσεγγιστική ανάλυση	
Υγρασία (wt. %, υγρή βάση)	4.7
Τέφρα (wt. %, επί ξηρού)	0.4
Πτητικά (wt. %, επί ξηρού)	80.5
Μόνιμος άνθρακας (wt. %, επί ξηρού)	14.4
Στοιχειακή ανάλυση (wt.%, επί ξηρής βάσης)	
C	50.6
H	6.3
N	0.10
S	0.006
Cl	0.02
O	42.4
LHV (MJ kg^{-1} ξηρής βιομάζας)	19.6

Ένα ρεύμα αερίου σύνθεσης διαχωρίζεται πριν την καύση στο φλόγιστρο της εγκατάστασης και οδηγείται είτε για ανάλυση είτε για αξιοποίηση σε μια εργαστηριακή εγκατάσταση σύνθεσης MeOH, η οποία φαίνεται στο Σχήμα 15. Η διάταξη αποτελείται από ένα σύστημα ανάμιξης αερίων με ελεγκτές παροχής μάζας, μια σειρά από αντιδραστήρες για τον καθαρισμό του αερίου από προσμίξεις και έναν καταλυτικό αντιδραστήρα για τη σύνθεση MeOH. Στην παρούσα μελέτη, πραγματοποιήθηκε τροποποίηση της πειραματικής διάταξης, κατά την οποία παρακάμφθηκαν οι αντιδραστήρες καθαρισμού του αερίου σύνθεσης (FB1 και FB2) και χρησιμοποιήθηκε ο θερμαινόμενος αντιδραστήρας FB3 για τις δοκιμές προσρόφησης.

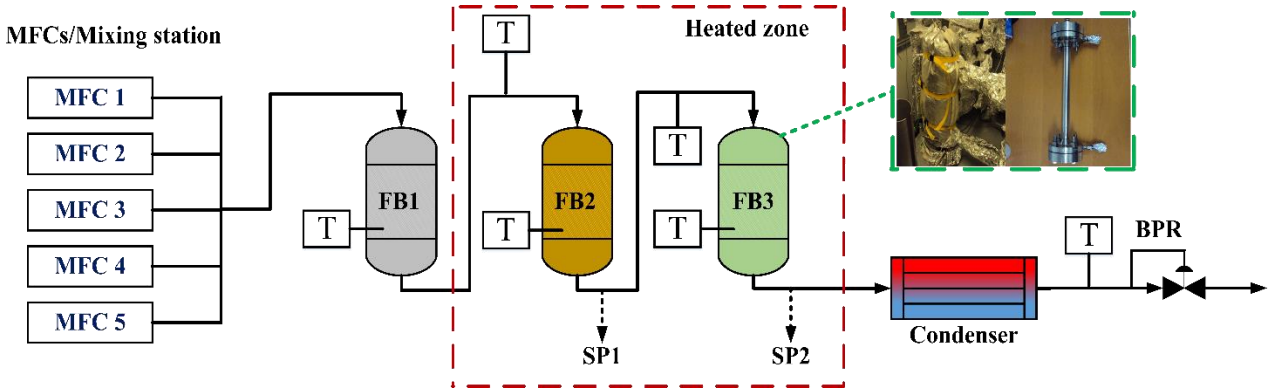

Σχήμα 15: Εργαστηριακή διάταξη καθαρισμού αερίου σύνθεσης και σύνθεσης MeOH στο ETC.

Κατά τη διάρκεια κάθε δοκιμής πραγματοποιήθηκαν συνεχείς αναλύσεις του αερίου σύνθεσης μέσω αναλυτή micro-GC (Varian 490 GC), ενώ οι αναλύσεις των θειούχων ενώσεων και των πισσών ανάντη και κατάντη της κλίνης FB3 πραγματοποιήθηκαν μέσω GC-PFPD και GC-FID αναλυτών (Varian CP-3800), αντίστοιχα. Οι συνθήκες λειτουργίας τόσο της εγκατάστασης αεριοποίησης όσο και της κλίνης προσρόφησης φαίνονται αναλυτικότερα στον Πίνακα 8.

Πίνακας 8: Συνθήκες λειτουργίας αεριοποιητή, κλίνης προσρόφησης και παράμετροι δειγματοληψίας.

	Αεριοποίηση	
Παράμετρος	**Δοκιμή 1**	**Δοκιμή 2**
Τύπος βιομάζας	Σουηδικές πελέτες ξύλου	
Θερμοκρασία αεριοποίησης (°C)	1274	1282
Πίεση αεριοποίησης (barg)	6.0	6.0
Παροχή βιομάζας (kg h^{-1})	120.0	120.0
λ (–)	0.40	0.39
Παροχή νερού στο σύστημα ψύξης (L min^{-1})	25.5	23.0
Έξοδος αερίου από τον αεριοποιητή (°C)	96.3	107.6
Διάρκεια σταθερής κατάστασης (min)	170	90
Αριθμός δειγμάτων αερίου από SP1	3	3
	Διάταξη προσρόφησης σε AC	
Παράμετρος	**Δοκιμή 1**	**Δοκιμή 2**
Τύπος AC	CECA ACM40-4WA	
Μάζα AC (g)	5.013	5.065
Θερμοκρασία FB3-TC (°C)	100	150
Πίεση προσρόφησης (bar)	1.1	1.1
Παροχή αερίου (NL min^{-1})	4.0	4.0
Διάρκεια δοκιμής (min)	110	60
Αριθμός δειγμάτων αερίου από SP2	6	8

3.3.2 *Αποτελέσματα αεριοποίησης και προσρόφησης θείου και πισσών από αέριο σύνθεσης*

Η λειτουργία του αεριοποιητή κονιοποιημένου καυσίμου ισχύος 1 MW_{th} ακολούθησε τρεις φάσεις, το στάδιο της προθέρμανσης με αντιστάσεις, το στάδιο της καύσης για την περαιτέρω αύξηση της θερμοκρασίας και τελικά το στάδιο της αεριοποίησης. Η θερμοκρασία του αντιδραστήρα και η περιοχή τιμών του λ κατά τα στάδια αυτά φαίνεται στο Σχήμα 16.

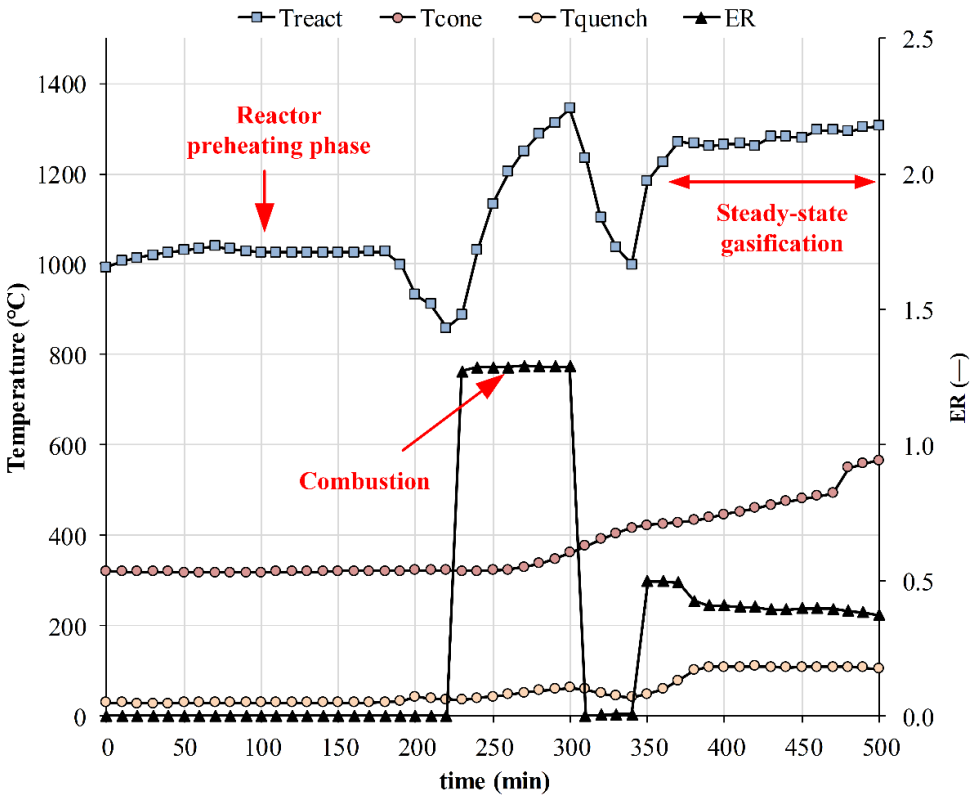

Σχήμα 16: Θερμοκρασία και λ αεριοποίησης ως συνάρτηση του χρόνου κατά την εκκίνηση και τη λειτουργία σε σταθερή κατάσταση (Δοκιμή 2).

Όπως φαίνεται στον Πίνακα 9, τα CO και H_2 ήταν τα κύρια συστατικά του αερίου σύνθεσης. Και στις δύο δοκιμές μετρήθηκε χαμηλή συγκέντρωση των υδρογονανθράκων, όπως των CH_4 και C_2H_4, γεγονός που μπορεί να αποδοθεί στην υψηλή θερμοκρασία της τεχνολογίας αεριοποίησης. Επιπλέον, στον Πίνακα 10 φαίνονται τα αποτελέσματα των αναλύσεων χρωματογραφίας για ενώσεις θείου και πίσσες. Οι δύο αντιπροσωπευτικές ενώσεις που μετρήθηκαν στο αέριο σύνθεσης ήταν οι H_2S και C_6H_6. Μια ενδιαφέρουσα παρατήρηση είναι η αδυναμία να επιτευχθεί πλήρης επαναληψιμότητα όσον αφορά τη σύσταση του αερίου σύνθεσης, ακόμα και υπό πανομοιότυπες συνθήκες αεριοποίησης με το ίδιο καύσιμο. Επιπλέον, βρέθηκε συσχέτιση των συγκεντρώσεων CH_4, C_2H_4 και C_6H_6 στο αέριο σύνθεσης σε συμφωνία με προηγούμενα αποτελέσματα [156].

Πίνακας 9: Σύσταση αερίου σύνθεσης (μέση τιμή και σ για τα κύρια αέρια) των Δοκιμών 1 και 2.

	Δοκιμή 1		**Δοκιμή 2**	
Ένωση	**Συγκέντρωση (vol.%, επί ξηρού)**	***σ* (vol.%)**	**Συγκέντρωση (vol.%, επί ξηρού)**	***σ* (vol.%)**
CO	49.02	0.40	47.38	0.85
H_2	28.98	0.34	28.15	0.59
CO_2	13.98	0.32	15.50	0.21
CH_4	1.83	0.25	1.25	0.10
C_2H_4	0.04	0.01	0.02	~0.00

Πίνακας 10: Συγκέντρωση H_2S και C_6H_6 στο αέριο σύνθεσης κατάντη του αεριοποιητή.

Δοκιμή 1/Αρ. δείγματος	**H_2S (ppmv)**	**C_6H_6 (ppmv)**
1	3.8	146.8
2	5.8	186.1
3	5.6	176.5
Μέση τιμή	5.1	169.8
σ	0.9	16.7
Δοκιμή 2/Αρ. δείγματος	**H_2S (ppmv)**	**C_6H_6 (ppmv)**
1	78.5	62.8
2	76.7	87.6
3	85.7	80.2
Μέση τιμή	80.3	76.9
σ	3.9	10.4

Οι καμπύλες διαρροής για την προσρόφηση των H_2S και C_6H_6 φαίνονται στα Σχήματα 17 και 18, αντίστοιχα.

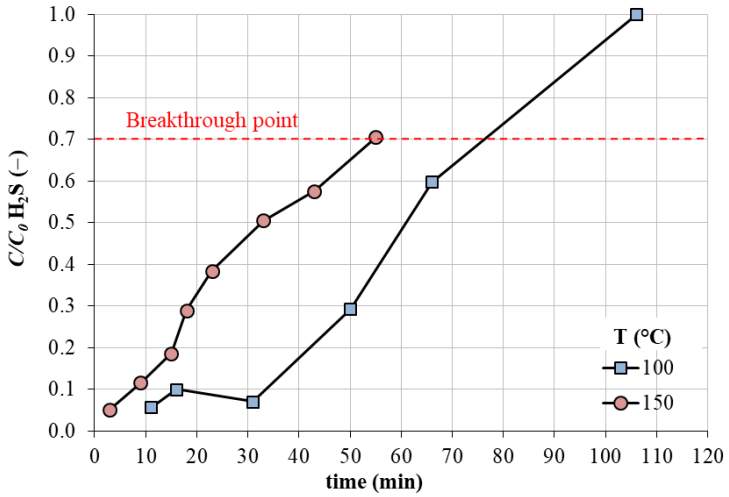

Σχήμα 17: Καμπύλες διαρροής για την προσρόφηση H_2S σε AC στους 100 και 150 °C.

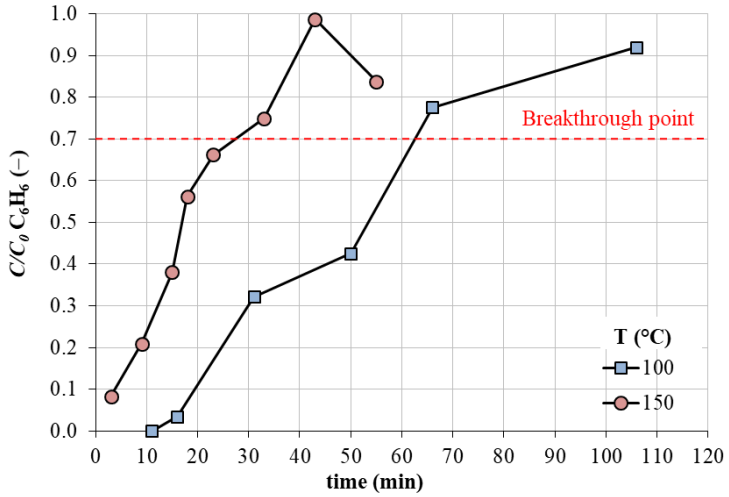

Σχήμα 18: Καμπύλες διαρροής για την προσρόφηση C_6H_6 σε AC στους 100 και 150 °C.

Επιπρόσθετα, τα αποτελέσματα των δοκιμών προσρόφησης με πραγματικό αέριο σύνθεσης συνοψίζονται στον Πίνακα 11.

Πίνακας 11: Σύνοψη αποτελεσμάτων προσρόφησης των H_2S και C_6H_6 σε AC.

Παράμετρος / **Δοκιμή**	**1**		**2**	
Ένωση	H_2S	C_6H_6	H_2S	C_6H_6
Παραδοχή διαρροής C/C_0 (–)	0.70	0.70	0.70	0.70
Χρόνος διαρροής (min)	76	63	55	27
Χωρητικότητα AC (mg g^{-1})	0.57	18.76	3.14	9.18
Χωρητικότητα του S (mg S g^{-1})	0.53	–	2.95	–

Σε κάθε περίπτωση, βρέθηκε πως η παρουσία C_6H_6 στο αέριο σύνθεσης έχει αρνητική επίδραση στην προσροφητική ικανότητα του AC. Η παρατήρηση ήταν εντονότερη στην περίπτωση της Δοκιμής 1, κατά την οποία μετρήθηκε επιπλέον πολύ χαμηλή συγκέντρωση του H_2S. Η αύξηση της θερμοκρασίας μείωσε το χρόνο διαρροής και για τις δύο ενώσεις, ενώ η ακανόνιστη κλίση των καμπυλών διαρροής μπορεί να αποδοθεί στη διακύμανση της συγκέντρωσης των αερίων κατά τη διάρκεια κάθε δοκιμής.

3.4 Συμπεράσματα

Στο κεφάλαιο αυτό διερευνήθηκε πειραματικά η προσρόφηση οργανικού και ανόργανου θείου σε φυσικώς ενεργοποιημένο άνθρακα (AC) σε συνθήκες υψηλών θερμοκρασιών. Αρχικά, πραγματοποιήθηκαν εργαστηριακές δοκιμές με χρήση του C_4H_4S ως χαρακτηριστική OSC. Μελετήθηκε η επίδραση τεσσάρων παραμέτρων (θερμοκρασία, *GHSV*, συγκέντρωση ένωσης και περιεκτικότητα σε υγρασία) στην χωρητικότητα του υλικού και στις καμπύλες διαρροής. Διαπιστώθηκε ότι εντός του εύρους των μελετώμενων παραμέτρων, η θερμοκρασία έχει την εντονότερη επίδραση στη μείωση της προσροφητικής ικανότητας του υλικού, δεδομένου ότι σε θερμοκρασία 200 ° C το υλικό διατηρεί λιγότερο από το 10% της χωρητικότητάς του στους 100 ° C. Μία αύξηση στην συγκέντρωση C_4H_4S βρέθηκε επίσης να επηρεάζει την προσροφητική ικανότητα του υλικού (η δεύτερη πιο σημαντική παράμετρος μετά τη θερμοκρασία). Σε υψηλότερες θερμοκρασίες και συγκεντρώσεις απορρόφησης, η κλίση της καμπύλης διαρροής ήταν μεγαλύτερη. Όταν αυξάνεται η θερμοκρασία, αυτή η τάση μπορεί να αποδοθεί στην υψηλότερη παροχή όγκου δια μέσου της κλίνης, στις λιγότερο ευνοϊκές ισόθερμες και στην αυξημένη διάχυση στους πόρους του υλικού, ενώ μια αύξηση της συγκέντρωσης βελτιώνει την κινητήρια δύναμη προσρόφησης. Μια μικρή προσθήκη H_2O στο ρεύμα του αερίου (3 vol.%) βρέθηκε να μειώνει τη χωρητικότητα και το χρόνο διαρροής, γεγονός που υποδηλώνει ότι είναι απαραίτητη μια περαιτέρω διερεύνηση της ταυτόχρονης προσρόφησης H_2O/C_4H_4S. Μια τέτοια μελέτη θεωρείται ιδιαίτερα σημαντική όταν η κλίνη AC επιτελεί ρόλο παγίδας θειούχων ενώσεων οι οποίες δεν δεσμεύτηκαν κατά το στάδιο της διεργασίας AGR, δεδομένης της παρουσίας H_2O στο καθαρό αέριο σύνθεσης όταν η διεργασία AGR πραγματοποιείται σε υψηλή θερμοκρασία. Επιπλέον, στην παρούσα μελέτη εφαρμόστηκαν υψηλές τιμές του *GHSV* και διαπιστώθηκε ότι η μεταβολή της παροχής αερίου δεν επηρεάζει την χωρητικότητα του υλικού, παρά μόνον προκαλεί μείωση του χρόνου διαρροής πριν τον κορεσμό. Φαίνεται λοιπόν ότι η ρόφηση του C_4H_4S παρουσιάζει παρόμοια χαρακτηριστικά ως προς τη συγκεκριμένη παράμετρο με δημοσιευμένα αποτελέσματα για την προσρόφηση DMS σε ACs. Το μοντέλο ισόθερμης τύπου Langmuir μπορεί να περιγράψει επαρκώς την επίδραση της θερμοκρασίας και της συγκέντρωσης στη χωρητικότητα του υλικού ($R^2 > 0.99$). Από την άλλη πλευρά, το μονοπαραμετρικό μοντέλο τύπου Henry μπορεί να χρησιμοποιηθεί μόνον για μια πρώτη εκτίμηση των τιμών χωρητικότητας.

Σε συνέχεια της προαναφερθείσας μελέτης, το ίδιο υλικό δοκιμάστηκε για την ταυτόχρονη προσρόφηση θείου και πισσών από πραγματικό αέριο σύνθεσης. Οι δοκιμές αεριοποίησης διεξήχθησαν σε αεριοποιητή τεχνολογίας EFG που τροφοδοτήθηκε με ξυλώδη βιομάζα. Το αέριο σύνθεσης ήταν πλούσιο σε CO και H_2, ενώ μετρήθηκε χαμηλή περιεκτικότητα σε υδρογονάνθρακες. Το γεγονός αυτό αποδίδεται στις υψηλές θερμοκρασίες λειτουργίας του αεριοποιητή (> 1200 °C). Οι αναλύσεις GC-FID και GC-PFPD των δειγμάτων του αερίου έδειξαν ότι τα C_6H_6 και H_2S ήταν οι κύριες ενώσεις πισσών και θείου, αντίστοιχα. Μία από τις ιδιαιτερότητες αυτών των δοκιμών ήταν η μεταβολή των συγκεντρώσεων των προσμίξεων, παρά την συνεπή

αναπαραγωγή των παραμέτρων λειτουργίας του αεριοποιητή. Παρόλο που αυτή η παρατήρηση καθιστά πιο δύσκολη την άμεση σύγκριση, μπορούν να ληφθούν χρήσιμες πληροφορίες σχετικά με τις επιδόσεις του υλικού υπό αντιπροσωπευτικές συνθήκες λειτουργίας. Οι δοκιμές έδειξαν ότι η χωρητικότητα του θείου μπορεί να μειωθεί λόγω της προσρόφησης ελαφρών πισσών, ιδιαίτερα όταν η συγκέντρωση του C_6H_6 στο αέριο σύνθεσης ξεπέρασε τα 150 ppmv (αναλογία όγκου H_2S:C_6H_6 = 1:30). Από την άλλη πλευρά, η ειδική χωρητικότητα θείου αυξήθηκε σημαντικά όταν η αναλογία όγκου των H_2S και C_6H_6 στο αέριο σύνθεσης ήταν περίπου 1:1 (80 ppmv έκαστο) στους 150 ° C. Υπό αυτές τις συνθήκες, μετρήθηκαν υψηλότερες τιμές της χωρητικότητας θείου σε σύγκριση με τις δοκιμές C_4H_4S με προσομοιωμένο αέριο (στα 30 ppmv συγκέντρωση εν τούτοις), το οποίο μεταφράζεται σε αντίστοιχη συνολική πρόσληψη μάζας και για τις δύο ενώσεις θείου.

Συνολικά, μπορεί να εξαχθεί το συμπέρασμα ότι οι ACs μπορούν να χρησιμοποιηθούν για την αποθείωση του αερίου σύνθεσης από H_2S και OSCs σε συνθήκες "θερμού" καθαρισμού αερίων κατάντη μιας διεργασίας AGR. Παρ' όλα αυτά, πρέπει να λαμβάνεται υπόψη η επίδραση της σύστασης του αερίου σύνθεσης και ειδικότερα των ενώσεων ελαφρών πισσών που δεν έχουν συλλεχθεί στη διεργασία AGR, ενώ επίσης σημαντικό ρόλο παίζει και το ποσοστό H_2O στο αέριο. Εντούτοις, κατά την ειδική περίπτωση όπου οι ελαφριές πίσσες αξιοποιούνται ή μετατρέπονται καταλυτικά σε κατάντη διεργασίες, υλικά πιο επιλεκτικά ως προς τις ενώσεις θείου θα πρέπει να αξιολογηθούν.

4 Απορρόφηση CO_2 σε καθαρά και ενισχυμένα διαλύματα ανθρακικού καλίου

4.1 Βιβλιογραφική ανασκόπηση και πλαίσιο μελέτης

Στις διεργασίες χημικής απορρόφησης, δύο στήλες διαχωρισμού είναι απαραίτητες: η πρώτη συνεισφέρει στο διαχωρισμό των όξινων αερίων από το αέριο μίγμα μέσω απορρόφησης στον υγρό διαλύτη, ενώ στη δεύτερη στήλη, τα όξινα αέρια διαχωρίζονται από το υγρό διάλυμα (αναγέννηση). Η μελέτη κατάλληλων διαλυτών για τη διεργασία είναι ιδιαίτερα σημαντική, ενώ οι διαλύτες αξιολογούνται με βάση διάφορα κριτήρια όπως η θερμότητα αναγέννησης, η χωρητικότητα σε όξινα αέρια, ο ρυθμός απορρόφησης, η τοξικότητα, η διαβρωτική συμπεριφορά, το κόστος και η θερμοχημική σταθερότητα [198]. Διάφοροι τύποι αμινών εξετάζονται λόγω της βελτιωμένης διαλυτότητας του CO_2 και της βελτιωμένης κινητικής των αντιδράσεων [199]. Ωστόσο, η χρήση διαλυμάτων με βάση αμίνες σχετίζεται με ορισμένα προβλήματα, όπως η υψηλή ειδική θερμότητα αναγέννησης, η διάβρωση του εξοπλισμού και ζητήματα αποδόμησης και απωλειών σε υψηλές θερμοκρασίες λειτουργίας. Τα υδατικά διαλύματα K_2CO_3 προσπερνούν διάφορα από τα εμπόδια αυτά. Η λειτουργία της απορρόφησης σε υψηλή θερμοκρασία (κοντά στο ατμοσφαιρικό σημείο κορεσμού) είναι ευεργετική ως προς τη μείωση της θερμότητας αναγέννησης [200], ενώ το K_2CO_3 είναι θερμοχημικά σταθερό και μη πτητικό [201]. Επιπρόσθετα, ένα από τα βασικά μειονεκτήματα που χαρακτηρίζουν τα συγκεκριμένα διαλύματα είναι ο χαμηλός ρυθμός απορρόφησης σε σχέση με τις πρωτοταγείς αμίνες [203]. Για το λόγο αυτό, ιδιαίτερο ενδιαφέρον υπάρχει για την βελτίωση των ιδιοτήτων των διαλυμάτων μέσω παρασκευής μιγμάτων με πρόσθετα αμίνες, αμινοξέα κ.α.

Στο κεφάλαιο αυτό παρουσιάζεται η επίδραση τεσσάρων (4) προσθέτων στη διαλυτότητα και το ρυθμό απορρόφησης του CO_2 σε υδατικά διαλύματα K_2CO_3. Μια πρώτη σειρά δοκιμών απορρόφησης CO_2 πραγματοποιήθηκε με δύο διαφορετικές συγκεντρώσεις K_2CO_3 (1.81 M και 2.53 M) χωρίς τη χρήση προσθέτων σε έναν αναδευόμενο αντιδραστήρα και τα αποτελέσματα χρησιμοποιήθηκαν για την επαλήθευση της πειραματικής μεθοδολογίας μέσω σύγκρισης με τις θεωρητικές εκτιμήσεις του μοντέλου electrolyte-NRTL στο Aspen Plus™. Μετά τις συγκεκριμένες δοκιμές οι οποίες χρησιμοποιήθηκαν και ως δοκιμές αναφοράς, εξετάστηκε η επίδραση της προσθήκης μιας πρωτοταγούς αμίνης (MEA), μιας τριτοταγούς αμίνης (MDEA), μιας διαμίνης (Πιπεραζίνη) και ενός αμινοξέος (Γλυκίνη) στη διαλυτότητα του CO_2 σε υψηλή θερμοκρασία (100 και 120 °C). Ενώ οι περισσότερες μελέτες εστιάζουν στη λειτουργία σε χαμηλή θερμοκρασία απορρόφησης [202, 207, 214, 215, 217, 221, 228, 229], η παρούσα εργασία εστίασε σε υψηλές θερμοκρασίες στις οποίες υπάρχουν λίγα δεδομένα διαλυτότητας [216]. Επιπλέον, στο κεφάλαιο αυτό παρουσιάζονται πειραματικά αποτελέσματα για τη διαλυτότητα του CO_2 σε διαλύματα K_2CO_3 ενισχυμένα με γλυκίνη για τα οποία ελάχιστες μελέτες είναι διαθέσιμες [230].

4.2 Μηχανισμοί αντιδράσεων

Η συνολική αντίδραση μεταξύ CO_2 και υδατικών διαλυμάτων K_2CO_3 δίνεται από την A2

$$K_2CO_{3(l)} + H_2O_{(l)} + CO_{2(aq)} \rightleftharpoons 2KHCO_{3(aq)} \qquad A2$$

ενώ αναλυτικότερα το σύστημα των χημικών αντιδράσεων δίνεται στον Πίνακα 12. Για τιμές pH > 9, η A7 είναι η αντίδραση που καθορίζει την κινητική της απορρόφησης. Διάφοροι μηχανισμοί βελτίωσης της κινητικής της απορρόφησης αποδίδονται στα ενισχυμένα διαλύματα [231, 232]. Ο βασικότερος μηχανισμός είναι ο σχηματισμός ενός ενδιάμεσου αμφιτεριόντος (zwitterion) που έπειτα χάνει ένα πρωτόνιο προς σχηματισμό καρβαμιδίου, όπως στην περίπτωση των πρωτοταγών αμινών (βλ. MEA).

Πίνακας 12: Χημικές αντιδράσεις για τη χημική απορρόφηση του CO_2 σε διαλύματα H_2O-K_2CO_3.

Αντιδράσεις	
$CO_{2(g)} \rightleftharpoons CO_{2(aq)}$	*A3*
$CO_{2(aq)} + 2H_2O_{(l)} \rightleftharpoons HCO_{3(aq)}^- + H_3O_{(aq)}^+$	*A4*
$K_2CO_{3(s)} \rightleftharpoons 2K_{(aq)}^+ + CO_{3(aq)}^{2-}$	*A5*
$CO_{3(aq)}^{2-} + H_2O_{(l)} \rightleftharpoons HCO_{3(aq)}^- + OH_{(aq)}^-$	*A6*
$OH_{(aq)}^- + CO_{2(aq)} \rightleftharpoons HCO_{3(aq)}^-$	*A7*
$2H_2O_{(l)} \rightleftharpoons H_3O_{(aq)}^+ + OH_{(aq)}^-$	*A8*

Οι αντιδράσεις που σχετίζονται με την προσθήκη MEA σύμφωνα με τον μηχανισμό σχηματισμού αμφιτεριόντος είναι οι A9-A11.

$$CO_2 + RNH_2 \rightleftharpoons RNH_2^+COO^- \quad A9$$

$$RNHCOO^- + H_2O \rightleftharpoons RNH_2 + HCO_3^- \quad A10$$

$$RNH_3^+ + H_2O \rightleftharpoons RNH_2 + H_3O^+ \quad A11$$

Περισσότερες λεπτομέρειες για τους μηχανισμούς των αντιδράσεων του CO_2 με τις ενώσεις MEA, PZ, γλυκίνη (Gly) και MDEA υπάρχουν στις εργασίες [207], [228], [229] και [234], αντίστοιχα.

4.3 Υλικά, πειραματική διάταξη και μεθοδολογία

Για τις πειραματικές δοκιμές, τα K_2CO_3, MEA, MDEA, PZ και Gly που χρησιμοποιήθηκαν είχαν καθαρότητα ≥ 99.0 %, ενώ για την παρασκευή των διαλυμάτων χρησιμοποιήθηκε απιονισμένο νερό. Ακόμη, οι καθαρότητες των αερίων N_2 και CO_2 ήταν 99.8% και 99.7%, αντίστοιχα. Σε κάθε πειραματική δοκιμή χρησιμοποιήθηκε σταθερός αρχικός όγκος διαλύματος (400 mL). Το σύνολο των πειραματικών δοκιμών παρουσιάζεται στον Πίνακα 13.

Πίνακας 13: Πίνακας δοκιμών απορρόφησης CO_2 σε καθαρά και ενισχυμένα υδατικά διαλύματα K_2CO_3.

Σύσταση K_2CO_3 (M)	**Πρόσθετο/ συγκέντρωση (M)**	**Πρόσθετο/K_2CO_3 γραμμομ. κλάσμα (-)**	**Θερμοκρασία (°C)**
1.81	χωρίς/-	-	80, 100, 120
2.53	χωρίς/-	-	80, 100, 120
1.81	PZ/0.58	0.32	100, 120
1.81	PZ/1.16	0.64	100, 120
1.81	MEA/0.82	0.45	100, 120
1.81	MDEA/0.25	0.14	100
1.81	MDEA/0.84	0.46	100
1.81	Gly/0.67	0.37	100

Μια απεικόνιση της πειραματικής εγκατάστασης που κατασκευάστηκε και χρησιμοποιήθηκε φαίνεται στο Σχήμα 19. Η διάταξη αποτελείται από δύο δοχεία πίεσης από ανοξείδωτο χάλυβα 316L που φέρουν θερμαινόμενη επένδυση εξωτερικά για τη ρύθμιση της θερμοκρασίας. Το πρώτο δοχείο χρησιμοποιείται για την προθέρμανση των αερίων (εδώ CO_2) πριν αυτά οδηγηθούν στο δοχείο απορρόφησης, το οποίο φέρει μαγνητικό αναδευτήρα για την βελτίωση των φαινομένων μεταφοράς στον αντιδραστήρα. Στο δοχείο απορρόφησης τοποθετείται ο υπό εξέταση διαλύτης στην αρχή κάθε δοκιμής, ενώ μια αντλία κενού (KNF Laboport N86 KT.18) χρησιμοποιείται για την απομάκρυνση αερίων προσμίξεων από το σύστημα σωληνώσεων. Η διάταξη φέρει θερμοστοιχεία τύπου K για τη μέτρηση της θερμοκρασίας στην υγρή και αέρια φάση, καθώς και μεταδότες πίεσης (WIKA S-10, 0-6 bar abs, ακρίβεια ± 0.03 bar) για την μέτρηση της πίεσης. Οι μετρήσεις αποθηκεύονται συνεχώς από ένα σύστημα καταγραφής δεδομένων.

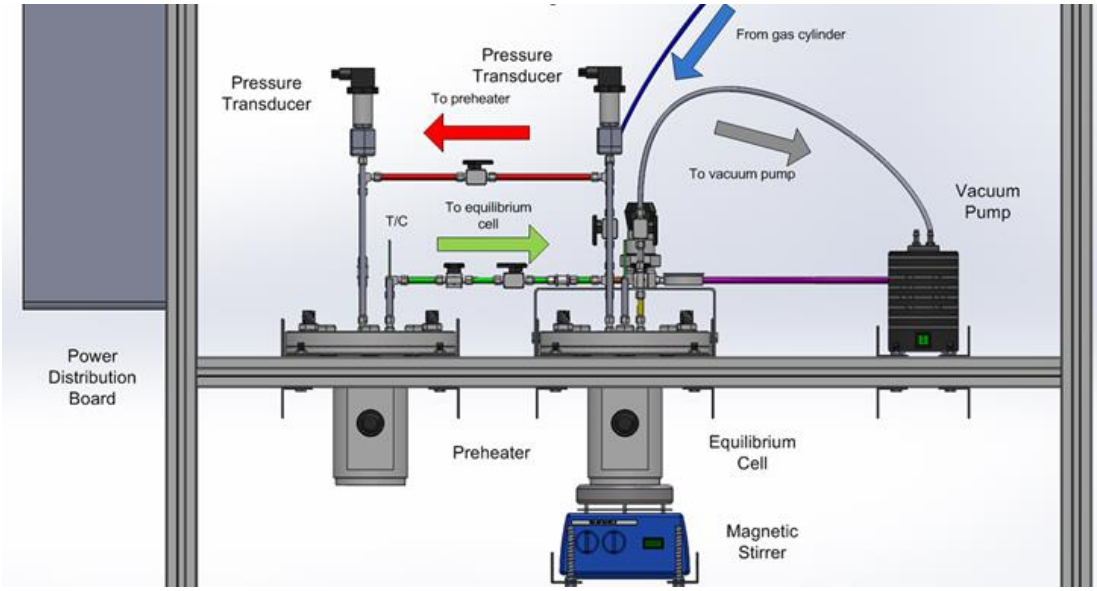

Σχήμα 19: Πειραματική εγκατάσταση μέτρησης της διαλυτότητας αερίων με ασυνεχή μέθοδο.

Τα στάδια της πειραματικής μεθοδολογίας φαίνονται καλύτερα στο Σχήμα 20. Η μεθοδολογία χωρίζεται στα στάδια της εκκένωσης του δοχείου απορρόφησης, προθέρμανσης του υγρού διαλύτη στο δοχείο απορρόφησης και του CO_2 στο δοχείο προθέρμανσης μέχρι την επίτευξη ισορροπίας φάσεων εντός του δοχείου απορρόφησης, ακολουθούμενα από διαδοχικές εγχύσεις CO_2 στο δοχείο ισορροπίας μέχρι να καλυφθεί ένα συγκεκριμένο εύρος μερικών πιέσεων του αερίου (και αντίστοιχα, νέα σημεία ισορροπίας φάσεων). Η κάθε έγχυση CO_2 στο δοχείο απορρόφησης πραγματοποιείται σχεδόν ακαριαία (~ 1 s), ενώ η παραδοχή της ισορροπίας υιοθετείται όταν για χρονικό διάστημα 40 min η μεταβολή της πίεσης στο δοχείο απορρόφησης είναι μικρότερη από 0.01 bar.

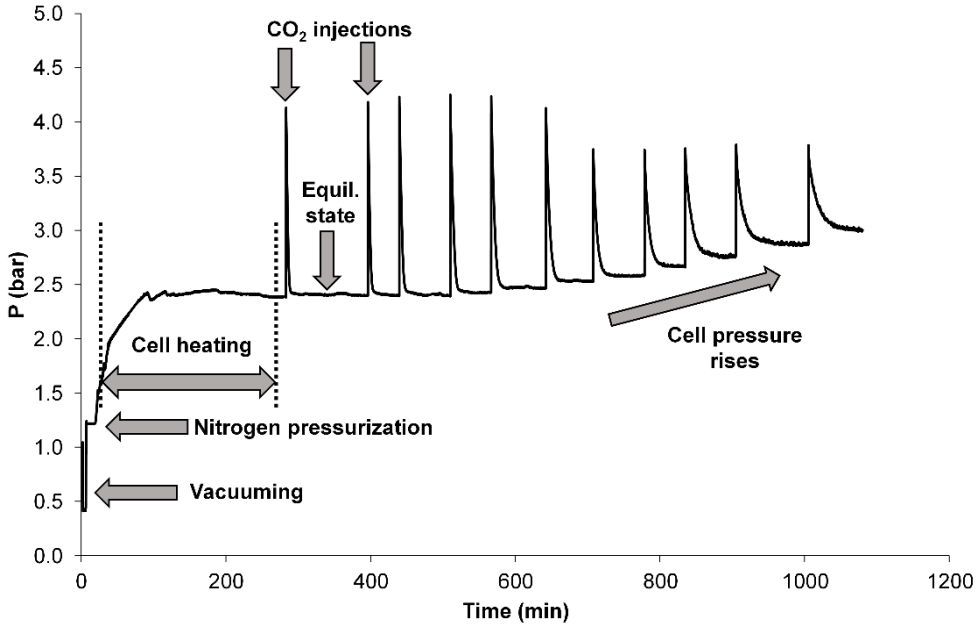

Σχήμα 20: Προφίλ πίεσης εντός του δοχείου απορρόφησης και στάδια πειραματικής μεθοδολογίας.

Η διαλυτότητα του CO_2 κατά την έγχυση j συμβολίζεται ως C_{CO_2} (mol/L) και ορίζεται ως ο λόγος των moles του CO_2 στην υγρή φάση προς τον αρχικό όγκο του διαλύτη σύμφωνα με την Εξ. 5

$$C_{CO_2} = \frac{n_{CO_2,j,sol}}{V_s} \qquad Εξ.\ 5$$

ενώ επίσης χρησιμοποιείται ο λόγος ανθράκωσης (loading) a ως ο λόγος των moles του CO_2 στην υγρή φάση προς το άθροισμα των moles του K_2CO_3 και των προσθέτων στην υγρή φάση κατά την έναρξη της δοκιμής σύμφωνα με την Εξ. 6

$$a = \frac{n_{CO_2,j,sol}}{n_{K_2CO_3} + n_{promoter}} \qquad Εξ.\ 6$$

Η αβεβαιότητα της μετρούμενης διαλυτότητας προσδιορίστηκε από τη σχέση της Εξ. 7 [238]

$$\delta C_{CO_2} = \left\{ \sum_{i=1}^{N} \left(\frac{\partial C_{CO_2}}{\partial u_i} \delta u_i \right)^2 \right\}^{\frac{1}{2}} \qquad Εξ.\ 7$$

όπου N είναι ο αριθμός όλων των u_i μεταβλητών που υπόκεινται σε μετρήσεις και δu_i είναι η αβεβαιότητα της μέτρησης για την κάθε μεταβλητή και βρέθηκε να είναι της τάξης του ± 4 %.

4.4 Αποτελέσματα

4.4.1 Επαλήθευση πειραματικής μεθοδολογίας μέσω σύγκρισης με το μοντέλο electrolyte-NRTL

Για την επαλήθευση της πειραματικής μεθοδολογίας πραγματοποιήθηκε σύγκριση των αποτελεσμάτων με τις προβλέψεις του θερμοδυναμικού μοντέλου electrolyte-NRTL. Δύο διαφορετικά θερμοδυναμικά μοντέλα καταστρώθηκαν: το πρώτο μοντέλο περιλάμβανε τις προεπιλεγμένες παραμέτρους αλληλεπίδρασης που ορίζονται στο λογισμικό Aspen Plus, ενώ το δεύτερο προέκυψε μέσω ανάλυσης παλινδρόμησης με πειραματικά δεδομένα από τη βιβλιογραφία (βλ. Κεφάλαιο 6), όπως συχνά εφαρμόζεται για τη βελτιστοποίηση των θερμοδυναμικών μοντέλων που περιγράφουν διαλύματα K_2CO_3 [234]. Η σύγκριση των πειραματικών αποτελεσμάτων της παρούσας εργασίας για τα υδατικά διαλύματα καθαρού K_2CO_3 σε σχέση με τις εκτιμήσεις των δύο θερμοδυναμικών μοντέλων φαίνονται στα Σχήματα 21 και 22.

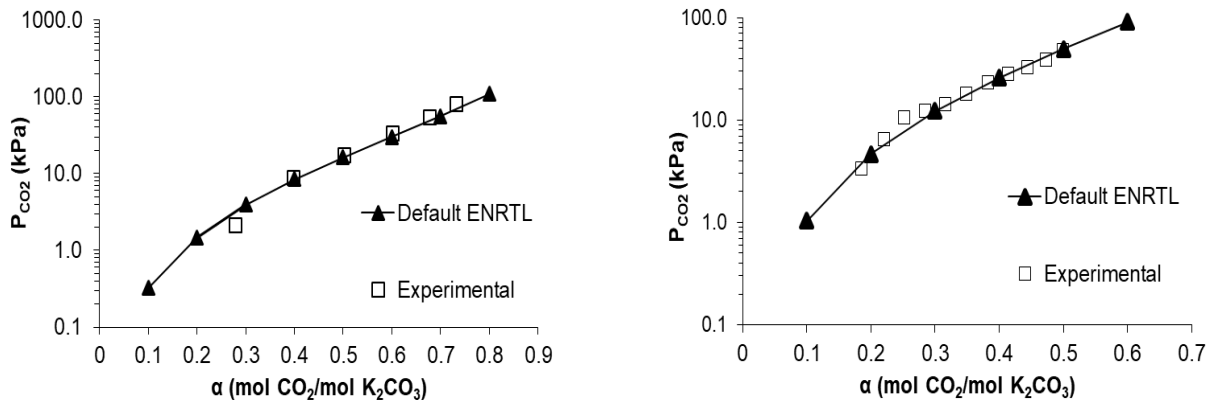

(a) (b)

Σχήμα 21: Πειραματικά αποτελέσματα και εκτιμήσεις του μοντέλου electrolyte-NRTL με προεπιλεγμένες παραμέτρους αλληλεπίδρασης για το υδατικό διάλυμα 1.81 M K_2CO_3 στους (a) 80 °C και (b) 120 °C.

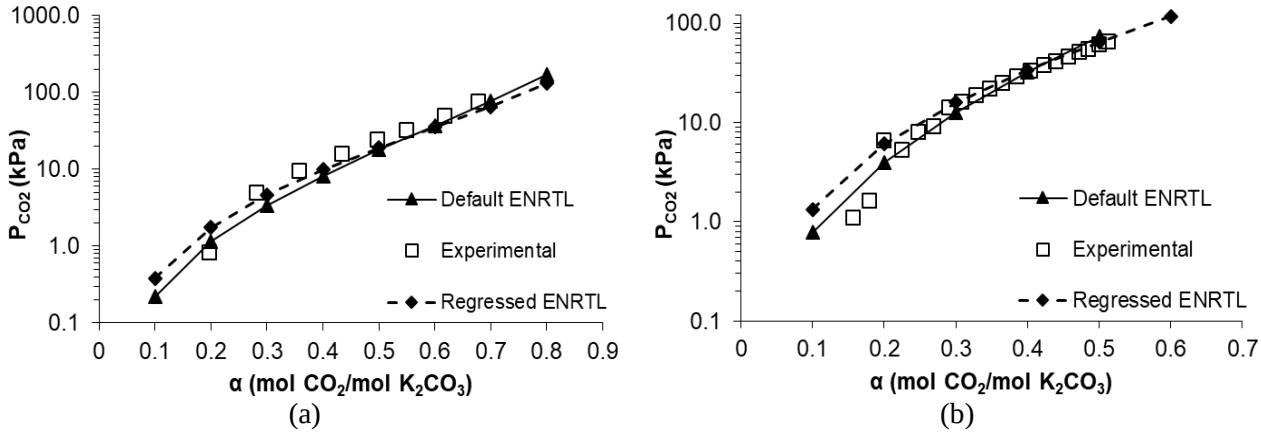

Σχήμα 22: Πειραματικά αποτελέσματα και εκτιμήσεις του μοντέλου electrolyte-NRTL που προέκυψε από παλινδρόμηση πειραματικών δεδομένων (από τη βιβλιογραφία) για το υδατικό διάλυμα 2.53 M K_2CO_3 στους (a) 80 °C και (b) 120 °C.

Είναι φανερό πως τα πειραματικά αποτελέσματα βρίσκονται σε καλή συμφωνία με τις εκτιμήσεις του μοντέλου electrolyte-NRTL. Η πειραματική μεθοδολογία μπορεί να χαρακτηριστεί επομένως αξιόπιστη για την μελέτη των διαφορετικών διαλυτών της παρούσας εργασίας. Αξίζει να σημειωθεί πως ενώ για τις δοκιμές με χαμηλή συγκέντρωση K_2CO_3 στο διάλυμα η συμφωνία με το μοντέλο electrolyte-NRTL με τις προεπιλεγμένες παραμέτρους ήταν ιδιαίτερα καλή, σε υψηλή συγκέντρωση βρέθηκε πως η χρήση ενός μοντέλου που έχει προκύψει από ανάλυση παλινδρόμησης επιτυγχάνει καλύτερη συμφωνία.

4.4.2 Πειραματικά αποτελέσματα διαλυτότητας CO_2

Οι καμπύλες ισορροπίας για τη διαλυτότητα του CO_2 σε διαλύματα με και χωρίς πρόσθετα στους 100 και 120 °C δίνονται στα Σχήματα 23 και 24.

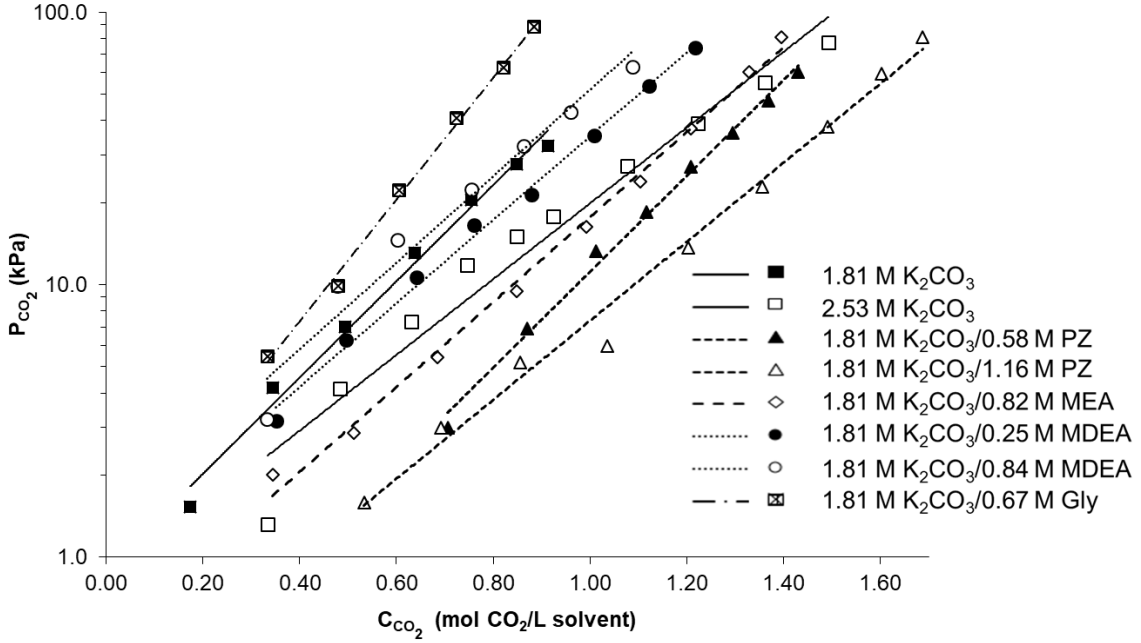

Σχήμα 23: Επίδραση των προσθέτων στη διαλυτότητα του CO_2 σε διάλυμα 1.81 M K_2CO_3 στους 100 °C.

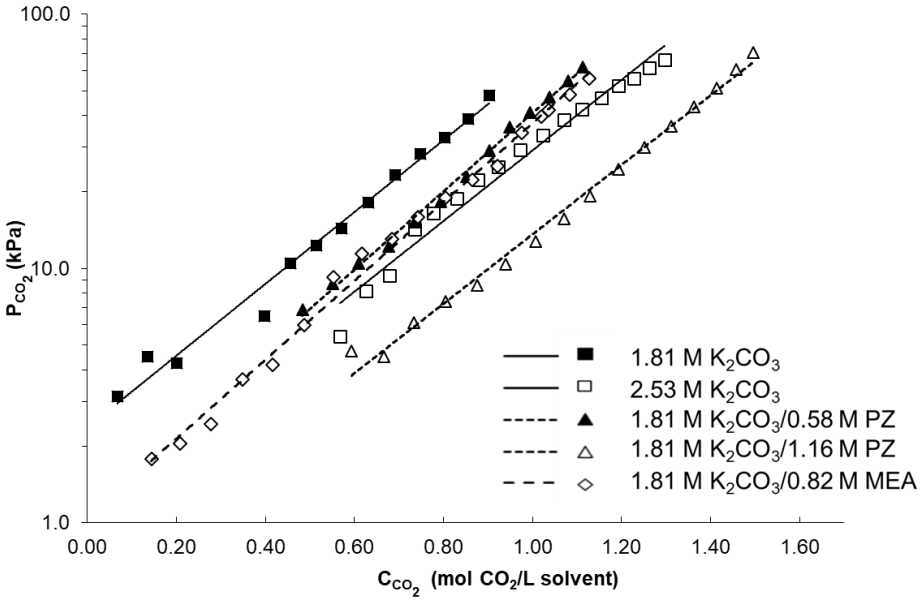

Σχήμα 24: Επίδραση των προσθέτων στη διαλυτότητα του CO_2 σε διάλυμα 1.81 M K_2CO_3 στους 120 °C.

Βρέθηκε πως η συγκέντρωση του K_2CO_3, ο τύπος των προσθέτων και η θερμοκρασία επηρεάζουν τη διαλυτότητα του CO_2. Και για τα δύο θερμοκρασιακά επίπεδα που μελετήθηκαν, η χρήση πρόσθετης PZ σε υψηλότερη συγκέντρωση επέφερε τη σημαντικότερη μείωση της μερικής πίεσης του CO_2 σε σχέση με τα διαλύματα χωρίς πρόσθετα (1.81 M και 2.53 M K_2CO_3). Τα διαλύματα με πρόσθετη MEA και PZ χαμηλότερης συγκέντρωσης μπορούν να βελτιώνουν τη διαλυτότητα σε σχέση με τα διαλύματα αναφοράς επίσης, ενώ σε θερμοκρασία 120 °C παρουσιάζουν διαλυτότητα αντίστοιχη με το διάλυμα συγκέντρωσης 2.53 M. Η προσθήκη MDEA και Gly από την άλλη πλευρά φαίνεται να αυξάνει την μερική πίεση του CO_2 πάνω από το διάλυμα.

4.4.3 Πειραματικά αποτελέσματα ρυθμού απορρόφησης CO_2

Η επίδραση των διαφόρων προσθέτων στο ρυθμό απορρόφησης του CO_2 φαίνεται στα Σχήματα 25 και 26.

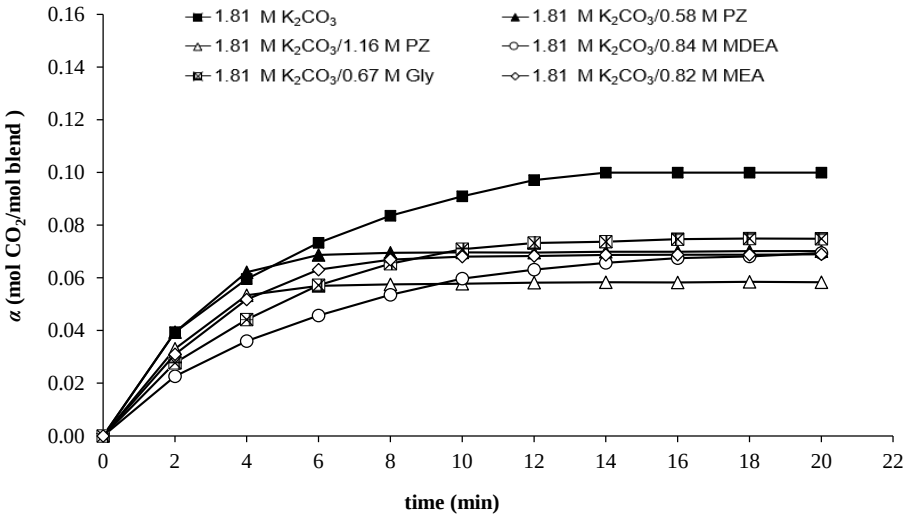

Σχήμα 25: Επίδραση των προσθέτων στον ρυθμό απορρόφησης του CO_2 για φρέσκους διαλύτες ($P_{CO_2,gs}$=180 kPa για ενισχυμένα διαλύματα, $P_{CO_2,gs}$=200 kPa για καθαρά υδατικά διαλύματα K_2CO_3, T=100 °C).

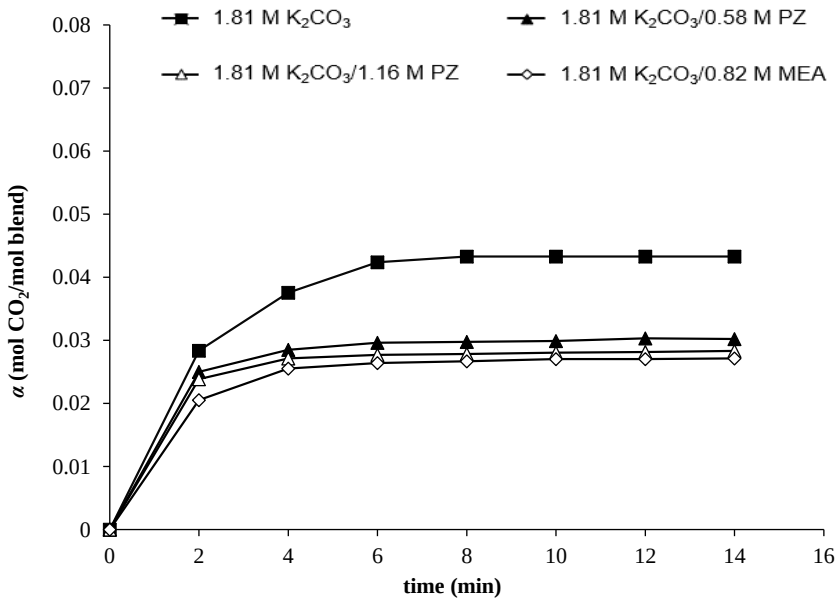

Σχήμα 26: Επίδραση των προσθέτων στον ρυθμό απορρόφησης του CO_2 για φρέσκους διαλύτες ($P_{CO_2,gs}$=80 kPa για ενισχυμένα διαλύματα, $P_{CO_2,gs}$=90 kPa για καθαρά υδατικά διαλύματα K_2CO_3, T=120 °C).

Τα αποτελέσματα στα συγκεκριμένα διαγράμματα αναφέρονται στην απορρόφηση του CO_2 σε φρέσκο διαλύτη (1ο σημείο ισορροπίας μετά την αρχική έγχυση CO_2 στο δοχείο απορρόφησης). Γενικά βρέθηκε πως η προσθήκη PZ και MEA σε διαλύματα K_2CO_3 βελτιώνει σημαντικά το ρυθμό απορρόφησης σε σχέση με το διάλυμα αναφοράς, ιδιαίτερα σε θερμοκρασία 100 °C. Στη θερμοκρασία αυτή, φαίνεται πως το διάλυμα που περιέχει 1.16 M PZ χαρακτηρίζεται από το μέγιστο ρυθμό απορρόφησης. Εντούτοις, η αύξηση της θερμοκρασίας βελτίωσε την κινητική της απορρόφησης με αποτέλεσμα αρχικά τη μείωση του χρόνου κορεσμού του διαλύματος K_2CO_3 χωρίς πρόσθετα, και επιπλέον επέφερε παραπλήσια αποτελέσματα ρυθμού απορρόφησης για τα διαλύματα με MEA και PZ.

4.5 Συμπεράσματα

Σε αυτό το κεφάλαιο παρουσιάστηκε μια πειραματική διερεύνηση της διαλυτότητας και του ρυθμού απορρόφησης του CO_2 σε καθαρά και ενισχυμένα διαλύματα (με πρόσθετα) K_2CO_3. Για τα υδατικά διαλύματα K_2CO_3 χωρίς πρόσθετα, διεξήχθησαν δοκιμές στους 80 °C, 100 °C και 120 °C με δύο διαφορετικές συγκεντρώσεις K_2CO_3 και τα πειραματικά αποτελέσματα επικυρώθηκαν επιτυχώς έναντι των αποτελεσμάτων προσομοίωσης που ελήφθησαν με το θερμοδυναμικό μοντέλο electrolyte-NRTL με προεπιλεγμένες παραμέτρους ζεύγους αλληλεπίδρασης (βιβλιοθήκες Aspen Plus™), καθώς και με τροποποιημένες παραμέτρους που προέκυψαν μέσω ανάλυσης παλινδρόμησης με πειραματικά δεδομένα από τη βιβλιογραφία. Τα πρόσθετα Gly, MDEA, MEA και PZ δοκιμάστηκαν στους 100 °C, ενώ τα τελευταία δύο δοκιμάστηκαν επίσης στους 120 °C. Όσον αφορά τα καθαρά υδατικά διαλύματα K_2CO_3, η διαλυτότητα του CO_2 αυξάνεται με μείωση της θερμοκρασίας ή με πυκνότερο διάλυμα. Όσον αφορά τη χρήση προσθέτων, η προσθήκη PZ βελτιώνει σημαντικά τη διαλυτότητα και το ρυθμό απορρόφησης του CO_2. Η προσθήκη MEA έχει επίσης θετικό αντίκτυπο στη διαλυτότητα και στο ρυθμό απορρόφησης, αλλά σε μικρότερο βαθμό σε σύγκριση με την PZ. Από την άλλη πλευρά, η MDEA μπορεί δυνητικά να βελτιώσει τα αποτελέσματα της διαλυτότητας όταν προστίθεται σε μικρότερες ποσότητες, ωστόσο, όταν χρησιμοποιείται σε υψηλότερες συγκεντρώσεις μειώνει τη διαλυτότητα του CO_2. Λαμβάνοντας υπόψη ότι δεν μετρήθηκε αξιοσημείωτη επίδραση στο ρυθμό απορρόφησης, η MDEA δεν συνιστάται ως πρόσθετο για υδατικά διαλύματα K_2CO_3. Τέλος, η προσθήκη καθαρής και μη επεξεργασμένης Gly, ακόμη και σε χαμηλή συγκέντρωση, περιορίζει τη διαλυτότητα του CO_2.

Με βάση την εργαστηριακή μελέτη διαλυτών που παρουσιάστηκε στο κεφάλαιο αυτό, τα πρόσθετα με τις καλύτερες επιδόσεις σε υψηλές θερμοκρασίες απορρόφησης, δηλ. οι PZ και MEA, εξετάστηκαν περαιτέρω σε θεωρητικό και πειραματικό επίπεδο. Στο Κεφάλαιο 5 διερευνάται πειραματικά η απορρόφηση μιγμάτων CO_2

και ελαφρών πισσών σε καθαρά υδατικά διαλύματα K_2CO_3 και σε υδατικά διαλύματα MEA-K_2CO_3, καθώς η παρουσία τέτοιων προσμίξεων στο αέριο σύνθεσης από την αεριοποίηση στερεών καυσίμων είναι αναμενόμενη. Στο Κεφάλαιο 6, πραγματοποιείται μοντελοποίηση της διεργασίας AGR με και χωρίς πρόσθετα στο διάλυμα K_2CO_3 στο λογισμικό Aspen Plus™.

5 Απορρόφηση μιγμάτων διοξειδίου του άνθρακα/ελαφρών πισσών από διαλύματα ανθρακικού καλίου

5.1 Πλαίσιο μελέτης

Η διατήρηση των πισσών στο αέριο σύνθεσης της αεριοποίησης μπορεί να είναι ευνοϊκή κατά την περίπτωση που αυτές είναι αξιοποιήσιμες κατάντη των διεργασιών καθαρισμού. Για παράδειγμα, όταν οι ελαφριές πίσσες διατηρούνται στο αέριο σύνθεσης μπορούν να μετατραπούν σε μη συμπυκνώσιμα αέρια π.χ. το τολουόλιο μπορεί να μετατραπεί σε CO και CH_4 παρουσία καταλυτών $NiO/MgO/Al_2O_3$ [245]. Ειδικά για τις ενώσεις BTX, οι Coll et al. συμπέραναν πως παρουσιάζουν μεγαλύτερο βαθμό μετατροπής παρουσία καταλυτών με βάση το Ni σε σύγκριση με άλλες αρωματικές ενώσεις που συναντώνται στο αέριο σύνθεσης [246]. Καθότι οι ενώσεις αυτές δεν συμπυκνώνονται παρά μόνο σε πολύ χαμηλές θερμοκρασίες, παρουσιάζει ενδιαφέρον η επίδραση που έχουν οι διεργασίες AGR στην απομάκρυνσή τους από το αέριο σύνθεσης. Για παράδειγμα, οργανικοί διαλύτες σε χαμηλότερη θερμοκρασία απορρόφησης σχετίζονται με υψηλότερα ποσοστά δέσμευσης ελαφριών πισσών [134].

Στο πλαίσιο αυτό, στο παρόν κεφάλαιο μελετάται η ταυτόχρονη προσρόφηση CO_2 και ελαφριών πισσών από διαλύματα K_2CO_3. Η μελέτη στοχεύει στην ποσοτικοποίηση της χωρητικότητας των διαλυτών για τα CO_2, C_6H_6 και C_7H_8 (τα βενζόλιο και τολουόλιο ως δύο από τις κύριες ενώσεις που μπορούν να μετατραπούν κατάντη της διεργασίας AGR σε μια μονάδα σύνθεσης SNG). Επιπλέον, διερευνάται η επίδραση της περιεκτικότητας πρόσθετης MEA στη διεργασία απορρόφησης.

5.2 Υλικά, πειραματική εγκατάσταση και μεθοδολογία μετρήσεων

Τα καθαρά αέρια που χρησιμοποιήθηκαν ήταν τα N_2, CO_2 και CH_4 με καθαρότητες 99.8%, 99.7% και 99.995%, αντίστοιχα (99.999% για υπερκάθαρο N_2 για βαθμονόμηση του αναλυτή) και η προμήθειά τους έγινε από την Air Liquide Hellas. Τα υπόλοιπα χημικά αγοράστηκαν από τις Fisher Chemical, Lach-Ner (Tech-Line) και Merck Hellas με τις ακόλουθες καθαρότητες: K_2CO_3 99.6%, MEA 99.5 %, C_6H_6 99.9% και C_7H_8 99.9%. Όλα τα διαλύματα παρασκευάστηκαν με απιονισμένο νερό, ενώ σε κάθε δοκιμή χρησιμοποιήθηκε διάλυμα σταθερής μάζας 500 g.

Η διάταξη που αναλύθηκε στο Κεφάλαιο 4 τροποποιήθηκε για τις δοκιμές της συνδυασμένης απορρόφησης πισσών και CO_2. Μια σχηματική απεικόνιση της εγκατάστασης φαίνεται στο Σχήμα 27. Η νέα διάταξη αποτελείται από 3 βασικά υποσυστήματα: το σύστημα ανάμιξης αερίων και πισσών, τον αντιδραστήρα και το σύστημα δειγματοληψίας και ανάλυσης της αέριας φάσης. Το σύστημα ανάμιξης αερίων ενσωματώνει τρεις (3) ελεγκτές παροχής μάζας για τη ρύθμιση της ροής (Omega FMA 5400 εύρους παροχής 0-2000 NmL min^{-1} για το N_2, Tylan FC-280s εύρους παροχής 0-700 NmL min^{-1} για το CO_2 και Aalborg GFC 17 εύρους παροχής 0-200 NmL min^{-1} για το CH_4). Οι πίσσες (σε υγρή μορφή σε θερμοκρασία περιβάλλοντος) διοχετεύονται σε θερμαινόμενους συνδέσμους ανάμιξης μέσω αντλιών σύριγγας (New Era NE-300 και NE-1000), οι οποίες μπορούν να λειτουργήσουν ανεξάρτητα μεταξύ τους. Όλες οι σωληνώσεις κατάντη του συστήματος ανάμιξης φέρουν θερμαντική ταινία με ρύθμιση θερμοκρασίας μέσω ελεγκτών PID. Το μίγμα των αερίων κατευθύνεται στον αντιδραστήρα, ο οποίος είναι αναδευόμενος και στον οποίο τοποθετείται ο προς μελέτη διαλύτης. Πρόκειται για το ίδιο δοχείο πίεσης από χάλυβα 316L που χρησιμοποιήθηκε στις δοκιμές ασυνεχούς απορρόφησης, με τη διαφορά ότι φέρει σύστημα διασκορπισμού του αερίου στην υγρή φάση. Κατάντη του αντιδραστήρα ακολουθεί μια θερμαινόμενη γραμμή υψηλής θερμοκρασίας (180 °C). Το αέριο μίγμα τροφοδοτείται στον αναλυτή Gasmet DX4000 FTIR, όπου πραγματοποιείται ανάλυση της σύστασης βάσει φασματοσκοπίας FTIR. Ακόμη, η διάταξη είναι εξοπλισμένη με θερμοστοιχεία και μετρητικά πίεσης (αντίστοιχα με αυτά που περιγράφονται στο Κεφάλαιο 4). Ακόμη, μια γραμμή σωληνώσεων για την παράκαμψη του αντιδραστήρα χρησιμεύει στην απευθείας σύνδεση του συστήματος ανάμιξης με τον αναλυτή FTIR.

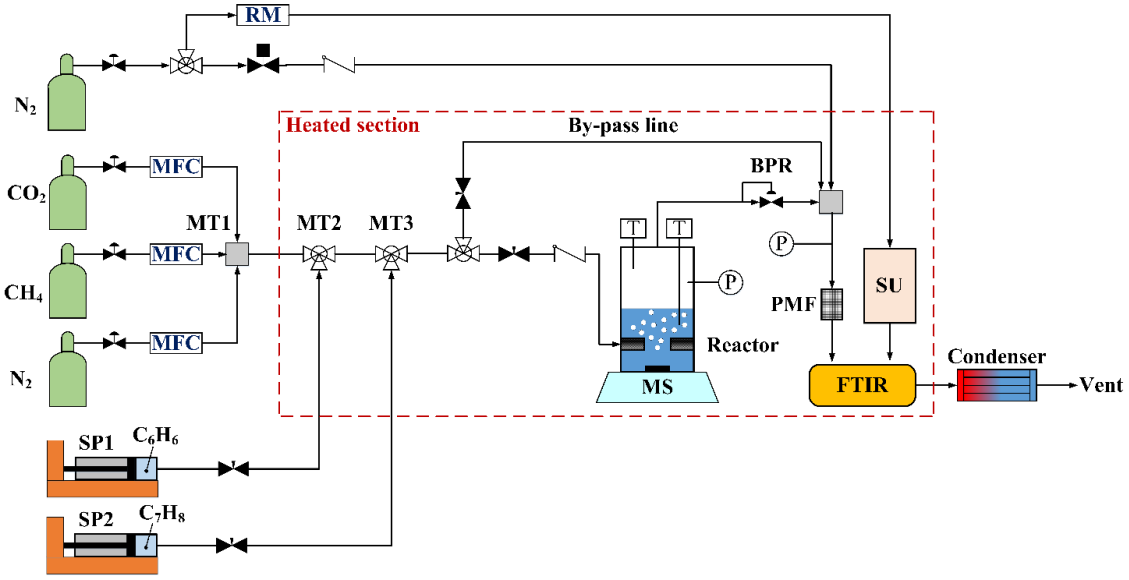

Σχήμα 27: Τροποποιημένη διάταξη απορρόφησης αερίων με ανάλυση αέριας φάσης (RM: παροχόμετρο, MFC: ελεγκτής παροχής μάζας, MT: σύνδεσμος ανάμιξης, SP: αντλία σύριγγας, MS: μαγνητικός αναδευτήρας, BPR: ρυθμιστής ανάντη πίεσης, PMF: φίλτρο σωματιδίων, SU: μονάδα δειγματοληψίας).

Το σύνολο των πειραματικών δοκιμών φαίνεται στον Πίνακα 14. Όλες οι δοκιμές πραγματοποιήθηκαν σε ατμοσφαιρική πίεση και περιεκτικότητα των CO_2 και CH_4 στο αέριο 15 vol.% και 3 vol.%, αντίστοιχα. Ιδιαίτερη σημασία δόθηκε στην αντιμετώπιση διαφόρων προβλημάτων που αφορούσαν τη λειτουργία της διάταξης. Το πρώτο από αυτά ήταν η αντιμετώπιση ταλαντωτικών φαινομένων των αντλιών σύριγγας. Στο Σχήμα 28 φαίνονται δύο εναλλακτικές που εξετάστηκαν για τη βελτιστοποίηση της διάταξης έγχυσης πισσών. Η μείωση του μεγέθους της σύριγγας από 5 mL σε 1 mL βρέθηκε να μειώνει την τυπική απόκλιση της περιεκτικότητας της ένωσης (εδώ νερό) κατά περίπου 65%, ενώ η χρήση ελαστικής σωλήνωσης PVC οδήγησε σε μείωση της τυπικής απόκλισης κατά περίπου 50%. Ένα δεύτερο ζήτημα ήταν η περιορισμένη μεταφορά μάζας εντός του αναδευόμενου αντιδραστήρα. Δοκιμάστηκαν διαφορετικοί τύποι διασκορπιστών και τα αποτελέσματα φαίνονται στο Σχήμα 29. Έτσι, υιοθετήθηκε η επιλογή του πορώδους μεταλλικού διασκορπιστή 2 μm που εξασφάλισε σημαντική μείωση του απαιτούμενου χρόνου για τον κορεσμό των διαλυμάτων.

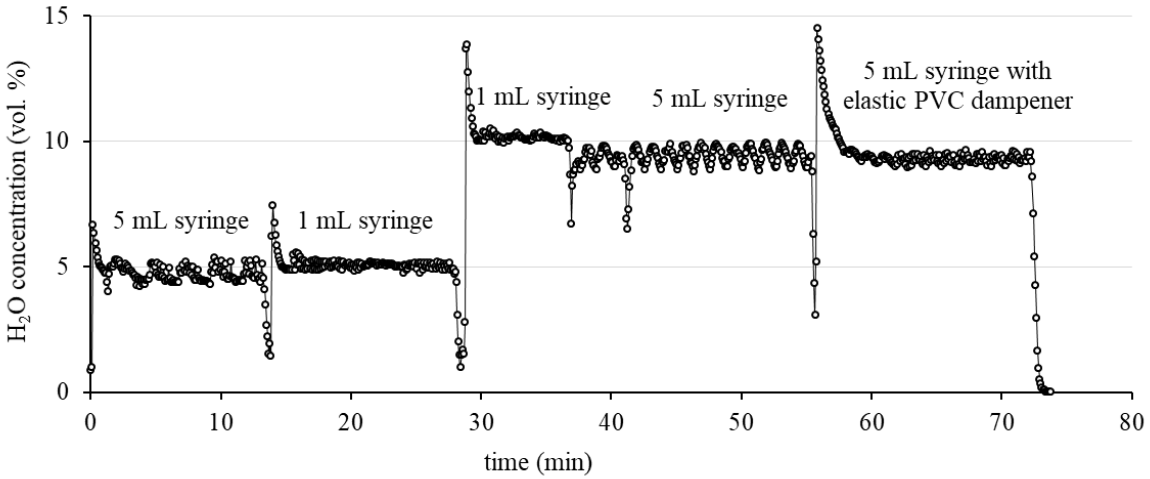

Σχήμα 28: Σταθερότητα έγχυσης αντλιών σύριγγας: επίδραση του μεγέθους της σύριγγας και της χρήσης ελαστικού σωλήνα τροφοδοσίας.

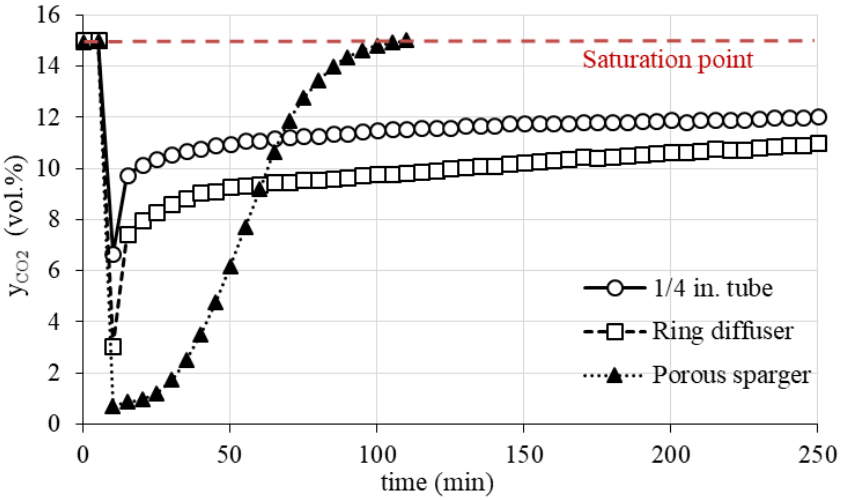

Σχήμα 29: Σύσταση CO_2 στο αέριο εξόδου (vol.%) συναρτήσει του χρόνου για διαφορετικούς τύπους διασκορπιστών.

Πίνακας 14: Πίνακας δοκιμών απορρόφησης μιγμάτων C_6H_6/CO_2 και C_7H_8/CO_2 σε διαλύματα K_2CO_3 με ή χωρίς προσθήκη MEA.

Δοκιμή	**Περιεκτικότητα K_2CO_3 (wt.%)**	**Περιεκτικότητα MEA (wt.%)**	**Θερμοκρασία (°C)**	**Τύπος/ Περιεκτικότητα πισσών (ppmv)**
1	25	–	60	–
2	25	–	70	–
3	25	–	60	C_6H_6/1000
4	25	–	60	C_6H_6/2000
5	25	–	70	C_6H_6/1000
6	25	–	70	C_6H_6/2000
7	25	–	60	C_7H_8/1000
8	25	–	60	C_7H_8/2000
9	25	–	70	C_7H_8/1000
10	25	–	70	C_7H_8/2000
11	25	1	60	–
12	25	1	70	–
13	25	5	60	–
14	25	5	70	–
15	25	1	60	C_6H_6/1000
16	25	1	60	C_6H_6/2000
17	25	1	70	C_6H_6/1000
18	25	1	70	C_6H_6/2000
19	25	1	60	C_7H_8/1000
20	25	1	60	C_7H_8/2000
21	25	1	70	C_7H_8/1000
22	25	1	70	C_7H_8/2000
23	25	5	60	C_6H_6/1000
24	25	5	60	C_6H_6/2000
25	25	5	70	C_6H_6/1000
26	25	5	70	C_6H_6/2000
27	25	5	60	C_7H_8/1000
28	25	5	60	C_7H_8/2000
29	25	5	70	C_7H_8/1000
30	25	5	70	C_7H_8/2000

Το τρίτο ζήτημα ήταν η επαρκής βαθμονόμηση του αναλυτή FTIR. Στο πλαίσιο αυτό πραγματοποιήθηκε μελέτη για την επιλογή των βέλτιστων περιοχών ανάλυσης για όλες τις ενώσεις ενδιαφέροντος, ενώ επιλέχθηκε να γίνει αναβαθμονόμηση των περισσότερων ενώσεων για τις οποίες δεν υπήρχαν επαρκή φάσματα αναφοράς.

5.3 Αποτελέσματα

Τα αποτελέσματα της διαλυτότητας του CO_2 για τις διαφορετικές πειραματικές δοκιμές φαίνονται στο Σχήμα 30.

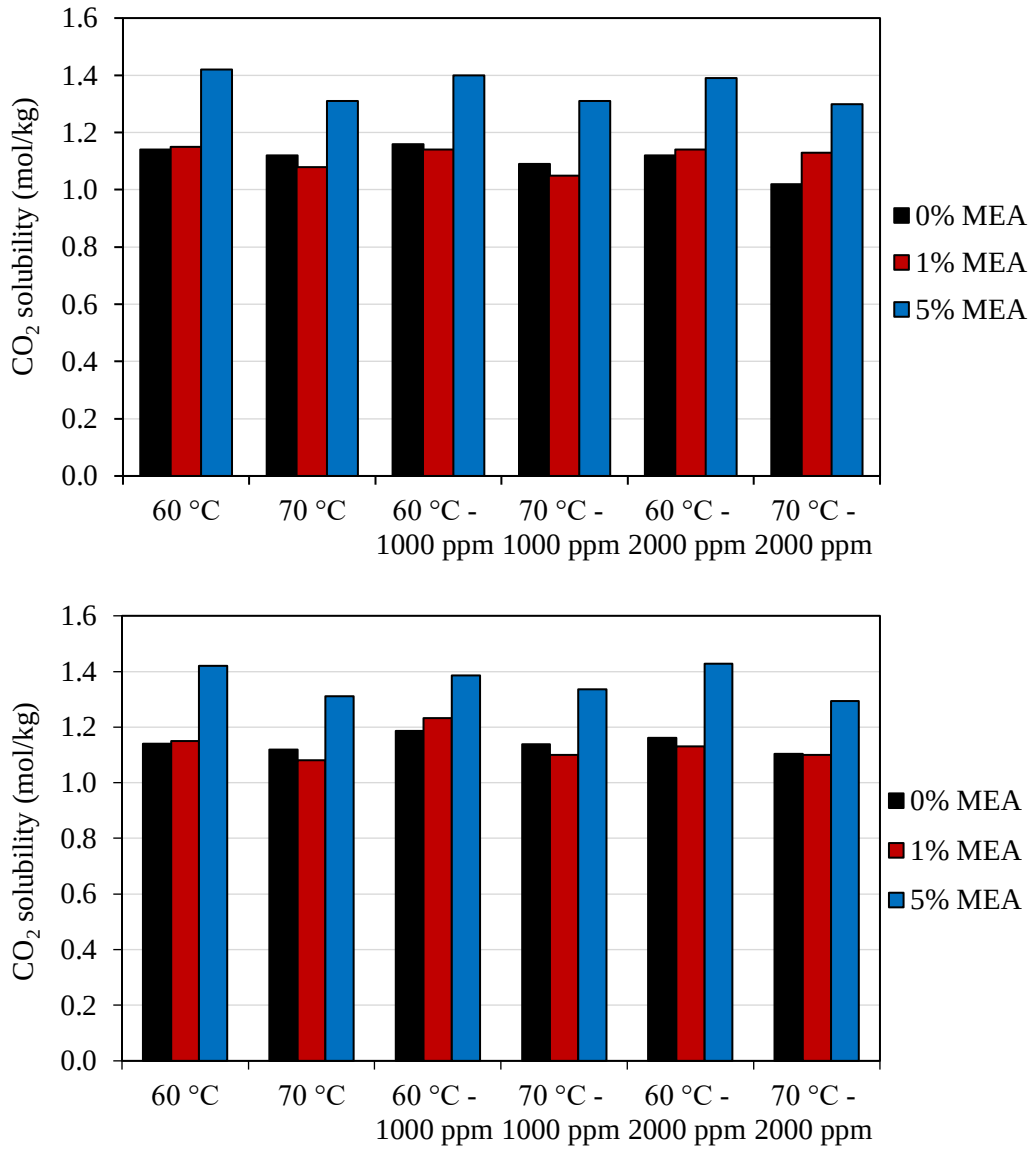

Σχήμα 30: Επίδραση της προσθήκης MEA στη διαλυτότητα του CO_2 για μίγματα $CO_2/C_6H_6/CH_4$ (πάνω) και $CO_2/C_7H_8/CH_4$ (κάτω).

Κατά τη διάρκεια της μελέτης, η μερική πίεση του CO_2 ήταν περίπου 22 kPa για όλες τις δοκιμές. Μπορεί να σημειωθεί ότι εντός των περιοχών μεταβολής των παραμέτρων, οι τιμές διαλυτότητας σε κατάσταση κορεσμού ήταν στο εύρος 1.02-1.43 mol kg^{-1} διαλύτη. Η θερμοκρασία έχει αρνητική επίδραση στη διαλυτότητα του CO_2, ωστόσο, το αποτέλεσμά της φαίνεται να είναι μάλλον αμελητέο όταν δεν προστίθεται MEA στο διάλυμα. Όταν αυξάνεται η περιεκτικότητα σε MEA αντιθέτως, η επίδραση της θερμοκρασίας γίνεται σημαντική, γεγονός που μπορεί να αποδοθεί στην αυξημένη θερμότητα απορρόφησης λόγω σχηματισμού καρβαμιδίου. Εκτός από τη

βελτίωση της διαλυτότητας του CO_2, η χρήση πρόσθετης MEA σε περιεκτικότητα 5 wt.%. βελτίωσε σημαντικά το ρυθμό απορρόφησης όπως φαίνεται στο Σχήμα 31. Αντίθετα, η προσθήκη 1 wt.% MEA στο διάλυμα βρέθηκε να επιφέρει ασήμαντη μεταβολή σε σχέση με το μη ενισχυμένο διάλυμα K_2CO_3.

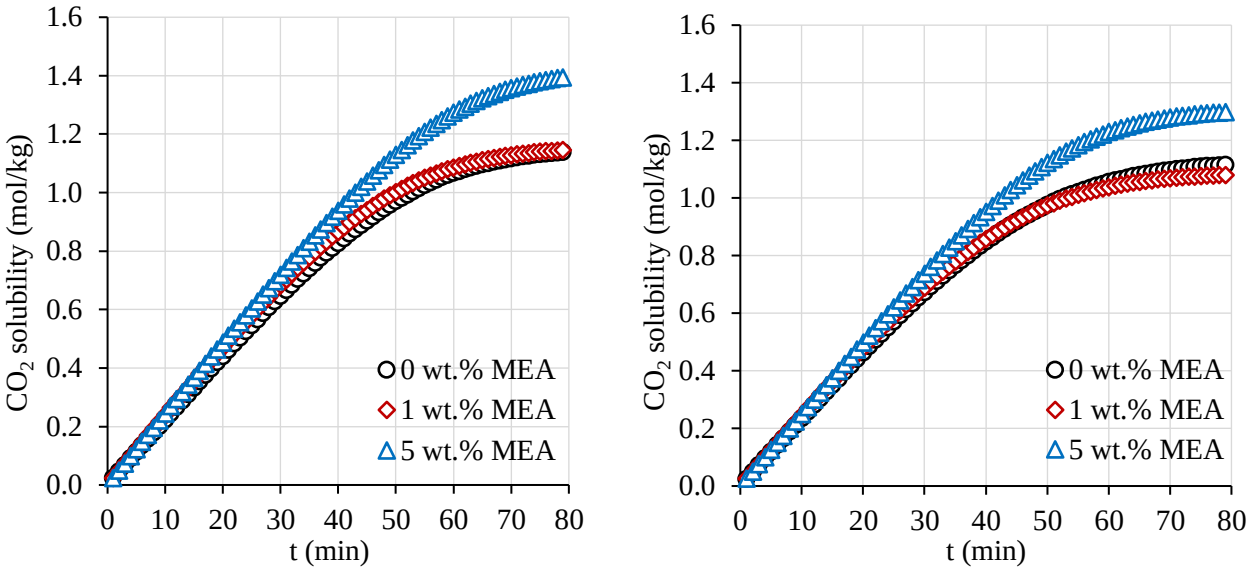

Σχήμα 31: Επίδραση της MEA στο ρυθμό απορρόφησης του CO_2 σε ενισχυμένα διαλύματα K_2CO_3 στους 60 °C (αριστερά) και 70 °C (δεξιά) και σύγκριση με το υδατικό διάλυμα 25 wt.% K_2CO_3.

Ακόμη, μπορεί να σημειωθεί ότι πολύ χαμηλές τιμές διαλυτότητας βρέθηκαν και για τις δύο ενώσεις πισσών, με τις υψηλότερες τιμές στα 1.65 και 1.72 mmol kg^{-1} για τα C_6H_6 και C_7H_8, αντίστοιχα. Αυτό οφείλεται στην διαφορά πολικότητας μεταξύ VOC και διαλυτών [255], καθώς και στην υψηλή θερμοκρασία. Παρόλα αυτά, το συγκεκριμένο αποτέλεσμα μπορεί να θεωρηθεί επιθυμητό όταν επιδιώκεται κατάντη αξιοποίηση των ενώσεων (όπως η αναμόρφωση πισσών με καταλύτες Ni).

5.4 Συμπεράσματα

Σε αυτό το κεφάλαιο παρουσιάστηκε μια επέκταση της εργασίας που παρουσιάστηκε στο Κεφάλαιο 4. Η μελέτη αφορούσε τη διερεύνηση της απόδοσης των υδατικών διαλυμάτων K_2CO_3 (χωρίς πρόσθετα και με προσθήκη MEA) προς την ταυτόχρονη απορρόφηση CO_2 και ελαφρών πισσών που συναντώνται στο αέριο σύνθεσης. Δύο χαρακτηριστικές ενώσεις μελετήθηκαν, συγκεκριμένα τα βενζόλιο (C_6H_6) και τολουόλιο (C_7H_8).

Η μελέτη συμπέρανε ότι η προσθήκη μικρής ποσότητας MEA της τάξεως 1 wt.% δεν έχει αξιοσημείωτη επίδραση στην διαλυτότητα του CO_2 σε σύγκριση με την περίπτωση που καθαρό K_2CO_3 προστίθεται αποκλειστικά στο υδατικό διάλυμα. Η θερμοκρασία επιδεινώνει τη διαλυτότητα του CO_2 σε όλους τους διαλύτες, ωστόσο, διαπιστώθηκε πως η επίδραση είναι σημαντικότερη για το διάλυμα που προάγεται με MEA περιεκτικότητας 5 wt.%. Από την άλλη πλευρά, η αύξηση της θερμοκρασίας κατά 10 °C έχει πολύ μικρή επίδραση στην διαλυτότητα του CO_2 για μικρότερες συγκεντρώσεις MEA ή καθαρό K_2CO_3. Στο Κεφάλαιο 4 εξήχθη το συμπέρασμα πως η προσθήκη MEA μπορεί να βελτιώσει το ρυθμό απορρόφησης του CO_2 σε υδατικά διαλύματα K_2CO_3 σε υψηλές θερμοκρασίες (≥ 100 °C). Στο παρόν κεφάλαιο φάνηκε πως η προσθήκη MEA (5 wt.%) στο διάλυμα μπορεί να βελτιώσει το ρυθμό απορρόφησης CO_2 ιδιαίτερα όταν η συγκέντρωση CO_2 στην υγρή φάση αυξάνεται πάνω από ~ 0.8 mol kg^{-1}. Από την άλλη πλευρά, μετρήθηκαν πολύ χαμηλές τιμές διαλυτότητας των C_6H_6 και C_7H_8 (< 2 mmol kg^{-1}). Τέλος, δεν παρατηρήθηκε σημαντική επίδραση στη διαλυτότητα του CO_2 όταν προστέθηκαν ενώσεις BTX στο μίγμα των αερίων.

6 Θερμοδυναμική μοντελοποίηση και μοντελοποίηση διεργασίας AGR μέσω διαλυμάτων ανθρακικού καλίου

6.1 Πλαίσιο μελέτης

Όπως επισήμαναν και οι Isa et al. σε μια πρόσφατη δημοσίευση βιβλιογραφικής ανασκόπησης [283], υπάρχει ανάγκη για μελέτες συγκριτικής αξιολόγησης ως προς την επίδραση διαφόρων παραμέτρων λειτουργίας στην κατανάλωση θερμότητας για αναγέννηση και ηλεκτρισμού των μονάδων δέσμευσης CO_2 με ενισχυμένα διαλύματα K_2CO_3. Στην πράξη, ενώ ορισμένες εργασίες είναι διαθέσιμες στη βιβλιογραφία για τη δέσμευση CO_2 από καυσαέρια, απαιτείται περαιτέρω διερεύνηση για τη δέσμευση CO_2 προ-καύσης. Σύμφωνα με τις γνώσεις του συγγραφέα, δεν υπάρχει διαθέσιμη μελέτη που να μελετά την επίδραση λειτουργικών παραμέτρων στην ενεργειακή κατανάλωση και αποδοτικότητα μιας διεργασίας AGR (τροφοδοτούμενης με αέριο σύνθεσης) με διαλύματα K_2CO_3 που ενισχύονται με PZ και η οποία λειτουργεί σε υψηλή θερμοκρασία. Επιπλέον, είναι σημαντικό να σημειωθεί ότι η μελέτη που παρουσιάζεται στο παρόν κεφάλαιο έχει ένα ακόμη ιδιαίτερο χαρακτηριστικό, το γεγονός ότι το H_2S θεωρείται ως είδος προς δέσμευση μαζί με το CO_2. Δύο μελέτες μοντελοποίησης βρέθηκαν σχετικά με την απορρόφηση του H_2S σε διαλύματα K_2CO_3, εκείνες των Dindore et al. [284] και Faiz και Al-Marzouqi [276]. Στην παρούσα εργασία παρέχεται η ακόλουθη συμβολή σε σύγκριση με τις προαναφερθείσες μελέτες:

α. Πραγματοποιήθηκε μοντελοποίηση της συνολικής διεργασίας απορρόφησης/εκρόφησης που δεν περιορίστηκε στη στήλη απορρόφησης.

β. Καταστρώθηκε ένα λεπτομερές θερμοδυναμικό μοντέλο electrolyte-NRTL με τροποποιημένες παραμέτρους αλληλεπίδρασης σε αντίθεση με τα πιο απλοποιημένα μοντέλα για τον υπολογισμό της διαλυτότητας των CO_2 και H_2S.

6.2 Μοντελοποίηση

6.2.1 Μεθοδολογία μοντελοποίησης

Το μοντέλο electrolyte-NRTL το οποίο χρησιμοποιήθηκε βασίζεται σε δύο κύριες παραδοχές, την άπωση μεταξύ όμοιων ιόντων και την υπόθεση τοπικής ηλεκτροουδετερότητας στο διάλυμα. Η έκφραση του μοντέλου για την ελεύθερη ενέργεια Gibbs περιλαμβάνει τρεις όρους, όπως φαίνεται στην Εξ. 8, συγκεκριμένα τις αλληλεπιδράσεις μεγάλης απόστασης κατά Pitzer-Debye-Hückel, τη διόρθωση Born και αλληλεπιδράσεις κοντινής απόστασης (μοντέλο NRTL).

$$\frac{G_m^{*E}}{RT} = \frac{G_m^{*E,PDH}}{RT} + \frac{G_m^{*E,Born}}{RT} + \frac{G_m^{*E,lc}}{RT} \qquad Εξ.\ 8$$

Οι παράμετροι ενεργειακής αλληλεπίδρασης στο μοντέλο electrolyte-NRTL εξαρτώνται από τη θερμοκρασία και έχουν τη μορφή της Εξ. 9 (εδώ για αλληλεπιδράσεις ηλεκτρολύτη-μορίου)

$$\tau_{ca,B} = C_{ca,B} + \frac{D_{ca,B}}{T} + E_{ca,B}\left[\frac{T^{ref} - T}{T} + ln\left(\frac{T}{T^{ref}}\right)\right] \qquad Εξ.\ 9$$

Οι παράμετροι *C*, *D* και *E* εκφράζονται στο Aspen Plus ως *GMELCC*, *GMELCD*, *GMELCE* και *GMELCN*, αντίστοιχα και προσδιορίστηκαν σύμφωνα με τη μεθοδολογία του Hilliard [285]. Τα πειραματικά δεδομένα που χρησιμοποιήθηκαν για την ανάλυση παλινδρόμησης φαίνονται στον Πίνακα 15.

Πίνακας 15: Πειραματικά δεδομένα για την ανάλυση παλινδρόμησης του μοντέλου electrolyte-NRTL για τα συστήματα CO_2-K_2CO_3-H_2O και CO_2-PZ-K_2CO_3-H_2O.

Σύστημα	**Τύπος δεδομένων**	**Σημεία**	**Θερμοκρασία και συγκέντρωση**	**Πηγή**
K_2CO_3-H_2O	Μέσος ιοντικός συντελεστής ενεργότητας	53	25 °C 0.014–50 wt.% K_2CO_3	[289]
	Ελάττωση τάσης ατμών	543	25–130 °C 2–50 wt.% K_2CO_3	[290]
	Ελάττωση τάσης ατμών	42	25–90 °C 0.048–0.51 wt.% K_2CO_3	[291]
	Θερμοχωρητικότητα	298	25–130 °C 2–50 wt.% K_2CO_3	[289]
$KHCO_3$-H_2O	Ελάττωση τάσης ατμών	10	25 °C 2–25 wt.% K_2CO_3	[290]
	Θερμοχωρητικότητα	214	5–130 °C 4–20 wt.% K_2CO_3	[289]
CO_2-K_2CO_3-H_2O	Διαλυτότητα CO_2	113	70–140 °C 20, 30, 40 wt.% K_2CO_3	[204]
CO_2-PZ- H_2O	Ολική πίεση	30	60–120 °C 2–4 m PZ Ανθράκωση 0.5–1.0	[292]
	Διαλυτότητα CO_2	14	40–70 °C 0.62 m PZ Ανθράκωση 0.2–1.0	[293]
	^{1}H NMR	101	10–60 °C 0.1–1.5 m PZ Ανθράκωση 0.15–0.97	[294]
CO_2-PZ-K_2CO_3-H_2O	Διαλυτότητα CO_2	38	39–110 °C 2.5–6.2 m K^+ 0.6–3.6 m PZ Ανθράκωση 0.37–0.74	[216]
	^{1}H NMR	41	27–70 °C 3.4–6.2 m K^+ 0.6–3.6 m PZ Ανθράκωση 0.38–0.65	[216]

Ωστόσο, το μοντέλο του Hilliard δεν έλαβε υπόψη την ταυτόχρονη απορρόφηση των CO_2 και H_2S, κυρίως λόγω του γεγονότος ότι αναπτύχθηκε για δέσμευση CO_2 από καυσαέρια. Η παρούσα εργασία επεκτείνει αυτό το μοντέλο ώστε να συμπεριλάβει την προσαρμογή της διαλυτότητας H_2S σε διαλύματα K_2CO_3. Με τη διόρθωση των καμπυλών VLE για τα όξινα αέρια, το μοντέλο μπορεί να εφαρμοστεί για τη διερεύνηση του καθαρισμού αερίων σύνθεσης. Οι πιέσεις ισορροπίας φάσεων των CO_2 και H_2S σε διαλύματα K_2CO_3 δημοσιεύτηκαν στην πηγή [288]. Τα πειραματικά δεδομένα από τη μελέτη αυτή χρησιμοποιήθηκαν για την διαδικασία παλινδρόμησης. Η ανάλυση παλινδρόμησης πραγματοποιήθηκε στο εργαλείο Data Regression System (DRS) του λογισμικού Aspen Plus. Η καταστατική εξίσωση της αέρια φάσης ήταν η Redlich-Kwong-Soave (RKS), ενώ οι σταθερές χημικής ισορροπίας υπολογίστηκαν στο Aspen Plus για το σύστημα αντιδράσεων με το K_2CO_3. Οι συντελεστές θερμοκρασιακής εξάρτησης των σταθερών χημικής ισορροπίας για τις αντιδράσεις της PZ ελήφθησαν από την πηγή [285], ενώ οι κινητικές σταθερές μπορούν να βρεθούν στις πηγές [286] και [287]. Για τη μοντελοποίηση των στηλών με πληρωτικό υλικό χρησιμοποιήθηκαν αναλυτικά μοντέλα που ενσωματώνουν εξισώσεις μεταφοράς (rate-based) στο λογισμικό Aspen Plus.

Το αέριο σύνθεσης προέρχεται από αλλοθερμική αεριοποίηση ορυκτού άνθρακα και προορίζεται για την παραγωγή SNG. Η σύσταση του καυσίμου και του αερίου σύνθεσης έχουν ληφθεί από την εργασία [134] και φαίνονται στον Πίνακα 16.

Πίνακας 16: Σύσταση καυσίμου και χαρακτηριστικά αερίου σύνθεσης.

Σύσταση ορυκτού άνθρακα			
Προσεγγιστική ανάλυση (as received)		**Στοιχειακή ανάλυση (as received)**	
Πτητικά (wt.%)	42.0	C (wt.%)	53.6
Μόνιμος άνθρακας (wt.%)	35.5	H (wt.%)	3.9
Τέφρα (wt.%)	3.5	O (wt.%)	19.2
Υγρασία (wt.%)	19.0	N (wt.%)	0.6
Θερμογόνος δύναμη (MJ kg^{-1})	19.8	S (wt.%)	0.35
Χαρακτηριστικά αερίου σύνθεσης			
H_2O (mole %)	36.39	Πίεση (bar)	20
CO_2 (mole %)	12.66	Θερμοκρασία (°C)	800
H_2 (mole %)	34.85	Παροχή μάζας (kg s^{-1})	3.5
N_2 (mole %)	0.13		
CH_4 (mole %)	3.29		
CO (mole %)	11.62		
H_2S (mole %)	0.06		

Η διεργασία AGR δίνεται στο Σχήμα 32. Πρόκειται για μια απλοποιημένη διάταξη απορρόφησης/εκρόφησης που μοντελοποιήθηκε στο Aspen Plus μέσω προσομοίωσης ανοικτού βρόγχου (open loop). Προκειμένου να διασφαλιστεί η διατήρηση των ισοζυγίων μάζας και ενέργειας, προστέθηκε στο μοντέλο μια σειρά προδιαγραφών σχεδιασμού (design specifications). Κάποιες βασικές παραδοχές της μοντελοποίησης δίνονται στον Πίνακα 17.

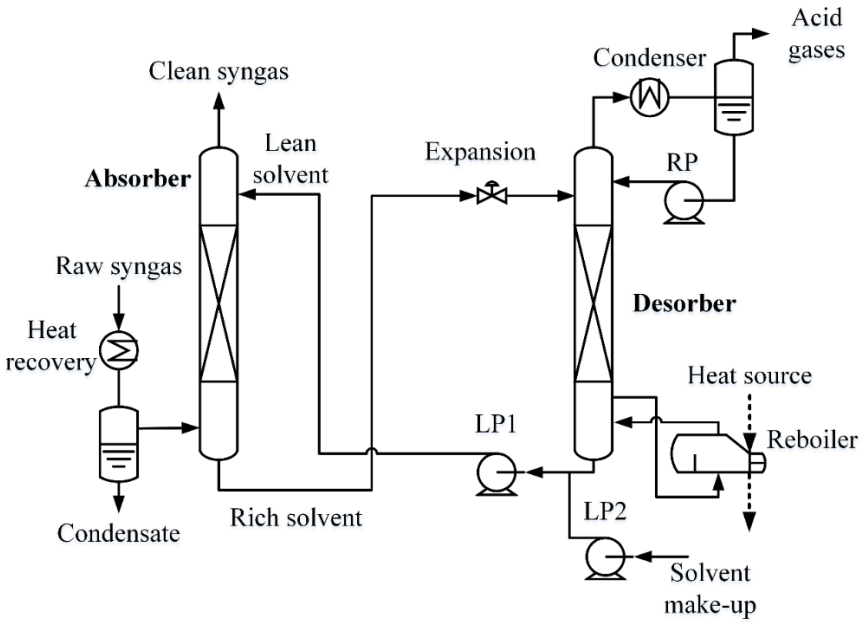

Σχήμα 32: Διάταξη της διεργασίας απορρόφησης/εκρόφησης όπως αυτή μοντελοποιήθηκε στο Aspen Plus.

Για τη μελέτη της επίδρασης των παραμέτρων λειτουργίας της διεργασίας, μεταβλήθηκαν οι τιμές της πίεσης στη στήλη απορρόφησης (10-18 bar), της πίεσης στη στήλη εκρόφησης (0.4-5.3 bar) και του λόγου ανθράκωσης πτωχού διαλύτη (0.24-0.44). Ακόμη, μελετήθηκαν 3 διαφορετικοί διαλύτες πλέον του διαλύματος αναφοράς 30 wt.% K_2CO_3:

- 6.5m K^+/0.65 m PZ με γραμμομοριακό λόγο PZ/K^+ ίσο με 0.1 ("PZ0.1"),
- 6.5 m K^+/1.3 m PZ με γραμμομοριακό λόγο PZ/K^+ ίσο με 0.2 ("PZ0.2") και
- 6.5 m K^+/1.95 m PZ με γραμμομοριακό λόγο PZ/K^+ ίσο με 0.3 ("PZ0.3").

Το ποσοστό δέσμευσης του CO_2 ήταν σταθερό (95%) σε όλες τις περιπτώσεις.

Πίνακας 17: Βασικές παραδοχές μοντελοποίησης για τη διεργασία AGR με K_2CO_3 (βλ. και Παράρτημα αγγλικού κειμένου).

Ροή μάζας (S)/Στοιχείο μοντέλου (B)	**Παράμετρος**	**Τιμή**
FEED (S: αέριο σύνθεσης, είσοδος)	Πίεση (bar)	20
	Θερμοκρασία (°C)	100
	Σύσταση (mole%)	(βλέπε Πίνακα 16)
ABS-LEAN (S: πτωχός διαλύτης)	Πίεση (bar)	18
	Θερμοκρασία (°C)	102
	Σύσταση	30 wt.% K_2CO_3
	Λόγος ανθράκωσης (–)	0.3/0.4
FLASH (B: απομάκρυνση συμπυκνώματος)	Πίεση (bar)	19.5 bar (είσοδος στήλης απορρόφησης) 1 bar (έξοδος στήλης εκρόφησης)
	Ενεργειακή κατανάλωση (kW)	Αδιαβατικός
ABS (B: στήλη απορρόφησης)	Αριθμός βαθμίδων (–)	5
	Πίεση (bar)	17
	Πληρωτικό υλικό	1-inch IMTP
	Πληρωμένο ύψος ανά βαθμίδα (m)	1.5
	Προσέγγιση στην πλημμύριση	0.75
STR (B: στήλη εκρόφησης)	Αριθμός βαθμίδων (–)	6
	Πίεση (bar)	1
	Πληρωτικό υλικό	1-inch IMTP
	Πληρωμένο ύψος ανά βαθμίδα (m)	1.5
	Προσέγγιση στην πλημμύριση	0.75
	Τύπος αναβραστήρα	Kettle
CNDSR (B: συμπυκνωτής στήλης εκρόφησης)	Πίεση (bar)	1
	Θερμοκρασία εξόδου αερίου (°C)	50
PUMP (B: αντλία διαλύτη)	Πίεση (bar)	18
	Απόδοση αντλίας (%)	70
	Ηλ/μηχανικός β.α. (%)	96
MX1 and MX2 (B: στοιχεία ανάμιξης)	Πτώση πίεσης (bar)	0
SPLIT (B: διαχωριστής συμπυκνωμάτων)	Πτώση πίεσης (bar)	0
	Λόγος διαχωρισμού (–)	Design spec M-BALANC
T-REGUL (B: μοντέλο ψύξης/θέρμανσης πτωχού διαλύτη)	Πίεση (bar)	18
	Ενεργειακή κατανάλωση (kW)	Design spec T-BALANC

6.2.2 Παράμετροι και δείκτες απόδοσης

Ο βαθμός δέσμευσης των CO_2 και H_2S δίνεται από τις Εξ. 10 και Εξ. 11, όπου τα $\dot{n}_{j,in/out}$ συμβολίζουν τη γραμμομοριακή παροχή (mol s^{-1}) της ένωσης j στη στήλη απορρόφησης.

$$CR_{CO_2}(\%) = \frac{\dot{n}_{CO_2,in} - \dot{n}_{CO_2,out}}{\dot{n}_{CO_2,in}} \, 100\% \qquad \textit{Εξ. 10}$$

$$CR_{H_2S}(\%) = \frac{\dot{n}_{H_2S,in} - \dot{n}_{H_2S,out}}{\dot{n}_{H_2S,in}}\ 100\% \qquad \textit{Εξ. 11}$$

Ο λόγος υγρού-αερίου *L/G* στη στήλη απορρόφησης δίνεται με βάση την παροχή μάζας των ρευμάτων, ενώ ο λόγος ανθράκωσης για τα συστήματα CO_2-K_2CO_3-H_2O και CO_2-PZ-K_2CO_3-H_2O δίνεται από τις Εξ. 12 και 13, αντίστοιχα.

$$a = \frac{[\mathrm{CO_2}] + [\mathrm{CO_3^{2-}}] + [\mathrm{HCO_3^-}] - \frac{[\mathrm{K^+}]}{2}}{\frac{[\mathrm{K^+}]}{2}} \qquad \textit{Εξ. 12}$$

$$a = \frac{[\mathrm{CO_2}] + [\mathrm{CO_3^{2-}}] + [\mathrm{HCO_3^-}] + [\mathrm{HPZCOO}] + [\mathrm{PZCOO^-}] + 2[\mathrm{PZ(COO^-)_2}] - \frac{[\mathrm{K^+}]}{2}}{\frac{[\mathrm{K^+}]}{2} + [\mathrm{PZ}] + [\mathrm{PZH^+}] + [\mathrm{HPZCOO}] + [\mathrm{PZCOO^-}] + [\mathrm{PZ(COO^-)_2}]} \qquad \textit{Εξ. 13}$$

6.3 Αποτελέσματα

Οι Πίνακες 18 και 19 παρουσιάζουν τη σύγκριση των εκτιμήσεων του θερμοδυναμικού μοντέλου electrolyte-NRTL με τα πειραματικά δεδομένα που χρησιμοποιήθηκαν για την ανάλυση παλινδρόμησης. Όπως φαίνεται, αν και οι αποκλίσεις παρέμειναν υψηλές σε κάποιες περιπτώσεις, το μοντέλο παλινδρόμησης πέτυχε να μειώσει σημαντικά τις τιμές *AARD* σε σχέση με το μοντέλο που χρησιμοποιεί προεπιλεγμένες παραμέτρους αλληλεπίδρασης στο Aspen Plus. Κάτι τέτοιο μπορεί να γίνει πιο εύκολα αντιληπτό και από το Σχήμα 33, στο οποίο φαίνονται οι καμπύλες ισορροπίας για το H_2S στο υδατικό διάλυμα K_2CO_3.

Πίνακας 18: Τιμές AARD μεταξύ πειραματικών δεδομένων και εκτιμήσεων του μοντέλου electrolyte-NRTL με προεπιλεγμένες και τροποποιημένες παραμέτρους αλληλεπίδρασης (μόνο K^+).

Πηγή	Τύπος δεδομένων	Σύσταση (wt.%)	Σημεία	Default eNRTL ***AARD*** **(%)**	Regressed eNRTL ***AARD*** **(%)**
[204]	Διαλυτότητα CO_2	20	31	33.9	9.6
[204]	Διαλυτότητα CO_2	30	26	24.2	9.2
[204]	Διαλυτότητα CO_2	40	67	41.6	14.7
Σύνολο			**124**	**35.3**	**11.9**
[288]	Διαλυτότητα H_2S	30	63	82.8	20.0
[288]	Διαλυτότητα H_2S	40	31	86.8	15.9
Σύνολο			**94**	**84.1**	**18.6**

Πίνακας 19: Τιμές AARD μεταξύ πειραματικών δεδομένων και εκτιμήσεων του μοντέλου electrolyte-NRTL με τροποποιημένες παραμέτρους αλληλεπίδρασης (μίγματα PZ/K^+).

Πηγή	Τύπος δεδομένων/ενώσεις	Σημεία	Regressed eNRTL ***AARD*** **(%)**
[216]	Διαλυτότητα CO_2	38	13.9
	^{1}H NMR για PZ/PZH^+		12.0
	^{1}H NMR για $PZCOO^-$/H^+PZCOO^-	41	9.2
	^{1}H NMR για $PZ(COO^-)_2$		19.7
Σύνολο		**130***	**12.9***

*Συνολικός αριθμός σημείων και *AARD* που περιλαμβάνει πειραματικά αποτελέσματα για υδατικά δ/τα PZ.

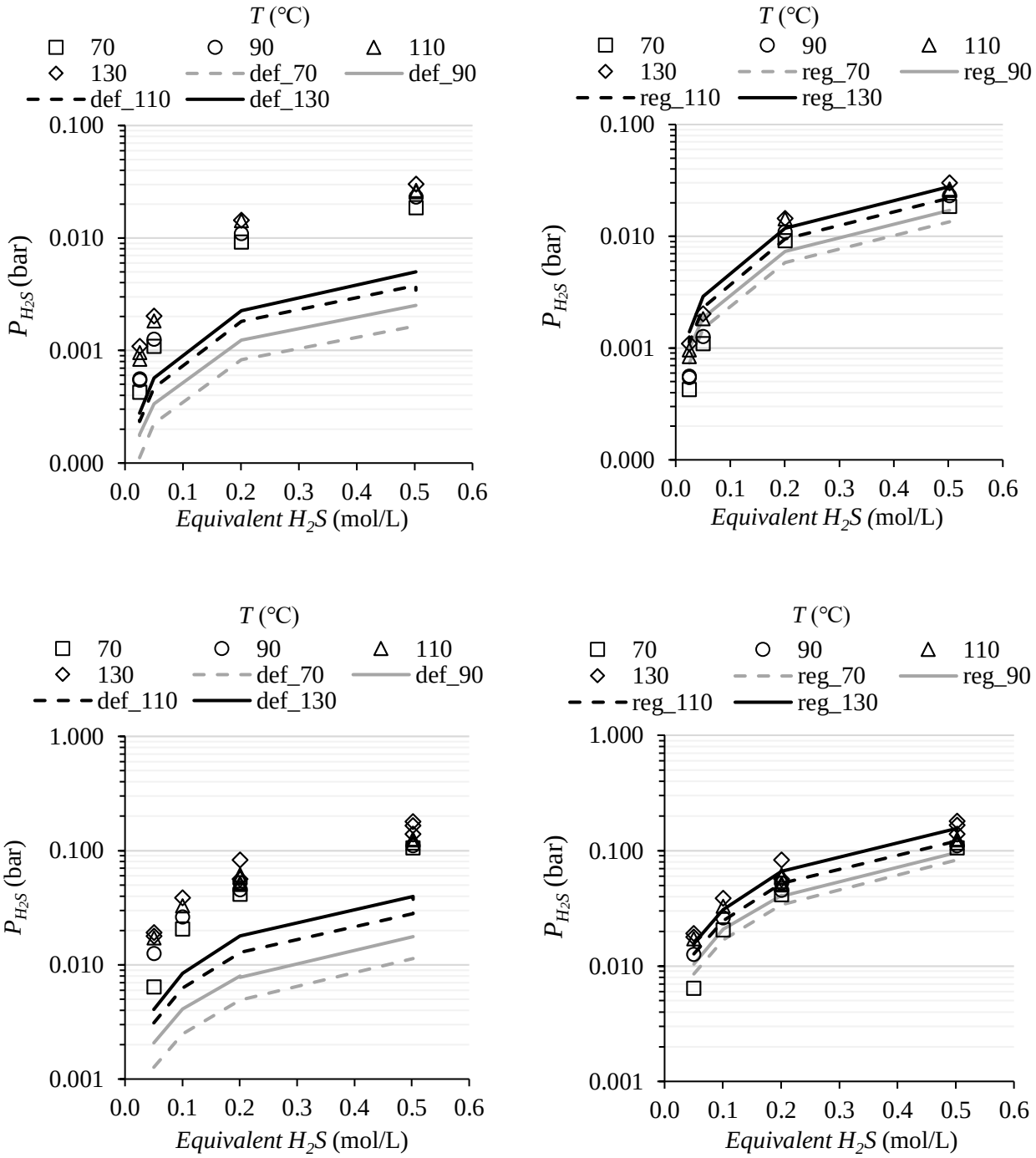

Σχήμα 33: Εκτιμήσεις μερικής πίεσης του H_2S (συνεχείς και διακεκομμένες γραμμές) πάνω από ισοδύναμο διάλυμα 30 wt.% K_2CO_3 στους 70, 90, 110 και 130 °C με προεπιλεγμένες (αριστερή στήλη) και τροποποιημένες παραμέτρους αλληλεπίδρασης του electrolyte-NRTL (δεξιά στήλη). Επάνω γραμμή: 33% μετατροπή σε ($KHCO_3$+KHS) εξαιτίας των CO_2 και H_2S. Κάτω: 66% μετατροπή σε ($KHCO_3$+KHS) εξαιτίας των CO_2 και H_2S. Τα σημεία αντιπροσωπεύουν πειραματικά δεδομένα από την πηγή [288].

Η επίδραση της πίεσης απορρόφησης φαίνεται στο Σχήμα 34. Η αύξηση της πίεσης στη στήλη απορρόφησης συντελεί στη μείωση της ειδικής θερμότητας για την αναγέννηση των διαλυτών, ενώ ταυτόχρονα μειώνει την απαιτούμενη ανακυκλοφορία διαλύτη στη διεργασία. Η αύξηση της περιεκτικότητας του διαλύματος σε PZ είναι ιδιαίτερα ευνοϊκή όταν η απορρόφηση πραγματοποιείται σε πιέσεις όχι μεγαλύτερες των 15 bar.

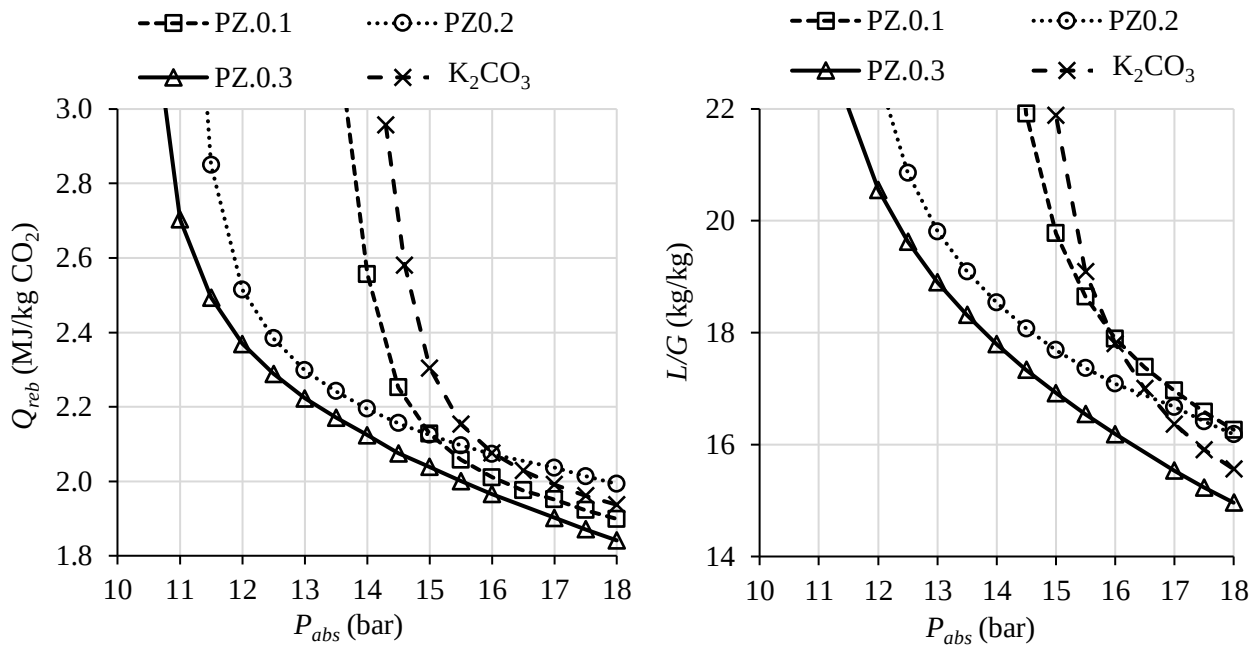

Σχήμα 34: Επίδραση της πίεσης απορρόφησης στην ειδική κατανάλωση θερμότητας για αναγέννηση (αριστερά) και στο λόγο L/G (δεξιά).

Η επίδραση του λόγου ανθράκωσης του πτωχού διαλύτη στη διεργασία φαίνεται στο Σχήμα 35. Για τιμές του α < 0.40, η χρήση πρόσθετης PZ δεν φαίνεται να προσφέρει πλεονέκτημα. Ωστόσο, με αύξηση του λόγου ανθράκωσης του πτωχού διαλύτη αυξάνεται σημαντικά η απαιτούμενη τιμή του λόγου *L/G* καθιστώντας ευνοϊκή τη χρήση προσθέτου στο διάλυμα.

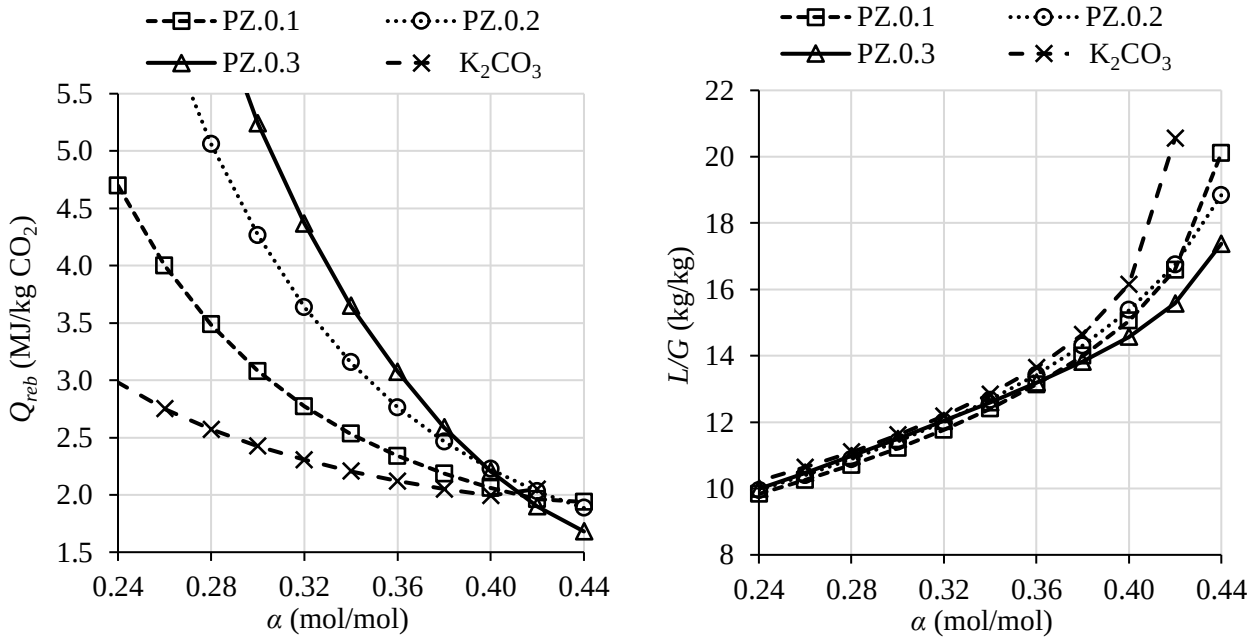

Σχήμα 35: Επίδραση του λόγου ανθράκωσης του πτωχού διαλύτη στην ειδική κατανάλωση θερμότητας για αναγέννηση (αριστερά) και στο λόγο L/G (δεξιά).

Η επίδραση της πίεσης στη στήλη εκρόφησης στη διεργασία φαίνεται στο Σχήμα 36. Η λειτουργία της στήλης υπό κενό μειώνει την ειδική κατανάλωση θερμότητας για αναγέννηση όλων των διαλυτών, ωστόσο ευνοεί περισσότερο τα διαλύματα χωρίς PZ ή με πολύ μικρή περιεκτικότητα σε PZ. Μάλιστα στην συγκεκριμένη περίπτωση υπάρχει το πλεονέκτημα ότι η θερμότητα αναγέννησης μπορεί να προσδοθεί σε χαμηλή

θερμοκρασία (< 100°C) καθιστώντας εφικτή την αξιοποίηση απορριπτόμενης θερμότητας. Αντίθετα, η προσθήκη PZ σε μεγαλύτερη περιεκτικότητα επιτρέπει τη λειτουργία της στήλης εκρόφησης σε μεγαλύτερη πίεση, καθώς η κλίση της καμπύλης της ειδικής θερμότητας αναγέννησης μειώνεται με αύξηση της σύστασης σε PZ.

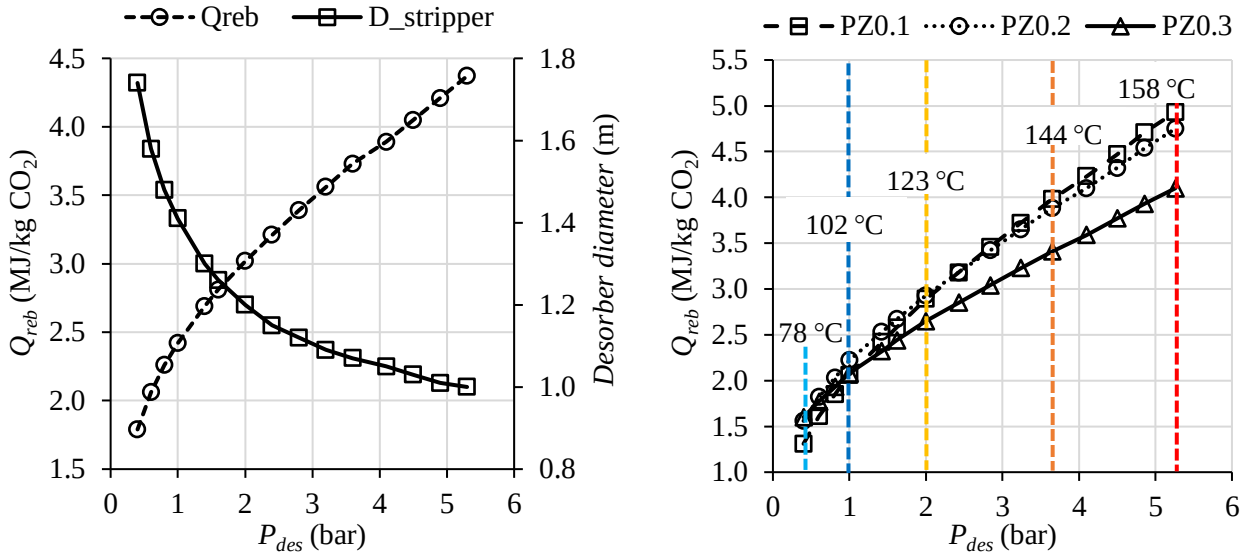

Σχήμα 36: (Αριστερά) Επίδραση της πίεσης εκρόφησης στην ειδική κατανάλωση θερμότητας για αναγέννηση και στη διάμετρο της στήλες εκρόφησης για υδατικό διάλυμα K_2CO_3 με a=0.3 και σταθερή τιμή L/G. (Δεξιά) Επίδραση της πίεσης εκρόφησης στην ειδική κατανάλωση θερμότητας για αναγέννηση για τους διαλύτες PZ0.1, PZ0.2 και PZ0.3 με a=0.4 και σταθερή τιμή L/G. Οι τιμές της θερμοκρασίας εκφράζουν το σημείο βρασμού του διαλύματος στη συγκεκριμένη πίεση.

Ακόμη, τα Σχήματα 37 και 38 δείχνουν την απόδοση δέσμευσης του H_2S και τη διαφυγή PZ με το καθαρό αέριο σύνθεσης, αντίστοιχα.

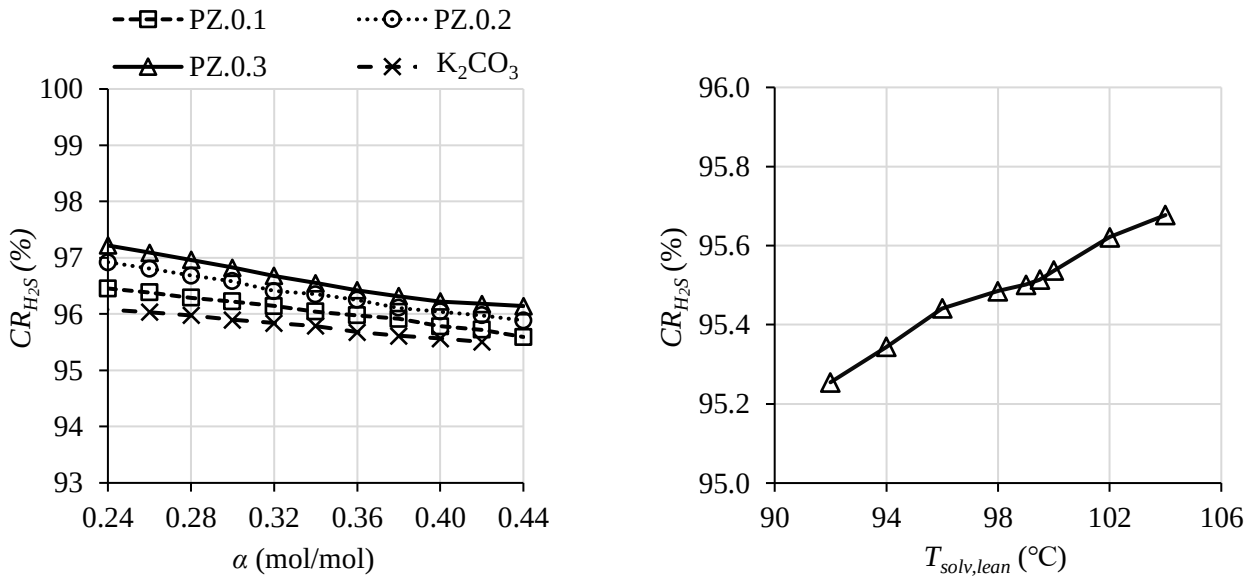

Σχήμα 37: (Αριστερά) Επίδραση του λόγου ανθράκωσης του πτωχού διαλύτη στο βαθμό απορρόφησης του H_2S από το αέριο σύνθεσης και (δεξιά) επιδραση της θερμοκρασίας του πτωχού διαλύτη στο βαθμό απορρόφησης του H_2S (υδατικό διάλυμα καθαρού K_2CO_3).

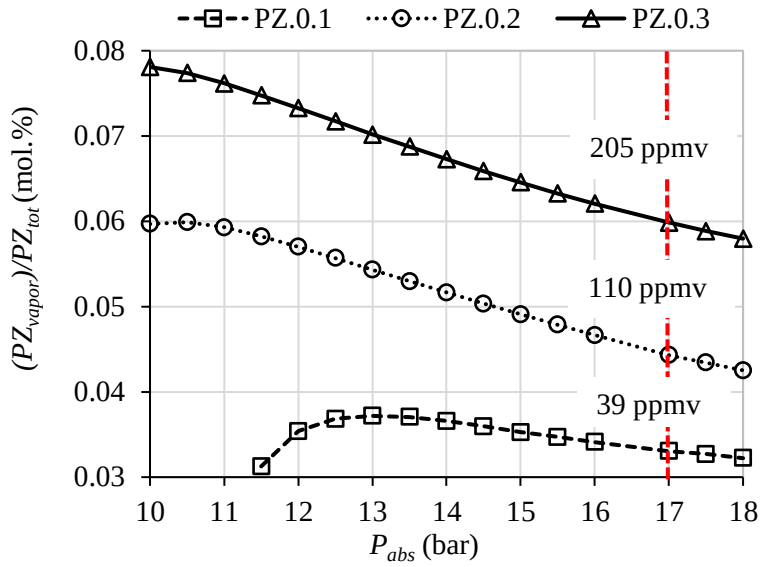

Σχήμα 38: Επίδραση της πίεσης απορρόφησης και της περιεκτικότητας σε PZ στις εκπομπές PZ από τη στήλη απορρόφησης.

Το ποσοστό δέσμευσης του H_2S έφτασε μέχρι περίπου 97%, ενώ ήταν σταθερά πάνω από το ποσοστό δέσμευσης του CO_2. Ωστόσο, αν και φαίνεται η διεργασία να είναι οριακά πιο επιλεκτική για το H_2S, δεν μπορεί να εξασφαλίσει το ποσοστό δέσμευσης που απαιτείται από καταλύτες που είναι επιρρεπείς σε δηλητηρίαση από θειούχες ενώσεις. Η αύξηση της πίεσης απορρόφησης και της θερμοκρασίας του πτωχού διαλύτη βελτιώνει την απόδοση καθαρισμού του H_2S, ενώ αύξηση του λόγου ανθράκωσης δυσχεραίνει την αποθείωση του αερίου σύνθεσης. Η διαφυγή της PZ βρέθηκε να υπερβαίνει τα 200 ppmv ιδιαίτερα για μεγαλύτερη περιεκτικότητα PZ στο μίγμα, τιμή αρκετά υψηλότερη σε σχέση με δημοσιευμένες τιμές για απορρόφηση CO_2 από καυσαέρια με υδατικά διαλύματα PZ σε χαμηλή θερμοκρασία (10-66 ppmv) [236, 301].

6.4 Συμπεράσματα

Σε αυτό το κεφάλαιο αναπτύχθηκε ένα μοντέλο της διεργασίας AGR με διαλύματα K_2CO_3 στο λογισμικό Aspen Plus™ με στόχο τη δέσμευση CO_2 και H_2S από αέριο σύνθεσης που προέρχεται από αεριοποίηση άνθρακα και προορίζεται για τη σύνθεση SNG. Σκοπός ήταν η διερεύνηση της επίδρασης της χρήσης προσθέτων, καθώς και των παραμέτρων λειτουργίας στην απόδοση της διεργασίας. Συγκεκριμένα, αξιολογήθηκαν υδατικά διαλύματα καθαρού K_2CO_3 και διαλύματα με πρόσθετη PZ (με διαφορετικές περιεκτικότητες PZ στο διάλυμα) ως υποψήφιοι διαλύτες για τα όξινα αέρια. Παρά το γεγονός ότι μελέτες μοντελοποίησης της διεργασίας για τη δέσμευση CO_2 από καυσαέρια με μίγματα PZ/K_2CO_3 είναι διαθέσιμες στη βιβλιογραφία, η παρούσα μελέτη επικεντρώθηκε στη δέσμευση προ-καύσης σε αυξημένη θερμοκρασία και πίεση. Πραγματοποιήθηκε προσαρμογή των παραμέτρων δυαδικής αλληλεπίδρασης του μοντέλου electrolyte-NRTL μέσω ανάλυσης παλινδρόμησης πειραματικών δεδομένων, καθώς οι προεπιλεγμένες παράμετροι του Aspen Plus™ εμφανίζουν σημαντικές αποκλίσεις σε σχέση με τις πειραματικές τιμές. Βρέθηκε πως το θερμοδυναμικό μοντέλο που καταστρώθηκε με βάση πειραματικά δεδομένα για τους μέσους συντελεστές ενεργότητας, την ελάττωση της τάσης ατμών, τη θερμοχωρητικότητα των διαλυμάτων, τη διαλυτότητα των CO_2 και H_2S και την κατανομή των ειδών PZ μπορεί να εξασφαλίσει μια ακριβέστερη περιγραφή του συστήματος σε σύγκριση με τις προεπιλεγμένες παραμέτρους του Aspen Plus. Η σχετική απόκλιση για τα υδατικά διαλύματα K_2CO_3 βρέθηκε να είναι μικρότερη από 12% όταν απορροφάται μόνο το CO_2, ενώ αυξήθηκε σε 18.6% για το σύστημα H_2S-CO_2-K_2CO_3-H_2O.

Το θερμοδυναμικό μοντέλο που προέκυψε από την ανάλυση παλινδρόμησης συνδυάστηκε με μοντέλα ρυθμού (μεταφοράς θερμότητας και μάζας, κινητικής κλπ.) στο Aspen Plus για την μοντελοποίηση της διεργασίας AGR. Η μεταβολή της πίεσης απορρόφησης, της πίεσης εκρόφησης και του λόγου ανθράκωσης του πτωχού

διαλύτη επηρέασε την απόδοση της διεργασίας και ειδικότερα την αναλογία μάζας υγρού προς αέριο, την ειδική κατανάλωση θερμότητας του αναβραστήρα και την απόδοση καθαρισμού του H_2S. Διαπιστώθηκε ότι όταν η διεργασία λειτουργεί με διαλύματα που προάγονται με PZ, παρόμοια ειδική κατανάλωση θερμότητας για αναγέννηση με τα υδατικά διαλύματα καθαρού K_2CO_3 είναι εφικτή σε χαμηλότερη πίεση της στήλης απορρόφησης. Η λειτουργία της στήλης απορρόφησης σε υψηλότερη πίεση ωφελεί τόσο τα ενισχυμένα όσο και τα υδατικά διαλύματα K_2CO_3 χωρίς πρόσθετα, γεγονός που υποδηλώνει την καταλληλότητα της τεχνολογίας για δέσμευση CO_2 πριν την καύση. Επίσης, απαιτείται μεγαλύτερος λόγος ανθράκωσης φτωχού διαλύτη όταν η PZ χρησιμοποιείται ως πρόσθετο στο διάλυμα, αποτέλεσμα που αποδίδεται στην υψηλότερη θερμότητα εκρόφησης. Οι εκπομπές PZ στα ενισχυμένα διαλύματα βρέθηκαν να είναι υψηλότερες σε σύγκριση με τις εκπομπές που συμπυκνωμένων υδατικών διαλυμάτων PZ για απορρόφηση CO_2 από καυσαέρια. Έτσι, θα πρέπει να ληφθούν υπόψη οι αλληλεπιδράσεις της PZ με καταλύτες κατάντη της διεργασίας AGR. Διαπιστώθηκε ότι όταν ο λόγος ανθράκωσης υπερβαίνει τιμές της τάξης του 0.42, οι απαιτούμενες τιμές L/G αυξάνονται απότομα. Επιπρόσθετα, η λειτουργία της στήλης εκρόφησης σε αυξημένη πίεση βρέθηκε να ωφελεί διαλύτες με υψηλότερο γραμμομοριακό κλάσμα PZ. Τέλος, η απόδοση δέσμευσης H_2S ήταν σταθερά υψηλότερη από το επίπεδο δέσμευσης του CO_2 από τη διεργασία.

7 Ενεργειακή και εξεργειακή ανάλυση ενός σταθμού αεριοποίησης για συμπαραγωγή ηλεκτρισμού/MeOH με CCS

7.1 Πλαίσιο μελέτης

Στο Κεφάλαιο 6 της διδακτορικής διατριβής παρουσιάστηκε η μοντελοποίηση της διεργασίας AGR με διαλύματα K_2CO_3 και μελετήθηκε η επίδραση των κυρίων παραμέτρων λειτουργίας στην ενεργειακή κατανάλωση της στήλης εκρόφησης και το βαθμό καθαρισμού του H_2S. Ωστόσο, ενδιαφέρον παρουσιάζει η επίπτωση της ενσωμάτωσης της διεργασίας απορρόφησης/εκρόφησης σε σταθμούς αεριοποίησης. Συγκεκριμένα, στο παρόν κεφάλαιο μελετάται η ενσωμάτωση της διεργασίας AGR σε σταθμούς αεριοποίησης βιομάζας με συνδυασμένο κύκλο (BIGCC) για αποκλειστική ηλεκτροπαραγωγή, αλλά και συμπαραγωγή ηλεκτρισμού και MeOH. Η αξιολόγηση παρουσιάζεται από ενεργειακή και εξεργειακή σκοπιά. Η αναγνώριση των κύριων διεργασιών που συνεισφέρουν στην εξεργειακή καταστροφή στο σταθμό αποτελεί το πρώτο σημαντικό στάδιο για την περαιτέρω βελτιστοποίηση της διεργασίας.

7.2 Διατάξεις σεναρίων BIGCC και μεθοδολογία μοντελοποίησης

Τα τρία σενάρια τα οποία μοντελοποιήθηκαν στο λογισμικό Aspen Plus παρουσιάζονται στο Σχήμα 39. Η μοντελοποίηση της διεργασίας αεριοποίησης βασίστηκε στον αεριοποιητή ρευστοποιημένης κλίνης του IGT [318], εισάγοντας ημι-εμπειρικές συσχετίσεις για τη θεώρηση καταλυτικής αεριοποίησης [304, 319] και τη δέσμευση θείου εντός της κλίνης [320]. Ως καύσιμο για τον αεριοποιητή χρησιμοποιούνται υπολείμματα ξυλείας με αρχική υγρασία 30 wt.%, τα οποία ξηραίνονται με καυσαέρια από το Λέβητα Ανάκτησης θερμότητας (ΛΑΘ) του σταθμού. Το O_2 τροφοδοτείται από μια μονάδα κρυογονικού διαχωρισμού αέρα (ASU), η οποία μοντελοποιήθηκε στο Aspen Plus ως διεργασία διαχωρισμού με συνδυασμό απόσταξης υψηλής και χαμηλής πίεσης [321, 322]. Ακολουθεί θερμός καθαρισμός του αερίου σύνθεσης για πίσσες (καταλυτικός αντιδραστήρας), σωματίδια, HCl και H_2S. Στην περίπτωση των σεναρίων που ενσωματώνουν τη διεργασία AGR, ένα ή δύο στάδια για την αντίδραση WGS ακολουθούν το σύστημα θερμού καθαρισμού του αερίου (ανάντη της AGR). Η διεργασία AGR χρησιμοποιεί διάλυμα 30 wt.% K_2CO_3 και το αέριο σύνθεσης εισέρχεται για καθαρισμό με θερμοκρασία 122 °C. Τα απαέρια από τη στήλη εκρόφησης που είναι πλούσια σε CO_2 ψύχονται και συμπιέζονται μέχρι τα 100 bar για αποθήκευση. Το αέριο σύνθεσης καίγεται στον αεριοστρόβιλο είτε απευθείας είτε αφότου αναμιχθεί με συμπιεσμένο N_2 από τη μονάδα ASU, ώστε να περιοριστεί η περιεκτικότητα του H_2 σε επίπεδα < 50 vol.%. Ο ΛΑΘ της εγκατάστασης παράγει ατμό για ηλεκτροπαραγωγή, αλλά και ικανοποίηση των αναγκών της διεργασίας (μέσο αεριοποίησης, θερμική κατανάλωση κ.α.).

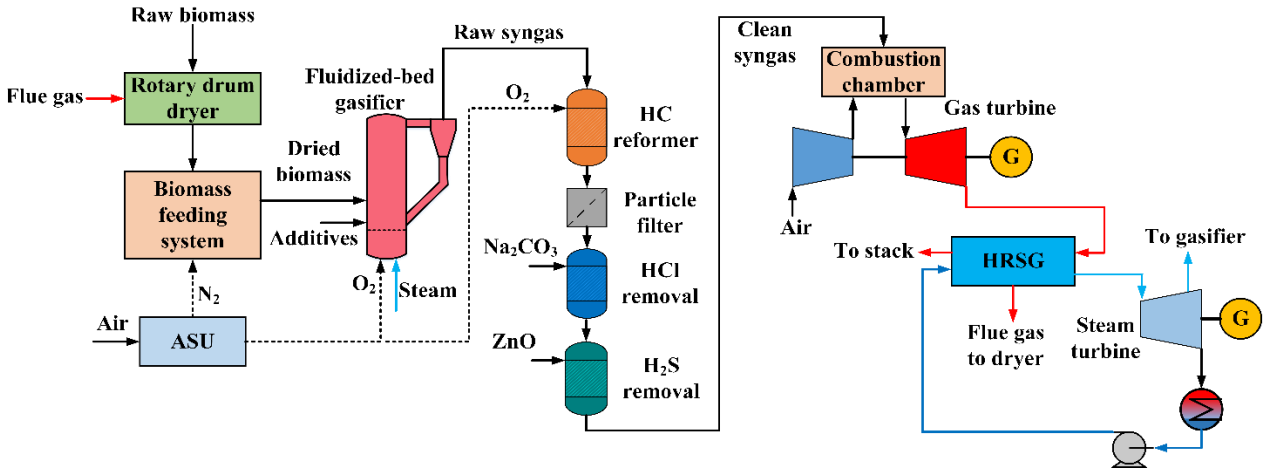

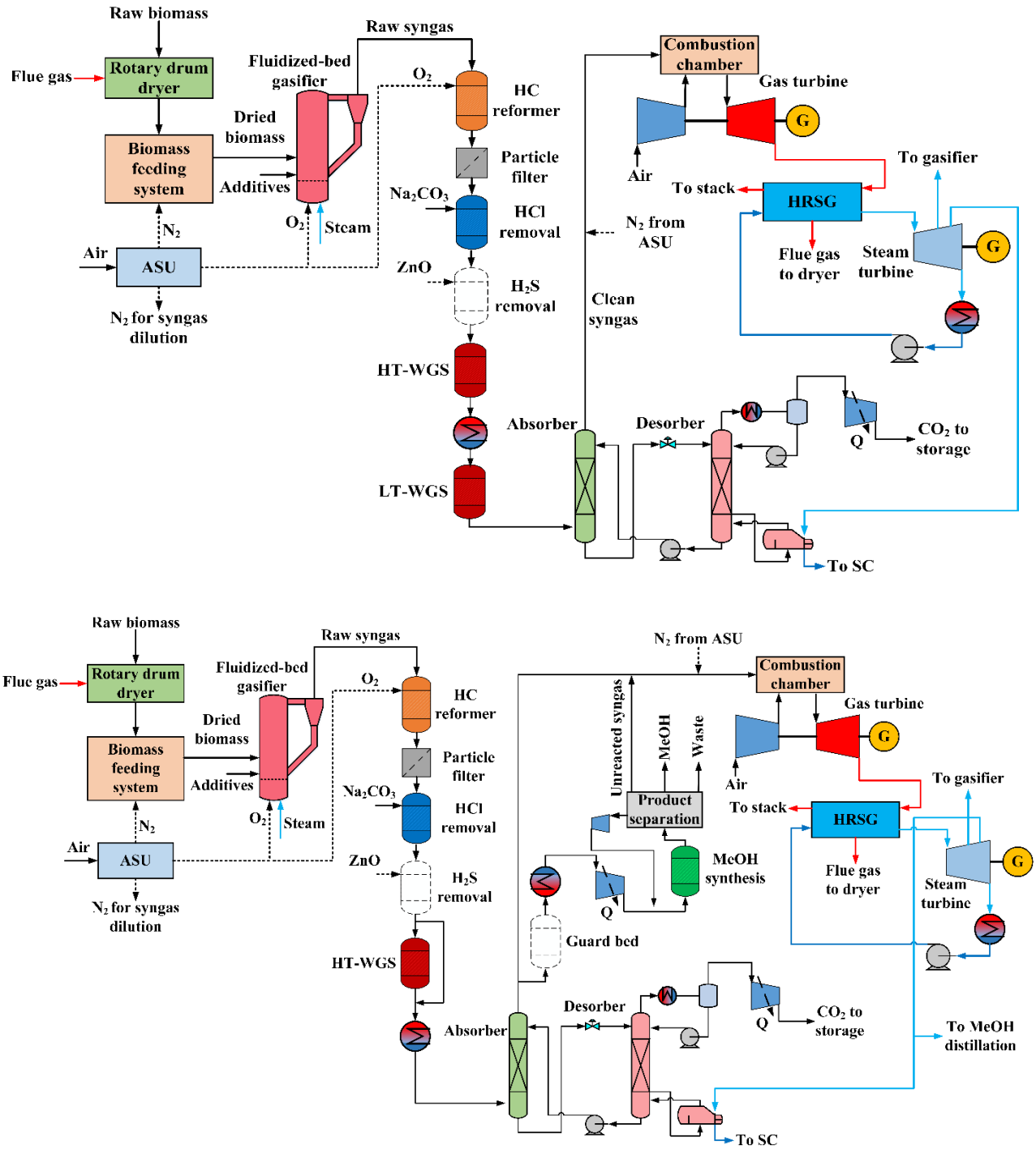

Σχήμα 39: Διατάξεις σταθμών BIGCC της παρούσας μελέτης. (Πάνω) Σταθμός BIGCC αναφοράς για ηλεκτροπαραγωγή χωρίς CCS (Σενάριο Ι), (μέση) σταθμός BIGCC για ηλεκτροπαραγωγή με CCS (Σενάριο ΙΙ), (κάτω) σταθμός BIGCC για συμπαραγωγή MeOH και ηλεκτρισμού με CCS (Σενάριο ΙΙΙ).

Για την περίπτωση του Σεναρίου ΙΙΙ, όπου πραγματοποιείται συμπαραγωγή ηλεκτρισμού/MeOH, χρησιμοποιήθηκε ένα κινητικό μοντέλο Langmuir-Hinshelwood-Hougen-Watson (LHHW) για τη μοντελοποίηση του αντιδραστήρα σύνθεσης. Οι παράμετροι για το κινητικό μοντέλο ελήφθησαν από την εργασία των Van-Dal και Bouallou [329]. Η διεργασία σύνθεσης λειτουργεί με ένα ποσοστό ανακυκλοφορίας του αερίου σύνθεσης κατά 60%, ενώ η υπόλοιπη ποσότητα καίγεται στον αεριοστρόβιλο του σταθμού. Ο Πίνακας 20 συνοψίζει τις βασικές παραδοχές που έχουν χρησιμοποιηθεί στη μοντελοποίηση.

Πίνακας 20: Παραδοχές μοντελοποίησης των σεναρίων BIGCC.

Υποσύστημα	**Παράμετρος**	**Τιμές**
ASU	Πίεση HP στήλης/LP στήλης/booster (bar)	5.5/1.6/30
	Λόγος διαχωρισμού αέρα για booster (−)	0.2
	Καθαρότητα O_2 (vol.%)	≥ 95.0
	Βαθμίδες στηλών διαχωρισμού HP/LP (−)	30/35
Ξηραντήρας	Θερμοκρασία καυσαερίου εισόδου/εξόδου (°C)	220/95
Αεριοποιητής	Θερμοκρασία/πίεση (°C/bar)	900/29
	Θερμοκρασία O_2 (°C)	200
	Θερμοκρασία ατμού (°C)	350
	Απόδοση μετατροπής άνθρακα (%)	98
	Βαθμός αποθείωσης (% του S)	60
	Απώλειες θερμότητας (% επί HHV)	1
Αντιδραστήρας αναμόρφωσης	Θερμοκρασία εξόδου (°C)	910
	Μετατροπή πισσών και C_{2+} (%)	99
	Μετατροπή CH_4 (%)	70
	Μετατροπή NH_3 (%)	90
Δέσμευση HCl (Na_2CO_3)	Θερμοκρασία εισόδου αερίου (°C)	420
Δέσμευση H_2S (ZnO)	Θερμοκρασία εισόδου αερίου (°C)	350
Αντιδραστήρες WGS	Θερμοκρασία εισόδου WGSHT (°C)	350
	Θερμοκρασία εισόδου WGSLT (°C)	200
Μονάδα AGR	Περιεκτικότητα K_2CO_3 (wt.%)	30
	Πίεσης στήλης απορρόφησης (bar)	25
	Πίεσης στήλης εκρόφησης (bar)	1.5
	Λόγος ανθράκωσης πτωχού διαλύτη (−)	0.3
	Θερμοκρασία εισόδου αερίου (°C)	122
Αποθήκευση CO_2	Συμπιεστής, πίεση αποθήκευσης (bar)	3-stage, 100 bar
Αεριοστρόβιλος	Λόγος πίεσης	15
	Πτώση πίεσης (% της εισόδου)	4
	TIT_{max} (°C)	1230
	Πολυτροπικός β.α. συμπιεστή (−)	0.90
	Ισεντροπικός β.α. στροβίλου (−)	0.88
	Έξοδος καυσαερίου (°C)	550
ΛΑΘ	Θερμοκρασία εξόδου (°C)	75
	Πίεση HP/RH/LP (bar)	110/30/4.2
	Θερμοκρασία εισόδου βαθμίδας HP (°C)	520
	Ελάχιστη θερμοκρασιακή προσέγγιση στο ΛΑΘ (°C)	20
Ατμοστρόβιλος	Ισεντροπικός β.α., όλες οι βαθμίδες (−)	0.82
	Πίεση συμπύκνωσης(bar)	0.06
Σύνθεση MeOH	Θερμοκρασία/πίεση σύνθεσης (°C/bar)	234/52.5
	Ανακυκλοφορία syngas (%)	60
	Λόγος H_2/CO στην είσοδο (−)	2.5
	GHSV (h^{-1})	4000
	Καθαρότητα MeOH (wt.%)	≥ 99.0
Εναλλάκτες θερμότητας	Ελάχιστη θερμοκρασιακή προσέγγιση, αέριο/υγρό και αέριο/αέριο (K)	10/20
Συμπιεστές	Πολυτροπικός β.α. (−)	0.8
Αντλίες	Β.α. αντλίας (−)	0.78
Εκτονωτές	Ισεντροπικός β.α. (−)	0.88
Λοιπά	Πτώση πίεσης* (% της πίεσης εισόδου)	1
	Μηχανικός β.α. για συμπιεστές, αντλίες κλπ. (−)	0.99
	Β.α. γεννήτριας (−)	0.98

*για τους εναλλάκτες θερμότητας και τους αντιδραστήρες

Για κάθε σενάριο εξετάστηκαν παραλλαγές ως εξής:

- Στο Σενάριο I, οι υποπεριπτώσεις I-LS, I-MS και I-HS αναφέρονται σε λόγο μάζας ατμού προς βιομάζα στον αεριοποιητή 0.60, 0.87 (βασική περίπτωση) και 1.09, αντίστοιχα.
- Στο Σενάριο II, οι υποπεριπτώσεις II-50%, II-70% και II-90% υποδεικνύουν το ποσοστό δέσμευσης του CO_2.
- Στο Σενάριο III, οι υποπεριπτώσεις III-25% MeOH και III-50% MeOH αναφέρονται στο ποσοστό της συνολικής παροχής αερίου σύνθεσης κατάντη της διεργασίας AGR που οδηγείται για σύνθεση MeOH.

Οι βαθμοί ενεργειακής και εξεργειακής απόδοσης των σεναρίων δίνονται στις Εξ. 14 και Εξ. 15

$$\eta = \frac{\dot{m}_{MeOH} LHV_{MeOH} + P_{el,net}}{\dot{m}_{biom} LHV_{biom}} \qquad \textit{Εξ. 14}$$

$$\varepsilon = \frac{\dot{m}_{MeOH} e_{MeOH} + P_{el,net}}{\dot{m}_{biom} e_{ch,biom} + E_{air,ASU} + E_{air,GT} + E_w} \qquad \textit{Εξ. 15}$$

όπου $P_{el,net}$ είναι η καθαρή ηλεκτρική ισχύς (MW), $\dot{m}_{biom}$ η παροχή βιομάζας (kg s^{-1}), LHV_{biom} η κατώτερη θερμογόνος δύναμη της βιομάζας (MJ kg^{-1}), $\dot{m}_{MeOH}$ η παροχή μάζας της MeOH (kg s^{-1}), LHV_{MeOH} η κατώτερη θερμογόνος δύναμη της MeOH (MJ kg^{-1}), e_{MeOH} η ειδική χημική εξέργεια της MeOH (MJ kg^{-1}), $E_{air,ASU}$ η εξέργεια του αέρα που παρέχεται στην ASU (MW), $E_{air,GT}$ η εξέργεια του αέρα που παρέχεται στο GT (MW) και E_w η εξέργεια του νερού συμπλήρωσης στο σταθμό (MW).

7.3 Αποτελέσματα

Το Σχήμα 40 παρουσιάζει την επίδραση της εισερχόμενης ποσότητας ατμού στον αεριοποιητή στην ποιότητα της αεριοποίησης. Η αύξηση του *STBR* αυξάνει την περιεκτικότητα του H_2 και το λόγο H_2/CO, γεγονός που είναι επιθυμητό για διεργασίες σύνθεσης με βάση το H_2. Ωστόσο, παρατηρείται ταυτόχρονα σημαντική αραίωση του αερίου σύνθεσης με ατμό (μέχρι σχεδόν 50 vol.%), αφού ένα σημαντικό μέρος του δεν καταναλώνεται σε αντιδράσεις αεριοποίησης. Παράλληλα, η αύξηση του *STBR* αυξάνει τον απαιτούμενο λόγο αέρα καύσης για τη διατήρηση σταθερής θερμοκρασίας αεριοποίησης.

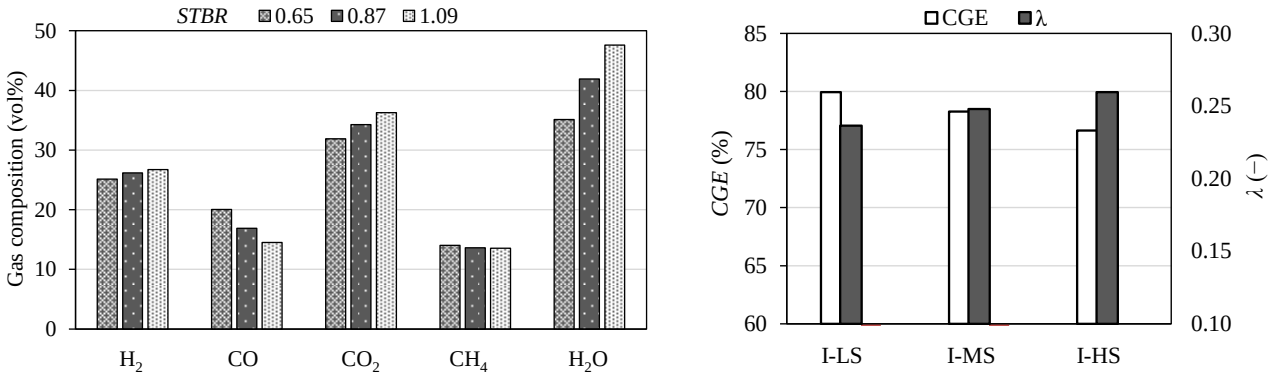

Σχήμα 40: (Αριστερά) Επίδραση του STBR στη σύσταση του αερίου σύνθεσης (επί ξηρού εκτός του H_2O) και (δεξιά) επίδραση του STBR στα λ και CGE για τα Σενάρια I-LS, I-MS και I-HS.

Ο ενεργειακός βαθμός απόδοσης βρέθηκε να υπερβαίνει το 45% για τις περιπτώσεις των διατάξεων χωρίς CCS, αποτέλεσμα που μπορεί να αποδοθεί στο σύστημα θερμού καθαρισμού του αερίου σύνθεσης. Η ενσωμάτωση της διεργασίας AGR με διαλύματα K_2CO_3 (Σενάριο II) προκάλεσε μείωση του ενεργειακού βαθμού απόδοσης κατά 6.5, 9.0 και 11.5 ποσοστιαίες μονάδες (50, 70 και 90% δέσμευση CO_2). Σχετικά με τον εξεργειακό βαθμό απόδοσης, ενδιαφέρον παρουσιάζει το γεγονός ότι το Σενάριο III-50% MeOH παρουσιάζει μεγαλύτερη τιμή σε σχέση με το Σενάριο αναφοράς I-MS, γεγονός που οφείλεται στην αυξημένη εξεργειακή απόδοση της σύνθεσης

της MeOH από αέριο σύνθεσης. Οι μέγιστες τιμές του εξεργειακού βαθμού απόδοσης κυμάνθηκαν κοντά στο 38%.

Το Σχήμα 41 παρουσιάζει τις ηλεκτρικές ιδιοκαταναλώσεις του σταθμού για κάθε σενάριο. Για τις περισσότερες υποπεριπτώσεις, η μονάδα διαχωρισμού αέρα είναι υπεύθυνη για τη μεγαλύτερη ηλεκτρική κατανάλωση στο σταθμό, ειδικά κατά τις περιπτώσεις ηλεκτροπαραγωγής χωρίς CCS. Με αύξηση του ποσοστού δέσμευσης του CO_2 παρατηρείται σταδιακή αύξηση των ηλεκτρικών ιδιοκαταναλώσεων για αποθήκευση του CO_2, αλλά και για την αραίωση του αερίου σύνθεσης που οδηγείται στο θάλαμο καύσης του αεριοστροβίλου με N_2. Η ηλεκτρική κατανάλωση της μονάδας AGR δεν υπερβαίνει το 5% των συνολικών ηλεκτρικών ιδιοκαταναλώσεων.

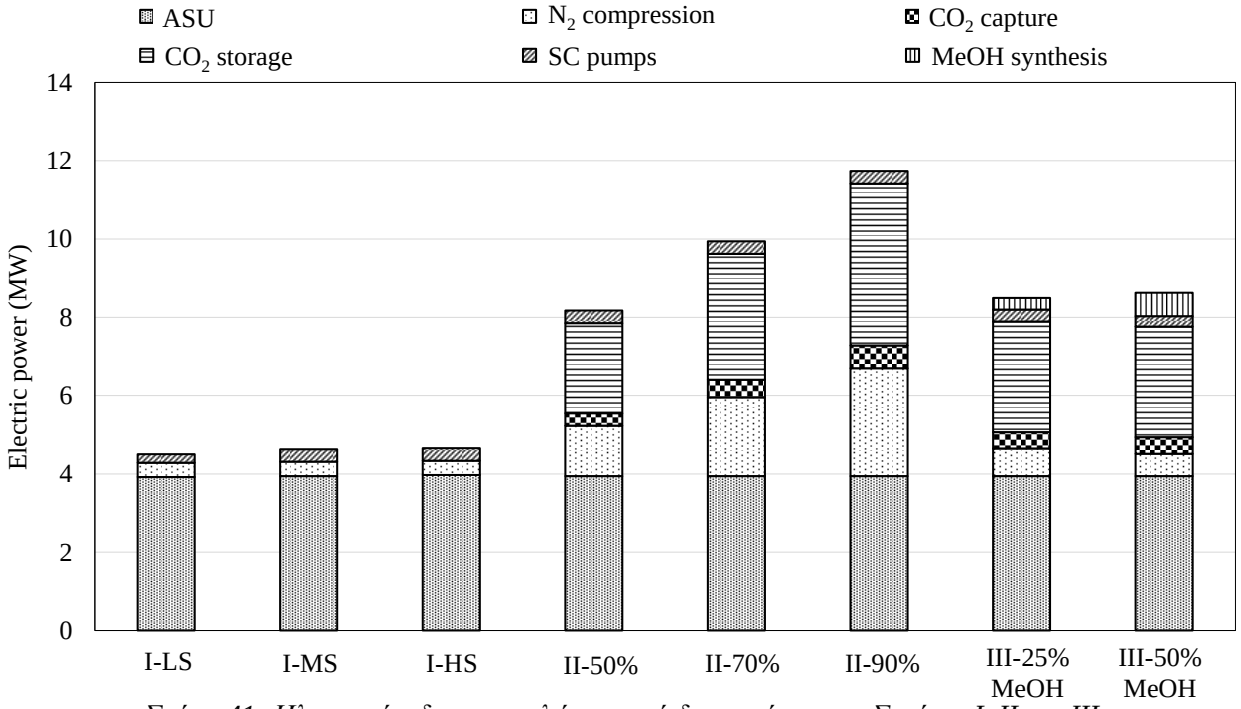

Σχήμα 41: Ηλεκτρικές ιδιοκαταναλώσεις ανά διεργασία για τα Σενάρια I, II και III.

Ακόμη, το Σχήμα 42 παρουσιάζει το εξεργειακό ισοζύγιο και την κατανομή της καταστροφής εξέργειας ανά διεργασία των Σεναρίων I, II και III. Όπως είναι αντιληπτό, η καταστροφή εξέργειας καταλαμβάνει ποσοστό μεγαλύτερο του 50% επί της εισερχόμενης εξέργειας στο σταθμό. Για το Σενάριο I, η λειτουργία του αεριοποιητή με μεγάλη περίσσεια ατμού αυξάνει την καταστροφή εξέργειας της αεριοποίησης. Συνδυαστικά, το άθροισμα της συνεισφοράς του αεριοστροβίλου και του αεριοποιητή υπερβαίνουν το 75% της συνολικής καταστροφής εξέργειας στο σταθμό, ακολουθούμενα από τη μονάδα του ατμοστροβίλου και τη διάταξη θερμού καθαρισμού του αερίου σύνθεσης (~ 5% έκαστο). Από το Σενάριο II φαίνεται πως η μονάδα CCS ευθύνεται για ένα ποσοστό εξεργειακής καταστροφής της τάξεως του 5-10%, ανάλογα με τη δέσμευση CO_2 στο σταθμό BIGCC. Τέλος, η συμπαραγωγή MeOH και ηλεκτρισμού στο σταθμό μειώνει την καταστροφή εξέργειας κατά περίπου 9 ποσοστιαίες μονάδες σε σχέση με το Σενάριο II-90% και 6 ποσοστιαίες μονάδες σε σχέση με το Σενάριο I-MS.

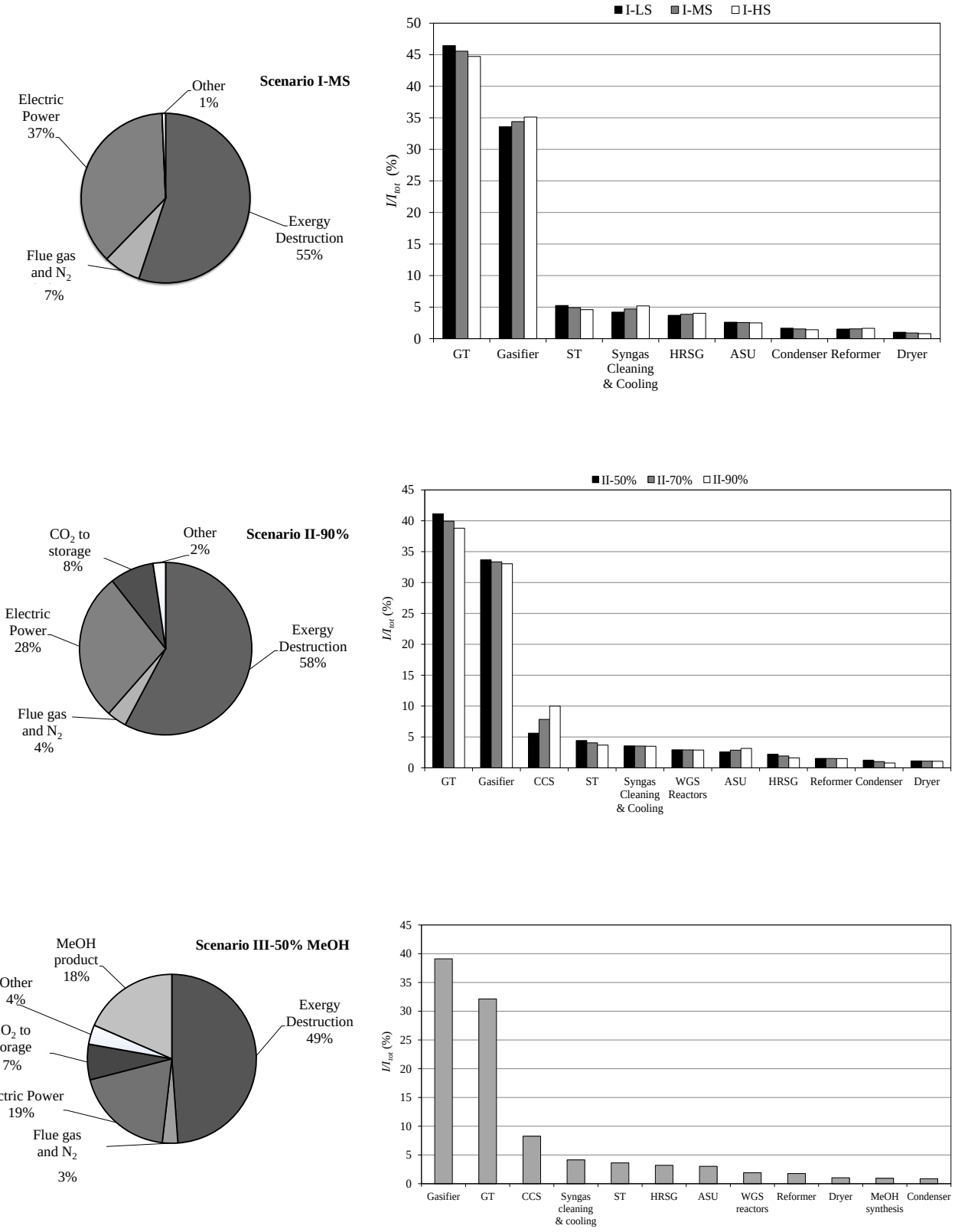

Σχήμα 42: (Αριστερή στήλη) Εξεργειακό ισοζύγιο των σεναρίων BIGCC I-MS (πάνω/αριστερά), II-90% (μέση/αριστερά) και III-50 % MeOH (κάτω/αριστερά) ως προς την εξέργεια εισόδου. (Δεξιά στήλη) Καταστροφή εξέργειας ανά διεργασία για τα Σενάρια I-LS, I-MS, I-HS (πάνω/δεξιά), Σενάρια II-50%, II-70%, II-90% (μέση/δεξιά) και το Σενάριο III-50% MeOH (κάτω/δεξιά).

7.4 Συμπεράσματα

Στο παρόν κεφάλαιο βρέθηκε πως μια μονάδα IGCC με βιομάζα και θερμό καθαρισμού αερίου σύνθεσης είναι εφικτό να επιτύχει υψηλό βαθμό απόδοσης που υπερβαίνει το 46%. Η ενσωμάτωση διεργασιών AGR με αποθήκευση CO_2 επιφέρει μείωση του ενεργειακού βαθμού απόδοσης μέχρι 11.5 ποσοστιαίες μονάδες κατά μέγιστο, όταν η διεργασία AGR βασίζεται σε υδατικά διαλύματα K_2CO_3. Η μείωση του εξεργειακού βαθμού απόδοσης κατά την ενσωμάτωση της συγκεκριμένης τεχνολογίας για δέσμευση CO_2 είναι αντίστοιχη και ελαφρώς μειωμένη σε σχέση με τη διεργασία φυσικής απορρόφησης Selexol και σημαντικά μικρότερη σε σχέση με τη διεργασία χημικής απορρόφησης με MEA. Τέλος, η εφαρμογή συμπαραγωγής ηλεκτρισμού και MeOH αποτελεί κατάλληλη επιλογή για την υβριδοποίηση ενός σταθμού ηλεκτροπαραγωγής με βάση την αεριοποίηση, παρέχοντας οφέλη ως προς την αξιοποίηση της εισερχόμενης εξέργειας στο σύστημα.

8 Συμπεράσματα διατριβής

Στην πρώτη ενότητα αυτού του κεφαλαίου συνοψίζονται τα κύρια συμπεράσματα της παρούσας εργασίας, ενώ ακολουθεί παράθεση κάποιων καινοτόμων στοιχείων της διατριβής.

8.1 Κύρια συμπεράσματα της διατριβής

Η έρευνα στην παρούσα εργασία βασίστηκε πάνω σε δύο κατευθυντήριες γραμμές. Η πρώτη περιλάμβανε την πειραματική διερεύνηση υδατικών διαλυμάτων ανθρακικού καλίου (K_2CO_3) και προσροφητικών υλικών ενεργού άνθρακα για εφαρμογές καθαρισμού αερίων σύνθεσης και απομάκρυνσης CO_2, H_2S, οργανικών θειούχων ενώσεων και ελαφρών πισσών. Η δεύτερη κατευθυντήρια γραμμή αφορούσε τη μοντελοποίηση της διεργασίας AGR με βάση διαλύματα K_2CO_3, τη θερμοδυναμική της ανάλυση και την ενσωμάτωσή της σε μονάδα αεριοποίησης συνδυασμένου κύκλου (IGCC) για συμπαραγωγή ηλεκτρισμού και MeOH. Τα κύρια συμπεράσματα συνοψίζονται παρακάτω.

8.1.1 Συμπεράσματα από πειραματικές δοκιμές διαλυτών και προσροφητικών υλικών

Η προσρόφηση οργανικών και ανόργανων ενώσεων θείου (δοκιμές για οργανικές θειούχες ενώσεις με εργαστηριακά αέρια και δοκιμές σε πραγματικό αέριο σύνθεσης, αντίστοιχα) σε φυσικώς ενεργοποιημένο ενεργό άνθρακα υπό συνθήκες υψηλής θερμοκρασίας διερευνήθηκε πειραματικά ως μέτρο για τη μείωση της περιεκτικότητας των θειούχων ενώσεων και ειδικά για εφαρμογές κατάντη καταλυτικής σύνθεσης. Τα αποτελέσματα παρουσιάστηκαν στο Κεφάλαιο 3. Μετά από μεταβολές των παραμέτρων των δοκιμών προσρόφησης οργανικών θειούχων ενώσεων σε ευρύ φάσμα τιμών, διαπιστώθηκε ότι η θερμοκρασία έχει τη μέγιστη επίδραση στη μείωση της χωρητικότητας του C_4H_4S, το οποίο χρησιμοποιήθηκε ως αντιπροσωπευτική ένωση. Στην υψηλότερη θερμοκρασία διενέργειας των πειραμάτων (200 °C), ο ενεργός άνθρακας διατηρεί λιγότερο από το 10% της χωρητικότητας σε σχέση με τις μετρήσεις που πραγματοποιήθηκαν στους 100 °C. Επίσης διαπιστώθηκε ότι η μεταβολή της συγκέντρωσης των οργανικών θειούχων ενώσεων στην είσοδο επηρεάζει την προσροφητική ικανότητα του υλικού, έχοντας τη δεύτερη μεγαλύτερη επιρροή μετά τη θερμοκρασία. Επιπρόσθετα σημειώθηκε έντονα απότομη κλίση της καμπύλης προσρόφησης. Αυτή αποδίδεται σε υψηλότερο ογκομετρική παροχή στην κλίνη, λιγότερο ευνοϊκές ισόθερμες και αυξημένη διάχυση στους πόρους (για αύξηση της θερμοκρασίας), καθώς και βελτίωση της κινητήριας δύναμης προσρόφησης (για αύξηση της συγκέντρωσης). Η προσρόφηση του μοντέλου οργανικών θειούχων ενώσεων σε συνθήκες υψηλής θερμοκρασίας βρέθηκε να αναστέλλεται από την παρουσία υγρασίας, ακόμη και σε χαμηλή συγκέντρωση (3 vol.%) στο μίγμα αερίων. Αποτέλεσμα ήταν η μείωση τόσο του χρόνου διαρροής όσο και της χωρητικότητας του C_4H_4S. Το συγκεκριμένο γεγονός μπορεί να είναι μεγίστης σημασίας όταν η κλίνη ενεργού άνθρακα είναι εγκατεστημένη ως στάδιο περαιτέρω αποθείωσης μετά από διεργασίες AGR προ-καύσης, δεδομένου ότι το αέριο που εξέρχεται από τη μονάδα AGR δεν θα είναι απαλλαγμένο από υγρασία. Ο ρόλος της υγρασίας στην προσρόφηση οργανικών θειούχων ενώσεων μπορεί να υποβαθμιστεί όταν το σύστημα λειτουργεί σε υψηλότερη θερμοκρασία, ωστόσο, η επίδραση αυτής της στρατηγικής στη χωρητικότητα του υλικού θα πρέπει επίσης να ληφθεί υπόψη. Από την άλλη πλευρά, διαπιστώθηκε ότι η επίδραση που έχει η παράμετρος *GHSV* στην προσροφητική ικανότητα είναι αμελητέα και επηρεάζει μόνο το χρόνο διαρροής. Επιπρόσθετα, η στατιστική ανάλυση έδειξε ότι ένα μοντέλο ισόθερμης τύπου Langmuir περιγράφει επαρκώς την χωρητικότητα του ενεργού άνθρακα για το C_4H_4S.

Ακολούθως διεξήχθησαν πειραματικές δοκιμές με πραγματικό αέριο από πιλοτικής κλίμακας βιομαζική μονάδα αεριοποίησης 1 MW_{th}. Οι κύριοι ρυπαντές στο αέριο ήταν οι ενώσεις H_2S και C_6H_6, ενώ οι οργανικές ενώσεις με μεγαλύτερα μόρια σχεδόν εξαλείφθηκαν λόγω της υψηλής θερμοκρασίας αεριοποίησης που υπερβαίνει τους 1250 °C. Μία δυσκολία κατά τη διάρκεια των δοκιμών υπό συνθήκες αεριοποίησης είναι το γεγονός της διακύμανσης σύστασης του αερίου σύνθεσης. Οι δοκιμές έδειξαν ότι η προσροφητική ικανότητα σε θείο μειώθηκε λόγω των επιδράσεων της παράλληλης προσρόφησης με C_6H_6 και ιδιαίτερα όταν η συγκέντρωση του C_6H_6 στο αέριο υπερβαίνει κατά πολύ την περιεκτικότητα σε θείο. Από την άλλη πλευρά, η χωρητικότητα σε θείο αυξήθηκε δραματικά όταν η αναλογία όγκου μεταξύ των H_2S και C_6H_6 στο αέριο ήταν περίπου 1:1, ακόμη και σε υψηλές θερμοκρασίες προσρόφησης. Συνολικά, μπορεί να εξαχθεί το συμπέρασμα ότι τα υλικά ενεργού άνθρακα μπορούν να χρησιμοποιηθούν για την αποθείωση του αερίου σύνθεσης από υδρόθειο και οργανικές θειούχες ενώσεις υπό «θερμές» συνθήκες καθαρισμού αερίων κατάντη της διεργασίας

AGR. Παρ 'όλα αυτά, η επίδραση της σύστασης του αερίου σύνθεσης και ειδικά της υγρασίας και των ενώσεων ελαφρών πισσών θα πρέπει να ληφθούν υπόψη κατά το σχεδιασμό της διεργασίας.

Η απορρόφηση του CO_2 από υδατικά διαλύματα K_2CO_3 σε υψηλή θερμοκρασία μελετήθηκε μέσω πειραματικών δοκιμών στο Κεφάλαιο 4. Το πρώτο μέρος της έρευνας αφορούσε την απορρόφηση CO_2 σε καθαρά υδατικά διαλύματα K_2CO_3 χωρίς πρόσθετα σε αναδευόμενο αντιδραστήρα ασυνεχούς λειτουργίας και τα πειραματικά δεδομένα χρησιμοποιήθηκαν επιτυχώς για την επικύρωση της πειραματικής μεθοδολογίας μέσω σύγκρισης με τα αποτελέσματα θερμοδυναμικής προσομοίωσης. Για αυτή τη σύγκριση χρησιμοποιήθηκε ένα θερμοδυναμικό μοντέλο βασισμένο στη θεωρία electrolyte-NRTL (η ανάπτυξή του αναλύθηκε στο Κεφάλαιο 6). Όσο αναφορά τα διαλύματα χωρίς πρόσθετα, η διαλυτότητα του CO_2 αυξάνεται με μείωση της θερμοκρασίας ή με πυκνότερο διαλύτη. Τέσσερα διαφορετικά πρόσθετα δοκιμάστηκαν (γλυκίνη, MDEA, MEA και PZ) σε συνθήκες υψηλής θερμοκρασίας. Όσον αφορά τα πρόσθετα που διερευνήθηκαν, διαπιστώθηκε ότι η χρήση της PZ βελτιώνει ταυτόχρονα τη διαλυτότητα του CO_2, αλλά και το ρυθμό απορρόφησής του. Η προσθήκη MEA έδειξε οφέλη τόσο για τη διαλυτότητα όσο και για το ρυθμό απορρόφησης, αλλά σε μικρότερο βαθμό σε σχέση με την PZ. Σε αντίθεση με τα άλλα πρόσθετα, η MDEA μπορεί δυνητικά να βελτιώσει τη διαλυτότητα όταν προστίθενται σε μικρότερες ποσότητες, αλλά μειώνει τη διαλυτότητα του CO_2 σε υψηλή συγκέντρωση στο διάλυμα. Λαμβάνοντας υπόψη τις επιδόσεις της προσθήκης MDEA και της καθαρής γλυκίνης σε υδατικά διαλύματα K_2CO_3, αυτά τα πρόσθετα δεν συνιστώνται ως πρόσθετα απορρόφησης. Με βάση τη μελέτη διαλογής, τα πρόσθετα με την καλύτερη επίδοση κατά τη διάρκεια αυτών των δοκιμών απορρόφησης υψηλής θερμοκρασίας, δηλ. οι PZ και MEA, εξετάστηκαν περαιτέρω στο πλαίσιο της παρούσας διατριβής.

Ως επόμενο στάδιο, εξετάστηκε η απορροφητική ικανότητα τόσο του καθαρού υδατικού διαλύματος K_2CO_3 όσο και του ενισχυμένου με MEA για τον καθαρισμό μιγμάτων CO_2 και ελαφρών πισσών (Κεφάλαιο 5). Η μελέτη αποκάλυψε ότι η προσθήκη μιας μικρής ποσότητας MEA στο εύρος του 1% κατά βάρος δεν έχει αξιοσημείωτη επίδραση στην διαλυτότητα του CO_2 σε σύγκριση με την περίπτωση που προστίθεται αποκλειστικά K_2CO_3 στο διάλυμα. Η αύξηση της θερμοκρασίας επιδεινώνει τη διαλυτότητα του CO_2 σε όλους τους διαλύτες, ωστόσο, πιο εμφανής επίδραση διαπιστώθηκε όταν αυξήθηκε η συγκέντρωση MEA στον ενισχυμένο διαλύτη. Από την άλλη πλευρά, η αύξηση της θερμοκρασίας κατά 10 °C έχει πολύ μικρή επίδραση στην απορροφητική ικανότητα του διαλύματος για μικρότερες συγκεντρώσεις προσθέτων ή για διαλύτη μόνο με K_2CO_3. Η προσθήκη MEA 5% κατά βάρος στο διάλυμα μπορεί να βελτιώσει το ρυθμό απορρόφησης του CO_2, ειδικά όταν η συγκέντρωση του CO_2 στην υγρή φάση αυξηθεί πάνω από ~ 0.8 mol kg^{-1} . Από την άλλη πλευρά μετρήθηκαν πολύ χαμηλές συγκεντρώσεις C_6H_6 και C_7H_8 στο διάλυμα, γεγονός που μπορεί να αποδοθεί στη διαφορά μεταξύ πολικότητας των πτητικών οργανικών ενώσεων και του διαλύτη. Τέλος, δεν παρατηρήθηκε επίδραση στη διαλυτότητα του CO_2 όταν προστέθηκαν πίσσες στο μείγμα αερίων.

8.1.2 Συμπεράσματα από τη θερμοδυναμική ανάλυση και μοντελοποίηση διεργασιών

Στο Κεφάλαιο 2, αναπτύχθηκε ένα μοντέλο ισορροπίας μέσω της ελαχιστοποίησης της ενέργειας Gibbs στο λογισμικό Aspen Plus και οι πειραματικές μετρήσεις, που διεξήχθησαν σε μια μονάδα αναβράζουσας ρευστοποιημένης κλίνης αεριοποίησης των 3 MW_{th} με ξύλο και αέρα ως οξειδωτικό μέσο, χρησιμοποιήθηκαν για την επικύρωσή του. Η χρήση διόρθωσης για την αντίδραση WGS συνέβαλε στην επίτευξη καλύτερης συμφωνίας των αποτελεσμάτων του μοντέλου με τα πειραματικά δεδομένα, υποδεικνύοντας ότι η αντίδραση μπορεί να είναι ενεργή κατά τη διάρκεια της ψύξης του αερίου. Η επιλογή του CH_4 ως μοναδικού υδρογονάνθρακα που προκύπτει κατά το στάδιο της πυρόλυσης στο μοντέλο φαίνεται να μην είναι κατάλληλη, καθώς τα αποτελέσματα προσομοίωσης και τα πειραματικά δεδομένα δεν συμφωνούν. Αντίθετα, ένα τροποποιημένο μοντέλο που περιλαμβάνει επιπλέον το σχηματισμό C_2H_4 και τη διόρθωση της αντίδρασης WGS κατά τη διάρκεια της ψύξης εκτιμά ικανοποιητικά τα κύρια συστατικά του αερίου προϊόντος. Προκειμένου να βελτιωθεί η ακρίβεια του μοντέλου χρειάζονται περισσότεροι ημι-εμπειρικοί συσχετισμοί που αφορούν την επίδραση του τύπου καυσίμου και των παραμέτρων αεριοποίησης στην ποιότητα του αερίου σύνθεσης. Ωστόσο, το ημι-εμπειρικό μοντέλο ισορροπίας που αναπτύχθηκε στο Κεφάλαιο 2 μπορεί να θεωρηθεί ως ένα ευέλικτο εργαλείο για τη μοντελοποίηση της αεριοποίησης ξυλώδους βιομάζας και την ανάπτυξη μοντέλων σε επίπεδο σταθμού που θα ενσωματώνουν κατάντη διεργασίες αξιοποίησης του αερίου σύνθεσης.

Στο Κεφάλαιο 6, αναπτύχθηκε ένα μοντέλο στο λογισμικό Aspen Plus για την προσομοίωση της διεργασίας θερμού ανθρακικού καλίου με στόχο την ταυτόχρονη δέσμευση CO_2 και H_2S από αέριο σύνθεσης προερχόμενο από αεριοποίηση άνθρακα (κατάλληλο για τη διεργασία παραγωγής SNG). Η μελέτη επικεντρώθηκε στην επίδραση των προσθέτων και των παραμέτρων λειτουργίας στην απόδοση της διεργασίας. Διαλύματα με και χωρίς προσθήκη PZ αξιολογήθηκαν με βάση τα αποτελέσματα που προέκυψαν από τις πειραματικές δοκιμές διαλυτών στο Κεφάλαιο 4. Αποδείχθηκε ότι υπήρχαν σημαντικές αποκλίσεις μεταξύ των πειραματικών δεδομένων και των εκτιμήσεων του μοντέλου electrolyte-NRTL όταν αυτό ενσωματώνει τις προεπιλεγμένες τιμές των παραμέτρων αλληλεπίδρασης. Η προσαρμογή του θερμοδυναμικού μοντέλου με πειραματικά δεδομένα για τους μέσους ιοντικούς συντελεστές ενεργότητας, την ελάττωση της τάσης ατμών, τη θερμοχωρητικότητα διαλύματος, τη διαλυτότητα CO_2 και H_2S, αλλά και την κατανομή των ειδών PZ στο διάλυμα οδήγησαν σε ακριβέστερη προσομοίωση του συστήματος στο Aspen Plus. Παρ 'όλα αυτά, είναι απαραίτητη η περαιτέρω βελτίωση του μοντέλου, προκειμένου να μειωθούν οι αποκλίσεις σε ένα προτεινόμενο εύρος απόκλισης ± 10%. Η διεργασία με ενισχυμένα διαλύματα μπορεί να επιτύχει αντίστοιχη ενεργειακή κατανάλωση (στον αναβραστήρα της στήλης εκρόφησης) με τα καθαρά υδατικά διαλύματα K_2CO_3 σε χαμηλότερη πίεση της στήλης απορρόφησης. Η αύξηση της πίεσης απορρόφησης ήταν επωφελής τόσο για τα ενισχυμένα όσο και για καθαρά υδατικά διαλύματα K_2CO_3, γεγονός που υποδηλώνει την καταλληλότητά της διεργασίας ως τεχνολογίας δέσμευσης CO_2 προ-καύσης. Μια υψηλότερη τιμή του λόγου ανθράκωσης του πτωχού διαλύτη για τα διαλύματα που έχουν ενισχυθεί με PZ μπορεί να αντισταθμίσει την αυξημένη θερμότητα εκρόφησης που τα χαρακτηρίζει. Η διερεύνηση για την επίδραση της πίεσης εκρόφησης σε σχέση με την απόδοση της διεργασίας κατέληξε στο συμπέρασμα ότι η αυξημένη πίεση μπορεί να ωφελήσει τη διεργασία με διαλύτες που έχουν μεγαλύτερη περιεκτικότητα PZ (μικρότερη αύξηση του θερμικού φορτίου στον αναβραστήρα). Από την άλλη πλευρά, η εκρόφηση σε ατμοσφαιρική πίεση ή ακόμα και υπό κενό είναι προτιμότερη για διαλύματα K_2CO_3 με χαμηλή θερμότητα εκρόφησης. Τέλος, παρά το γεγονός ότι η δέσμευση του H_2S ήταν σταθερά υψηλότερη από το επίπεδο δέσμευσης του CO_2, η περιεκτικότητα σε θείο στο καθαρό αέριο δεν θα μπορούσε να ικανοποιήσει τις απαιτήσεις για καταλυτική σύνθεση με καταλύτες που είναι επιρρεπείς σε δηλητηρίαση από θειούχες ενώσεις. Το ζήτημα αυτό τονίζει περαιτέρω την ανάγκη για μια κατάντη διεργασία (π.χ. AC σε αυτήν την εργασία) για να επιτευχθούν χαμηλά επίπεδα θείου.

Στο Κεφάλαιο 7, η διεργασία AGR που μοντελοποιήθηκε στο Κεφάλαιο 6 ενσωματώθηκε σε διατάξεις βιομαζικών μονάδων αεριοποίησης με συνδυασμένο κύκλο (BIGCC) και καθαρισμό αερίου σύνθεσης υπό θερμές συνθήκες. Οι περιπτώσεις παραγωγής ηλεκτρικής ενέργειας και συμπαραγωγής ηλεκτρικής ενέργειας και MeOH με δέσμευση και αποθήκευση του διοξειδίου του άνθρακα (CCS) μοντελοποιήθηκαν στο λογισμικό Aspen Plus. Τα αποτελέσματα της προσομοίωσης χρησιμοποιήθηκαν για την εκτίμηση της ενεργειακής και εξεργειακής απόδοσης, όπως και την καταστροφή της εξέργειας σε διαφορετικά στάδια και υποσυστήματα του σταθμού. Όσον αφορά τη διεργασία αεριοποίησης, υψηλότερη τιμή του λόγου του παρεχόμενου ατμού προς την εισερχόμενη βιομάζα (*STBR*), για αεριοποίηση με μείγμα O_2/H_2O, μειώνει την απόδοση της αεριοποίησης και αυξάνει τον απαιτούμενο λόγο αέρα καύσης για την αυτοθερμική διεργασία. Αν και η χαμηλότερη τιμή του λόγου *STBR* είναι προτιμότερη από την άποψη της απόδοσης της διεργασίας, πρέπει να γίνει συμβιβασμός για να εξασφαλιστεί η απαιτούμενη περίσσεια ατμού για τις διεργασίες κατάντη, δηλαδή την καταλυτική διεργασία αναμόρφωσης πισσών και τη διεργασία της αντίδρασης μετατόπισης WGS (σενάρια BIGCC-CCS). Οι υπολογιζόμενες αποδόσεις χωρίς εφαρμογή CCS υπερέβησαν το 46%, με το κύριο ποσοστό της συνολικής ηλεκτρικής ιδιοκατανάλωσης στο σύστημα να καταναλώνεται από τη μονάδα διαχωρισμού αέρα. Αντίθετα, όταν η διεργασία AGR με K_2CO_3 είναι εγκατεστημένη ανάντη του αεριοστροβίλου (δέσμευση CO_2 ίση με 90%), το μερίδιο της ηλεκτρικής κατανάλωσης των συμπιεστών N_2 για αραίωση του αερίου σύνθεσης και το μερίδιο των συμπιεστών CO_2 για αποθήκευση είναι συγκρίσιμα με αυτό της μονάδας διαχωρισμού αέρα. Η θερμοδυναμική αξιολόγηση κατέληξε στο συμπέρασμα ότι, ανάλογα με το επίπεδο δέσμευσης CO_2 (50 έως 90%), η τεχνολογία χημικής απορρόφησης προ-καύσης μέσω θερμών υδατικών διαλυμάτων K_2CO_3 επιφέρει μείωση στην ενεργειακή απόδοση της τάξης των 6.5-11.5 ποσοστιαίων μονάδων. Επιπλέον, η μείωση στην εξεργειακή απόδοση είναι παρόμοια και ελαφρά χαμηλότερη από αυτή της διεργασίας με φυσική απορρόφηση μέσω της τεχνολογίας Selexol και σημαντικά χαμηλότερη σε σύγκριση με χημική απορρόφηση με MEA. Παρατηρήθηκε επιπλέον σημαντική μείωση στην ολική καταστροφή της εξέργειας στα σενάρια συμπαραγωγής MeOH και ηλεκτρικής ενέργειας της τάξεως των 9 ποσοστιαίων μονάδων σε σύγκριση με το σενάριο αναφοράς για ηλεκτροπαραγωγή με CCS. Το μεγαλύτερο μέρος της εξεργειακής καταστροφής λαμβάνει χώρα στον αεριοστρόβιλο και στον αεριοποιητή. Για την περίπτωση αποκλειστικής ηλεκτροπαραγωγής με CCS, διαπιστώθηκε ότι η μονάδα CCS (συμπεριλαμβανομένων των συμπιεστών CO_2) είναι υπεύθυνη για το 5-10%

της συνολικής εξεργειακής καταστροφής ανάλογα με το ποσοστό δέσμευσης, ενώ για την περίπτωση της συμπαραγωγής ηλεκτρισμού και MeOH το ποσοστό αντιστοιχεί σε περίπου 8%.

8.2 Καινοτόμα στοιχεία διατριβής

Οι πτυχές της διατριβής που συμβάλλουν στη γνώση συνοψίζονται παρακάτω.

- Πειραματικές δοκιμές αεριοποίησης σε μονάδες μεσαίας κλίμακας με ξυλώδη βιομάζα: σε αεριοποιητή αναβράζουσας ρευστοποιημένης κλίνης BFB ισχύος 3 MW_{th} και σε αεριοποιητή τύπου EFG ισχύος 1 MW_{th}.
- Διερεύνηση της επίδρασης του σχηματισμού C_2 υδρογονανθράκων και της διόρθωσης της αντίδρασης μετατόπισης WGS (και του συνδυασμού τους) στην ικανότητα πρόβλεψης της σύστασης αερίου σύνθεσης από βιομάζα με ένα απλοποιημένο μοντέλο αεριοποίησης.
- Πειραματικά δεδομένα για τη διαλυτότητα του CO_2 σε ενισχυμένα διαλύματα K_2CO_3 (4 πρόσθετα) σε συνθήκες σχετικές με τη δέσμευση CO_2 προ της καύσης σε υψηλές θερμοκρασίες (μερική πίεση CO_2 μέχρι 100 kPa και θερμοκρασίες έως 120 °C).
- Πειραματική μελέτη της απόδοσης ενεργού άνθρακα σε σχέση με την προσρόφηση οργανικών θειούχων ενώσεων και H_2S από αέριο σύνθεσης υπό θερμές συνθήκες καθαρισμού. Εκτός από τις κοινές παραμέτρους διερεύνησης των μελετών προσρόφησης (π.χ. θερμοκρασία, μερική πίεση), μελετήθηκε η επίδραση του H_2O και των ελαφριών πισσών στην απόδοση καθαρισμού.
- Παρουσιάστηκε μελέτη για τη συνδυασμένη δέσμευση μειγμάτων CO_2/ελαφρών πισσών από υδατικά διαλύματα K_2CO_3. Αυτή είναι μια νέα πιθανή κατεύθυνση για τις μελέτες επιλογής διαλυτών (όταν διεργασίες απομάκρυνσης όξινων αερίων προ-καύσης λαμβάνονται υπόψη).
- Μοντελοποίηση της διεργασίας AGR βασισμένη σε θερμοδυναμικό μοντέλο electrolyte-NRTL με τροποποιημένες παραμέτρους αλληλεπίδρασης για διαλύματα K_2CO_3 με και χωρίς προσθήκη PZ. Μελέτη της διεργασίας συνολικά, η οποία δεν περιορίστηκε στην απόδοση καθαρισμού της στήλης απορρόφησης.
- Ανάπτυξη μοντέλων σταθμών αεριοποίησης βιομάζας, οι οποίοι φέρουν σύστημα θερμού καθαρισμού αερίου και διεργασία AGR με υδατικά διαλύματα K_2CO_3.
- Αξιολόγηση της ενεργειακής/εξεργειακής απόδοσης σταθμών BIGCC με CCS (διαλύματα K_2CO_3) για ηλεκτροπαραγωγή και συμπαραγωγή ηλεκτρισμού και MeOH.